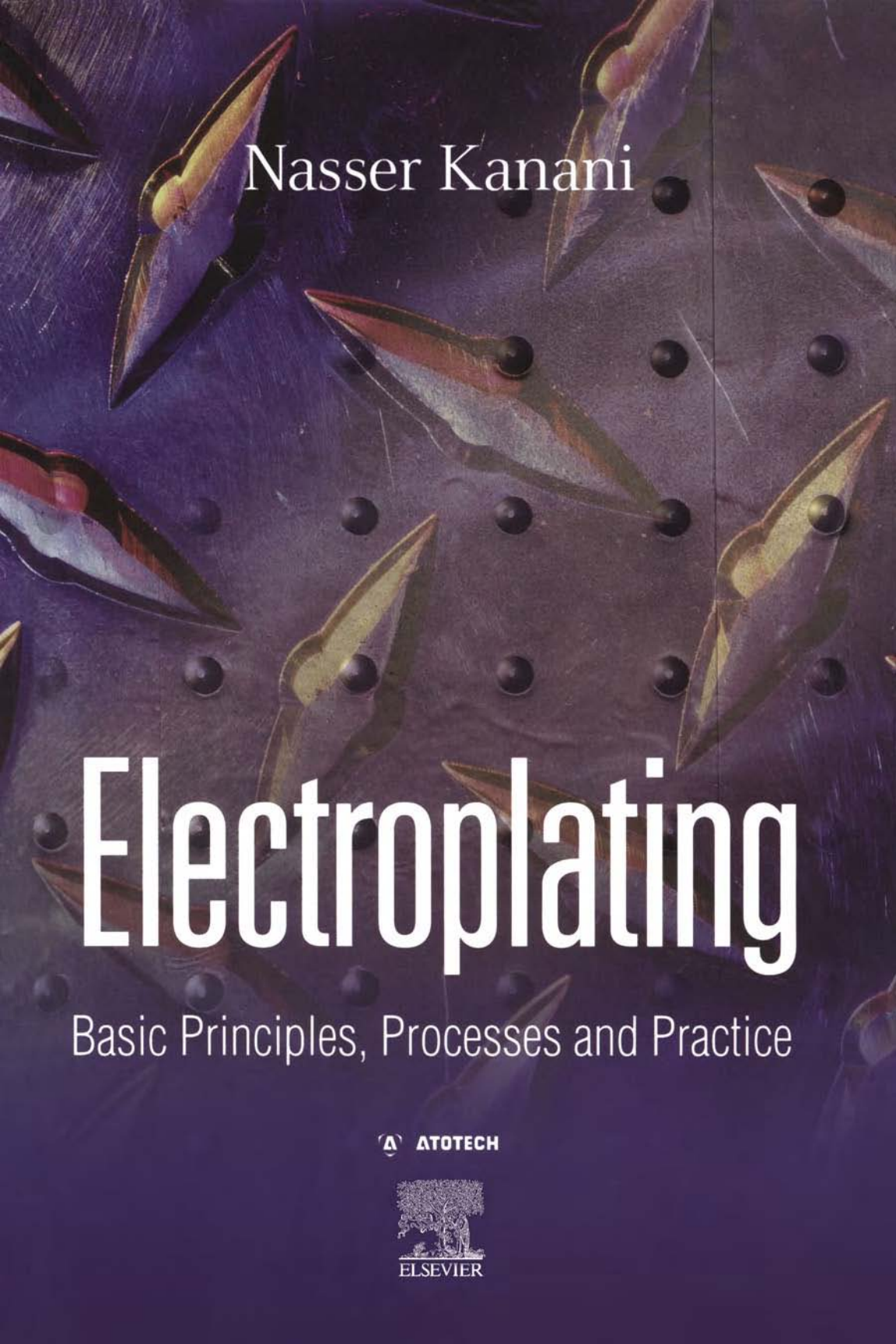
Nasser Kanani
Electroplating
Basic Principles, Processes and Practice
ATOTECH
ELSEVIER

Electroplating – Basic Principles, Processes and Practice

This Page Intentionally Left Blank

Electroplating – Basic Principles, Processes and Practice

Nasser Kanani
Atotech Deutschland GmbH,
Berlin, Germany

ELSEVIER

Elsevier
The Boulevard, Langford Lane, Kidlington, Oxford OX5 1GB, UK
Radarweg 29, PO Box 211, 1000 AE Amsterdam, The Netherlands

First edition 2004
Reprinted 2005, 2006

British Library Cataloguing in Publication Data
Kanani, Nasser
Electroplating: basic principles, processes and practice
1. Electroplating
I. Title
671.7'32

ISBN 1856174514

For information on all Elsevier publications
visit our website at books.elsevier.com

Printed and bound in Great Britain by MPG Books Ltd, Bodmin, Cornwall

Table of Contents

This Page Intentionally Left Blank

Preface

This book offers an introduction to the fundamentals of the processes used, and their practical implementation in modern electroplating. It aims to bring together in a logical sequence, elements of both scientific and the practical aspects of the subject in a manner that will be of use to both scientists in the discipline and also those involved in more practical aspects of the subject. Every effort has been made to include the latest developments, both practical and conceptual. The contents of the book and its purpose are broadly described below.

First: What is the main role of electroplating? How does the technology respond to the ever-more demanding requirements made of it? What are the implications against a background of ever-scarcer raw materials and pressures to minimise use of energy?

Chapter 1 addresses these issues and explores the technical aspects of electroplating, its uses in a modern industrial society and the economic and ecological goals it has achieved.

Second: Which materials can be coated using electrochemical methods? How should components made of such materials be designed and manufactured in order that, after coating, they can fulfil the decorative or functional requirements made of them?

Chapter 2 seeks to address these issues. The structure of metals, alloys and plastics and their properties, are examined. The concepts of 'Design for Plating' and 'Construction for Plating' are explained.

Third: What electrolytes are available for the coating of suitably designed and manufactured components and what are their specific features? How can the various demands be matched to one another? Under what conditions is optimal performance achieved? What is the function of electrolyte additives?

Chapter 3 uses practical examples to explain these questions; some actual electrolytes are illustrated with examples of their application, showing how their performance can be optimised.

Fourth: Which deposition processes can be used to coat components made of mixed materials? How can one coat components of widely differing size and geometry?

Chapter 4 not only describes the most well-established processes but also presents the most recent developments in the field. Some of these allow the deposition of coatings with entirely new properties.

Fifth: What are the mechanisms taking place in the initial stages of deposition? To what extent do they influence the microstructure and thus the properties of the

resulting layers? To what extent can such processes be controlled or modified to bring about a specific desired property?

In Chapter 5, the processes of nucleation and growth at the atomic level are described, as well as the various factors such as deposition conditions, which can affect such processes and thus the properties of deposited layers formed.

Sixth: To what extent can one monitor or observe the nucleation and growth processes in-situ, and thereby influence them?

Chapter 6 describes techniques, some relatively recent, which allow observations of the electrodeposition process and the effect of additives to be made *in situ*.

Seventh: What are the mechanisms which control adhesion between substrate and coating? How can we measure the adhesion of coatings to a substrate and how can we optimise this?

Chapter 7 considers the significance of adhesion in terms of the functionality of the coated component and describes the various methods for qualitative or quantitative measurement of adhesion.

Eighth: How significant is the question of coating thickness and distribution of coating thickness across the surface of a component? What are the main techniques for measurement of coating thickness used in metal finishing? Is it possible to measure the growth of coating thickness during the actual deposition process?

Chapter 8 discusses not only the traditional techniques for thickness measurement but also the more recent developments in this field. With some of these, it is possible to follow the growth in thickness on a printed circuit board during the actual manufacturing process.

Ninth: What is the relationship between the chemical composition of the coating and its properties? What are the implications of surface composition for the functionality of the coating? What methods are available to determine the chemical composition of a coating especially in the near-surface region?

Chapter 9 describes the most important analytical methods with their advantages and drawbacks and their significance and predictive powers in the context of metal finishing processes.

All of these chapters, although thematically linked with one another and set out in a logical sequence, have been at written in such a way that they can also, where appropriate, be consulted on a stand-alone basis. The reader is thus at liberty to read systematically through the entire book or to consult chapters of specific interest. Schematic diagrams and illustrations are have been used within the individual chapters to make easier, the understanding of the sometimes complex inter-relationships.

This book would undoubtedly never have been written without any encouragement of Mrs S. Spinoza, the former Editor-in-chief of the journal *Metalloberfläche* and Professor Jantsch, the publisher of this journal, both of whom continuously encouraged the author to write this book. He is most deeply grateful to them both.

The numerous illustrations and diagrams used in the book were prepared with the greatest care by Mrs Huesmann (Atotech Marketing Service) to whom the author is much indebted. Thanks are also due to colleagues at Atotech Materials Science who carried out many of the laboratory investigations and analyses referred to. They include Mrs Küssmann, Mrs Larondelle, Mrs Liske, Mr Nitsche and Mr Posthumus.

The author is also most grateful to Senior Management at Messrs Atotech Deutschland GmbH for permission to quote internal research reports in the writing of this book and for general facilities and support and encouragement provided..

Finally, the author is more than happy to acknowledge the contributions of his many colleagues listed below (all of them working at Atotech Deutschland GmbH) who took the trouble to read through and offer comments on the various chapters of the book. These were: Dr Pietsch (Chapters 1, 2, 4, 5, 7, 8 and 9), Dr Richtering (Chapter 3) and Dr Vogel (Chapter 6). Their valuable and constructive suggestions, most of which have been incorporated, are most gratefully acknowledged here.

Berlin, October 2004 N. Kanani

This Page Intentionally Left Blank

CHAPTER 1

Metal Finishing – A Key Technology?

1.1 Introduction

Metallic and non-metallic materials which require enormous amounts of energy for their production, form one of the pillars on which our technical civilisation is constructed. Their evolution has profoundly influenced the shape of the world in which we live. A huge range of objects, be they tools, components, sub-assemblies, machines or entire plants are constructed from a range of materials, often in painstaking manner. These materials will, in most cases, have a limited lifetime, which depends strongly on the action of external factors and the operating environment. There are usually mechanical interactions between components in contact with one another. Sometimes there will be chemical or electrochemical reaction with the environment which, by attacking the surface, will sooner or later damage functionality. In the worst case, this can lead to a catastrophic breakdown, hazardous both for humans and the environment. In many cases, materials are constantly being pushed further and further towards the limits of their properties. Whether to save weight or the cost of materials, there is unremitting pressure for components to be dimensioned to the very minimum. One might almost say that, in the absence of any compensating measures, this is a process which is destined to end in failure of the component or assembly in question.

The surface of a material or component might be deemed, because of its atomic structure, to be the most vulnerable site for various forms of attack. This could be mechanical, chemical, electrochemical or thermal, in nature. The effects may be present individually or in combination. They may arise as a tension, or as an impact or perhaps intermittently. Table 1.1 offers an attempt to classify such possible processes, any or all of which can lead to damaging changes at the surface [1].

As raw materials become scarcer, it is necessary to use them as efficiently as possible. At the same time it is a reasonable prediction that future constraints on energy use, will apply further pressure to use materials in the most cost-effective possible way.

1.2 Coating Technologies

The recognition that one might protect a surface from environmental attack, by application of an organic, inorganic or metallic coating, so extending the life of not just the surface, but the entire component or equipment, was one of the major advances in the history of technology. The implications, in allowing the use of less

Table 1.1 Surface change as a result of external influences.

Surface in contact with:	Resulting surface change due to:
Atmospheric air	Soiling, weathering
Hot gases	Oxidation, scaling
Flowing liquids	Cavitation, erosion
Micro-organisms	Microbiological damage
Chemicals	Chemical or electrochemical corrosion
Mechanical contact	Tribological damage, wear

material or a less expensive material, coupled with the associated energy savings, have the profoundest economic consequences and underline the huge economic significance of surface engineering. The coating processes shown in Table 1.2 serve to illustrate the diversity of available and economically important processes which are commercially available and can be used to protect surface functionality and so extend the life of the component or equipment in question. The processes shown are intended to be representative and it is not suggested this listing is in any way comprehensive [2, 3].

Whatever coating technique is used, it is almost invariably necessary to use the appropriate pretreatment and cleaning of the surface to maximise the performance of the coating. The processes shown in Table 1.2 will be briefly described below with comments highlighting major differences between them.

1.2.1 Vacuum Evaporation

With chemical vapour deposition (CVD) processes, very hard coatings can be formed under the action of pressure and heat by deposition of substances from gaseous species (sometimes known as 'precursors') containing the metal to be deposited, often using additional reactive gases. By contrast, deposition of protective coatings using physical vapour deposition (PVD) involves the metal itself in the gas phase, formed by evaporation of the solid. In the case of cathodic vacuum evaporation in a sputter coater, noble gas ions are generated and are fired at the metal cathode, causing metal ions to evaporate and strike the surface of the substrate with sufficient energy to ensure an adherent coating.

1.2.2 Weld-Surfacing; Molten Metal Coating Processes

In this class of process, sometimes known as hard-facing, not only the coating material itself but also a thin zone at the substrate surface are brought together in the

Table 1.2 Coating processes used to protect functional surfaces.

Process	Process variants
Evaporation	Chemical vapour deposition (CVD) Physical vapour deposition (PVD) Sputtering
Hot metal processes	Weld-surfacing Hot-dip galvanising Roll-coating
Painting	Application of inorganic coatings Application of organic coatings Application of low-friction coatings
Thermal spraying	Atmospheric-pressure plasma spraying Low-pressure plasma spraying Flame spraying
Metallising	Electroless metal coatings Electroplated metal coatings

molten state, using a technique closely related to welding. As a result of diffusion, a pore-free and strongly adhering surface coating is formed. In another, commercially very important process known as hot-dip galvanising, the metallic substrate to be coated is immersed in a bath of the molten metal coating metal or alloy. This results in the formation of an alloy (strictly speaking, an intermetallic) layer at the interface between substrate and the molten metal, which, after withdrawing the component from the metallic melt, gives a metallic coating layer on solidification. A quite different technology is roll-coating or metal cladding. Here, the cladding is applied to the metallic substrate that has been previously coated with electrodeposited nickel or with a nickel fine-gauge sheet as interlayer, held in place and used as an adhesion promoter. When the melting points of the two metals are widely separated, the cladding process is carried out by the application of pressure.

1.2.3 Organic Coating, Painting

Liquid inorganic paints, used to coat functional surfaces contain chromium and phosphorus compounds with aluminium powder as a pigment. They are applied using spray guns to the surface of the material and after standing and drying, are fired at 350°C. Organic paints are applied to the component surface in a similar manner and are cured again after air drying. This can take place at temperatures up to 200°C. In addition, there are special paints which can survive exposure for extended times at up to 500°C. Special low-friction paints can be applied to a surface with spray guns and serve as solid lubricants. As before, after drying, the paint film is cured. Depending on the lubricating surface and binder, such paints can be used at temperatures between 260 and 800°C.

1.2.4 Thermal Spraying

In atmospheric plasma spraying, the coating material in powdered form is applied to the surface using a carrier gas in a plasma flame, with considerable mechanical force. In the low-pressure plasma spray process, the difference is that the coating process takes place in a vacuum chamber. In flame spraying, the material to be applied is in wire or powder form and is sprayed using an acetylene oxygen flame in a molten state onto the surface. Typical coating thicknesses in these types of processes are range from 0.1 μm to several centimetres.

1.2.5 Metallising

In addition to the coating processes detailed above, the metallising of surfaces has special importance. Here a metallic protective layer is applied to a surface as a coating for the component. Usually, this is carried out in aqueous medium. The metallic salt of the metal to be deposited, dissolved in solution, ionises and the metal cation is then discharged to form the metal itself, using an external voltage source. In other cases, a reduction medium is present in the electrolyte. These processes are described as electrochemical or electroless surface metallising, respectively (see Chapter 4). The latter process is widely used for metallising non-conducting materials such as

plastics. The electrochemical method, also known as electroplating, is used for deposition onto metallic or other electrically conducting substrates, or to build up greater thicknesses on layers previously formed by electroless deposition.

The range of materials which, after the appropriate pretreatment and cleaning, can be coated in this way is extensive. In addition to plastics, it includes low-carbon and high-alloy steels, aluminium, magnesium and nickel alloys as well as cobalt and titanium based materials. In special cases, ceramic materials can also be metallised in this way.

1.3 Electroplating Processes

The electroplating of components both large and small, the latter sometimes known as mass plating is carried out using special equipment. Depending on the size and geometry of the components to be plated and the plating processes to be used, a distinction is made between rack plating, mass plating, continuous plating and in-line plating [4–8].

1.3.1 Rack Plating

Finished components or semi-manufactures, which, because of their size, shape or special features of construction, cannot be mass finished, are attached to racks, that is, fixtures suitable for immersion in the plating solution. Thus mounted, these are subjected to a suitable pretreatment and cleaning sequence, then plated and in some cases, subjected to a post-treatment. The process is sometimes known as batch-plating. The attaching of components to the rack is usually done manually, often by means of copper wire. After this the racks are transferred, often by hand, to the first of the process tanks. After immersion for the prescribed time, the rack is withdrawn and moved on to the next bath, and so on until the sequence is completed. Finally, the plated components are thoroughly rinsed and dried and taken to the loading bay.

Manual rack plating of this type (so-called manual plant) is by definition labour-intensive and thus relatively expensive. However, it comes into its own when dealing with bent or tubular components. In such cases, the components mounted on the racks must be immersed in solution and agitated in such a way that electrolyte residues are completely drained [6]. A degree of automation is found in the so-called semi-automatic plating plant. In this, the racks after they have been manually passed from tank to tank, in which they are mechanically agitated, are then automatically returned, after unloading, to the beginning of the cycle. In most cases, the racks are raised and lowered into the sequence of tanks using an overhead conveyor which is manually controlled. The main advantage of this approach is the reduction in the amount of manual labour involved [6].

A much-favoured system is the so-called fully automatic one in which the racks carrying the work are automatically transferred through the sequence of plating, post-treatment and rinsing tanks. The entire process is controlled either by a computer or a programmable logic controller (PLC) and not only the plating process itself, but the loading and unloading of the parts before and after plating are also

controlled by the computer. In its most advanced form, bath analysis, dosing with additives, monitoring and control of bath temperatures and duration of bath immersion time are all automated.

1.3.2 Mass Plating

Among the various types of components which are plated, are small items such as screws or nuts. Rack-plating is not a feasible proposition in cases where throughputs may be millions of items per day. They are therefore processed by one or other methods known collectively as 'mass finishing'. Depending on their geometry, dimensions and shape, the plating of such items require special equipment. The most widely used system uses the so-called plating barrel. Also found are plating bells and vibratory plating units. Mass plating, though it offers many advantages, it is not suitable for delicate parts where there is a danger of deformation, scratching, or entanglement. Correct operation can minimise such dangers, and avoiding over-loading, under-loading, use of correct rotation speeds and adding 'ballast' to the work-load are among the means of ensuring optimum results.

1.3.2.1 Barrel plating

Plating barrels, which have proved their worth in treatment of large quantities of small items by the mass finishing approach, are perforated barrels which are either cylindrical or polygonal in shape. Typically they rotate around either a horizontal or an inclined axis. For optimum performance, they are loaded with a single type of component, of a shape allowing the load to tumble readily during rotation of the barrel rather than rotating *en masse* as the barrel turns.

The barrel is usually loaded with small components which have been previously treated either mechanically or chemically in some previous operation. After loading, the barrel is sequentially transferred from pre-treatment tanks, through the various processing solutions and then on to post-treatment, after which it is withdrawn from solution. The entire sequence may be carried out semi-automatically with electric hoists, or it may be completely automated using a flight bars mounted on rails in much the same way as in various types of rack plating plant. The emptying of barrels and a drying of their plated contents can likewise be automated. The barrel rotation is powered in most cases by an electric motor which may have its own power supply or (less satisfactorily) it may draw power from the plating busbars. Barrels up to 2 m long and up to 1 m in diameter are used on larger plants. At the other extreme, they may be smaller than 5 cm in height and diameter.

1.3.2.2 Bell plating

Plating bells are polygonal, bell-shaped containers which rotate around a vertical or near-vertical axis. They are perforated around their periphery and their floor and are specially suitable for the plating of smaller quantities of work. In consequence, they require smaller volumes of electrolyte. After loading with the work, the units are immersed in the electrolyte tanks and, after the prescribed length of time, withdrawn when plating is complete. In contrast to plating barrels, a useful feature of

plating bells is that they allow random samples of the work to be withdrawn during operation without interrupting the plating process, for process monitoring and quality control.

1.3.3 Continuous Plating

The plating of metal strip, wire and tube is carried out in so-called continuous plating plants. In these, the items to be plated move continuously past either one row or between two rows of anodes at a substantial rate [5, 7]. It follows that operating conditions in such plants may be completely different from those found in the analogous batch plating operations. Provided the geometry of the work being plated is simple and uniform, the process can deliver excellent results. Given the high deposition rate found in such plants, the necessary dwell time is a function of line speed and the length of the plating tank. For various reasons, it is sometimes necessary to configure such plants as a series of plating tanks through which the work passes, one after the other. Because of the high current densities used, electrolytes used in such continuous processes are characterised by their very high metal ion concentration and very high electrolytic conductivity. Since no great amount of throwing power is required, such electrolytes often contain no additives. Being very highly automated, such plants often require a minimum of supervision and maintenance.

A major advantage of continuous plating lines arises in the case of plated metal strip. In this case, coatings on either side of the metal strip need not be of the same thickness, resulting in great savings in the use of the raw materials and energy.

1.3.4 In-line Plating Processes

A development in recent years has been the integration of the plating and finishing processes into the main production line. This can bring many benefits including a significant reduction in use of eco-unfriendly materials [8]. In-line plating also allows some pretreatment stages to be omitted, thanks to closer control of the plating and production lines and this again can reduce the consumption of chemicals. The main benefits from using this approach, both economic and environmental can be summarised as follows:

- Savings in chemicals used
- Reduced effluent discharge
- Complete recycling of chemicals used in the process solutions
- Reduced energy consumption

Figure 1.1 indicates possible investment savings resulting from in-line plating (shown shaded grey) brackets shown in grey [8].

From this sketch, it can be seen that using this approach, the investment costs for storage and transport of materials are significantly reduced [8]. In addition, the cost-intensive processes which may be required to protect a surface being transferred from one location to another can then be eliminated.

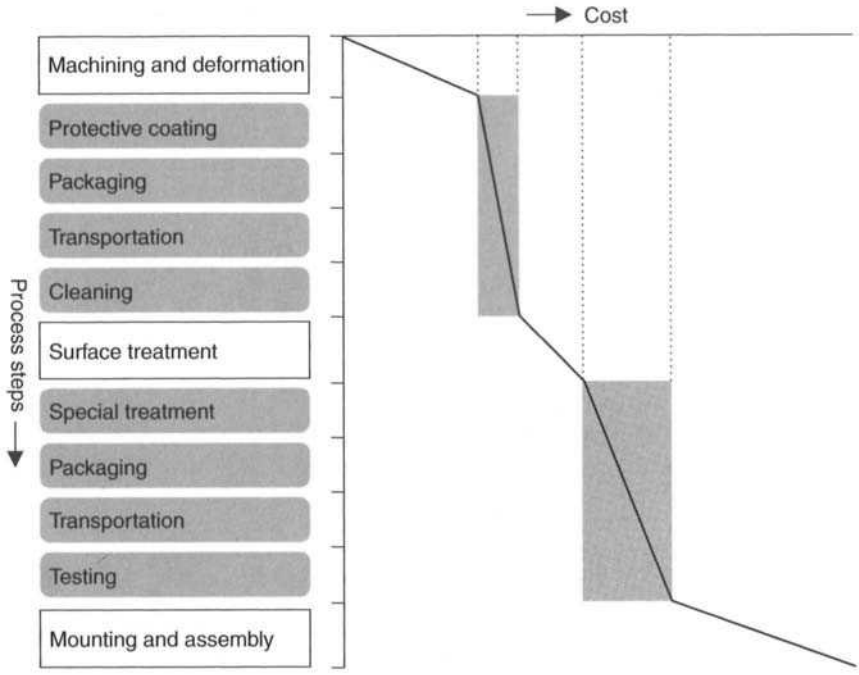

Figure 1.1 Cost reductions achieved with in-line plating.

1.4 Electroplating and its Key Role

The leading German metal finishing agency, Gütegemeinschaft Galvanotechnik e.V. defines metal finishing and its role as follows [9]:

'Metal Finishing' is a term embracing the surface treatment and finishing of metals and non-metals, in which a metallic coating is formed from an aqueous solution or a molten salt by means of an electrochemical reaction. The properties of such coatings are determined by the deposition process as well as pretreatment and post-treatments.

Metal finishing can be said to have transformed itself within a few decades from what was mainly an empirical craft, into a key technology, grounded on scientific principles. Coating methods have been systematically developed in terms of the composition and properties of the layer(s) required. Specific process parameters such as the deposition rate, deposition efficiency and throwing power of each electrolyte have been specially developed to meet the required specifications. In this way, one can now deposit either pure metal or alloy coatings of virtually any composition. The properties of such metallic coatings are often different from those of the corresponding massive metal or alloy. The reason for this lies in the microscopic or sub-microscopic structure of such metal layers (see Chapter 2). Thus, the Vickers microhardness value is one of the simplest ways of demonstrating such differences. From the data in Table 1.3 it will be clear that electrodeposited metal coatings are uniformly harder than their counterparts prepared by metallurgical methods.

Table 1.3 Vickers microhardness (HV) for selected metals.

Metal	Manufacturing process	
	Metallurgical	Electrodeposition
Cadmium	30	50
Chromium	350	1000
Cobalt	200	500
Copper	50	150
Nickel	150	500
Zinc	30	130
Tin	10	10

Table 1.4 Protective layers and coatings formed by metal finishing.

Type of coating	Example
Metallic	Chromium, hard chromium precious metals (gold, platinum, palladium, rhodium, silver) copper, nickel, zinc, tin
Multi-layered	Copper + nickel: copper + nickel + chromium
Alloy coatings	Gold–copper–cadmium; copper–nickel–chromium; nickel–cadmium; nickel–cobalt; nickel–phosphorus; zinc–cobalt, zinc–iron; zinc–nickel; tin–lead; tin–cobalt
Composite coatings	Chromium + alumina; cobalt +chromium carbide; cobalt +chromium oxide; (nickel–phosphorus) + SiC; (nickel–phosphorus) + PTFE
Conversion coatings	Blacking, chromating, phosphating
Anodised coatings	Anodised aluminium, anodised magnesium; anodised titanium
Electroforming	Iron, copper, nickel, nickel–cobalt

Metal finishing as defined above, also includes the formation of conversion coatings. Composite coatings with a metal matrix and non-metallic inclusions (also known as dispersion coatings) are finding growing application, while selective deposition is useful, for example, to repair defective or worn coatings, thus allowing recycling of components. Parts with complex shapes and surface topography can be manufactured by electroforming. Table 1.4 shows but a few of countless such examples.

1.4.1 Metallic Coatings

In the following, some of the examples shown in Table 1.4 and their typical applications are examined.

1.4.1.1 Chromium coatings

Electroplated chromium coatings are notable for their high resistance to tarnish, their high hardness and wear resistance as well as their low coefficient of friction

resistance to cold welding. With a thickness of 0.2–0.6 μm and a bright silver to matt appearance, they are widely used as decorative finishes. Thanks to this, special design effects can be achieved. While chromium deposits from hexavalent electrolytes are silver with a blueish tinge, those formed from trivalent chromium baths can have an attractive smoky appearance. Black chromium deposits can also be formed, and a thickness from 0.5 to 2.0 μm is often used for optical equipment and cameras. In contrast to decorative chromium, hard chromium deposits are usually much thicker, from 10 to 500 μm. They are typically applied to cylinder bores, valves and piston rods of diesel locomotive engines. As a result, service intervals between overhauls can be increased from around 10.000 km to over a million kilometres [10]. Hard chromium plated components are widely used in the mining and aircraft industries and for hydraulics and metal deformation equipment. They are also used in the finishing of medical and surgical equipment.

1.4.1.2 Precious metal coatings

Even the very thinnest of precious metal coatings can be highly effective. The electrodeposition of these metals is therefore of special importance in electrical engineering, electronics, optics and the aerospace industries as well as in the construction of chemical apparatus. Using special equipment, a selective plating, for example, of electrical contacts or stamped strip, can be applied in such a way as to minimize the use of these valuable metals. In another example, silver-plated waveguides for high-frequency transmission are as efficient as those made from the massive silver but far less expensive. Electrodeposition also allows a coating of gold alloys with virtually unlimited range of carat values in order to meet specific technical requirements [10]. Such gold alloy coatings are invaluable in situations where metal allergy might be a problem. That such coatings also provide superb corrosion protection needs no further emphasis. Palladium coatings are used not only for decorative purposes but also for their low coefficient of friction and higher hardness in electrical contacts and plug connectors.

1.4.1.3 Nickel coatings

Nickel coatings are most widely used for their high corrosion resistance, coupled with an attractive visual appearance. Thus, taps and sanitaryware, automotive components and light fittings are but a few examples of this widely used coating. The metallising of plastics using nickel, gives such components a metallic appearance, a higher reflectivity and low weight – a valuable combination of properties. In electroforming too, nickel coatings are widely used for their higher hardness, wear- and corrosion-resistance.

1.4.1.4 Zinc coatings

In the automotive industry, more than any other, the corrosion protection of functional components is considered to be vital. For this reason, such components are usually zinc-plated. Thereafter, such components are usually conversion coated, then sealed. In the past, chromate conversion coatings were the most widely used. Today, on account of environmental legislation restricting use of Cr(VI), alternative conversion coatings have been, and are being, developed. The corrosion resistance of

conversion coated, zinc-plated components is so effective that the number of such components used in most vehicles, continues to increase. The pleasing colours of chromated finishes have in the past obviated the need for painting. However, as chromates cease to be used, this issue will have to be reconsidered. Thick-film Cr(III) passivates are blue in colour.

1.4.1.5 Multi-layered coating systems

Multi-layered coatings based on copper, nickel, chromium, in that order, applied to either metal or plastic components, provide an attractive visual appearance as well as excellent corrosion- and wear-resistance. As such, they play a significant part in automotive design. In addition, such coatings impart to plastic components many of the surface properties of massive metals, while retaining the benefits of weight-saving available from use of plastics. Other benefits of metallic coatings include enhanced scratch resistance, hardness, stiffness, heat resistance, an electrically conductive surface and an attractive appearance. A further important function for metallised plastics is in the field of electromagnetic screening, where these coatings provide a shielding whether from incoming or emitted electromagnetic radiation (so-called 'electro-smog'). In some cases only partial metallising is needed to achieve the necessary screening.

1.4.1.6 Alloy coatings

It is often the case that the requirements demanded of a metal coating cannot be met by a pure metal. In such cases it may be that an alloy coating will meet such requirements. Thus, alloy coatings of gold–copper–cadmium have shown excellent corrosion resistance. Nickel–cobalt alloys are used in electroforming on account of their very high strength, in the production of cross-wires and telescopic sights. Electroless nickel coatings with 8–15% phosphorus content are used to deposit coatings of uniform thickness over the most geometrically complex shaped items where they provide excellent corrosion and wear resistance, and good solderability and weldability. Tin cobalt coatings are used for their attractive visual appearance, being advocated as alternatives to bright chromium [10]. Coatings of zinc–cobalt, zinc–iron and zinc–nickel are superbly corrosion resistant, far superior to pure zinc. For this reason they are increasingly used in the automotive industry.

1.4.1.7 Composite coatings

Composite coatings with an electrodeposited metal matrix and non-metallic inclusions have excellent wear resistance and permit emergency dry-running of machinery. Nickel coatings with 8–10 vol% of silicon carbide are used to increase the life of internal combustion engine cylinder bores, for example, in portable chain saws. Although such coatings have also been used with aluminium cylinder blocks, they have been largely superseded by alternative coating methods. Composite coatings based on chromium carbide in a cobalt matrix are used as wear-resistant coatings in gas turbines where they are required to perform for extended periods at temperatures of up to 800°C. Chromium deposits with alumina inclusions are used in piston rings for diesel engines. Single crystal diamonds locked into a nickel matrix form the cutting edge in tools such as chainsaws, grinding discs or dental drills [11].

1.4.1.8 Conversion coatings

Conversion coatings are, strictly speaking, those formed by a reaction of the metal on the surface of the substrate (be it the bulk metal or a metallic coating) with a solution such as, for example, chromic acid which reacts with the metal to form an insoluble chromate. These coatings greatly increase the corrosion resistance of the component and are of particular importance for use with coatings of zinc and its alloys. These very thin chromate coatings may be transparent, blue, yellow, olive or black. As such they can also fulfil a decorative function. In addition, they are excellent adhesion promoters for organic coatings. That chromate coatings can be differently coloured, is sometimes utilised to distinguish between types of component. In the case of aluminium and its alloys, solutions consisting of mixed chromic and phosphoric acids are similarly used. Use of hexavalent chromium compounds, because of their potential carcinogenicity, is nowadays heavily restricted. However, similar principles apply to many other types of conversion coating such as phosphates or trivalent chromium compounds.

1.4.1.9 Anodised coatings

Both wear- and corrosion-resistance of components made of aluminium or its alloys can be significantly improved by anodic oxidation of the surface [12]. The resulting anodised layer, typically 5–25 μm thick can be used in this state or otherwise is ideally suited for a subsequent coloring process. There are several technologies for this. Thus particles of dyestuff may be used to impregnate the oxide pores to give an almost limitless range of colors. Alternatively, a metal such as tin or copper can be electrodeposited into the base of the oxide pore to form a range of colours such as gold, bronze, yellow through to dark brown or black. Finally, by close control of oxide layer thickness, interference colours can be created. Colours formed by the last two methods are virtually immune from light-fading [10]. Anodised aluminium (alloy) components are widely found in the construction industry, in aerospace, in the electronics industry and computer construction as well as in optical and medical equipment.

1.4.1.10 Electroforming

Metallic components with the most complex shapes and surface structures can be produced using a special technique known as electroforming [5, 13]. This technique can be used over a wide range of sizes, from tools for the production of micro-precision components, for example, gearwheels for watches, to the very large surface areas used in automotive or aerospace rocket chambers with integral cooling channels, virtually impossible to produce by any other method. The process begins with a mold or mandrel, made of wax, plaster, plastic or metal having the negative shape of the component to be produced. These are then electroplated with a metallic layer so thick that it retains its shape after the mandrel is removed. Electrolytes used for this process must have good throwing power so that the metal is deposited in all recesses and in the corners of the model (see Chapter 3). Only in this way can the model surface be exactly replicated. After sufficient thickness has been laid down, the electroformed component is parted from the mandrel and, where necessary, is further finished. Other applications of electroforming include machine construction, in the

Table 1.5 Hardness, wear-resistance and coefficient of friction of electroplated or electroless coatings.

Coating	Deposition rate (μm/min)	Hardness HV	Wear ($mg \times 10^{-3}$)[1]	Coefficient of friction
Hard chromium	0.6–0.8	800–1100	0.9	0.15–0.18
Nickel[2]	1–10	200–450	4–5	0.4–0.6
Nickel (PTFE)	1–2	300	4–5	0.15–0.3
Nickel (SiC)	2–5	400–500	0.4–0.6	0.5–0.7
Nickel[3]	0.3	400–(700)	(2)–4	0.3–0.4
NiP (PTFE)	0.05–0.8	300–(700)	(0.7)–3	0.1–0.2
NiP (SiC)	<0.3	500–(>1000)	(0.2)–0.4	0.5–0.7
Ni–Co–P (CF_x)	1–2	700–(1200)	2–3	0.1–0.15

Note: Figures in parentheses are data after heat treatment.
[1]Data using Taber Abraser.
[2]Electrodeposited.
[3]Electroless deposition (the hardness values given in parentheses are achieved after heat treatment.).

printing industry (where they are known as electrotypes) and in dentistry for custom forming of dental crowns and inlays.

1.4.2 Areas of Application

From the foregoing, the vital role of metal finishing in a wide range of applications can be appreciated, indeed in some cases, makes such applications feasible. Electroplated coatings must possess, according to their end use, various properties, either functional or decorative or both. Use of the correct coating can increase the life-time and service-interval of components or entire machines many times over. The parameters shown in Table 1.5, which include hardness, wear-resistance and coefficient of friction of either electroplated or electrolessly deposited coatings are proof of this [14].

Table 1.6 collates the most important properties of electrodeposited coatings and gives examples for their practical application in a range of industrial settings [15].

The examples shown in Table 1.6 demonstrate how, by using electrodeposition processes to apply the correct type of coating, it is possible to enhance the properties of a substrate in specific ways. Thus, while the substrate material may provide adequate mechanical properties, a coating can be necessary to provide sufficient corrosion protection, wear-resistance, hardness or tensile strength. This also highlights the difference between coatings with decorative and functional purposes, indeed coatings are often designated along these lines. Thus, functional coatings are applied to improve corrosion- and wear-resistance including dry-running or to improve solderability and weldability. These coatings must also permit subsequent machining or manufacturing operations. In the case of decorative coatings, aesthetics are the primary concern, though adhesion of coating to substrate should not be overlooked. Increasingly, however, it is demanded that functional equipment should also be visually attractive, and to make a sharp division between functional and

Table 1.6 Properties and application examples of electrodeposited coatings.

Coating property	Application purpose	Example
Optical properties		
Colour	Aesthetic appearance	Brass-plated furniture and lighting fittings
Brightness	Decorative appearance/reflectivity	Chromium-plated taps, silver mirrors
Physical Properties		
Electrical conductivity	Current conduction on surface	Copper tracks on printed circuit boards
Thermal conductivity	Improved heat transfer on surface	Copper-plated saucepan bottoms for electric cookers
Magnetic conductivity	High coercivity	Cobalt–nickel alloys on magnetic storage
Chemical properties		
Chemical protection	Resistance to chemical attack	Lead–tin coatings as etched resistance for printed circuit boards
Corrosion protection	Resistance to corrosion attack	Zinc and its alloys on steel components
Mechanical properties		
Ductility	Improved plastic preforming	Copper coatings on drilling punches in multi-layer printed circuit boards
Hardness	Improved adhesive wear-resistance	Nickel or phosphorus coatings for mining equipment
Technological properties		
Friction reduction	Improved dry-running	Lead–tin–copper coatings
Adhesion	Improved adhesion	Brass coatings on steel wires
Solderability	Soldering without aggressive fluxes	Zinc–lead coatings on printed circuit board tracks
Lubricity	Improved mobility	Copper plating for wire drawing
Wear resistance	Improved lifetime	Hard chromium-plated tools
Machinability	Metal machining	Copper coatings on printing cylinders

decorative coatings could in many cases be misguided. The bottom line is to optimise functionality and appearance of component and coating, having regard to economic and environmental factors.

1.5 Requirements for Metal Finishing

It is evident that there is hardly a branch of industry and manufacturing industry where metal finishing does not play an important role. Metal-finished components are found in architecture, in the textile and furniture industries, in machinery construction and in aerospace, as well as in the electrical and electronic industries. Increasingly, coatings are a critical issue in precision engineering and medical technology. Coatings are used in optical instruments, domestic appliances, in sporting or camping equipment and also in fashion accessories where their functional and/or decorative role can be critical. Thus metal finishing, perhaps uniquely, is evident in every aspect of daily life. Hardly anything is manufactured that is not in some way subjected to a finishing process.

1.5.1 Quality and Cost Effectiveness

In order to meet the requirements imposed by designers and production engineers, the following are the main requirements made of electroplated coatings [16, 17]:

- as thin as possible with uniform thickness,
- smooth surface,
- dense and the fine-grained structure,
- good adhesion to the substrate,
- high corrosion resistance,
- freedom from internal stress,
- sufficient ductility,
- high hardness and strength,
- high wear resistance,
- uniform and low coefficient of friction.

These properties should be able to be specified as appropriate, and coatings should be reproducible to such specifications. A given coating can be applied with widely varying properties. Thus, for example, copper coatings used in electrical or electronic applications must have the highest possible electrical conductivity, whereas for copper coatings on printing cylinders, this is not important but hardness is at a premium. In many cases, a combination of specific properties is required, for example, a combination of corrosion- and wear-resistance. At times, two apparently opposed properties are specified such as a high tensile strength and at the same time high ductility. In all cases it is assumed that these metallic coatings will retain their decorative and functional properties for the entire lifetime of the item over which they are applied.

Other requirements imposed by product designers or production engineers on electroplating may include the following:

- choice of coating to have no implications for the substrate used, the assembly means employed or any other final machining or interconnection methods involved;
- the coating process will not affect the substrate properties;
- the dimensional tolerances of the component will not be compromised;
- there should be no problems in repairing the component;
- coating and delivery should be as rapid and cost-effective as possible.

In laying down specifications and requirements, it should be clear to all concerned that coating properties can be influenced by countless factors [18]. These include the type of substrate material, the nature of the surface prior to plating, cleaning and pretreatment of the component surface, the composition of the electrodeposition electrolyte and the conditions under which it operates and finally any mechanical, thermal or chemical post-treatment of the substrate/coating combination

Given the fact that the various interactions take place between substrate and coating at the atomic level, the nature and condition of the substrate surface is critical.

It should be chemically and physically a homogeneous, free from pores or cracks and should exhibit no folds, shrinkage or scaled surfaces. In the case of non-metallic substrates, the surface should be able to be activated.

Equally important is the construction and geometry of the component to be coated. In the industry jargon one speaks of 'fit-for-plating' or 'design-for-plating' [1, 5, 19, 20]. By this term is meant not only a correct choice of substrate material(s) but also the joining and assembly techniques employed. It is simple to construct a product using more than one metal or alloy, and the metal finishing of 'mixed metal' assemblies is possible. Such mixed-metal construction will, however, restrict the range of surface treatment processes one can use. The following key points should be borne in mind by designers and production engineers:

- Design of edges, corners and profiles with subsequent plating in mind.
- Avoiding locations where gas bubbles formed during plating, might be trapped.
- Avoiding geometries where process solution might be trapped.
- Designs allowing coated surfaces to be machined after coating.
- Use of appropriate materials of construction.
- Plating of components prior to a riveting.
- Recognising that subsequent plating of soldered surfaces may increase costs.
- Configuring welds so that seams and adjacent heat affected zones (HAZs) can be readily accessed for cleaning, etc.
- Ensuring that tubes and other hollow sections to be plated on the outside only are free from internal cracks.
- In the case of items to be mass plated, designing such that entanglement or clumping does not become a problem.

Those involved in product design must be helped to recognise that components or assemblies which are unsuitably constructed, will not only be difficult to plate at a uniform thickness but will also exhibit irregularities at the coating surface. Problems may then appear only when the component is exposed to thermal, mechanical or chemical action. The coating may then, for example, lift from the substrate thereby exposing the unprotected surface of the substrate to the environment.

The examples shown in Fig. 1.2 emphasise how important it is to design for plating at the earliest stage of a project. Optimum results will be obtained only when the design and construction of the component are carried out with the subsequent finishing in mind.

1.5.2 Ecology and the Environment

The task of the metal finisher is to provide surface coatings for components, tools, appliances and high-volume small parts which are reasonably priced and fit-for-purpose, that is to say, they are able to provide protection, ensure functionality and extend component life. Over the years, developments in metal finishing have delivered these requirements, on the basis of continuous improvements. Increasingly, however, a further requirement has been added, which is to carry out these operations in an ecologically and environmentally responsible manner. This includes minimising

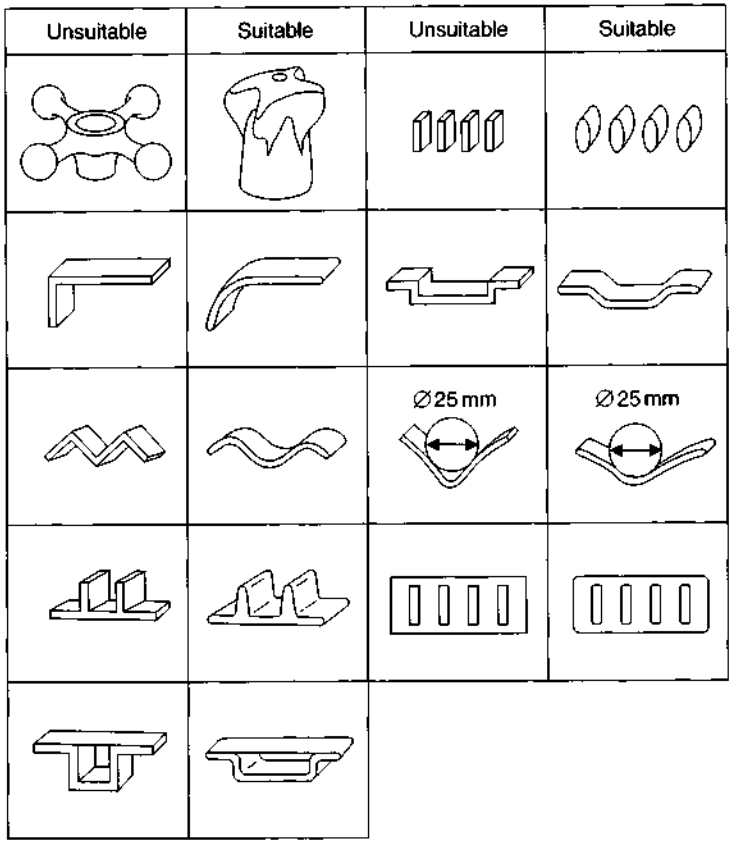

Figure 1.2 Some examples of geometries suitable and unsuitable for plating [19].

use of raw materials and energy, and disposing of waste products or recycling these is a responsible manner. Most metal finishing plans are equipped to carry out such recycling and waste treatment functions. It is true that construction and operation of these calls for substantial capital investment and on-going operating costs. However, it is accepted today that there is no avoiding this responsibility.

Thanks to the development and introduction of low-waste technologies, and the use of more sophisticated rinse techniques, it is now possible to recover waste materials and purify air emissions and effluent with far less effort and energy use than hitherto [4]. Furthermore, there is a continuing drive to use electrodeposition solutions with the lowest possible metal ion content, and as free as possible from complexing agents, while also minimising rinse water volumes used, all in order to minimise the impact of metal finishing on the environment.

A promising avenue of approach for the future appears to be what is known as process-integrated environmental protection. The underlying philosophy here is to minimise waste at the point of use, as opposed to the so-called 'end-of-pipe' approach which is to treat whatever effluent and waste that arises, without enquiring whether it might be reduced [21, 22]. Ideally, minimum waste technology

becomes a closed-loop system. The desire for 'zero-discharge' metal finishing plants has been for some time established, and though it may never be possible to completely eliminate all waste, there are locations where this comes close to being the case. This philosophy is now enshrined in German law, under the slogan www ('Waste avoidance, waste minimisation, waste recycling'). In some cases at least, those who have succeeded in implementing this, have been pleasantly surprised in finding that it can also bring financial, as well as ecological benefits.

References

[1] Czichos, H., Konstruktionselement Oberfläche, *Konstruktion* 37 (1985) H. 6, 219–227.

[2] Haefer, R.A., Oberflächen- und Dünnschicht-Technologie, Teil I und II, Springer-Verlag, Berlin, 1987

[3] Bode, E., *Funktionelle Schichten*, Hoppenstedt Technik Tabellen Verlag, Darmstadt, 1989.

[4] Autorenkollektiv, *Galvanotechnisches Fachwissen*, VEB Deutscher Verlag für Grundstoffindustrie, Leipzig, 1982.

[5] N. N., *Taschenbuch für Galvanotechnik*, Bd. 1 Verfahrenstechnik, 13. Auflage, LPW-Chemie GmbH, Neuß, 1988.

[6] N. N., *Korrosionsschutz von Stahlteilen durch galvanisches Verzinken*, Informationsschrift der Arbeitsgemeinschaft der Deutschen Galvanotechnik (AGG) Düsseldorf.

[7] Kreisel, R., Galvanische Anlagen und Ausrüstungen, in *Technologie der Galvanotechnik*, herausgegeben von B. Gaida und K. Aßmann, Eugen G. Leuze Verlag Saulgau/Württ, 1996.

[8] Mollath, G., Kriterien für fertigungsflußintegrierte Oberflächentechnik, Galvaniktagung Oberflächentechnik – Wirtschaftliche Perspektive, Berlin, Mai 1997.

[9] Gütegemeinschaft Galvanotechnik e.V., *Gütesicherung in der Galvanotechnik*, Eugen G. Leuze Verlag, Saulgau/Württ., 1987, 2/2.

[10] Metzger, W., Galvanisieren bietet heute viele Möglichkeiten, teure Metalle einzusparen, *Sonderdruck aus Maschinenmarkt*, Heft 6 (1982) 2–5.

[11] Metzger, W., Wichtige Verfahren zur galvanischen Veredelung von Oberflächen, *Sonderdruck aus Maschinenmarkt*, Heft 25 (1982) 6–8.

[12] N. N., *Oberflächenschutz und attraktive Optik durch Eloxal*, Informationsschrift der Arbeitsgemeinschaft der Deutschen Galvanotechnik (AGG), Düsseldorf.

[13] N. N., *Galvanoformung*, Informationsschrift der Arbeitsgemeinschaft der Deutschen Galvanotechnik (AGG), Düsseldorf.

[14] Fuchs, R. and Paulet, J.-F., Ökonomisch und ökologisch vertretbare Verschleißschutzschichten auf Aluminium-Formteilen, *Praxis-Forum Tagung Oberflächentechnik High-Tech-Finishing*, TCI Verlag GmbH, Berlin, 1992.

[15] Autorenkollektiv, *Praktische Galvanotechnik*, 4. Auflage, Eugen G. Leuze Verlag, Saulgau/Württ., 1984.

[16] Illgner, K.H., Forderungen des Ingenieurs an die Galvanotechnik, *Galvanotechnik* 71 (1980), Nr. 5, 452–457.
[17] Merz, H., Anforderungen an die Oberflächen-Veredlung, *Oberflächen Werkstoffe* Nr. 1–2 (1995) 8–9.
[18] Dini, J.W., *Electrodeposition*, Noyws Publications, Park Ridge, USA, 1993, 2.
[19] Simon, H. and Thoma, M., Funktionelle Bauteiloberflächen durch angewandte Galvanotechnik, *Konstruktion* 37 (1985) 6, S.235–214.
[20] N. N., *Galvanisiergerechtes Konstruieren*, Informationsschrift der Arbeitsgemeinschaft der Deutschen Galvanotechnik (AGG), Düsseldorf.
[21] Fischwasser, K., Galvanotechnik 2001, *Metalloberfläche* 52 (1998) 6, 446–447.
[22] Fischwasser, K., Blittersdorf, R. and Schwarz, R., Stoffverlustminimierte Prozeßtechnik – Eine Systemlösung in der Galvanotechnik und Metallchemie, *Metalloberfläche* 51 (1997) 5, 338–342.

This Page Intentionally Left Blank

CHAPTER 2

Materials that can be Electroplated

2.1 Introduction

Items destined for electroplating are almost invariably either metallic or non-metallic. Steels (ferrous alloys) and other non-ferrous metals fall into the first category, with plastics and ceramics as examples of the latter.

Whatever the substrate, careful cleaning and, in some cases, pretreatment, are essential precursor steps to forming a satisfactory substrate–coating combination, with the properties required for practical service. These cleaning and pretreatment stages are almost always specific to the substrate-surface treatment process in question. No further details will be given here, since the subject is adequately treated elsewhere.

Setting out from the knowledge that the nature of the surface of the substrate, be it metallic or non-metallic, affects the characteristics of the surface layer, it is necessary to consider the atomic structure of metals and alloys, as well as the molecular structure of plastics. Given that this volume deals predominantly with metallic coatings, the main emphasis in what follows will be on metals and alloys.

2.2 Metals

Of the numerous metals used as substrates, only rarely are those of high purity used. In practice, metallic substrates are overwhelmingly alloys containing two or more components, which may themselves be metallic or non-metallic. The reason, as has been known for thousands of years, is that alloying can create a material with properties superior to those of any pure metal. The atomic structure of pure metals and special features of alloys, are considered below.

Metals are polycrystalline materials, that is, they are built up from a multiplicity of small crystals, these being only very rarely perfectly ordered and free of atomic lattice defects. The hallmark of the perfect crystal is a totally ordered and symmetrical structure, extending over a distance of numerous inter-atomic spacings. This is described as long-range ordering. Figure 2.1 illustrates an example, in this case as the so-called simple cubic crystal lattice. The inter-atomic distance a, which usually lies in the range 0.25–0.5 nm for metals, is known as the lattice constant.

Where the lattice constants along the three axes x, y, z differ from one another, and are designated a, b, c, a structure such as that shown in Fig. 2.2 results. To describe such a structure, we invoke the concept of the so-called *unit cell*, which is the smallest unit embodying all the features of the continuous lattice. This is seen in the bottom left-hand corner of Fig. 2.2 shown in heavier lines. The three lattice constants, a, b, c and the angles α, β, γ, formed between the three axes are marked. In the case of a cubic structured lattice, these three angles are all equal to one another, with value 90°. The crystal planes of an idealised simple cubic crystal is shown in Fig. 2.3.

Truly perfect crystals are never found in practice. Instead, crystalline structures invariably show lattice defects. Such crystals, on account of their defective structure are known as crystallites or grains. According to their deviation from perfection, they are known as zero- uni- or two-dimensional lattice defects, or as point defects, edge defects and planar defects, respectively.

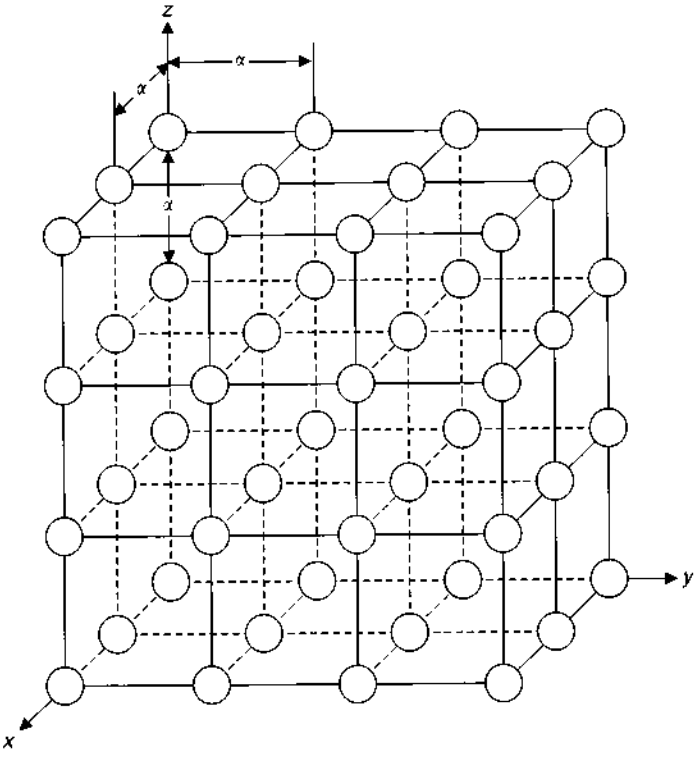

Figure 2.1 Spatial configuration of atoms in an idealised simple cubic structure with lattice constant α.

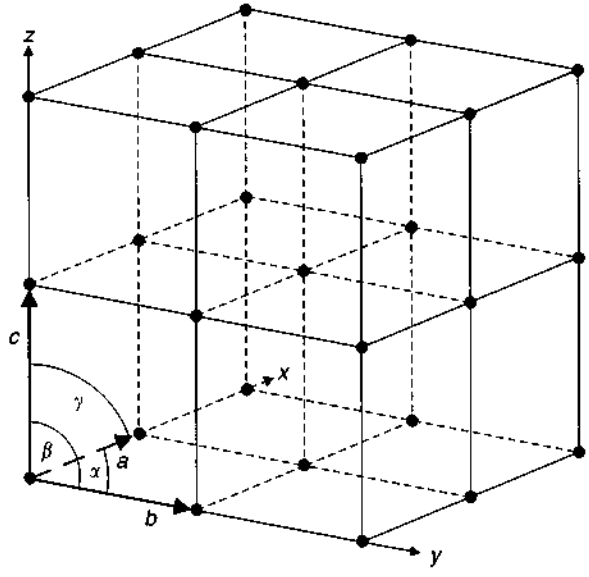

Figure 2.2 Spatial configuration of atoms in an idealised crystal lattice with lattice constants a, b and c.

2.2.1 Zero-Dimensional Lattice Defects

These defects are usually of one of two kinds. Either a site in the lattice is unoccupied (lattice vacancy) or an 'extra' atom is squeezed into the lattice between two lattice sites (interstitial occupancy).

The first of these, the presence of an unoccupied site, is usually the result of an atom migrating from the bulk of the crystal to the surface, leaving a vacancy behind. This can result in lattice distortions or surface defects, as shown in Fig. 2.4.

An expression giving the vacancy concentration, c_L, in an actual crystal is:

$$C_L = Ne^{-(E_L/KT)} \tag{2.1}$$

In this equation, N denotes the number of lattice sites, E_L is the energy required to dislocate a vacancy from the interior of the crystal to its surface, $k = 1.38 \times 10^{-23}$ is the Boltzmann constant, and T the absolute temperature in Kelvin. From this expression, it follows that the vacancy concentration is a function of the energy of vacancy formation and the temperature. Table 2.1 lists some values of energies for vacancy formation and also that required for migration of such vacancies, that is, energy required for a vacancy relocation.

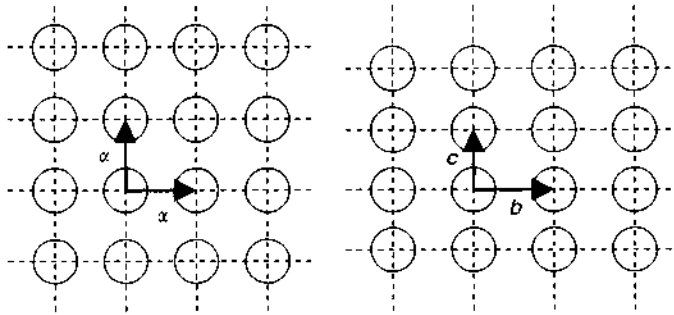

Figure 2.3 (Right): Crystal plane of an idealised simple cubic crystal with lattice constant α. (Left): The same but with three different lattice constants, a (normal to the image plane) and b, c (as shown).

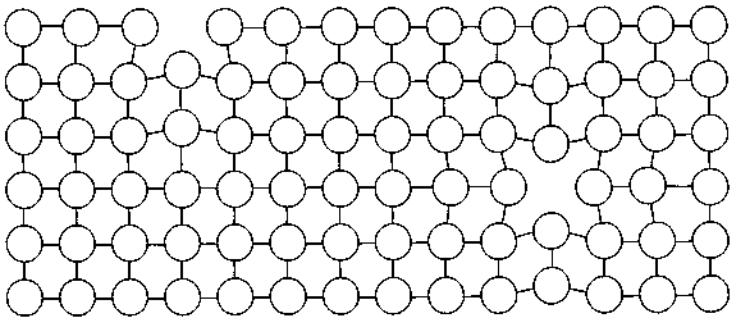

Figure 2.4 Elastic lattice distortions within an actual crystal and sub-microscopic defect sites at the crystal surface, resulting from presence of vacancies.

Table 2.1 Energies of vacancy formation and migration for selected metals [1].

Metal	Formation energy [eV]	Migration energy [eV]
Au	0.96–1.00	0.55–0.80
Ag	1.02–1.10	0.83–0.88
Cu	1.00–1.40	0.70–1.20
Pt	1.20–1.40	1.10–1.50
Al	0.74–0.79	0.50–0.60
Ni		≈1.50

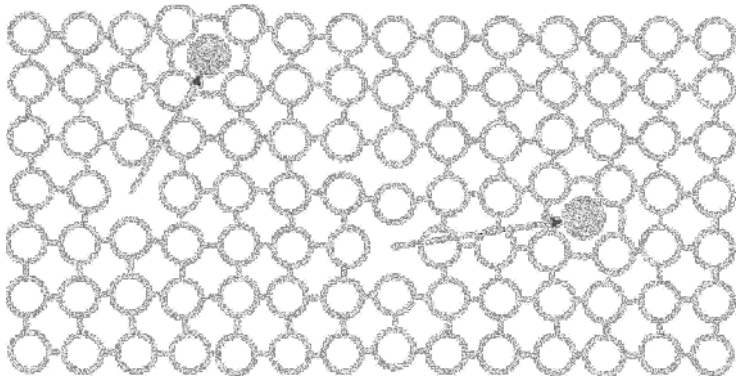

Figure 2.5 Elastic lattice strains in an actual crystal with sub-microscopic unevenness at the crystal surface, caused by the presence of interstitial atoms.

Using Eq. (2.1), it can be calculated that the vacancy concentration in a copper crystallite at 1100 K with a formation energy of 1.1 eV will be 10^{-5}. Otherwise expressed, at this temperature, one in 100,000 lattice sites will be vacant. This implies a distance between adjacent vacancies of only a few interatomic spacings.

As a general rule, one can state that for most metals, the vacancy concentration below the melting point will be around 10^{-4}, that is to say 100 million vacancies per square millimetre of lattice plane. As the temperature decreases, the number of vacancies falls in exponential manner, until at room temperature, it might be 10^{-12}, that is, one vacancy per square millimetre lattice plane.

The degree of mobility of atoms in the interior of a crystal lattice is strongly linked to the number of vacancies and, especially in the case of strongly temperature dependent processes, of which solid-state diffusion in the crystalline state is one example, the existence of vacancies are the main means by which such migration takes place.

Where an atom is found, not at a lattice site but – as shown in Fig. 2.5 – between two lattice sites, it is known as an interstitial atom. These are formed when atoms vacate their lattice positions but remain in the bulk of the lattice. The process is known as the Frenkel mechanism and results in formation of vacant lattice sites and interstitial atoms, in equal numbers. As a consequence, there is no change in the volume of the crystal lattice.

Defining the energy required to move an atom from a lattice site to an interstitial position as E_Z, the number as n and the number of possible interstitial sites as N', one obtains the expression:

$$n \approx \sqrt{(N \cdot N') \cdot e^{-E_z/kT}} \tag{2.2}$$

From this equation, it follows that, thanks to the much higher energy required to create an interstitial atom the concentration of these, even at elevated temperatures, is negligible.

2.2.2 One-Dimensional Lattice Defects

Actual examples of this type of defect, that is linear defects, are demonstrated by so-called dislocations, which are predominantly of two types, namely screw- or step-dislocations. In the strictest sense, these two types are extreme cases. In reality, one usually encounters 'mixed' dislocations, a combination of both types.

Figure 2.6 shows the change from the ideal lattice plane for a simple cubic-structured crystal to the occurrence of a screw-type dislocation.

From this representation, it will be evident that the existence of a screw-type dislocation, shown by the symbol ⊙, gives rise to a circular distortion of the lattice plane. This is depicted more clearly in Fig. 2.7. This also shows the dislocation line (VL), that is, the axis of rotation of the screw dislocation.

The spiral-shaped form of the lattice plane around the screw dislocation results in the fact that, after a complete circuit of the dislocation line, one arrives at the adjacent lattice plane. The distortion line cannot, thus, terminate within the crystal, but must either carry through to the surface or form a closed circle within the

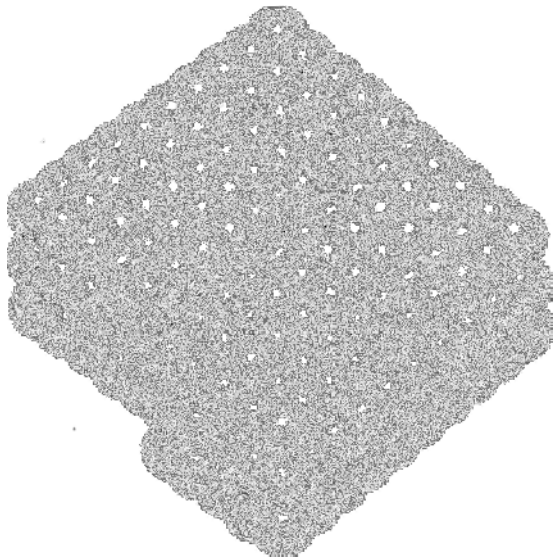

Figure 2.6 Schematic representation of a screw-type dislocation in a simple cubic-structured actual crystal [2].

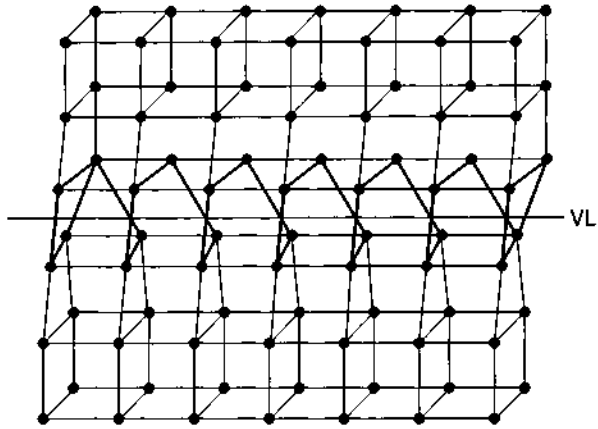

Figure 2.7 Spiral distortion of the lattice plane in an actual crystal caused by a screw dislocation [3].

crystal itself. The presence of a screw dislocation is evident in that it causes elastic lattice distortions in the surrounding regions of the crystal. The lattice distortion energy, E_o caused by a screw dislocation can be expressed, on the basis of theory as

$$E_o \sim \ln(r_1 / r_o) \tag{2.3}$$

Here, the two parameters r_1 and r_o are lengths, which can be defined as follows: r_o is an arbitrary distance from the dislocation line while r_1 is the dimension of the real crystal. According to Eq. (2.3), the distortion energy of a screw-type dislocation decreases as the natural logarithm of the distance from the dislocation. This implies that screw-type dislocations give rise to far-reaching stresses in the surrounding crystal lattice. The mobility of screw-type dislocations within individual crystallites under the influence of external forces is a major explanation for the plastic deformation of metals and alloys. In the case of metal deposition, screw dislocations have special importance in that they allow a continuous growth of the deposit to continue. At the points on the surface of the individual crystallites where these defects emerge, the growth process can proceed without a need for prior formation of nuclei (see Chapter 5).

A step dislocation, designated as ⊥, can be considered as approximating as being equal to 'half' a lattice plane spacing, as shown in Fig. 2.8 which shows the lattice being compressed. The lower edge of the half lattice plane is marked as a dislocation line (VL). It is located in the slip-plane (GL) of the lattice and at right angles to the drawing [5].

The image reproduced in Fig. 2.9 shows a step dislocation in a 10^{-2} μm thick germanium single crystal [6]. The photograph was taken using a 100 kV electron microscope with resolution of 3×10^{-4} μm. The lines represent the lattice planes in the crystal. Their separation is 3.27×10^{-4} μm. The only half-inserted additional lattice plane can be clearly seen.

As with screw-type, so also for step dislocations, the dislocation line must either terminate at the surface or form a closed loop within the bulk of the material.

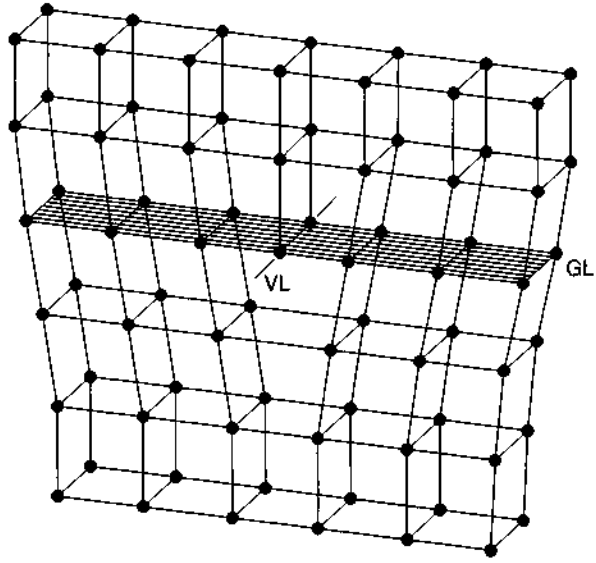

Figure 2.8 Formation of a step dislocation in a simple cubic crystal, resulting from the insertion of a 'half' lattice plane into the lattice [4].

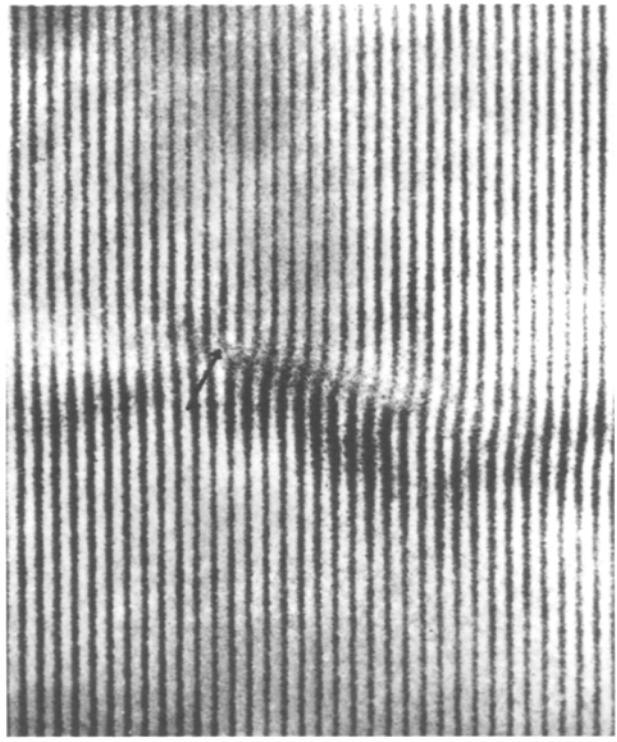

Figure 2.9 Step dislocation in 10^{-2} μm thick germanium single crystal [6].

The sketch shown in Fig. 2.8 shows how insertion of an additional lattice plane gives rise to distortion in the crystal lattice. The lattice atoms in the vicinity of the inserted plane are compressed, whereas those atoms in the underlying regions of the crystal are pulled apart from one another. The interface between these two crystalline regions is known as a slip-plane and is shown schematically in Fig. 2.10.

From this, it follows that under the effect of a shear force, a step dislocation can be shifted to left or right. As a result, the dislocation line moves along the slip-plane in a particular crystallographic slip direction. This movement of the dislocation line is what determines the plastic deformability of a real crystal.

The dislocation energy, $E_\perp$ of a step dislocation is expressed by the equation

$$E_\perp = \tfrac{1}{2}E_\circ \tag{2.4}$$

From this it follows that the dislocation energy of a step-type dislocation is larger than that of a screw-type one. Thus, step-type dislocations are associated with extensive elastic tensile or compressive stress in the lattice of an actual crystal. This is visualized in Fig. 2.11.

The total length of dislocation lines per unit volume is defined as the dislocation density and expressed in units of (mm/mm^3) or ($1/cm^2$). For metals not subjected to deformation, typical values might be 10^6–10^8 mm/mm^3. This corresponds to a total length of around 1 km dislocation lines per mm^3. Cold-working causes a substantial increase in this, to around 10^{12} cm^{-2}, that is, a length of around 10,000 km/mm^3. The resulting severe lattice distortions, specially affect the mechanical properties of the metal.

If one recognises that the crystal structure and the lattice constants of the metallic substrate and the metallic deposit formed on its surface will almost certainly differ, it is obvious there will be no complete match or alignment of the atomic lattices of the two partners at the interface between them. Figure 2.12 describes this situation and shows how the formation of step dislocations can be envisaged.

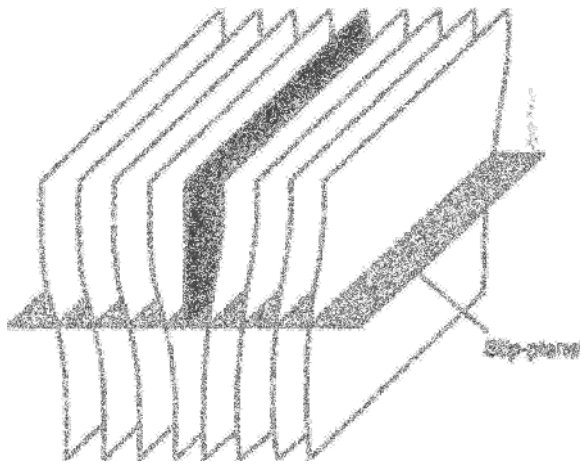

Figure 2.10 Schematic representation of a slip-plane [7].

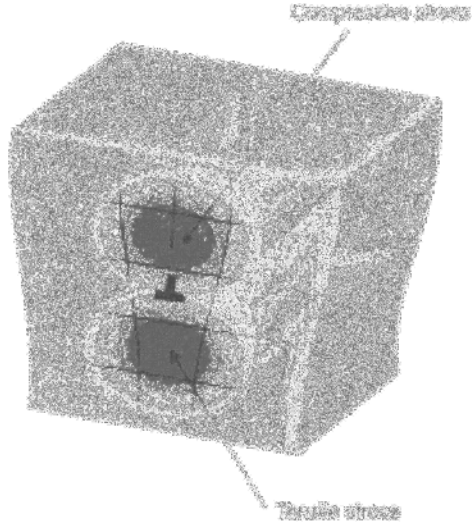

Figure 2.11 Geometry and extent of elastic compression and tensile stress around the dislocation line of a step dislocation in a real crystal [8].

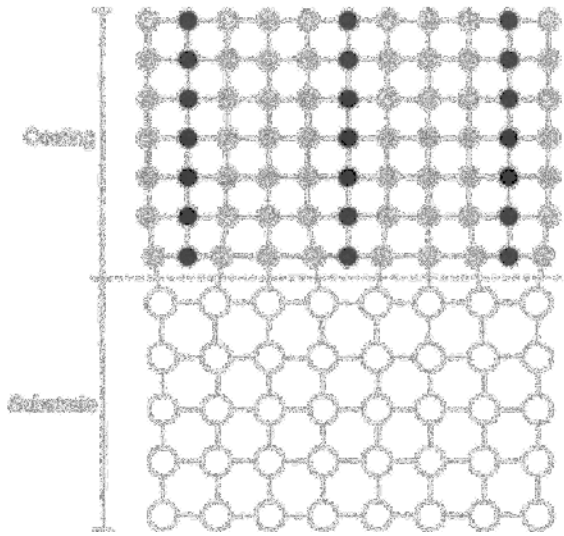

Figure 2.12 Formation of step dislocations when two simple cubic-structured lattices with different atoms and unequal lattice constants are juxtaposed.

In bringing together two simple cubic-structured crystal lattices (representing the substrate–coating combination) but with disparate atoms and lattice constants, it follows that step dislocations must form at their interface, in order to allow a matching up of the two metals or alloys. Appreciating this is crucial to an understanding of the interaction of substrate and coating, and the extent of these

dislocations critically affects the properties of the deposited layer. Thus, for example, they determine the adhesion and plastic deformation of the deposited metal layer.

2.2.3 Two-Dimensional Lattice Defects

The crystallites or grains which form the building blocks of metallic materials are arranged, in terms of their orientation, in more or less statistical distribution. In some circumstances, a preferred orientation is observed and this is known as the 'texture'. In every case, these are separated from one another at grain boundaries. Such structures are the best-known exemplars of two-dimensional or linear defects. Within this category, a distinction can be made between the so-called large- and small-angle grain boundaries. In this case, only the former will be considered, since it is these which form the actual grain boundaries between adjacent crystallites. As seen in Fig. 2.13, this is the case when, as a result of the growth process, growing crystallites are bounded on all sides by others in the same state.

The atomic structure of a large-angle grain boundary is shown in Fig. 2.14. It is characterised by the random orientation of the atoms so that no systematic array exists, between the two adjacent crystal lattices. The pronounced lattice deformation at the interfacial region creates a zone without any structure, that is, amorphous. The main difference between a crystalline and an amorphous state is seen in Fig. 2.15.

Whereas the crystalline state is characterised by a highly ordered atomic structure, extending over a considerable distance (long-range ordering), in the case of an amorphous material, one can see a modest amount of short-range ordering, that is, very small, sub-microscopic regions in which ordering can be found.

The large-angle grain boundaries are zones of enhanced energy, this being the larger the greater the difference in orientation of adjacent grains. Once the angle reaches 30°, however, no further energy increase is found.

A special form of grain boundary is found with so-called 'twinning'. This can occur under defined circumstances, for example, when two crystallites, both free from lattice distortion, form a common boundary. This, for example, is the case when two

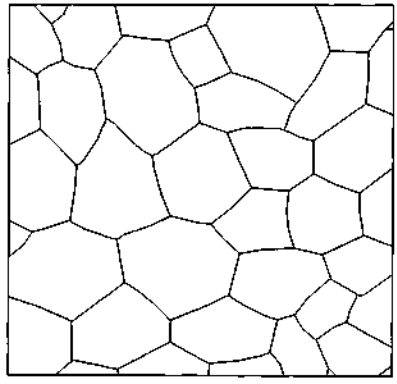

Figure 2.13 Formation of large-angle grain boundaries following crowding of growing crystallites with random orientation.

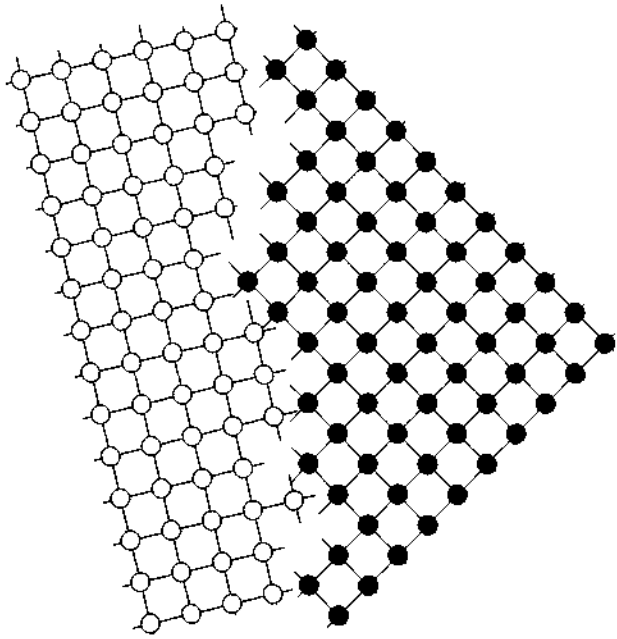

Figure 2.14 Atomic structure of a large-angle grain boundary between two adjacent crystallites of different orientation.

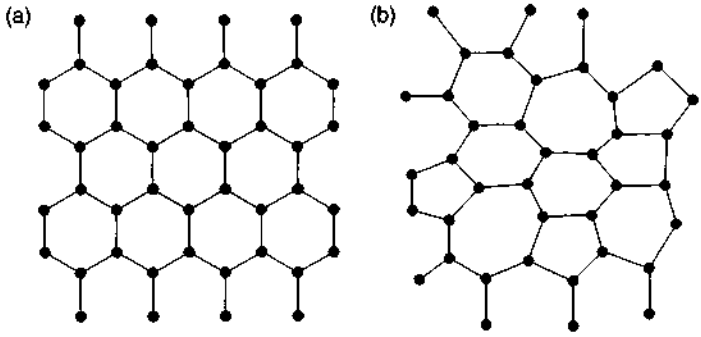

Figure 2.15 Structural difference between crystallites with long-range ordering (a) and in a mainly amorphous state with localized areas of short-range ordering(b).

crystallites come into contact oriented as the mirror image of one another. The necessary prerequisite is that the resulting atomic stacking, as shown in Fig. 2.16, occurs along the so-called twinning boundary. This means that the lattice planes of the adjacent crystallites can be brought together, as a result of a folding at the twinning boundary. Such cases are known as coherent twinning boundaries. By contrast, a so-called incoherent twinning boundary is formed when the folded zone does not extend through the entire crystallite. Figure 2.16 shows examples of both these cases.

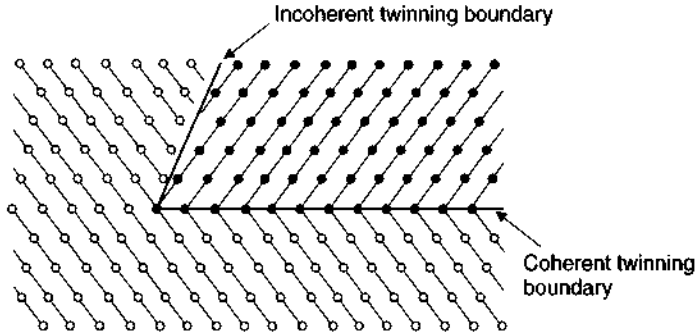

Figure 2.16 Formation and development of coherent and incoherent twinning boundaries between two crystallites (the first displaying mirror symmetric atom stacking) [1].

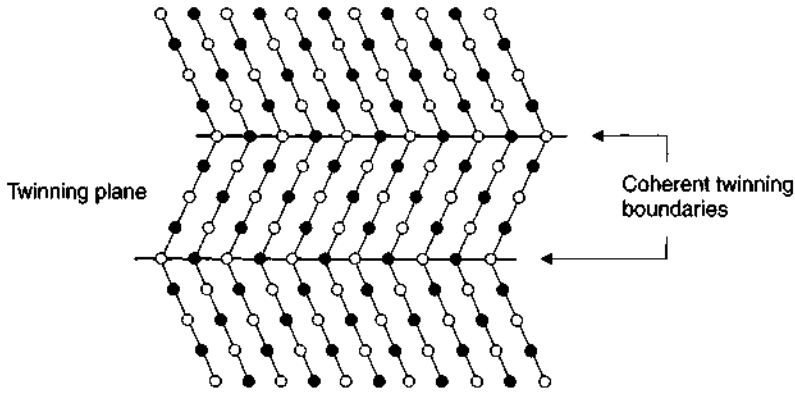

Figure 2.17 Formation of a twinning plane between two coherent twinning boundaries.

Figure 2.17 shows formation of a twinning plane, sandwiched between two coherent twinned grain boundaries.

Coherent grain boundaries appear under the optical microscope as straight lines, whereas incoherent grain boundaries appear to be irregular. An idealized visualization of both types, as might appear under a microscope, is shown in Fig. 2.18.

The crystal defects summarised above exert a profound influence on the mechanical, physical and chemical properties of polycrystalline metals. Table 2.2 is an attempt to summarise these, but without taking into full account of some of the often complex synergistic effects.

Specially noteworthy is the action of line defects on the mechanical properties of a metal. Figure 2.19 shows an idealised plot of the fracture strength of a crystalline material as a function of lattice defects.

The term 'theoretical strength' is used here to designate any mechanical force which can be applied to break the atomic binding forces between neighbouring lattice planes in a defect-free crystal structure. It is many times greater than the experimentally obtained value for the fracture strength of a crystalline material.

Table 2.2 Crystal defects and their effect on the physical and mechanical properties of metals.

Defect type	Effects
Point defect Vacancy, interstitial atoms	Electrical and thermal conductivity
Line defect Screw and step dislocation	Mechanical properties, strength, ductility, hardness
Plane defect Large angle grain boundaries, twinning boundaries	Creep and corrosion resistance

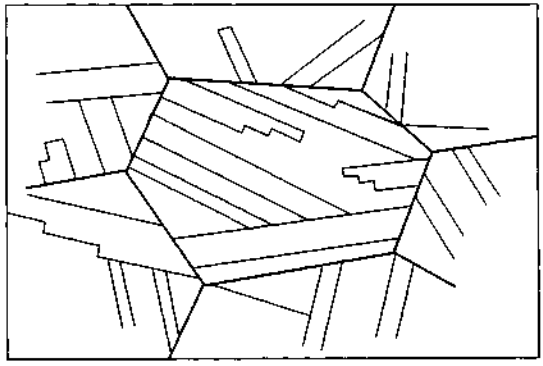

Figure 2.18 Idealised visualisation of coherent and incoherent twinning boundaries as seen under an optical microscope [8].

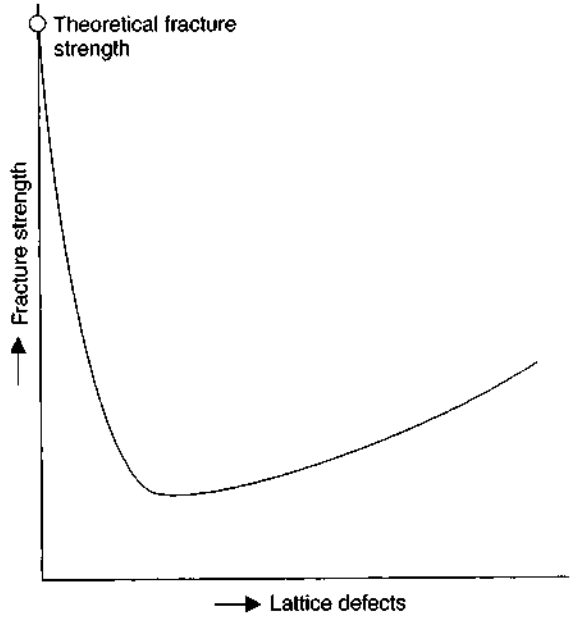

Figure 2.19 Idealised plot of the fracture strength of a crystalline material as a function of lattice effects.

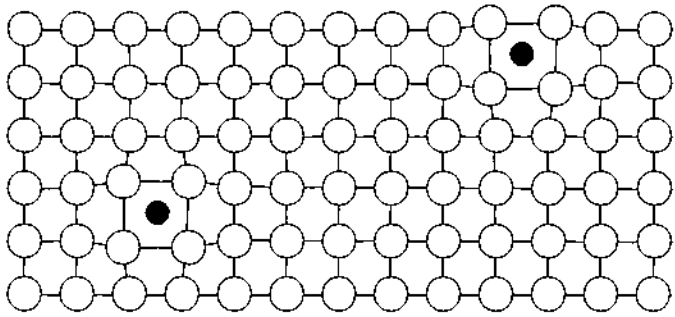

Figure 2.20 Formation of an insertion-type alloy by incorporation of foreign atoms at interstitial sites in the lattice, where these have smaller atomic radii than the parent atom.

2.3 Alloys

As noted above, in practice, pure metals are very rarely used in manufacturing of finished products or semi-manufactures, since they cannot in most cases, offer the required range of properties. Only using an alloy of two or more metals, or metals and non-metals, can the best combination of properties be achieved. Considered at the atomic level, this usually implies the insertion of foreign atoms into the lattice structure of the so-called parent metal. Usually, this is the metal present in the highest amount. Depending on the type of foreign atom and the amount inserted, a range of modified crystal lattices will result [9].

2.3.1 Interstitial Solid Solutions

Sometimes known as insertion structures, these alloys are formed when the atomic radius of the foreign atom is smaller than that of the parent metal atom. In this case, the foreign atoms are statistically distributed at interstitial sites in the lattice. The resulting structure is shown in Fig. 2.20.

The presence of interstitial foreign atoms, dissolved to form an alloy, gives rise to elastic distortions in the crystal lattice of the parent metal, and these affect a number of properties. In cases where there is localised enrichment of foreign atoms within individual grains of the parent metal, these are known as incoherent deposits or inclusions. The effect of such inclusions is mainly on the chemical properties and corrosion resistance of the alloy. An example is shown in Fig. 2.21.

2.3.2 Substitutional Solid Solutions

Where the atomic radius of the foreign atom is of a size comparable to that of the parent metal, and in defined situations, for example, unlimited mutual solubility of the two components, then the foreign atom may be incorporated into the lattice on a substitutional basis, where one foreign atom occupies a site formerly occupied by a parent metal alloys. This is known as an exchange or substitution mixed crystal or alloy and is depicted in Fig. 2.22.

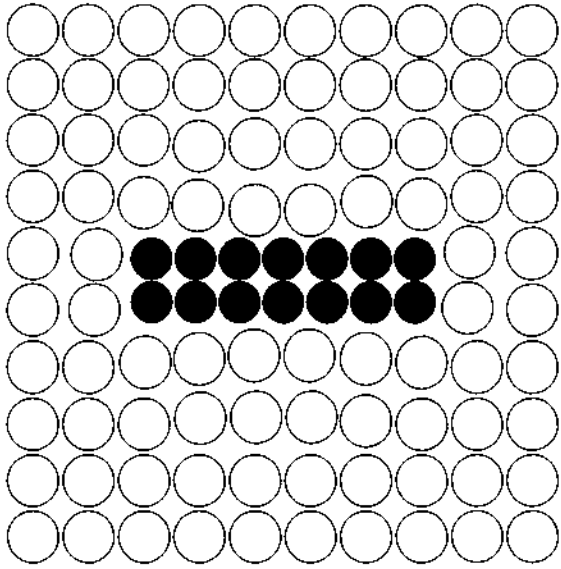

Figure 2.21 Formation of localised foreign atom enrichment within a grain of the parent metal.

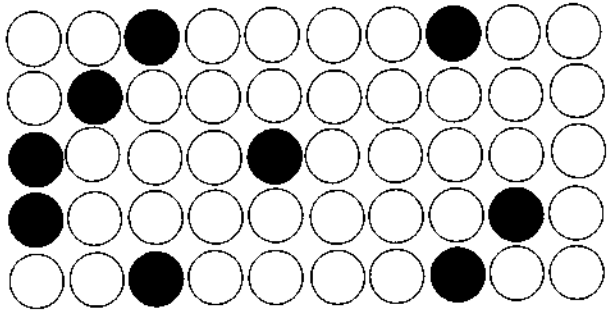

Figure 2.22 Formation of a substitution-type mixed crystal or alloy where the foreign atom has radius similar to that of the parent atom.

Although lattice distortions, in this type of mixed crystal, can be negligible since there is no significant volume change, the properties of the resulting alloy can be substantially different from that of the parent metal. As a crude approximation, the properties of such alloys, provided they remain single-phase, are intermediate between those of the two constituent metals, and in proportion to the amounts of each metal present.

In cases where the foreign atom has atomic radius greater than that of the parent metal, one-for-one substitution is only possible in certain circumstances. In this case, however, the properties of the resulting alloy can differ significantly from that of the parent metal. This situation is shown in Fig. 2.23.

Alloys, be they homogeneous (single-phase) or heterogeneous (multi-phase), are polycrystalline materials and can incorporate all the defects, dislocations, vacancy sites, etc., which were previously discussed in the context of a single metal. They are equally prone to large-angle grain boundaries between adjoining grains of different orientation. As with pure metals, there are amorphous zones of enhanced energy and activity at which foreign atoms can concentrate. These are known as grain boundary impurities, or preferential grain boundary enrichments, and Fig. 2.24 shows a schematic representation.

Figure 2.25 shows a schematic of such grain boundary enrichment as seen under an optical microscope. That such accumulations, be they larger or smaller, of foreign atoms can drastically affect the chemical and mechanical properties of an alloy, goes without saying.

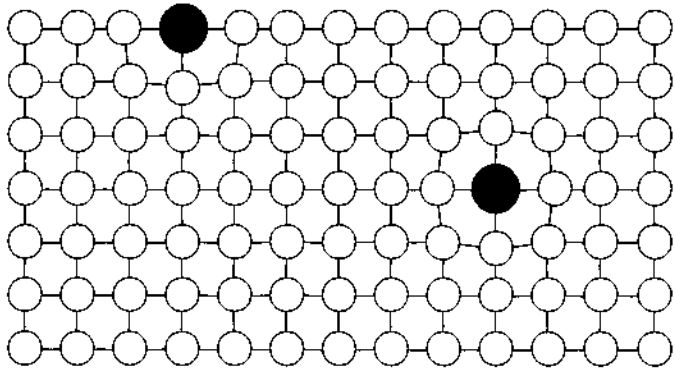

Figure 2.23 Lattice strain and volume change in a parent metal lattice caused by presence of foreign atoms of radius greater than that of the parent metal.

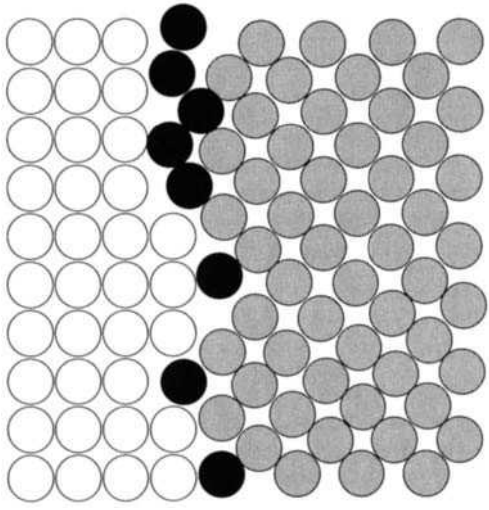

Figure 2.24 Preferential deposition of foreign atoms at a large-angle grain boundary in an alloy.

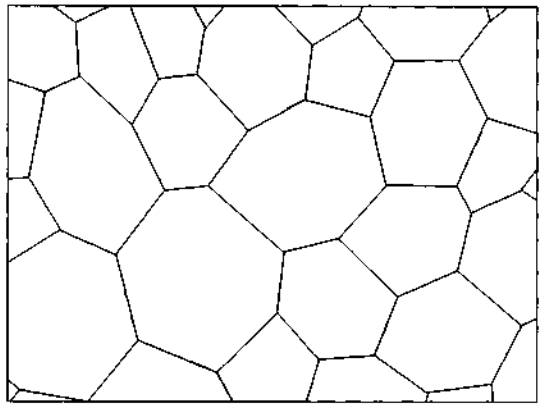

Figure 2.25 Idealised optical microscope image of deposition at grain boundaries of a metal.

2.4 Plastics

Plastics, also known as polymers are almost always organic compounds, though some inorganic (silicon-based) polymers are also known. As polymer science and technology develop, this class of compounds is being used in an ever-widening range of applications, usually to replace metal components. Polymers are normally of low density and often exhibit a high resistance to corrosion or other chemical attack, as well as being readily mouldable. They have their drawbacks too, however. Thus, they readily become brittle at low temperatures, and lose mechanical strength above 100°C.

It is these, in some way contradictory, properties that presently restrict the areas of application for plastics. If one compares plastics with metals, in terms of their physical, chemical and technological properties, it is found, as Table 2.3 demonstrates, that these two groups of very important engineering materials have little in common.

There are exceptions to the listing of properties in Table 2.3, with some metals being softer than most plastics, a few plastics being intrinsically electrically conducting, etc.

Plastics are almost always based on a carbon skeleton, onto which are incorporated other atoms or radical groupings of hydrogen, oxygen, nitrogen, chlorine and fluorine. In contrast to metals, where the basic unit is an atom, the 'building block' for plastics is a low molecular weight molecule, known as a monomer. A polymer is formed from these monomers, usually from a single type of monomer, but a so-called copolymer is assembled from two or more different monomer types. The chemical reactions for forming polymers may be addition reactions, where one monomer is simply chained to another, or condensation types, in which two monomers are linked with loss of a simple radical or functional grouping. Polymers may also be formed from macromolecules.

Table 2.3 Comparison between metals and plastics in terms of their physical, chemical and technological properties.

Property	Metals	Plastics
Physical		
Electrical conductivity	High	Low
Thermal conductivity	High	Low
Coefficient of thermal Expansion	Low	High
Reflectance	High	Low
Magnetic	Yes	No
Chemical		
Chemical resistance	Low	High
Corrosion resistance	Moderate	Moderate to high
Technological		
Specific Weight	High	Low
Specific strength	High	Moderate
Wear resistance	High	Low
Hardness	High	Low

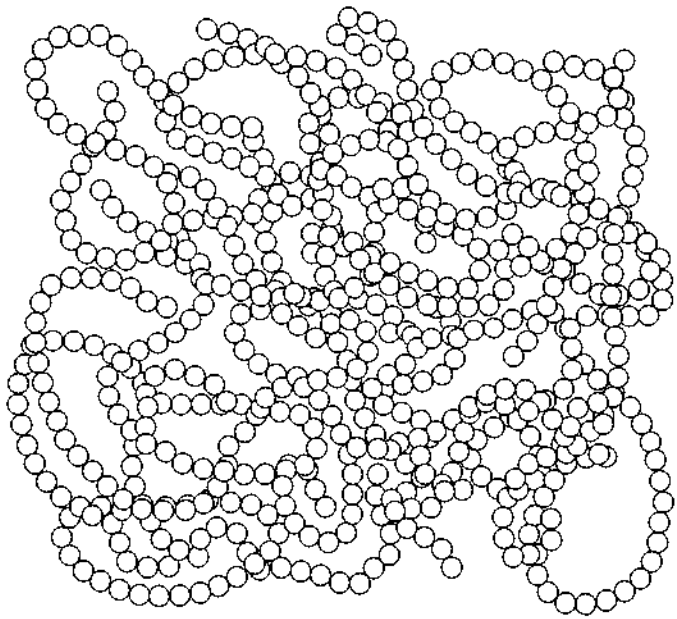

Figure 2.26 Schematic representation of the molecular structure of a polymeric material [10].

2.4.1 Amorphous Polymers

Macromolecules are found as very long chains or threads, and because of their length and resulting flexibility, such molecules form non-crystalline, predominantly amorphous structures. Figure 2.26 shows an idealised schematic of such an

amorphous structure. The small circles of which the structure is formed indicate monomers rather than atoms.

These long molecular chains, as indicated in Table 2.4, can be linear, entangled with one another, or branched [11].

Cohesion of the macromolecular groupings is brought about, other than by mechanical attachments, mainly by intermolecular bonding forces. The mechanical properties of polymeric materials are thus mainly due to their molecular structure and the juxtaposition of their molecular chains.

2.4.2 Partly Crystalline Polymers

The configuration of atoms in a molecular chain can also lead to crystalline features, where the interatomic bonding forces are specially large. In one example of this, strands of macromolecules lie between the amorphous zones in a bundled form, such that the plastic assumes a partially crystalline structure. This is shown in Fig. 2.27.

Both the amorphous and crystalline parts of a polymer can exist either in totally random and unoriented form, or they can be oriented. The unoriented, amorphous polymer can, however, become ordered, either as a result of external influences or thanks to the action of intermolecular bonding forces, with the polymer acquiring a preferred orientation. In partially crystalline polymers too, both oriented and unoriented structures can be seen. The oriented crystalline condition is recognisable in that the partly bundled macromolecules, form up parallel to one another, whether as a result of external forces or intermolecular bonding forces, and

Table 2.4 Structure and generic properties of thermosetting and thermoplastic plastics.

	Type of Plastic	
	Thermosetting	Thermoplastic
Structure	Three-dimensional polymerized Macromolecule Spatially polymerized molecule	Uni-dimensional chain-structured Macromolecule Thread-like molecule
	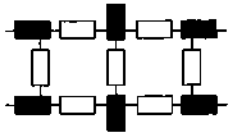	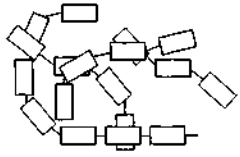
Chemical binding	Macromolecules and macromolecular groups: primary bonds, Valence bonds	Macromolecules: primary bond macromolecular groups: secondary bonds, Van der waals forces
	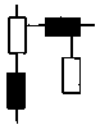	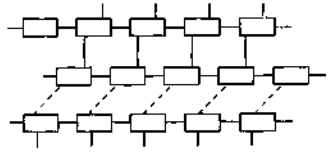

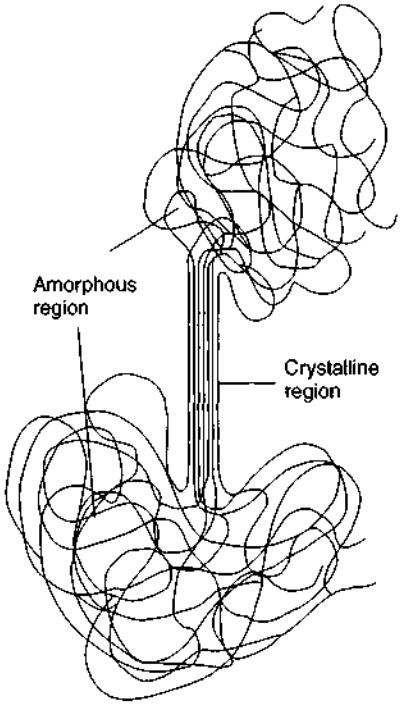

Figure 2.27 Schematic representation of a partially crystalline structure of a polymeric material with amorphous basis [12].

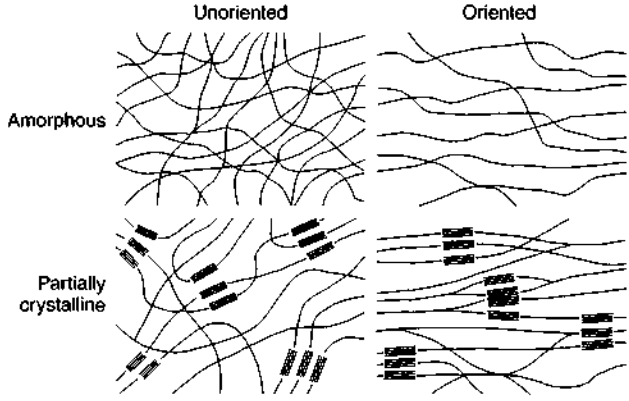

Figure 2.28 Molecular structure and orientation for amorphous and partially crystalline polymers [3].

a preferred orientation is found. Figure 2.28 shows these different conditions in schematic form.

Among the ways in which amorphous and partially crystalline polymers differ from one another, is in their change of specific volume with temperature. A comparison with metals is illuminating, and this is seen in Fig. 2.29.

In the case of polycrystalline metals, specific volume increases significantly with temperature until the melting point T_S is reached (Fig. 2.29a). At this point, the crystalline structure is lost and a sudden jump in specific volume is observed, as shown in the plot. Above the melting point, a further increase in volume takes place, with total loss of order as the amorphous state of the melt is assumed.

A hallmark of the behaviour of amorphous plastics, as temperatures increase is the so-called 'glass transition temperature' (T_g) (Fig. 2.29c). Below this temperature, there is virtually no movement of the long-chain molecules.

As temperature increases, so does the vibrational motion of the long-chain molecules, resulting in an increase in specific volume (Fig. 2.29c). As the glass transition temperature is reached, there is a 'thawing' of the amorphous structure which is manifested in an increase in the value of the function $V = f(T)$. Since this transition is not usually sharply defined, a value for T_g is best obtained from the intersection of the curves either side of the transition. Above T_g, a further increase in specific volume is seen. However, the long-chain structure of the macromolecules remains up to the melting point, and only above this point do the chains break down.

The thermal behaviour of partially crystalline plastics is intermediate between that of fully crystalline materials and those which are amorphous. In this case, thanks to the amorphous zones between the crystallites, some molecular movement is possible, even at lower temperatures, and increasing temperature enhances this. As a partially crystalline material is heated, the crystalline portions initially

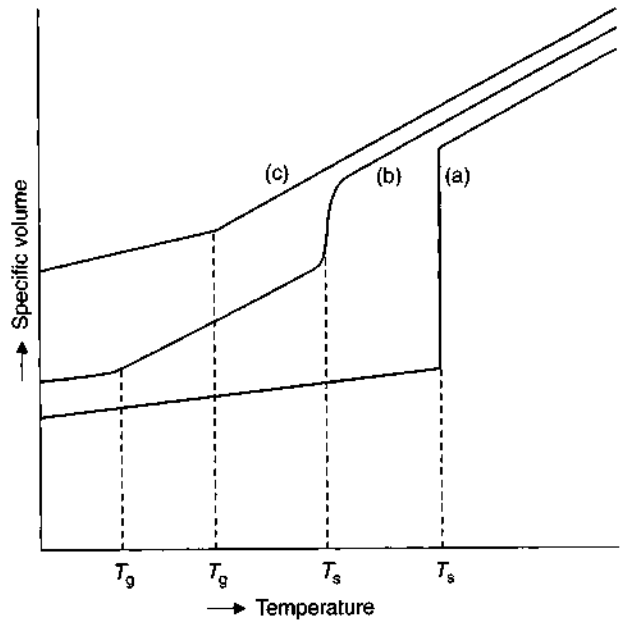

Figure 2.29 Change in specific volume caused by temperature variation for an amorphous (c) and partly crystalline (b) polymer with, for comparison, a polycrystalline metal (a) [14].

retain their structure, whereas the amorphous zones progressively break down as they approach the glass transition temperature (Fig. 2.29b). Further increase in temperature results in a loosening of the crystalline structure, until the melting point is reached, when – as in all liquids – virtually all vestiges of structural features disappear. The ratio of crystalline to non-crystalline (amorphous) material, designed as the degree of crystallinity, is thus the determining factor governing the behaviour of partially crystalline materials when heated. The greater the degree of crystallinity, the greater are the values of density, mechanical strength, hardness, and melting point of the plastic, as also the retention of these at elevated temperatures.

2.4.3 Intrinsically Conductive Polymers

Polymers differ from metals inasmuch as they are predominantly based on directional, covalent bonds. It is a characteristic of such bonding that the electrons are mainly localised. This is the main reason why polymers are usually good electrical insulators.

In the case of so-called intrinsically conductive polymers, one is dealing with an organic compound which, by suitable means, can be made electrically conductive [15–32]. The oldest-established conducting polymers are the so-called filled polymers. At some stage in the production of the plastic, conductive metal particles, such as those of gold, silver or lead are incorporated, or sometimes conductive carbon black (soot) or stainless steel fibres. Filled electrically conductive polymers are not classified as intrinsically conducting. The electrical conductivity of the resulting composite depends on the fraction of conducting particles incorporated, although there is a threshold effect, since until sufficient concentration of conductive particles is reached to allow these to contact one another, they remain insulated by the surrounding insulating polymer matrix. The development of such conductivity is known as a 'percolation network' [21]. Figure 2.30 illustrates the development of electrical conductivity in such a situation. As a rule of thumb, some 20% by weight of metallic particles is necessary for such materials to become conductive.

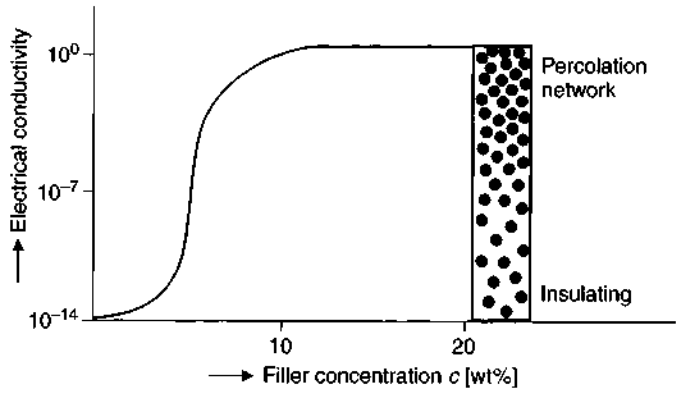

Figure 2.30 Dependence of the electrical conductivity of a filled polymer on composition [21].

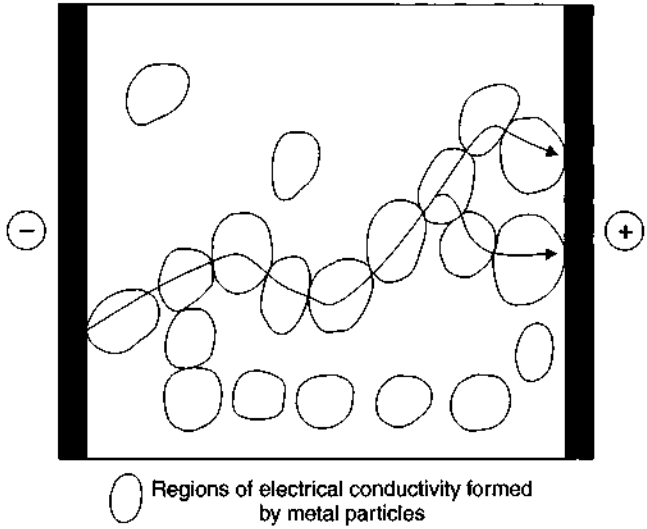

Figure 2.31 Current-conducting pathways formed by metal-to-metal particle contacts, in an insulating matrix [15].

This approach suffers from two main drawbacks. In the first place, only a modest range of conductivity values can be reliably achieved, typically from 10^1 to 10^4 S/cm [15]. Second, as Fig. 2.31 shows, at low metal particle concentrations, little or no particle-to-particle contact is found, and the composite remains essentially an insulator.

Pathways, formed where particle-to-particle contact is established, allow passage of current and so confer electrical conductivity on these materials. Where no intermetallic contact exists, the material remains an insulator under low voltage gradients. As the applied voltage increases, electrical conductivity develops but only by virtue of electrical discharges, which 'hop' from one metallic particle to the next, but usually causing catastrophic breakdown of the material as this occurs. At the other extreme, where very high metal particle concentrations exist, the composite acquires conductivity close to the value for the massive metal of which the particles are made.

A further drawback of these filled polymers is that the metal particles, whose density is almost invariably greater than that of the polymer, tend to settle during processing (see Fig. 2.30), unless means are adopted to avoid this, resulting in an inhomogeneous material.

For some years now, an entirely different class of material has been known, the so-called intrinsically conductive polymers. These have reported DC conductivities[1] from 10^{-14} to 10^3 S/cm, and contain no metallic inclusions. Figure 2.32 demonstrates the difference between intrinsically conductive polymers, and their filled analogues, in terms of their conductivities [16, 19, 32].

Figure 2.33 shows, for the purpose of comparison, the energy level bands of a metal, a semiconductor and an insulator, and this explains the conduction mechanism involved in the case of intrinsically conductive polymers.

[1] Referred to in the following simplified treatment simply as 'conductivity'.

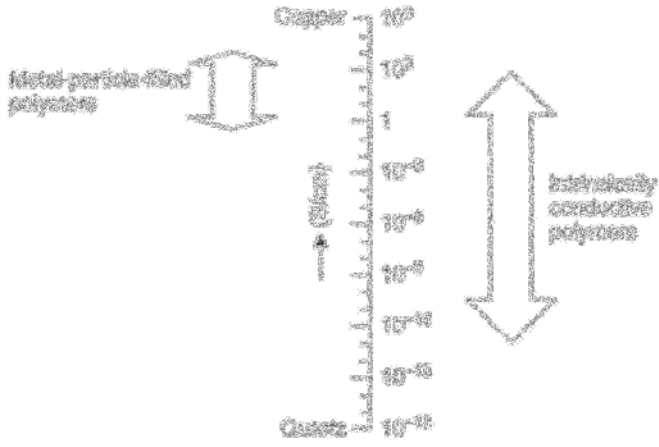

Figure 2.33 Comparison of conductivities of metal-particle-filled plastics with intrinsically conductive polymers

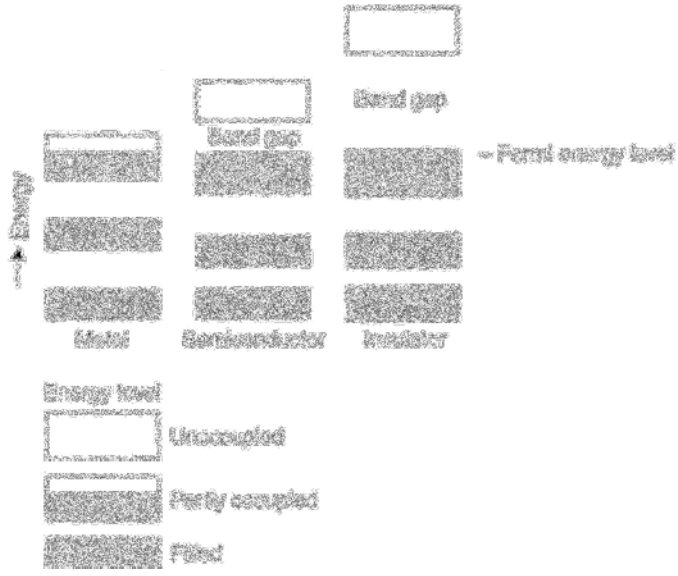

Figure 2.33 Comparison of energy bands of metals, semiconductors and insulators in terms of the band energy model.

According to band theory, electrons are mobile only in partly filled band levels and thus, fully occupied or totally vacant bands can make no contribution to electrical conductivity.

That metals possess only partly filled bands at the Fermi level implies that the resulting electron mobility allows passage of charge (i.e. current) under an electrical gradient. In the case of semiconductors, all the energy bands up to the Fermi level are fully occupied, while those above are vacant. The difference between the highest filled energy level and the vacant level above it (band gap) is relatively small, typically

0.5–1.5 eV, thereby allowing thermally excited electrons to jump from the valence to the conduction band. In the case of an insulator, this band gap is much larger, usually >3 eV. At normal temperatures, this gap is too great for thermally excited electrons to be promoted to the conduction band.

Polymers are usually based on long-chain carbon atom skeletons, which can be linear, or linked five- or six-membered rings. Most of the spare bonds are taken up with hydrogen atoms, though nitrogen and sulpfur are also found in some polymers. In their normal form, polymers behave as insulators or semiconductors, whose band structure they share. Thus, there is a substantial band-gap between the valence and conduction bands and only by doping with charge donors or acceptors, can a degree of electrical conductivity be achieved [16]. Acceptors are electron recipients such as I, AsF_5, BF_4, ClO_4^- and $FeCl_3$ whereas electron donors include the alkali metals.

Doping in this way results in modification of the polymer band structure such that electrons can be promoted from the valence band (p-doping) or injected into the conduction band (n-doping). Such doped polymers then become conductive since either

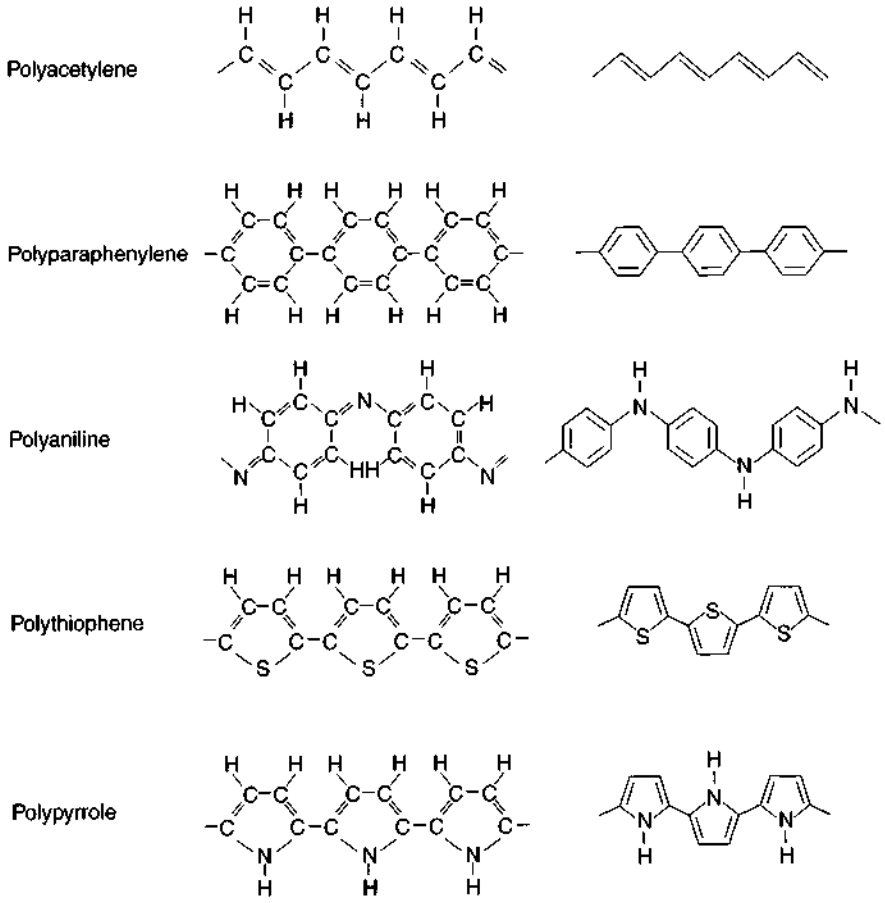

Figure 2.34 Chemical structures of the most important intrinsically conductive polymers.

valence or conduction bands are then partly filled. The doping process introduces positive or negative charge centers into the polymer chain. To balance the electrical charge on the dopant, ions of the opposite charge are located in the polymer matrix.

The electrical conduction mechanism in intrinsically conductive polymers is not yet fully understood. However, it is believed to involve islands of charge (solitons, polarons and bipolarons) which form around the counter-ions [16, 19, 20]. It is also believed that electron hopping between polymer chains contributes far more to conductivity than electron transport along the length of a polymer chain.

The most important and most thoroughly researched intrinsically conductive polymers are polyacetylene, polyparaphenylene, polyaniline, polythiophene and polypyrrole, whose chemical structures are shown in Fig. 2.34 [16–29]. Polyanisidine has also been reported.

In terms of its structure, polyacetylene is the simplest of these polymers. The chemical and structural transitions which are necessary to transform an insulating into a conductive polymer, can be quite simply illustrated in the case of this species [15]. As shown in Fig. 2.35, polyacetylene can be formed by dehydrogenation of polyethylene. The compound has a carbon atom backbone on which, in contrast to polyethylene, there is only one pendant hydrogen atom per carbon. As a result, there is a two-electron overlap at each adjacent carbon, in place of the bond

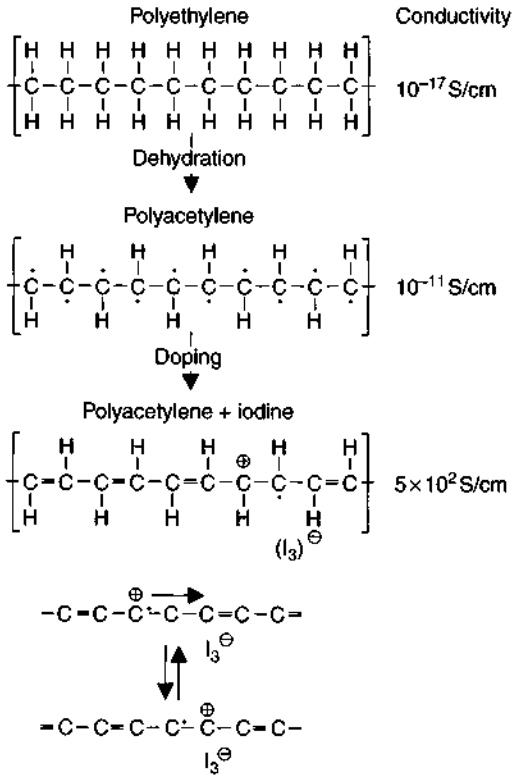

Figure 2.35 Synthesis of polyacetylene and changes in its conductivity on doping with iodine [15].

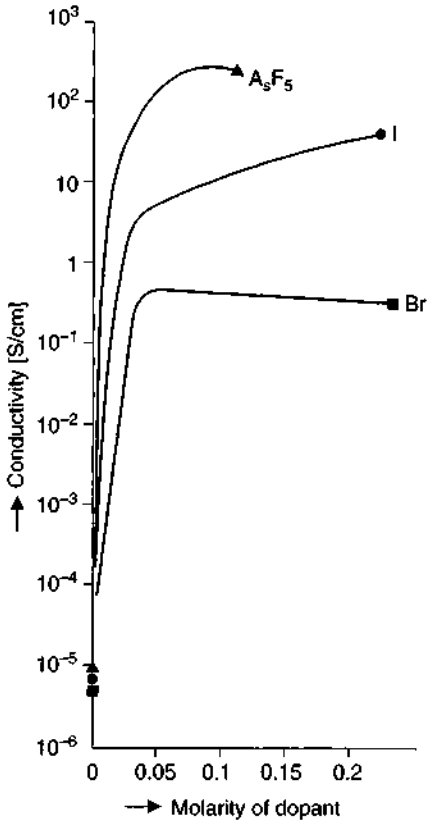

Figure 2.36 Increase in specific electrical conductivity of trans-polyacetylene by doping with Br, I or AsF_5 [19].

to hydrogen previously there. This is a π-electron orbital at right angles to the C–C bond. The carbon atoms are thus linked alternately with double and single bonds along the chain, although these continuously switch with one another. This is known as 'conjugate bonding', which can be considered as an intermediate state between single and double covalent bonds, and is a feature found in most conductive polymers.

On standing, polyacetylene has a substantial affinity for oxygen, thanks to its electron acceptor property. This results in an increase in electrical conductivity from typically 10^{-17} to 10^{-11}. Doping with iodine creates positive and mobile charge carriers, which further increase its conductivity by some 13 orders of magnitude to 5×10^2 S/cm. The effect of doping with bromine or AsF_5 rather than iodine, is shown in Fig. 2.36.

From this diagram, it can be seen that, after doping, polyacetylene has a conductivity comparable to the less conductive metals, such as bismuth.

A key criterion for practically useful intrinsically conductive polymers is their environmental stability, not least expressed in terms of their conductivity in air. Temperature effects and shelf-life are likewise critical. Figure 2.37 shows the effect

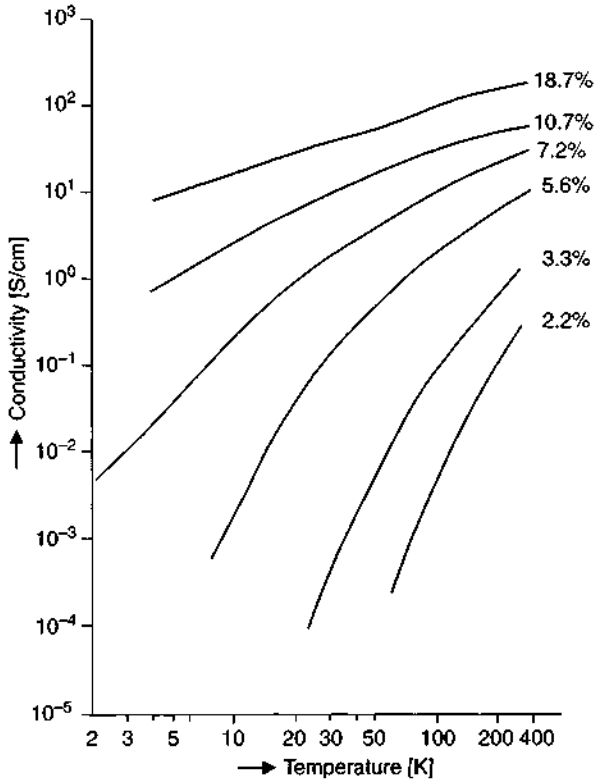

Figure 2.37 Temperature dependence of the electrical conductivity of iodine-doped polyacetylene at various dopant concentrations [16].

of iodine dopant concentrations versus temperature. The figure shows how lightly-doped polyacetylene is much more susceptible to temperature effects than when the material is more heavily doped.

Figure 2.38 shows the effects of storage in air on weakly iodine-doped polyacetylene at various temperatures, and reveals that, provided temperatures are not too high, conductivity is stable over time.

Another conductive polymer that has attracted much technological interest, is polypyrrole. This is electrochemically synthesised in a process whereby the oxidation and incorporation of counter-ions all occur during the reaction [17]. Typically, the conductivity of this polymer is around 10^2 S/cm and it is more stable in its time and temperature behaviour than polyacetylene. Figure 2.39 shows these effects.

As the foregoing diagrams show, and hardly surprisingly, the loss of conductivity is greater, the higher the storage temperature. Figure 2.40 shows this for polypyrrole with the anion of benzosulfonic acid as counter-ion, compared with iodine-doped polyacetylene.

Thus, whereas the conductivity of polyacetylene decreases by a factor of 1000 over 30 days, a slight reduction in conductivity is observed only after 200 days in polypyrrole.

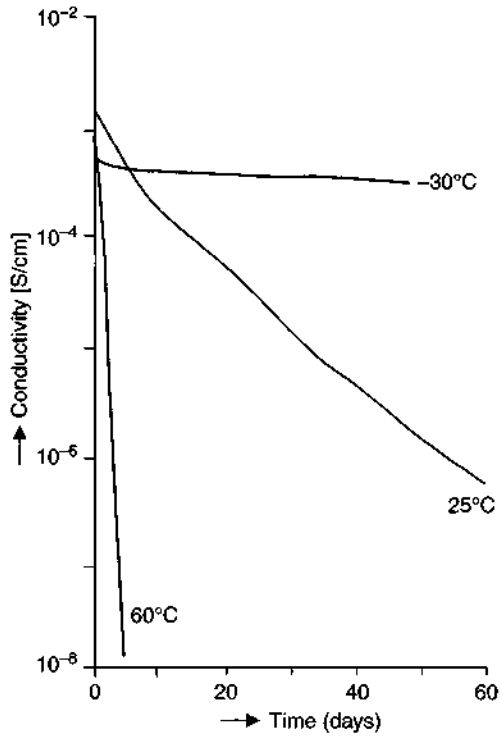

Figure 2.38 Effect of time on electrical conductivity of weakly iodine-doped polyacetylene when stored in air at various temperatures [18].

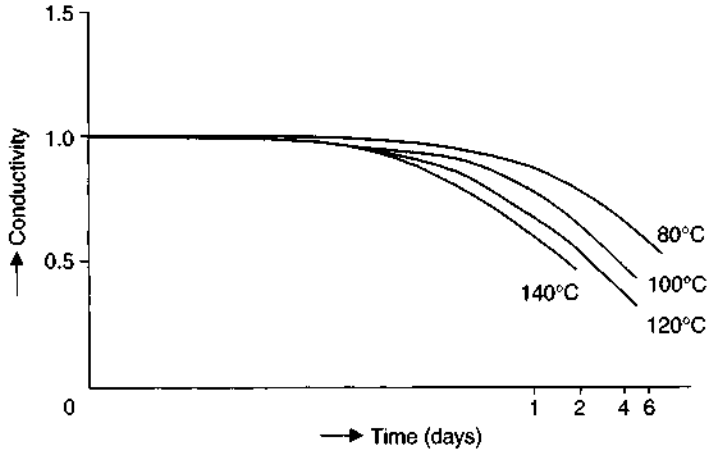

Figure 2.39 Change of electrical conductivity over time for polypyrrole at various temperatures [17].

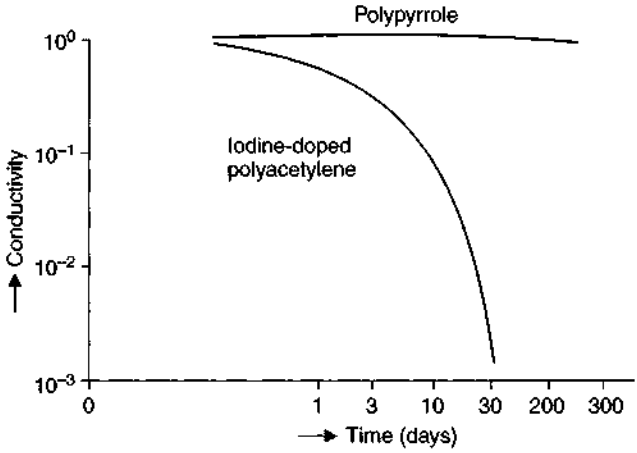

Figure 2.40 Change of conductivity over time for polypyrrole and polyacetylene [17].

The key issues in technical application of intrinsically conducting polymers are their resistance to elevated temperatures and oxygen, and the extent to which they retain their conductivity under in-service conditions. Their ease of formability is also important. Among other applications, they have been used to prevent build-up of static charge on metal housings, for photovoltaic panels and in fuel cells. They are widely used in single and multi-layered printed circuit boards [30–36].

References

[1] Böhm, H., *Einführung in die Metallkunde*, Bibliographisches Institut, Mannheim, 1968.

[2] Kröner, E., Versetzungen in Kristallen in *Moderne Probleme der Metallphysik*, herausgegeben von A. Seeger, Springer-Verlag, Berlin, 1965.

[3] Guy, A.G., *Metallkunde für Ingenieure*, Akademischer Verlagsgesellschaft, Frankfurt/M., 1970.

[4] Lange, K., Gleitung, in *Lexikon der Werkstofftechnik*, herausgegeben von H. Gräfen, VDI Verlag GmbH Düsseldorf, 1991.

[5] van Vlack, L.H., *Elements of Materials Science*, Addison-Wesley Publishing Company, California, 1971.

[6] Weizel, H., *Festkörperphysik*, in Physik – gestern, heute, morgen, (Autorenkollektiv), Heinz Moos Verlag, München, 1971.

[7] Genzel, L., *Die feste Materie, Atome und Elektronen im Festkörper*, Umschau Verlag, Frankfurt/M., 1973.

[8] Hayden, H.W., Moffatt, W.G., and Wulff, J., *The Structure and Properties of Materials*, Volume III: Mechanical Behavior, John Wiley & Sons, New York, 1965.

[9] Cottrell, A.H., *An Introduction to Metallurgy*, Edward Arnold Publishers, London, 1971.

[10] Hayden, H.W., Moffatt, W.G., and Wulff, J., *The Structure and Properties of Materials*, Volume I: Structure, John Wiley & Sons, New York, 1965.
[11] Ehrentraut, P., Eigenschaften und Einsatz von Kunststoffen in der Beschichtung, *Metalloberfläche* 22 (1968) 10, 289–294.
[12] Autorenkollektiv, *Werkstoffe der Elektrotechnik und Elektronik*, VEB Deutscher Verlag für Grundstoffindustrie, Leipzig, 1979.
[13] Neumann, A. (Hrsg.), *Werkstoffe mit Zukunft*, Urania-Verlag, Leipzig, 1977.
[14] Katzer, F., *Werkstofftechnik*, VEB Verlag, Berlin, 1988.
[15] Weddigen, G., Elektrisch leitende Kunststoffe, *Physik in unserer Zeit*, Nr. 4 (1983).
[16] Roth, S., Metallisch leitende Polymere, in *Elektrisch leitende Kunst stoffe*, Technische Akademie Esslingen, Symposium 15–16 April, 1985.
[17] Münstedt, H., Physikalisches Altern von intrinsisch elektrisch leitfähigen Polymeren, in *Elektrisch leitende Kunststoffe*, Technische Akademie Esslingen, Symposium 15–16 April, 1985.
[18] Menke, K. and Roth, S., Chemische Stabilität metallisch leitender Polymere, in *Elektrisch leitende Kunststoffe*, Technische Akademie Esslingen, Symposium 15–16 April, 1985.
[19] Menke, K. and Roth, S., Metallisch leitfähige Polymere I, *Chemie in unserer Zeit*, Nr. 1 (1986) 1–8.
[20] Menke, K. and Roth, S., Metallisch leitfähige Polymere II, *Chemie in unserer Zeit*, Nr. 2 (1986) 33–43.
[21] N. N., Elektroaktive organische Materialien, in *Neue Chancen durch neue Stoffe*, Schriftenreihe des Fonds der Chemischen Industrie, Heft 27, Frankfurt a. M., 1986.
[22] Ku, C.C. and Liepius, R., *Electrical Properties of Polymers*, Hanser Publishers, Munich, 1987.
[23] Alcacer, L. (editor), *Conducting Polymers Special Applications*, D. Riedel Publishing Company, Dordrecht/Holland, 1987.
[24] Kaner, R.B. and MacDiarmid, A.G., Elektrisch leitende Kunststoffe, *Spektrum der Wissenschaft*, April (1988) 54–59.
[25] Mair, H.J. and Roth, S. (Hrsg.), *Elektrisch leitende Kunststoffe*, Carl Hanser Verlag, München, 1989.
[26] Salanek, W.R., Clark, D.T. and Samualsen, E.B., *Science and Applications of Conducting Polymers*, Adam Hilger, Bristol, 1991.
[27] Ewe, T., Polymere unter Strom, *Bild der Wissenschaft* 11 (1991) 16–20.
[28] Haupt, S.G., Riley, D.R. and McDevitt, J.T., Conductive polymer/high-temperature superconductor composite structures. *Adv. Mater.* No. 10 (1993) 755–756.
[29] Bäuerle, P., Intrinsically conducting polymers – quo vadis?, *Adv. Mater.* No. 12 (1993) 879–885.
[30] Sailor, M.J. and Curtis, C.L., Conducting polymer connections for moleclular devices, *Adv. Mater.* No. 9 (1994) 688–692.
[31] Clery, D., After Years in the dark, electric plastic finally shines, *Science*, 263 (1994) 1700–1703.
[32] Bischoff, S., Dunsch, L. and Plieth, W., Leitfähige Polypyrrol-Schichten, *Metalloberfläche* 50 (1996) 23–25.

[33] Kanani, N., Bressel, B. and Meyer, H., A direct electrolytic copper plating process for printed circuit boards, *Interfinish 92. International Congress for Surface Finishing*, 1992, pp. 1260–1275.

[34] Whitlaw, K.J., The use of conductive organic coatings for metallisation of printed circuit boards, *Trans. Inst. Metal Finish.* 70(3) (1992) 135–140.

[35] Meyer, H. and Szimmat, K., Die Durchkontaktierung von Leiterplatten auf Basis von leitfähigen Polymeren, *ZEV-Leiterplatten* 3 (1992) 18–24.

[36] Lewis, R., Are your holes conjugated?, *Trans. Inst. Metal Finish.* 71(4) (1993) 149–155.

This Page Intentionally Left Blank

CHAPTER 3

Electrolytes for the Deposition of Metal Coatings

3.1 Introduction

Aqueous electrolytes, used in metal finishing for electrodeposition of metal coatings, are principally solutions of metal salts, which, in solution, dissociate to form electrically charged anions and cations. These ions can be simple metal cations, Me^{z+}, positively charged complex ions or hydrogen ions, H^+. Also present will be ionised acid species, negatively charged complexes or hydroxyl anions, OH^-. Figure 3.1, which shows by way of illustration, the copper–sulfate ion system, also makes clear that the charged ions themselves are surround by an outer sheath of water molecules, held by electrostatic forces to the ions themselves. The orientation of these water molecules is seen to differ according to whether they surround a positively or a negatively charged ion. The reason for this lies in the dipole nature of water molecules. The same is also true for complex ions which, in comparison to simple ions, have a more complex structure. The reason for this is that complex species are higher-order compounds, built up from first-order species. In many of their properties, they differ markedly from the simple compounds of which they are formed.

The build-up of a complex can be described as follows. Around a central ion, in many cases, a heavy metal, are spatially arranged other ions or uncharged molecules (Fig. 3.2). These are often referred to as ligands. The central ion can coordinate, in this way, a greater number of outer ions or radicals than its normal valency would imply. This being the case, the conventional, simple means of formulating a chemical compound is no longer adequate.

The bonding between the central ion and the ligands is predominantly electrostatic or also non-polar bonding. The number of ligands is expressed as the so-called coordination number. There is no correlation between the valence number of the central ion and the coordination number, which is often 4, 6 or 8 in value. The reason for this lies in rules, which are an expression of steric ordering. Figure 3.3 shows the three most commonly found spatial configurations.

Since the ligand species are usually larger than the central ion, the latter is more or less completely shielded, with the result that its chemical properties are usually extensively modified.

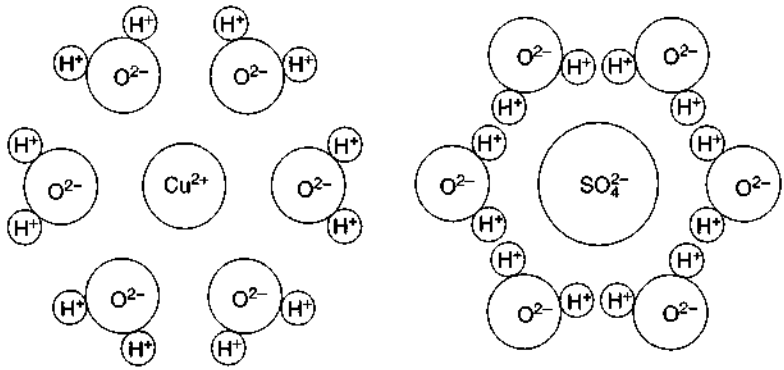

Figure 3.1 Formation of hydration sheaths around a positively and a negatively charged ion, as illustrated by copper (cation) and sulfate (anion).

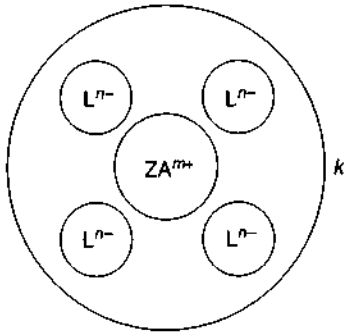

Figure 3.2 Schematic arrangement of a complex. ZA^{m+} is the central ion, L^- the ligands (m, n are the charge numbers, k can be positive, negative or uncharged) [1].

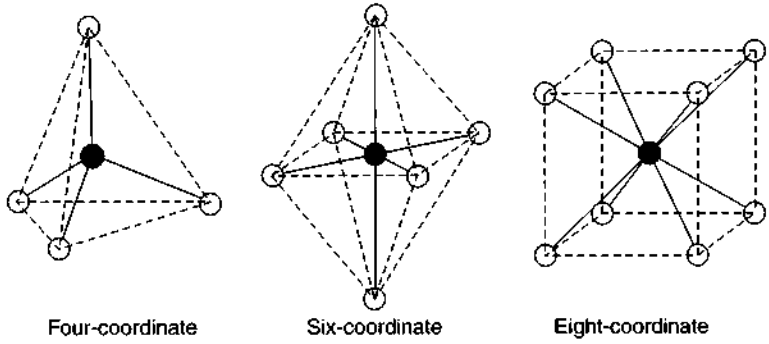

Figure 3.3 The most commonly found coordination structures of metal complexes (● = central ion, ○ = ligands) [2].

Many electrolytes used in Metal Finishing are based on complexes. A typical example would be potassium hexacyanoferrate(II), in which six CN ligands surround a central iron ion. The species dissociates as shown below:

$$K_4[Fe(CN)_6] \longrightarrow 4K^+ + \begin{bmatrix} & CN & \\ CN & & CN \\ & Fe & \\ CN & & CN \\ & CN & \end{bmatrix}^{4-} \qquad (3.1)$$

In addition to ligands which possess only one coordination site used in complex formation, there are other species with more than one coordination points allowing them to envelop the central ion. Complexes formed on this basis are known as 'chelated' and the ligands are known as 'chelating species' or 'chelants' (from the Latin, crab's pincers). Examples of these include ethylenediamine tetraacetic acid (EDTA) and ethylenediaminetetra-2-hydroxpropane (quadrol), with chemical formulae $\{(HOOC{-}CH_2)_2N{-}CH_2{-}CH_2{-}N(CH_2{-}COOH)_2\}$

or $\{CH_3CH(OH)CH_2)_2–N–CH_2–CH_2–N(CH_2CH(OH)CH_3)_2\}$. The structural formulae of these are shown below:

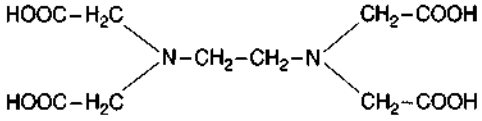

EDTA

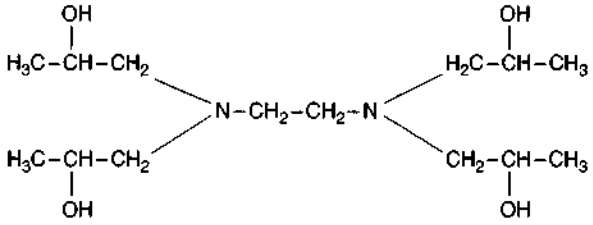

Quadrol

Using EDTA as example, it is seen that the two nitrogen atoms bond at two coordination sites, the four oxygen atoms of the acetate grouping bond at four coordination sites [3, 30].

3.2 Electrodeposition Electrolytes

The electrodeposition of metal coatings in industrial metal finishing is usually based on aqueous electrolytes, known in the industry as electrodeposition baths or simply, baths. Their primary constituent is the metal salt of the metal to be deposited, then in most cases an acid or alkali to promote conduction. In some cases the bath is buffered. In addition, there will be additives to promote the electrodeposition process or optimise the deposit properties.

The metal deposition is brought about either by current flow from an external power source, or by addition of a strong reducing agent, which sets up a coupled anodic and cathodic reaction. Depending on which of these is the case, the terms 'electrodeposition' or 'electroplating' or 'electroless deposition' are used (see Chapter 4). The term 'plating' usually refers to electroplating, but retains a degree of ambiguity.

3.2.1 Electroplating Electrolytes

Over the last few decades, hundreds of different plating baths have been developed to allow or optimise the deposition of metals or alloys. A useful means of characterising such baths is in terms of their operating pH. In terms of this, one has acid, neutral and alkaline baths, where the pH values are usually <3, ≈ 7 and >9, respectively. In the following, examples of each of these three are detailed. In all three cases, it is vital to avoid significant pH changes during the electrodeposition process. For this reason, all plating electrolytes have added acid, alkali or buffers.

3.2.1.1 Acid electrolytes

Acid electrolytes are usually based on simple metal salts such as sulfates or chlorides, less commonly are phosphates or sulfamates encountered. Also present is a high concentration of the parent acid, partly to optimise electrical conductivity, partly to minimise pH changes. The metal salts will dissociate as usual, into their constituent anions and cations. A typical example is the so-called 'acid copper' [4] typically constitutes as:

150–250 g/l copper(II) sulfate pentahydrate $CuSO_4 \cdot 5H_2O$
30–75 g/l sulfuric acid (d = 1.84 g/cm^3)
30–150 mg/l chloride (Cl^- ion)

The copper salt is the source of the metal ions. From a copper sulfate solution alone, copper deposits will be mossy, coarse-crystalline and brittle. Only after the parent acid is added will a compact, fine-grained and ductile deposit be formed. In addition, by increasing electrolyte conductivity, the process can be carried out at a lower voltage, reflecting a smaller ohmic drop in solution.

To this acidified sulfate solution, brightening additives are usually added (see Section 3.2.1.4.1), whose function is self-evident. Addition of chloride ions is critical for the correct functioning of such brighteners, and the concentration of this is usually in the range 30–150 mg. At chloride concentrations <20 mg/l, striated and rough deposits are formed. Above the higher limit, matt deposits are found and the covering power falls off (see Section 3.2.1.5.2).

This type of electrolyte is usually operated in the temperature range 20–45°C and at current densities of 1–20 A/dm^2.

Another example of an acid deposition bath is the high-chloride nickel electrolyte, typically of composition:

200 g/l nickel(II) chloride hexahydrate $NiCl_2 \cdot 6H_2O$
up to 100 g/l nickel(II) sulfate heptahydrate $NiSO_4 \cdot 7H_2O$
30–50 g/l boric acid, H_3BO_3

The pH in this system lies in the range 2.5–4 [5] with the boric acid as buffer to maintain a constant pH. Operating conditions are 40–70°C and deposition current density of 3–10 A/dm^2. There are also electrodeposition baths using organic or inorganic complexes as source of the metal ions. Thus, fluroboric acid $H[BF_4]$ is the basis of well-know fluroborate electrolytes, while hexaflurosilicic acid $H_2[SiF_6]$ is likewise the parent acid of flurosilicate baths [5]. In both cases, the metal is present in cationic form.

Equally, however, there are metal ion complexes where the metal is anionically charged [5]. These include hexavalent chromic acid (for chromium plating) and acid gold baths, based on the anion $[HCr_2O_7]^-$ and $[Au(CN)_2]^-$, respectively.

3.2.1.2 Neutral electrolytes

Under this heading are included systems which operate in the weakly-acid to weakly alkaline range. Since these are poorly conducting, they are not in common use. (hydrogen cations and hydroxyl anions have far the greatest electrolytic conductivity).

An important exception to this, however, are the neutral zinc plating baths, operating in the pH range 7.5–8.8. They contain two or more zinc-containing complexes, which must be maintained in a given concentration ratio. The first of these are complexes of ammonium chloride zincate, of composition $Zn[(NH_3)_2Cl_2]$ or $Zn[(NH_4)_2Cl_4]$, with the second category being zinc chelated with polyhydroxy-carboxylic acid.

Thus a typical composition of such an electrolyte would be [6]

26–52 g/l zinc (as the metal)
105–165 g/l chloride (as Cl^- ion)
45–90 g/l chelating agent

Another example of a neutral electrolyte is that used for electrodeposition of precious metals, which incorporate added salts to increase their conductivity. So a typical composition for a neutral (pH 6.8–7.5) gold bath might be [7]:

7 g/l gold (as the potassium dicyanoaurate(I), $K[Au(CN)_2]$)
7 g/l copper (as potassium cyanocuprate(I) $K_2[Cu(CN)_3]$)
28 g/l sodium dihydrogen phosphate NaH_2O_4

This bath is used at 65–75°C with a deposition current density of 0.5–1 A/dm^2. One final example of a neutral electrolyte is that for forming gold–palladium–nickel alloys in which both cationic and anionic metal ion complexes are present as $[Pd(NH_3)_4]^{2+}$ or $[Ni(NH_3)_6]^{2+}$ and $[Au(CN)_2]^-$ or $[Au(SO_3)_2]^{3-}$ [5].

3.2.1.3 Alkaline electrolytes

This category is best sub-divided as cyanide-containing and cyanide-free types. It might be noted here that in both cases, alkaline electrolytes react slowly with carbon dioxide in air to form alkaline metal or other metal carbonates. Anything that increases electrolyte-to-air contact, such as agitation or air-sparging, will accelerate the rate of carbonate formation. Above a certain concentration, carbonates in solution will adversely affect the metal deposition process and will have to be removed, using either a physical or chemical approach.

3.2.1.3.1 Cyanide-containing electrolytes

Electrolytes are designated as 'cyanide-containing' when they contain significant amounts of so-called 'free cyanide', that is, an excess of the simple KCN or NaCN. This will dissociate in solution, to form the constituent ions. It is vital that such solutions be at all times kept sufficiently alkaline, for if this is not so, HCN, the deadly hydrocyanic acid will form and be liberated in gaseous form (also known as 'Prussic acid gas'). In fact, accidents due to this are extremely rare. In spite of this, metal finishers are under on-going pressure to replace cyanide-based processes with those not containing this species.

Citing an example, such as cyanide copper solution [4], is helpful.

The copper(I) cyanide, CuCN, which acts as the source of the metal, is not soluble in water, but can be made so by addition of an alkali metal cyanide (NaCN or KCN).

This leads to the formation of a cyanide complex, as:

$$CuCN + 2NaCN \rightarrow Na_2[Cu(CN)_3] \quad (3.2a)$$

$$CuCN + 2KCN \rightarrow K_2[Cu(CN)_3] \quad (3.2b)$$

Dissociation of the complex salt sodium (or potassium) tricyanocuprate(I) takes place as shown:

$$Na_2[Cu(CN)_3] \rightarrow 2Na^+ + [Cu(CN)_3]^- \rightarrow 2Na^+ + Cu^+ + 3(CN)^- \quad (3.3a)$$

$$K_2[Cu(CN)_3] \rightarrow 2K^+[Cu(CN)_3]^{2-} \rightarrow 2K^+ + Cu^+ + 3(CN)^- \quad (3.3b)$$

It follows that the presence of a significant amount of 'free cyanide' (as the sodium or potassium salt) as well as free alkali are necessary for the functioning and safe operation of this system, not just to solubilize the copper cyanide, but also for the following reasons:

(a) Cyanides will slowly break down, either by anodic oxidation or homogeneous or heterogeneous (catalysed) air oxidation. Alkali is removed, as explained above, by carbonate formation.

(b) If there is insufficient free cyanide to solubilise the copper salt, the anodes will become encrusted with the insoluble metal cyanide, their rate of dissolution will be reduced and the electrolyte may become depleted of copper ions. In some cases, because the effective anode area is reduced, the current density will increase and polarisation or passivation may occur.

(c) In the absence of sufficient cyanide in solution, the electrodeposited copper will be powdery rather than forming a dense adherent layer.

A typical cyanide copper electrolyte (low copper type) would have the following composition:

25 g/l copper(I) cyanide CuCN
30 g/l sodium cyanide NaCN
3 g/l sodium sulfite Na_2SO_3
6 g/l sodium carbonate Na_2CO_3

Such a bath operates at pH 12, at a temperature of 20–30°C and a current density of 2–2.5 A/dm^2. The particular characteristics of this electrolyte lend themselves to copper-plating of undercoats on zinc diecastings.

A similar copper electrolyte, but with higher copper content, is made up as [8]:

270 g/l potassium tricyanocuprate(I) $K_2[Cu(CN)_3]$
10–30 g/l sodium cyanide NaCN
10 g/l potassium cyanide KCN
5 g/l sodium sulfite Na_2SO_3
5 g/l sodium hydroxide NaOH

This electrolyte too, has pH 12, and will also include brightening additives. It would normally be operated at 65°C and at a current density of 1.5–4 A/dm^2.

Table 3.1 Composition of alkaline cyanide zinc plating baths [6, 9].

Constituents	Concentration [g/l]		
	High cyanide	Medium cyanide	Low cyanide
Zn	30–50	15	17–15
NaCN	75–150	40	10–30
NaOH	75–150	90	80–150

Other examples of alkaline cyanide baths are used for deposition of zinc, silver and gold. In the case of zinc, cyanide electrolytes are categorised as low, medium or high cyanide. Typical compositions for these are shown in Table 3.1.

In many cases, some 25–30 g/l of sodium carbonate is also added, to increase bath stability, and small quantities of sulfides may be added, in order to precipitate out, as the highly insoluble metal sulfide, any metallic impurities.

Of the greatest importance, when operating cyanide zinc solutions, is not only the zinc ion concentration, but also the ratio of NaCN and NaOH to the zinc ion concentration, in order to ensure uniform thickness distribution. In practice, one uses the so-called '*M*-factors', which are defined as follows:

$$M_{CN} = \frac{NaCN}{Zn}$$

$$M_{OH} = \frac{NaOH}{Zn}$$

Such *M*-factors can be used to determine the trade-off between highest useable current density and optimum throwing power. Thus, a high M_{CN}- factor, that is, high NaCN content, implies a lower useable current density but good throwing power (see Section 3.2.1.5.3). Thus, when zinc plating components of complex geometry or with pronounced profiles, a high M_{CN} factor is desirable. By contrast, a high M_{OH} factor, that is, high NaOH concentration, is preferred when high deposition rates are desired, even at the expense of covering power [9].

Being able to 'fine tune' such zinc electrolytes for a particular application is thus a useful attribute. In addition to examples of cyanide electrolytes cited above, one might also list those in use for deposition of a range of alloys, including copper–zinc, copper–tin, gold–copper–cadmium or gold–copper–zinc [5].

3.2.1.3.2 Non-cyanide alkaline electrolytes

Under this heading, one could list a range of zinc baths used for rack or barrel plating of small parts. Cited compositions for such electrolytes are 12–14 g/l zinc and 120–160 g/l NaOH, or 11–13 g/l zinc and 110–150 g/l NaOH [9]. The optimum ratios of NaOH to zinc are 8–10. The higher the zinc and NaOH concentrations, the higher the current efficiency, other things being equal.

These cyanide-free alkaline zinc electrolytes lack the stability of their cyanide-containing counterparts, and are mainly used where (for whatever reason) it is desired to avoid the use of cyanides, but without sacrificing the benefits of uniform

deposit thickness distribution. These systems are usually operated at 18–35°C and at a deposition current density of 0.5–6 A/dm^2 [9].

3.2.1.4 Electrolyte additives

In addition to metal salts, electrodeposition electrolytes usually contain various other species. Thus both inorganic and organic salts, acids or alkalis will be added to increase electrolyte conductivity. Other species, both organic or inorganic, may be added for specific purposes, for example, to increase bath stability, or improve levelling or metal distribution, or to optimise the chemical, physical or technological properties of the deposited metal (corrosion resistance, brightness or reflectivity, hardness, mechanical strength, ductility, internal stress, wear-resistance or solderability).

In working with such additives, it should be recognised that they are often effective over only a defined concentration range, and should their concentrations fall outside this range, all kinds of problem can arise either in the deposition process or the deposit properties. In the following sections, such addition agents are considered in greater detail.

3.2.1.4.1 Brightening agents

In metal finishing, bright or highly reflective surfaces (the terms are usually synonymous) can be of both decorative and functional importance, if for no other reason that bright surfaces require less mechanical finishing, after plating, if indeed any at all.

Defining brightness or reflectivity of a surface as the extent to which incident light is reflected, it follows that surface roughness and unevenness are antithetical to good reflectance. Reflective surfaces are characterised by a crystallite size at the surface of less than 0.3 μm^2. Thus, highly reflective deposits are found under conditions where fine-grained deposits are formed. To achieve this, it is long-established practice to add metallic or organic compounds, known as brighteners or brightening agents. Their use is based on empiricism, there being no certain means of predicting their effects. In the same way, selecting the most appropriate such compound(s) will usually be based on trial-and-error.

Two different types of brightener are recognised, the first being brightener carriers, the second, brightener additives [10–12].

Addition of brightener carriers, also known as primary brighteners or Class I brighteners, leads to a significant grain refining action in the deposited metal. While this greatly increases the brightness of the metal, it will not impart a mirror-finish or anything close to this. Among the best-known brighteners of this type are [13]

- sulfonamides
- sulfonimides
- benzenesulfonic acids (mono-, di- or trisulfonic acids)
- napthalenesulfonic acids (mono-, di- or trisulfonic acids)
- alkylsulfonic acids
- sulfinic acids
- arylsulfonesulfonates.

These primary brighteners are essential components of a complete brightening system, in that they reinforce the efficacy of Class II or secondary brighteners, the

Table 3.2 Some commonly used brighteners [14].

Designation	Structural formula
Thiourea	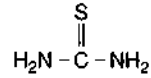
Acylthiourea	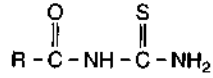
Mercaptoalkylsulfonic acid	$HS-C_nH_{2n}-SO_3H$
Bis-(sulfoalkyl)-disufide	$[S-C_nH_{2n}-SO_3H]_2$
Thiocarboxylic acid amide	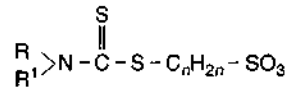
Thiocarbazone	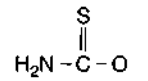
Thiosemicarbazone	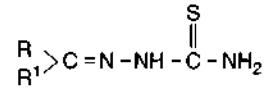
Thiohydantoin	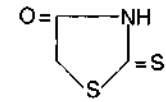

latter being rarely used without the former. Class II brighteners, even at very low concentrations, impart a near-mirror finish to the deposited metal. The most important of these are listed in Table 3.2.

Out of a very large number of potential Class II brighteners, only a few are used in practice, largely because – although many such species are highly effective in their brightening action, they can adversely affect process or deposit properties in other ways. In order to minimise this, secondary brighteners are usually employed with a primary brightener in a combination known for the compatibility and synergy of both.

A number of electrolytes form bright deposits only in a comparatively narrow temperature and current density operating window. Figure 3.4 shows this for chromium deposition.

As Fig. 3.4 shows, at any given temperature, a range of current densities exists, within which bright deposits can be formed. Alternatively, at any given current density, there is range of temperatures in which the same is true. Figure 3.4 is valid only for a particular chromium electrolyte system, and depending on concentrations of species used, and the catalyst, similar diagrams can be drawn, though the general shape of these is similar. At a given temperature, the widest possible range of operating current densities is desirable, especially when items of complex geometry or with deep profiles are involved, as in such cases, there will be marked variations in

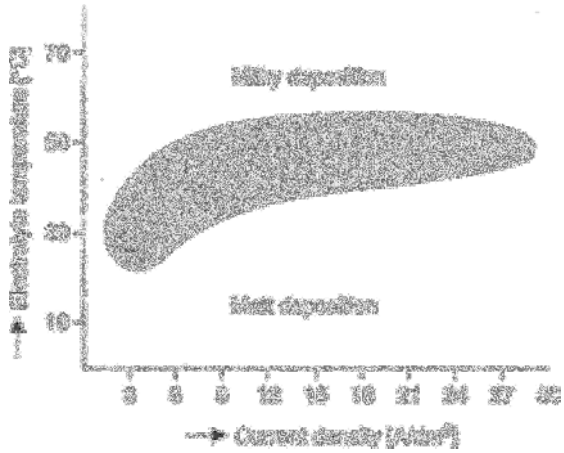

Figure 3.4 Operating window for bright chromium deposition as function of deposition temperature and current density [8, 15].

current density at different locations on the work. An approach such as that shown in Fig. 3.4 is essential in ensuring that bright deposits are formed over the entire surface, however complex this might be.

There are many theories to explain the brightening action of this class of additive. Most probably, the effect is due to a controlling effect, and perhaps a rate-limiting action, on the electrocrystallisation step. Such theories link with the accepted mechanism for metal electrodeposition, based on a nucleation and growth at a series of centres. From the growth nuclei, grains develop with a range of sizes and orientations. It is assumed that the brighteners are preferentially adsorbed on the developing growth peaks, thereby inhibiting further growth at these points. Having no alternative, the electrocrystallisation is forced to continue in the valleys rather than the peaks, whereby a levelling action results. The end result is a smooth and shiny surface. It follows that brightening is associated with a levelling action as well.

3.2.1.4.2 Levelling agents

Either before or after electroplating, it may be necessary for the work to be mechanically finished, using grinding, then polishing stages, and these can significantly add to the overall cost [16], especially when the deposited metal is hard, for example, hard chromium. Levelling agents can act to smooth pre-existing irregularities in the surface, such as pits or scratches and thus they compensate for poor surface quality of incoming work.

The levelling action of an electrolyte, that is to say its ability to form a smoother surface than that of the original substrate, is defined as 'levelling power' [11, 17–19]. By levelling action is implied the deposition of a greater thickness of metal in the depths of a groove than at its outer edge. This can be quantitatively expressed as:

$$E = \frac{d_t - d}{R_z} \cdot 100\% \tag{3.4}$$

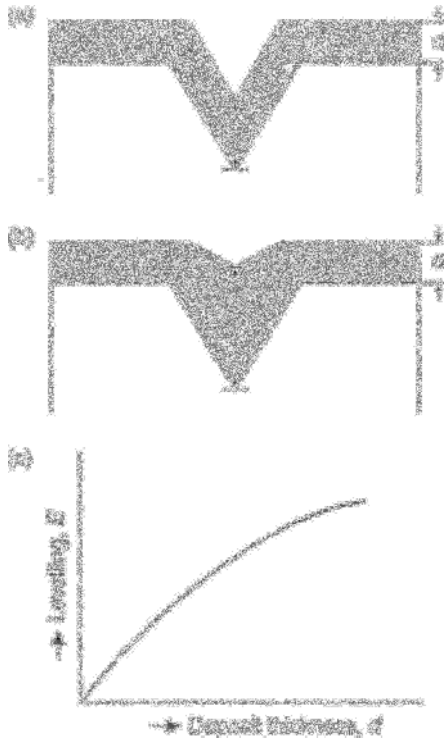

Figure 3.5 Illustration of levelling action: (a) geometric levelling; (b) true levelling; (c) levelling as function of deposit thickness.

In Eqn (3.4), E is the levelling effect, d_t the deposit thickness at the base of the groove, d the overall deposit thickness and R_z the roughness of the substrate.

A distinction is made between geometric and true levelling. In the former case, the key factor is that the deposit is thicker at the bottom of a groove than at the edge (Fig. 3.5a). The effect is measured in terms of the geometry and shape of the groove. The hallmark of true levelling is a higher metal deposition rate in the groove than at the adjacent areas (Fig. 3.5b) and this results when the so-called levelling agents or levellers are added to the electrolyte. The manner in which these additives work is by restricting the rate of metal deposition, but only at those locations where they are freely supplied, specifically at peaks and edges. The levelling action of such species can vary quite widely, apart from which it is usually temperature dependant and can often be enhanced by work movement or solution agitation. Levelling action is a function of deposit thickness and increases as thickness increases (Fig. 3.5c).

Certain electrodeposition electrolytes are specially effective in their levelling action. These include bright nickel, whose levelling action is shown in Fig. 3.6. On a polished surface of a copper–zinc alloy, grooves were formed using a scribing diamond with loading 0.5 N. Onto this scribed surface, bright nickel was deposited at 58°C, pH 4.0 and a cathodic current density of 4 A/dm^2.

From this sequence of cross-sections, it can be seen that as a result of the pronounced levelling action of the bright nickel, deposition occures initially in the

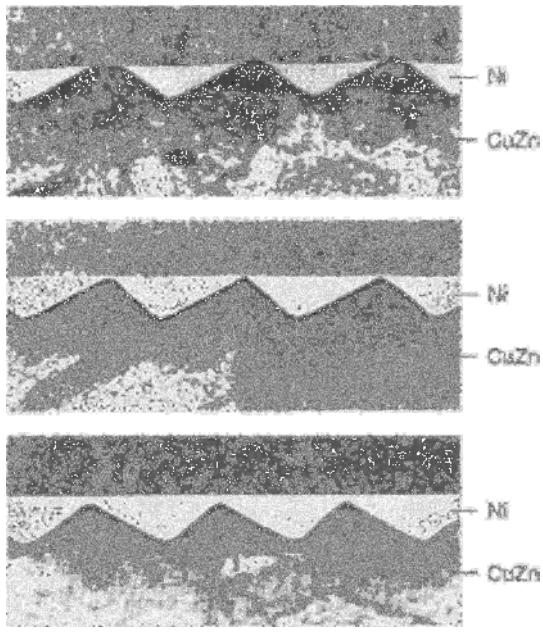

Figure 3.6 Dependence of bright nickel levelling action on deposition time. From top down, 7, 14 and 21 min V = 350:1 [5].

grooves. The levelling effect increases as the deposit thickness grows so that, after sufficient time, the troughs and peaks have been effectively levelled.

A negative levelling action is defined as a situation where less metal is deposited in the depths of a groove than at the outer surfaces, that is to say that the electrodeposition enhances the surface roughness. This effect is observed with some cyanide electrolytes.

3.2.1.4.3 Surfactants (wetting agents)

Plating baths will usually contain wetting agents, also known as surfactants. These are characterised by their asymmetry and dipolar nature (•–). They have a hydrophilic ('water loving') 'head' (•) and a hydrophobic ('water-repellent') 'tail'⁻. Surfactants can be 'anionic', 'cationic' or 'non-ionic' depending on the charge at the hydrophilic end. The polar hydrophilic radicals are typically $-COO^-$ or $-SO_3^-$ groupings, while the hydrophobic part of the molecule might be a non-polar aliphatic long-chain hydrocarbon [20, 21]. Non-ionic surfactants are themselves uncharged, acquiring their charge from ions present in aqueous solution [17].

Wetting agents are surface-active species, that is, they act by accumulating at a surface or interface. At an air–electrolyte interface, they are oriented with hydrophilic head into solution, the hydrophobic tail to the air-side. In this way they reduce the surface tension of a liquid.

Chromium plating afford a good example of the working of such wetting agents. In this process, chromium deposition is accompanied by a substantial evolution of hydrogen gas at the cathode (work) surface. These bubbles rise to the electrolyte surface and there explode, thereby forming a mist of the chromic acid

Table 3.3 Classification of surface-active agents (n = 10–20; m = 8–16; o = 5–20) [20].

Type	Hydrophilic grouping	Example	Designation
Anionic	$-COO^{\ominus}$	$CH_3-(CH_2)_n-COO^{\ominus}$ with $Na^{\oplus}$: basic soap; with K^{+}: lubricating soap	Soaps
	$-O-SO_2-O^{\ominus}$	$CH_3-(CH_2)_n-O-SO_2-O^{\ominus}$	Fatty alcohol sulfates
	$-SO_2-O^{\ominus}$	$CH_3-(CH_2)_n-SO_2-O^{\ominus}$	Alkyl sulfonates
		$CH_3-(CH_2)_m-C_6H_4-SO_2-O^{\ominus}$	Alkylarylsulfonates
Cationic	$-N^{\oplus}(CH_3)_3$	$CH_3-(CH_2)_n-N^{\oplus}(CH_3)_2\ Cl^{\ominus}$	Alkyltrimethyl-ammoniumchloride
Amphoteric, zwitterionic	$-N^{\oplus}(CH_3)_2-CH_2-CO-O^{\ominus}$	$CH_3-(CH_2)_n-N^{\oplus}(CH_3)_2-CH_2-CO-O^{\ominus}$	N-alkylbetain
Non-ionic	$-O-(CH_2-CH_2-O-)_L-H$	a) $CH_3-(CH_2)_m-O-(CH_3-CH_2-O-)_L-H$	Polyethyleneglycol adducts of  with (a) alkyl alcohols (b) alkyl phenols (c) fatty acids
		b) $CH_3-(CH_2)_m-C_6H_4-O-(CH_2-CH_2-O-)_L-H$	
		c) $CH_3-(CH_2)_n-C(=O)-O-(CH_2-CH_2-O-)_L-H$	

electrolyte[1], which is extremely hazardous to health, and indeed to nearby equipment. As a result, powerful air-extraction facilities are essential. If, however, a wetting agent is added, usually a fluorinated type capable of withstanding the powerful oxidising action of chromic acid, the surface tension will be reduced from, typically 70 to 20 mN/m and the extent of chromic acid mist formation is greatly reduced [22]. At the same time, a thin and compact layer of foam is formed at the surface which substantially reduces evaporative losses from the electrolyte.

Wetting agents or surfactants also build up at the solid–liquid interface of the work, immersed in the electrolyte. The hydrophilic groups are hydrated and drawn towards the aqueous phase, with the hydrophobic end being weakly adsorbed onto the work surface. With this degree of ordering imposed at the interface, the interfacial tension is reduced, that is, the work surface becomes more easily wetted by the electrolyte, with several resulting benefits to the electrodeposition process.

In metal finishing, anionic or non-ionic surfactants are most often used. The lowering of surface tension facilitates the release of gas bubbles adhering to the work surface, whether these be cathodically evolved hydrogen or trapped air. Where such bubbles adhere to the surface, their shielding action results in little electrodeposition occurring and they can be the cause of pitting or deposit porosity. Table 3.3 gives a classification of surface-active agents.

[1] Hexavalent chromium compounds are toxic and carcinogenic.

Addition of surface-active agents also results in the following:

- certain organic compounds, insoluble or poorly soluble in water can be solubilised or their distribution in solution made more uniform;
- coagulation and sedimentation of suspended solid matter as dirt in solution which would otherwise lead to rough or porous deposits, is reduced;
- crystal growth is inhibited and a brightening action of the deposit results;
- draining of adherent electrolyte, on withdrawing the work from solution is improved, drag-out losses are reduced.

It should be noted that the type of surface-active agent best used is very much linked to the particular electrolyte employed, and a poor choice can result in all manner of adverse consequences in process operation. Maintaining the optimum concentration is also critical. If too low, some or all of the benefits listed above may not come into play, while if too high, the deposit properties may be adversely affected. Finally, the choice of wetting agent may be influenced by the type of electrolyte agitation being used, whether air-sparging, work-movement or eductor.

3.2.1.5 Electrolyte properties

The aim of the electrodepositor will usually be to form dense, uniform and adherent metal coatings. Of the countless factors which are important for this, the electrolyte and its properties are vital, and this is discussed below.

3.2.1.5.1 Electrolytic conductance

Whereas, in a metal, electric current flows by means of free electrons, the passage of current in an aqueous solution of ionised species is due to the migration of ions, molecules or atoms bearing a positive or negative charge. In some important aspects, these two mechanisms behave differently, and conduction of the latter type is therefore known as electrolytic conductance, as opposed to electrical conductance found in a metal. Electronic conductors are sometimes known as Class I conductors, electrolytic conductors as Class II. Worth noting that under a wide range of conditions, both types of conductors obey Ohm's law. Arguably, the key feature of aqueous electrolytes is that the compounds dissolved in them, have partly or completely ionised. It is by the movement of such charged ions that electric current can be passed through the solution. For further details and data, see Refs. [8, 23]. The key issues are the degree of dissociation of the dissolved species in solution, and the so-called ionic mobility, reflecting the fact that under a given potential gradient, some ions travel faster than others, and are thus a more effective means of carrying charge.

In broad terms, it is usually assumed that inorganic acids, alkalis and metal salts are close to 100% dissociated (see Table 3.4), metal salts of organic acids, such as copper acetate, are partly dissociated, while, for example, organic acids range from being highly dissociated (formic, acetic) to being almost undissociated (butyric, oleic acids).

Ions formed by dissociation of the parent species travel across the electrolyte between anode and cathode, under the influence of the potential gradient established by application of a voltage. Cations (positively charged) travel to the cathode (the negative pole) and anions, negatively charged, move in the opposite direction to

Table 3.4 Degree of dissociation of selected acids and salts.

0.1 N solution of	Degree of dissociation [%]
H_2SO_4	96
HNO_3	92
HCl	91
H_3PO_4	81
NaOH	80
KOH	73
$ZnCl_2$	24
Na_2SO_4	13
NaCl	12
$ZnSO_4$	0.17
$CuSO_4$	0.01

Table 3.5 Ionic mobility values for selected ions.

Ion	v [cm/h]
H^+	11.34
OH^-	6.01
Cl^-	2.25
K^+	2.18
SO_4^{2-}	2.13
NO_3^-	2.09
Ag^+	1.76
Fe^+	1.73
Na^+	1.32
Cu^{2+}	1.04

the anode. Their ionic mobility is defined as rate of travel (in cm/s) under unit potential gradient (volt/cm = 1). It should be noted that since all ions in aqueous solution carry a hydration sheath, what is actually measured is the rate of travel of the hydrated ion. This explains why, for example, in the alkali metal series, the larger ions such as Rb^+ travel faster than the apparently smaller ions such as Li^+, the reason being that the latter carries a larger hydration sheath.

A selection of ionic mobility values is shown in Table 3.5. It will be noted that the hydrated proton and hydroxyl ions have the highest mobility values, and this is due to the fact that, for these two species, an additional charge transport mechanism operates. It should be emphasised that the foregoing description is greatly simplified. Factors such as solution viscosity (itself linked to temperature) and ionic activity (a measure of concentration, but corrected for other effects) are also important.

In terms of the simplified theory presented here, one might expect a solution undergoing electrolysis to become depleted, as ever more anions migrate in one direction to the anode, and cations to the cathode. In practice, such effects are only significant under very special conditions. Working against ionic depletion are effects such as solution agitation (including natural convection) and diffusion under the effect of a concentration gradient (Fick's law). Chapter 4 provides further insights.

Table 3.6 Specific conductivity of selected electrolytes [19].

Electrolyte	$\chi \times 10^{-5}$[m/Ω mm^2]
Zinc, sulfuric acid	0.49 (at 25°C)
Nickel	1.04 (at 50°C)
Copper, sulfuric acid	1.10 (at 25°C)
Copper, cyanide	2.15 (at 60°C)
Zinc, cyanide	2.52 (at 25°C)
Chromium	6.57 (at 50°C)

These explain the apparent paradox that chromium can be electroplated (at a cathode) from hexavalent $Cr_2O_7^{2-}$ ions when in fact one might expect such ions to be repelled from a cathode.

For electrolytes, as for metallic or inorganic conductors, the concept of specific conductivity, χ or its reciprocal ρ, specific resistivity, is useful. These can be visualised as the conductivity (or resistivity) of a cube of the material or liquid, to which Ohm's law is applied, that is, current is measured across opposing faces of the cube under a voltage gradient of 1 V/cm. Conductance is thus expressed as (m/Ω mm^2) or (mS/cm) where S (the siemens) = [1/Ω]. Some examples of specific conductivity are given in Table 3.6.

It is seen that the electrical conductivity of metals, for example silver, with $\chi = 63$, and copper with $\chi = 60$ is of order 10^6 higher than the best conducting electrolytes. Thus, 30% sulfuric acid solution at 18°C has a conductivity 800.000 times lower than copper.

In order to increase the conductivity of electrodeposition baths, acids or alkalis or salts are often added, and these are known as 'supporting electrolytes'. In the case of acid electrolytes, chloride and acids are used for this purpose, with chlorides alone being used with neutral solutions and, for alkaline solutions, sodium hydroxide or cyanide.

In order to compare the conductance of several electrolytes, a rational basis for doing so must be established. In practice, this is done by comparing values for 1 M solutions (also known as c_{Mol}) or as c_{Ae} the molar equivalent concentration.[2] In the first case, molar conductivity is expressed as:

$$\Lambda_m = \frac{\chi}{c_{Mol}}[\mathrm{cm^2/\Omega \cdot mol}] \tag{3.5}$$

and in the second case as the equivalent conductance χ_{Ae}

$$\Lambda_{Ae} = \frac{\chi}{c_{Ae}}[\mathrm{cm^2/\Omega \cdot val}] \tag{3.6}$$

The conductivity of an electrolyte is a function of the degree of dissociation, the mobility of the individual ions, the temperature (and thus viscosity) and the electrolyte composition. It should be noted that not only the ionic mobility but also the charge carried by each ion, as well as their concentrations. The hydration sheaths on

[2] The equivalent weight of an atom is its atomic weight divided by valence value.

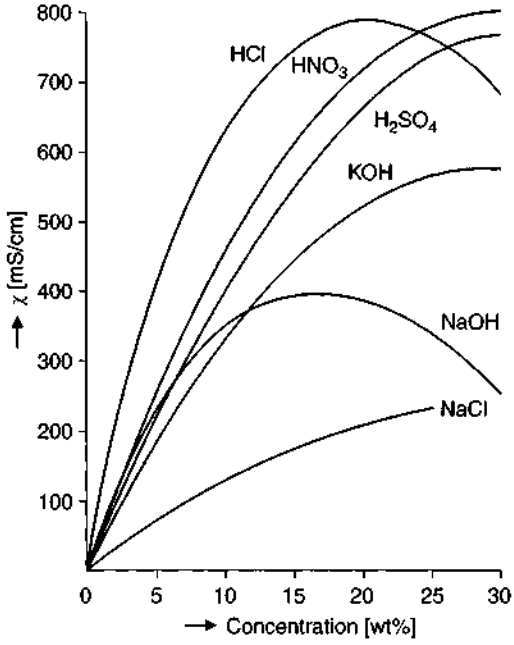

Figure 3.7 Conductivity of various electrolytes as functions of their concentration [24].

the ions play no part in the overall charge transport process. Some values for specific conductivity of selected electrolytes are plotted versus their concentrations in Fig. 3.7. It is seen that conductivity initially increases with concentration, after which a maximum value is reached. In the gradients of these plots and also the concentration values at which maximum conductivity is reached, there are significant differences between the various species shown.

The reason why, at higher concentrations, the linear relationship between conductivity and concentration breaks down, is ascribed to electrostatic interactions between neighbouring ions. These become more significant as concentration increases and this interaction decreases the effective rate of ionic mobility.

The marked decrease in conductivity at the highest concentrations is due to the greater coulombic forces acting between the ever-closer ions in solution. This can lead to a loose association of oppositely charged ions, which are effectively neutral and thus no longer contribute to the overall solution conductivity.

While, in principle, the electrolytic conductivity of a solution has no effect on the properties of the deposited metal, in cases where it is too low, certain adverse effects will appear. These include:

- Primary current distribution deteriorates, with the result that disproportionately heavy deposition occurs at leading edges and corners of the work. More generally, the outcome is less uniform metal distribution.
- Because the resistance is higher, more heat will be generated by the passage of the same current through the electrolyte (i^2R effect), the result being

increased electrical energy required, and perhaps more cooling of the solution being necessary.

High concentrations of alkali metal or alkaline earth metal cations, as well as cationic impurities in solution, all adversely affect solution conductivity.

3.2.1.5.2 Covering power

The term 'covering power' is used to describe the extent to which an electrodeposition electrolyte can cover the entire surface of an object being plated, with reasonably uniform thickness, including at least some deposition in recesses and cavities.

It is accepted that metal deposition begins only above a certain deposition potential, the value of which depends on the surface, and the metal being deposited. For an electrodeposition bath to exhibit covering power, the so-called minimum covering-power current density must be applied.

Estimation of covering power is frequently determined using the so-called Hull cell, named after its American inventor [DIN 50957, 5, 17]. As Fig. 3.8 shows, this is a miniature electrodeposition tank, but one in which the cathode is angled with respect to the anode. As a result, when a voltage is applied across the anode and cathode, the resulting current density will vary along the length of the cathode, being highest at the point it is closest to the anode. In this way, one can, within a single test run, assess the effect of varying current density. After such a run, the cathode is removed and inspected. At the highest current densities, the deposit may be burned. At the lowest current densities, no deposition may be observed. Thus the Hull cell allows the determination of the so-called 'operating window', the current density range over which acceptable deposition occurs. An electrolyte is said to have good covering power when satisfactory metal deposition extends into the lowest current density range.

Covering power is largely a reflection of the energy of nucleation at the work surface. Among the parameters affecting it, are the nature of the substrate surface, its composition and the operating conditions. Covering power usually increases with increasing current density and decreases with increasing temperature.

Covering power is specially important in the case of chromium plating, since it is generally poor for this metal anyway. A uniform deposit will result only when high

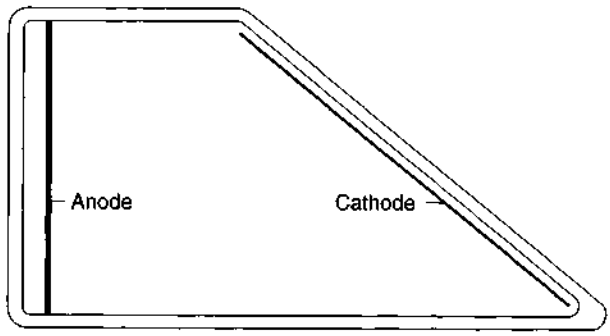

Figure 3.8 Hull cell for experimental determination of covering power of electroplating solutions.

current densities are used and total current densities can be up to 100% greater than the actual chromium deposition current density [19] with copious co-evolution of hydrogen. Typically, a uniform chromium deposit will form in 1–3 min. Further deposition is then carried out at reduced current density.

In general, alloy steels with high carbon content as well as cast iron and aluminium and its alloys all require relatively high current densities to achieve covering, as compared with unalloyed steel, copper and nickel [19].

3.2.1.5.3 Macro-throwing power

In the electrodeposition of metals, the depositing metal film does not grow uniformly at the same rate across the surface, reflecting the various factors which influence the rate of crystal growth.

Macro-throwing power is a term used to describe the ability of an electrolyte to lay down as nearly as possible, a uniformly thick deposit across the surface of an object. The more this is so, the better the throwing power, and thus throwing power can be used as a predictor for the uniformity of a deposit. It will be clear that good covering power is a pre-requisite for good macro-throwing power.

The macro-throwing power of an electrolyte is a manifestation of the extent of primary and secondary current density distribution in the system [17, 19].

Primary current distribution is the outcome of Ohm's law, applied to the dimensions and geometry of the spatial anode–cathode configuration and the shape of the electrolyte container. As seen in Figs. 3.9(a) and (b), there is a concentration of electrical lines of force at edges, points and corners. The result is a higher current density at these points and, in most cases, heavier deposition. The higher the electrolyte resistance, the greater such enhanced effects at edges, etc., will be. The parallel field lines shown in Fig. 3.9(c) are never achieved in practice.

Secondary current distribution reflects the electrochemical behaviour of the system, mainly in terms of the overvoltage at the cathode (polarisation). This is total overvoltage, and thus includes the various types of overvoltage which impede the rate of metal deposition. Overvoltage, or polarisation, is thus an expression of the difference between actual potential and the theoretical, reversible potential under conditions of current flow. The higher the overvoltage, the more uniform is metal distribution and anything that results in increased overvoltage will thus result in

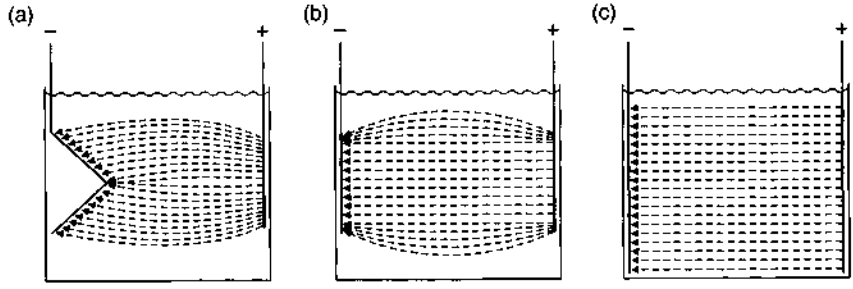

Figure 3.9 Primary current density distribution as a function of the electrical field between anode and cathode.

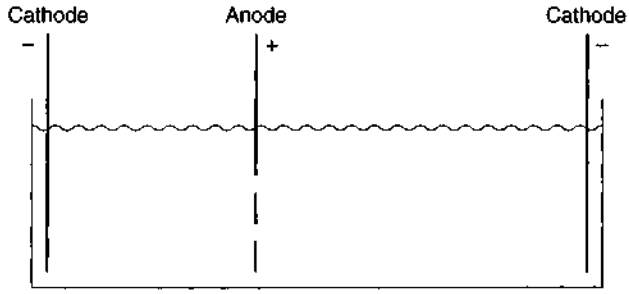

Figure 3.10 Haring–Blum cell for experimental determination of throwing power of electrodeposition electrolytes [25].

more uniform current density. Included in such effects are electrolyte composition, electrical conductivity and electrolyte agitation as well as deposition current density.

The experimental determination of macro-throwing power can be made either using a Hull cell or a Haring–Blum cell (Fig. 3.10).

A rectangular, open-topped electrolyte container is equipped with two cathodes, one at each end, of the same size, shape and material. Between these, is positioned an anode made of perforated mesh or similar construction. This anode is placed closer to one cathode than to the other, typically 1:5 in terms of the two anode–cathode spacings. The aim, though it is never completely achieved, as a result of edge-effects, is to replicate the uniform field shown in Fig. 3.9(c).

Assuming that the electrolyte resistances in the two compartments reflect the respective anode–cathode spacings, and are thus 1:5, one would expect, on the basis of primary current distribution effects, five times more metal distribution at the cathode of the shorter of the two compartments. In such a case, the macro-throwing power would be taken as zero. In practice, various electrolyte effects intervene and rather different values are obtained. These alter the amount of electrodeposited metal on the more distant cathode and result in positive values of macro-throwing power. Macro-throwing power is defined using the equation

$$S = \frac{L - M}{L + M - 2} \cdot 100\% \tag{3.7}$$

where S is the throwing power, L the distance between anode and cathode and M the ratio of deposited metal on the nearer and farther cathodes.

It should be noted that two Haring–Blum cells, each with anode positioned in the ratio 1:5 vis-à-vis the two cathodes, but of different total length will give different results. Some authors, especially when using poorly conducting electrolytes, advise against perforated anodes, since current can flow through the perforations, creating spurious effects. Instead, a planar anode giving a seal between the two electrolyte compartments is suggested.

For cyanide- or sulfuric acid-based copper electrolytes, this method gives values of 25–30% and 2–5%, respectively [26] showing that cyanide copper electrolytes have a macro-throwing power far superior to that of acid copper. In general, it can be

asserted that complex-type electrolytes and those containing brightening additives have good macro-throwing power. Thus, in the case of copper plating components with complex geometry, cyanide copper or cyanide-free alkaline copper are the electrolytes of choice, where a uniform deposit is desired.

In practice, it is clear that the uniform electrical field which the Haring–Blum cell sets out to create, is rarely achieved. The electrical field is distorted by the shape of the work being plated, and by the means by which the work is attached to the racks, the configuration of anodes, etc. In practice, despite its poor performance in the Haring–Blum cell, a satisfactorily uniform deposit can be obtained using an acid copper electrolyte.

A far more challenging situation, in terms of macro-throwing power, is found with hexavalent chromium electrodeposition [25], which is inferior even to acid copper. In some cases, this requires that the chromium be electroplated from the trivalent electrolyte. In this case too, electrolyte agitation and increased temperature can lead to reduced macro-throwing power.

3.2.1.5.4 Micro-throwing power

Given that many components being electroplated have far from perfectly smooth surface, micro-throwing power is important. This is the extent to which metal electrodeposition occurs at the outer plane of the substrate or at the base of valleys or cracks. In principle, electrodeposition at these latter sites is hindered, in that access of fresh electrolyte and dispersal of exhausted electrolyte are hindered. Micro-throwing power becomes important in such situations, and is an expression of tertiary current distribution. The less metal that is deposited on peaks and outer planes, the better is the micro-throwing power. Micro-throwing action is achieved by preferentially activating the metal surfaces at the base of cracks or valleys, ensuring that those species which promote electrodeposition are concentrated there, while at the same time inducing inhibitors to adsorb at the outer surfaces [27]. In many cases it is found that micro-throwing power is inversely related to macro-throwing power. When the one is good, the other is not, and vice versa. Micro-throwing power thus acts to bring about a levelling (see also Section 3.1.4.2).

3.2.2 Electroless Deposition Electrolytes

Electroless deposition, also known as chemical deposition (see Chapter 4) is brought about when, to an electrolyte similar to those used in electroplating, a chemical reducing agent is added. Metal ions are thus reduced to metal at the surface of the work, not by externally applied current, but by the oxidation of the chemical reductant at the metal surface [31].

Examples of such systems include the widely used electroless nickel, where the deposited nickel includes a significant amount of phosphorus, when hypophosphite is the reducing agent used. Though such systems are used to deposit metallic coatings over metal substrates, they are also able to deposit a metal on non-conductors, such as plastics, once these have been activated. The basis of this hugely important activity, so-called 'metallising of plastics' is described in Chapter 4. In the case of electroless nickel, the deposits typically contain from 3 to 15 wt% phosphorus. After

heat-treatment, a range of Ni–P intermetallics are formed, whose hardness and corrosion resistance are superior to those of conventionally electroplated nickel.

The nickel salt used is usually the sulfate hexahydrate, $NiSO_4 \cdot 6H_2O$, with sodium hypophosphite as reductant. This is usually in the form of colourless hygroscopic crystals, molecular weight 107 and readily water soluble (100 g $NaH_2PO_4 \cdot H_2O$ per 100 g water at 25°C).

Table 3.7 shows the composition of commonly used electroless nickel systems and the deposition conditions used. These so-called hypophosphite electrolytes have a pH of 4.6–5.6. Operated at 85–95°C, they deposit Ni–P coatings at a rate of 10–30 μm/h. Operating under the simplest conditions, they have a finite life, typically expressed as 2–10 MTO (metal turnover) [28] where 1 MTO implies a complete depletion of the nickel content of the bath. It is clear that to achieve this, the bath will need to be several times replenished with fresh nickel salts to make good the nickel removed from solution. In the past, accepted practice was to dispose of the bath after 30–80 g/l nickel had been deposited from it [28]. One can continue to use the bath for much longer, but the deposit properties will suffer. However, more recently, numerous processes for bath life extension have been published, many based on removal of the orthophosphite ions formed. The so-called EDEN (electrodialysis of electroless nickel) process claims that when used, the life of an electroless nickel bath is virtually infinite.

As Table 3.7 suggests, the Type III system is in many ways the best of the three. It uses lower nickel and hypophosphite concentrations, has higher stability, that is to say is less prone to spontaneous deposition. It has a high deposition rate and longer bath life. Bath life is here defined as the age of the bath before metal deposits exhibit properties inferior to those from a virgin bath. The Type III system can be operated at high pH and temperatures to give greater deposition rates. Against this, it must be noted that the lower phosphorus content gives a deposit with somewhat reduced corrosion resistance, as compared to that from Type I and Type II systems.

Table 3.7 Compositions and operating parameters for three proprietary electroless nickel systems.

Bath constituents and operating parameters	Type I	Type II	Type III
Nickel content [g/l]	7.3	7.3	6.3
Sodium hypophosphite [g/l]	40	40	30
pH	4.6–5.2	4.6–5.2	4.8–5.6
Bath temperature [°C]	86–92	86–92	88–95
Deposition rate [μm/h]	12–14	13–15	18–25
Bath life [MTO] (metal turn over)[1]	5–6	5–7	9–12
Bath life (g/l Ni)	37–44	37–50	57–63
Bath loading [dm^2/l]	up to 2	up to 2	up to 3
Agitation/air sparging	Required	Required	Required
Filtration	Continuous	Continuous	Continuous
Bath stability	High	High	Very high
P content of deposit [%]	10–11	11–12	8–9

[1] MTO equates to the depletion of the entire nickel content of the bath.

In order to avoid too high a concentration of free nickel ions in solution, complexants are added at concentrations up to 0.2 M. These form stable nickel complexes, reducing the concentration of free nickel ions while providing an available reservoir of the metal. This represses the tendency for nickel ions to precipitate as the hydroxide, which otherwise readily occurs in weakly acid solutions.

The stability of nickel hypophosphite baths can be compromised by local overheating in solution, by too high a concentration of reactants and by the presence of trace impurities in solution. The formation of suspensions of insoluble species such as nickel hydroxide or nickel phosphate can have the same effect, since such solid particles can act as nucleation sites for spontaneous electroless deposition to occur. For this reason, such solutions usually include stabilisers (cadmium, lead, tin, thiourea, etc.) to prevent spontaneous metal deposition. The concentration of these species must be carefully adjusted. At too low a concentration they will not have any effect, at too high a concentration, they will make any metal deposition difficult to initiate. Their concentration depends on the nickel ion concentration and the ratio of work surface area to bath volume. Where excessive nickel deposition on the walls of the tank is observed, a higher concentration of stabiliser is called for. In the opposite sense, when a discolouring is observed on the edges of work, indicating too thin a nickel deposit, the stabiliser concentration should be reduced. Typically, stabiliser concentration lies in the range 1–6 ppm.

Also present in most electroless nickel formulations is a so-called accelerator which activates the hypophosphite anions and increases the availability of free nickel ions. The effect is to accelerate film growth kinetics without detriment to the action of the stabiliser. A further bath constituent, in many cases, is a wetting agent, to increase the wettability of the work surface, thereby aiding the release of adherent bubbles and promoting more uniform deposit growth.

The concentrations of these species, and also the pH buffer used, are in practice reached on the basis of a compromise, in which bath stability and high deposition rates are the primary aims.

Another very widely used electroless deposition system is electroless copper, used to metallise plastics, which include the substrates of printed circuit boards. The main constituents are the copper salt, the reducing agent, alkali and the complexing agent. The copper salt used is normally the Cu(II) sulfate pentahydrate. The reducing agent is a 37% aqueous solution of formaldehyde. NaOH is added to reach a pH of 11–13. The complexant depends on the system used, but is usually EDTA, quadrol or tartaric acid [29]. Stabilisers are adsorbed at the copper nuclei, otherwise surrounded by solution, thereby minimising their further growth.

Copper deposition from this solution takes place at 20–35°C, typically with deposition rate of 5 μm/h. The main bath constituents are

10 g/l copper sulfate pentahydrate; $CuSO_4 \cdot 5H_2O$
10 g/l sodium hydroxide: NaOH
50 g/l potassium sodium tartrate KOOC–CH(OH)–CH(OH)–COONa
10 g/l formaldehyde: HCHO, 37%
10–100 mg/l stabiliser

3.2.2.1 Electrolyte additives

In theory, it should be possible to operate an electroless bath containing nothing but metal salt and reducing agent. In practice, the result would be either a system so unstable that spontaneous metal deposition occurred, and/or that the deposited metal would not possess the desired properties. Spontaneous deposition can be triggered by catalytically active foreign particulates, suspended, often homogeneously, in solution. Metal ions are reduced at such suspended particles, which act as nucleation sites. Following an initial metal deposition, often no more than a few atoms, an uncontrolled metal deposition follows.

To repress such effects, a range of organic or inorganic additives are included in such bath formulations, to increase bath stability, to control the metal deposition process and to regulate the metal deposition rate, both too fast or too slow being undesirable. At the same time, such additives are used to optimise deposit properties such as hardness, ductility, solderability, wear- and corrosion-resistance, as well as minimising internal stress and increasing deposit brightness. No single additive can bring about all of these modifications and in practice, a combination of addition agents is used. The selection of such additives and the combinations and concentrations in which they are used, make the difference between successful and unsuccessful operation of such baths and the resulting deposit properties. Some of the additives act diametrically opposite ways to one another, and some act (for example) as accelerators at low concentrations, and inhibitors at higher concentrations. It would be no exaggeration to suggest that the remarkable advances in plating bath formulations in recent years have been the result of development of improved additives and combinations of these. The composition and nature of such additives lies at the core of intellectual property, and they are rarely disclosed, save in the patent literature. In what follows, the most important bath constituents are discussed.

3.2.2.1.1 Reducing agents

Apart from the metal salt, the reducing agent is the most important constituent of electroless deposition systems, and the following key points should be made:

- The concentration of reducing agent is critical. Increasing this will usually lead to an increase in metal deposition rate.
- The reducing agent plays a critical role in determining the bath stability.
- The composition and microstructure of the deposited metal and thus its properties, are largely determined by the nature of the reducing agent.

The importance of the choice of reducing agent is indicated by the fact that it is usually indicated when describing a deposition system, for example, as 'Electroless nickel–phosphorus'. Some of the best-known electroless deposition systems are listed in Table 3.8.

The power and ranking of reducing agents is indicated by their redox potential value and for a chemical reduction to take place, this value must be more negative than the redox potential value of the metal/metal ion couple. However there should not be too great a potential difference between the two values, if a deposit with

Table 3.8 Frequently used electroless metal deposition systems [28].

Reducing agent	Chemical formula	Molecular weight [g/mol]	Available electrons	Redox potential [V]	Used for:
Sodium hypophosphite	$NaH_2PO_2 \cdot H_2O$	106.90	2	−1.57 alkaline −1.38 acidic	Nickel, Cobalt
Sodium borohydride	$NaBH_4$	37.80	8	−1.24 alkaline	Nickel, Cobalt
Formaldehyde	HCHO	30.03	2	−1.11 alkaline	Copper, Silver
Dimethyl-aminoborane	$(CH_3)_2NH \cdot BH_3$	58.90	6	−1.18 alkaline	Nickel, Copper, Silver
Hydrazine	N_2H_4	32.00	4	−1.16 alkaline	Nickel

satisfactory properties is to be formed. Thus sodium hypophosphite ($E = -1.57$ V) is ideal for reducing nickel ions ($E = -0.25$ V) though it is not suitable for reducing the more noble copper ions ($E = 0.34$ V). The latter require an alternative reducing agent with a higher redox value, and formaldehyde ($E = -1.11$ V) is used in this case.

3.2.2.1.2 Stabilisers

A constant preoccupation in operation of electroless plating systems is to avoid spontaneous and uncontrolled metal deposition. Unlike electroplating baths which cannot operate unless electrical energy is supplied, electroless deposition systems are thermodynamically unstable, and spontaneous metal deposition is prevented only so long as a catalytically activated surface is absent. To minimise the danger of this happening, so-called stabilisers are added and form an essential part of all electroless metal deposition systems. The concentration of these species is very low, and were this not the case, their effectiveness would be so great that metal deposition would not occur even when this was desired. Stabilisers operate by masking off those nuclei which would otherwise act as initiators for the reduction process, and it is generally assumed they do so by adsorbing at the surface of these finely divided particles, which are often held in suspension, thereby impeding further nucleation reactions. Of course, there will also be adsorption of the stabiliser on the work surface, where it can likewise impede any metal deposition.

Stabilisers can be metallic or non-metallic. In the former category, are found lead, cadmium and tin, and in the latter class, divalent sulfur compounds such as thiourea, lead or tin sulfides or sodium methyl xanthates are used.

3.2.2.1.3 Complexing agents

Though they act in quite another way, metal complexing agents are used in electroless deposition systems for various reasons, one of which is to prevent spontaneous metal reduction and deposition. By complexing the metal, the danger of its precipitation as an insoluble compound is largely avoided. Complexing agents are species which form ionic compounds with the metal to be deposited. These ionic complexes often behave quite differently from the simpler ions of the metals they include. The complexation of a metal can be seen as a means of stabilising it, and making it less readily available for any form of reaction. Indeed, the metal ion will not be available

Table 3.9 Some commonly used complexing agents for electroless deposition systems.

Designation	Chemical formula
EDTA	$(HOOC–CH_2)_2N–CH_2–CH_2–N(CH_2COOH)_2$
NTA	$N(CH_2–COOH)_3$
EDTP	$((HO)_2PO–CH_2)_2N–CH_2–CH_2–N(CH_2–PO(OH)_2)_2$
Quadrol	$(CH_3CH(OH)CH_2)_2N–CH_2–CH_2–N(CH_2CH(OH)CH_3)_2$
Malic acid	$HOOC–CH(OH)–CH_2–COOH$
Citric acid	$HOOC–CH_2–C(OH)(COOH)–CH_2–COOH$
Lactic acid	$HOOC–CHCOH–CH_3$

unless the complex is decomposed. If the metal ion is too strongly bound in such a complex, it will not be released for reduction and no metal deposition will take place. The strength with which the metal is locked up in a complex is expressed in terms of the stability constant of a given metal–ligand system.

Though complexation cannot change the total amount of metal ions in a closed system, it will lower the concentration of 'free metal ions'. The greater the stability constant, the more that metal ions will be complexed and the lower the concentration of 'free' metal ions. There are no firm rules for assessing the concentration of complexing agents, though this is often much lower than that of the other main bath constituents. Complexing agents affect bath stability, ease of deposition initiation and deposition rate. Since they will be slowly but systematically lost from the system by drag-out, their concentration must be monitored and losses made good by dosing.

Recognising that the deposition conditions can critically affect the mechanical and other properties of the deposit, it will be recognised that the complexation process offers a key to control of the deposition reaction. Complexing agents would appear to form an essential part of many aqueous metal finishing and surface treatment processes. On the debit side, however, these species can be environmentally harmful and a number of them call for special effluent treatment techniques in order that they are broken down and made harmless.

3.2.2.1.4 pH buffers

Electroless metal deposition systems operate in a relatively narrow pH window, and this must be strictly maintained if the deposit properties are not to be compromised. However metal deposition is almost invariably accompanied by hydrogen evolution and the loss of this hydrogen will drive the solution to become more alkaline as hydrogen ions are lost from the system. In some cases, the redox values of the metal ion, or the complex holding it, or the reducing agent can be affected by change in pH, and so influence the overall process. Such effects are minimised by including in the bath formulation, a pH buffering system. These are described in most physical chemistry textbooks. Such buffer systems operate in a defined pH range and will normally be effective over about 2 pH units within that range. They are usually based on a weak acid or weak alkali and its metal salt and as long as at least some of both buffer species remain in solution, they will prevent any marked excursions of pH.

3.2.2.2 Electrolyte monitoring

When operating electroless deposition systems, the following rules should be followed.

The chemicals used in electroless bath formulations must be of higher than normal purity, and as such, will be more expensive than lower quality grades. This has to be accepted as an inherent part of the process cost.

The deposition rate for most electroless processes is rather lower than that for the analogous electrodeposition reaction. This implies that for thicker deposit, relatively longer tank times are involved.

Maintaining the recommended concentrations of metal ions and other species in the bath, is critical. When depositing very thick layers, there should be sufficient metal in the bath (in ionised form) to allow such deposit to form without significant depletion of the bath. After such deposition, the bath must be replenished, but doing so in the middle of a deposition operation is not recommended. Satisfactory deposit quality will only be obtained when the concentration of all species in the system lie within the permitted ranges. When this is not so, and indeed when the concentrations of by-products such as phosphite, accumulates above permitted levels, not only will deposit quality suffer, but spontaneous metal deposition may occur or the electrolyte may become inactive. In either case, the electrolyte becomes unusable with financially adverse consequences.

In summary, the composition of an electroless plating bath will change during operation, becoming depleted in reactants, accumulating impurities and reaction products and all of these will affect deposit properties, usually adversely. For this reason, monitoring bath composition, density, pH and deposition conditions such as temperature, is absolutely essential. Some comments on these are made below.

3.2.2.2.1 pH value

pH (defined as $-\log c_{H+}$) is a measure of the hydrogen ion concentration in solution. In all but the most dilute solutions, the concept of concentration is usually replaced by that of 'activity' which can be seen as a measure of concentration, but with adjustment to take account of interaction of neighbouring species in solution. At higher concentrations, a given ion will be less 'active' than would be the case in dilute solutions. The above definition can then be replaced by $pH = -\log a_{H+}$. The pH value of a metal deposition electrolyte is critical, because it can influence:

- the electrical conductivity of solution,
- the extent of corrosion of the substrate immersed in solution,
- the deposition rate,
- the co-evolution of hydrogen,
- the deposit properties.

Figure 3.11 illustrates the effect of pH on metal deposition rate for the electroless nickel–phosphorus system. Such solutions are buffered, as described above, to

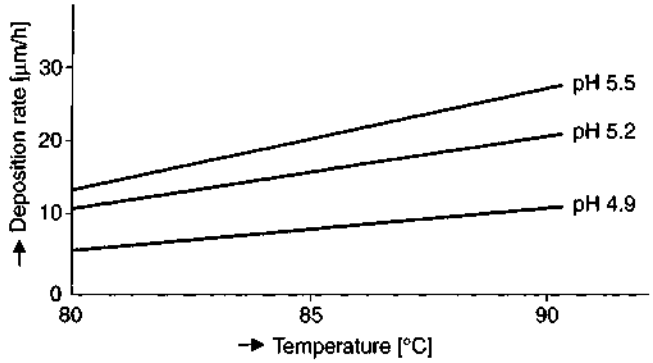

Figure 3.11 Effect of pH on deposition rate of electroless nickel–phosphorus.

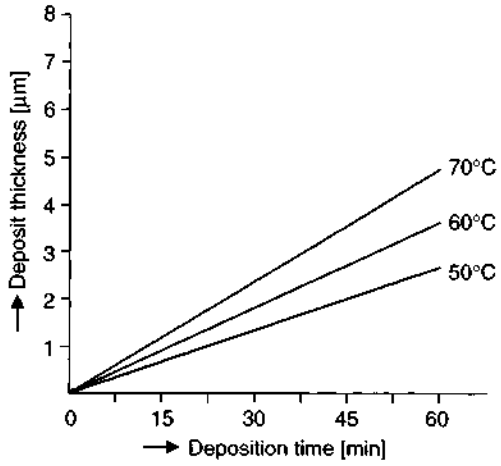

Figure 3.12 Effect of bath temperature on deposit thickness for electroless palladium deposition.

maintain the correct pH value. Even modest pH changes can affect not only the deposition rate but also the amount of phosphorus included in the deposit. The latter exerts a considerable influence on the mechanical and chemical properties of the deposit.

3.2.2.2.2 Electrolyte temperature

Maintaining close temperature control of the deposition bath is one of the most important criteria in operating electroless deposition processes. It determines deposition rate and bath stability, as Fig. 3.12 shows. Under actual operating conditions (e.g. components from a cold storeroom being introduced into a hot bath), bath temperatures can vary by several degrees celsius. Increase in temperature will result in a higher electrolytic conductivity, and because all reaction rates are accelerated, will increase the rate of consumption of additives in solution.

References

[1] Oehme, E., Chemie für Galvaniseure – Bildung und Zerstörung von Komplexen, *Oberfläche-Surface* 25/Heft 12 (1984) 434.

[2] Aßmann, K., Verfahren zur Abwasserbehandlung, in: *Technologie der Galvanotechnik*, herausgegeben von B. Gaida and K. Aßmann, Eugen G. Leuze Verlag Saulgau/Württ., 1996.

[3] Hoffmann, R., *Chemie für die Galvanotechnik*, Eugen G. Leuze Verlag Saulgau/Württ., 1988.

[4] Roth, E., Galvanisch hergestellte Metallüberzüge – Kupfer und seine Le gierungen, in: *Praktische Galvanotechnik* 4. Auflage, Autorenkollektiv, Eugen G. Leuze Verlag, Saulgau/Württ., 1984.

[5] *LPW Taschenbuch für Galvanotechnik*, Bd. 1 Verfahrenstechnik, 13. Ausgabe, 1988.

[6] Jelinek, T.W., Galvanisch hergestellte Metallüberzüge – Zink, in: *Praktische Galvanotechnik*, 4. Auflage, Autorenkollektiv, Eugen G. Leuze Verlag, Saulgau/Württ., 1984.

[7] Knödler, A., Galvanisch hergestellte Metallüberzüge – Gold und seine Legierungen, in: *Praktische Galvanotechnik*, 4. Auflage, Autorenkollektiv, Eugen G. Leuze Verlag, Saulgau/Württ., 1984.

[8] Gaida, B., *Galvanotechnik in Frage und Antwort*, Eugen G. Leuze Verlag, Saulgau/Württ., 1983.

[9] Ramisch, J. and Jelinek, W., Zink und Zinklegierungen, in: *Technologie der Galvanotechnik* herausgegeben von B. Gaida und K. Aßmann, Eugen G. Leuze Verlag, Saulgau/Württ., 1996.

[10] John, W., Galvanisch abzuscheidende Metalle – Nickel, in: *Technologie der Galvanotechnik*, herausgegeben von B. Gaida und K. Aßmann, Eugen G. Leuze Verlag Saulgau/Württ., 1996.

[11] Kanani, N., Abscheiden von Metallen ohne äußere Stromquelle in: *Technologie der Galvanotechnik*, herausgegeben von B. Gaida und K. Aßmann, Eugen G. Leuze Verlag, Saulgau/Württ., 1996.

[12] Dini, J.W., *Electrodeposition, The Materials Science of Coating and Substrates*, Noyes Publications, Park Ridge, NJ, USA, 1993.

[13] Brugger, R., Galvanisch hergestellte Metallüberzüge – Nickel, in: *Praktische Galvanotechnik*, 4. Auflage, Autorenkollektiv, Eugen G. Leuze Verlag, Saulgau/Württ., 1984.

[14] Dietz, K.H., Kontrolle organischer Zusätze im sauren Kupferbad für die Leiterplattenfertigung, *Galvanotechnik* 78 (1987) Nr. 8, 2290–2298.

[15] Jelink, T.W., Galvanisch hergestellte Metallüberzüge – Chrom, in: *Praktische Galvanotechnik*, 4. Auflage, Autorenkollektiv, Eugen G. Leuze Verlag, Saulgau/Württ., 1984.

[16] Andreas B., Vorbehandlungsverfahren Schleifen und Polieren, in: *Technologie der Galvanotechnik*, herausgegeben von B. Gaida und K. Aßmann, Eugen G. Leuze Verlag, Saulgau/Württ., 1996.

[17] Dettner, H.W., *Lexikon für Metalloberflächen-Veredlung*, Eugen G. Leuze Verlag, Saulgau/Württ., 1989.

[18] Schulz-Harder, J., Ein neuer Mechanismus des Einflusses von Badzusätzen auf die Stromdichteverteilung bei der Metallabscheidung auf rauhen Kathoden und seine experimentelle Begründung, Dissertation TU Berlin, 1971.
[19] Autorenkollektiv, *Galvanotechnisches Fachwissen*, VEB Deutscher Verlag für Grundstoffindustrie, Leipzig, 1982.
[20] Latscha, H.P., Was sind eigentlich Tenside?, *GIT Fachzeitschrift Labor* 1 (1987) 29–30.
[21] Fabry, B., Tenside – Eigenschaften, Rohstoffe, Produktion, Anwendungen, *Chemie in unserer Zeit*, Nr. 4 (1991) 214–222.
[22] Ludwig, R., Galvanisch abzuscheidende Metalle – Chrom, in: *Technologie der Galvanotechnik* herausgegeben von B. Gaida und K. Aßmann, Eugen G. Leuze Verlag, Saulgau/Württ., 1996.
[23] Jelinek, T.W., Galvanische Verfahren in der Praxis, in: *Praktische Galvanotechnik*, 4. Auflage, Autorenkollektiv, Eugen G. Leuze Verlag, Saulgau/Württ., 1984.
[24] Oehme, F., Chemie für Galvaniseure – Die Leitfähigkeit von Lösungen, *Oberfläche-Surface* 25/Heft 7 (1984) 213–214.
[25] Lausmann, G.A. and Unruh, J.N.M., *Die galvanische Verchromung*, Eugen G. Leuze Verlag Saulgau/Württ., 1998.
[26] Todt, H.-G., Technische Aspekte der cyanidischen und sauren Verkupferung, *Sonderdruck aus Galvanotechnik*, Heft 12 (1967).
[27] Plieth, W., Schröder, N, and Sandmann G., Qualitätssicherung, Analytik und Prozeßoptiemierung bei der Kupferabscheidung, in Kupferschichten – Herstellung, Eigenschaften und Anwendungen, herausgegeben von N. Kanani, Eugen G. Leuze Verlag, Saulgau/Württ., 2000.
[28] Riedel, W., *Funktionelle Chemische Vernicklung*, Eugen G. Leuze Verlag, Saulgau/Württ., 1989.
[29] Ehrich, H.-J., Moderne Aspekte der chemischen Verkupferung zur Herstellung gedruckter Schaltungen, *Galvanotechnik* 68 (1977) 960–969.
[30] Ehrich, H.-J., Herstellung gedruckter Schaltungen, in: *Technologie der Galvanotechnik*, herausgegeben von B. Gaida und K. Aßmann, Eugen G. Leuze Verlag, Saulgau/Württ., 1996.
[31] Frick, W., Metallabscheidung ohne äußere Stromquelle, *Galvanotechnik* 76 (1985) 5, 548–551.

This Page Intentionally Left Blank

CHAPTER 4

Processes for the Deposition of Metallic Coatings

4.1 Introduction

A metallic coating can only be deposited onto a substrate from an aqueous solution of a metal salt if there are sufficient electrons available, from whatever source, to neutralise the metal ions in solution, allowing the metal itself to form in the zero-valent state. In practice, there are two main sources of such electrons, each forms the basis of a technologically important process. The first of these is the so-called electroless or chemical deposition, which does not involve any external source of voltage or electron source. The second is the electrolytic deposition, where electrons are supplied from an externally applied voltage. Figure 4.1 provides an overview of both types and a variant, which is laser-induced deposition. The latter is a relatively new concept, reflecting the development of laser technology. It can be applied to either of the two main types of deposition. In the following treatment, these processes will be more closely examined.

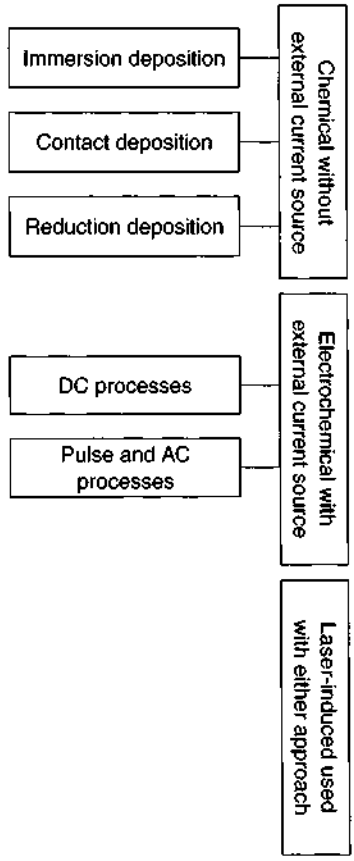

Figure 4.1 Chemical and electrochemical processes for deposition of metallic layers.

4.2 Electroless Metal Deposition

The hallmark of this type of process is the absence of any external power source. Although they operate on very different bases, one should include three different types of process under this heading. Immersion plating, contact plating and chemical reduction plating. The first two are used only in very special situations [1]. The last of the three is easily the most important and indeed 'electroless deposition' is widely used as a synonym for chemical reduction plating [2].

The operating principle of chemical deposition is shown in Fig. 4.2. The discharge of metal ions present in solution is achieved using a chemical reductant, R^{H+} in solution. This is not added to the solution, but is already present at the point the work is immersed in the electrolyte.

A major advantage of chemical (electroless) deposition is that it can be used to metallise non-conductive surfaces, such as plastics, glass or ceramics. This requires a suitable pretreatment, in order to 'activate' these surfaces. This consists of a sequence of steps in which the surface of the work is modified, allowing spontaneous deposition to take place.

The best-known and perhaps economically most significant example is the metallising of printed circuit boards, and in particular, the through-holes in order to provide a conductive path from one side of a board to the other, or through a multilayer stack. Printed circuit boards are usually made of glass fibre–reinforced epoxy resin. The activation involves a number of stages, perhaps the most important of which is application of a $SnCl_2/PdCl_2$ solution, prier to electroless copper plating. Palladium nuclei form on the electrically non-conducting hole walls and these act as growth centers for the subsequent electroless copper deposition.

4.2.1 Deposition of Metal Layers

The overall process taking place in electroless deposition can be formulated as a true chemical reaction, in which no electron transfer is explicitly shown. This conceals,

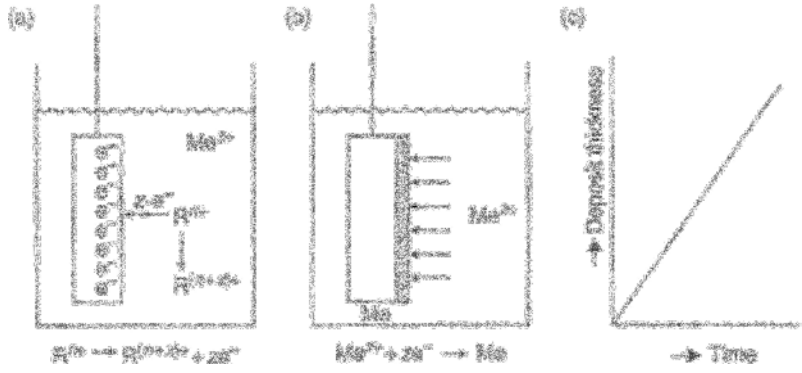

Figure 4.2 Principle of electroless deposition: (a) oxidation of the reductant; (b) reduction of the metal ion, leading to formation of the metal layer; (c) plot showing rate of deposition (expressed as thickness) versus time.

however, the actual electrochemical nature of the process, which can be written for the reduction of a z-valent metal as follows

$$R^{n+} \rightarrow R^{(n+z)+} + z \cdot e^-$$

$$\frac{Me^{z+} + z \cdot e^- \rightarrow Me}{R^{n+} + Me^{z+} \rightarrow R^{(n+z)+} + Me} \qquad (4.1)$$

This is known as a coupled reaction, comprising two half-reactions, the one anodic, the other cathodic. Because the electrons donated by the reductant have nowhere to go, other than being accepted by the metal ion, the rates of these two half-reactions (in the absence of any complicating factors), have to be equal, and indeed to proceed at the rate of the slower of the two. In practice, the hydrogen evolution reaction offers a secondary, additional, cathodic reaction.

The net outcome of the coupled reactions, as seen in Eq. (4.1), is the deposition of the metal. Clearly it is desirable that the metal deposit on the surface of the work to be plated. However, this is not always the case. Thus, the metal can deposit in finely divided form in the electrolyte itself, and can also deposit on the walls of the electrolyte containing tank. Ensuring that the surface of the work to be plated is the preferable deposition site, must be a key aim. Although the substrate does not appear to be formally involved in Eqs. (4.1), it functions as a catalyst for the point cease, unless the growing deposit itself were able to act as catalyst. Fortunately, in most cases, it does so, and thus as long as sufficient reductant and metal salt remain in solution, there is no limit to the thickness of an electroless deposit. For this reason, the process is often described as being 'autocatalytic'. In this behaviour, 'electroless deposition' processes differ from 'displacement plating' (Fig. 4.1). In this process, also known as cementation or immersion plating, a steel nail (for example) is immersed in copper sulfate solution. The less noble iron atoms dissolve, and an electron exchange takes place with the iron atoms ionising, and an equal number of copper ions being reduced to the metallic state. However, once the steel has become obscured by being covered with a thin layer of copper (usually less than 1 μm thick), the driving force for the reaction is removed and further reaction ceases. These two processes, the one driven by a chemical reductant in solution, the other by a simple exchange of metal atoms at a surface, should not be confused.

Metals which have been deposited by true electroless processes are shown in Fig. 4.3. It should be noted that the metalloids, such as boron and phosphorus, have no technological significance as deposits in their pure state, but are important only as components of electroless deposited alloys.

4.2.2 Deposition of Alloys

Electroless deposition of alloys is arguably of technological importance no less than that of pure metals, with nickel–phosphorus and nickel–boron being the best-known examples. The former tend to be classified according to their phosphorus content, usually ranging between 2 and 15 wt% P. For $P < 8\%$, the deposits will usually be crystalline. For $P > 10\%$, the deposit will usually be amorphous and both forms possess superb mechanical and chemical properties. The main constituents of electroless nickel–phosphorus electrolytes are the nickel salt, the complexing agent

Ia	IIa	IIIa	IVa	Va	VIa	VIIa	VIII			Ib	IIb	IIIb	IVb	Vb	VIb	VIIb	O
1 H																1 H	2 He
3 Li	4 Be											5 B	6 C	7 N	8 O	9 F	10 Ne
11 Na	12 Mg											13 Al	14 Si	15 P	16 S	17 Cl	18 Ar
19 K	20 Ca	21 Sc	22 Ti	23 V	24 Cr	25 Mn	26 Fe	27 Co	28 Ni	29 Cu	30 Zn	31 Ga	32 Ge	33 As	34 Se	35 Br	36 Kr
37 Rb	38 Sr	39 Y	40 Zr	41 Nb	42 Mo	43 Tc	44 Ru	45 Rh	46 Pd	47 Ag	48 Cd	49 In	50 Sn	51 Sb	52 Te	53 I	54 Xe
55 Cs	56 Ba	57 La	72 Hf	73 Ta	74 W	75 Re	76 Os	77 Ir	78 Pt	79 Au	80 Hg	81 Tl	82 Pb	83 Bi	84 Po	85 At	86 Rn
87 Fr	88 Ra	89 Ac	104 Ku														

Figure 4.3 Periodic table showing metals and metalloids which can be deposited in an electroless manner.

and the reducing agent (see Chapter 3) and the main functions of these are self-evident. The reducing agent is also, however, the source of the metalloid phosphorus which is co-deposited with the nickel as Ni–P. Again, self-evidently, the redox potential of the reducing agent should be more cathodic than that of the metal/metal ion couple being reduced (in this case nickel). However it should not be too much more negative, since in this case, the enhanced nucleation rate can result in spontaneous reduction in solution, leading to an utterly useless, finely divided suspension of the metal in the electrolyte. The redox potential of the hypophosphite is -1.065 V at pH 7. At pH 4.5, the value becomes -0.88 V. Hypophosphite is thus an ideal reducing agent for nickel ions over a considerable pH range.

The reduction mechanism of this reaction has not been completely elucidated, and remains to some extent, contentious. That the process involves simultaneous coupled electrochemical reactions, one anodic, the other cathodic, is however not in dispute, and experimental measurements leave no doubt on this [3, 4]. Taking this concept one step further, it is assumed that anodic and cathodic sites are formed at the substrate surface, these being differentiated in terms of physical and/or chemical inhomogeneities and that the alloy deposit is formed in this way. The anodic half-reaction is generally accepted as being:

$$[H_2PO_2]^- + H_2O \rightarrow [H_2PO_3]^- + H_{ads} + H^+ + e^- \qquad (4.2)$$

It is assumed that at catalytically active regions of the substrate, the hypophosphite anion is reduced to the phosphite anion, on the right-hand side of the equation. The hydrogen is formed partly as a proton, partly as atomic hydrogen. H_{ads} which is adsorbed at the metal surface. Thereafter it may become absorbed into the metal, or combine with another H_{ads} to form molecular (gaseous) hydrogen. The formation of protons results in an increase in acidity, initially in the near-electrode region, then through the bulk of solution. The cathodic process(es) are taken to be:

$$Ni^{2+} + 2 \cdot e^- \rightarrow Ni \qquad (4.3)$$

Table 4.1 Electroless nickel deposition parameters and their significance in the process and in determining deposit properties.

Deposition parameter	Significance for:
Bath temperature	Deposition rate, bath stability, adhesion, appearance of deposit
Bath pH	Deposition rate, deposition initiation and bath stability. Deposit properties and composition
Deposition rate	Thickness, appearance, structure, morphology
Deposition potential	Deposition rate and deposition initiation
Filtration	Bath stability and surface properties of deposit
Work movement, bath agitation	Structure, appearance and uniformity of deposit

$$[H_2PO_2]^- + 2H^+ + e^- \rightarrow P + 2H_2O \quad (4.4)$$

$$2H^+ + 2 \cdot e^- \rightarrow H_2 \quad (4.5)$$

These represent, in formal terms, the formation of metallic nickel, elemental phosphorus and hydrogen. Summing reactions (4.2) and (4.3), one obtains:

$$Ni^{2+} + 2[H_2PO_2]^- + 2H_2O \rightarrow Ni + 2[H_2PO_3]^- + H_2 + 2H^+ \quad (4.6)$$

As seen, the deposition of metallic nickel is accompanies by hydrogen evolution. The molar ratio of metal to hydrogen formed in this way is between 1:1.76 and 1:1.93 [3]. Summing reactions (4.2) and (4.4), one obtains:

$$2[H_2PO_2]^- + H^+ \rightarrow P + [H_2PO_3]^- + H_{ads} + H_2O \quad (4.7)$$

This reaction explains how phosphorus is formed. Finally, the catalytic decomposition of hypophosphite is seen by combining equations (4.2) and (4.5):

$$[H_2PO_2]^- + H_2O + H^+ + e^- \rightarrow [H_2PO_3]^- + H_{ads} + H_2 \quad (4.8)$$

Table 4.1 summarises the effect of deposition parameters and the properties of the deposited Ni–P coating.

4.2.3 Deposition of Composite Coatings

Deposits consisting of a metal matrix in which particles of a second phase are distributed, either uniformly or with a concentration dependant on depth from the surface, are known as composite coatings or as dispersion coatings. They can be formed either by electrodeposition or, as discussed here, by electroless deposition. The finely divided second phase particles which may range in size from 10 μm down to the nanometre range are may be inorganic or organic. Occasionally, they are metallic. Incorporation of such particles can greatly improve the mechanical properties of the deposit, notably friction and wear behaviour. Depending on the intended function of the coating, the second phase particles can be ceramics such as borides, carbides or oxides, they may be sulfides or PTFE (solid lubricants and low-friction), diamond or metallic, notably chromium which, after heat-treatment, yields alloys of the MCrAlY family. Table 4.2 shows some of these, as used with an Ni–P matrix [5].

Table 4.3 Commonly used second-phase particles in electroless nickel matrix composite coatings.

Carbides	Oxides	Miscellaneous
Cr_3C_2	Al_2O_3	cBN
SiC	Cr_2O_3	CaF_2
TiC	SiO_2	Diamond
	TiO_2	MoS_2
		PTFE

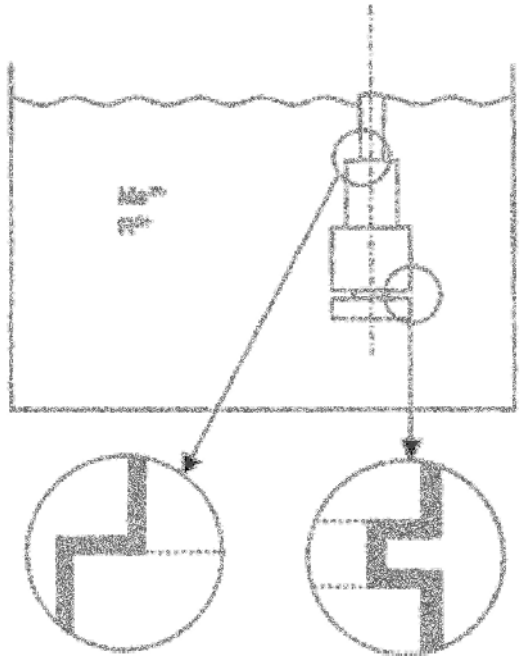

Figure 4.4 Electroless deposition makes possible uniform thickness coatings, even over the most complex geometries.

4.2.4 Coating Thickness Distribution

Electroless nickel deposition offers a number of advantages, as compared with electrodeposition. First and foremost are the very high hardness and wear-resistance of the deposit. (It should be noted that similar values of these parameters can be obtained by electrodeposition from a nickel + hypophosphite electrolyte.) Perhaps more important is the fact that electroless metal deposits are highly uniform in thickness not only across a flat surface, but equally in recesses and undercuts and irrespective of the work geometry. In this, they differ markedly from the analogous electrolytic processes, where work geometry and positioning with respect to the anode, can significantly affect metal thickness variation. This can be seen in Fig. 4.4 which shows a component with relatively complex geometry.

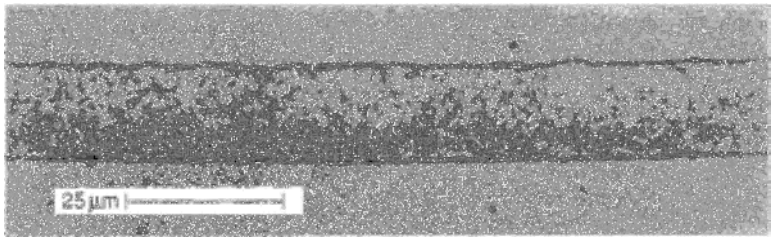

Figure 4.5 Thickness uniformity of an electroless copper deposit (see text).

The scanning electron microscopic image of a 15 µm thick copper deposit shown in Fig. 4.5 again shows the remarkably uniform deposit thickness. The substrate in this case was the plastic acrylonitrile–butadiene–styrene (ABS) and after deposition, the plastic was dissolved away in acetone, leaving a free-standing foil [6]. Following this, the copper was plated on both sides with nickel, and metallographically sectioned.

The basis of the very uniform metal thickness distribution in electroless deposition, lies in the very high macro-throwing power of the reductant used. Macro-throwing power is defined, as the ability of a deposition system to form a deposit of high thickness uniformity over the entire surface of a component. In many cases, ensuring uniform deposit thickness is critical in the context of maintaining close dimensional tolerances. To assure this, unimpeded access of electrolyte to all parts of the surface is essential. That remarkably uniform thicknesses can be obtained even over the most extreme variations in geometry is seen in Fig. 4.6, which shows a metallographic cross-section of an ink-jet printer nozzle. Made of brass, the internal bore of 80 µm width was coated with a nickel–phosphorus deposit of 10.5±0.5 µm thickness.

4.3 Electrolytic Metal Deposition

The fundamental principle of the electrodeposition of a metal is shown in Fig. 4.7. From this, it is seen that when a metal is immersed in an electrolyte solution, under certain conditions, a spontaneous dissolution takes place whereby metal atoms leave the metal lattice to form positively charged ions (cations) which migrate into the electrolyte. As a result of this so-called anodic dissolution, an excess of positively charged ions is found in the immediate vicinity of the metal electrode. Their departure leaves an equal and opposite negative charge on the metal. Electrostatic charge attraction has the opposite effect and seeks to pull the positively charged ions back to the negatively charged metal. These processes, which can be described as a dynamic equilibrium, can be represented as:

$$Me \rightleftharpoons Me^{z+} + z \cdot e^{-} \tag{4.9}$$

The double arrow indicates that equilibrium is reached by virtue of the process going from left to right and vice versa at the same rate. The potential difference $\Delta\varphi = \varepsilon_{Me/Me^{z+}}$ (sometimes known as the metal–solution potential difference) has a fixed value for a given metal, immersed in a solution of standard composition, pH

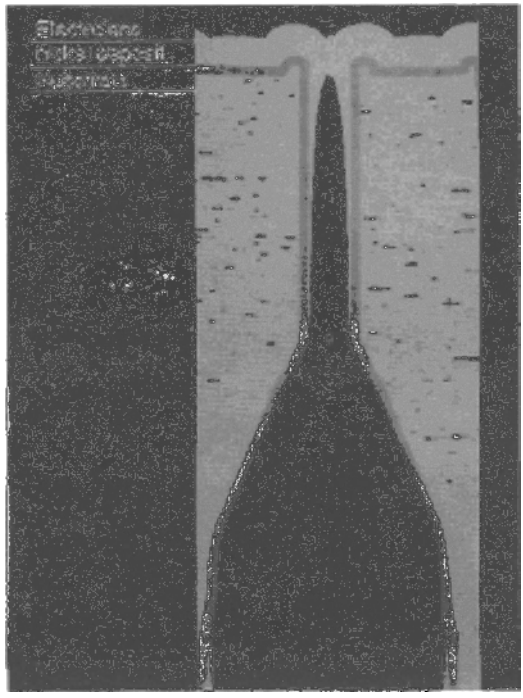

Figure 4.6 Uniformly thick 10 μm electroless nickel–phosphorus deposit on the internal 80 μm bore of an ink-jet printer nozzle.

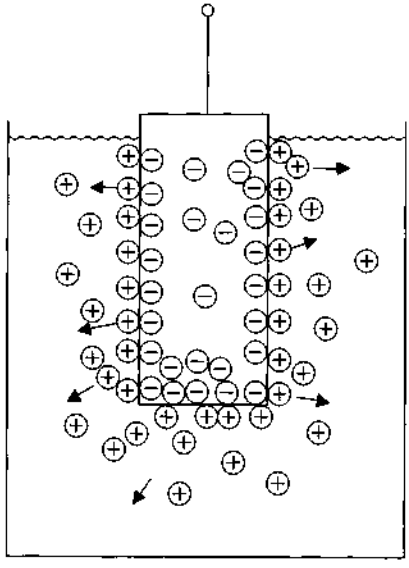

Figure 4.7 Spontaneous establishment of a charge at a metal–solution interface for a metal immersed in aqueous solution.

and temperature. The foregoing treatment does not explain what drives the metal atoms out of the lattice, or how the necessary energy to do so is acquired. The main source of such energy lies in the free energy of hydration of the metal ions so formed. The equilibrium thereby developed is discussed in Chapter 5.

The process of anodic dissolution or cathodic metal deposition implies movement of charge and thus constitutes an electric current, which is denoted as anodic or cathodic, respectively. Under a purely arbitrary convention, anodic current (I_a) is deemed to be positive, cathodic current, I_c, is negative. In some cases, *total* current is the relevant parameter. In other cases, current density, that is, current per unit surface area, is the critical parameter. Current density is sometimes denoted by i_a or i_c, and j is another symbol found in the literature for this. At equilibrium, the anodic and cathodic currents are equal, and no net current then flows. This can be represented as:

$$|I_c| = |I_a| = I^0 \quad \text{or} \quad |i_c| = |i_a| = i^0 \tag{4.10}$$

Here, i^0 is the so-called exchange current density. In many sources, it is shown as i_0. It is an indication of the rate at which the dynamic equilibrium shown in Eq. (4.9) is taking place. Under equilibrium conditions, no nett reaction takes place. However, if the metal is no longer at open circuit, but attached by means of a wire, for example, to an electron source or electron sink, this equilibrium will be disturbed. Attached to an electron source, more electrons will flow into the metal, which will become more negatively charged, and will attract more cations from solution. The metal is then said to be cathodic, and electrodeposition takes place. If the metal is connected to an electron sink, the metal will become positively charged, or 'anodic' and repulsion of metal cations will be encouraged, in other words, anodic metal dissolution.

The first of these is the basis of metal deposition or electroplating. Until quite recently, the process was carried out using direct current (DC). More recently, the benefits of using interrupted current or even cathodic current with periodic polarity reversal, have become clear and this is known as pulse current plating.

4.3.1 Direct Current Electrodeposition

DC electrolysis can be represented as in Fig. 4.8, where two electrodes, immersed in solution, are connected to the output of a DC current source [7]. The cathode, onto which the metal (or alloy) is deposited, may itself be a metal or it might be a semiconductor or a non-metallic conductor such as graphite. Also shown in the figure, is the anode. The primary purpose of this is to complete the electrical circuit, and as metal cations are removed from solution as the metal, so one or more balancing processes must take place at the anode to remove anions and thereby maintain overall charge neutrality in solution. The anode may or may not fulfil a second function, which is to provide a source of fresh metal to replace that which has been removed from solution by deposition at the cathode. Anodes fall into two classes. Sacrificial anodes are made of the same metal that is being deposited, e.g. copper. A copper anode will anodically dissolve, so releasing into solution copper ions to replace those which have been deposited at the cathode. Ideally the anodic process would be the absolute mirror-image of that taking place at the cathode. In practice, one or both processes are less than 100% efficient, and some sort of adjustment is required. The

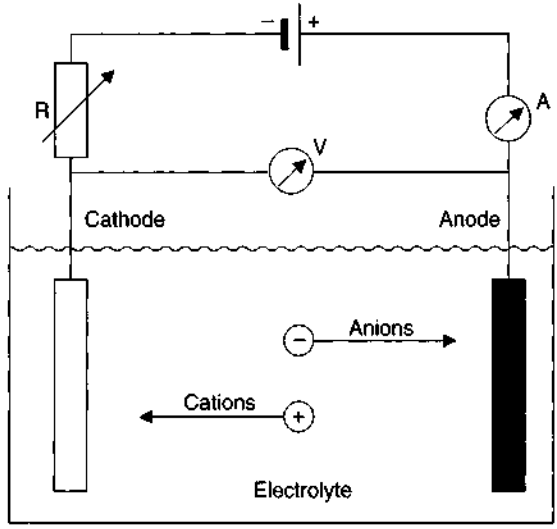

Figure 4.8 Main components of a DC electrolysis system.

second type of anode is the so-called permanent anode, typically platinum coated titanium. Where these are used, metal ion depletion from solution is made good by adding metal to solution in the form of a metal salt, for example, copper sulfate.

The application of an external current source upsets the equilibrium shown in Eq. (4.9) and depending on the polarity of the connection, will tilt the equation from left to right or vice versa and the greater the voltage of the external source, the faster the forward or backward reaction component will proceed. The equilibrium condition shown in Eqs. (4.9) and (4.10) (no nett reaction) will cease to hold, and a nett electrochemical reaction will be observed. The potential driving this is known as the overpotential (η) and is defined as:

$$\eta = |\varepsilon - \varepsilon_{Me/Me^{z+}}| \tag{4.11}$$

The overpotential will be be either anodic (η_a) or cathodic (η_c), driving the reaction in the anodic or cathodic direction respectively. Assuming that the charge-transfer reaction which takes place across the electrical double-layer is the only rate-determining step in the cathodic process, the overpotential can be more specifically defined as activation overpotential, η_D. This is the energy required to overcome the reaction activation energy barrier, and the greater the overpotential, the faster will the reaction proceed, in the same way as increase in thermal energy (temperature) will increase the rate of a chemical reaction. Activation overpotential is most significant in those redox couples (or irreversible reactions) with a low exchange current density (i^0). In short, the greater the exchange current density, the more reversible it will be, and the lower the activation energy barrier which divides the two states of Eq. (4.9). The rates of anodic metal dissolution and cathodic metal deposition can be represented by the following kinetic equations:

$$i_a = i^0 \times e^{(\alpha \cdot z \cdot F/RT)\eta_D} \tag{4.12}$$

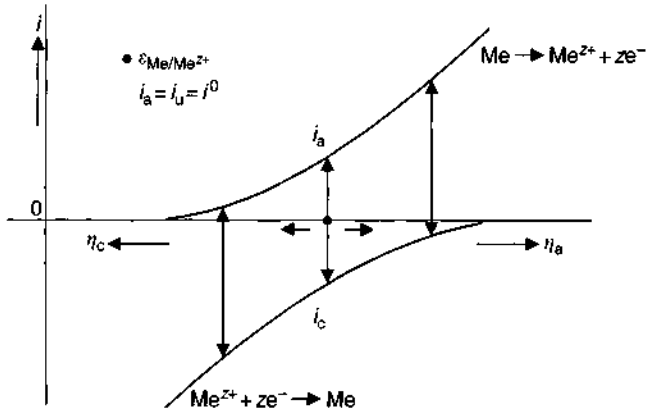

Figure 4.9 Polarisation plot showing the rates of both the anodic dissolution and cathodic metal deposition as function of potential.

$$i_c = -i^0 \times e^{-[(1-\alpha)\cdot z\cdot F/RT]\eta_D} \tag{4.13}$$

In these equations, α is the so-called transfer coefficient, which is usually assumed to be 0.5 but can have any value $0 < \alpha < 1$. α denotes the potential dependence of the forward charge transfer reaction, $(1 - \alpha)$ denotes the potential dependence of the reverse reaction. R is the gas constant (8.135 J/mol/K), and T the absolute temperature. For a given current density, the activation overvoltage is given by the following equation:

$$\eta_D = \frac{RT}{(1 - \alpha \cdot z \cdot F)} \cdot \ln\left(\frac{i^0}{i_c}\right) \tag{4.14}$$

This makes clear why a reduction of the exchange current density, for example, by poisoning of the cathode surface, results in an increase in overvoltage.

Figure 4.9 is a so-called polarisation (current density versus potential or overpotential) plot, in this case showing both the anodic and cathodic curves.

4.3.1.1 Deposition of metal layers

If a voltage is applied across the two electrodes in an electrolysis cell, a current consisting of electron flow, will be set up, with these moving from the anode, through the external circuit and back to the cathode. The anode will thereby dissolve anodically, and the cations so formed will migrate to the cathode. Anions present in solution will move in the opposite direction towards the anode. Current will thus flow through the solution by virtue of the movement of these charged ions and this is known as ionic current, or electrolytic conductance.

Of critical importance in electrodeposition, is the mechanism by which metal cations are delivered to the cathode, and the means for their replenishment as they are lost to solution by deposition at the cathode. The rate at which fresh ions (and also uncharged species required for reaction) are delivered to the cathode surface from the bulk of solution, depends on the prevailing hydrodynamic conditions at and near the cathode surface. There are three main mechanisms involved in delivery of ions to the electrode surface, these being migration (under a potential gradient), diffusion (under a concentration gradient) and convection (movement of the electrolyte liquid itself).

4.3.1.1.1 Migration

Voltage applied across the electrodes of an electrolysis cell sets up an electrical field between anode and cathode. Assuming that the electrolytic conductivity of the electrolyte is the same at all points in solution, the potential gradient is given by the voltage across the solution (excluding overvoltage at the electrodes) divided by the distance between the electrodes. The magnitude of this potential gradient determines the rate at which ions move through solution. The term 'migration' is understood here as the movement of charged species in solution under a potential gradient. The effect operates throughout the solution, anions being electrostatically attracted to the anode, cations to the cathode. The progress of such ions through solution is impeded by collisions with solvent molecules and viscous drag as the ions, with their hydration sheaths, move through the liquid. The ions thereby acquire a given velocity, depending on the nature of the ion, the potential gradient, solution viscosity, etc. These velocities are very low, of the order of micrometres per second. It follows that the overall contribution to the supply of ions resulting from the migration process is very small, and can generally be neglected.

4.3.1.1.2 Convection

In contrast to the preceding and following transport mechanisms which involve the movement of species through an electrolyte, convection can be said to be the movement of reactants, etc. with the electrolyte. The so-called 'convective mass transport' results from movement of the bulk solution, whether by stirring, movement of the work through the solution (deliberate measures to enhance convection, known as 'forced convection') or by the natural circulation of a liquid caused by adventitious differences in solution density caused by thermal effects. Such movement of solution ceases to be significant in the region immediately adjacent to the electrode surface, where a liquid layer sometimes known as the 'stagnant layer' or more usually as the 'diffuse layer' is formed. Movement of ions etc across this diffuse layer takes place by diffusion (see below). Convection is important not only because it moves the solution (with dissolved species) up to the diffuse layer, but also because the thickness of the diffuse layer is determined by convective action. The stronger the agitation (pumping, stirring, air-sparging) the thinner is the diffuse layer with benefits considered below.

4.3.1.1.3 Diffusion

The penultimate step, before charge transfer takes place at the electrode surface, is the migration of species, both charged and uncharged, across the diffuse layer. The driving force here is the concentration gradient, more formally expressed as chemical potential. The concentration of species at the electrode surface will, under open circuit conditions, be much the same as that in bulk solution. However, once current flows, species will, by their reaction, be removed at the electrode surface and a concentration gradient will be established. The tendency of species to move from regions of high concentration to those of lower concentration, are what drive the diffusion process, and this is enshrined in Fick's laws of diffusion. The thickness of the 'diffuse layer', also known as the Nernst or Nernstian layer, is denoted by δ. Without forced convection, in a static solution, δ would be approx 0.2 mm. Under conditions of forced convection, this value will decrease, and can reach values as low as 0.001 mm. It is generally assumed that diffusion is the only significant transport mechanism operating within

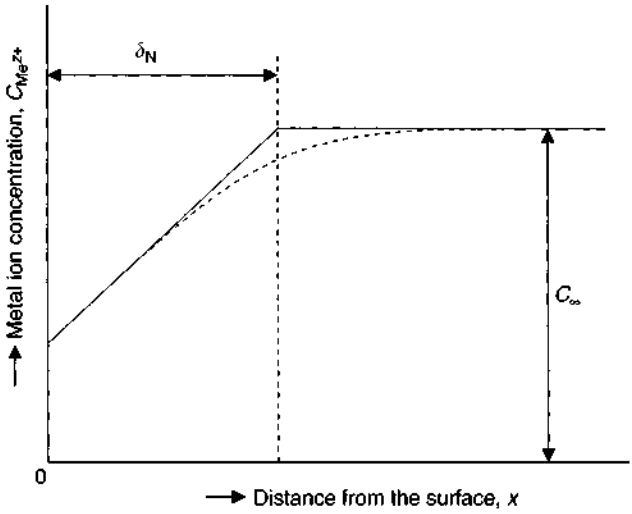

Figure 4.10 Metal ion concentration profile as a function of distance from the surface.

the Nernstian layer. Figure 4.10 shows what might be described as a concentration–depth profile. It shows the electrode surface as a vertical line on the left of the diagram. The vertical dashed line indicates the outer edge of the Nernst layer. The solid line shows the concentration profile predicted by the Nernst equation, the curved dashed line shows typical experimental results.

Figure 4.10 depicts the situation in a typical electrolysis and shows how the concentration of reactants is depleted at the electrode surface. In the extreme case, the concentration of reactants at the electrode surface is zero. Otherwise expressed, the species arriving at the electrode surface react instantly. This industrially important limiting case is mathematically represented by Eq. (4.17).

The flux of cations through the diffuse layer, expressed as mol/s/cm^2 is known as the diffusion current density n^*. It is a function, as Fick's law indicates, of the concentration gradient across the Nernst layer, as expressed in Eq. (4.15), where D is the diffusion coefficient, $c_{Me^{z+}}$ is the metal ion concentration in bulk solution, c_k is the concentration at the electrode surface:

$$n^* = D\frac{dc}{dx} = D\frac{(c_\infty - c_c)}{\delta_N} \tag{4.15}$$

At 100% cathode efficiency, the cathode current density[1] i_c (A/cm^2) is given by the following expression:

$$i_c = z \cdot F \cdot D\frac{(c_\infty - c_c)}{\delta_N} \tag{4.16}$$

[1] Cathode current efficiency, θ is defined as the ratio of weight of deposited metal to that predicted by theory, $\times 100$. This percentage is a measure of the efficiency.

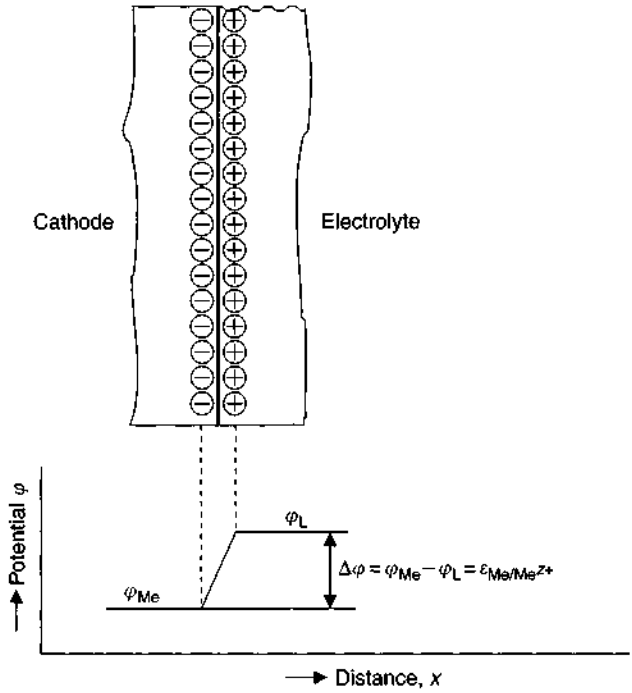

Figure 4.11 Structure of the electrical double layer at a metal–solution interface.

where z is the number of electrons per ion being transferred, F the Faraday constant (96,490 C/equivalent). The cathodic current density is proportional, as shown in Eq. (4.16), to the value of $(c_\infty - c_c)/\delta_N$, the Nernstian concentration gradient. The metal ion concentration decreases from outside to inside of the Nernstian layer. If the current density is further increased, there comes a point where $c_c = 0$. The current is then said to have reached the diffusion-limited current density, or mass-transport-limited current density. Increasing the voltage, at this point, will then (on this simplified theory) bring no further increase in current. We can then rewrite Eq. (4.16) in a simplified form as

$$i_D = z \cdot F \cdot D\frac{c_\infty}{\delta_N} \tag{4.17}$$

The rate of metal deposition is then limited to this value, mass-transport being the rate-determining step. The diffusion-limiting current density i_D represents the maximum current density at which the metal can be deposited under the given hydrodynamic conditions. In practice, metals deposited under these conditions tend to be powdery or friable and of no practical use except where there is a deliberate intention to produce metal powders.

Having crossed the Nernst diffusion layer, the metal ions face a further barrier separating them from the electrode surface, namely the electrode double layer (see Chapter 5). This is formed, as indicated earlier, by the aggregation of electrons on one side of the interface, and metal ions on the other. As a first approximation, as shown in Fig. 4.11, this can be modeled as an electrolytic capacitor. In this scheme,

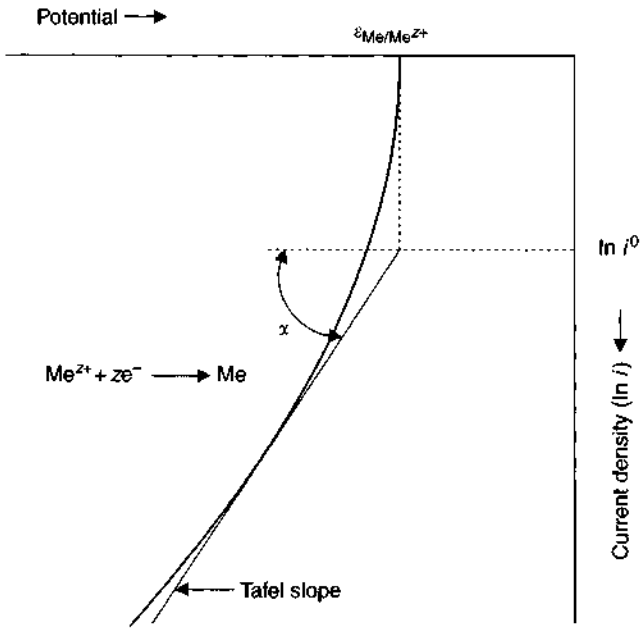

Figure 4.12 Dependence of cathodic current density on potential. Graphical determination of $\varepsilon_{Me/Me^{z+}}$, i^0 and α by drawing a tangent to the curve.

$\Delta\varphi$ is the difference between the potential of the metal electrode, φ_{Me} and that of the solution, φ_L (it should be noted that although $\Delta\varphi$ is an extremely important parameter, there are no simple means of directly measuring it).

The rate of metal electrodeposition, up to the point where diffusion limiting conditions set in, is governed by Eq. (4.13). In the following treatment, it will be shown how the key parameters in this equation, $\varepsilon_{Me/Me^{z+}}$, i^0 and α, can be determined by graphical representation of the data. In Fig. 4.12, the natural logarithm of the cathodic current density is plotted versus potential.

As this representation shows, the value of the equilibrium potential can be derived from the asymptotic value of the log function. The corresponding exchange current density is derived by drawing a tangent and is given by the intersection of the tangent with the asymptotic value of the current–potential plot. This value, which is proportional to the transfer coefficient, is known as the Tafel slope, named after the German scientist who first derived an empirical relationship linking current density and overpotential.

Cathodic deposition of metals is initiated by discharge of metal ions which are already in close proximity to the electrode. Thus, at the onset of the process, the rate-determining step is the movement of the charged species through the electrical double layer to the electrode surface. This leads to a depletion of the dischargeable metal ions in the near-electrode region, and metal electrodeposition can only continue if these are replenished from bulk solution. It follows that, in most cases (except at very low current densities and high metal ion concentrations), the deposition process is increasingly mass-transport controlled. In the limiting case, where mass transport

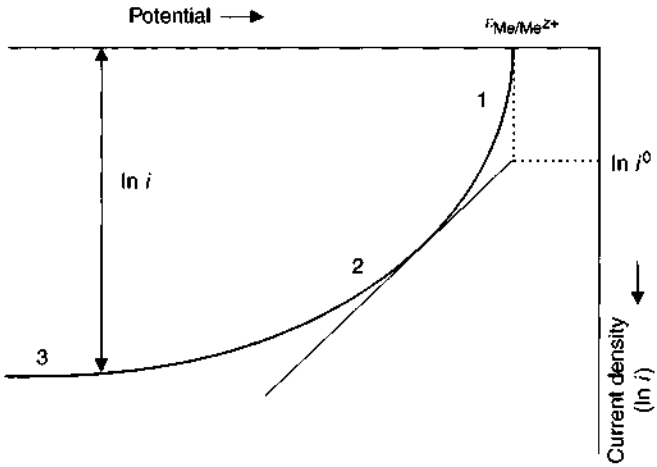

Figure 4.13 Shape of the current–voltage plot: (1) under activation control and (3) under diffusion control; (2) intermediate region with both mechanisms rate-determining.

Ia	IIa	IIIa	IVa	Va	VIa	VIIa	VIII			Ib	IIb	IIIb	IVb	Vb	VIb	VIIb	O
1 H																1 H	2 He
3 Li	4 Be											5 B	6 C	7 N	8 O	9 F	10 Ne
11 Na	12 Mg											13 Al	14 Si	15 P	16 S	17 Cl	18 Ar
19 K	20 Ca	21 Sc	22 Ti	23 V	24 Cr	25 Mn	26 Fe	27 Co	28 Ni	29 Cu	30 Zn	31 Ga	32 Ge	33 As	34 Se	35 Br	36 Kr
37 Rb	38 Sr	39 Y	40 Zr	41 Nb	42 Mo	43 Tc	44 Ru	45 Rh	46 Pd	47 Ag	48 Cd	49 In	50 Sn	51 Sb	52 Te	53 I	54 Xe
55 Cs	56 Ba	57 La	72 Hf	73 Ta	74 W	75 Re	76 Os	77 Ir	78 Pt	79 Au	80 Hg	81 Tl	82 Pb	83 Bi	84 Po	85 At	86 Rn
87 Fr	88 Ra	89 Ac	104 Ku														

Figure 4.14 Periodic table showing those metals (inside frame) which can be electrodeposited from aqueous solution [5].

becomes the rate controlling stage, the current-potential plot assumes the form seen in Fig. 4.13.

In practice, it must be recognised that only certain metals can be electrodeposited from aqueous solution and these are shown in Fig. 4.14 enclosed within the frame.

4.3.1.2 Deposition of alloy layers

The picture drawn above, based on the discharge of a single ionic species at the cathode, is rarely encountered in practice. Rather, it is normal to find the simultaneous electrodeposition of two or more ionic species, the best-known case being the (undesired) co-evolution of hydrogen. However that more than one metal ion can be simultaneously deposited can be turned to good use in that it is possible to electrodeposit alloys, rather than single metals [8, 9].

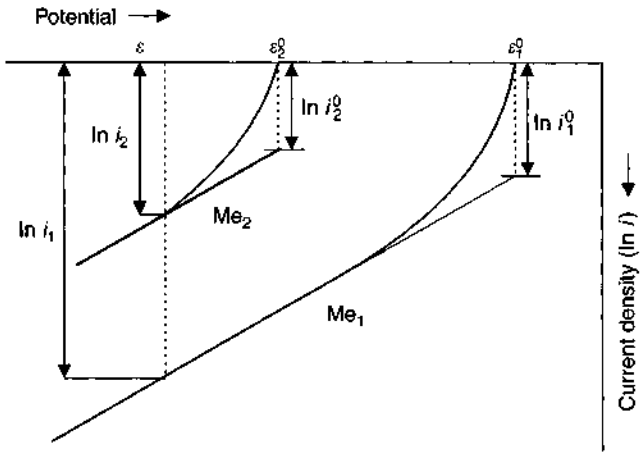

Figure 4.15 Simultaneous electrodeposition of two metals, Me_1 *and* Me_2 *under DC electrolysis, given that* $\varepsilon_1^0 > \varepsilon_2^0$, $i_1^0 > i_2^0$, $\alpha_1 = \alpha_2 = \alpha$.

The simultaneous electrodeposition of two metals Me_1 and Me_2 (which may or may not form a single-phase binary alloy) is best considered in terms of their two polarisation plots. Here, the following points should be made:

- Me_1 is more noble than Me_2 ($\varepsilon_1^0 > \varepsilon_2^0$),
- the exchange current density $i_1^0 > i_2^0$,
- the deposition process is wholly under activation control, such that $\eta_{D1} \neq \eta_{D2}$.

Given these assumptions, the following different cases can be considered.

The case where the transfer coefficients α_1 and α_2 have the same value. This is represented by Eq. (4.13).

$$i_1 = -i_1^0 \times e^{[-(1-\alpha_1)\cdot z\cdot F/RT]\cdot\eta_{D,1}} \tag{4.18}$$

$$i_2 = -i_2^0 \times e^{-[(1-\alpha_2)\cdot z\cdot F/RT]\cdot\eta_{D,2}} \tag{4.19}$$

The corresponding current–potential plots for electrodeposition of metals Me_1 and Me_2 are depicted in Fig. 4.15.

Deriving the ratio of the two cathodic current densities, i_1 and i_2:

$$\frac{i_1}{i_2} = \frac{i_1^0}{i_2^0} e^{[(1-\alpha)\cdot z\cdot F/RT]\cdot(\eta_{D,2}-\eta_{D,1})} \tag{4.20}$$

The following conclusion is obtained. For the simultaneous deposition of two metals, the ratio of their deposition current densities is a function of their exchange current densities and the separation of their reversible potentials. The greater the exchange current density of Me_1 and the more anodic its equilibrium (reversible) potential than the corresponding values for Me_2, the more Me_1 will be deposited, as compared with Me_2.

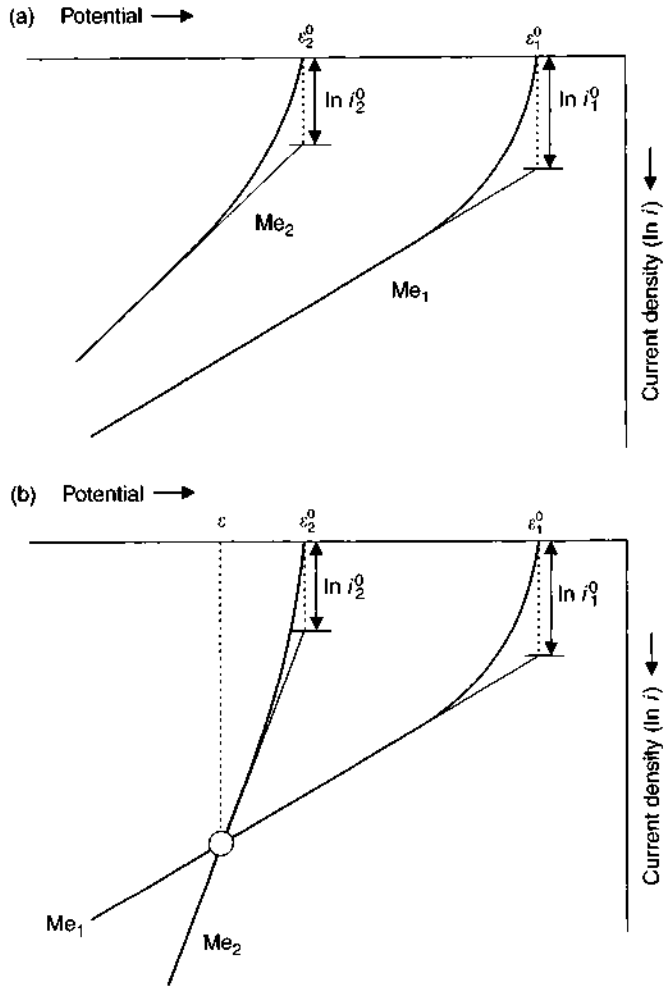

Figure 4.16 Simultaneous deposition of metals Me_1 *and* Me_2 *under DC electrolysis, given that* $\varepsilon_1^0 > \varepsilon_2^0$, $i_1^0 > i_2^0$, $\alpha_1 < \alpha_2$ *(top) and* $\alpha_1 \ll \alpha_2$ *(bottom).*

The condition $\alpha_1 = \alpha_2$ is an approximation which does not always *hold*, and in general, the transfer coefficients for different cathodic reactions are not identical, though in many cases they are close to 0.5. However to the extent that the transfer coefficients are not identical, the slopes of the polarisation plots (Tafel slopes) will differ [10]. This is seen in Fig. 4.16(a) and (b), which shows the current–voltage plots for the cases $\alpha_1 < \alpha_2$ and $\alpha_1 \ll \alpha_2$, respectively.

It follows that as α_2 increases, the amount of metal Me_2 compared with Me_1 likewise increases. In the case where α_2 becomes much larger, the current–voltage plot for Me_2 will intersect that for Me_1 (Fig. 4.16b) with the following consequences: at deposition potentials more positive than ε, Me_1 is preferentially deposited. At deposition potentials more negative than ε, more Me_2 will be deposited. At potential ε, the

point at which the two lines intersect, the deposition current densities for the two metals are equal ($\ln i_1 = \ln i_2$). As a consequence, the two metals will be deposited in equal amounts at this potential. (this assumes n, the number of electrons in the charge transfer, is the same, and that 'equal amounts' is expressed in atomic mass, rather than straightforward weight). The cathodic deposition efficiency will then be 50% for each metal, but not as defined in Section 4.3.1.1 (which is the mass definition) but as atomic percent efficiency. The wider conclusions to be drawn from this are that, when seeking to electrodeposit an alloy, it is best when the polarisation curves for the two lie as close as possible together, and in the ideal case, rarely if ever found in practice, the two curves would be identical.

The listing of reversible potentials for metal deposition–dissolution, widely quoted in many textbooks, almost invariably quotes values for metal–metal ion couples in their uncomplexed aqueous solution. Once such metal ions are complexed, however, for example as cyanides, their values of ε ($Me/Me_{complex}$) will almost certainly be different. Thus, when it is not possible to deposit an alloy because the ε values of the parent metals are too far apart, it may be possible to complex the metal ions in such a way that their ε values become much closer, so meeting the conditions set out above. Thus, the principle that the more noble of two metals will be deposited at a more anodic potential may, in some circumstances, be reversed. Complexation will also usually result in a much lower concentration of free metal cations (most of these being instead bound as a complex ion). The resourcefulness of the electrochemist thus lies in selecting complexing electrolytes which bring together the deposition potential of the constituent metal ions, while meeting the various other requirements. Inspection of the electrolyte formulations for alloy deposition illustrates how this has been achieved.

The principles set out above, assume that the deposition reaction is activation controlled (charge-transfer controlled). If, however, as inevitably happens as the current density is increased, the reaction becomes diffusion controlled (mass-transfer controlled), then the situation changes. Under these conditions, the relative rates of discharge of Me_1 and Me_2 will be a function simply of their relative concentrations and diffusion coefficients (the hydrodynamic conditions and Nernst layer thickness is the same for both species). This is illustrated in Fig. 4.17. Here, Me_1 is the more noble of the two metals and it is seen that in the potential range $\varepsilon_1^0 > \varepsilon_2^0$, Me_1 will be deposited exclusively. As the potential becomes more cathodic, and reaches the value ε_2^0, Me_2 will also begin to be deposited, though at a rate less than Me_1. As the potential is made still more cathodic, the point is reached, at ε where the two metals deposit at the same partial current density. However, after this point, the deposition current for Me_2 becomes greater, and the current–potential plot for Me_1 flattens out (current no longer a function of potential), the classic indication of a diffusion-limited reaction.

This somewhat complex picture can be summarised as follows for a solution containing two or more different metals (assumed to be carrying the same charge):

- At low overpotentials, the metal with the most noble reversible potential, ε, will deposit at a faster rate.

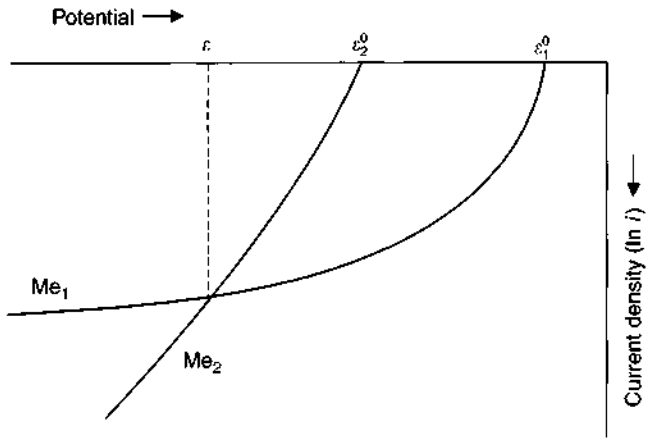

Figure 4.17 Simultaneous electrodeposition of two metals under DC conditions. Me_1 *has the more anodic value of* ε (ε_1^0) *and therefore is deposited exclusively, until the overpotential is increased to the point* ε_2^0 *when* Me_2 *also begins to deposit, though not as fast as* Me_1. *At the overpotential value* ε, *the curves interest and the deposition currents are the same. Above this, the curve for* Me_1 *begins to flatten out, indicating the onset of diffusion control.*

- By selecting a suitable complexing agent, the value of ε for a given metal ion can be shifted by several hundred millivolts, and the ranking of two or more metals can be altered.
- As the overpotential increases, the overall reaction will shift from charge transfer to the so-called 'mixed' control, and then to mass-transport control.
- At higher overpotentials where the electrodeposition reactions will be under mass-transport control, the relative deposition rates of two or more metals will depend on their concentrations and the diffusion coefficients of the metal-containing ions.

The reader is reminded, however, of a statement made above, which is that in general, metals electrodeposited under mass-transport controlling conditions will form powdery deposits of no practical use.

The foregoing picture holds only under the condition that the two deposition reactions do not interfere with one another. This is only rarely the case.

A broad overview is given in Fig. 4.18 which shows virtually all conceivable binary alloys, noting which of these have been deposited in practice [5, 11]. Some form the basis of widely used commercial processes, others have been demonstrated in the laboratory.

4.3.1.3 Deposition of composite coatings

The properties of electrodeposited metals or alloys can be substantially modified, usually for the better, by arranging that finely divided particles are co-deposited with the metal or alloy, thereby becoming incorporated into a metallic matrix [12–16]. This is usually accomplished either by arranging for the particles to remain suspended in solution, or for them to settle onto a horizontal cathode surface over

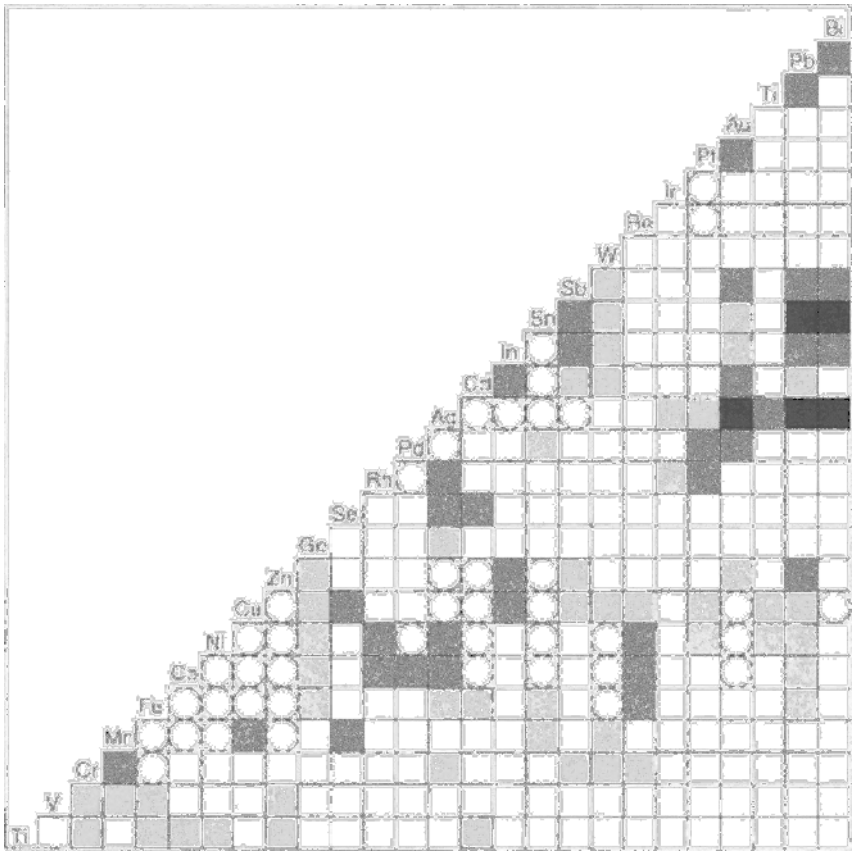

Figure 4.18 Status chart for electrodeposition of binary alloy: ○ = *demonstrated on the technical scale,* ■ = *currently used in practice,* □ = *reported in laboratory study [11].*

which the metal electrodeposits. Such particles may be inorganic (oxides, carbides, diamond), metallic (chromium) or organic (PTFE). The amount of second-phase particles thereby incorporated will be a function of the deposition conditions (pH, temperature, viscosity, concentration of particles in suspension, hydrodynamic conditions) and to the extent these parameters affect the zeta potential, this too is important. The particle size will be from 30 μm downwards, more recently there has been emphasis on nanometer-sized particles of 100 nm or less. The incorporation of such particles affects both the structure of the metallic deposit and its properties. Thus internal tensile stress can be reduced and thus the propensity to crack (particles can act as crack-stoppers). Surface properties such as friction and wear will likewise be modified, and bonding characteristics also.

The choice of second-phase particle for incorporation depends on the function it is desired to enhance. For increased hardness, tensile strength and high-temperature characteristics, hard compounds such as the carbides of chromium, silicon, titanium or tungsten can be used, as can the oxides of titanium, silicon, aluminium and zirconium. Titanium nitride has also been used. Where tribological factors are

Table 4.3 Overview of electrodeposited composite coatings.

Matrix metal	Oxides	Carbides	Sulfides	Sulfates	Others
Ag	Al_2O_3	SiC			
Au	Al_2O_3	SiC			
Cd	Fe oxide	SiC, WC			
Co	Various oxide				Natural or synthetic mica
Cr	Al_2O_3				
Cu	Al_2O_3, CeO_2, TiO_2, ZrO_2	SiC, WC, ZrC	MoS_2	$BaSO_4$, $SrSO_4$	Mica, graphite
Fe	Al_2O_3, Fe oxide	SiC, WC	MoS_2		Natural or synthetic mica
Mn		SiC			
Ni	Al_2O_3, BeO_2, CdO, CeO_2, Fe oxide, MgO, SiO_2, ThO_2, TiO_2, ZrO_2	SiC, VC, WC	MoS_2	$BaSO_4$	Boron nitride, Teflon (PTFE), mica

Table 4.4 Industrially important composite coatings (in grey) and possible future developments.

Composite coating	Application areas
$Co–Cr_2O_3$/Co–Ni–Cr_2O_3	High-temperature resistant coatings, aerospace
Me + graphite, Me + oil	Wear-resistant coatings including dry-running
Ni–Al_2O_3 + Cr-layer	For decorative uses
Ni–BN, Ni–graphite, Ni–MoS_2	Automotive industry
Ni–PTFE	Low-friction coating, automotive industry
Ni–SiC	Wear-resistant coating, automotive industry
Ni + diamond	For microelectronic uses
Ni + $NiFeS_2$, Cu + Cu_2O, Ni + TiO_2	Catalytically active surfaces
Ni + Cr + Al + Si + TiC	Dense, temperature-resistant coatings
Zn + SiO_2	Corrosion-resistant coatings

important, boron nitride, graphite, fluorinated graphite, molybdenum disulfide and PTFE are used. The action of such solid lubricants is usually initiated after a thin outer skin of pure metal has been worn away, after which their respective actions begin to operate. Many other species have also been used as second phase. Among these, three will be mentioned, namely diamond (for obvious reasons), metallic chromium particles which, after heat-treatment, alloy with the matrix to form an alloy which could not have been formed by simple electrodeposition of ions. Lastly, a technology has been developed for incorporation of micro-capsules which can be filled with whatever species is desired, liquid or solid, this being released as the surface wears away to expose fresh capsules. One particular application of composite coatings is the provision of surfaces which can, under emergency conditions, continue to function in the dry-running, that is, in the unlubricated state.

The properties of composite coatings depend also on the particle size and distribution of the second phase. The growing use of sub-micro metre particle sizes

(100 nm or less) has been mentioned and in certain applications, the second-phase must be high-temperature resistant, that is it must neither break down nor alloy with the matrix metal. The presence of such particles can create a dispersion-hardening effect in that they hinder dislocation formation in the grain, and act as pinning agents. In the same way, they can also hinder grain growth resulting from annealing.

Table 4.3 gives an overview of matrix-second phase combinations while Table 4.4 shows those which are of industrial importance [16].

Where it is desired to achieve a uniform distribution of second phase through the matrix (and in some cases, a graded rather than a uniform distribution is sought), the second phase particles must be uniformly suspended in the electrolyte. For this to be so, the tendency to settle under gravity must be constantly overturned, by means of stirring, pumped electrolyte flow, ultrasonic agitation or air injection.

Sacrificial anodes are made of the same metal that is being deposited, for example, copper. A copper anode will anodically dissolve, so releasing into solution copper ions to replace those which have been deposited at the cathode. Ideally, the anodic process would be the absolute mirror-image of that taking place at the cathode. In practice, one or both processes are less than 100% efficient, and some sort of adjustment is required. The second type of anode is the so-called permanent anode, typically platinum coated titanium.

In the case of very fine particles, a suitable surfactant is frequently added which, after ionising in solution, adsorbs on the surface of the particles and then orient themselves according to their electric charge. The repulsive electrostatic forces thereby minimise coagulation of the particles, which could result in settling [15].

A number of workers have investigated the mechanism of the electrodeposition of composites, and most of their proposed mechanisms involve one or more of the following three processes [13, 16].

1. Electrophoretic movement of positively charged particles to the cathode.
2. Adsorption of the particles at the electrode surface by van der Waals forces.
3. Mechanical inclusion of the particles into the layer.

The most important of these models, which offer a quantitative relationship for the incorporation rate of the particles into the matrix, are listed in Table 4.5 [16]. These models are all, to a greater or lesser extent, approximate solutions, based on simplifying assumptions. As a result, they cannot be used for exact quantitative predictions. Even so, they are of value in pointing the way towards advances in the technology. They allow one to envisage the overall deposition process in terms of five discrete steps, shown in Fig. 4.19.

These steps mark the progress of particles from the bulk solution to their incorporation in the deposit. The first stage postulates formation of an electro-active ionic cloud surrounding the particle, as soon as these are introduced into the electrolyte. Under the action of convection, these ionically enveloped particles are transported to the hydrodynamic boundary layer, migrate across this and are conveyed by diffusion to the cathode. After the ionic cloud is wholly or partly reduced, the particles are deposited and incorporated in the matrix as the metal ions are discharged, so 'burying' the inert particles.

Table 4.5 Theoretical models for calculating incorporation rates of particles into a metal matrix.

Saifullin–Kablilova model	m = wt% of particles incorporated in coating c_p = particle concentration in electrolyte ρ_M = density of matrix metal ρ_p = particle density
Bazzard–Boden model	r_p = particle radius A = electrochemical equivalent of matrix metal i = current density t = deposition time
Guglimi model	c_v = vol. fraction of particles in suspension α = vol. fraction of particles in matrix A_M = atomic mass of matrix metal i^o = exchange current density β, V_o = constants z = valence of matrix metal k = constant for particle–cathode interaction
Kariapper–Foster model	dV_p/dt = volume per cm^2 and per s adsorbed particles N^* = number of interparticulate collisions
Valdes–Chieh model	i_p = rate of incorporation of particles into coating k^o = electrochemical rate constant c_ξ = concentration of electroactive species adsorbed on cathode
Celis–Roos–Buelens model	N_{Ion} = number of ions passing through diffuse layer N_p^* = number of particles in electrolyte N_{Ion}^* = number of ions in electrolyte i_{tr} = current density at transition from reaction to concentration overvoltage Φ = constant related to interaction between free and adsorbed ions (Φ = 0; charge transfer mechanism) W = probability of particle being incorporated in layer

4.3.1.4 Deposition of 'sandwich layers'

Not only can one deposit simple metal layers, alloys and composite coatings but electrodeposition methods can also be used to form so-called 'sandwich layers'. These consist of two or more layers, one above the other. The individual layers are usually extremely thin, typically in the nanometer range, and are formed under special condition. Such alternating sandwich deposits are increasingly important in micro- and nanotechnology and their special physical and chemical properties make them attractive in the wider field of metal finishing.

The underlying principle for deposition of such systems is as follows. A given metal will only be electrodeposited when the potential is more negative than its reversible potential, $\varepsilon_{Me/Me^{z+}}$ as given by the Nernst equation

$$\varepsilon_{Me/Me^{z+}} = \varepsilon^0_{Me/Me^{z+}} + \frac{R \cdot T}{z \cdot F} \cdot \ln \frac{a_{Me^{z+}}}{a_{Me}} \tag{4.21}$$

where $\varepsilon^0_{Me/Me^{z+}}$ is the standard reversible potential, $a_{Me^{z+}}$ the activity (effective concentration) of metal ions in solution, and a_{Me} the activity of the pure metal (by definition = 1).

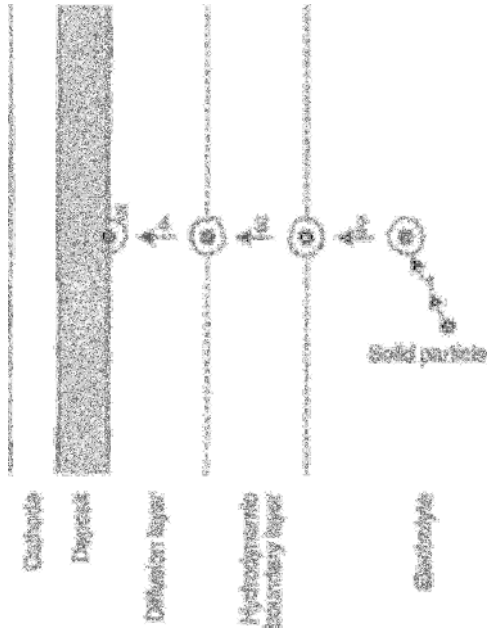

Figure 4.19 Process steps in codeposition and incorporation of a solid particle into the deposit: formation of an ion cloud around the particle (1); transport by means of convection (2); transport by diffusion (3); reduction reaction (4); adsorption (5) [14].

The hypothetically reversible reaction, $Me^{z+} + z \cdot e^- \rightarrow Me$ is driven in the cathodic direction (left to right) by application of a cathodic potential, ε. Deposition can only begin when ε is more cathodic than $\varepsilon_{Me/Me^{z+}}$ and the metallic phase so formed, is only stable in aqueous solution so long as this remains the case. The Nernstian equilibrium potential $\varepsilon_{Me/Me^{z+}}$ thus represents the upper (anodic) limit of thermodynamic stability. It is usual to discuss metal electrodeposition in terms of the cathodic overpotential which drives the process ($\eta < 0$) (note: potential values (ε) will normally be designated + or −, and are referenced to a potential standard or reference such as the hydrogen electrode. The overvoltage, η refers to a specific reaction being driven in a specified sense (anodic or cathodic) and is not therefore assigned any polarity).

In spite of the foregoing, metal deposition can sometimes occur at potentials anodic to the reversible value of $\varepsilon_{Me/Me^{z+}}$, thereby apparently contravening the thermodynamics of the system. This phenomenon, known as underpotential deposition (UPD), is an adsorptive process, which proceeds only as far as a monolayer of the deposited metal [17] and can be a precursor stage for subsequent metal electrodeposition on a foreign substrate surface. The phenomenon is important in the context of sandwich layer formation. Depending on whether only one adsorbable metal ion Me'^{z+} or several such, Me''^{z+}, Me'''^{z+} ions are present in solution, a single or multiple layer system can be formed, as, for example [Me]/Me'/Me''/Me''', ... where [Me] is the metallic substrate. Figure 4.20 shows the build-up of such a sandwich system from two or three components. The thickness of the first layer of Me' can be one (Fig. 4.20a) or more monolayers (Fig. 4.20b). In addition to sandwich layers (Fig. 4.20c), alloy layer systems can also be formed (Fig. 4.20d).

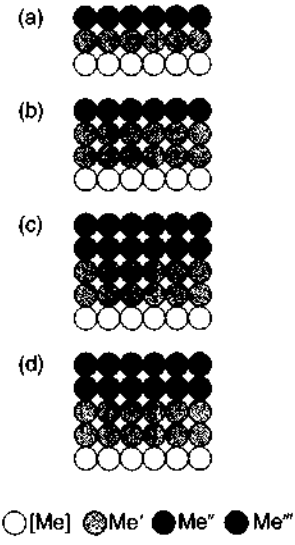

Figure 4.20 Schematic representation of the build-up of a duplex (a, b) and triplex (c) sandwich layer system, and an alloy system (d).

An impressive example of this technology is the formation of a three-component layer system based on silver, lead and thallium over gold [Au]/Ag/Pb/Tl [18]. A (111) gold single crystal used as substrate, provides the orientation. For the deposition of defined monolayers, the following concentrations of metal salts are used:

Silver: 10^{-5} M $AgClO_4$
Lead: 10^{-5}–5×10^{-3} M $Pb(ClO_4)_2$
Thallium: 10^{-3} M $Tl(ClO_4)$
Supporting electrolyte: 0.5 M $NaClO_4$ + 10^{-3} M $HClO_4$

The procedure is as follows: initially silver is deposited in the underpotential and overpotential range. The silver ion concentration is kept low, so that a silver film of thickness 0.2–5 monolayers is formed under diffusion control on the exposed gold surface in the underpotential region. By maintaining the electrode for a longer time in the overpotential range, the thickness can then be continuously increased to several monolayers. Next, by stepping the potential towards the reversible value for lead deposition, underpotential deposition of this metal occurs. Silver deposition continues to take place, but because the concentration of silver ions is so low, the process is diffusion controlled and several orders of magnitude less than the activation-controlled lead deposition. The resulting incorporation of silver in the lead deposit is thus negligible. In order to form the thallium layer, one has to combine two, two-component systems, namely [Au]/Ag/Pb and [Ag]/Pb/Tl [18]. The properties of the resulting three-component system are then determined by both two-component systems.

By suitable means, the sequence of metals on the substrate can be reversed.

The literature contains numerous reports on deposition of such multilayer sandwich systems, some of which are based on use of a single, multicomponent bath (as above) while others involve transfer of the work from one solution to another.

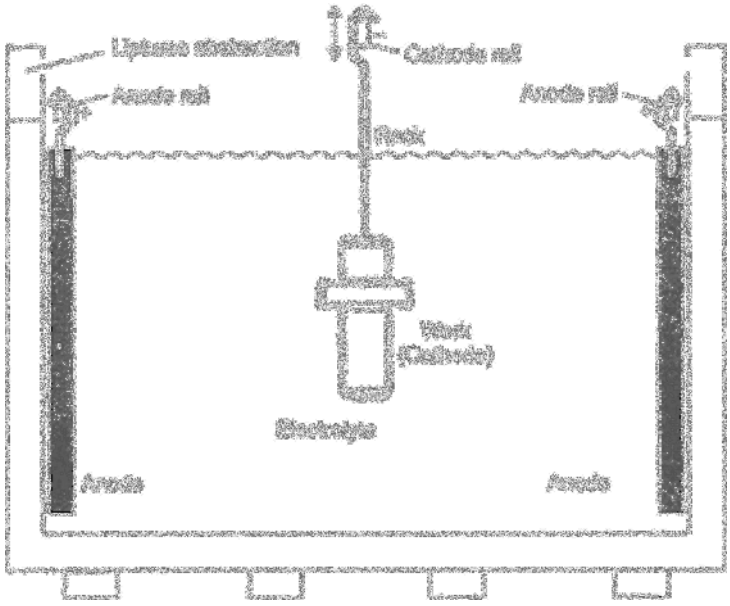

Figure 4.21 Main components of a metal electroplating tank using DC [5].

4.3.1.5 Deposit thickness distribution

Figure 4.21 is a sketch of a DC metal electrodeposition bath.

The work to be plated is the cathode; the anodes are positively polarised. A distinction is made between soluble and insoluble anodes. In the latter case, the source of metal ions is from soluble metal salts which are added to the solution. In the case of soluble anodes, these dissolve anodically, releasing the ions which are then deposited at the cathode. Ideally, the rate of anodic dissolution exactly matches the rate of cathodic metal deposition so that the concentration of ions in solution remains the same. In practice, this is rarely the case, and either the anodic or cathodic process is more efficient, resulting in build-up or depletion of metal ions in solution, respectively. The quality of the anode metal, its purity and metallic structure can all affect the dissolution rate and the quality of the cathodic deposit.

The metal ions, after migrating to the cathode, are there discharged. The deposition rate can be calculated using Faraday's law. Here θ denotes the cathode current efficiency*

$$v = \theta \frac{i_c}{zF} [\text{mol}/(\text{cm}^2\text{s})] \tag{4.22}$$

As seen in Fig. 4.22, and in contrast to the case of electroless deposition (Section 4.4) the deposit thickness is not uniform.

A better insight is obtained by inspection of Fig. 4.23 where both types of deposition process were used to coat a screw thread, first with electroless, then with electroplated nickel. It is seen that whereas the electroless Ni–P deposit is substantially

*See Footnote on page 100.

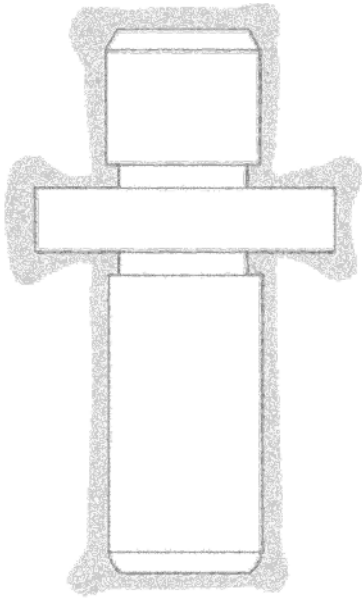

Figure 4.22 Non-uniform deposit thickness distribution found when electroplating a component with complex geometry using DC.

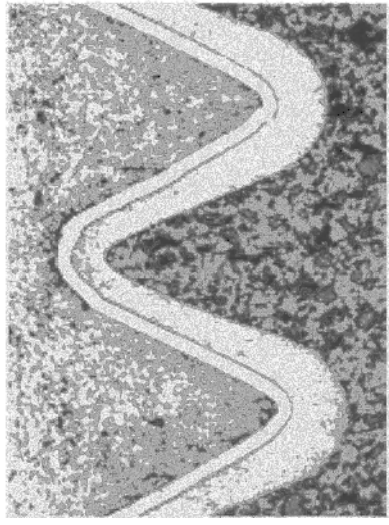

Figure 4.23 Metallographic cross-section of a screw thread, initially plated with electroless nickel, thereafter with electrodeposited nickel (etched in H_2O_2/H_2SO_4, 200 V).

uniform in thickness, the electroplated deposit is about half as thick in the recesses as it is on the outer ridges of the screw thread.

Such non-uniform thickness distribution from electroplated deposits is specially pronounced in samples of complex geometry. The causes of this unwelcome behaviour

are the variations in local current density, these in turn being a reflection of non-uniform electrical field between anode and cathode (see Chapter 3). The pattern of these field-lines is mainly determined by geometric factors, such as the size, shape and positioning of anodes and cathode. Field-lines are very rarely parallel, and tend to be more closely-spaced at protruding edges and corners on the component being plated, as shown in Fig. 4.24.

The surface morphology is also important, especially when, as in Fig. 4.25, there are pronounced roughness peaks.

As Fig. 4.24 shows, the cause of the unevenly distributed metal thickness is due to the fact that the incoming ions, heading towards various parts of the cathode, have to travel along longer or shorter lines of force during their diffusion. Equation (4.15) expresses the cathodic current density for the condition that diffusion of metal ions to the cathode is the rate-determining step. The next step in the mechanism is transport through the Nernst layer, across which there is a linear concentration gradient. In those cases where the surface roughness or other protrusions at the cathode surface are less than the Nernst layer thickness, incoming ions reaching these peaks have a shorter distance to travel than those destined for depressions or the principal plane of the cathode. Metal deposition is thereby favored at these 'high points' and deposit thicknesses there will be greater than in surrounding depressions. As a consequence, the roughness will become more pronounced as a result of the electrodeposition [19]. In theory, at least, one could space the anode and cathode so far apart that the distance between peaks and valleys at the surface became insignificant. In practice, this would not be feasible. However much the same effect can be

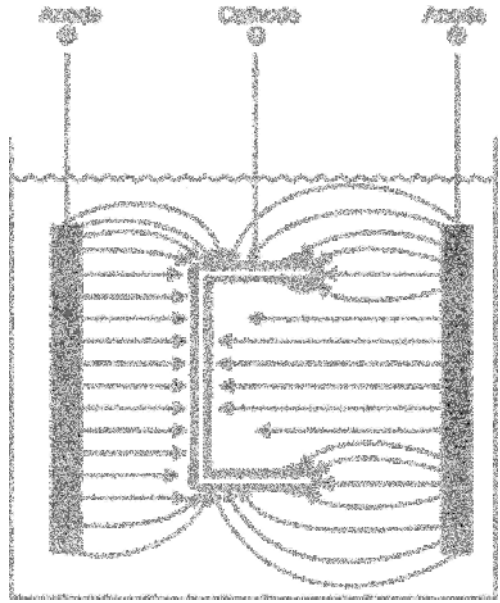

Figure 4.24 Pattern and distribution of lines of electrical equipotential force between anode and cathode as the cause of non-uniform current density and metal distribution.

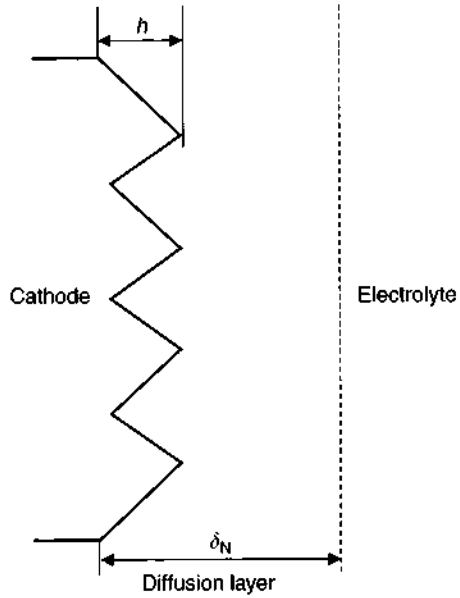

Figure 4.25 Enhanced metal deposition at roughness peaks on the cathode work surface as a result of an inhomogeneous potential field.

achieved by interposing a mesh, or perforated plate, made of a non-conducting material, between anode and cathode. While this significantly improves metal distribution, it does so at a price – which is an increase in cell voltage and thus the energy required.

One widely used approach to improve metal distribution, is to improve the so-called levelling power of the electrolyte, that is, its ability to reduce the extent of roughness of the substrate, by preferential deposition into depressions, resulting in a smoother surface. Such electrolytes contain special additives for this purpose (see Chapter 3). In the case of components with a simple geometry, the problem can often be mitigated by appropriate positioning of the anodes (Fig. 4.26).

A further example, shown in Fig. 4.27, illustrates the use of so-called auxiliary anodes, which operate to improve the uniformity of the potential field and thus the thickness of metal deposited. The figure also shows how deposition is enhanced at the corners and edges of the work, the so-called 'dog-bone' effect and this too, can be repressed using auxiliary anodes.

4.3.2 Pulse Plating Processes

Electrodeposition using pulsed currents, usually known as 'Pulse plating', is a relatively new approach [20–36]. Though electrodeposition was traditionally carried out using DC, a modification of this by use of current interruption or even current reversal, goes back many years, as does the use of AC, superimposed on DC. Given that only electromechanical switchgear was then available, the timescale of these operations was many seconds in duration. Only with modern electronic switching

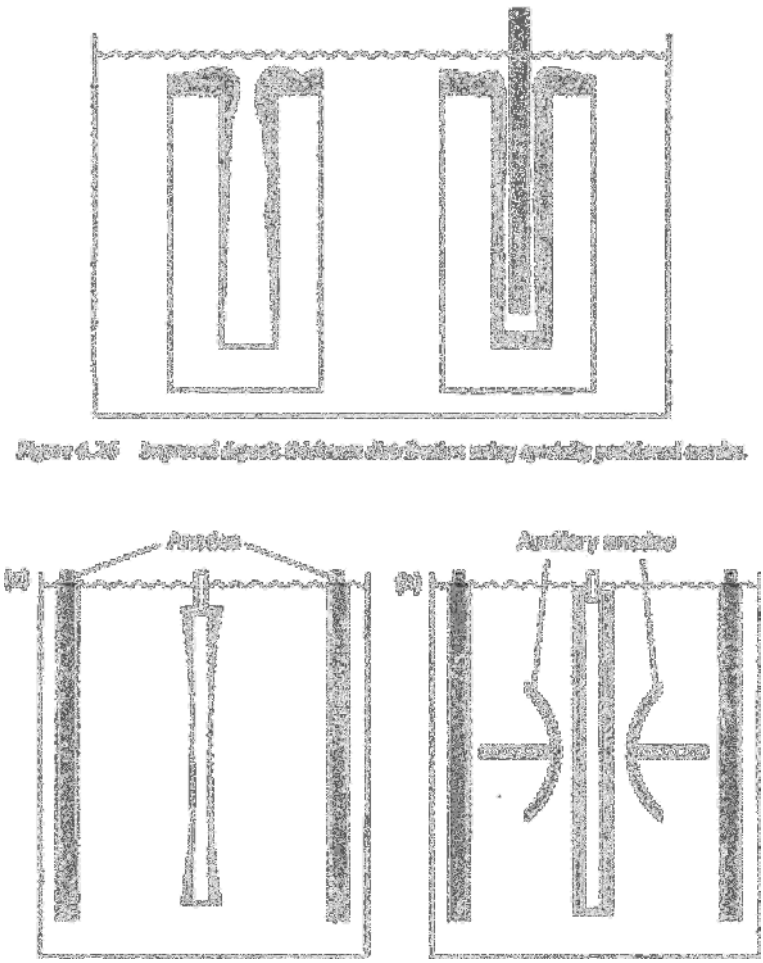

Figure 4.27 Metal thickness distribution: (a) without auxiliary anodes and (b) with auxiliary anodes [5].

has it become possible to create the short duration, but heavy current square-wave pulses shown in Fig. 4.28. These pulses can be unipolar ('on–off') or bipolar (current reversal, with or without additional 'rests') [21, 28]. In all cases, the option remains to use pulses alone, or to superimpose these on a DC feed. Figure 4.28 shows the most common variants. In the case of the bipolar pulse, metal deposition occurs in the cathodic pulse with a limited amount of metal being re-dissolved in the anodic period. This repeated deposition and partial re-dissolution can improve the morphology and indeed the physical properties of the deposit.

In Fig. 4.28, the area enclosed by the square waves represents electrical charge ($i \times t$). Areas designated as 'k' represent metal deposition charge. Those with 'a', the re-dissolution. Clearly k must be greater than a, or no net deposition would take place. Also to be seen in Fig. 4.28 are the rest periods between pulses, when no current flows. For some deposition processes, even more complex pulse trains than

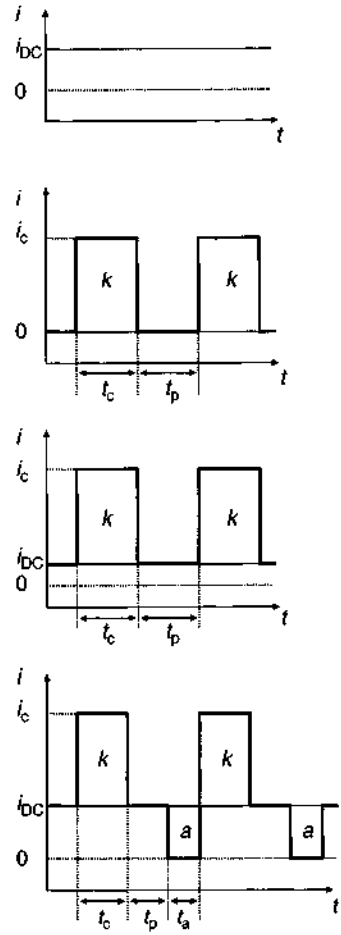

Figure 4.28 Typical current–time sequences (pulses) used in metal deposition by pulse plating. Top to bottom: simple square-wave; square-wave superimposed on DC; square-wave superimposed on DC with polarity reversal. (uppermost: conventional DC electroplating current).

those shown in Fig. 4.28 have been used. The function of the rest periods and reverse pulses is complex, and partly based on empiricism. However, it is clear that during the rest period, the concentration of metal ions in the Nernst layer can be replenished, so that when the cathodic polarity is again switched on, the deposition process takes place with a higher concentration of metal ions than would be found using all but the lowest DC current densities. It will also be noted that, as a consequence of pulsing, the electrical double layer, which is analogous to an electrolytic capacitor, is repeated charged up and discharged. It should also be pointed out that, although the cathodic current might be applied for less than half the total time (Fig. 4.28), the overall metal deposition rate can be as great or even greater than that obtained with DC alone.

One implication of pulse plating is that, in addition to the usual independent variables in electrodeposition (pH, temperature, current density, bath composition,

agitation) one now acquires further degrees of freedom in terms of pulse duration, polarity, pulse height, etc. Expressing these as i_c (cathodic pulse height), t_c (duration), t_{off} (off-time), i_a (anodic pulse height), t_c and i_{DC} (DC current over which pulses are imposed), it is seen that at least five additional variable are now added to the list. These parameters can be used to calculate current densities at each point in the sequence, though it has to be said, with the process now being describable as 'non-steady-state', the concept of current density has little practical significance and it may be more meaningful to think in terms of total cathodic and total anodic charge passed over time, or their algebraic sum.

Table 4.6 summarises the range of independently variable parameters.

Taking the three variables, current density, pulse duration and off-time, a fourth parameter can be uniquely defined, namely mean current density, I_m. In formal terms, this may be compared with a corresponding DC current density. In order to achieve current densities comparable to DC, when pulsing, higher pulse current densities must be used, in order to compensate for the off-times. A widely used parameter is $t_c/(t_c + t_p)$. Multiplied by i_c, this gives mean current density, and the expression is sometimes referred to as 'percent on-time' or 'duty-cycle'.

4.3.2.1 Deposition of metal layers

A typical plating cell for use with pulsed currents is sketched in Fig. 4.29. Just as much as with DC plating, the various transport mechanisms for replenishment of metal ions to the cathode, especially diffusion, play a key part in the process. However, and in contrast to DC plating processes as shown in Fig. 4.10, two, rather than one, diffusion layers are formed at the cathode surface. A greatly magnified sketch of these is shown in Fig. 4.30.

As a result of convective processes in solution, the metal ions migrate from the bulk of solution to the outer edge of the diffusion layer, δ_s which is analogous to that found in DC electrodeposition systems. Thereafter, they move closer to the cathode, entering the so-called pulse-diffusion layer δ_p which is immediately adjacent to the cathode surface.

This layer builds up and collapses in synchronism with the pulse frequency, and the concentration of metal ions within it, follows suit. The repetition of this cycle of layer formation and collapse with the corresponding change in metal ion concentration is known as the 'quasi-steady-state'. The thinner the pulse diffusion layer, the

Table 4.6 Independently variable parameters in pulse plating and mean current density [22].

Current form	Selectable variables	Mean current density
Direct current	1	$i_m = i_{DC}$
Square-wave pulse	3	$i_m = i_c \frac{t_c}{t_c + t_p}$
Square-wave superimposed on DC	4	$i_m = i_c \frac{t_c}{t_c + t_p} + i_{DC}$
Bipolar square-wave pulse	5	$i_m = \frac{i_c t_c - i_a t_c}{t_a + t_c + t_p}$

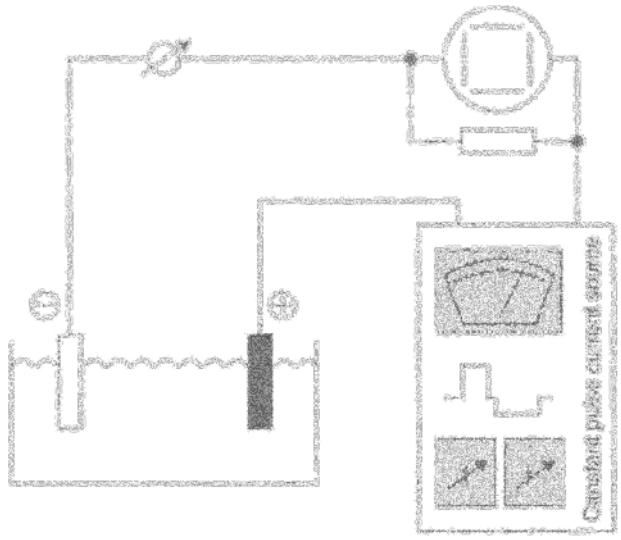

Figure 4.29 Experimental plant for metal electrodeposition by pulse plating.

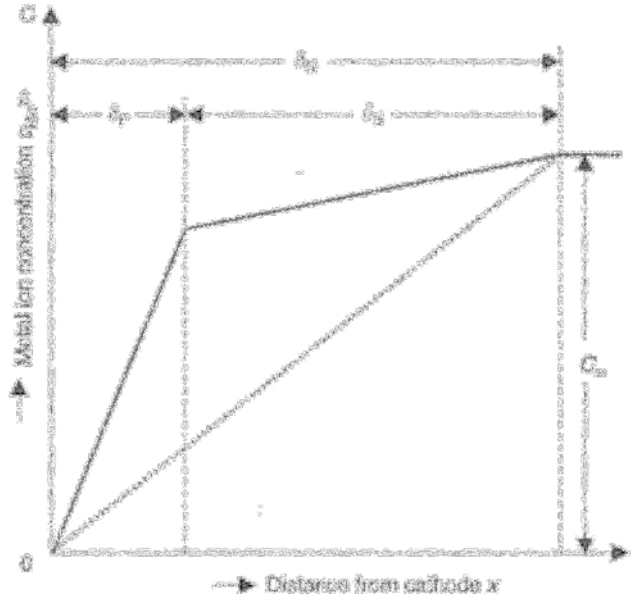

Figure 4.30 Structure of the diffusion layers during pulse plating (δ_N, Nernstian diffusion layer; δ_s, steady-state diffusion layer; δ_p, pulse diffusion layer in a quasi-steady-state [22].

better it can follows the contours of the surface, implying that all areas of the cathode surface are equally accessible. The total thickness of the diffusion layer, δ_N denotes an expansion of the Nernstian diffuse layer which forms during DC electrolysis. The sequence of metal ion concentrations within the layers, δ_s, δ_p and δ_N is shown in Fig. 4.30.

The pulsed current not only affects the structure of the diffusion layer, but also that of the electrical double layer which forms at the metal–solution interface (Fig. 4.11). This layer, only a few Angstroms thick, can be compared, as previously noted, to a parallel plate condenser with closely spaced plates and thus a very high capacitance value.

In order to move to a potential region where metal deposition can take place, this 'electrolytic condenser' must first be charged and the time taken to do this depends on a number of physical and chemical factors and also the current density. If the magnitude or direction of the applied current changes, as is the case when a current pulse is applied, then the electrode potential changes and so too does the structure of the double layer. In pulse plating, the time taken for this change will normally be far shorter than the pulse duration itself or the time between pulses.

The complex conditions obtaining during metal electrodeposition can be demonstrated in the following example based on a simple cathodic square-wave pulse [21]. Such a current is characterised in terms of the cathodic current density, I_c, the pulse duration, t_c and the off-time, t_{off}. The times are usually of the order of some milliseconds and the foregoing three parameters are independently variable. Once determined, the fourth parameter, mean current density, i_m is then fixed.

As the schematic in Fig. 4.31 shows, the pulsed metal deposition is accompanied by characteristic concentration changes at the cathode surface. In the schematic, the current pulses, i_c, the metal ion concentration as a function of time, $c_{Me^{z+}}$ and the concentration of the reduction product, c_R at the cathode surface, are all shown.

The metal ion concentration at the cathode surface falls, during the first pulse, from $c_{Me^{z+}}$ to $c'_{Me^{z+}}$. It then increases during the off-time to a value $c''_{Me^{z+}}$, once again decreases during the second pulse, increasing again in the second off-period and so on. Thus, in this quasi-steady-state, a metal ion concentration at the cathode surface prevails which is significantly higher than would be found in DC electrodeposition, designated as $c^E_{Me^{z+}}$.

During cathodic metal electrodeposition, other species can be simultaneously formed, both metallic or non-metallic and in some cases, these can be incorporated

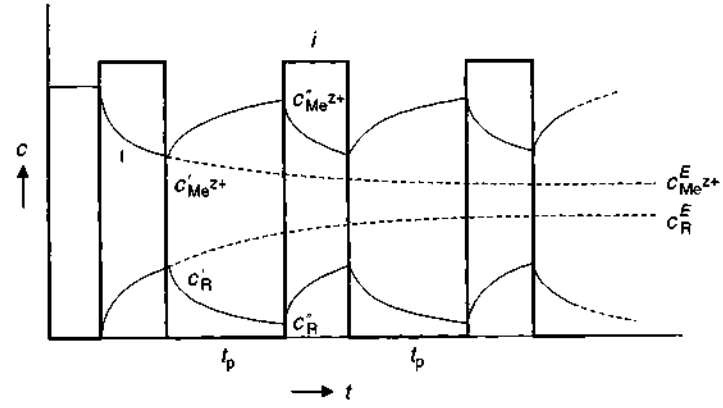

Figure 4.31 Variation with time of metal ion concentration, $c_{Me^{z+}}$ and concentration of reduction product, c_R during pulsed electrodeposition of a metal.

into the deposited metal. Equally, they can diffuse into the bulk electrolyte and it is a feature of pulse plating that this can continue during the off-times. Because of this, the probability of such co-evolved products being incorporated into the deposited metal, is reduced and pulse-deposited metals are thus usually of higher purity than their DC-deposited analogues.

In the example shown, the concentration of reduction product c_R at the cathode surface fell, at the end of the first pulse, to c'_R, and after the second pulse, to c''_R. This progressive decrease continues until the quasi-steady-state is reached, the value being significantly lower than would be the case with DC electrolysis (cE_R).

An impressive example of the decrease in reduction products at the cathode surface following a current pause, is seen in pulse plating of palladium. Palladium is notorious for its very high absorption of hydrogen and it has been shown that, on deposition from an ammoniacal nitrite–nitrate electrolyte, the hydrogen content of the deposited metal is far lower after pulse plating than with DC [25] as shown in Fig. 4.32. Note in this figure that the steep decline in hydrogen content as the off-time increases, appears independent of the pule current density, i_c. Presumably the hydrogen desorbs during the off-time.

It has also been suggested that the high current density at the beginning of a pulse creates a more strongly reducing environment at the cathode surface and thereby enhances the cleaning action, presumably by cathodic desorption. This in turn increases the number of sites where metal deposition can occur and improves adhesion of the deposited metal. In addition, the increased current density is thought to increase the free energy of the charge carriers, thereby increasingly the number of nucleation processes. Pulsed current deposits thereby tend to be more fine-grained and denser (less porous) and better adhering than their DC deposited analogues (see Chapter 8, Section 8.4.2).

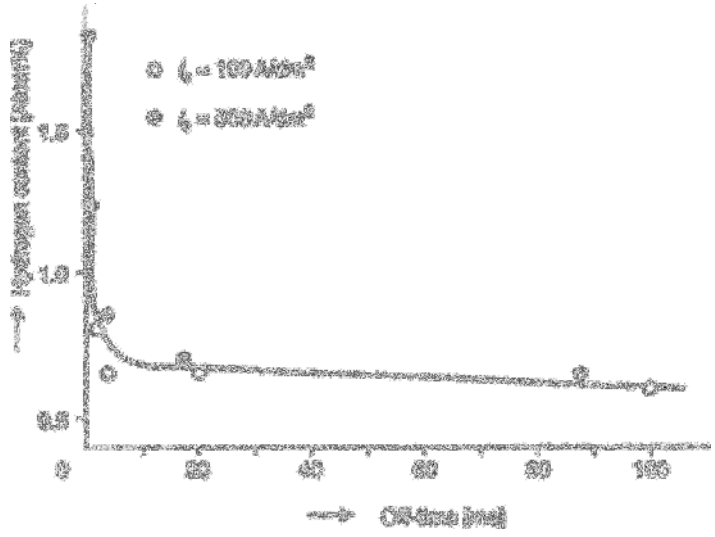

Figure 4.32 Hydrogen content of a pulse plated palladium deposit as function of off-time. pH 9, i_m = 15 A/dm² [25].

Pulse plating has been used on an industrial scale for deposition, among others, of cadmium, copper, nickel and zinc to name but a few. It is increasingly used in the printed circuit board industry for copper deposition (see Fig. 4.37) [27–36].

4.3.2.2 Deposition of alloy layers

Most of what has been previously noted for the pulse deposition of pure metals, applies equally to the electrodeposition of alloys consisting of two or more components. However, some additional points should be noted:

- The current densities used in pulse plating are, in general, high and are many times the value of the mean current density. It follows that electrodeposition takes place at more cathodic potentials than would be the case with DC electrodeposition. Thus, in the pulse plating of a binary alloy, the potential of the less noble component can be shifted so far to the positive direction that its deposition will be favored against the second component. The precondition for this is that there is a sufficient concentration of the less noble component in solution. If this is not the case, its concentration at the cathode surface will fall to zero during the pulse and then, even though the deposition potential is increased, no further increase in the proportion of the metal in the deposit, will result.
- The co-evolution of hydrogen which often accompanies metal deposition leads to a pH increase in the near-electrode layer, and this can strongly affect the composition of the deposit. In the case of pulse plating, this effect is less marked, since hydrogen ions can diffuse in during the off-time.
- In the case of pulse plating, the metal ion concentration at the electrode surface is higher at the beginning of the pulse than it would be in DC plating. This is not to suggest that overall higher deposition rates can be achieved, since the higher rates which prevail during the pulse, are offset by the pause time when no deposition occurs.
- In the case of DC electrolysis, the current efficiency of metal deposition decreases as soon as the limiting current density is exceeded, and the same is true with pulse plating. There is, though, a difference in that whereas in the pulse deposition of a single metal, one normally seeks not to exceed the limiting current density, this is not always possible when depositing an alloy.
- The effect of the pulse regime used, on the deposit composition may be different in two situations, the first where the deposition mechanism of one component is activation controlled and the second component diffusion controlled, and on the other hand, a situation where the rate-determining process for both components is the same.
- Each new current pulse initiates a nucleation process, resulting on the one hand, in a depletion of metal ions in the diffusion layer, and on the other, a grain-refining effect in the deposited metal or alloy. The current pauses allow a replenishment of metal ions in the diffusion layer. As a result, it may be possible to produce deposit compositions by pulsing, which cannot be achieved using DC conditions.

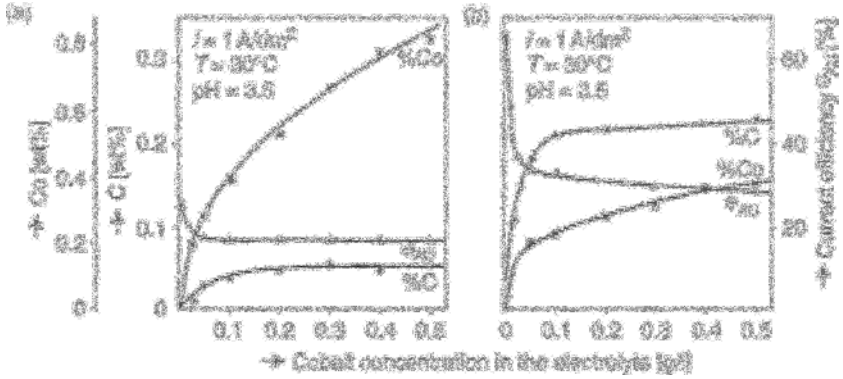

Figure 4.33 Cobalt and carbon content of gold–cobalt alloys deposited with (a) pulsed current and (b) DC [21].

Figure 4.33(a) shows an example of pulse deposition of an alloy. The composition of the gold–cobalt alloy from an acid electrolyte is primarily a function of the cobalt concentration [21]. Alloys of this composition are widely used, for example in electrical contacts. Figure 4.33(b) shows, for comparison, the same type of alloy formed using DC electrodeposition.

It is seen that the cobalt concentration in the pulse-plated deposit is twice that in the DC plated deposit. At the same time, the carbon content in the former deposit is a quarter of that found in the DC deposit. These observations confirm some of the assertions made above, regarding pulse plating. Pulsing favours deposition of the less noble cobalt and thus its concentration in the deposited alloy. The carbon content is lower, because the carbon-containing reaction products have an opportunity to diffuse out of the diffusion layer and back into bulk solution during the off-times.

Pulse plating is also used to deposit gold–nickel, silver–palladium and nickel–phosphorus deposits.

4.3.2.3 Deposition of multilayers

The term multilayer is taken to mean a sequence of two metals, alternately deposited one above the other. The number of such layers, which can consist of a metal or an alloy, is in theory unlimited. Such multilayers are also referred to as CMM (compositionally modulated multilayers), indicating that the deposition process can be modulated (usually by a complex pulse sequence) to create successive layers of alternating composition [37–42].

Such multilayers exhibit electrical, magnetic, optical, chemical and mechanical properties quite distinct from their parent metals or alloys. They are, in effect, new materials and that they are difficult to form other than by electrodeposition, promise an exciting extension to the range of surface coatings and associated applications made possible by electroplating. Such multilayers can be produced by means of two main techniques, known as the dual bath technique (DBT) and single bath technique (SBT).

In the first of these, also known as the dual plating process (DFPP), the component is alternately immersed first in one electrolyte and a deposit is ladid down, then it is

transferred to the second electrolyte where a different deposit is formed, then back to the first bath and so on. The advantages of this approach are:

- One can use established and proven electrolyte systems
- Very thin metal or alloy films can easily be formed
- Any combination of films can be formed, provided each can be individually deposited.

Against these advantages, must be set certain drawbacks:

- The deposition process must be continually interrupted as the sample is transferred between baths
- A danger exists of cross-contamination due to drag-out from each bath
- Additional steps may be necessary between transfers, such as rinsing or re-activation
- As a result of the above, the process will probably be more time-consuming.

In most cases, the drawbacks of the DBT have been deemed to outweigh the benefits, so that the SBT approach is used instead. In this case, the metal ions required to form both deposit layers, are included in a single electrolyte. To avoid their simultaneous deposition, a large potential span must exist between the deposition potential of the metals in question and this can be arranged by adjusting their respective concentrations and/or using complexed ions, whose deposition potential can be many hundreds of millivolts different from the uncomplexed form. The most satisfactory approach is to create a situation where modulation of current will result in the deposition of a different composition at higher or lower currents.

At lower current densities, the more noble of the species present will be deposited in the form of the pure metal. If the current density is increased, the less noble species will also be deposited thus leading to alloy formation. To avoid this, and to bring about the desired result of two pure metal films being alternately deposited, the more noble metal should be present at so low a concentration that its deposition is diffusion controlled. Pulse deposition is in fact specially well suited to deposition of such alternate pure metal layers. Variants of this, shown in Fig. 4.34 include the double- and triple-pulse processes.

In the former, as shown in Fig. 4.34(a), the first pulse is used to deposit the more noble metal, the second the less noble. The sequence is driven by a time-dependant potential step-function such that the lower current density reaches a potential slightly below the deposition potential of the more noble metal. This approach, however, precludes formation of alternating layers where each metal is relatively pure.

In the triple-pulse process (Fig. 4.34b), the current pulse is followed by an open-circuit rest. The idea being that after deposition of the less noble metal, the electrode potential quickly recovers to reach a value just less than the deposition potential of the more noble metal. In contrast to the double-pulse method, one finds here a uniform change of potential with time, with a steep drop after the rest period. By this means, alternate layers, each compositionally quite distinct from the other, can be formed.

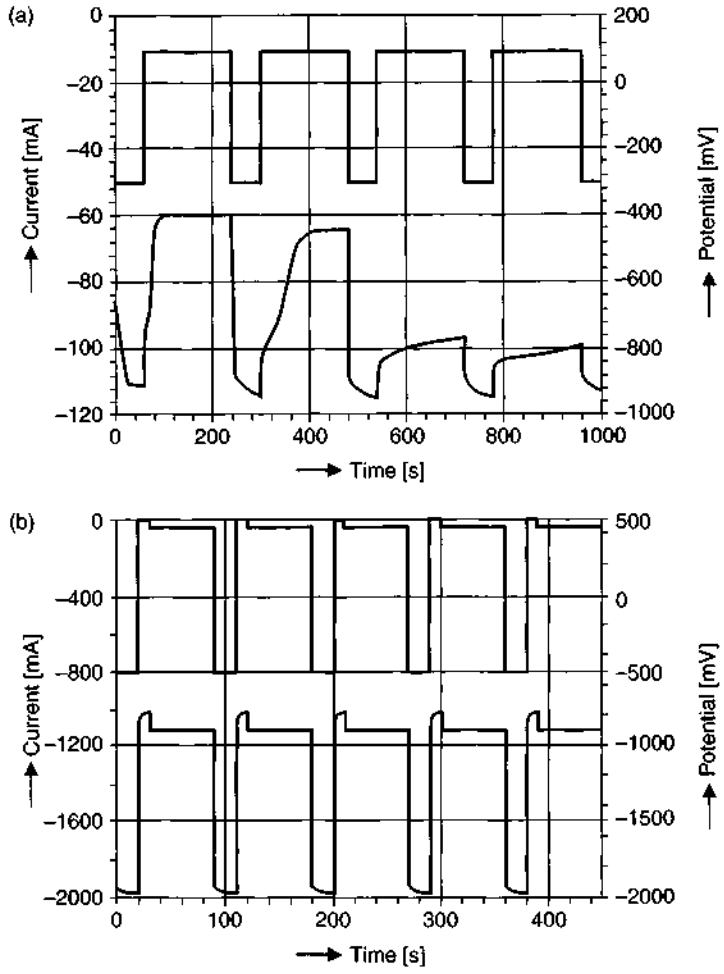

Figure 4.34 Current and potential as function of time for (a) double-pulse and (b) triple pulse deposition.

Examples of multilayers formed by pulse plating include silver–copper, platinum–cobalt and palladium–cobalt. The purity of these is shown in Table 4.7. The reason why the layers of the less-noble metals, cobalt and copper, are less pure than the nobler metals, silver, platinum and palladium, is that alloy formation is possible during their deposition.

The SEM image shown in Fig. 4.35 shows the built-up of a platinum–cobalt multilayer.

Apart from multilayers based on two relatively pure metals, systems based on alternate layers of two different alloys can be formed. This presupposes that variation of current can be used to modify the deposit composition. The SEM image in Fig. 4.36 gives an example of such an alloy.

Table 4.7 Purity of pulse-plated multilayers [40].

Multilayer	Composition
Silver	96% Ag, 4% Cu
Copper	87% Cu, 13% Ag
Platinum	82% Pt, 18% Co
Cobalt	64% Co, 36% Pt
Palladium	96% Pd, 1.5% Co, 2.5% P
Cobalt	35% Co, 63% Pd, 2, 0% P

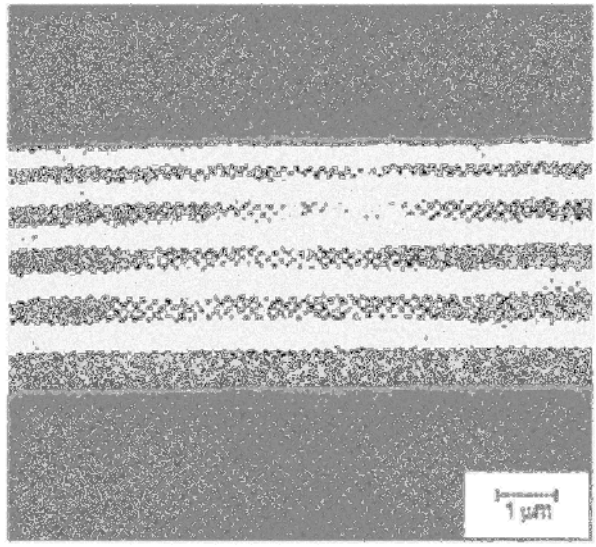

Figure 4.35 SEM image of a platinum–cobalt multilayer system [4.40].

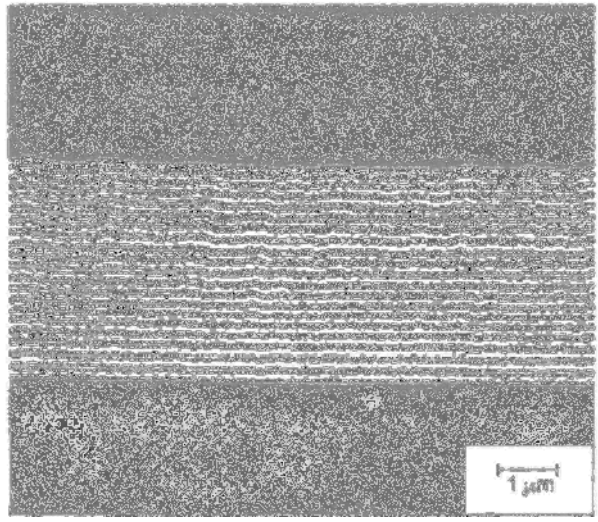

Figure 4.36 SEM image of a gold–cobalt alloy multilayer system [40].

Production of multilayers using the single bath technique offers the following advantages:

- No need to transfer work from one bath to another
- No intermediate processing between baths required
- Current density modulation does not require elaborate equipment
- Process is less time-consuming.

Against this, certain drawback should be noted:

- A specially formulated electrolyte is required which may require development
- Range of possible deposits is limited by availability of metal salts and metal complexes
- It is not always possible to avoid some alloying at the interface between two layers.

4.3.2.4 Deposition of composite layers

The deposition of metal matrix composites where the second phase is electrically conducting, is more difficult than the co-deposition of non-conducting particles. The incorporation of second-phase particles in the growing metal matrix is usually governed by the adhesive forces at the particle–electrolyte interface, since these determine the transport of the particle through the diffusion layer, and its behavior there. In contrast to non-conducting particles, whose maximum incorporation rate, determined by the weak adhesion forces, is reached only when a given flow-rate is reached in solution, the behaviour of conducting particles is rather different. Incorporation of these species begins only when the deposition itself commences and is mass-transport determined. The rate of incorporation remains virtually constant, once the layer is saturated with these species and, because of the strong adhesion forces in this case, is barely affected by hydrodynamic conditions in the electrolyte. Other significant parameters in the case of electrically conductive species include the stability of the particles in the electrolyte and their behaviour after incorporation in the growing deposit. Last but not least, the possible effect of such conductive particles on current distribution must be considered.

Thus, it appears that the behaviour of electrically conducting particles and the factors which influence them, are quite different from those acting in the case on non-conducting particles. It has been shown that modulation, for example, pulse plating, can be used in the deposition of metal matrix composites. Thus the deposition of nickel–cobalt matrix layers with zirconium inclusions over carbon-fibre reinforced carbon (CFRC) components was carried out in this way [23]. CFRC, itself a composite, is based on carbon fibers in a carbon matrix. This type of material is widely used for heat shields in space vehicles or as insulation in high-temperature furnaces. The high-temperature stability of CFRC can be further improved by coating it with a crack-free, non-porous composite coating which, by suppressing oxidation of the carbon, allows the material to function up to the limit of its thermal stability. Heat-resistant composite coatings include binary or ternary alloys of aluminum, chromium, iron, cobalt, nickel and silicon in various compositions, and suitable metal particles are incorporated into such alloys. Most such alloys cannot be simply electrodeposited from a solution. In the case of nickel and cobalt, this is straightforward since the

reversible potentials of the two metals lie close to one another. The co-deposition of chromium is problematic, because of its very different reversible potential. However, the incorporation of zirconium particles in a nickel–cobalt matrix seems to be entirely feasible. The process is based on an electrolyte with a Ni : Co concentration ratio of 8 : 2 to 2 : 8. Zirconium particles of mean size 1–5 μm and at a suspension concentration of 50 g/l. A current pulse regime of 50 : 20 was found optimal [23]. The Ni–Co matrix with Zr second phase deposit showed no significant internal stress. Nor were surface pores, pits or cracks due to hydrogen bubbles a problem, since the hydrogen was able to diffuse away from the surface in the off-time. These deposits showed no dendritic growth at edges and surface rugiosities, such as might have been expected where electrical field lines were most concentrated. Presumably the zirconium particles behave as an electrically neutral species. The surface structure of this deposit did not display any non-uniformity at least up to a 3 mm thickness.

4.3.2.5 Deposit thickness distribution

On the whole, pulse deposition, accompanied by some re-dissolution in the anodic phase, results in a more uniform deposit thickness distribution than the analogous DC process. The micro-sections shown in Fig. 4.37 illustrate this.

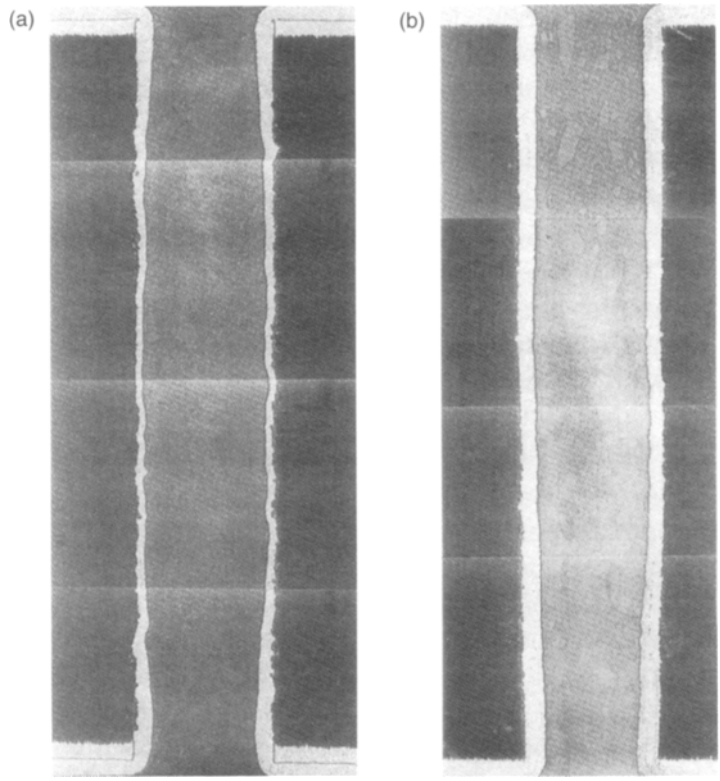

Figure 4.37 Thickness distribution of copper deposited in printed circuit board through-holes. (a) DC (i_{DC} = 8 A/dm², v_H = 0.6 m/min); (b) pulse plated (i_m = 8 A/dm², v_H = 0.6 m/min).

The figure shows a DC-plated and pulse-plated copper deposit, 35 μm thick, as used in through-hole contacting of printed circuit boards. Both deposits were formed in a horizontal plating plant, through which the printed circuit board is horizontal transported at constant rate (v_H) and against which electrolyte is flowed from below. By contrast with DC (Fig. 4.37a), the pulse-plated deposit (Fig. 4.37b) shows a far more uniform thickness distribution. The reason for this lies in the fact that, in the case of DC, more copper is laid down in high current density areas such as the edges of through-holes and on corners, than in lower current density areas such as in the middle of a through-hole. When pulse plating is used, the short anodic pulses result in a re-dissolution of excess copper at edges and corners, thus creating more uniform deposition. From a statistical assessment of thickness measurement data (Fig. 4.38), the much more pronounced thickness variations for DC deposits can be seen.

It is seen that Δd, the difference between maximum and minimum deposit thicknesses is 31 μm for DC conditions, but only 19 μm in the case of pulse-plated copper.

4.3.3 Laser-induced Metal Deposition

More recent studies [43–57] have shown that under the action of a focused laser beam, metal deposition can be accelerated. In at least one case, experiments showed the deposition rate to be increased 1000-fold [43]. According to the literature [45], using laser power densities of 103 kW/cm^2, deposition rates of 10 μm/s are possible. Using this approach, known as laser-induced or laser-enhanced deposition, it is

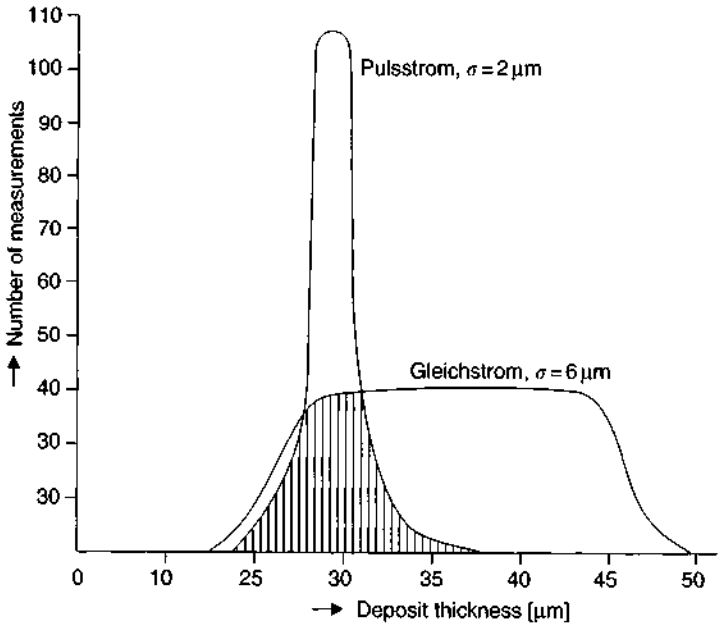

Figure 4.38 Statistical treatment of copper deposit thickness for (a) DC deposition and (b) pulse deposition (σ = standard deviation).

also possible to selectively deposit a metal, and this has been demonstrated using a steered laser beam both with electrolytic and electroless deposition processes.

4.3.3.1 Electrodeposition

Figure 4.39 is a schematic showing the equipment used for laser-induced DC metal deposition.

The equipment consists mainly of a laser head with focusing optics and the electrolysis cell. The most suitable laser is an argon ion type. The focused laser beam passes through a hole in the anode, through the electrolyte and impinges on the cathode surface. The diameter of the focused beam is given by the following expression [50]:

$$D_{\min} = 1.27 \cdot \frac{\lambda \cdot f}{d} \tag{4.23}$$

Here, λ denotes the wavelength, D the diameter of the impinging laser beam and, f is the focal value of the lens.

The energy density of the laser beam used is typically in the range 0.1–2 kW/cm^2 [43, 44, 47]. For continuous laser irradiation, there will be significant local heating at the impingement point of the laser beam. To minimise this, intermittent rather than continuous light is used, this being achieved with an optical chopper. The length of the light pulses is then typically 0.5–40 ms [47]. In other work, it was shown that local heating occurred also when the laser beam impinged on the rear-side of the cathode [43]. This experimental observation suggests that photolytic effects are not significant, bearing in mind the high concentration and high mobility of the charge-carrying species.

To create an actual pattern of deposited metal at the surface, a suitable beam-width must be provided, capable of being steered in an X–Y plane. This is done by mounting the electrolysis cell on an X–Y table, driven by stepper motors [47].

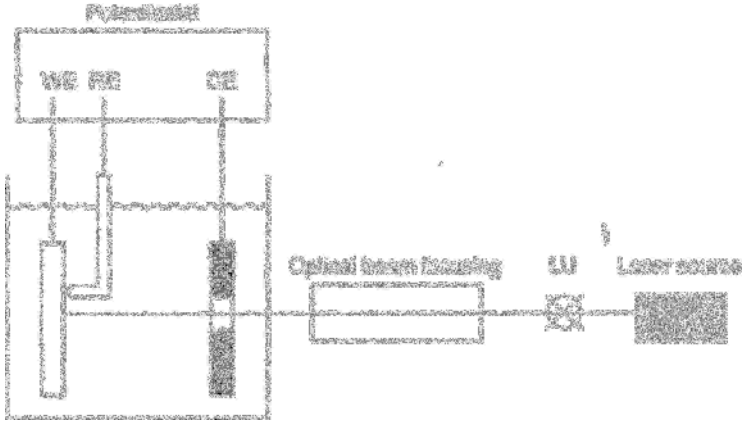

Figure 4.39 Experimental equipment for laser-induced metal deposition. WE = working electrode (substrate). CE = counter electrode RE = reference electrode. LU = mechanical beam chopper.

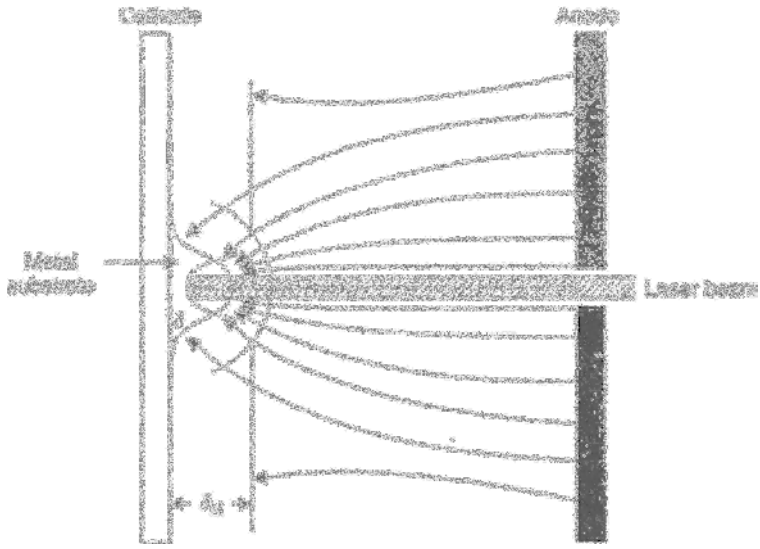

Figure 4.40 Local heating at the incidence area of a laser beam: — electrical field lines; ····· lines of equipotential [46].

Alternatively, the laser beam can be steered by a moveable mirror as described in [43]. Either method allows the dwell time of the incident laser beam and its energy to be controlled. Using such methods, thin tracks of 2 μm width were formed on a substrate surface [50].

The processes involved in this technique can be satisfactorily thermally modeled [43, 44, 47]. The assumption is that part of the incident laser beam is absorbed by the substrate. This brings about local heating at the solid–liquid interface, resulting in a temperature gradient around the irradiated surface area and surrounding electrolyte. The sketch in Fig. 4.40 illustrates the concept.

It should be noted that the thickness δ, of the zone heated by the laser beam, is significantly less than the thickness of the Nernstian diffusion layer, δ_N. The heating of the electrolyte is caused by heat conduction. This sets up a local convection which enhances mass transport in the irradiated zone. The strongly enhanced mass transport due to this micro-convection increases the local current density and thus the local deposition rate. Figure 4.41 compares the enhancement of electrolyte agitation caused by air sparging, ultrasonics and laser irradiation, and underlines the importance of thermally induced local convection [45].

Using very high energy laser beams, local boiling of the electrolyte can occur, resulting in even more pronounced micro-agitation. The literature reports localised electrolyte temperatures of up to 120–140°C in such cases [43, 44].

The resulting steam bubbles enhance local mass-transport even further in that temperature-dependent parameters such as the diffusion coefficients of the metal ions to be deposited, are also favored. The same massive micro-agitation also reduces the thickness of the Nernstian diffuse layer and this leads (Eq. (4.16)) to an increase in the diffusion-limited current density, i_D and thus the rate of metal deposition.

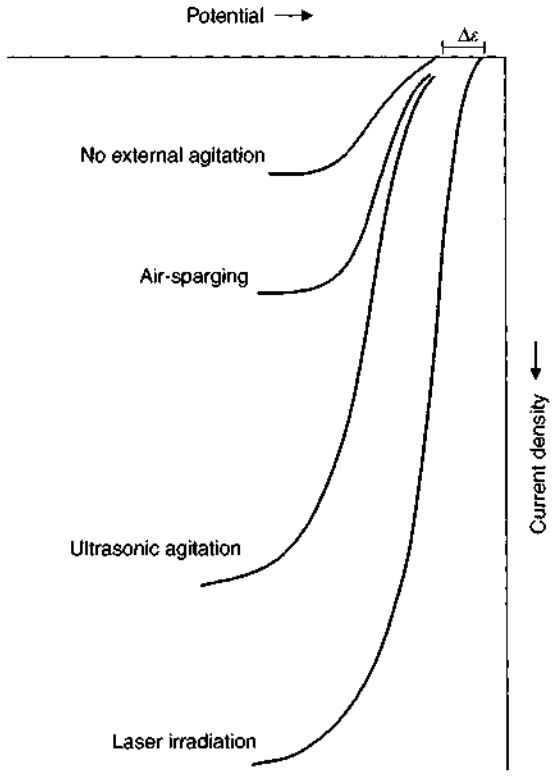

Figure 4.41 Potential shift Δε and increase in deposition current density caused by various types of intensive electrolyte agitation.

Local heating of the irradiated area of the cathode–electrolyte interface has a further beneficial outcome, resulting from the thermodynamics. As implicit in Fig. 4.42, increasing temperature shifts the reversible potential to a more noble value, again favouring the deposition process.

This temperature effect is most pronounced in the low overpotential region, in that metal deposition is charge-transfer limited.

The extent of the shift in reversible potential caused by heating is a specific function of the substrate–electrolyte combination in question. The resulting increase in current density is typically two orders of magnitude [54]. At higher current densities, where the process becomes mass-transport limited, the role of micro-agitation becomes less important and in this situation, the increase in deposition current density made possible by laser irradiation, is only enabled when additional metal ions are added [43].

It might also be noted that the shift of electrode potential to more noble potentials, described above, is increased as the laser beam power increases, as shown in Fig. 4.43 which uses copper deposition to illustrate the point.

The shift of electrode potential, irrespective of whether it is caused by thermal or energetic stimuli, leads to formation of a local galvanic couple between the irradiated

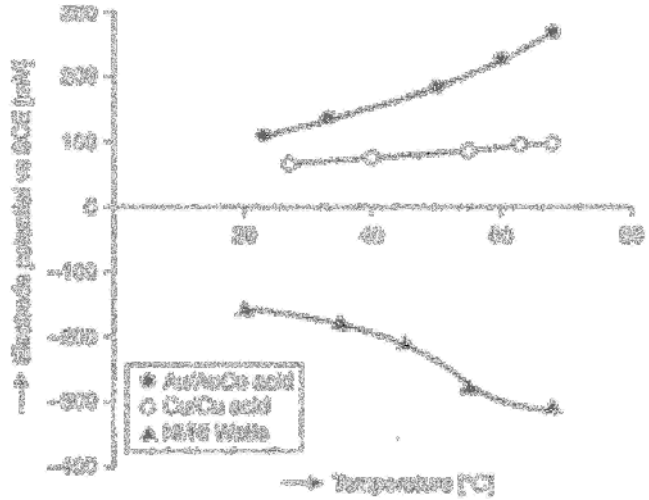

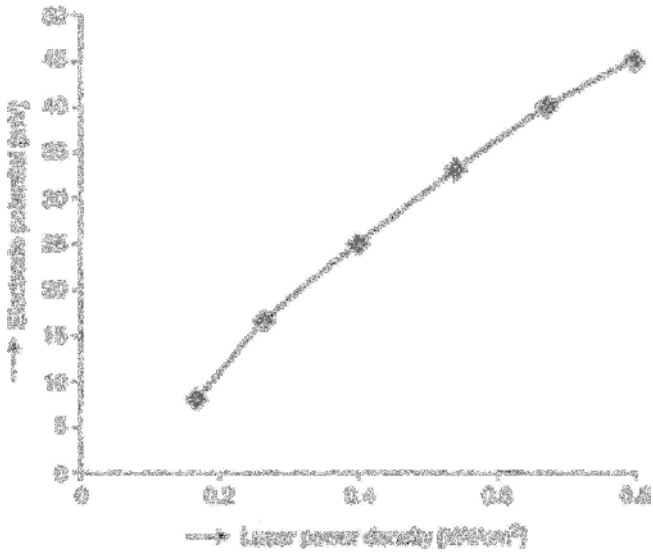

Figure 4.43 Shift in reversible metal deposition potential with increasing laser power, illustrated by the $Cu/CuSO_4$ system [47].

zone and the non-irradiated areas surrounding it. If the electrode potential is shifted to more positive values, as is the case with copper or gold (Fig. 4.42), the irradiated zone behaves cathodically, the surrounding non-irradiated zone becomes anodic. Thus, in the case of the $Cu/CuSO_4$ system, enhanced copper deposition is found in the irradiated zone whereas in the surrounding, cooler zone, metal dissolution occurs.

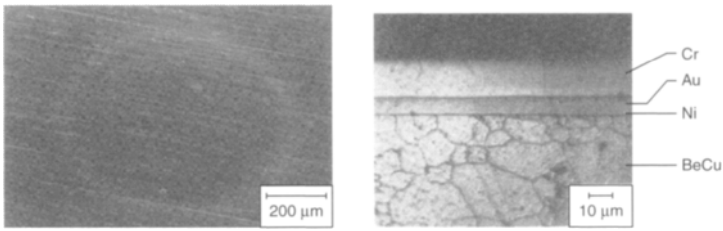

Figure 4.44 SEM and metallographic cross-section of a laser-induced gold deposit (beam diameter 800 µm, deposit thickness, 10 µm).

The reverse is found with those metals where the reversible potential shifts to a more negative region, as for example Ni/Ni^{2+} (Fig. 4.42)

In this case, anodic metal dissolution takes place in the irradiated zone, while metal deposition occurs in the surrounding un-illuminated areas. Figure 4.44 shows an SEM and cross-section metallograph of a laser–induced gold deposit on a beryllium–copper substrate with nickel interlayer.

4.3.3.2 Electroless deposition

Laser irradiation can not only initiate electroless metal deposition, but also accelerate it. The effects previously discussed, of local heating and shift of reversible potential, operate in this case also. The following point should be noted. Electroless deposition will usually operate only above a given minimum threshold temperature. This can be utilized to form selective metal deposits, for if the electrolyte temperature is maintained below the threshold, then deposition will occur only where local heating from the impinging laser beam is found. As described before, a shift of reversible potential caused by local heating, sets up a galvanic couple between irradiated and non-irradiated surrounding areas, with enhanced metal deposition in one or other of these regions, as detailed above.

Laser-induced metal deposition has been found to work well for electroless copper, nickel and gold electrolytes [47–53]. The relatively modest deposition rates from these electrolytes at lower temperatures can be increased by up to a factor of 100, when suitable laser illumination is provided.

4.3.3.3 Surface morphology

A characteristic of laser-deposited metals is their rather coarse-grained, even cauliflower-like surface morphology [47, 49, 50, 53]. This is attributed to the very high local current densities and temperatures. Use of specially formulated electrolytes and additives can modify the morphology, and overvoltage and pH also affect the deposit structure. In certain cases, these parameters can be used to bring about grain refinement [47]. It should be noted that when using lasers as described here, a perfect delineation between irradiated and non-irradiated zones is not possible. There will always be some sort of transitional zone between the former and the latter, and in this zone, a scale-like deposit can be formed [54].

4.3.3.4 Application areas

To fully exploit the potential of laser-induced metal deposition, certain measures must be taken. First, every effort must be made to maximise the proportion of laser energy irradiating the surface to be plated, ensuring that it is there absorbed and converted to thermal energy. The wavelength of the laser light should be such as to minimise the amount absorbed by the solution. This requires that the presence of suspended particles or gas bubbles be held to a minimum. There will also be losses of laser energy due to light scattering. In the same way, the surface of the electrode to be coated should be so arranged as to maximise the amount of laser light absorption and its conversion into thermal energy. The thermal conductivity of the cathode material plays a critical role in this, for the higher this is, the faster will the heat formed by the laser beam be conducted away, and the lower will be the temperature rise, and thus the increase in deposition rate. Substrates with poor thermal conductivity will thus give rise to the highest local temperature increases. Equally, it is desirable that the laser beam be as closely focused on the surface as possible, so that a small focal spot can cause the greater local heating. This is specially important for thicker substrates, where radial and lateral conductive heat flow offer paths for heat loss from the surface, thereby minimising local temperature elevation.

One particularly important application of this technology is in the production of electronic components, whereby the most finely defined patterns and conductive tracks, in the micrometre range, can be formed. The technology can also be used for repair or re-working of such features on defective printed circuit boards. Another example is in the formation of miniature electrical contacts, where selective plating has long been important.

In spite of this, the substantial investment costs involved can prove a disincentive to installation of such equipment. Key factors here include the choice of laser (wavelength and power rating) as well as operating mode (continuous or pulsed, pulse duration and frequency). A further restricting factor is the thickness of the substrate on which the deposit is to be formed. For relatively thick substrates, especially those with high thermal conductivity, higher powered lasers are required, for reasons explained above. Focusing the laser beam to a small area will increase the energy density, but limits the area over which the enhanced deposition is found.

In spite of this, it should be clear that laser technology, while not in its infancy, is still very much a developing process and this is reflected in a decrease in the price of laser equipment. For this reason alone, one is entitled to look forward to a steady expansion of areas in which laser-enhanced metal deposition will be industrially used.

References

[1] Kanani, N., Abscheidung von Metallen ohne äußere Stromquelle, in: *Technologie der Galvanotechnik*, herausgegeben von B. Gaida and K. Aßmann, Eugen G. Leuze Verlag, Saulgau/Württ., 1996.

[2] Frick, W., Metallabscheidung ohne äußere Stromquelle, *Galvanotechnik* 76 (1985) 5, 548–551.

[3] Gawrilow, G.G., *Chemische (stromlose) Vernicklung*, Eugen G. Leuze Verlag, Saulgau/Württ., 1974.

[4] Riedel, W., *Funktionelle Chemische Vernicklung*, Eugen G. Leuze Verlag, Saulgau/Württ., 1989.
[5] Simon, H. and Thoma, M., Funktionelle Bauteiloberflächen durch angewandte Galvanotechnik, *Konstruktion* 37 (1985) 6, 235–214.
[6] Kanani, N., Untersuchung der Schichteigenschaften von Kupferüberzügen aus außenstromlosen Bädern, *Galvanotechnik*, 80 (1989) 12, 4242–4260.
[7] Wendt, H., Elektrolyse in: *Ullmanns Encyklopädie der technischen Chemie Band* 3, Verlag Chemie, Weinheim, 1973.
[8] Raub, E. and Müller, K., Grundlagen der Metallabscheidung, in: *Handbuch der Galvanotechnik Band* I, herausgegeben von H. Dettner and J. Elze, Carl Hanser Verlag, München, 1969.
[9] Fischer, H., Galvanotechnik, in: *Ullmanns Encyklopädie der technischen Chemie Band 12*, Verlag Chemie, Weinheim, 1976.
[10] Bockris, J. O'M. and Reddy, A.K.N., *Modern Electrochemistry*, Volume 2, Plenum Press, New York, 1972.
[11] Liebscher, H., Legierungsabscheidung; Entwicklung, Möglichkeiten und Grenzen der Anwendung, 18. Ulmer Gespräch, *Neue Schichtsysteme für die Industrie*, Eugen G. Leuze Verlag, Saulgau/Württ., 1996.
[12] Haefer, R.A., *Oberflächen- und Dünnschicht-Technologien*, Teil I, Springer-Verlag, Berlin, 1987.
[13] N.N., *Taschenbuch für Galvanotechnik*, Band 1, 13. Ausgabe, LPW-Chemie, GmbH, Neuß 1988.
[14] Celis, J.-P., *et al.* Mechanism of electrolytic composite plating: survey and trends, *Trans. Inst. Metal Finish.* 69 (1991) 4, 133–139.
[15] Müller, K.-P., *Praktische Oberflächentechnik*, Vieweg & Sohn Verlaggesellschaft mbH, Braunschweig, 1996.
[16] Celis, J.-P. and Fransaer, J., Wohin führt die elektrolytische Dispersionsabscheidung? *Galvanotechnik* 88 (1997) Nr. 7, 2229–2235.
[17] Budevski, E., Staikov, G. and Lorenz, W.J., *Electrochemical Phase Formation and Growth*, VCH Verlagsgesellschaft mbH, Weinheim, 1996.
[18] Pauling, H.J. and Jütter, K., Sandwich-Schichten, Teil 1 und 2, *Metalloberfläche* 49 (1995) 3/4, 167–171, 259–262.
[19] Dossenbach, O., Die Bedeutung des Stofftransports in der Galvanotechnik, *Galvanotechnik* 73 (1982) 11, 1184–1189.
[20] Ibl, N., Zur Kenntnis der Metallabscheidung mittels Pulselektrolyse, *Metalloberfläche* 33 (1979) 2, 51–59.
[21] Knödler, A., Abscheidung von Legierungen mittels Pulse-Plating., 4. Ulmer Gespräch, *Die Herstellung von Legierungsüberzügen in der Galvanotechnik und aktuelle Anwendungen*, Deutsche Gesellschaft für Galvanotechnik e.V., Düsseldorf, 1982.
[22] Landolt, D., Allgemeine Überlegungen zum Einfluß der Stromform auf die Metallabscheidung, *Oberfläche-Surface*, 1 (1984) 6–15.
[23] Sova, V., Aufbau der Legierungen durch Dispersions-Pulse-Plating-Verfahren, *Proceedings of the 3rd International Congress for Surface Technology, SURTEC-Kongreß*, Berlin '85, VDE-Verlag GmbH, Berlin, 1985.
[24] Paatsch, W., Galvanotechnik mit Strompulsen, *Metalloberfläche* 40 (1986) 9, 387–390.

[25] Puippe, J. Cl. and Leaman, F., Pulse-Plating, *Schriftenreihe Galvanotechnik* 21, Eugen G. Leuze Verlag, Saulgau/Württ., 1986.
[26] Pearson, T. and Dennis, J.K., Facts and fictions about pulseplating, *Trans. Inst. Metal Finish.* 69 (1991) 3, 75–79.
[27] Pearson, T. and Dennis, J.K., The effect of pulsed reverse current on the polarization behaviour of acid copper plating solutions containing organic additives, *J. Appl. Electrochem.* 20 (1990) 196–208.
[28] Pearson, T. and Dennis, J.K., Effect of pulsed reverse current on the structure and hardness of copper deposits obtained from acidic electrolytes containing organic additives, *Surf. Coat. Technol.* 42 (1990) 69–79.
[29] Kalantary, M.R. and Gabe, D.R., Pulse plating of copper for printed circuit board technology, *Metal Finish.* April (1991) 21–27.
[30] Coughlan, S., Improved plating of small holes and other benefits found using pulse plating of acid copper in PCB manufacture, *Trans. Inst. Metal Finish.* 73 (1995) 2, 54–57.
[31] Baltrusch, S., Der Einfluß von Umkehr-Pulsstrom auf den inneren Aufbau und die Eigenschaften galvanischer Nickelschichten aus dem WATTS-Bad, *Dissertation*, Humboldt-Universität zu Berlin, 1996.
[32] Whitelaw, K.J., Pulse periodic reverse copper plating of high aspect ratio holes, *Proceedings ICP Printed Circuits Expo 1997*, March 9–13, 1997, pp. S.13.1.1–S.13.1.9
[33] Woodman, A.S., Anderson, E.B. and Kimble, M.C., Additive-free plating of high aspect ratio through-holes, *Proceedings ICP Printed Circuits Expo 1997*, March 9–13, 1997, pp. S.13.3.1–S.13.3.8
[34] Holtzman, M., WST, a total systems approach to pulse plating, *Proceedings ICP Printed Circuits Expo 1997*, March 9–13, 1997, pp. S.13.4.1–S.13.4.4.
[35] Retallik, R.C., Periodic Pulse Reverse Plating: Installation and Qualifikation eines verbesserten Verkupferungsprozesses für die Herstellung von Leiterplatten, *Produktion von Leiterplatten und Systemen* 1 (1999) 63–68.
[36] Senge, G., Conversion of DC plating processes to reverse pulse plating process, from qualification to mass production, *IPC Printed Circuits Expo 1999*, March 14–18, 1999, Long Beach, CA, pp. S.15.2.1–S.15.2.11.
[37] Tench, D.M. and White, J.T., Consideration in electrodeposition of compositionally modulated alloys, *J. Electrochem. Soc.* 137 (1990) 10 3061–3064.
[38] Zabludosky, V.A., Fedotova, N.V. and Shtapenko, E.F., Structure, texture and properties of metallic multilayers deposited by a program-controlled pulse current method, *Trans Inst. Metal Funish.* 74 (1996) 3 106–107.
[39] Zabludovsky, V.A. and Shtapenko, E.F., The obtaining of cobalt multilayers by programme-controlled pulse current, *Trans. Inst. Metal Finish.* 75 (1997) 5 203–204.
[40] Zielonka, A., Neue Werkstoffe durch elektrochemisch abgeschiedene Multilayer, *Galvanotechnik* 88 (1997) 4, 1122–1129.
[41] Atanassov, A. and Celis, J.-P., Extrem dünne Sandwich-Metallschichten, *Metalloberfläche* 51 (1997) 2, 93–100.
[42] Chawa, G., Wilcox, G.D. and Gabe, D.R., Compositionally modulated zinc alloy coatings for corrosion protection, *Trans. Inst. Metal Finish.* 76 (1998) 3 117–120.

[43] Gutfeld, von R.J. and Puippe, J.Cl., Erhöhung der Metallabscheidungsund der Metallauflösungsgeschwindigkeit durch Laser-Strahlen, *Oberfläche-Surface* 22/Heft 9 (1981) 294–297.

[44] Puippe, J.Cl., Acosta, R.E. and Gutfeld, von R.J., Investigation of laser-enhanced electroplating mechanisms, *J. Electrochem. Soc.* 128, 12 (1981) 12 2539–2545.

[45] Gutfeld, R.J. von and Romankiw, L.T., Laser enhanced plating, *Gold Bull.* 4 (1982) 15, 120–125.

[46] Romankiw, L.T., Electrochemical technology in electronic today and its future: a review, *Oberfläche-Surface* 25, Heft 8 (1984) 238–247.

[47] Friedrich, F. and Raub, Ch. J., Zur Möglichkeit der laserunterstützten. Elektrolyse *Metalloberfläche* 38 (1984) 6, 237–243.

[48] Zahavi, J., Tamir, S. and Halliwell, M., Laser-induced deposition on semiconductor and polymeric substrates, *Plating Surf. Finish.* 2 (1986) 57–64.

[49] Raub, Ch. J., Baumgärtner, M. and Khan, H.R., Laserunterstützte elektrolytische Abscheidung aus Goldelektrolyten, *Metalloberfläche* 40 (1986) 9, 371–374.

[50] Friedrich, F. and Raub, Ch. J., Untersuchungen zur laserunterstützten Palladiumabscheidung, *Galvanotechnik* 77 (1986) 2658–2664.

[51] Raub, Ch. J., Khan, H.R. and Baumgärtner, M., high temperature gold deposition from acid cyanide baths, *Gold Bull.* 19 (1986) 3, 70–74.

[52] Khan, H.R., Baumgärtner, M. and Raub, Ch. J., High temperature electrodeposition of gold–iron, gold–cobalt and gold–nickel layers and their properties, *Proceedings of the Symposium on Electrodeposition Technology. Theory and Practice* L.T. Romakiw, (Editor) The Electro- chemical Society, NJ 1987, 165–178.

[53] Khan, H.R., Kittel, M.U. and Raub, Ch. J., Laser-induced selectiv deposition on metal using elektroless gold, *Plating Surf. Finish.* 8 (1988) 58–64.

[54] Paatsch, W., Laser-induzierte Metallabscheidung aus wäßrigen Elektrolyten, *Metalloberfläche* 42 (1988) 8, 365–369.

[55] Gesemann, R., Laseraktivierung und Lasermetallisierung von dielektrischen Substraten aus chemisch-reduktiven Bädern, *Galvanotechnik* 81 (1990) 2, 454–459.

[56] Morgenstern, T. and Schultze, J.W., Laser deposition of metals and polymers in Si-microstructures, *Electrochim. Acta* 42 (1997) 3057–3064.

[57] Sato, Y. *et al.*, Laser-enhanced palladium electroless plating, *Trans. Inst. Metal. Finish.* 75 (1997) 1 4–6.

CHAPTER 5

Electrodeposition Considered at the Atomistic Level

5.1 Introduction

The electrodeposition of metallic layers from aqueous solution is based on the discharge of metal ions present in the electrolyte at a cathodic surface (the substrate or component.) The metal ions accept an electron from the electrically conducting material at the solid – electrolyte interface and then deposit as metal atoms onto the surface. The electrons necessary for this to occur are either supplied from an externally applied potential source or are surrendered by a reducing agent present in solution (electroless reduction). The metal ions themselves derive either from metal salts added to solution, or by the anodic dissolution of the so-called sacrificial anodes, made of the same metal that is to be deposited at the cathode. The process is shown in idealised form in Fig. 5.1.

In fact, the process is more complex, involving a number of intermediate stages. The most important of these are:

- Transport of the hydrated metal ion or complex from bulk solution to the cathode.
- Stripping the hydration sheath from the metal ion at the metal–solution interface.
- Charge transfer with formation of adsorbed atom (ad-atom) at the cathode surface.
- Formation of crystal nuclei by diffusion of the ad-atoms at the cathode surface.
- Fusion of thermodynamically stable crystal nuclei to form a metallic layer.

These individual steps are shown together in Fig. 5.2, with the understanding that this is a simplified depiction of the actual process.

Transport of metal ions from the bulk solution to the cathode surface is primarily due to convection and diffusion. The discharge of ad-ions to form ad-atoms takes place within the electrolyte double layer, which forms spontaneously at the metal–solution interface. Although the metal ions lose most of their charge in this process, a residual charge remains, and thus also a part of their hydration sheath.

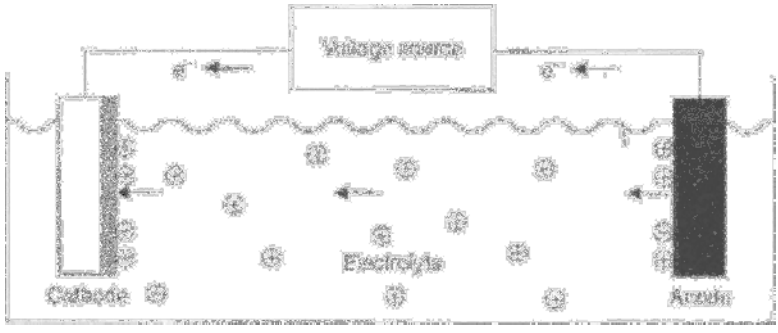

Figure 5.1 Migration of metal ions from a sacrificial anode to the cathode with formation of a metal deposit on the surface.

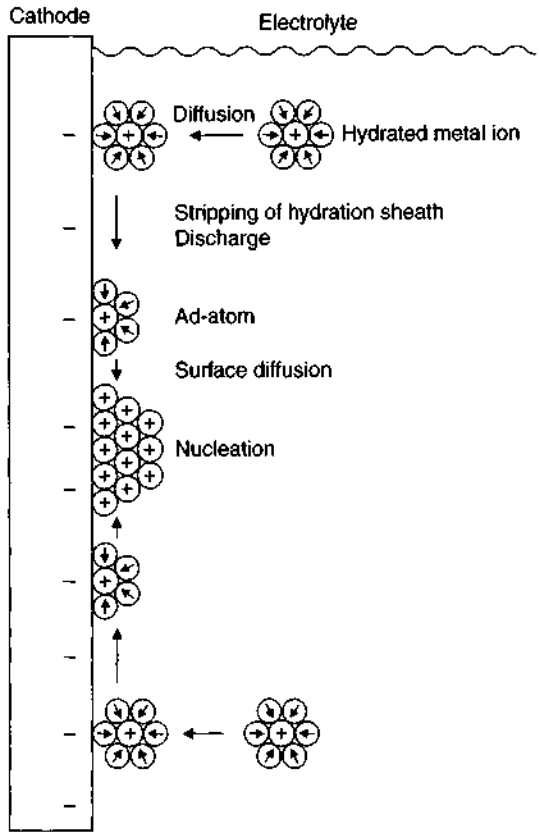

Figure 5.2 Migration of hydrated metal ions to a cathode, surrender of the hydration sheath, formation of ad-atoms, formation of crystal nuclei at the cathode surface.

In this state, and after passing through the electrolytic double-layer, they are adsorbed on the cathode surface where they form ad-atoms. In order that a coherent metal film is formed, two further coupled stages must occur, known as nucleation and (crystal) growth, or as 'electrocrystallisation'. Nucleation results from diffusion-controlled migration of the ad-atoms on the surface, and this lateral diffusion should in no way be confused with solution diffusion processes which have been previously discussed. The growth process begins once the nuclei have reached a critical size.

5.2 Structure of Metal Ions

Ions that are subsequently deposited onto the cathode, are very rarely, if at all, present in solution in simple form. Almost invariably, they are surrounded by other atoms, molecules or ions, especially water molecules. In the latter case, the geometric structure of the water molecule, shown in Fig. 5.3, plays a determining role.

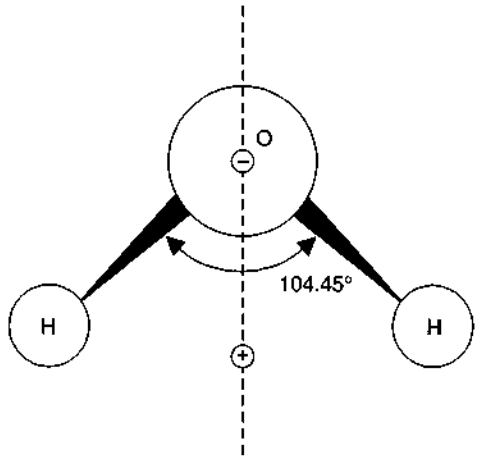

Figure 5.3 Schematic representation of the structure of a water molecule, shown as a dipole [1].

The angle of 104.45°, formed between the two hydrogen–oxygen bonds shown in Fig. 5.3 results from the strong dipole forces within the water molecule. The electrostatic attraction between the positively charged metal ions and the water molecules, results in the formation of the hydration metal ions, also referred to as solvated ions, which are sheathed with a layer of water molecules. Their structure is sometimes denoted by the generalized formula $[Me(H_2O)_x]^{z+}$ where Me^{z+} is a metal ion of valency z, while x denotes the number of water molecules. Figure 5.4 shows such a structure, with an anion for comparison. Two cautions should be noted here. First, the salts of most metals in their solid state, are often hydrated and although this is written in a form very similar to that above, the two situations are completely different. Second, the term 'x' above, should not be taken literally. In fact the metal ion is surrounded by several layers of water molecules, each layer being more loosely bound than the one inside it.

From the foregoing, it will be seen that cations and anions, partly because of their different diameters, but also because of the 'triangular' structure and polar character of the surrounding water molecules, behave very differently in terms of their hydration behaviour. In the case of the positively charged cations, the oxygen atoms face inwards, while for the negatively charged anions, it is the hydrogen atoms which do so, as shown in Fig. 5.4. Cations, as a result, are more fully hydrated than anions, this being due to the smaller ionic radius of the cations.

The number of water molecules surrounding a metal ion to form the primary (innermost) hydration sheath can be between 1 and 10. Since the interaction between the metal cation and the surrounding water molecules is mainly electrical, an electric field is formed around the cation. However, the primary hydration sheath does not entirely screen the metal cation and there is also an ordering of water molecules outside this inner sheath, where a secondary hydration sheath can be said to exist. That the outer sheath is more weakly bound to the metal cation, is shown by

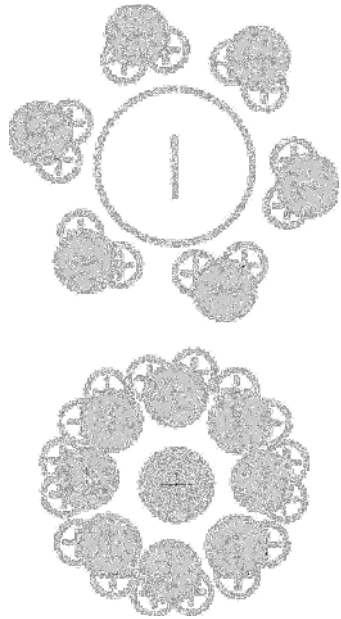

Figure 5.4 Hydrated cation or anion. In the case of cations, water molecules are oriented with oxygen atoms facing inwards, for anions, the hydrogen atoms face inwards [2].

the fact that, as the cation approaches the cathode surface, it retains the primary water sheath, while losing the outer ones.

5.3 Structure of the Electrical Double Layer

Although both the cathode and the electrolyte layer adjacent to it, could be described as 'condensed matter', their properties are completely different. Because of this, as soon as a metal is immersed in aqueous solution, and electrically charged double layer forms at the interface between the two. The structure of this electrochemical double-layer (EDL) profoundly influences the kinetics of the metal deposition process [3–9]. Numerous publications, mainly in the period 1950–1970 considered how best to model the EDL and possibly the most refined was the BDM model [4]. The main classical models are described below.

5.3.1 Helmholtz–Perrin Model

According to this model, the double-layer structure can be represented by a rigid array of charged species at the metal–solution interface. The model implies that electrons (on the cathode side) and metal ions (electrolyte side), co-exist in equal measure. The separation between them is of order one ionic radius. This model is shown in Fig. 5.5.

According to this model, the properties of the electrical double layer resemble those of a parallel plate condenser, for which the capacitance value is constant.

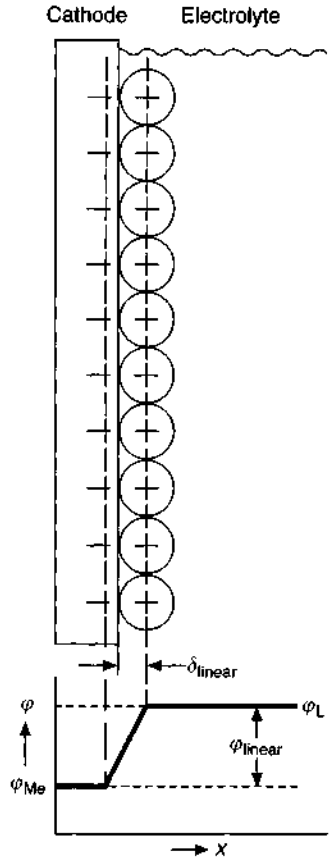

Figure 5.5 Helmholtz–Perrin model of the electrical double-layer; the potential gradient at the interface is shown below. $\Delta\varphi = \varphi_L - \varphi_{Me} = \varphi_{DL}$.

The potential gradient within the Helmholtz layer, δ_H is linear;

$$\left(\frac{d\varphi}{dx}\right)\delta_{linear} = \text{const.} \tag{5.1}$$

The Helmholtz–Perrin model is an extremely simplified concept of the actual situation. Thus it ignores the statistical spatial distribution of metal ions in front of the cathode surface, which is due to the twin effects of electrostatic attraction on the one hand, and random motion caused by thermal motion on the other. As a result, the actual spatial charge distribution in the dilute electrolyte layer adjacent to the cathode, is not taken into account by this model. However, the model does offer a reasonably satisfying representation for higher concentration electrolytes.

5.3.2 Gouy–Chapman Model

This model sets out, quite correctly, from the premise that as a result of convection in solution, especially for dilute electrolytes, there will be a loss of ordering and

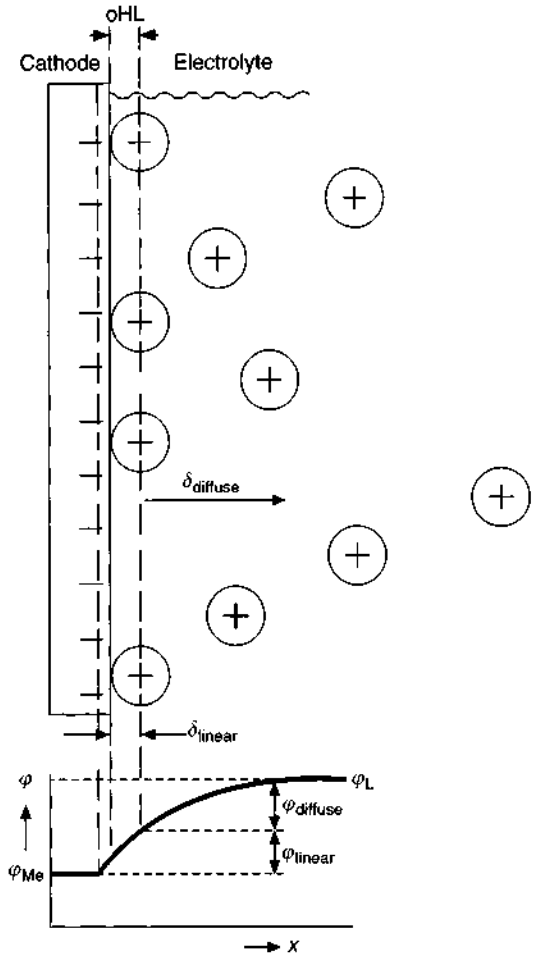

Figure 5.6 Gouy–Chapman model of the electrical double-layer; the potential gradient at the interface is shown below. $\Delta\varphi = \varphi_{DL} + \varphi_{diffuse}$.

structure for the ionic distribution in the near-cathode layer. As a result, the concentration of metal ions falls off in exponential manner, with increasing distance from the cathode, falling to approximately zero in the bulk of solution. For this reason, only a few of the metal ions are attracted to the cathode surface by interfacial forces, the remainder being distributed in a spatially random manner in the immediate vicinity of the cathode. This, in its description of the electrical double layer, the Gouy–Chapman model distinguishes between two potential regions. The first is a rigidly structured region in which the potential increases steeply, in linear manner. Outside this, in the diffuse layer, there is an exponential change in potential. This is shown in Fig. 5.6.

The Gouy–Chapman model thus embodies a rigid, inner portion of the electrical double layer where metal ions are adsorbed at the cathode surface, outside which is a layer of electrolyte immediately adjacent to the cathode, representing a spatially

distributed ionic charge. In this outer layer, convective thermal motion of the ions results in the degree of order becoming less pronounced, as the distance from the cathode surface increases. Within the inner layer (Helmholtz layer), there is a steep and near-linear potential gradient. In the outer, Gouy–Chapman layer which extends outward to bulk solution, there is an exponential change of potential versus distance. Given certain assumptions, the potential change across the diffuse layer, δ_{diff}, can be represented as

$$\left(\frac{d\varphi}{dx}\right)\delta_{diff} = \sqrt{\frac{2RT}{\varepsilon}\sum_{i=1}^{s} c_i\left[\exp\left(-\frac{z_i F\varphi}{RT}\right) - 1\right]} \qquad (5.2)$$

In this expression, R is the gas constant, T the absolute temperature, ϵ the dielectric constant, c_1 the metal ion concentration in bulk solution, z_1 the charge on the metal ions, and F is the Faraday constant. The spatial charge density is determined by summing all the charges. For dilute electrolytes, the thickness of the diffuse layer is of order 10^{-4} cm while for more concentrated electrolytes, values of 10^{-7}–10^{-8} are typical, thus becoming comparable in thickness to that of the inner layer.

5.3.3 Stern–Graham Model

Even the Gouy–Chapman model of the double layer is unable to accurately represent the prevailing condition in the near-cathode electrolyte layer, and this for the following reasons: at the cathode surface, spontaneous formation of an adsorbed layer of iriented water dipoles takes place, comparable to the primary hydration sheath around the metal ions. It can also happen that certain types of organic molecules or surface-active anions displace the primary adsorbed water layer, becoming adsorbed on the negatively charged cathode surface. This is known as specific adsorption or contact adsorption. This initally surprising observation, which has been many times experimentally confirmed results from the fact that anions, in the electrolytic double layer, behave quite diffferently from cations. Because of their greater ionic radius, they are less strongly hydrated than the cations. Thus, after partial loss of water molecules, they can approach close to the cathode surface and there interact with it. Equally, chemical interaction between the dehydrated anions and the cathode can occur. Specifically adsorbed anions are so strongly adsorbed at the cathode that they lose their hydration sheath and they thus approach the surface more closely than the hydrated cations, whose hydration sheaths prevent a closer approach. While retaining their hydration sheaths, the cations are adsorbed at the cathode surface by coulombic forces, and the magnitude of these depends on the potential of the cathode. The concepts embodied in the Stern–Graham model of the electrolyte double-layer are illustrated in Fig. 5.7(a).

The plane of mean charge of specifically adsorbed anions is defined as the inner Helmholtz layer, and thus encloses an adsorbed layer of water molecules, electrostatically attracted to the cathode surface and there oriented, as well as certain surface-active species present in solution. The spatial extent of this region is known as the inner Helmholtz layer (iHL). In the same way, the mean geometric location of charge centres due to metal ions adsorbed at the cathode is known as the outer Helmholtz

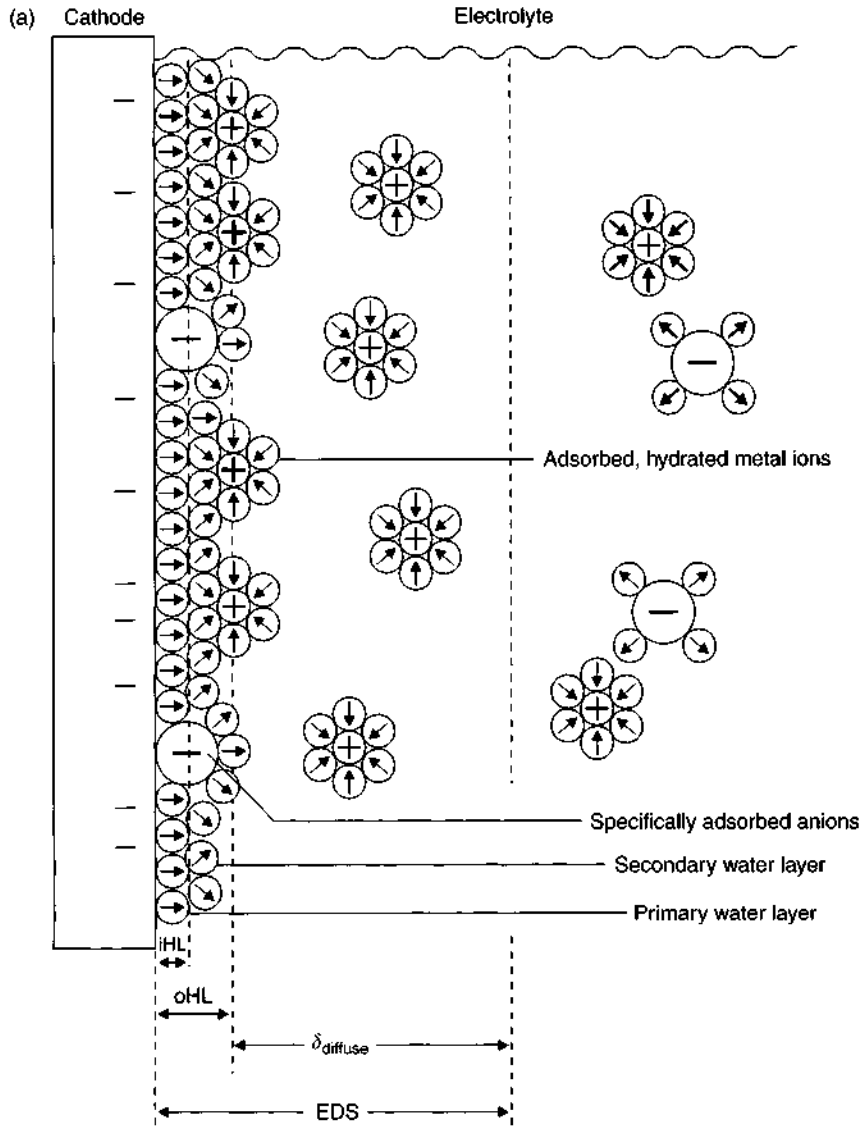

Figure 5.7 Stern–Graham model of the electrolyte double-layer: (a) electrostatically adsorbed primary water layer/specifically adsorbed anions [9]; (b) potential versus distance from the metal–solution interface, $\Delta\varphi = \varphi_{linear} + \varphi_{spec} + \varphi_{diffuse}$ [8].

layer (oHL), and so defines the outer limit of the rigid Helmholtz layer. Beyond this, lies the so-called diffuse layer in which metal ions are fully mobile, and whose spacing from one another is a function of total ionic concentration in bulk solution. The concentration of positively charged ions in this layer is governed by the need to maintain overall charge neutrality, including those charged species adsorbed at the electrode surface. The potential–distance profile across the electrolyte double-layer, according to the Stern–Graham model, is shown in Fig. 5.7(b).

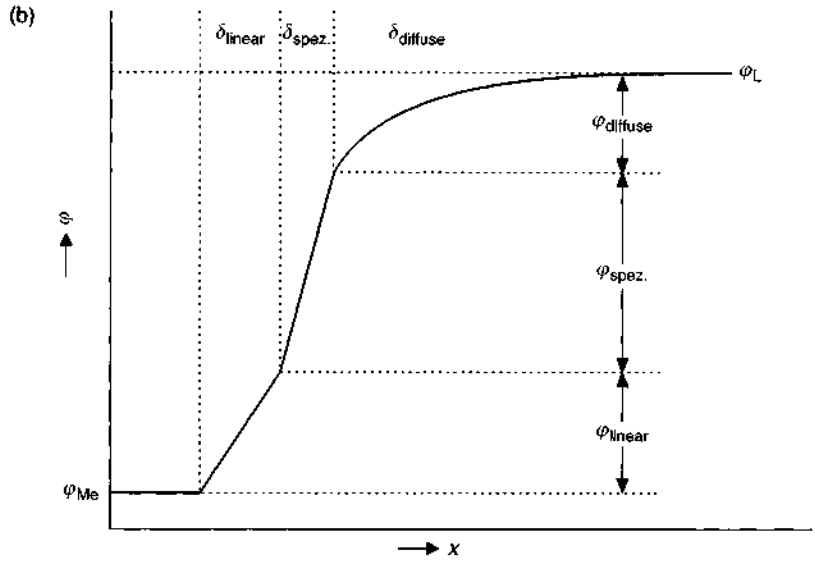

Figure 5.7 Continued.

5.4 Rate-Determining Steps in Electrode Reactions

In the path that begins with a metal ion in bulk solution, and ends with its incorporation as a metal atom into a metal lattice forming on the cathode surface, there are numerous discrete stages. Any one of these can, in certain circumstances, be 'rate-determining', or as one might say, the 'bottleneck'. The first step is for the ions to move from bulk solution to the vicinity of the cathode. This is mainly achieved by means of convection, that is to say the ion moves because the surrounding solution moves. 'Natural convection' is the movement of liquid due to convection currents. 'Enhanced convection' (see Fig. 4.41) is the result of various forms of agitation. The migration of ions through solution under the potential gradient between anode and cathode also contributes to the overall transport process, though it is normally small in comparison with convective mass-transport. The ions then reach the outer part of the Nernstian diffuse layer, and diffuse across this, driven by a concentration gradient. Convection ceases to operate to any significant extent within the Nernst layer, and the concentration gradient is the difference between metal ion concentration in bulk solution, and that at the cathode surface, where it can fall to zero (e.g. Eq. (4.16). Convection may not operate within the Nernst layer, but it can reduce its thickness δ_N and thereby increase the concentration gradient. Once immediately adjacent to the cathode, the ions must transit the electrolytic double-layer, after which they become adsorbed ad-atoms. These, by lateral diffusion across the surface, come together to form actual metal atoms. Only at this point can such metal atoms incorporate themselves into the crystal lattice, a process which follows nucleation and growth of the deposit layer.

The technologist, as much as the scientist, is concerned to identify the rate-determining step (r.d.s) and remove or minimise the 'bottleneck'. Although each step in the sequence is associated with its own overvoltage, so that total overvoltage is the sum of the individual overvoltage components. In some cases, increasing the overvoltage will accelerate the reaction, though not when the r.d.s is mass-transport-limited (see, e.g., Fig. 4.13).

Thus, the expression 'overvoltage' should more rigorously be sub-divided into concentration overvoltage, activation (or charge transfer) overvoltage, crystallisation overvoltage and resistance overvoltage [9–11]. In metal electrodeposition, several of these, perhaps even all of them, may be operative. One then refers to total overvoltage, η_{tot}, the sum of the individual overvoltages:

$$\eta_{tot} = \eta_c + \eta_D + \eta_K + \eta_w \tag{5.3}$$

Among the factors determining total overvoltage are the type of electrolyte, the cathodic current density and the particular metal being deposited. As a rule, charge-transfer and concentration overvoltages are the dominant terms. Of the two, the transit of the metal ion through the electrolyte double layer is often the critical step and it follows that charge-transfer overvoltage can be the r.d.s. This notwithstanding, overvoltages associated with preceding or following steps can often not be ignored.

5.4.1 Concentration Overvoltage

The origin of concentration overvoltage, η_c, stems from the fact that, during electrolysis, a concentration difference will be set up between metal ions in bulk solution and a lower concentration at the cathode surface (Eq. (4.16)). Metal cations are discharged to form metal at a faster rate than they can be supplied from bulk solution. In the limiting case, charge transfer occurs as soon as the cations reach the cathode surface. Their effective concentration there is then zero, and increase in overpotential brings no further increase in reaction rate. The electrodepositor will make every effort to avoid this situation occurring in practice, not least because metal deposits formed under these conditions are powdery and virtually of no practical use.

Concentration overpotential can be further sub-divided into reaction overpotential and diffusion overpotential. The first of these comes into play when the metal ions, on their way to the cathode surface, are involved in a chemical reaction which is so slow that it becomes rate-determining. Typical examples of such reactions are hydration or dehydration processes or the formation or decomposition of a complex, all of these being processes which precede the actual charge-transfer reaction. Reaction overvoltage can also result from certain chemical reactions taking place close to the cathode but subsequent to charge transfer. The fusion of ad-atoms at the cathode by surface diffusion is an example of this. In most cases, however, these reactions preceding or following the actual charge transfer are more rapid than the charge-transfer reaction, and in this case, reaction overvoltage is not of major significance.

Diffusion overvoltage, as its name implies is linked to the diffusion of metal ions prior to their discharge. In the course of the reaction, as explained above, a depletion

of metal ions for subsequent charge transfer, occurs. A concentration gradient of these metal ions then forms in the diffusion layer. This reaches a maximum, as explained above and in Eq. (4.16), when the metal ion concentration at the surface, $c_{surf} = 0$. The various terms in Eq. (4.16) indicate factors which are important in minimising this problem, such as ensuring the highest possible metal ion concentration in solution, and the most vigorous possible solution agitation, to minimise the diffusion layer thickness (δ). Concentration overvoltage can also become significant if the path between anode and cathode is in any way obscured, or if the cathode surface is for any reason blocked, usually with foreign species present in solution. None of the foregoing actually explains how the concentration overpotential arises. In broad terms, this is an expression of the Nernst equation, which describes the establishment of a potential difference when a given ion is present at two different concentrations.

5.4.2 Charge-Transfer Overpotential

The main prerequisite for electrochemical metal deposition, is a charge transfer at the cathode, of an incoming hydrated metal ion at the metal–solution interface. The driving force for the process is a linear potential difference between the metal surface and the outer Helmholtz layer. The exponential portion across the diffuse double-layer, shown in Figs. 5.6 and 5.7(b) does not come into play. The charge-transfer process can thus be described in the following formal terms. The hydration sheath around the metal ions is deformed or perhaps splits sufficiently wide open so that the ion can traverse the rigid Helmholtz layer and come close enough to the cathode surface for the charge transfer to take place. From the cathode side, the electrons tunnel through the Helmholtz layer and trigger the discharge process. A hindering of the charge transfer process is thus expressed as charge-transfer overvoltage or activation overvoltage, η. This is almost invariably found in metal electrodeposition reactions.

5.4.3 Crystallisation Overvoltage

The metal electrodeposition reaction takes place in two consecutive and coupled stages. The first of this is formation of thermodynamically stable crystal nuclei at certain points on the cathode, followed by their growth. Both process can be expressed in terms of a characteristic overvoltage, generally known as crystallisation overvoltage, η_K. It should be noted that the nucleation usually contributes more to the overvoltage than the growth stage, the former having a higher activation energy. Incorporation of metal atoms into the crystal lattice can only take place at certain growth sites. Should metal ions be discharged at other points on the surface, they are forced to diffuse at the surface until they encounter a growth site. Crystallisation overpotential thus becomes significant when the nucleation and growth stages become rate-limiting, as a result of slow diffusion of metal atoms on the surface. Given that the concentration of ad-atoms at the surface is subject to marked local variation, it is often the case that there are significant differences in crystallisation overpotential at various points on the surface.

5.4.4 Resistance Overvoltage

Resistance overvoltage, or ohmic overvoltage η_R is an expression of potential drop outside the electrolyte double-layer, and (in contrast to other forms of overvoltage) follows Ohm's law, that is, a linear relationship with current. Examples of this include the electrolyte resistance of the Nernst diffuse layer, formation of a film of reactants or products at the cathode surface or some other multilayer, such as an oxide. Such a film can be a poorly conducting solid or it can be a liquid film, which completely covers the cathode surface and thus hinders access of metal ions as reactant species. Resistance overvoltage can thus also be included in the charge-transfer overvoltage. In experimental terms, however, the resistive term is readily identifiable in the overall overvoltage.

5.5 Electrocrystallisation

In their operation and effects on the properties of electrodeposited metal coatings, the nucleation and growth processes which constitute electrocrystallisation, have much the same resistive effects as crystallisation processes in general. The main difference is that, in the case of electrocrystallisation, the metal atoms required for nucleation must first be present. This follows from the fact that the hydrated or complexed metal ions which transfer across the metal–solution interface, and are then charge-neutralised at the cathode surface, form local crystal nuclei. By contrast, when crystallisation from molten metal occurs, the uncharged metal atoms congregate to from crystal nuclei, which then grow spontaneously, as soon as a critical size is reached. For a better understanding of the complex processes involved in electrocrystallisation, the processes involved in solidification of a molten metal will be described [12].

5.5.1 Nucleation

5.5.1.1 Homogeneous nucleation

When a molten metal is cooled, the first crystal nuclei are formed as soon as the temperature falls below the melting point. The process results not only in a so-called change-of-state but also in a thermodynamic change, with thermal energy being released or taken up, as the state changes. The so-called Gibbs free energy (G) of all elements is set, by definition, as zero. However, this is true only for each element in a defined state (liquid, solid, gaseous) and at a given temperature. Tables are available reporting the free energy of elements in other physical states, and for most compounds. The Gibbs free energy differences between elements in their various states or elements and compounds formed from them, are expressed as ΔG, which can be positive or negative as heat is released or taken up. The solidification of n metal atoms to form a crystal nucleus, usually with a contraction in volume, itself makes a contribution to the free energy balance and is designated ΔG_V. As they solidify, the metal atoms lose kinetic energy; ΔG_V thus represents energy liberated from the system and, by definition, is designated, under the most widely used convention, with a

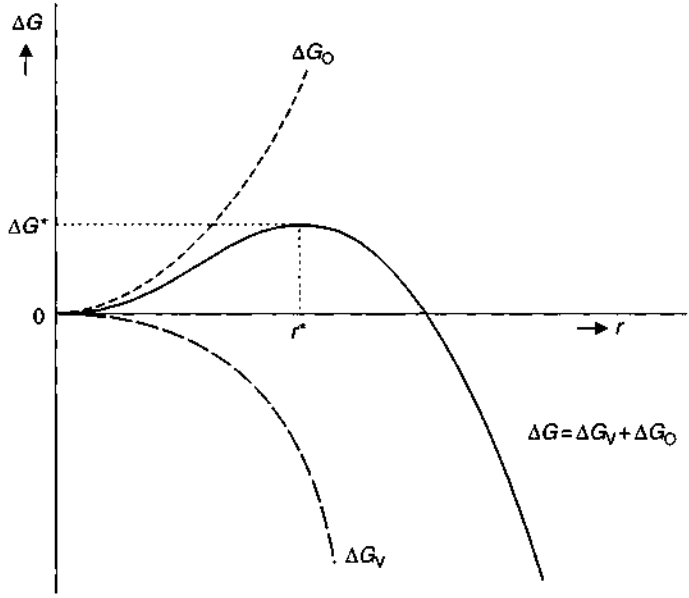

Figure 5.8 Change in free energy, ΔG as a function of the radius r, of a nucleus. ΔG = maximum energy of formation of a nucleus.*

minus sign. On the other hand, as a solid nucleus is formed, an interface must be set up between this nucleus and the surrounding melt. For this, some surface work is required, which therefore is positive, and represented as ΔG_O. The surface energy γ between the crystal surface and the melt, depends on the metal in question and the surface area of the nucleus. The total change in Gibbs free energy, ΔG, for the formation of a spherical nucleus of radius r, volume $V_K = (4/3)\pi r^3$ and surface area $F_K = 4\pi r^2$ is the sum of the energy contributions, ΔG_V and ΔG_O

$$\Delta G = \Delta G_V + \Delta G_O = -(4/3)\pi r^3 \cdot \Delta g_v + 4\pi r^2 \gamma \qquad (5.4)$$

The term Δg_V here signifies the change in free energy for a given volume of the solidified material.

The reason for basing this on a spherical nucleus is legitimate in that one must consider the surface area to volume ratio and thus the minimum required surface energy to form a nucleus. The plot for ΔG_V and ΔG_O and the resulting free energy change, ΔG as a function of nucleus radius, that is, the number of metal atoms in the nucleus, are shown in Fig. 5.8.

If the radius, r, of a crystal nucleus, forming in the midst of the solidification process, is larger than the critical nucleus radius $r^* = 2\gamma/\Delta g_V$, then it will continue to grow, since its further grow results in a decrease in the free energy of the system $d(\Delta G)/dr < 0$. It follows that crystal nuclei with $r > r^*$ are thermodynamically stable and will probably grow. Conversely, for the condition $r < r^*$, the nucleus is not thermodynamically stable and is likely to contract in size, ultimately disappearing as

it dissolves. Further growth of such small nuclei would imply an increase in Gibbs free energy, $d(\Delta G)/dr > 0$.

ΔG^* signifies the thermodynamic energy barrier which must be overcome in order to initiate a homogeneous nucleation process. It indicates the maximum energy of nucleus formation required to form a nucleus of critical size. Differentiation of Eq. (5.4) gives an expression for the energy of formation of a nucleus:

$$\Delta G^* = \frac{16\pi\gamma^3}{3\Delta g_v^3} \tag{5.5}$$

5.5.1.2 Heterogeneous nucleation

The homogeneous nucleation mechanism described above represents a special case, and the requisite energetic conditions are only occasionally found. Much more commonly found is a situation where nucleation and growth initiates at the container wall or perhaps around a solid foreign particle in the melt. These are known as initiation sites and their *modus operandi* is that they act as active centres, reducing the height of the activation energy barrier for formation of nuclei of greater than the critical size. A precondition of this process is that the initiation sites are not wetted by the molten metal. The degree of wetting can be expressed as the wetting or contact angle, θ. Figure 5.9 illustrates formation of a cup-shaped crystal nucleus at the wall of a melt crucible.

For the change in free energy $\Delta\overline{G}$ taking place in heterogeneous nucleation, the following equation holds, based on the same assumptions as that for homogeneous nucleation:

$$\Delta\overline{G} = -(1/3)\pi r^3 \cdot (2 - 3\cos\theta + \cos^3\theta) \cdot \Delta G_v + 2\pi r^2 \cdot (1 - \cos\theta) \cdot \gamma \tag{5.6}$$

The first term in the above equation represents energy released in formation of a cup-shaped nucleus. The second term, by contrast, identifies the energy required to form a stable and isotropic interface between the crystal nucleus and the melt. According to the above equation, the change in free energy is not only a function of the radius of the nucleus, but also of the wetting angle. Figure 5.10 shows this relationship in terms of three values of wetting angle.

R^* symbolises the minimum critical radius for a stable nucleus, capable of growth. The energy of formation of such a nucleus, ΔG^{**}, can be derived from Eq. (5.6).

$$\Delta\overline{G}^* = \frac{16\pi\gamma^3}{3\Delta g_v^2}\left[\frac{2 - 3\cos\theta + \cos^3\theta}{4}\right] = \Delta G^* \cdot \frac{f(\theta)}{4} \tag{5.7}$$

For the hypothetical case, $\theta = 0°$, that is, a complete wetting of the wall surface by the nascent crystal nucleus, one obtains $\Delta G^{**} = 0$, which expresses a condition where spontaneous crystallisation from the melt can occur, with no activation energy barrier. Conversely, for $\theta = 180°$, that is, no wetting of the container wall by the growing nuclei, the relationship $\Delta G^{**} = \Delta G^*$ is obtained.

This condition corresponds to homogeneous nucleation and demands the highest energy of formation of a nucleus. For wetting angles between 0 and 180°, values of ΔG^{**}, are somewhat smaller that energies of formation in homogeneous nucleation.

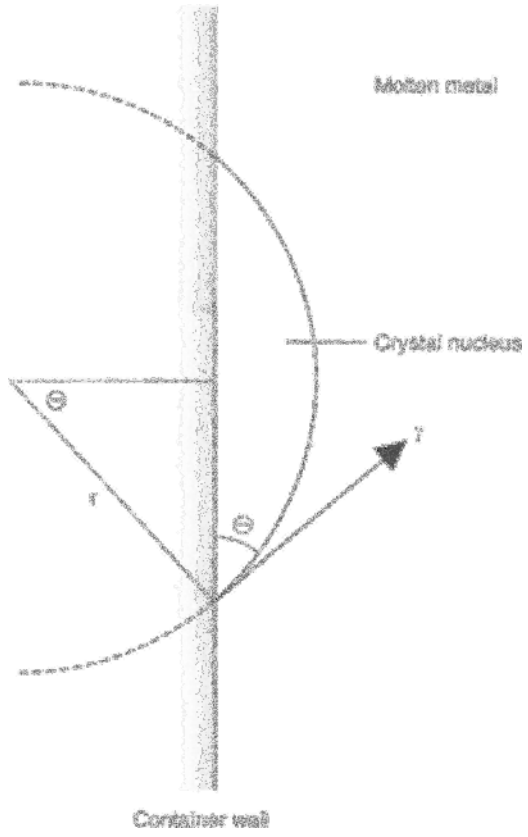

Figure 5.9 Formation of a cup-shaped crystal nucleus at the melt container wall by heterogeneous nucleation.

For example, for $\theta = 90°$, the maximum value of nucleus formation energy required would be half that required in homogeneous nucleation ($\Delta G^{**} = 0.5\Delta G^{*}$). The process of heterogeneous nucleation is, however, increasingly difficult as the wetting angle condition follows $90° < \theta < 180°$ since the value of ΔG^{**} continues to increase. For $\theta = 180°$, the value of ΔG^{**} reaches a maximum and is, as noted above, equal to ΔG^{*}.

Armed with this theoretical treatment, the electrocrystallisation process can be seen in terms analogous to nucleation from a melt. The mechanism can be considered in terms of an agglomeration of ad-atoms at the cathode surface which, having reached a critical size, can then grow further by taking up further ad-atoms. The necessary precondition for this is that all the metal ions involved, transfer through the electrolytic double-layer, to reach the cathode. After an initial constriction as they pass through the primary outer water layer, they then pass through the electrolytic double layer and then make contact with the crystal lattice at the cathode surface. Under the effect of the potential field, the hydration sheath is split open, resulting in more or less complete neutralisation. If, during this process, the incoming metal ions impinge on a specifically adsorbed ion, they must attempt to circumvent this, since the activation energy barrier to pass directly through would be extremely high. The discharge of complexed

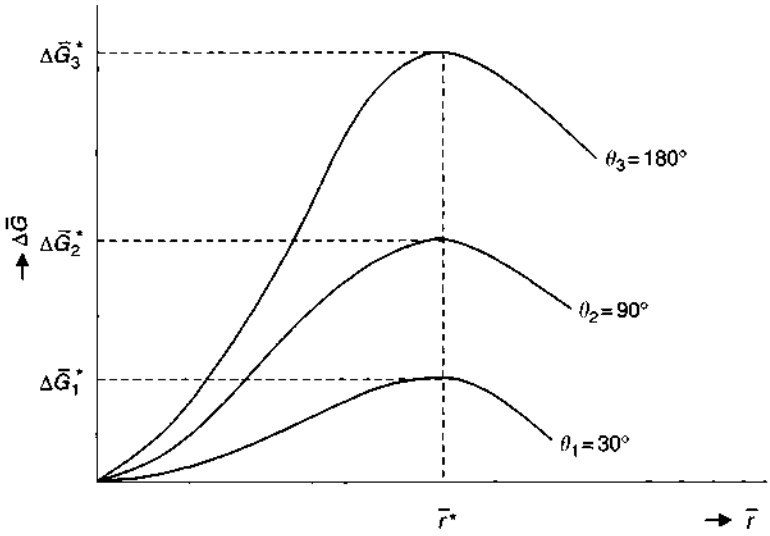

Figure 5.10 Change of free energy in heterogeneous nucleation as a function of the radius of the nucleus r, and the wetting angle θ (r = critical nucleus radius value).*

metal ions is subject to similar restrictions, and subjected to the strongly deforming effect of the steep potential gradient within the electrolytic double-layer, they shed most if not all of the complexing ligands in the Helmholts layer.

For the formation of nuclei of at least the critical size, there are seen (Fig. 5.11) to be two options. Either the metal ions passes directly to the cathode surface, at locations acting as nucleation sites, where this is energetically favoured and where nuclei of at least the critical size can form or, at they pass through sites which are energetically less favourable. In the latter case, lateral movement of ad-atoms across the surface is necessary to form nuclei of the critical size.

The lateral diffusion of ad-atoms at the surface can be visualised as shown in Fig. 5.12. As they approach the cathode, the hydrated metal ions lose a part of their hydration sheath and thus retain a partial charge. In this specially low energy state, they diffuse across the cathode surface to the nearest growth site. Depending on the location and state of the resulting crystal nucleus, four different types of site are recognised (Fig. 5.15). These are point sites, and one-, two- and three-dimensional sites (edge, plane or corner sites, respectively).

5.5.1.2.1 Zero-dimensional nuclei

This description covers the deposition of individual ad-atoms onto an active site at the cathode surface. Formation of such nuclei requires the smallest of all energies of nucleation.

5.5.1.2.2 One-dimensional nuclei

This situation arises when a series of ad-atoms congregate along the edge of a mono-atomic step at the cathode surface [13]. The nucleation energy required for this is somewhat higher than in the preceding case.

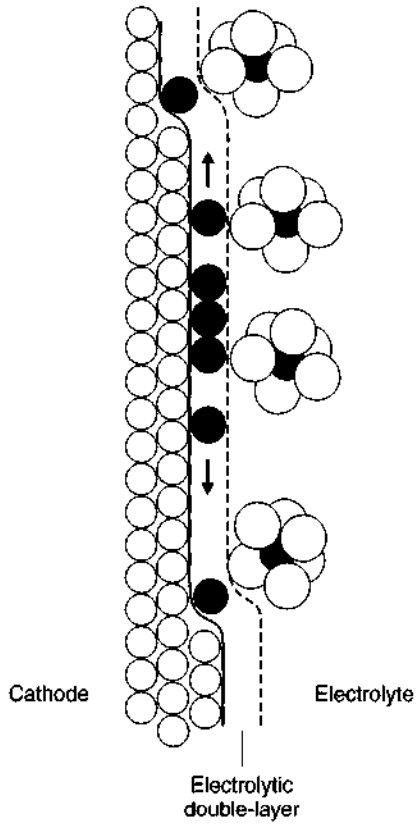

Figure 5.11 Passage of metal ions through the electrolyte double-layer to active sites; for example, step dislocations.

5.5.1.2.3 Two-dimensional nuclei

This situation relates to a planar agglomeration of ad-atoms, the orientation of which will often be related to that of the underlying cathode material. This effect is known as 'epitaxy' where the lattice structure of the deposit is either identical to that of the substrate, or very similar. As an example, consider the electrodeposition of tin onto iron [14, 15]. α-Iron is known to have a body-centred cubic (bcc) structure, whereas β-tin forms a tetragonal body-centred structure. Unit cells of these are shown in Fig. 5.13(a).

The epitaxially formed structure of intermetallic $FeSn_2$ on an iron substrate is shown in Fig. 5.13(b).

The oriented nucleation of the intermetallic phase $FeSn_2$ forming over the iron substrate can be shown as follows (Fig. 5.13b). Two rows of sites, formed from four adjacent α-iron unit cells remain in place following the formation of $FeSn_2$. At the same time, six rows of sites move out to create space for the newly incorporated tin atoms. The newly formed $FeSn_2$ *unit cell* consists of two vertical superimposed tetragonal face-centred Fe cells. Within these two Fe cells are enclosed four tin atoms, tetragonally positioned [14, 15].

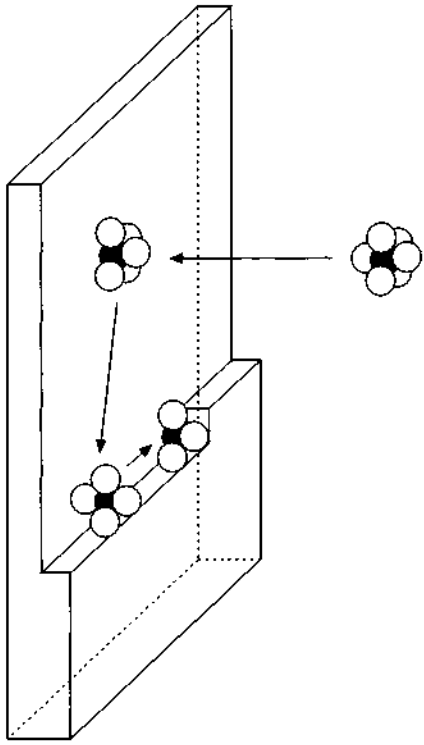

Figure 5.12 Lateral diffusion of ad-atoms at the cathode surface towards energetically favoured growth locations, for example, at steps or corners.

The required energy of nucleation for forming two-dimensional nuclei is thus greater than that required to form point or edge nucleation sites.

5.5.1.2.4 Three-dimensional nuclei

In this case, one is concerned with a spatial aggregation of ad-atoms whose lattice structure bears no relationship to that of the substrate. In practice, the conditions for forming such nuclei are extremely complex. In the case of a totally smooth and featureless cathode surface, the interaction between a crystal nucleus and the cathode metal depends on their respective lattice structures. Where the cathode surface is in some way patterned, and this is usually the case, the nature of such cathode features can strongly exercise influence on the nucleation process. Where lattice structures of substrate and the deposited metal are either identical or similar, then the nucleation may well exhibit epitaxial behaviour. Of special significance in three-dimensional nucleation, is the existence of lattice defects such as edges, corners and steps at the cathode surface, since these can act as active centres which not only trigger nucleation but also influence its subsequent course. As will be apparent from what has been written above, the nucleation energy for three-dimensional nuclei of critical size is larger than that for two-, one- or zero-dimensional types.

The nucleation energy values required to form these various nuclei are shown in Fig. 5.14.

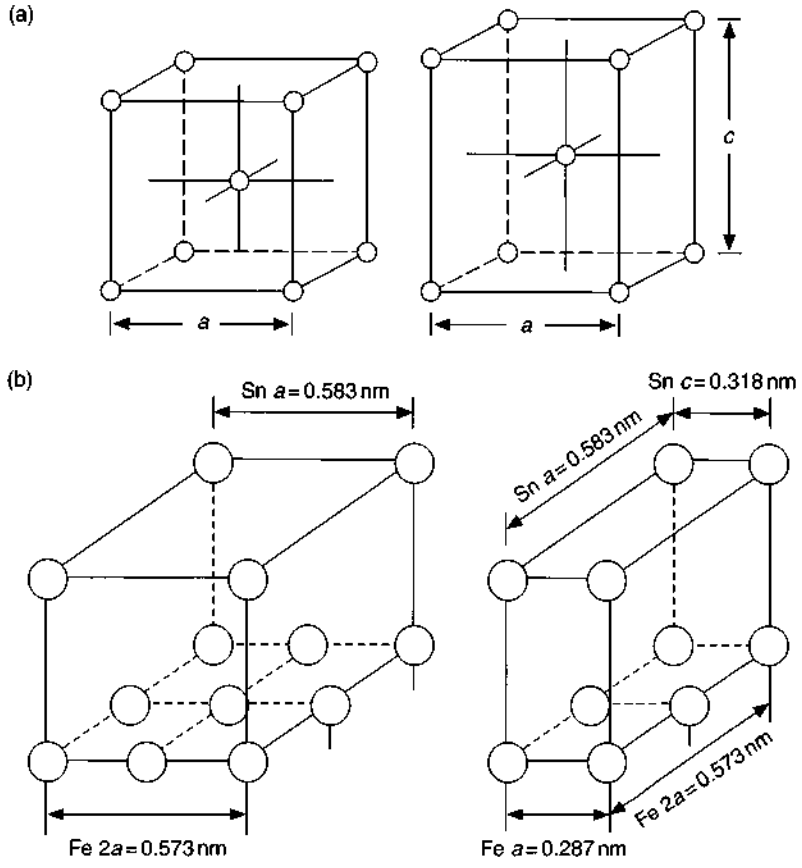

Figure 5.13 (a) Unit cell of a body-centred cubic structure of α-iron (left) and body-centred tetragonal β-tin (right). (b) Epitaxial growth of β-tin over body-centred α-iron. (Left) (001) tin plane over (100) plane of four Fe unit cells. Right:(100) tin plane over (100) plane of two Fe unit cells [14, 15].

The spontaneous growth of thermodynamically stable nuclei is, as noted earlier, a function of the reduction in free energy in the system. Figure 5.14 shows the change in free energy as a function of the radius of the nucleus in forming all four types. It can be seen that the maximum energy to form a nucleus of critical size increases strongly as one moves from zero- to three-dimensional types. Conversely, under comparable conditions, the rate of nucleation, dN_R/dt, that is the number N_K of nuclei forming in unit time, decreases strongly, as shown by Eq. (5.8).

$$\frac{dN_K}{dt} = a_K \cdot \exp\left(-\frac{\overline{\Delta G}^*}{RT}\right) \tag{5.8}$$

where a_K is a constant of the system. The critical nucleus size, above which spontaneous growth continues, is predominantly determined, for electrodeposition, by the

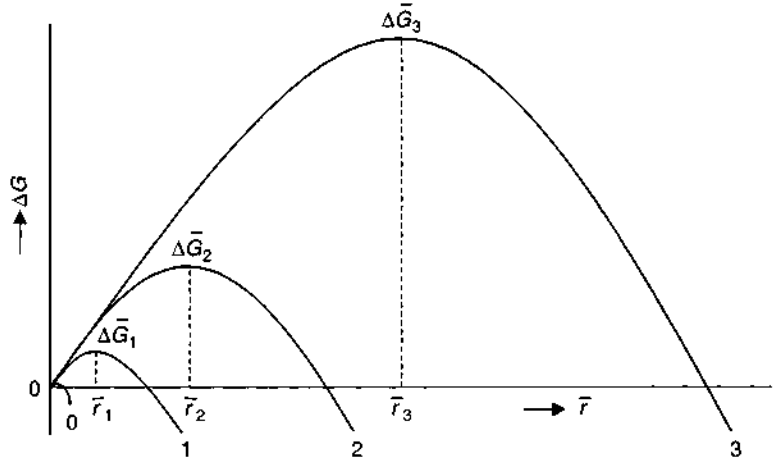

Figure 5.14 Change in free energy in the formation of zero-, one-, two- and three-dimensional crystal nuclei: ΔG_0^*, ΔG_1^*, ΔG_2^* and ΔG_3^* are the energies of nucleation for forming nuclei of a critical size [13].

crystallisation overvoltage, η_K as given by Eq. (5.9)

$$\eta_K = \frac{2\gamma V}{zF\bar{r}^*} = \frac{RT}{zF}\ln\frac{c_{ad}}{c_{ad}^\circ} \tag{5.9}$$

Here, V is the molar volume of a crystal nucleus of critical size, z is the number of electrons transferred, c_{ad} the concentration of ad-atoms at a growth site and c_{ad}° the concentration of ad-atoms in the equilibrium state.

From the foregoing, it can be seen that the crystallisation overvoltage and thus the rate of nucleation (as long as growth sites remain available) are the higher, the greater the concentration of ad-atoms.

5.5.2 Growth of Nuclei

The transition from ad-atoms, formed by metal ion discharge, to a crystalline state, and the subsequent growth of these crystalline nuclei, constitutes the final stage in the sequence of processes leading to formation of a metallic film by electrodeposition. Seen at the microscopic level, the process of crystal growth is the result of accretion of metal atoms at the location of stable crystal nuclei which have formed at the cathode surface. Note that crystal growth, in the case of electrocrystallisation (in contrast to the crystal growth situation in an electrically neutral medium such as molten metal), occurs with simultaneous effects due to lattice forces and electrostatic interactions. A further difference lies in the fact that, in the case of electrocrystallisation, the incoming hydrated or complexed metal ions are surrounded by foreign species such as other cations, anions and neutral molecules. In spite of these different energetic circumstances, analogies can be drawn between virtually all stages of electrocrystallisation and the crystallisation processes taking place in the electrically neutral environment of a molten metal.

5.5.2.1 The Kossel–Stranski Model

According to this theory, metal atoms are preferentially deposited at those sites on the cathode surface where their incorporation in the lattice releases the most energy. On this basis, one would anticipate preferential growth of nuclei at those locations where overall energy requirement is at a minimum. Such locations include edges, corners, steps and kinks. The latter are sharp breaks in dislocation lines. The interatomic forces of attraction within the lattice of the cathode metal are satisfied, thanks to the action of neighbouring atoms in the lattice. Metal atoms at the surface of the lattice, by contrast, have unbound valence bonds, which exert an effect in their immediate environment and this effect is most pronounced at the topographical features listed above, where one might say that individual atoms are more 'exposed'. It is for this reason that preferential metal deposition occurs at these locations, where the free energy required is at a minimum. These locations are also known as semi-crystalline. It should also be recollected that it is at these topographical features that the highest current density is found, and this can further accelerate the crystal growth process. Figure 5.15 illustrates the most commonly found surface defects.

Incoming ad-atoms build up, either directly or after lateral diffusion, at the defect sites on the cathode surface. The stability of growing nuclei formed at these locations

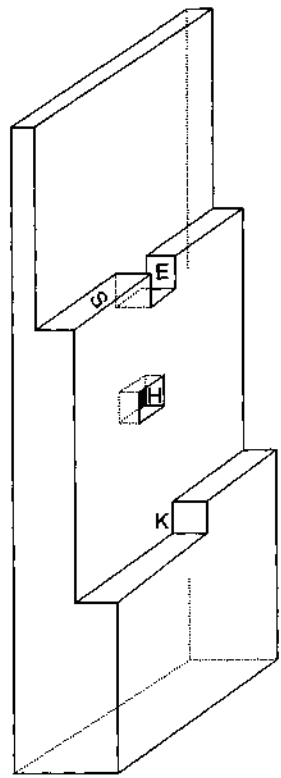

Figure 5.15 Growth sites at a cathode surface. E = corner; H = recess; K = edge; S = step.

is determined by the local lattice energy, and can be defined as that energy that is required to incorporate a further atom into the metal lattice at the cathode. In the case where the incoming ad-atoms combine to form a single, thermodynamically stable crystal nucleus, that is one capable of further undisturbed growth, the outcome will be formation of a single crystal. More commonly, though, electrodeposited layers are polycrystalline, that is they consist of a countless number of small grains or crystallites.

5.5.2.2 Growth types

Polycrystalline deposits can be characterised in terms of the size, shape, distribution and orientation of the crystallites. In fact, there are only a handful of basic types, which are described below [13, 16, 17]. In many cases, however, one can observe transitions between these types, where several types will be present. Metallographic sections are used to illustrate the following brief descriptions.

5.5.2.2.1 Field-oriented isolation type (FI type)

At overvoltages of 0–10 mV, a one-dimensional (point) nucleation is the norm. The nuclei grow to form individual crystallites, mostly oriented in the axis of the current field. Growth occurs slowly at the side faces of these crystallites, resulting in formation of smooth flanks. In technical terms, such deposits, which can be described as dendritic or acicular, are not welcome, and do not result in deposits with useful technical properties. An example of this type of deposit is shown in Fig. 5.16.

5.5.2.2.2 Substrate-oriented reproduction type (BR type)

At overvoltages of 10–100 mV, a two-dimensional nucleation takes place, permitting a flat-faced crystal growth. The axis of growth is normal to the growth plane and is determined by the rate of the slowest step in the sequence, the two-dimensional

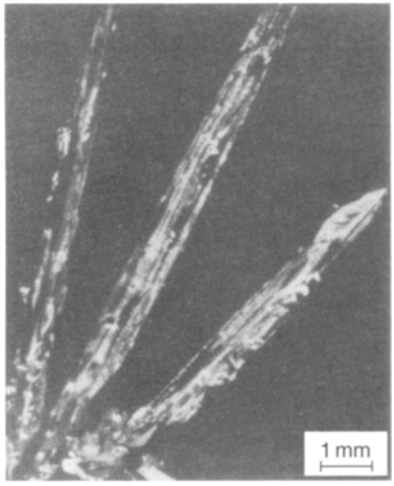

Figure 5.16 Field-oriented isolation type [17] silver crystallite.

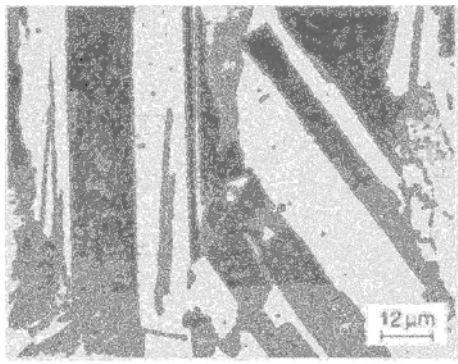

Figure 5.17 Substrate-oriented reproduction type [17] copper crystallite.

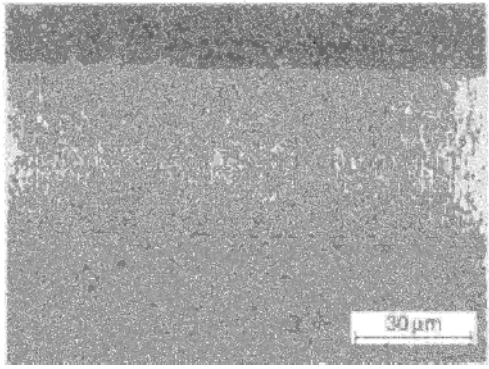

Figure 5.18 Field-oriented texture type [13] Co crystallite.

nucleation [13]. The crystallites in the deposit layer thus emulate the crystal structure of the substrate, a process described elsewhere as 'epitaxy'. These crystals usually form a coarse and compact structure. The technical properties of such deposits are primarily of interest to the extent that they emulate those of the underlying substrate. Figure 5.17 shows an example of such a BR-type.

5.5.2.2.3 Field-oriented texture type (FT type)

In the region 100–150 mV of total overvoltage, single crystallite initially form. As the overvoltage increases, more and more three-dimensional crystallites form. This results in a compact structure formed of fine fibre-shaped crystallites, which grow parallel to the electrical field lines, and whose boundaries are indistinct. At their boundaries, foreign particles can be incorporated. Neither the increased internal stress which this causes nor the pronounced anisotropy of the crystallites, is conducive to good technical properties of such films, and their practical use is accordingly restricted. Figure 5.18 shows an example of a FT-type crystallite.

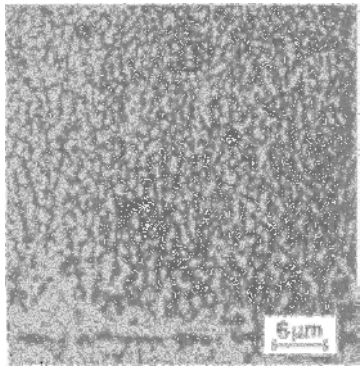

Figure 5.19 Randomly oriented dispersion type [17] Cu crystallite.

5.5.2.2.4 Randomly oriented dispersion type (UD type)

At overvoltages of >200 mV, as a result of high rates of electrocrystallisation, very small crystal nuclei can form, resulting in formation of a micro-structure of very fine, randomly oriented crystallites with no visible grain structure. Using an optical microscope, it is not possible in this case, to distinguish individual crystallites. The absence of any pronounced crystallite orientation is an indication that the nucleation process has a statistical basis. This type of structure is characterised by incorporation of finely divided foreign species, which act to stabilise the micro-structure of the deposited layer. Thanks to their excellent properties, deposits of this type are ideal for technical applications. Figure 5.19 is an example of this UD type.

5.5.2.2.5 Twinning transition type (Z type)

The Z-type designates the transition between FT (field-oriented texture type) and BR type (base-oriented reproduction type). This structure is formed when the crystallisation overvoltage is large enough to allow formation of two-dimensional nuclei. Under these conditions, the crystallographic twinning planes of the crystallite act as growth planes, on which twinned crystals can form. The twinning boundaries appear under the microscope as straight lines. Twinning can result in a reduction of the ductility of the deposited metal. An example of a Z-type crystallite is shown in Fig. 5.20.

5.5.2.3 Frank model

As noted previously, incoming ad-atoms form preferentially at the most energetically favorable sites for nucleation and growth, on the cathode surface and this continues until the defect sites which meet this description, are fully occupied and healed. Figure 5.21 shows how a continuing deposition process creates a new crystal plane.

As soon as the processes above have created a new and defect-free crystal plane, one might expect, on the basis of arguments used, that further growth would come to a halt. In fact, that growth continues, requires that two-dimensional nuclei form on the 'perfect' plane, and these act as new nucleation sites. This process can be seen as one wholly analogous with homogeneous nucleation, which was described

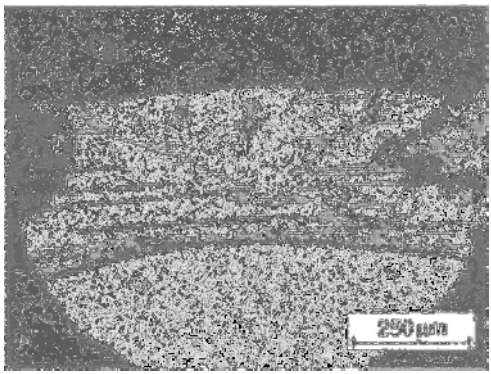

Figure 5.20 Twinning transition type [13] Fe crystallite.

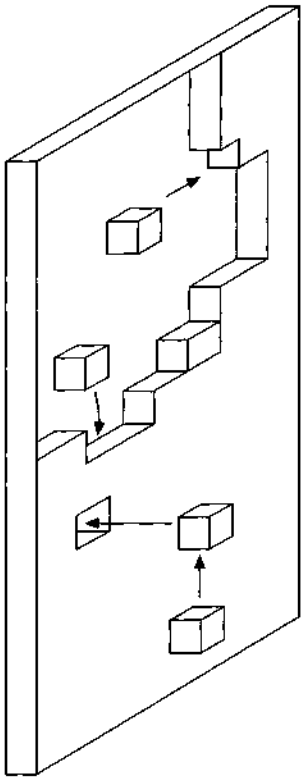

Figure 5.21 Formation of new lattice planes on the cathode surface, with elimination of existing growth sites.

previously. It implies that, in some way, small, adherent flat nuclei must form, which thanks to the normal Gaussian distribution of energy levels, grow to a sufficiently large size to become thermodynamically stable, at which point further growth can take place. The activation energy required for this to occur is, nevertheless, so high that its probability is low, and would require very high cathodic

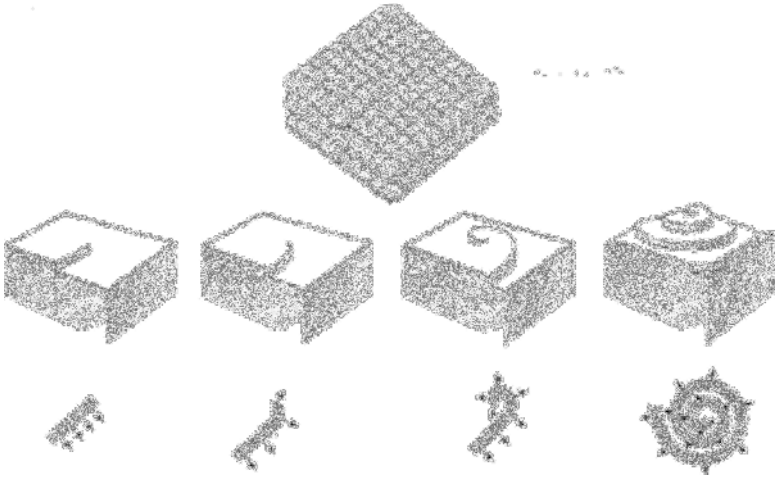

Figure 5.22 Spiral-formed crystal growth around the break-through point of a screw dislocation [20, 21].

current densities, of a magnitude not found in practice. This suggests that this particular mechanism is effectively precluded. However, the very large energy of formation required for two-dimensional nuclei vanishes if the Frank growth mechanism comes into play [18, 19]. This is based on a continuous crystal growth, with no requirement for a preceding nucleation. Instead of a growth at edges, corners or steps, growth takes place at defects in the substrate lattice. The initial assumption of this growth model is that the growing crystallites are themselves afflicted with a range of lattice defects.

Such defects include screw dislocations, formed by a spiral rotation of the lattice plane along an axis of rotation. They project from the surface of the cathode, and there form, as shown in Fig. 5.22, atomic-scale steps. These grow, as further metal atoms are deposited, and a spiral growth pattern continues. The axis of rotation of such screw dislocations, where steps are initiated, remains fixed.

The growth pyramid continues to form, and the lattice plane grows continuously as long as further metal atoms are supplied. In this way, a fresh lattice plane can form, covering the entire cathode surface. In this process, the screw dislocation remains a feature, and thus renders unnecessary, the formation of two-dimensional nuclei as a prerequisite for formation of a fresh lattice plane. The growth process then occurs in spiral mode, in which the spacing between the individual threads corresponds to the radius of a two-dimensional nucleus. In that the cathode surface is penetrated by numerous screw dislocations, there are enough growth centers to allow growth to occur at an accelerated rate. Confirmation of this mechanism can be seen in Fig. 5.23.

Protrusion of numerous screw dislocations from the cathode surface often result, in practice, to a roughening of the deposited metal surface.

The explanation is straightforward. At the tips of the screw dislocations, a concentration of field lines is found, which leads to higher local current densities and

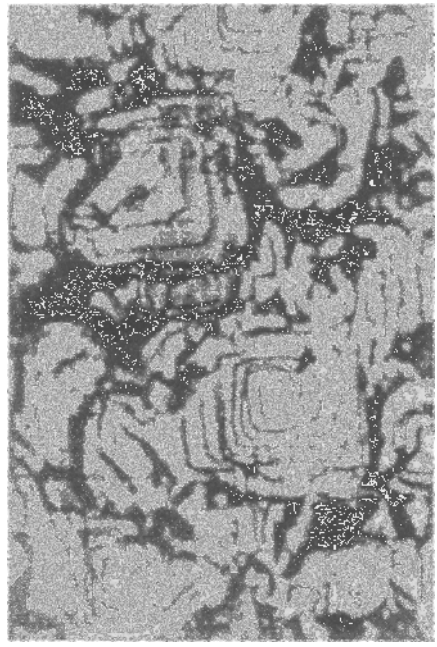

Figure 5.23 Spiral-formed growth [17] of a copper crystallite. Magnification 450×.

higher metal deposition rates. In the case of poorly conducting electrolytes, the roughening effect is further enhanced by metal ion depletion, which is more pronounced at the basal plane than at the tip. In extreme cases, a pyramidal growth leads to formation of needle-like deposits, and these are known as dendrites [22].

5.5.2.4 Factors influencing nucleation and growth

Nucleation and growth can be affected by a number of parameters, of which the most important are:

- the crystal structure and type of substrate material;
- the crystal structure of the deposited metal;
- the composition and pH of the electrolyte;
- the deposition conditions such as current density and temperature.

The effect of two of these parameters, the substrate and current density, will be considered further.

5.5.2.4.1 Substrate effects

Taking into consideration factors such as inter-atomic bonding forces and interactions between the substrate and the deposit forming over it, the substrate–deposit interface can be modeled, using a mechanism originally developed for growth from the gaseous or the molten phase. Taking the case where the bonding forces between

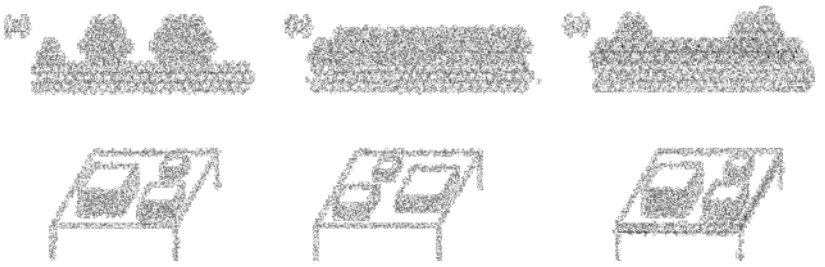

Figure 5.24 Growth of a deposit on a surface, showing the interface: (a) Volmer–Weber model; (b) Frank–van der Merwe model; (c) Stranski–Krastanov model [23, 24].

the atoms in the layer are stronger than those between the layer and the substrate, the Volmer–Weber model predicts formation of individual crystallites, which then grow in three dimensions over the substrate. In the opposite case, where the atomic forces between the atoms in the layer are weaker than those binding the layer to the substrate, and, arising from this, when both types of atom are of comparable size, the Frank–van der Merwe model holds, predicting epitaxial growth. In those cases, however, where the bonding forces beneath the atoms in the deposited layer are identical with those between atoms of the substrate metal, even if the atomic radii of the two metals is different, then the Stranski–Krastanov model holds. In the case, a thin epitaxial film is initially formed on the substrate surface, with a distorted or staggered atomic spacing, which then transforms to a three-dimensional crystal growth. The foregoing three models are seen in Fig. 5.24.

In the above descriptions of the growth processes at a deposit–substrate interface, the presence of the occasional foreign atom at the substrate surface has been ignored. In practice, there are a number of ways in which such atoms can be present. They may have been present in the first place or perhaps diffused in from solution during the electrodeposition process. Whatever their source, they can, by their presence, significantly affect the nucleation process. Thus, foreign atoms can block growth centres on the substrate surface, or they can occupy growth sites. In either case, the incoming metal atoms are then forced to seek out energetically less-favoured sites. This may result in formation of new nucleation sites, which implies an increase in the number of nuclei at the surface. This can substantially affect the two competitive processes of nucleation and growth. This effect offers a useful means of controlling or suppressing the nucleation processes which determine the deposit micro-structure, that is, the size, distribution and orientation of the crystallites in the deposited layer, all of which, in their turn, determine the deposit properties.

Crystal growth resulting from a continuous formation of new lattice planes can also be affected by the structure and surface morphology of the substrate, and this effect is specially marked in the case of thin deposits. Individual crystallites in such thin films will often adopt an orientation determined by the underlying substrate. In a similar manner, the size of crystallites in the deposit can be influenced by that of the crystallites in the substrate, with crystallites in the deposited film being fine-grained where those in the substrate are the same, and vice versa. Only above a

certain thickness of deposited film, will it assume a structure of its own, and at this point, the so-called 'substrate effect' disappears.

5.5.2.4.2 Effect of current density

Current density is one of the principal factors affecting the structure and morphology of an electrodeposited film, determining not only the deposition rate, that is, the rate of film growth, (Fig. 5.25) but also the size and distribution of the crystallites.

The metallographic sections shown in Fig. 5.26 testify to the effect of current density on deposit micro-structure, in this case an iron deposit formed from a sulfate electrolyte (pH 2.0, $T = 60°C$).

The effect of current density is even more significant when considering pulse current. In this case, using very short duration pulses, extremely thin diffusion layers are formed, since there is insufficient time for these films to grow any thicker. In this case, the current interruptions act to allow an equilibration of metal ion concentration.

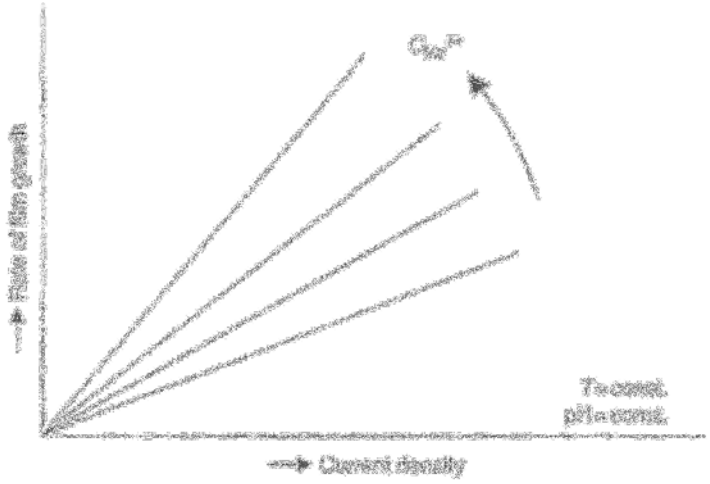

Figure 5.25 Effect of current density on the rate of deposit film growth at various metal ion concentrations

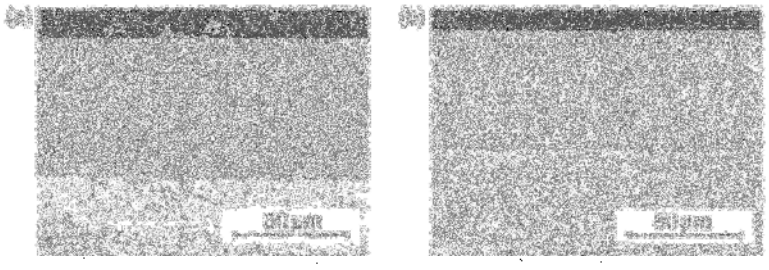

Figure 5.26 Effect of current density on the structure of deposited iron: (a) $I = 5$ A/dm^2; (b) $I = 10$ A/dm^2 [25].

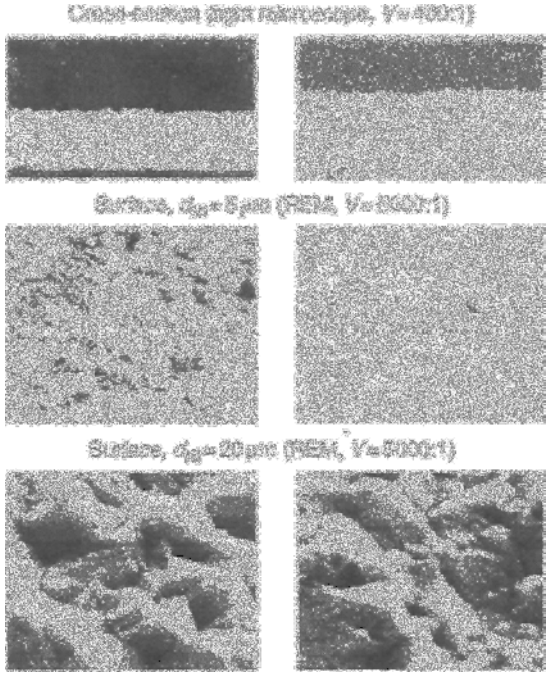

Figure 5.27 Structure build-up and surface morphology of DC and pulse-plated nickel: (left) I_{DC} = 47 mA/cm²; (right) pulse current, I_m = 47 mA/cm² [26].

One result of this is that a higher peak pulse current is necessary in order to deposit a given amount of metal in a set time, than would be the case with DC, in order to compensate for the off-time when no deposition occurs.

A consequence of using the higher current density in the case of pulsing is that higher deposition overpotentials result, which promote the nucleation process. In consequence, one would normally expect a finer-grained deposit. Figure 5.27 shows the cross-section and surface images of nickel, deposited from an additive-free Watts bath (240 g/l nickel sulfate, 30 g/l nickel chloride, both hydrated, and 30 g/l boric acid) under DC and pulsed-current conditions.

In both cases, the nickel deposits are strongly columnar in form with variable degree of lateral growth.

Another important point to be noted in the case of pulsed current deposition is that fact that reduction products, such as carbon, hydrogen and oxygen are able, to a large extent, to diffuse back into solution during the off-times and thereby less likely to be incorporated into the deposit. By selecting appropriate cathodic and anodic pulse current densities, desired reactions can be promoted, and by making use of specific adsorption and desorption, the extent of incorporation of certain species can be controlled. In summary, it can be stated that pulse plating not only allows higher deposition current densities, but also compositions which would not normally be possible using DC deposition.

5.6 Whisker Growth

It is well known that, over time, hair-like fibres can grow out of electrodeposited layers and these are known as whiskers [27–37]. An example is shown in Fig. 5.28. Formation of such whiskers is especially problematic in the electrical and electronics industries, since these whiskers can lead to short-circuits in a wide range of electrical appliances, especially printed circuit boards. In the latter case, as the conducting tracks are spaced ever closer together, the distance over which a whisker must grow, in order to cause catastrophic failure, becomes smaller and smaller. From this point of view, the problem is a growing one. According to the literature, whiskers can carry electrical currents of 10 mA, perhaps even 25 mA without melting [33].

Thus, it is reported that tin whiskers might have a resistance of 50 Ω and that these would begin to melt only with a current of 10 mA [35].

Whisker formation is usually classified as one of two cases. In one case, the metal atoms forming the whisker diffuse through the deposit layer to the location from which the whisker then grows. In this case, they do not diffuse through any other phase layer. This is known as spontaneous whisker formation (proper whiskers). In cases where whiskers are due to externally applied compressive stress, one refers to these as squeeze whiskers. Whereas the growth rate of spontaneous whiskers can be up to 1 cm/year under the most favourable conditions, squeeze whiskers can grow at up to 1 m/year.

The growth of both types of whisker can be satisfactorily modeled in terms of diffusion processes. Setting out from the observation that irregularities found at the whisker tip often remain unchanged over a period of time, it can be deduced that the metal atoms involved in the formation and growth of the whisker, are sourced by solid state diffusion from adjacent areas to the growth point. Two diffusion mechanisms can operate in this case, namely self-diffusion and grain-boundary diffusion. Which of these is of primary importance, can only be determined on a case-by-case basis, in which diffusion coefficients are measured. Comparison of values for diffusion coefficient, not only at ambient conditions but also at elevated temperatures,

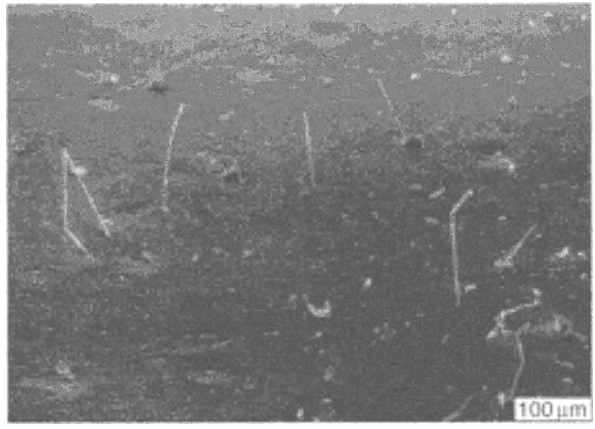

Figure 5.28 Whisker on the surface of zinc-plated steel cabinet (after 2 years in service).

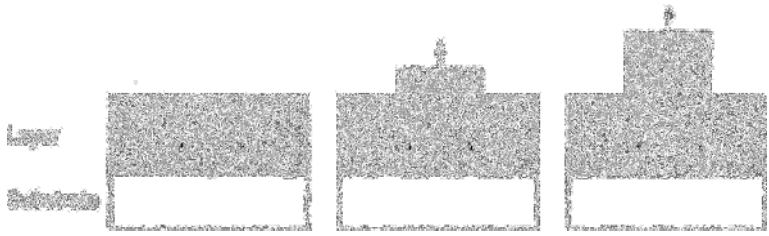

Figure 5.29 Whisker growth due to solid-state diffusion of metal atoms along grain boundaries in the deposited layer [32].

indicates that the contribution from self-diffusion is negligible, as compared with that from grain-boundary diffusion. Taking the case where diffusion of metal atoms along the grain boundaries in the deposited layer is the sole mechanism for whisker growth, the whisker formation process can be represented as shown in Fig. 5.29.

That the diffusion model for whisker growth is the correct one, is also supported by the observation that there is no reduction of deposit thickness in the region around the root of the whisker [37]. However, the diffusion mechanism is not the only process involved in whisker growth, as the following consideration makes clear. The volume of a whisker of 4 μm diameter and 1 mm length, growing out of a film 10 μm thick, represents a volume of 12.6 μm^3. This corresponds to an area of deposit of diameter 40 μm from which the whisker metal atoms must be sourced. Should several such whiskers form, close to one another, as is often the case, the question must then be asked, what forces are responsible for providing the metal atoms necessary for further whisker growth? Experiments suggest that compressive stress, present in the deposit layer, are the primary driving force for mass-transport of metal atoms [37]. These operate not only through lattice defects in the crystal, but also result from lattice dislocations, these last being often due to the presence of foreign species in the lattice. These impurities frequently derive from the deposition electrolyte, in which they are inadvertently present.

In addition to the growth mechanism described above, which operates via solid-state diffusion and is driven by compressive stress, a further mechanism should be noted, as a possible source of whisker formation and growth. This involves a spiral growth mechanism(Fig. 5.30) along the screw dislocations which can penetrate through to the outer surface of the deposited layer, where they form an atom-scale step at the point of their emergence (see Fig. 5.22). These steps are energetically favored grow locations, at which metal atoms can readily accrete. One can thus hypothesise a whisker growth process in which the metal atoms diffuse to the surface, using vacancy-hopping, after which, by surface diffusion, they congregate at these growth sites. In this way, step defects are built up around the axis of rotation of screw dislocations. Migration of metal atoms along the axis of the screw dislocation is favored by reduced displacement energies, which provides the driving force for spiral grain growth. A characteristic of whiskers formed by this mechanism is their sharp tip.

This mechanism is also invoked to explain the extremely high mechanical strength of such whiskers, in many cases close to the theoretical value. The tensile strength values shown in Fig. 5.31 are an indication of the very high values

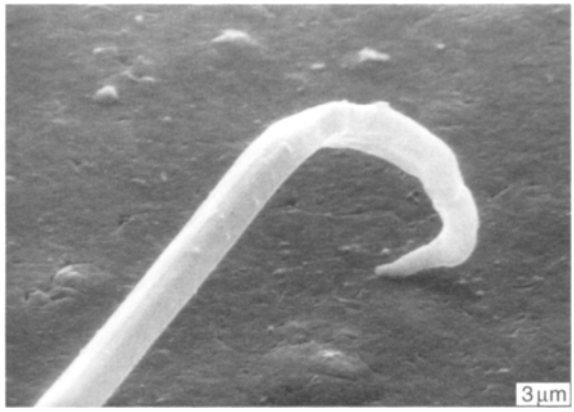

Figure 5.30 Tip of zinc whisker, formed as part of a spiral growth mechanism.

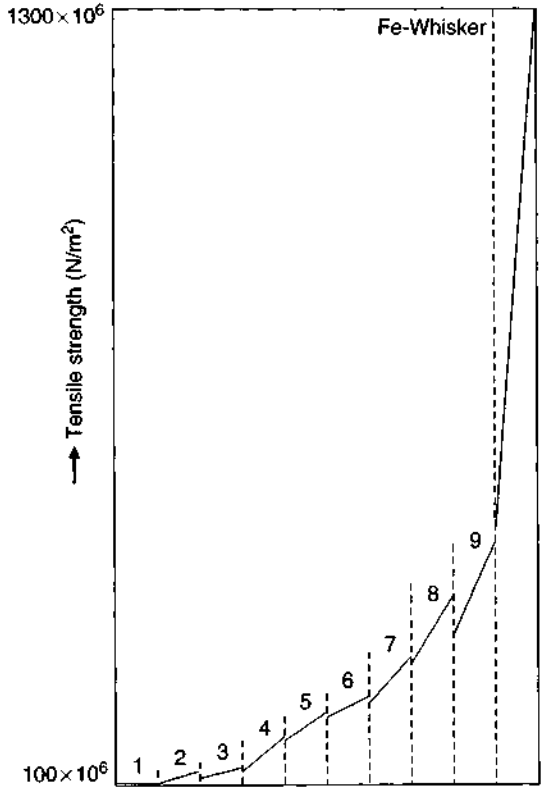

Figure 5.31 Tensile strengths: (1) iron single crystal; (2) α-iron; (3) fine-grained steel; (4) cold-drawn steel; (5) steel with pearlitic structure; (6) steel with transition structure; (7) steel with martensitic structure; (8) steel with martensitic structure, after tempering; (9) cold-drawn steel wire.

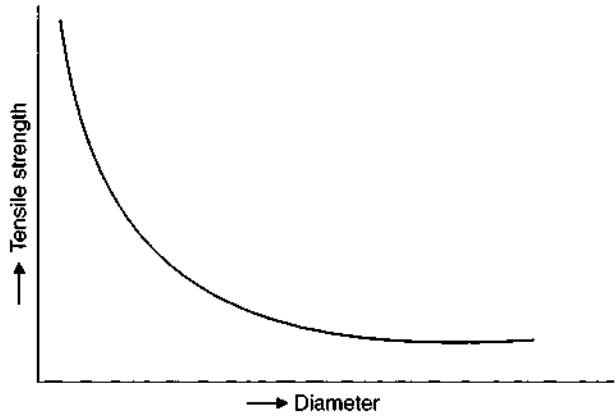

Figure 5.32 Tensile strength of a whisker as function of its diameter.

found for iron whiskers, as compared with other forms and structures of the same metal.

The experimental observation that the tensile strength of a whisker falls off rapidly with increasing diameter, suggests that a model based on a single axial screw dislocation, is not a valid explanation for the extremely high tensile strength of such whiskers. The decrease in tensile strength of a whisker, as its diameter increases, is shown schematically in Fig. 5.32.

References

[1] Hamann, C.H. and Vielstich, W. *Elektrochemie I*, Verlag Chemie, Weinheim, 1975.

[2] Dunsch, L., *Vom Ion zur Elektrode*, VEB Deutscher Verlag für Grundstoffindustrie Leipzig, 1983.

[3] Freise, V., Zur Theorie der diffusen Doppelschicht, *Zeitschrift für Elektrochemie*, Bd. 56, Nr. 8 (1952) 822–827.

[4] Bockries, O'M., Devanathan, M.A.V., and Müller, K., On the structure of charged interfaces, *Proc. Roy. Soc. A* 274, 55 (1963) 55–79.

[5] Dehahay, P., *Double Layer and Electrode Kinetics*, Interscience Publishers, New York, 1965.

[6] Conway, B.E., *Theory and Principle of Electrode Processes*, The Ronald Press Company, New York, 1965.

[7] Levine, S., Mingins, J. and Bell, G.M., The discrete effect in ionic double-layer theory, *J. Electroanal. Chem.* 13 (1967) 280–329.

[8] Beck, F., *Elektroorganische Chemie*, Verlag Chemie, Weinheim, 1974.

[9] Landsberg, R. and Bartelt, H., *Elektrochemische Reaktionen und Prozesse*, VEB Deutscher Verlag der Wissenschaften, Berlin, 1977.

[10] Hamann, C.H. and Vielstich, W., *Elektrochemie II*, Verlag Chemie, Weinheim, 1981.

[11] Schwabe, K., *Physikalische Chemie – Elektrochemie*, Band 2, Akademie-Verlag, Berlin, 1986.
[12] Kanani, N., Kristallisation und Transformation in binären Systemen, *Physik in unserer Zeit*, 13 (1982) 3, 71–80.
[13] Liebscher, H., Elektrochemische Metallabscheidung, in: *Oberflächenveredeln und Plattieren von Metallen*, herausgegeben von A. Knauschner, VEB Deutscher Verlag für Grundstoffindustrie, Leipzig, 1983.
[14] Schütz, W., Über gesetzmäßige Verwachsung von $FeSn_2$ mit α-Eisen beim Verzinnen von Weißblech, *Metalloberfläche* 25 (1971) 6, 190–194.
[15] Knauschner, A., Schmelztauchverfahren in: *Oberflächenveredeln und Plattieren von Metallen*, herausgegeben von A. Knauschner, VEB Deutscher Verlag für Grundstoffindustrie, Leipzig, 1983.
[16] Fischer, H., *Elektrolytische Abscheidung und Elektrokristallisation von Metallen*, Springer-Verlag, Berlin, 1950.
[17] Vetter, K.J., *Elektrochemische Kinetik*, Springer-Verlag, Berlin, 1961.
[18] Frank, F.C., Crystal growth and dislocation, *Z. Elektrochem.* 56 (1952) 822.
[19] Kaischew, R., Keimbildung bei der elektrolytischen Metallabscheidung, *Chemie-Ing.-Techn.* 39 (1967) 9/10, 554–562.
[20] Kitaigorodsky, A.I., *Order and Disorder in the World of Atoms*, Mir Publishers, Moscow, 1980.
[21] Kittel, C., *Einführung in die Festkörperphysik*, Oldenbourg Verlag, Mün- chen, 1969.
[22] Raub, E. and Müller, K., Grundlagen der Metallabscheidung, in: *Hand- buch der Galvanotechnik*, Band I, herausgegeben von H. Dettner und J. Elze, Carl Hanser Verlag, München, 1969.
[23] Landolt, D., Beziehung zwischen Herstellung, Struktur und Eigenschaften von PVD und galvanischen Schichtsystemen, in: *Neue Schichtsysteme für die Industrie*, 18. Ulmer Gespräch, Eugen G. Leuze Verlag, Saul- gau/Württ., 1996.
[24] Nicols, R.J., *et al.*, Classification of growth behaviour for copper on various substrates with in-situ scanning probe microscopy, *Surf. Sci.* 335 (1995) 110–119.
[25] Schmidt, C. *et al.*, Elektrolytische Eisenschichten, *Metalloberfläche* 52 (1998) 12, 968–974.
[26] Baltrusch, S., Der Einfluß von Umkehr-Pulsstrom auf den inneren Aufbau und die Eigenschaften galvanischer Nickelschichten aus dem WATTS-Bad, Dissertation, Humboldt-Universität zu Berlin, 1996.
[27] Hardy, H.K., The filamentary growth of metals, *Prog. Metal Phys.* 6 (1956) 45–73.
[28] Frank, J., Growth of whiskers in the solid Phase, *Acta Metall.* 6 (1958) 103–109.
[29] Blaha, F., Bemerkenswerte Eigenschaften dünner Metallfäden, *Metall. 1* (1959) 20–25.
[30] Wachholtz, R., Probleme der Whiskerentstehung auf metallischen Oberflächen, *Oberfläche-Surface* 2 (1970) 41–45.
[31] Glazunova, K.V. and Gorbunova, K.M., Spontaneous growth of whiskers from electrodeposited coatings, *J. Crystal Growth*, 10 (1971) 8590.

[32] Evans, C.C., *Whiskers*. Mills & Boon Limited, London, 1972.
[33] Jafri, A., Fighting whisker growth in the communication industry, *Plating* 4 (1973) 358–361.
[34] Dunn, B.D., Whisker formation on electronic materials, *ESA Sci. Techn. Rev.* (1976) 2, 1–10.
[35] Baker, R.G., Spontaneous metallic whisker growth, *Plating Surf. Finish.* (1987) 12.
[36] Hitch, T.T., Avoiding electrolytic and strain-induced shorting mechanisms, *Circuit World* 16 (1990) 2, 41.
[37] Kanani, N., Zink-Whisker, *Metalloberfläche* 52 (1998) 10, 782–788.

This Page Intentionally Left Blank

CHAPTER 6

In situ Observation of Electrodeposition

6.1 Introduction

It goes without saying that studying the structure of an electrodeposit provides valuable insight into its properties. Such insights are reinforced if such structural studies are complemented with data on deposit properties, such as hardness, ductility etc. Such studies are usually undertaken with techniques which are widely used in metallurgy and materials science, such as optical or electron microscopy, X-ray diffraction, etc. In many cases, these techniques can be used in their standard form. In some cases, they have to be somewhat adapted. Details of some of these are found in the following chapters. Such investigations are all concerned with the electrodeposited film after its formation is complete. Hardly surprisingly, attempts have also been made to observe the electrodeposition process as it is taking place, in situ. Until relatively recently, all such techniques were based on use of the optical microscope and a specially configured electrochemical cell. The far more powerful scanning electron microscope operates under vacuum, and was thus ruled out. Some work was carried out using *in situ* X-ray, *in situ* Raman spectroscopy and *in situ* infrared, all of which are reported in the literature. Most of these have been consigned to the drawer labeled 'scientific curiosities'. It has been noted that recent advances in lens design now allow use of high magnifications (e.g 500×) but with far greater object-to-lens working distance. It might have been though that this would trigger a renewed interest in *in situ* optical microscopy, but this seems not to have occurred. Although, as published work shows, optical microscopy is nowhere near as powerful a tool as the methods described below, its far lower price, coupled with the fact that such equipment already exists in many laboratories, makes it surprising that it seems not to be used at all today.

Without doubt, the development of the scanning probe microscope (SPM) [1–45] with its associated variants, the scanning tunnelling microscope (STM) and atomic force microscope (AFM) have drastically transformed our understanding of the electrodeposition process, allowing an *in situ* observation of the processes at the atomic level. In what follows, these instruments and their underlying principle will be briefly described, and their applications in electrodeposition R&D will be detailed.

6.2 Scanning Probe Microscope (SPM)

The operation of this instrument (sometimes known as scanning probe microscopy, but also as scanning tunnelling microscopy) is based on the interaction between the tip of a probe and the surface being studied. The extent of interaction depends on the distance between probe tip and substrate surface. If the probe tip, located at a distance of a few atomic diameters from the substrate surface, is rastered, and the resulting signal (I) recorded as this takes place, a three-dimensional plot can be recorded for the function $I = f(x, y)$ where x, y are the geometric coordinates in the plane of the substrate. The result is a topographical representation of the surface. The vertical resolution might be of order 10^{-3} nm. The horizontal resolution is a function of the shape and properties of the probe tip, and the x, y traverse mechanism.

Table 6.1 Specific comments on some SPM applications [32].

Method (Designation)	Probe	Working principle	*In situ*?	Data recorded
Scanning tunnelling microscopy (STM)	Metal tip	Quantum mechanical tunnelling effect	Yes	Topography, local density
Scanning force microscopy (SFM)	Tip attached to micro-beam	van der Waals forces	Yes	Topography, micromechanical properties
Scanning electrochemical microscopy (SECM)	Amperometric micro-electrode in insulated mounting	Detection of redox species close to probe tip	Only *in situ*	Topography, electrochemical reactivity
Scanning ion conductance microscopy (SICM)	Electrolyte filled micro-pipette with inner and outer electrodes	Conductivity between electrodes	Only *in situ*	Topography, ionic diffusion through pores
Near-field optical scanning microscopy (NOSM)	fibre-optic mounted lens	Reflection, Transmission, Luminescence, Scattering	Yes	Optical properties

Table 6.2 Comparison of optical microscopy (OM), scanning electron microscopy (SEM) and scanning probe microscopy (SPM).

	OM	SEM	SPM
Sample preparation	(Electro)polishing	Evaporation	None
Operating environment	Air	Vacuum	Air, liquid, vacuum
Depth of focus	Very small	Very large	Small
(x, y) resolution	1.0 μm	5 nm	0.1–1.0 nm
z-axis resolution	–	–	0.01 nm
Magnification	1000–2000	10–10^6	5×10^2–10^8

Some specifics of the most important SPM techniques are noted in Table 6.1, though it should be appreciated that as the method continues to be more widely used, the listing is in no way comprehensive.

By comparing SPM with optical microscopy or the SEM with respect to ease of sample preparation, operating environment, depth of focus, resolving power and magnification range, it is found that the SPM, especially in terms of its flexibility and resolution, is far superior to the other two techniques, as Table 6.2 makes clear.

Using SPM, the following data and information can be obtained in terms of the composition and structure of the surface being studied:

- Three-dimensional image of surface topography at magnification of 500 to 10 million times.

- Details of monatomic steps and other atom-scale surface defects and irregularities.
- Information as to the distribution and geometry of nuclei and clusters and the initial stages of the electrodeposition process.

6.2.1 Scanning Tunnelling Microscopy (STM)

6.2.1.1 Basics and techniques

An STM operates on the principle known as quantum-mechanical tunnelling. This lays down that electrons do not necessarily require sufficient kinetic energy to surmount an energy barrier; they can also tunnel through such potential energy barriers.

Tunnelling effects are a consequence of the fact that electrons behave, in quantum-mechanical terms, like waves, and indeed their behaviour can be expressed in terms of wave functions. Since the electrons are not uniquely associated with a specific point in a metal (giving rise to the term 'delocalised'), one can do no more than assign a given probability that an electron will occupy a particular point in space at a given time. In this way, the concept of 'electron clouds' arises and these form in close proximity to the outer limits of the object in question.

In cases where the electron clouds from two solid species overlap, electron exchange can occur. The condition for this to take place is that the electrons can cross the potential energy barrier between the two solid bodies. This process will be considered in terms of a metallic probe, whose tip is immediately adjacent to the surface of a metallic substrate. Figure 6.1 shows, in terms of their atomic structures, the probe tip and the substrate surface.

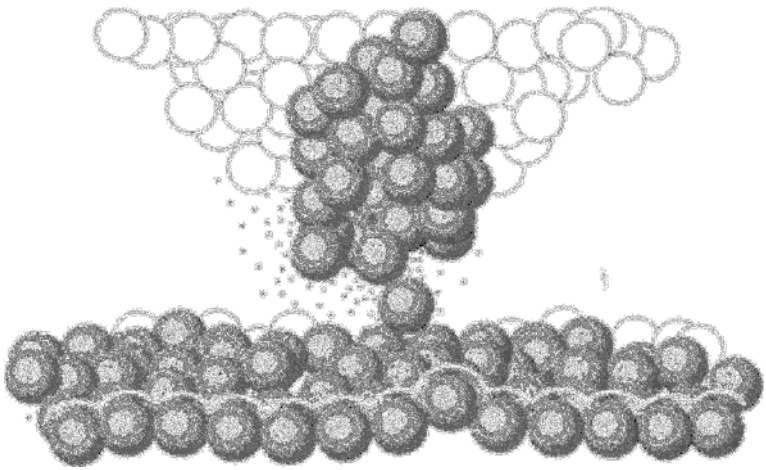

Figure 6.1 Electron exchange between a metallic tip and the surface of a metallic substrate resulting from overlapping electron clouds (courtesy of Wild-Leitz).

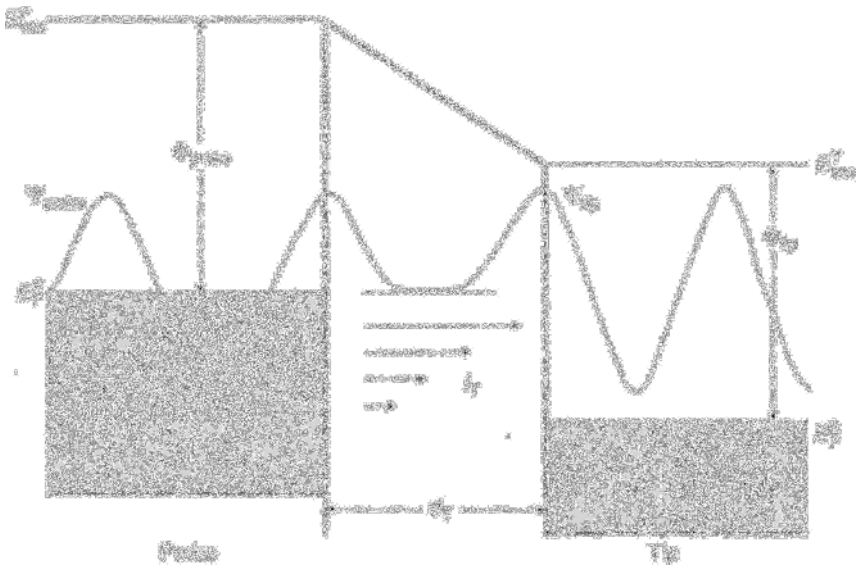

Figure 6.2 Formation of a potential energy barrier between sample surface and probe tip [27].

The potential energy barrier formed between the probe tip and the surface of the sample is shown schematically in Fig. 6.2. It is a function of the medium separating these two solids and is here assumed to be a vacuum.

The thicker line shows course of the potential energy of the electrons. The grey hatched areas depict filled energy states for the valence electrons which are responsible for the electrical conductivity. E^{P}_{F} is the Fermi energy of the sample, E^{S}_{F} that of the probe tip and these are the boundary values that divide occupied and vacant energy states. It is recognised that both in the sample and in the probe tip, energy levels will be filled with electrons up to the Fermi level. Φ_{probe} and Φ_{tip} designate the work-function, that is, the energy required to remove an electron from the Fermi level in the sample or the probe and take it, in vacuum, to an infinite distance. This determines the height of the potential energy barrier which forms between probe tip and sample. Ψ is the amplitude of the corresponding wave function. The square of this designates the probability of an electron residing at a given location. E^{P}_{vac} is the vacuum energy level of the sample, E^{T}_{vac} is that of the tip.

On account of the atomic dimensions of the tunnelling distance, d_T ($\leq$1 nm), that is, the distance between probe tip and sample surface, an overlap occurs of the electronic wave functions and thereby enables the electrons to tunnel through the energy barrier. The result is that by application of a so-called tunnel voltage U_T between sample surface and probe tip, a current will flow between the two, the so-called tunnel current, I_T. It is the sum of the partial currents which, as seen in Fig. 6.2, decrease as the separation between probe tip and sample surface, increases.

The tunnelling probability is determined by the distance through which the process must take place, and the height of the potential energy barrier. However, the electronic state of probe tip and sample, surface also determine the magnitude

of the tunnelling current. Of fundamental importance is the fact that the wave functions of the electrons which move in a vacuum between sample surface and probe tip, are exponential in nature. From this, it follows that the tunnel current, I_T, is a sensitive function of the tunneling length, d_T. This fact can be mathematically expressed, using a relationship originally developed to model two flat-plate electrodes, as shown below [1,2]:

$$I_T \sim \left(\frac{U_T}{d_T}\right) \cdot \exp\left(-A\sqrt{\Phi} \cdot d_T\right) \tag{6.1}$$

In this, the term $A = \sqrt{2m\,(4\pi/\lambda)}$ ($eV^{-1/2}\,nm^{-1}$) is a constant, where m is the mass of a free electron and $h = 6.626 \times 10^{-34}$ J s (Planck's constant). The term $\Phi = \frac{1}{2}(\Phi_{probe} + \Phi_{tip})$ is the arithmetic mean of the electronic work function for the sample surface and probe tip [27].

With typical values for $A \approx 0.1$ ($eV^{-0.5}\,nm^{-1}$) and $\varphi \approx 4$ eV, one can use Eq. (6.1) to show that a change in tunnelling length, that is, the distance between probe tip and sample surface of as little as 0.1 nm, results in a 1000-fold change in tunnel current. Put another way, if the tunneling length is increased by only 0.1 nm, the result is a 90% reduction in tunnel current. This implies that only the most prominent metal atom at the probe tip (Fig. 6.1) makes any significant contribution to the total tunnel current, with the current from the remaining metal atoms contributing progressively less and less, as their distance from the sample increases. It is this sensitive relationship between tunnel current and distance that underlies the incredibly high vertical resolution of the SPM, with values of 10^{-2}–10^{-3} nm.

By application of an electrical potential, the tunnel voltage, U_T between sample surface and probe tip, it is possible, as shown in Fig. 6.3, to control the extent of electron exchange and thus the tunnel current.

The direction of the tunnel current, I_T, depends on the polarity of the applied tunnel voltage U_T. The magnitude of the tunnel voltage also usually affects the dimensions of the potential energy barrier. In the example above, a negative polarity was used, so that the vacuum electron energy level, E^P_{vac} of the sample is higher than that of the probe tip, E^S_{vac} (Fig. 6.2).

Some practical details of scanning probe microscopy are noted below.

A fine metal needle,[1] with tip size ideally only a few atoms in diameter is brought to a distance of 0.5–1.0 nm of the sample surface, using piezo-ceramic positioning devices. However, the two should not be in actual contact since the resulting current would not then be solely due to the tunnelling effect and only when this condition is met, will the method function, with electronic interaction occurring between probe tip and individual atoms at the sample surface. Figure 6.4 shows an SEM image of a probe tip at a sample surface.

Applying a voltage of 2–2000 mV across the probe tip – sample interface gives rise to a tunnel current of 0.1–10 nA. Since the SPM (in contrast to an SEM) does not involve passage of free electrons, the SPM is largely independent of the medium

[1] The metal tips are usually made of various metals, preferably tungsten or platinum–iridium alloy.

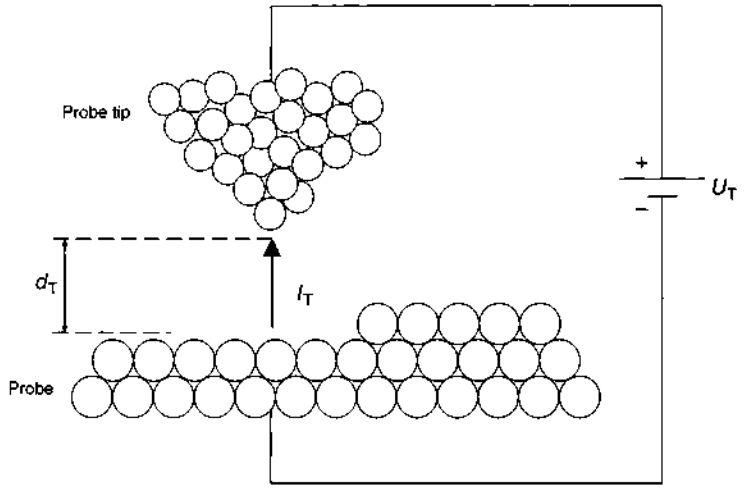

Figure 6.3 Effect on the tunnel current, an applied electrical voltage (tunnel voltage U_T) between sample surface and probe tip [22].

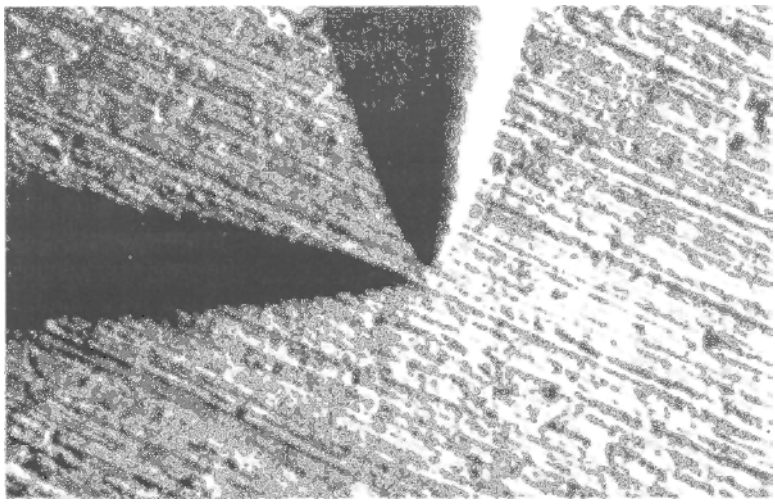

Figure 6.4 SEM image of an SPM probe tip close to, but not in contact with, a sample surface.

between probe tip and sample and can thus operate not only in vacuum, but equally in a gaseous or liquid environment.

The SPM is usually rastered and so, by repeated scans across a surface, a topographical image is built up. One of two operating modes will normally be used for this, namely *constant height mode* or *constant current mode*. The terms are self-explanatory, but Fig. 6.5(a) and (b) illustrates both approaches, with current being the variable in the former case, height in the second.

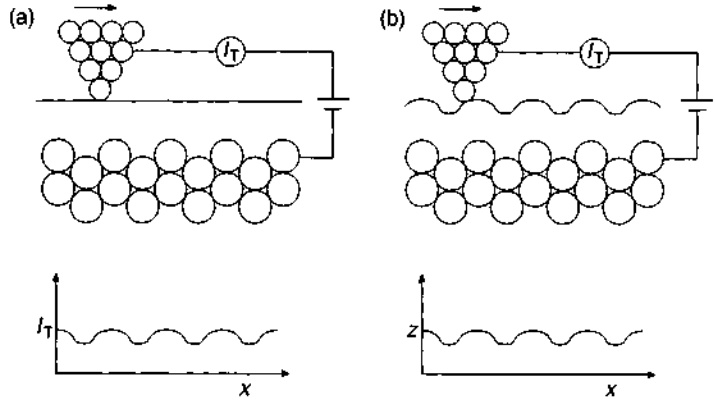

Figure 6.5 Schematic representation of the two methods of operating an SPM: (a) constant height mode and (b) constant current mode [6].

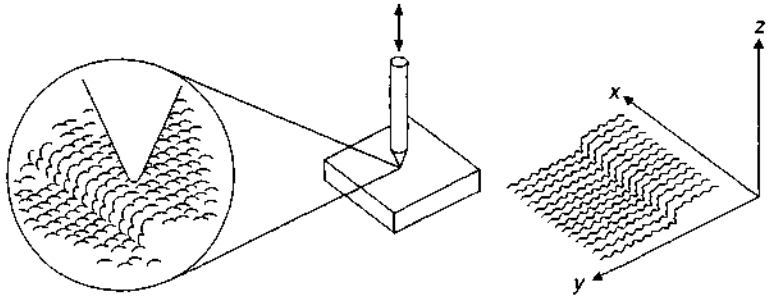

Figure 6.6 Vertical adjustment of SPM probe tip during surface scan of a sample with monatomic steps.

The constant height mode is best suited for use with a 'perfectly flat' surface. Since, however, these do not exist in practice, the *constant current mode* is more commonly used. As the probe tip traverses the surface of the sample, the current is sensed and then fed in a feedback circuit to a piezo-electric device which adjusts the probe tip height to maintain a constant current. The z-axis output is then plotted as shown in Fig. 6.6 [12].

From this, a topographical image of the surface can be constructed. However, bearing in mind that this is a contactless technique, it is not the physical profile of the sample that has been recorded, but the profile of its electronic properties. An SPM image should thus be viewed as a representation of the spatial distribution of electronic charge at the sample surface. The recorded tunnel current is related, in the first instance, to the Fermi levels of the surface atoms. In the case of metals, whose nucleus coincides with their charge centers, the tunnel current approximates well to the physical contour of the surface and the technique can be used to visualize such surfaces [22].

In terms of the vertical and lateral resolution of the SPM, the following points should be made. Since the height of the smallest surface irregularity is of the order

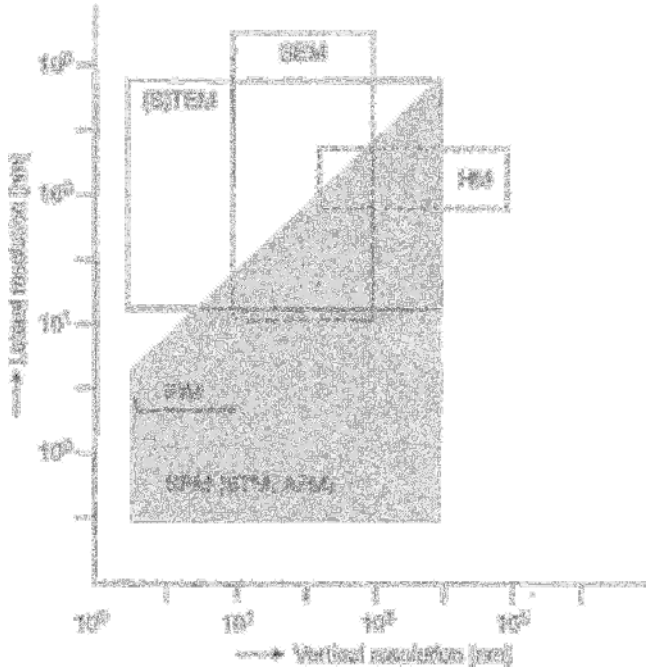

Figure 6.7 Resolution ranges of SPM (hatched area), compared with that of scanning (SEM), transmission (TEM), and scanning transmission (STEM) electron microscopes, high-resolution microscope (HM) and field ion microscope (FIM) [1].

of a single atom size, or perhaps less, the remarkable resolution of the SPM, due to the sensitivity of the current versus tip distance function, is of order <0.01 nm. This is a resolution, as Fig. 6.7 shows, unmatched by any other microscopic technique.

The lateral resolution is mainly determined by the shape and size of the probe tip. To a first approximation, it is $3\sqrt{R}$ where R is the radius of curvature of the probe tip [1, 2, 38]. On this basis, a lateral resolution of <10 nm would be obtained using a tip of radius of curvature 10 nm.

How important it is to maximise lateral resolution, that is, to use the finest possible tip, is illustrated by the following. If a surface is rastered with a tip of curvature radius 0.2 nm, and held 0.4 nm from the surface, then a scanned strip of 0.5 nm width will contribute some 80% of the tunnel current. To achieve a lateral resolution of 0.2 nm, probe tips are thus required of diameter no greater than a single atom.

Such tips can be prepared using special methods such as electrochemical etching [5] and the finest tips are most important when the sample surface topography exhibits features on an atomic scale. Most commonly, however, probe tips are not of single atom dimensions but are 'micro-tips' as shown in Fig. 6.8.

As a micro-tip (which can be considered as having a number of individual atomic tips) approaches a monatomic step feature at a surface, so that individual atomic tip that finds itself closest to the step edge, becomes the main current carrier, as shown schematically in Fig. 6.9.

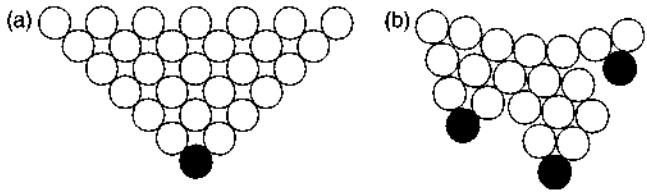

Figure 6.8 STM probe tips: (a) idealised single-atom tip; (b) 'micro-tip' with several 'tips'.

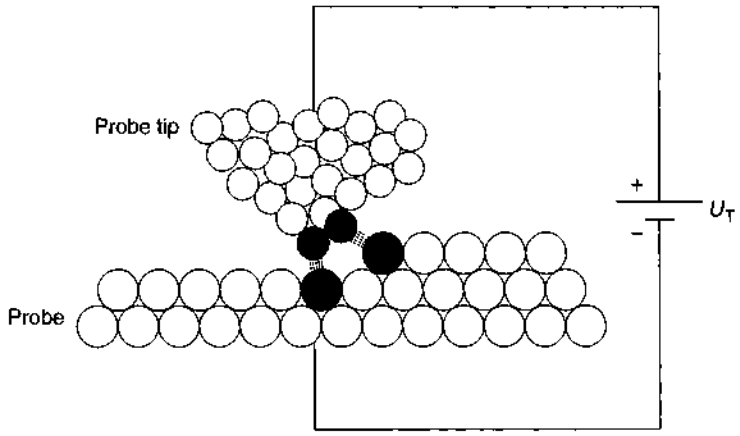

Figure 6.9 Tunnelling currents passing from more than one location at a micro-tip to the sample surface, as the tip is brought up to a monatomic step feature, showing how several 'tips' can operate simultaneously.

It should be noted (Fig. 6.9) that if, during a scan, the main tunneling current actually transfers from one tip atom to another, this will degrade the resulting reconstruction of the surface topography.

Some typical SPM parameters are listed below:

- Tunnelling voltage, U_T 10–1000 mV
- Tunnelling current, I_T 0.1–10 nA
- Tunnelling distance 0.5–1 nm
- Observation area 10–1000 nm^2

6.2.1.2 In situ *scanning tunnelling microscopy*

As was noted earlier, the STM can be used in a gaseous or liquid environment, and does not demand a vacuum. Thanks to this, it can be used for *in situ* observations of electrode reactions, such as electrodeposition. In this form, it is known as ECSTM (electrochemical scanning tunnel microscope) and has become one of the most powerful tools available to scientists studying electrochemical and electroless deposition mechanisms.

It is normally used (Fig. 6.10) in conjunction with the classical three-electrode cell, that is, working, counter and reference electrodes and these must be positioned close to, but not interfering with, the STM probe [7].

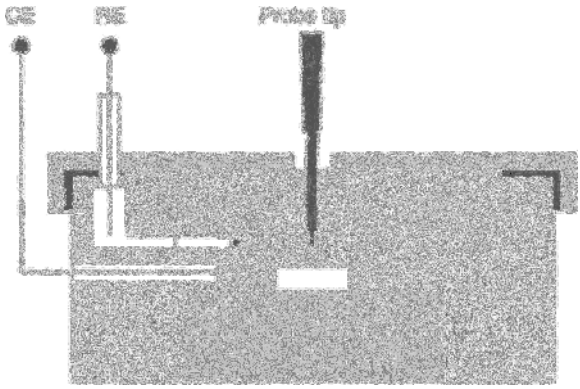

Figure 6.10 Schematic of an in-situ *electrochemical STM cell. WE = working electrode, CE = counter-electrode, RE = reference electrode.*

Care must be taken that no adventitious electrode reactions occur at the probe tip, since these would interfere with the tunneling current. Any faradaic reaction taking place at the scanning probe tip will almost certainly invalidate the data, for example by interfering with the feedback process earlier mentioned.

Various means are used to avoid such problems. The electrochemical and STM electrical circuitry should be rigorously isolated from one another, and the metal STM probe should be electrically masked by application of a suitable stop-off wax such as Apiezon, or similar medium (whatever is used must be chemically inert, not leaching organic species into solution), leaving only the very tip exposed [7]. By this means, the surface area of the probe can be reduced from (typically) 10^{-4}–$10^{-8}\,cm^2$ and this will reduce any faradaic current by the same proportion. If correctly carried out, this will reduce the faradaic current to $\leq 100\,pA$, at which level it can be neglected by comparison with tunnel currents in the range 1–250 nA [23]. In case of doubt, STM scans obtained at open circuit can be compared with those where faradaic current is passed, yet even this is not an infallible test, since coupled galvanic reactions can occur at open circuit.

The formation of two- and/or three-dimensional structures on the surface of a substrate to be electroplated, which constitute the initial stages of the deposition process are of great significance for the subsequent growth process and the properties of the deposit and studies of the conditions under which these structures form, accordingly important. By replicating the deposition, while observing it, in an *in situ* STM cell, detailed information as to the geometry and positioning of such structures can be obtained, with insights into the growth process [33,40]. Care must be taken, though, since (as indicated above), interferences of various kinds can distort or falsify the data.

Thus, the co-evolution of gas bubbles or formation of a gas film, or the formation of any kind of passive layer such as an oxide, can all introduce complications and possibly errors. Problems are also encountered with very rough surfaces when the tunnelling current from the probe tip may not evoke a response from the floor of deep 'valleys'. Impurities at the sample surface can result in unstable tunnel current

if they are transferred to the probe tip. In experiments on adsorbed surface species, surface impurities can falsify the results when they are indistinguishable from the adsorbed species.

6.2.1.2.1 Volmer–Weber mechanism

When a metal, Me, is in contact with an aqueous solution containing its ions, Me^{z+}, an equilibrium potential is set up, $E_{Me/Me^{z+}}$, which can be represented by the Nernst equation:

$$E_{Me/Me^{z+}} = E^0_{Me/Me^{z+}} + \frac{RT}{z \cdot F} \ln a_{Me^{z+}} \tag{6.2}$$

Here, $E^0_{Me/Me^{z+}}$ signifies the standard reversible potential, R is the universal gas constant, T the absolute temperature, z the valency of the metal ion, F the Faraday constant and $a_{Me^{z+}}$ the activity of the metal ions in solution.

If a potential E is applied to the system, more negative than the equilibrium potential $E_{Me/Me^{z+}}$, then metal ions will deposit from solution to form a layer at the substrate surface. This is known as overpotential deposition (OPD). Under these conditions, the deposition begins with formation of discrete nuclei or clusters as shown in Fig. 6.11, which then continue to grow in three dimensions.

A feature of OPD is that the bonding forces are stronger between atoms of depositing metal than between these atoms and the substrate surface. This growth mechanism, involving formation of three-dimensional nuclei followed by three-dimensional crystal growth, is known as the Volmer–Weber mechanism.

OPD corresponds to normal metal electrodeposition, that is, the conditions under which technical electroplating is normally carried out. The STM images shown in Fig. 6.12 show formation of three-dimensional copper islands on a Cu(111) substrate as part of a Volmer–Weber deposition process. The electrolyte is indicated in the figure legend, with deposition at −250 mV (all potentials in this section, unless otherwise noted, refer to the Cu/Cu^{2+} potential). Worth noting is the preferential deposition of the copper crystallites at atomic-scale surface defects, such as

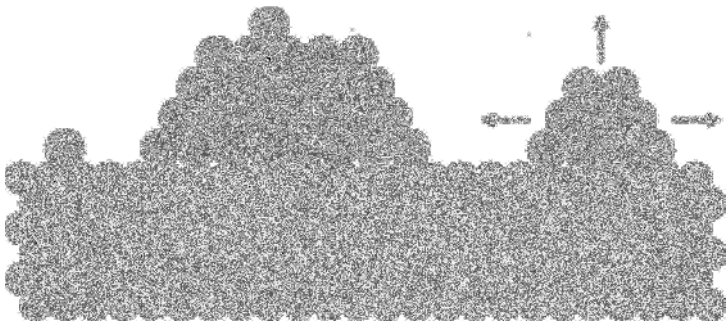

Figure 6.11 Formation of isolated three-dimensional metal nuclei at the surface of a similar substrate under OPD conditions [47].

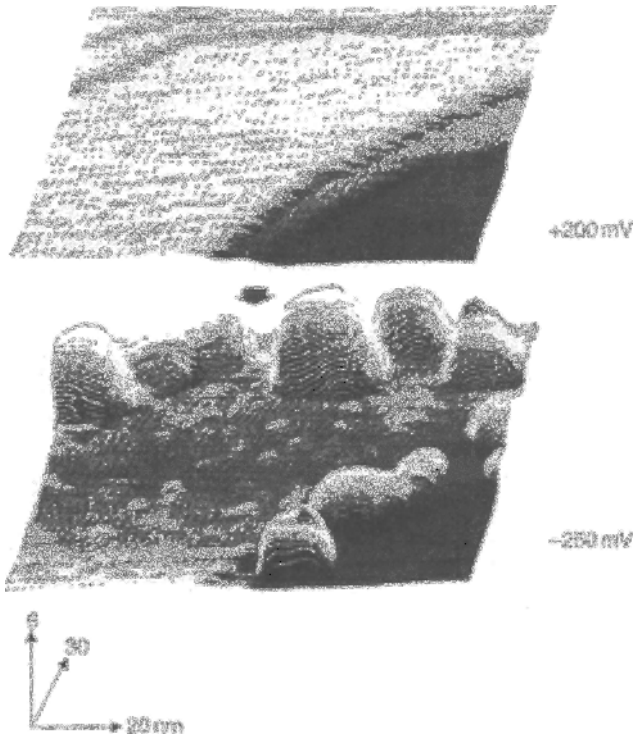

Figure 6.12 Volmer–Weber mechanism: in situ *STM images of three-dimensional copper islands on a Cu(111) substrate (electrolyte 0.05 M copper sulfate + 0.1 M sulfuric acid).*

atomic-scale step edges. Also notable is that a large part of the substrate surface remains uncovered, with no coherent copper deposit visible.

6.2.1.2.2 Frank–van der Merwe mechanism

Where, in contrast to the preceding case, metal ions are deposited on a surface of other than the same metal, the initial process involves deposition of one or more monolayers on the surface, with this taking place at potentials more positive than the equilibrium potential $E_{Me/Me^{z+}}$. Following this, a two-dimensional growth process sets in. For this case, schematically represented by the open circles in Fig. 6.13, the term underpotential deposition (UPD) is employed [24, 42, 43, 47]. The origin of this electrochemically important process lies in the fact that the bonding forces between the atoms of the depositing metal and those at the substrate surface, are stronger than those between the depositing metal atoms. An additionally important precondition is that the degree of 'mismatch' between the structures of substrate and deposited film, is minimal.

The formation of two-dimensional monolayers and subsequent two-dimensional growth is known as the Frank–van der Merwe mechanism.

The *in situ* STM image shown in Fig. 6.14 depicts the formation of a two-dimensional copper deposit on a gold(111) substrate. Electrolyte composition as shown in the figure legend.

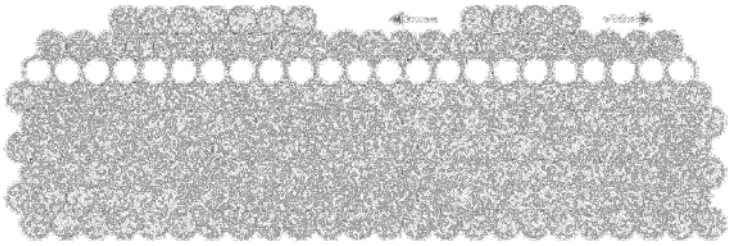

Figure 6.13 Formation of a monolayer (open circles) on the surface of a substrate metal other than that of the depositing metal under UPD conditions, with subsequent two-dimensional growth [47].

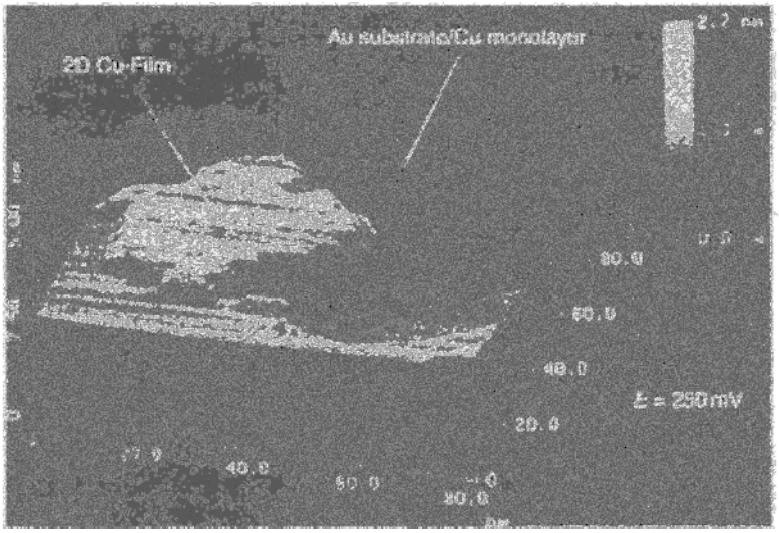

Figure 6.14 Frank–van der Merwe mechanism: in situ *STM image of a two-dimensional copper deposit, a Au(111) substrate (electrolyte: 1 mM copper sulfate + 0.1 M sulfuric acid + 3×10^{-4} M BT-B) [33, 36].*

In the initial stage of deposition, the potential was held for a few minutes at +10 mV in order to form a monolayer of copper under UPD conditions. Thereafter, deposition took place at −250 mV, where OPD took place. The *in situ* image of Fig. 6.14 shows a quasi two-dimensional deposit, forming from a step edge with a thickness of four to seven monolayers. The growth of this film in the *z*-axis direction was presumably restricted by the adsorption of BT-B.[2]

6.2.1.2.3 Stranski–Krastanov mechanism

In cases where a monolayer initially forms under UPD conditions, over which (in contrast to the Frank-van-der-Merwe mechanism), isolated three-dimensional structures then form, the process is known as the Stranski–Krastanov mechanism and is schematically represented in Fig. 6.15.

[2] BT-B, a benzothiazolium derivative, is added to proprietary copper plating solutions as a brightener.

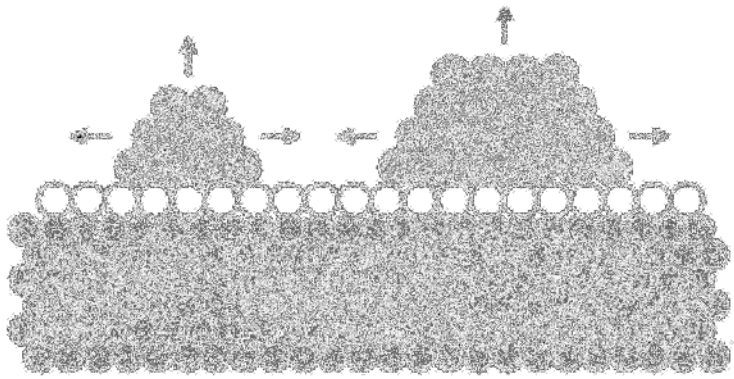

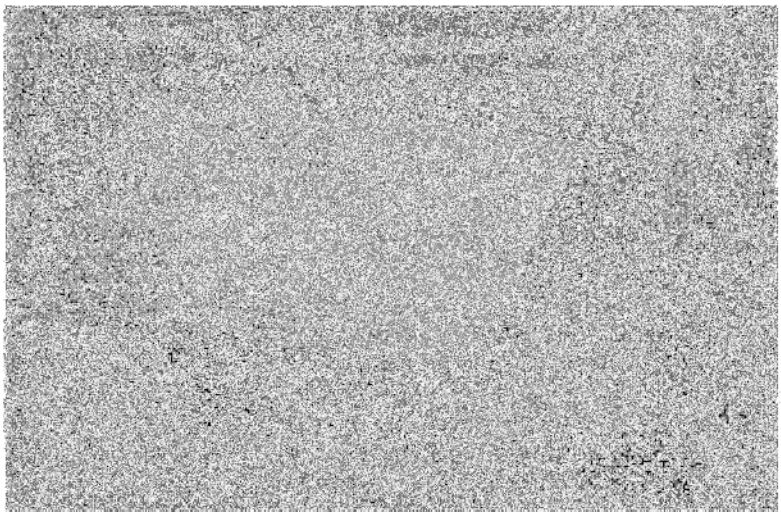

Figure 6.16 Stranski–Krastanov mechanism: in situ *STM image of three-dimensional copper islands on a gold(111) substrate. Electrolyte: 1 mM copper sulfate + 0.1 M sulfuric acid [33, 36].*

Two preconditions must be met for the Stranski–Krastanov mechanism to operate. First, the bond strengths between the metal atoms being deposited and the substrate atoms, must be stronger than those between the deposited atoms themselves. Second, the lattice 'mismatch' between substrate and deposited film (in contrast to the Frank–van der Merwe model) must be substantial [47].

The STM image reproduced in Fig. 6.16 shows the formation of isolated copper islands over a gold(111) substrate as formed by a Stranski–Krastanov mechanism.

The copper deposition took place from an electrolyte containing 1 mM copper sulfate, and 0.1 M sulfuric acid. At potentials anodic to the reversible potential $E_{Me/Me^{2+}}$, the initial deposit forms and epitaxial monolayer, under UPD conditions, completely covering the surface of the gold(111) substrate. This is due to the strong

interactions between the copper and gold substrate. The copper monolayer is deposited in an internally stressed state, since the Cu–Cu lattice spacing, at 0.256 nm is much closer than the Au–Au spacing, at 0.289 nm. If the potential is made more cathodic, OPD conditions obtain, and at −200 mV, three-dimensional copper crystals form, preferentially at defect sites on the surface. Formation of three-dimensional copper islands results in a relief of the internal stress.

6.2.1.2.4 Effect of electrolyte additives

The electrochemical STM is ideally suited to a study of the effect of electrolyte additives (see Chapter 3) on the nucleation and deposit growth processes. The *in situ* STM images shown in Fig. 6.17 chart the formation and growth of copper crystallites on a gold(111) substrate. Deposition was carried out in a 1 nM copper sulfate, 0.1 M sulfuric acid electrolyte.

The first image in the set shows the gold(111) surface prior to electrodeposition, at a potential of +150 mV in the UPD region. It offers a view of the atomic structure of the substrate surface. As soon as the potential is shifted cathodically, to a value of

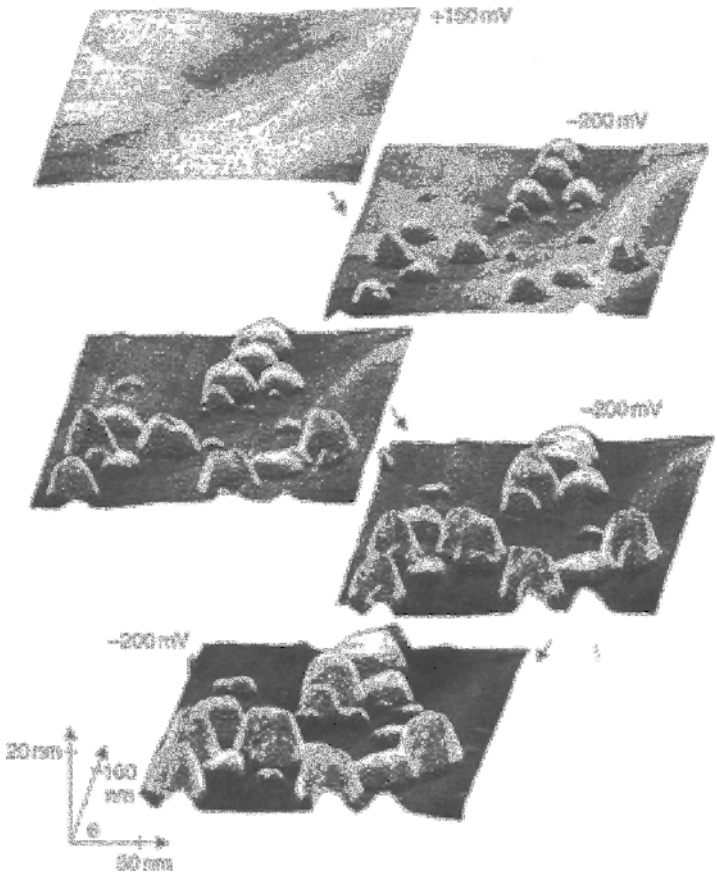

Figure 6.17 Formation and growth of copper crystallites on a gold(111) substrate (electrolyte: 1 nM copper sulfate + 0.1 M sulfuric acid [26].

−200 mV, the first copper crystallites are formed, now under OPD conditions, preferentially at surface atomic defect sites. Though the number of these crystallites remains unchanged, they begin to grow, as the subsequent photos in the series show. Nevertheless, a significant part of the substrate surface remains uncovered, since the growing crystallites have not joined together to form a coherent film.

If 10 mg/l of the organic additive crystal violet is added to the electrolyte, the degree of coverage improves, but only slightly.[3] The growth of the copper crystals in the z-axis remains unchanged, as the series of images in Fig. 6.18 shows. The first

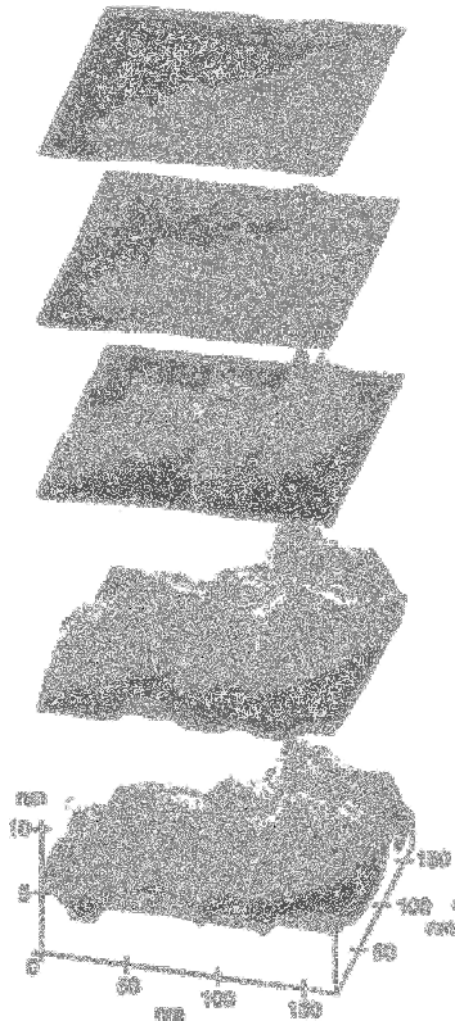

Figure 6.18 Effect of crystal violet additive on the growth of copper crystallites: 10 mg/l. crystal violet, otherwise as in previous figure [28, 29].

[3] Crystal violet, hexamethyl-*para*-rosaniline chloride possesses properties similar to those of organic dyestuffs, and is used in small concentrations in some proprietary copper electrolytes.

in-situ STM image in the set shows the gold(111) surface prior to copper electrodeposition, at a potential of +150 mV which is in the UPD region. The following images show the growth of copper crystallites at −150 mV which is in the OPD region. The images serve to show that, at the chosen concentration and deposition conditions, crystal violet is not effective in promoting formation of a continuous and coherent copper deposit on the substrate surface.

If, however, 10 mg/l BT-B are added to the solution, *in situ* STM images then show (Fig. 6.19) that the copper crystallites grow parallel to the surface, that is, in

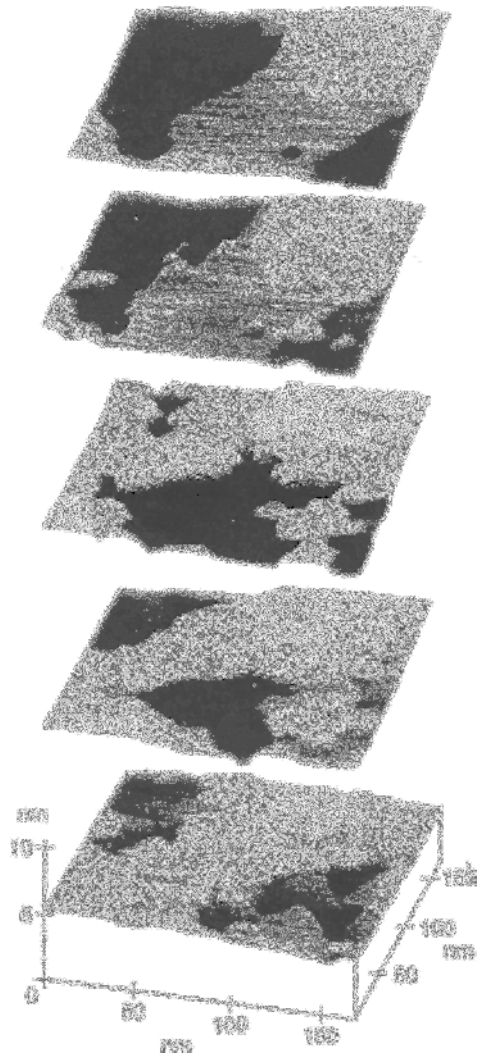

Figure 6.19 Effect of organic additive BT-B on the growth of copper crystallites at a gold(111) surface. Electrolyte: 1 mM copper sulfate + 0.1 M sulfuric acid + 10 mg/l BT-B [28, 29].

quasi-two-dimensional mode. The result is a smoother and denser copper deposit on the gold surface.

The first image in the series shows the gold surface prior to electrodeposition, at +150 mV, that is, in the UPD region. The remaining images show the growth of the copper deposit at −250 mV, that is, in the OPD region. The copper film appears to be growing laterally, in a quasi-two-dimensional mode, across the entire substrate surface.

The different effects of these two additives on the structure and growth of a copper deposit can also be seen in terms of the surface roughness profilograms in Fig. 6.20.

From the profilograms, it can be seen that addition of BT-B to the electrolyte, in contrast to use of crystal violet at comparable concentrations and deposition conditions, has a beneficial effect on formation of a smooth and continuous copper film that begins at the earliest stage of the deposition process.

6.2.1.2.5 Surface topography

In using the *in situ* STM apparatus to characterize deposited films, two different approaches can be used. In the first of these, the probe is withdrawn until the electrodeposition process is complete, and the substrate is completely covered. Only then is the probe tip brought close to the surface so that the tunneling current flows and the surface mapping process can begin. The resulting images are then recorded and interpreted. The advantage of this approach is that the probe tip will not in any way interfere with the deposition process. Thus, for example, the diffusion of metal ions from solution to the surface is not interfered with by the probe tip, which might otherwise partly shield the surface.

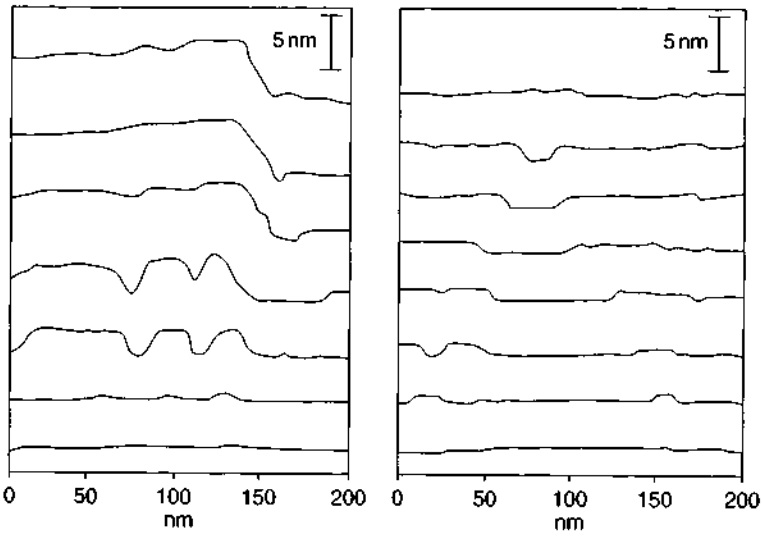

Figure 6.20 Profilograms showing the effect of organic additives on the growth of a copper deposit. Left, crystal violet; right, BT-B [29].

The drawback of this method is that it is extremely difficult, if indeed at all possible, to 're-visit' a specific part of the surface, especially when only very areas are in question or when substantial changes in surface topography have resulted after the electrodeposition.

In the second variant, the probe tip is initially close to the surface so that the tunnelling action is taking place, and data is continuously recorded so that real-time imaging can be carried out during the deposition process. The advantage of this method is that changes in surface topography can be continuously monitored throughout the various stages of the deposition process.

As an example, the deposition of palladium on a polished glassy carbon surface is shown in Fig. 6.21, as monitored by *in situ* STM [46].

The surface of the polished glass carbon is defect-rich, which favours anchoring of depositing Pd nuclei. The STM image in Fig. 6.21 shows the initial surface structure of the glassy carbon. Measurements indicate this to have a micro-roughness value of $R_a = 1.56$ nm.

Prior to Pd electrodeposition, the glassy carbon was activated by holding for 60 s in 0.1 N sulfuric acid at 1.24 V (SHE). The palladium was then deposited by pulse-plating (see Chapter 5, Section 5.2.2) with vigorous agitation using a magnetic stirrer.

The STM image (Fig. 6.22a) shows that complete surface coverage is achieved after 60 s. This takes the form, as the image shows, of agglomerates built up of smaller clusters each of some 15 nm diameter. The agglomerates themselves measure 150–220 nm across. From Fig. 6.22(b), it is seen that after 600 s, the

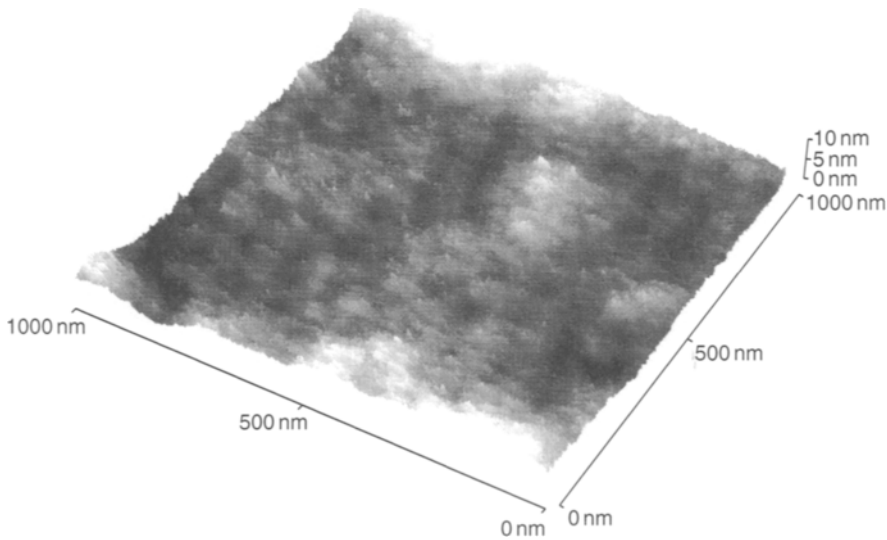

Figure 6.21 STM image of the surface of a glassy carbon substrate prior to palladium deposition.

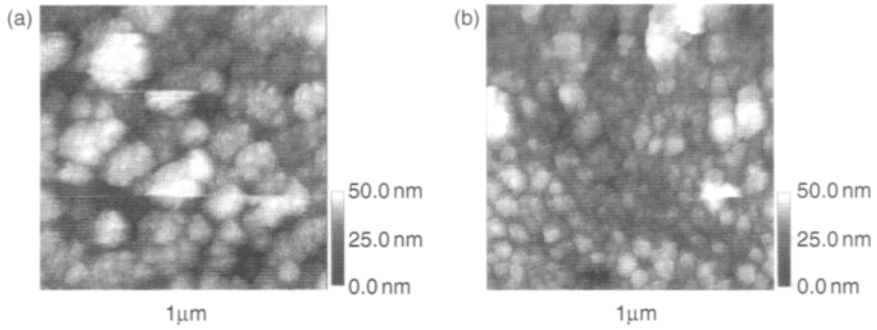

Figure 6.22 In situ *STM images of an electrodeposited palladium layer: (a) after 60 s (b) after 600 s.*

agglomerate size is 50–150 nm: the clusters have grown only slightly, being now 20–30 nm.

In the case of the 60-s image, flat structures can be identified between the agglomerates of the palladium layer, and these are most probably part of the substrate (Fig. 6.22a). Presumably, these are areas where no palladium has deposited. After 600 s, these areas are no longer visible, and the entire surface is covered with palladium (Fig. 6.22b)

The images seen in Fig. 6.23 reveal the effect of certain anions on the morphology of the deposited palladium. All were deposited at 0.287 V (versus SHE).

In all three cases, the palladium layer is formed of agglomerated clusters. The deposit is mainly quite thick and only the chloride-containing electrolyte exhibits individual pores of some 50–60 nm depth, probably reaching down to the substrate surface. In addition, the chloride ions are seen to lead to a rougher deposit surface.

6.2.1.2.6 Growth spirals

Not infrequently, hair-like growths, known as whiskers, are observed during an electrodeposition process (see Chapter 5, Section 5.5). They are not only visually undesirable, but can also lead to short-circuits in electrical circuits or on printed circuit boards.

The cause of such whiskers is the presence of so-called screw dislocations, which are a specific type of lattice defect in crystalline structures (see Chapter 2, Section 2.1.1.2). They give rise to a spiral dislocation in the lattice plane and thereby induce far-reaching stresses in the crystal. The axis of rotation of these defects, the dislocation line, rarely terminates within the crystal, and almost invariably emerges through the outermost plane, there protruding. In this way, a monatomic step dislocation is formed at the emergence point. Under some electrochemical conditions, these surface steps can be observed with the STM. This is because at the emergence point of the screw dislocation and in its immediate vicinity, zones of increased energy are formed and as such, are more easily subject to chemical attack. An example of this can be seen in Fig. 6.24.

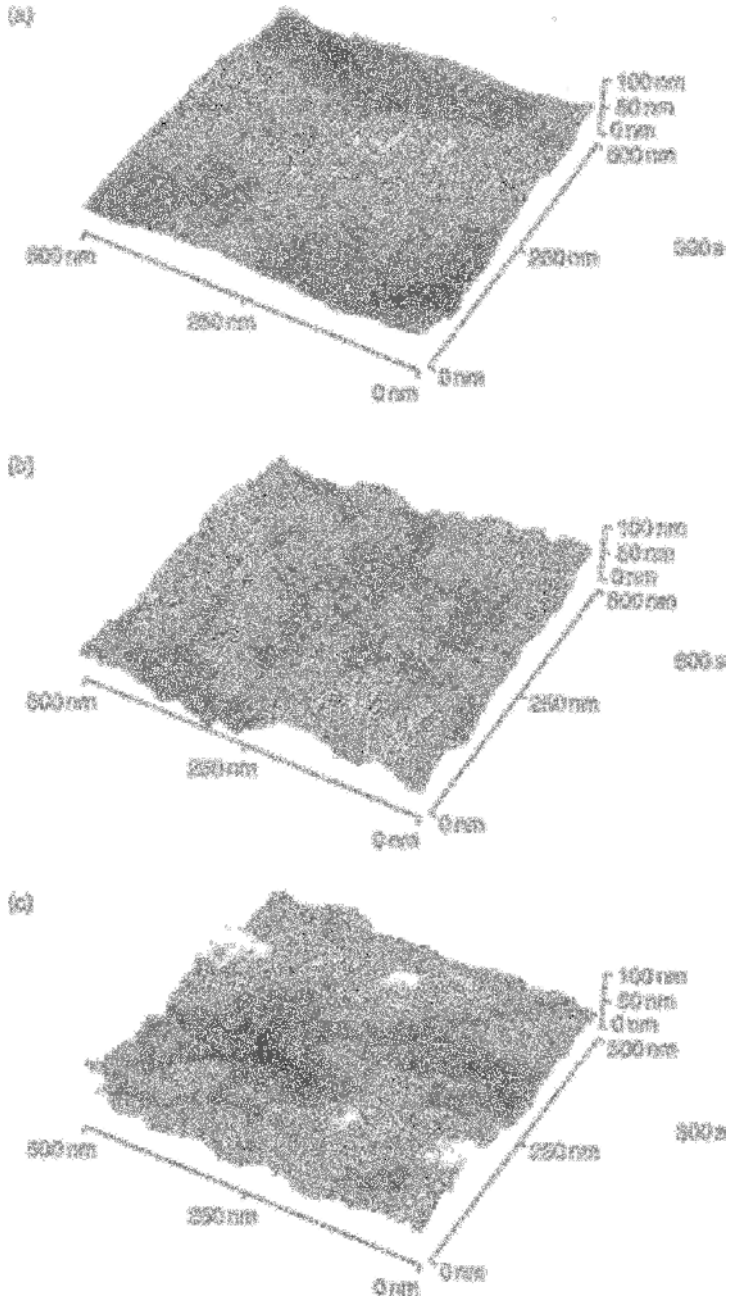

Figure 6.23 Effect of some anions on the surface morphology of electrodeposited palladium: (a) sulfate (R_a = 16 nm); (b) nitrate (R_a = 13 nm); (c) chloride (R_a = 23 nm).

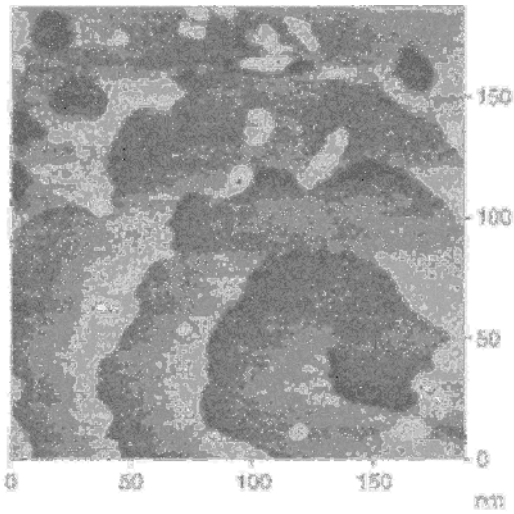

Figure 6.24 In situ *STM images of a screw-dislocation on a gold(111) plane (electrolyte: 5×10^{-3} M $Ag(CN)_2^- + 5 \times 10^{-1}$ M $HClO_4$, E = 300 mV, T = 298 K, I_T = 10 nA, probe tip Pt–Ir) [47].*

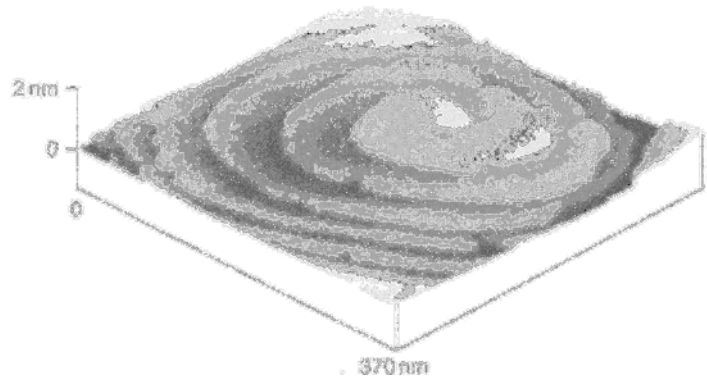

Figure 6.25 In situ *STM image of a spiral growth during copper electrodeposition onto a silver(111) substrate (electrolyte: 1 nM copper sulfate, 5×10^{-2} M sulfuric acid. T = 298 K, E = 80 mV) [47].*

Screw dislocations can also affect the deposition of metallic layers. In line with the Frank growth mechanism, a continuous crystal growth can take place at the emergence point of a screw dislocation, with not initial nucleation (see Chapter 5, Section 5.4.2.2). The result is a continuing deposition of depositing metal atoms at the emergence point which effectively extends the screw dislocation outwards into the electrolyte, so giving rise to the whisker morphology. The rotational axis of the screw dislocation does not move and becomes the axis of the newly formed spiral growth.

The *in situ* STM image in Fig. 6.25 shows such a growth spiral, here formed in electrodeposition of copper (details in legend) formed on a silver(111) substrate at ambient temperature.

Where the growth rate is anisotropic, that is, dependant on the crystallographic orientation, it is probable that growth spirals will form. Perfect polygonal growth spirals with rectilinear edges and sharp corners have, to date, only been observed during deposition at the lowest temperatures. In the case of deposition at room temperature, growth spirals will normally have rounded edges of nanometre dimensions.

Only rarely is it that a single screw dislocation emerges from the outer plane of a single crystal, then acting as a crystallization site for a growth spiral. In most cases there are two or more such defects. In these cases, growth spirals are only independent of one another if sufficient spacing occurs between them. When they are in close proximity, each influences the growth of the other, especially when, in their initial stages, their crystallographic axes are in opposing directions.

6.2.2 Scanning Force Microscopy (SFM)

6.2.2.1 Basics and process details

Scanning tunnelling microscopy, discussed above, employs an electrically conductive probe. For resolution of surface features at the atomic level and to obtain a three-dimensional representation of surface topography when the latter is electrically non-conducting, or poorly conductive, such as a plastic or passivated metal, STM is not a useful technique. Instead, a technique known as scanning force microscopy (SFM) or perhaps better-known as atomic force microscopy (AFM) is better used. Instead of employing the tunnel current effect, AFM uses a sharply tipped probe in direct contact with the surface. As this stylus is tracked across the surface, its vertical movement is recorded, having first been greatly magnified. The principle of the method is shown in Fig. 6.26. Examining this, many will recognise that AFM is in

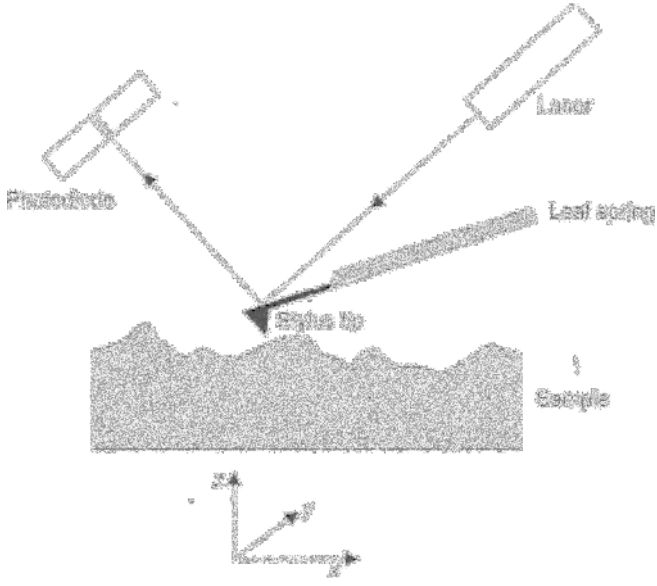

Figure 6.26 Operating principle of the atomic force microscope (AFM).

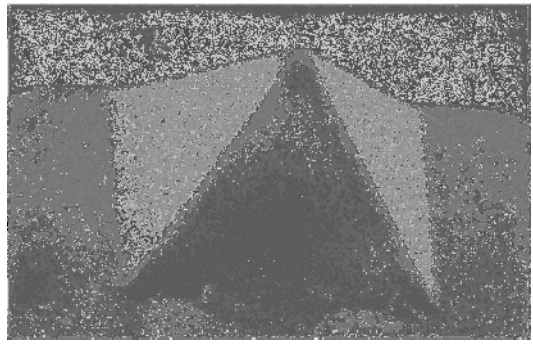

Figure 6.27 SEM image of a typical AFM stylus tip.

effect a refinement of the long-established profilometer which also uses a mechanical stylus in direct contact with the surface, but with less sensitive means of amplifying the vertical motion.

A finely pointed silicon single crystal[4] serves as the stylus tip, mounted at one end of a soft leaf-spring or cantilever, having a spring constant (k) between 0.1 and 1.0 N/m is tracked across the sample surface. The angle of attack of the tip is typically 54.7° and the radius of curvature less than 10 nm. The SEM image in Fig. 6.27 shows the geometry of a typical stylus tip.

As the stylus moves relative to the sample (or vice versa), the vertical movement of the stylus is optically amplified using the reflection from a laser beam reflected from the upper side of the leaf spring and impinging on a position-sensitive photodiode. The output from both halves of the diode is produced both in differential and summed modes. In order to compensate for fluctuations in laser output intensity, the difference of the individual outputs is split through the summed output. The differential output is a measure of the deflection of the leaf spring and thus indicative of the height of a feature on the sample surface. In practice, the output is digitized and the resulting x, y, z dataset is processed to provide a three-dimensional image of the surface topography.

The stylus tip, as it traverses the surface, experiences both attractive and repulsive forced. The former are due to effects such as magnetic and electrostatic attraction, as well as capillary[5] and van der Waals[6] forces, while the latter can be attributed to repulsion due to electron orbital forces. Such attractive or repulsive forces become

[4] The tip was formed, in this case, by preferential etching of the (100) plane of a silicon single crystal.

[5] Capillary forces are caused by thin films of contaminating species on the sample surface when exposed to the atmosphere. These can included condensed water molecules and other species present in air. Depending on the relative humidity, such films can range from 2.5 to 50 nm in thickness.

[6] Uncharged atoms can form electrical dipoles of variable moment, since their electrons are not rigidly held in a given location, but can be displaced. If two such atoms approach too closely to one another, an interaction takes place between their electrical charges, and this is known as the van der Waals force. Such forces are significantly weaker than normal atomic bonding forces.

measurable when the stylus tip approaches within a few nanometres of the sample surface. As the stylus tip approaches, the long-range attractive forces are the first to manifest themselves, thereby pulling the tip downwards. However, the closer the tip approaches the sample surface, the more significant become the short-range forces, which mainly act in a repulsive mode. These forces, acting on the stylus tip, whose magnitude F is estimated to be 10^{-13}–10^{-4} N, are transmitted to the leaf spring. The resulting vertical deflection of the lead spring, Δz, can be estimated using Hooke's law ($F = -k \times \Delta z$).

In analogy with the STM, which, as described, can operate in two modes (constant current mode or constant height mode), the AFM can be used in constant force mode and constant height mode.

In the first operating mode, the force acting on the leaf spring is maintained constant, using the differential output from the diode, through a feedback circuit to a piezo-electric position transducer which then alters the z-axis distance between sample surface and stylus tip. In the second operating mode, the z-axis piezo-electric transducer is not activated. Instead, the differential output from the photo-diode is fed to a computer for processing. Rather than giving an actual topography, the constant height mode produces a force map of the surface. This form of representation is specially well suited for the characterization of surfaces with atom-scaled features.

In this mode of operation, also known as *soft contact mode*, both attractive and repulsive forces are shown. The advantage of the method lies not only in its greater convenience, but also in that it allows a greater resolution to be obtained in that it also records the stronger repulsive forces. In addition, this mode of operation lends itself to use in a liquid environment.

If, on the other hand, the stylus tip is not brought too close to the sample surface, then only the attractive forces are recorded. This is known as the *non-contact mode*. In this case, the stylus is moved in the z-axis with pre-determined amplitude and frequency. The attractive forces create a difference between the applied and resulting frequencies which is registered and can be used to build a map of the surface topography. The advantage of this approach is that only small forces are applied to the sample surface. The method then is quasi-non-contact and can be used to study soft surfaces such as layers of organic molecules and crystals. In this mode too, the likelihood of any form of interaction between stylus and sample is minimal. Against this, it has to be said that the technique is more difficult and time-consuming to implement than the soft contact mode.

In interpreting AFM images, the following points should be noted: first, the relatively large tip angle can limit the resolution when studying steeply featured structures. Then, it should not be forgotten that in addition to z-axis forces, a lateral (x-axis) force acts on the stylus which sets up a frictional force. Depending on the tip geometry, this can affect the resolution.

6.2.2.2 In situ *atomic force microscopy*

The AFM can be used equally well in air, in vacuum or in an aqueous environment. The latter is of special importance in a study of electrodeposition nucleation and growth processes. Figure 6.28 shows the main features of an electrochemical AFM cell in schematic form.

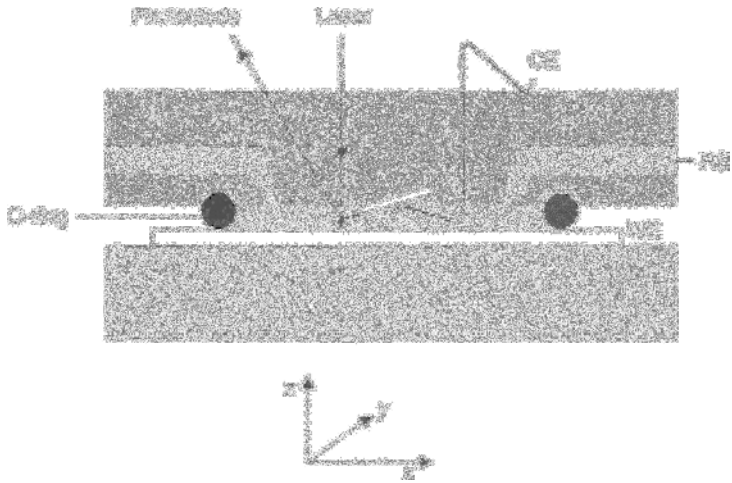

Figure 6.28 Schematic representation of an electrochemical AFM cell for in-situ *studies.*

As seen in the figure, an O-ring is used to seal the cell and this defines the volume of electrolyte used. The reference electrode RE is located in a separate reservoir. The counter-electrode (CE) is formed by the metal container to which the stylus is secured. The technique allows nucleation and growth processes to be followed, both in space and time and for the surface topography of deposited metals to be characterized. By the same token, the technique allows one to study the effect of electrolyte additives on deposit structure and properties under defined conditions. In such studies, full use is made of the special features of the technique (very high vertical resolution and high magnification).

In using the method, it must be recognised that the imaging process can, in certain circumstances, interfere with the reaction(s) taking place. Thus the stylus, by virtue of its proximity to the surface, can screen the electrode area beneath and immediately adjacent to it, impeding the flow of reactants inwards and/or products outwards and also electrically shielding the area below. In addition, there is a small interactive force between stylus tip and the electrode surface beneath it. This can, in some circumstances, be greater than the bonding forces between the nuclei forming on the surface or the forces between nuclei and substrate. Where this is so, the nuclei are displaced away from the tip and out of the image area.

In the following section, some actual examples of the use of the AFM are described, in which the technique was able to throw light on a particular problem or process.

6.2.2.2.1 Surface pretreatment

When metallising plastics, not least of the deposit is to be highly reflective, the plastic must first be coated with an electrically-conducting material. This 'activation' can be carried out by forming trace nuclei of noble metals such as palladium, or silver. At these catalytically active sites, subsequent electroless deposition of copper or nickel

can then be initiated, so forming a continuous and electrically conducting coating. Thereafter, the deposit can be further built up by means of electrodeposition. In order that the palladium or other noble metal nuclei are firmly anchored to the plastic surface, it must first be suitably pre-treated. This involves primarily a surface roughening, forming microscopic cavities and hollows, in which the metal nuclei can anchor themselves. This is brought about by etching. A widely used example of this is the chromic acid etching of ABS (acrylonitrile–butadiene–styrene). This both cleans the surface and renders it hydrophilic, that is, readily water-wettable. The etch typically contains 375 g/l chromium trioxide and 375 g/l concentrated sulfuric acid. The chromic acid, used at 60°C oxidatively attacks the double bonds in the rubber phase and dissolves out the rubber particles in some 8–12 min, leaving as a result, small cavities which they formerly occupied. The hard phase, styrene–acrylonitrile polymer, remains unattacked during this etching. The result is a 'roughened' surface. Figure 6.29(a) shows a sequence of AFM images obtained during such an etch, showing how the cavities and hollows develop over time. The first image shows the surface prior to etching. Figure 6.29(b) shows the development of such cavities with time.

The so-called 'press-stud' mechanism, invoked to explain the adhesion of such metal deposits on a polymer surface, is based on the growth of metal deposits within the cavity, so acting to lock the deposit onto the surface (see Chapter 7, Section 7.2.1) and the mechanism is specially invoked in the case of metallized ABS. The AFM image shown in Fig. 6.29(c) indicates the dimensions of the cavities formed in ABS once the rubber-phase butadiene particles have been etched out.

6.2.2.2.2 Surface activation

After the etching process has created the desired degree of surface roughness, the noble metal nuclei are deposited, in the finest possible state, at the surface and this step is known as 'activation'. There are two main variants, namely the colloidal and the ionogenic approaches. Both employ palladium as the nucleating metal.

In the colloidal process, the activating solution contains palladium particles of some 1 μm diameter, in colloidal suspension. In order to prevent their sedimentation, they are enveloped with a protective hydrated tin oxide colloid. In acid medium, these form positively charged spheres around the palladium particles. The palladium concentration in such solutions is of order 0.1 g/l. The activation is due to adsorption of these palladium particles, with their protective colloid, at the polymer surface.

In the ionogenic variant, a palladium complex is used, in which the ligands are nitrogen-containing compounds and this adsorbs on the polymer surface. The palladium concentration in these solutions ranges from 0.1 to 0.5 g/l. The amount of palladium adsorbed at the surface is somewhat less, in this approach, than with colloidal solutions.

In order to convey the Pd in solution to the polymer surface, a so-called accelerator is used. In the colloidal process, the role of the accelerator is to strip the protective colloid from the surface of the palladium particles, to leave the metal in an active form on the polymer surface. In the ionogenic process, where no particu-

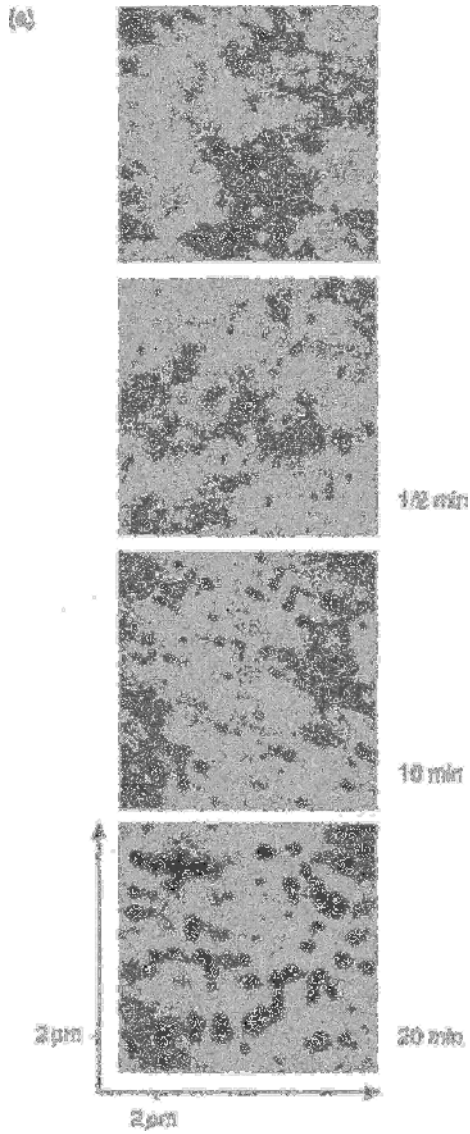

Figure 6.29 (a) AFM images showing the development and growth of cavities at the surface of ABS during a chromic–sulfuric acid etch process over time. (b) Increase in the number of cavities as a function of etch time. (c) ABS surface after 10 min chromic–sulfuric acid etch (AFM image).

lates are present, the accelerator is a reducing agent which converts adsorbed Pd-containing ions to the metal.

AFM is an ideal method for following the activation process, since it allows a visualization of both the distribution of the Pd nuclei and their size, and the manner in which these vary as various parameters are altered.

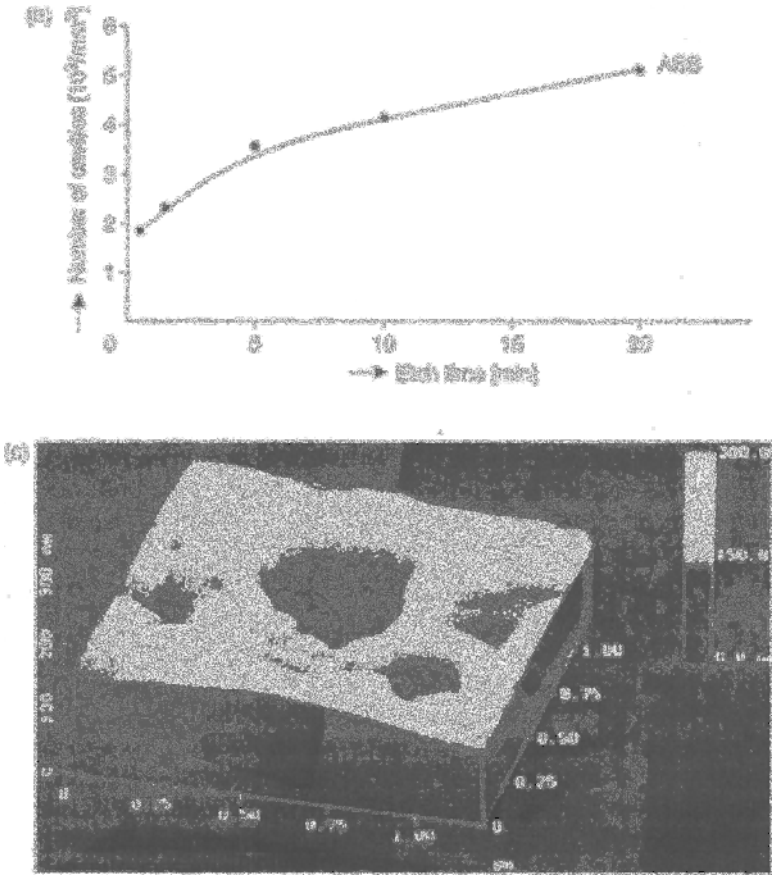

The *in situ* AFM images in Fig. 6.30 show the surface of untreated (top) and Pd-activated (below) polyimide film. Polyimide is ideal for such studies on account of its very smooth surface.

6.2.2.2.3 Through-hole contacting of printed circuit boards

The conventional means of through-hole contacting of drilled holes in multi-layer printed circuit boards consist in the activation and electroless copper plating of the hole walls, followed by electrodeposition of copper into these holes.

Because this process can be difficult, recent years have seen a search for alternative methods, hopefully both easier to carry out and also environmentally friendly. One solution has been the so-called 'direct metallising' method. This dispenses with the electroless copper, using instead some other means of making the hole walls electrically conducting. Electrically conducting polymers such as polypyrrole

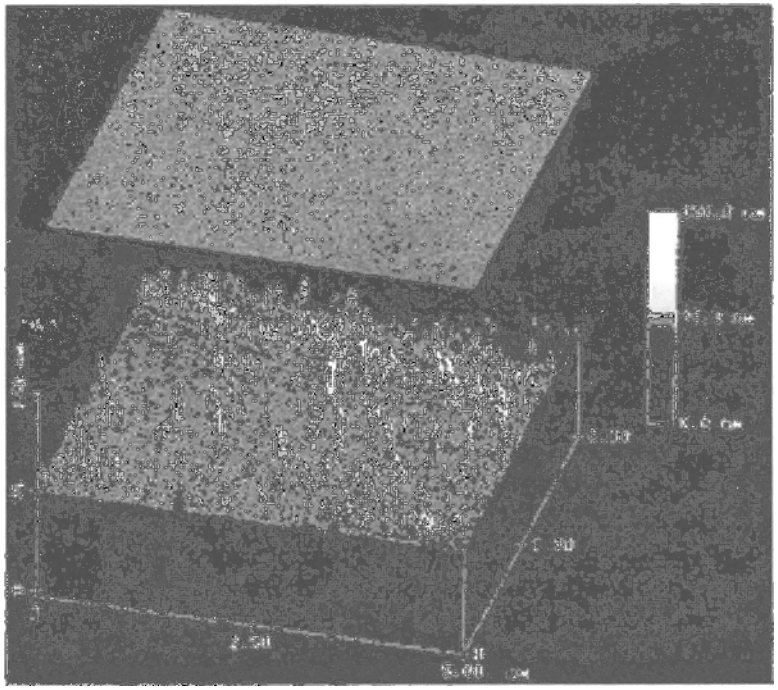

Figure 6.30 In situ *AFM images of untreated (top) and palladium-activated (below) polyimide film [28].*

have proved useful, and after application, allow copper electrodeposition as before. The nucleation and growth of electrodeposited copper on such surfaces is clearly of the greatest interest, and AFM has proved an ideal technique for visualizing the process.

Figure 6.31 shows such a sequence. The electrolyte was 1 mM copper sulfate + 0.1 M sulfuric acid [34]. The upper image shows the polypyrrole prior to electrodeposition at +50 mV (versus Cu/Cu^{2+}). Shifting the potential to −100 mV results in deposition of the first copper nuclei, which grow in three-dimensional mode (centre). If the potential is shifted to −150 mV (lower image), more numerous copper crystallites are seen to form.

6.2.2.2.4 Surface topography

The surface morphology of electroless or electrodeposited metals determines not only their physical, chemical and mechanical properties, such as reflectivity, corrosion- and wear-resistance, but also their coefficient of friction and dry-running behaviour. The primary variable are electrolyte composition and deposition conditions.

Using the AFM in *in situ* mode and with continuous observations, the effect of such variable is readily established. Electroless nickel–phosphorus deposits afford a good example of this.

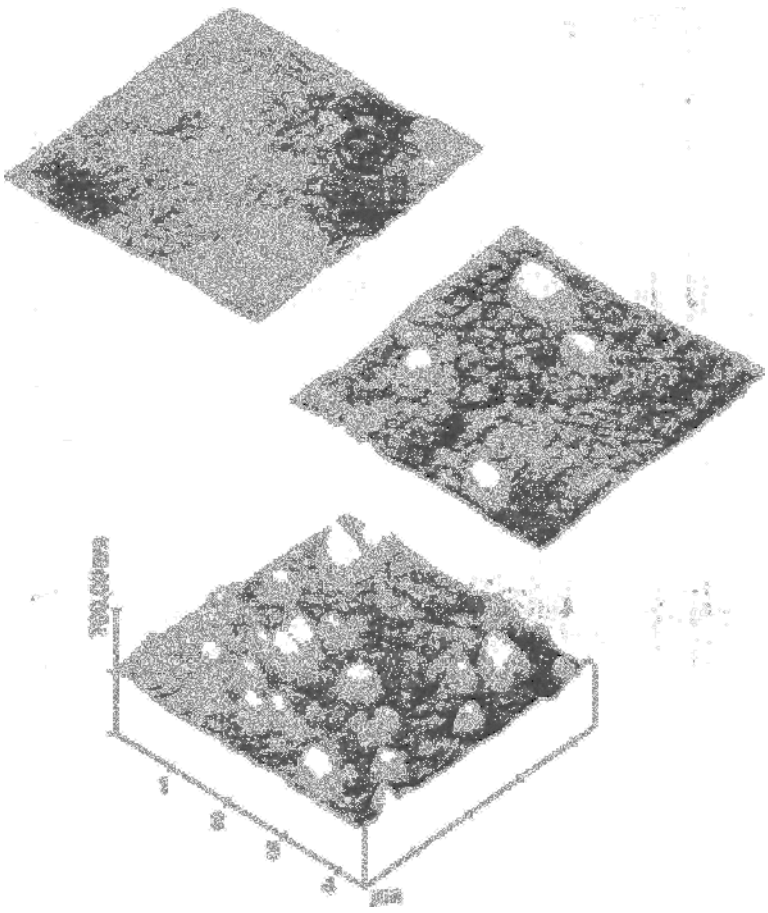

Figure 6.31 In situ *AFM images of formation and growth of copper crystallites on an electrically conductive polypyrrole substrate. For details, see text [34].*

Electroless nickel (EN) (usually an Ni–P alloy) has excellent functional properties, which can be further improved by heat-treatment. The *in situ* AFM images in Fig. 6.32 show the development of an electroless EN deposit with 12 wt% P, formed over a polished CrNi steel substrate. The surface of the steel was first mechanically polished with diamond dust (1 μm grade) to a roughness of 20 nm peak-to-peak. The sample, was then electropolished to a 10 nm mirror finish. The electroless Ni–P alloy deposition was triggered with a cathodic pulse (3 V for 1 s.)

This procedure is necessary since the mechanical polishing served to deactivate the substrate surface. In addition, electropolishing results in formation of an oxide film on the substrate surface, a few nanometres in thickness.

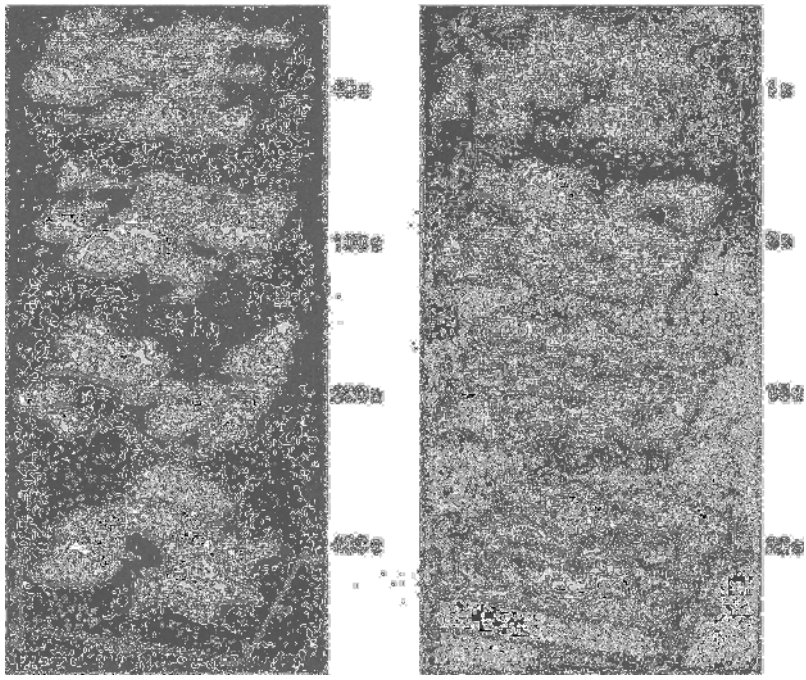

Figure 6.32 In situ *AFM images showing development of electroless Ni–P deposit on a CrNi steel substrate [20].*

After the application of the cathodic pulse, the substrate is covered with nodular deposit of Ni–P. The individual nodules are of order 200 nm in size with average height 75 nm. After 3 s, the uniformly nodular surface has a height of 25 nm. In places, larger nodules protrude of ca. 250 nm diameter and 100 nm height.

The frequency of these larger nodules is around $1/\mu m^2$. After 13 s, this value increases to $3/\mu m^2$. At the same time, the medium sized nodules increase in diameter to around 500 nm, with a mean height of 250 nm. The individual larger nodules begin to form as groups. After 20 s, one sees significant aggregations of nodules with around 800 nm diameter and 300 nm high. At 40 s, the surface is overwhelmingly covered with pronounced nodules of 300 nm diameter, 30 nm high. At some locations, larger nodules protrude above these, of diameter 500 nm and around 250 nm high. This surface morphology resembles that observed at 3 s, but with appreciably less roughness, now around 30 nm. After even longer deposition times, the surface becomes still smoother, with peak-to-peak value of 20 nm or so. Only a few of the larger nodules are now seen, those of 400 nm diameter and 40 nm height [20].

The *in situ* AFM images in Fig. 6.33 record the surface morphology of 1, 2, 3 and 4 μm thick EN deposits with 12 wt% phosphorus, deposited on previously cathodically degreased CrNi steel.

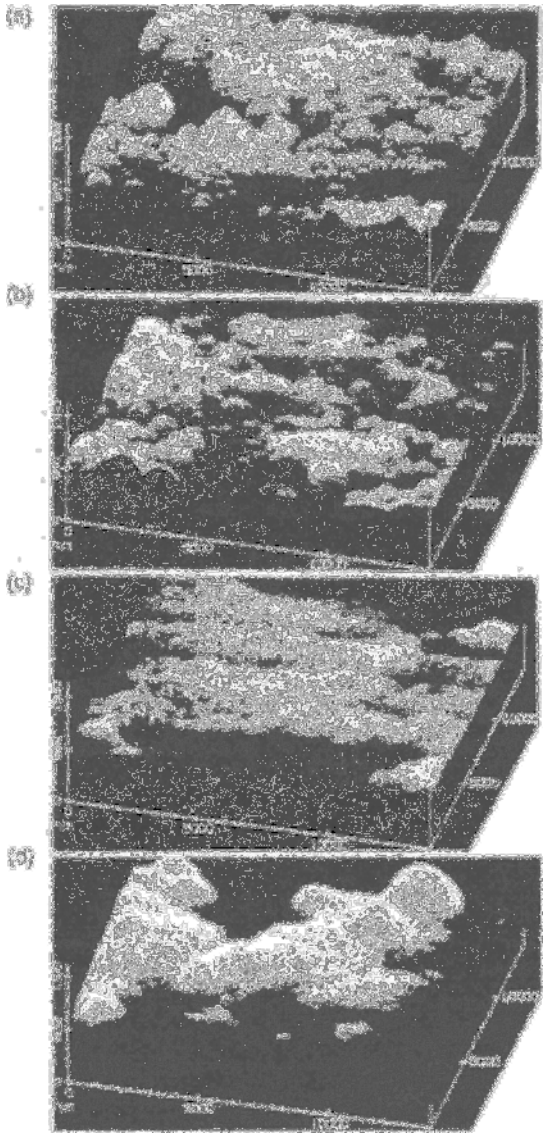

Figure 6.33 In situ *AFM images showing growth of electroless nickel-phosphorus on a cathodically degreased CrNi steel substrate: (a) 1 μm; (b) 2 μm; (c) 3 μm; (d) 4 μm [20].*

As the images show, the deposit covers the surface with a nodular deposit. The diameter and height of the individual nodules decrease as deposition proceeds, resulting in an increased number of the smaller nodules. At a deposit thickness of 4 μm, no individual nodules can be discerned. However, the deposit retains a regular, gently undulating appearance, punctuated with occasional larger bumps.

References

[1] Binnig, G. and Rohrer, H., 'Scanning tunnelling microscopy', *Helv. Phys. Acta*, 55 (1982) 726–735.

[2] Binnig, G., Rohrer, H., Gerber, Ch., and Weibel, E., Surface studies by scanning tunneling microscopy, *Phys. Rev. Lett.*, 49 (1982) 57–60.

[3] Binnig, G. and Rohrer, H., Scanning tunneling microscopy, *Surf. Sci.* 126 (1983) 236–244.

[4] Binnig, G. und Rohrer, H., Das Raster-Tunnelmikroskop, *Spektrum der Wissenschaft* 10 (1985) 62–68.

[5] Fink, H.-W., Mono-atomic tips for scanning tunneling, microscopy, *IBM J. Res. Dev.*, 30, (1986) 460–465.

[6] Hansma, P.K. and Tersoff, J., Scanning tunneling microscopy, *J. Appl. Phys.*, 61, (1987) 2, R1–R23.

[7] Wiechers, J., Entwicklung eines Rastertunnelmikroskops für elektrochemische Anwendung und in-situ Untersuchungen zur Struktur einer Gold Elektroden-Oberfläche, Diplomarbeit, Ludwig-Maximilians-Universität, 1988.

[8] Krebber, U., Tunnelmikroskopische Untersuchungen zur Belegung von Graphitoberflächen mit Palladium. Diplomarbeit, Westphälisch Wilhelms-Universität, 1988.

[9] Christoph, R. and Siegenthaler, H., In-situ scanning tunneling microscopy at potential controlled Ag(100) substrates, *Electrochimi. Acta* (Fisher Symposium) 1988.

[10] Fuchs, H., Strukturen-Farben-Kräfte: Wanderjahre der Raster-Tunnelmikroskopie, *Phys. Bl.* 45 4 (1989) 4, 105–115.

[11] Persch, G. and Strecker, H., Das Rastertunnelmikroskop, *Labor* 2000 (1989) 72–79.

[12] Rabe, J.P., Surface chemistry with the scanning tunneling microscope, *Adv. Mater.*, 1 (1989) 13–17.

[13] Uosaki, K. and Kita, H., Construction of an STM system and its application to electrodeposition of copper on polycrystalline platinum, *J. Electroanal. Chem.* 259 (1989) 301–308.

[14] Besenhard, J.O., Kanani, N., and Meyer, H., A STM study of Pd-catalyst for electroless Cu deposition on nonconductors by means of a modified graphite substrate, *J. Electrochem. Soc.*, 136, (1989) 12, 3608–3610.

[15] Behm, R.J., Garcia, N., and Rohrer, H., Scanning tunneling microscopy and related methods, *NATO ASI Series*, Kluwer Academic, Dordrecht, 1990.

[16] Hansma, P.K., *et al.*, Scanning probe microscopy of liquid–solid interfaces, *NATO ASI Series*, Kluwer Academic. Dordrecht, 1990.

[17] Siegenthaler, H. and Christoph, R., In-situ scanning tunneling microscopy in electrochemistry, *NATO ASI Series*, Kluwer Academic, Dordrecht, 1990.

[18] Heinzelmann, H., *et al.*, Force microscopy *NATO ASI Series*, Kluwer Academic, Dordrecht, 1990.

[19] Fricke, J., Folgeentwicklungen des Rastertunnelmikroskops, *Physik in unserer Zeit*, 5 (1990) 219–221.

[20] Pietsch, K.-H., Untersuchungen zum Wachstum und zur anodischen Auflösung von chemisch reduktiv abgeschiedenen Nickel-Phosphor-Schichten, Dissertation, TU Berlin, 1992.
[21] Rohrer, H., STM: 10 years after, *Ultramicroscopy* 42–44 (1992) 1–6.
[22] Neddermeyer, H., Rastertunnelmikroskopie an reinen und adsorbatbedeckten Oberflächen, *Chemie in unserer Zeit*, 1 (1992) 18–26.
[23] Kolb, D.M., Nichols, R.J., and Behm, R.J., The application of scanning tunneling microscopy to electrochemistry in: *Electrified Interfaces in Physics, Chemistry and Biology*, R. Guidelli, Kluwer Academic, Netherlands, 1992.
[24] Aindow, M. and Farr, J.P.G., The use of electrochemical scanning tunneling microscopy to study the initial stages of electrodeposition *in situ*; overpotential deposition of Pb and Pt on HOPG. *Trans. Inst. Metal Finish.* 70 (1992) 171–176.
[25] Haiss, W., Lackey, D., and Sass, J.K., A determination of copper overlayer structures on Au(111) in the presence of electrolyte additives, *Chem. Phys. Lett.* 200 (1992) 4, 343–349.
[26] Nichols, R.J., Batina, N. and Kolb, D.M., An in situ scanning tunneling microscopy study of bulk copper deposition and the influence of an organic additive, *J. Electroanal. Chem.* 330 (1992) 381–394.
[27] Koenders, L., Das Rastertunnelmikroskop eine Pinzette für Atome, *Physik in unserer Zeit*, 6 (1993) 260–266.
[28] Nichols, R.J., Schröer, D., Meyer, H., Application of SPM in the metal plating industry, *Scanning* 15 (1993) 266–273.
[29] Nichols, R.J., Bach, C.E., and Meyer, H., The effect of three organic additives on the structure and growth of electrodeposited copper: an in-situ scanning probe microscopy study. *Ber. Bunsenges. Phys. Chem.* 97 (1993) 1012–1019.
[30] Fuchs, H., SXM-Methoden, nützliche Werkzeuge für die Praxis, *Phys. Bl.* 50 1994) 9, 837–842.
[31] Welland, M., New tunnels to the surface, *Phys. World* 3 (1994) 32–36.
[32] Wittstock, G., Elektrochemische Rastermikroskopie zur Grenzflächecharakterisierung, *CLB Chemie in Labor und Biotechnik*, Heft 4 (1995) 166–167
[33] Nichols, J.R., and Baumgärtel, H., Classification of growth behaviour for copper on various substrates with in-situ scanning probe microscopy, *Surf. Sci.* 335 (1995) 110–119.
[34] Nichols, R.J., Schröer, D., and Meyer, H., An *in situ* scanning probe microscopy study of copper electrodeposition on conductive polypyrrole, *Electrochimi. Acta*, 40 (1995) 10, 1479–1485.
[35] Kanani, N., In-situ-/ex-Situ-Schichtkontrolle, *Metalloberfläche* 49 (1995) 3, 192–198.
[36] Bunge, E., Adsorption organischer Moleküle auf der Au(111) Elektrolde und ihr Einfluß bei der Kupferabscheidung: Eine *in-situ* STM-Studie, Dissertation, Freie Universität Berlin, 1996.
[37] Breuer, N., Kanani, N., and Meyer, H., Characterization of electrodeposited metal surfaces by scanning probe microscopy, *MST news* 21 (1997) 20–22.
[38] Lorenz, W.J. and Plieth, W. (Editors) *Electrochemical Nanotechnology*, Wiley-VCH, Weinheim, 1998.

[39] Kornyshev, A.A. and Sumetskii, M., Beyond the landscapes: imaging the invisible, in: *Electrochemical Nanotechnology*, W.J. Lorenz and W. Plieth (Editors), Wiley-VCH, Weinheim, 1998.

[40] Salvarezza, R.C. and Arvia, A.J., Roughness kinetics and mechanism derived from the analysis of AFM and STM imaging data, in: *Electrochemical Nanotechnology*, W.J. Lorenz and W. Plieth (Editors), Wiley-VCH, Weinheim, 1998.

[41] Aloisi, G., Cavallini, M., and Guidelli, R., Surface structure and electrochemistry: new insight by scanning tunneling microscopy in: *Electrochemical Nanotechnology*, W.J. Lorenz and W. Plieth (Editors), Wiley-VCH, Weinheim, 1998.

[42] Gewirth, A.A. and Niece, B.K., STM and AFM studies of the electrified solid–liquid Interface: monolayers, multilayers, and organic Transformations, in: *Electrochemical Nanotechnology*, W.J. Lorenz and W. Plieth (Editors), Wiley-VCH, Weinheim, 1998.

[43] Magnussen, O.M. *et al.*, Nucleation and growth at metal electrode surfaces in: *Electrochemical Nanotechnology*, W.J. Lorenz and W. Plieth (Editors), Wiley-VCH, Weinheim, 1998.

[44] Dietterle, M. and Kolb, D.M., In-situ Rastertunnelmikroskopie, Untersuchungen zu den Anfangsstadien der elektrolytischen Kupferabscheidung, *Metalloberfläche* 52 (1998) 5, 382–385.

[45] Smith, J.R., Campbell, S.A., and Walsh, F.C., The use of scanning probe microscopy in surface finishing and engineering, Trans. *Inst. Metal Finish.* 76 (1998) 4, B53–B61.

[46] Atotech Deutschland GmbH, interne Berichte.

[47] Budevski, E., Staikov, G., and Lorenz, W.J., *Electrochemical Phase Formation and Growth*, VHC Verlagsgesellschaft mbH, Weinheim, 1996.

This Page Intentionally Left Blank

CHAPTER 7

Adhesion and its Measurement

7.1 Introduction

The functionality of a coated component relies on the adhesion of coating to substrate and even the highest quality deposited film is useless if the substrate-to-coating bond fails. This is nowhere more so than in the case of corrosion or wear-resistant coatings which will fail in their intended function if even partial loss of adhesion occurs. The surface of the substrate is then exposed, and subjected to conditions for which it was never intended. In a different context, poor coating adhesion can lead to high electrical resistance between substrate and coating and can cause electrical components or circuits to fail. Loss of coating adhesion is equally unacceptable in the case of decorative plating, when the item becomes aesthetically unacceptable.

There can be many reasons for failed coating adhesion and external effects can also aggravate such problems, both those before application of the coating and also those acting after its application. Without question, poor cleaning and incorrect pre-treatment prior to plating are the most commonly found causes of poor adhesion, and the importance of carrying out these preliminary stages cannot be over-emphasized. In particular, degreasing and removal of any oxide films present, are critical.

Special care must also be taken in prior mechanical finishing operations. Grinding and polishing will often induce a thin and brittle surface layer which can be removed by subsequent pickling or the atomic hydrogen formed in electrolytic degreasing. However, this can lead to another undesirable phenomenon, namely hydrogen dissolution in the metal, resulting in hydrogen embrittlement. Atomic hydrogen diffuses into the metal, there combining to form molecular hydrogen which can result in very high compressive stresses in the substrate. The resulting shear forces at the substrate–coating interface can greatly reduce adhesion, as indeed can build-up of hydrogen gas pressure at the interface.

Insufficient adhesion should not, however, be automatically ascribed to poor cleaning or pretreatment. The composite, formed of substrate and coating, may be subjected to extreme conditions. To the extent that the physical, chemical, mechanical and thermal conditions affect substrate and coating to different extents or indeed in different ways, such effects can lead to loss of adhesion, such as blistering or localised lifting of coating.

The mechanisms governing adhesion of coatings to a substrate are not fully understood, although metallic, heteropolar or van der Waals forces are clearly important in this context. That increased micro-roughness of the substrate surface will in general improve adhesion, is indicative of the role of metal-to-metal interaction. In addition, the process of micro-roughening will increase the true surface area of the substrate and also the metal-to-metal contact area. In other terms, this increases the number of substrate-to-coating metal pairs which can then bond. In the following treatment, the most widely used methods for measurement of adhesion are described, together with an overview of adhesion theories.

7.2 Metal–Metal Adhesion

7.2.1 Diffusion Theory

Considering the adhesion between coating and substrate, vacancy diffusion is a key process in that it offers a site exchange mechanism at the coating-substrate interface. Lattice vacancies at the substrate surface (A) facilitate diffusion of atoms from the coating (B) into the substrate and vice versa. Figure 7.1 shows the concentration profile $c_A = f(x)$ before and after the onset of the interdiffusion.

The greater the number of vacancies in the substrate, the greater the extent of the interdiffusion and thus the co-mingling of the two types of atom. This mechanism assumes that the atomic radii of coating and substrate metals are of the same order of magnitude and that a certain mutual solubility is possible.

In those electrodeposited or electroless coating that usually exhibit large numbers of lattice vacancies, a vigorous atomic interdiffusion between substrate and coating

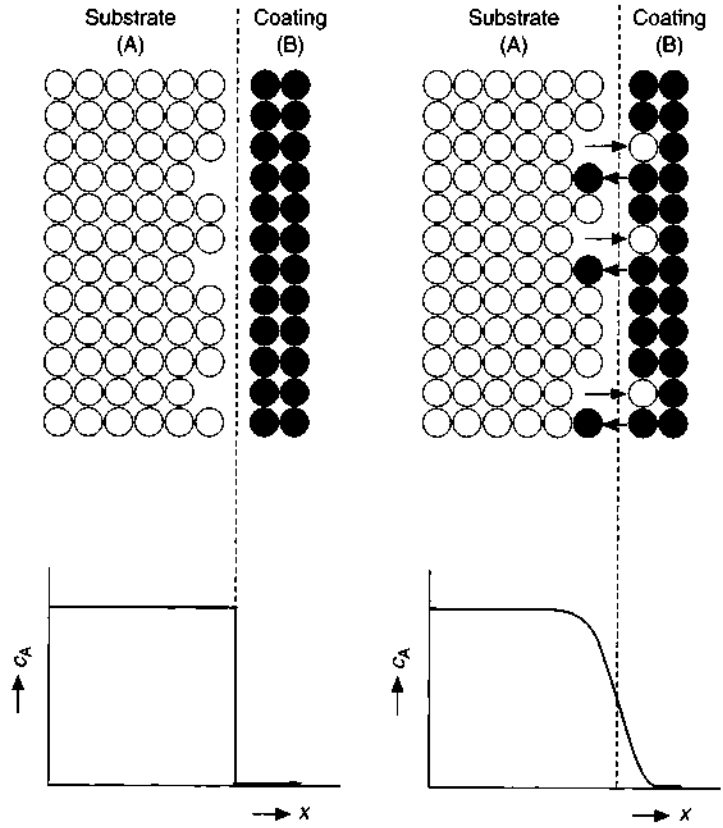

Figure 7.1 Concentration profile c_A before (left) and after (right) the onset of the diffusion process as a function of the diffusion path length x.

can take place. The process can be quantitatively described in terms of the two Fick's laws of diffusion. If n_A and n_B are the number of moles of atom types A and B, then the flux over time t, and a surface area F is given by Fick's first law as:

$$\frac{dn_A}{dt} = -F \cdot D_A \frac{dc_A}{dx} \tag{7.1a}$$

$$\frac{dn_B}{dt} = -F \cdot D_B \frac{dc_B}{dx} \tag{7.1b}$$

In the above equations, D_A and D_B (cm^2/s) are the diffusion coefficients of A and B, respectively, and x is the distance from the surface, that is, the diffusion path length. The extent of diffusion (flux) is then determined by the concentration gradient dc_A/dx and dc_B/dx respectively. The minus sign signifies that the mass transport is inversely related to the concentration gradient.

Fick's first law describes the steady state, in which the concentration gradients shown above, remain unchanged during the diffusion process. This assumption is not valid in the non-steady state in that the local concentrations change continuously as a function of time. This situation is represented by Fick's second law, which shows the variation of concentration with time at a given location, and assuming a constant diffusion coefficient, as a second-order differential equation.

$$\frac{\partial c_A}{\partial t} = D_A \cdot \frac{\partial^2 c_A}{\partial x^2} \tag{7.2a}$$

$$\frac{\partial c_B}{\partial t} = D_B \cdot \frac{\partial^2 c_B}{\partial x^2} \tag{7.2b}$$

If one assumes that substrate atoms can diffuse as fast, across the interface and into the coating as can the coating atoms into the substrate, that is, $D_A = D_B = D$, and also assumes that the diffusion coefficients are concentration-independent, that is, $D \neq f(c)$, then the changes in concentration $c_A = f(x)$ and $c_B = f(x)$ over distance are as seen in Fig. 7.2 [1, 2].

For the mean depth of permeation Δx_A and Δx_B of the diffusing atoms A and B, one then obtains the expressions:

$$\Delta x_A = \sqrt{D_A \cdot t} \tag{7.3a}$$

$$\Delta x_B = \sqrt{D_B \cdot t} \tag{7.3b}$$

where t is the time of the diffusion process.

In fact, the diffusion coefficients D_A and D_B are in many cases concentration dependent, but are invariably temperature dependent. The concentration dependence is expressed in terms of Fick's second law in the following differential equations

$$\frac{\partial c_A}{\partial t} = \frac{\partial}{\partial x}\left(D_A \cdot \frac{\partial c}{\partial x}\right) \tag{7.4a}$$

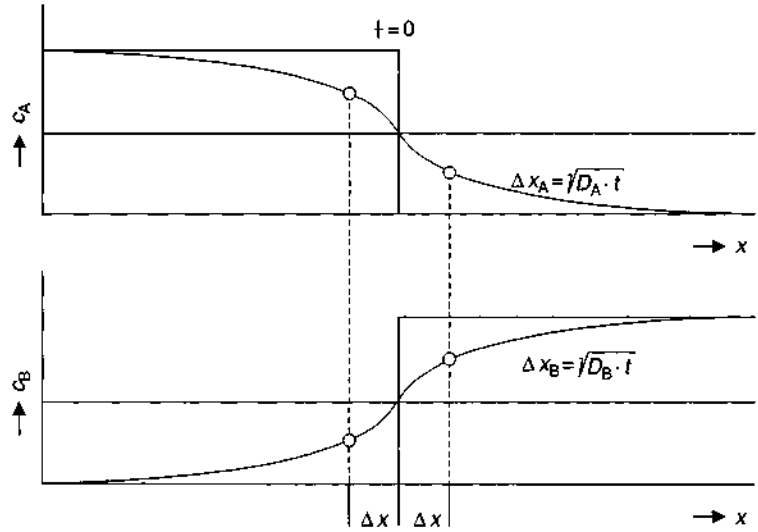

Figure 7.2 Concentration profiles for $c_A = f(x)$ and $c_B = f(x)$ under the condition $D_A = D_B = D \neq f(c)$.

$$\frac{\partial c_B}{\partial t} = \frac{\partial}{\partial x}\left(D_B \cdot \frac{\partial c}{\partial x}\right) \tag{7.4b}$$

The temperature dependence is expressed using an Arrhenius type equation

$$D_A = D_A^0 \cdot e^{-Q_A/RT} \tag{7.5a}$$

$$D_B = D_B^0 \cdot e^{-Q_B/RT} \tag{7.5b}$$

Here, D_A^0 and D_B^0 are diffusion constants and, Q_A and Q_B activation energies.

Because the diffusion process is so very temperature dependent, use of appropriate heat-treatment accelerates the interdiffusion and thus, in most cases, the adhesion of the coating. The conditions for this will reflect the substrate and coating metals in question, and the necessary time can be roughly calculated from Eq. (7.3).

The SEM images shown in Fig. 7.3 show electroless nickel deposited over steel, and heat-treated for about 1 h at 400–600°C in a neutral gas atmosphere. The depth profiles obtained using energy dispersive X-ray (EDX) analysis show the nickel concentrations at the steel/Ni–P interface as a function of heat-treatment temperature.

The contour of the nickel line, in the case of the as-deposited sample indicates that, even in this case, there has been a certain amount of interdiffusion of the nickel and iron. It is seen that as the heat-treatment temperature increases, so does the extent of the interdiffusion.

Figure 7.4 shows another example, in this case a tin-plated copper tube from a hot water system. The thickness of the tin ranges from 0.11 to 0.15 μm. In order to study the mutual diffusion of these two metals, samples were heated at 100°C for 3 weeks, in a neutral atmosphere.

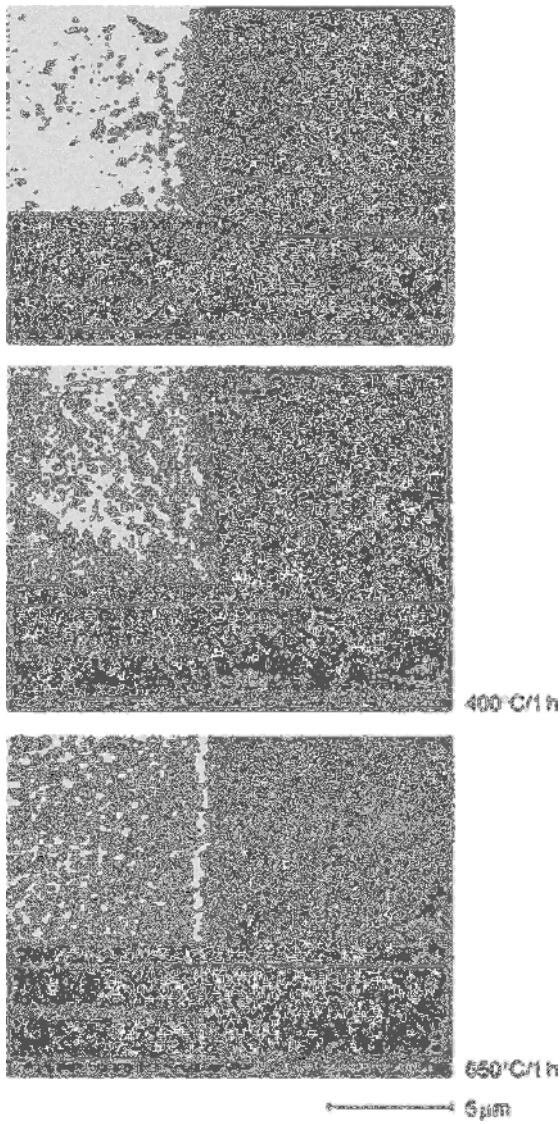

Figure 7.3 Formation of a diffusion layer (concentration profile of nickel) at the steel/Ni–P interface. Top: as-deposited. Center: heat-treated at 400°C/1 h. Bottom: 600°C/1 h.

The images, obtained using a field-emission SEM, show that even at 100°C after 168 h, a considerable amount of interdiffusion has taken place. This then leading to formation of an intermetallic, probably the ε-phase Cu_3Sn. It is seen that the diffusion of tin in copper becomes more pronounced with time, leading to an increase in the thickness of the intermetallic zone. It can also be seen that that at some locations (as indicated by the arrows), the tin layer has become totally dissolved by the copper. In Fig. 7.5, the concentration profiles for copper and tin are shown along a line marked as (+).

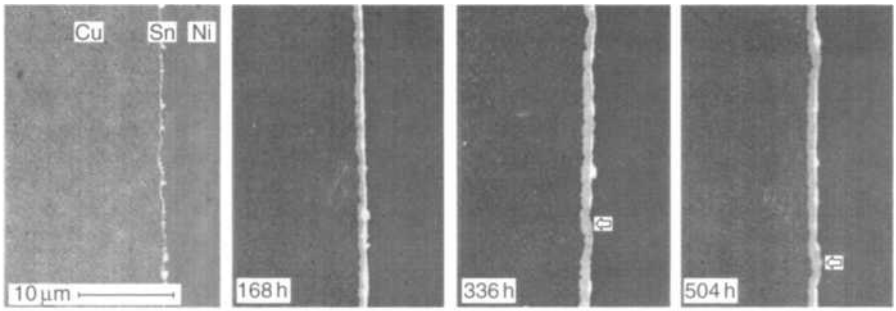

Figure 7.4 Interdiffusion of copper and tin at 100°C as function of heat-treatment time (Ni protective coating).

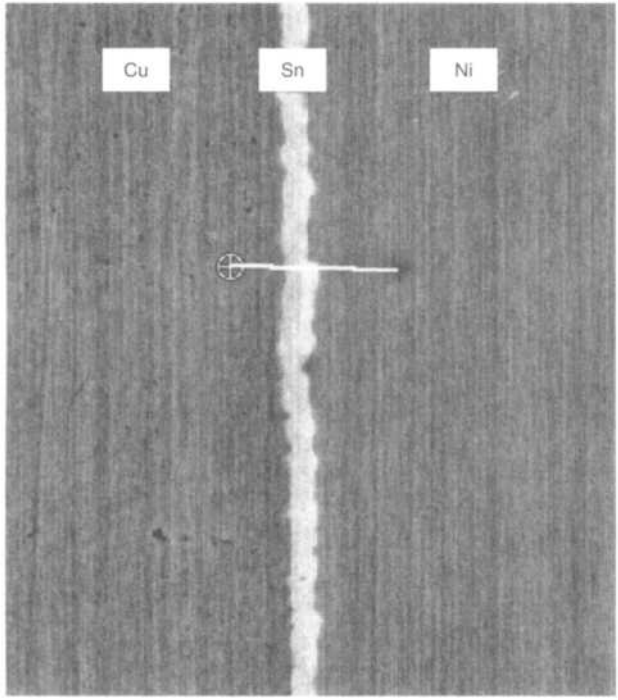

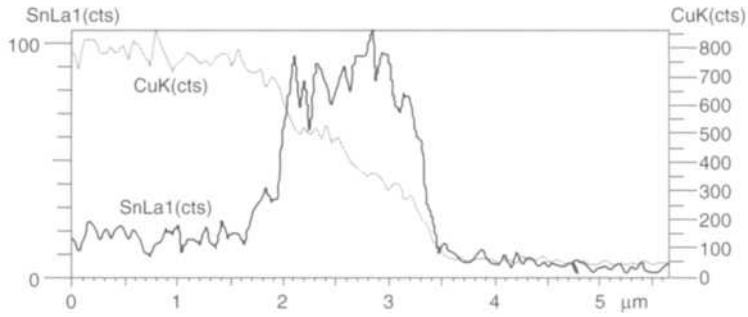

Figure 7.5 Concentration profiles of copper and tin along an analysis line.

Table 7.1 Concentrations of copper and tin along the analysis line (+) (12 points).

⊕	Cu	Sn
1	98.69	0.01
2	98.88	0.11
3	98.36	0.18
4	90.57	7.46
5	82.45	12.43
6	44.69	8.15
7	0.84	0.02
8	2.07	0.06
9	0.99	0.11
10	0.99	0.03
11	0.24	0.05
12	0.25	0.11

The quantitative analytical data for copper and tin concentrations along this line (beginning at (+)) are shown in Table 7.1.

The interdiffusion of the coating and substrate metals may not always work to the benefit of adhesion, since (as in the latter case), the same conditions can promote formation of a brittle intermetallic phase at the boundary, which can even result in lower adhesion values. This can take place when, for example, the diffusion rates of the two types of atom are very different. As a result, pores and cavities can form on that side of the interface from which the atoms diffuse most rapidly. This is known as the Kirkendall effect, and is usually accompanied by a marked decrease in adhesion. In addition, it can happen that the substrate atoms, when sufficient numbers diffuse into the coating, can modify the properties of the latter.

It should also be noted that grain boundaries and dislocations, as well as vacancy sites, offer favorable diffusion paths for migrating atoms. In both cases, diffusion is possible with lower activation energy than otherwise, in the case of grain boundaries because of strong lattice distortion, and in the case of dislocations because of linear lattice defects. It is for this reason that fine-grained materials, where there are fair more grain boundaries for diffusion to take place, give rise to better adhering coatings. In the opposite sense, some oxide films or other forms of surface contamination can act as diffusion barriers, resulting in poorer adhesion. Once again, one is reminded of the crucial importance of correct cleaning and pretreatment.

7.3 Polymer–Metal Adhesion

The surface of polymeric materials or components is usually prepared for coating by making it electrically conductive [3, 4]. The usual method is to allow precious metal nuclei to form as islets at the surface, these then catalysing electroless deposition, and often thereafter, a heavier deposit being electroplated (see Chapter 4, Section 4.2). The latter process allows any required thickness to be laid down. The metallographic

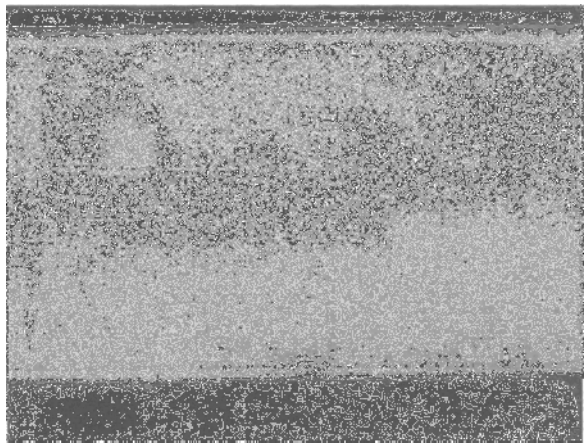

Figure 7.6 Layer build-up on a plastic component: from the bottom up: ABS/nickel/copper/nickel/chromium (500x).

cross-section in Fig. 7.6 shows such a deposit formed over the plastic ABS (acrylonitrile butadiene styrene), widely used in the automotive industry.

The adhesion between coating and substrate is strongly affected both by virtue of the polymer used and also its pretreatment. However, the deposition conditions and electrolyte composition also play a role. The diffusion theory of adhesion, discussed above and which appears a reasonably satisfactory model for metal–metal adhesion, proves an unsatisfactory model for adhesion of metallised plastics. For this reason, other models have been developed, some of which are detailed below [3–11].

7.3.1 'Press-stud' Theory

The theory based on a mechanical anchoring of coating to substrate, as applied to metillised coatings on plastics, is known as the 'press-stud' theory, and has been much studied using metallised ABS. This is a copolymer in which particles of butadiene are incorporated [3, 4]. Prior to metallising, the surface of ABS is roughened either mechanically or by chemical etching with chromic acid. The acts to remove the butadiene from the elastomeric skeleton, resulting, as seen in Fig. 7.7, in a proliferation of pores and cavities at the surface.

The adhesion of the metallic layer over the plastic is thereby attributed to a mechanical anchoring between the two components. The morphology and geometry of the pores and cavities at the ABS surface must be such as to allow ingress of the metal forming the outer layer, and so provide an anchoring. A critical parameter is the aperture angle and shape of the pores [6, 8]. Figure 7.8 provides a schematic of the situation.

The force required to part the metal coating from its ABS substrate can be estimated in terms of the 'press-stud' theory [3]. This assumes formation of spherical

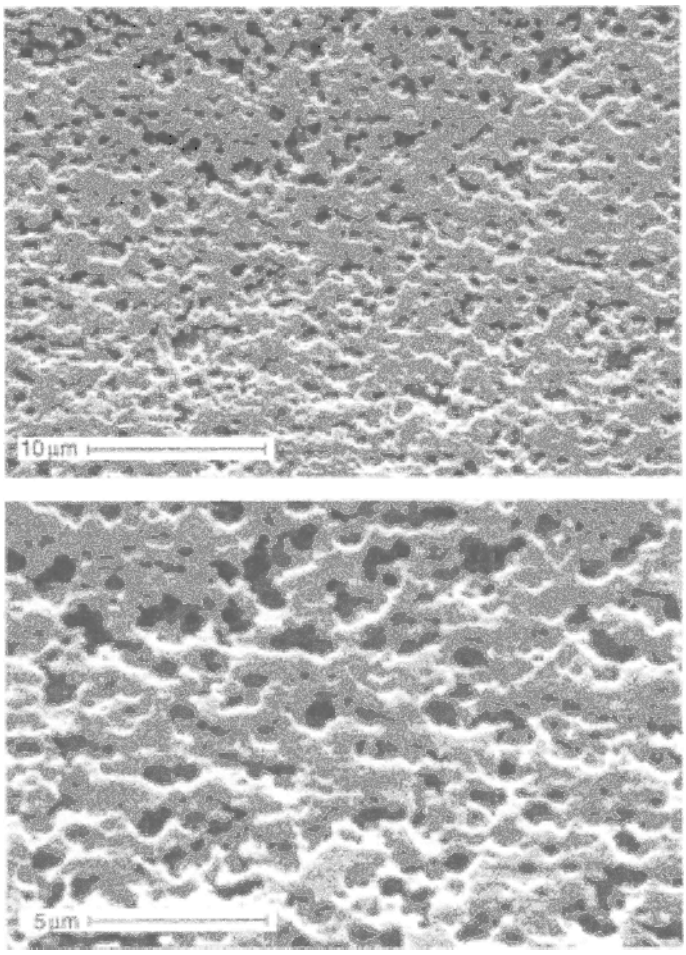

Figure 7.7 Appearance of an ABS surface after chromic–sulfuric acid etching.

hollows beneath the surface. The force K, required to withdraw a metal sphere of radius r from the acrylonitrile–styrene skeleton is then

$$K \approx 2\pi r\sqrt{a^2 + (r - \sqrt{(r^2 - a^2)^2}} \tag{7.6}$$

In this equation, $0 \leq a \leq r$ represents the distance of the centre of the sphere from the plane of the surface.

The same theory can be used to explain the good adhesion of metallic coatings to polypropylene (PP), which is some two to three times higher than that on ABS [4]. PP consists of both amorphous and partly crystalline phases, and because of its superior temperature resistance, is widely employed in engineering. The metal-to-PP adhesion is due, as seen in Fig. 7.9, to the fact that the amorphous regions are strongly attacked

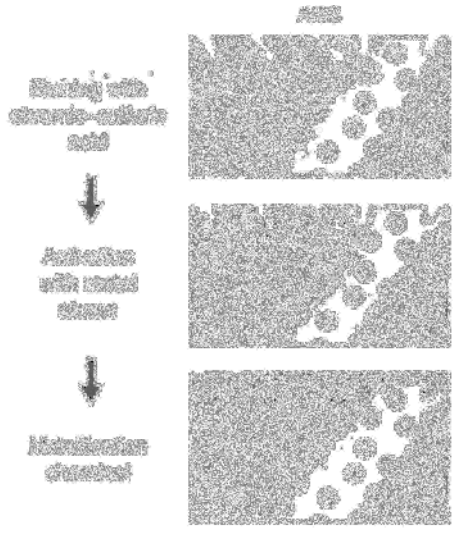

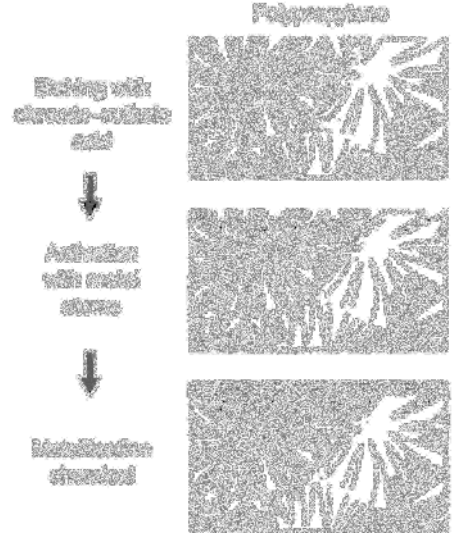

Figure 7.9 Etching, activation and electroless metallising of a polypropylene substrate [8].

by the chemical etch, and thus selectively dissolved out. The resulting pores and cavities create a rough surface which promotes mechanical anchoring.

If one records the metal-to-plastic adhesion value and plots this as a function of etch time, an optimum value is found at around 30 min, as seen in Fig. 7.10. The plots pass through a clearly defined maximum and adhesion improves with surface roughness, but only up to a given point, after which it falls off.

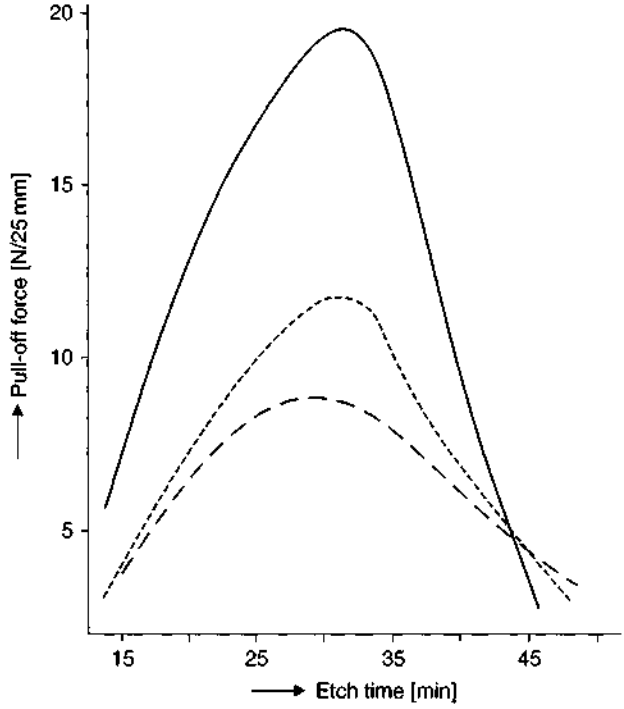

Figure 7.10 Pull-off force as an indication of adhesion between metal coating and polypropylene substrate as a function of etch time, for polymers with various degrees of crystallinity [7].

7.3.2 Wetting Theory

The wetting theory of adhesion for a metal-coated plastic substrate is based on surface energies of the two components and their interaction. The key element of the theory is that the polymer surface must be wetted by the electrolyte [8–11]. It is assumed that the extent of wetting is a function of the components forming the surface of the plastic. Satisfactory adhesion can only take place, according to this, when the surface is completely wetted by the metal. The work required to part the metal coating from the plastic substrate surface is designated as W_a, the work of adhesion [8, 9] and is given by the following expression:

$$W_a = \gamma_P + \gamma_P - \gamma_{PM} \tag{7.7a}$$

Here γ_P and γ_M describe the surface energies of plastic and metal, respectively, γ_{PM} is the interfacial surface energy.

According to this, a knowledge of the surface energy of the polymer being metallised allows an estimate of the expected adhesion value. The direct relationship between the work of adhesion W_a and the surface energy γ_P and γ_M lends support to the idea that, at least in some circumstances, the wetting theory is valid for

polymer-to-metal adhesion. Based on a hypothesis that surface energy consists of a dispersive (d) and a polar (p) component [8] one can then by analogy resolve the work of adhesion into a dispersive (W_a^d) and a polar (W_a^p) term:

$$W_a = W_a^d + W_a^p \tag{7.7b}$$

7.3.3 Electrostatic Theory

The electrostatic theory sets out from the existence of an electrolytic double layer (see Chapter 5) and applies the concept to the polymer–electrolyte interface, and seeks to explain the polymer/metal adhesion mechanism in these terms [6, 10, 11]. According to this theory, an electrical double-layer is formed as soon as the polymer is immersed in an electrolyte. However, the charge distribution and potential gradient across the double layer are not the key factors, because of the presence of precious metal nuclei at the polymer surface. Only after a complete metal surface has formed, as a result of the metallising process, can the charge distribution and potential gradients be unequivocally defined. Since the metal can donate electrons more easily than the polymer, its surface carries a positive charge and as a result, a higher electrical potential. The potential gradient across the electrolytic double layer for a polymer–metal combination is shown in Fig. 7.11.

Thus, according to this theory, adhesion is determined by the dielectric and electrical forces between polymer and metal. The more detailed theory underlying

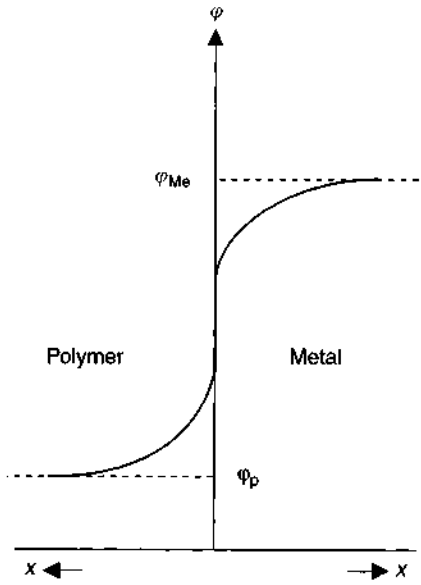

Figure 7.11 Potential profile across a polymer-metal interface [6,11].

this model is extremely complex, and a number of simplifying assumptions are employed [6].

7.4 Methods for the Determination of Adhesion

The term 'adhesion strength', also sometimes known as 'adhesive force' or 'pull-off force' allows us a means of quantitatively describing this key parameter. Being able to assign a quantitative value to the coating–substrate adhesion, can also provide insights into the physico-chemical forces involved. The term signifies the force required to part coating from substrate. In the case of metal-on-metal coating-substrate pairs, adhesive force can range between two extreme limits. When the lattice parameters and structures of the two are identical, that is, the coating can be seen as no more than an extension of the substrate and there is virtually no interfacial region between the two, the adhesion between the two will be much the same as the tensile value of the substrate metal. This is a situation very rarely encountered in practice, since the requisite conditions are difficult to fulfil. At the other extreme, adhesion values fall close to zero if, prior to metal electrodeposition, the substrate metal is deliberately passivated, and in this case, no metal-to-metal bond can form. Practical use is made of this, for example, in peeling thin metal films from an inert cathode, or parting an electroform from a metallic mandrel.

A definition of adhesive force assumes that the forces responsible, act normally to the plane of the substrate. In fact, external forces which can be used to part coating from substrate, often likewise act in the same axis. Sometimes, though, conditions arise where a shear force acts in the plane of the substrate–coating interface, as for example, the two materials have different coefficients of thermal expansion, and are subjected to temperature variations. The resulting force will then seek to move one relative to the other in the plane of their interface. Coatings applied to reduce friction, are also subjected to shear forces. When selecting a test method for study of adhesion, such factors should be borne in mind.

The measurement of adhesion is difficult, since the results can be affected by numerous factors. Strictly speaking, there is even today, no rigorous method for adhesion measurement, and in many cases, a 'yes/no' test procedure is applied. Such test methods tell us little or nothing about bonding forces and their efficacy.

Over time, numerous adhesion test methods have been developed, most of which fall into the two categories of qualitative and quantitative, and almost all of which are destructive in nature. Sharp delineation between the two categories is not in all cases possible. In the following, the most important and widely used test methods are described [12].

7.4.1 Qualitative Test Methods

These are often based on the various plastic or thermal properties of substrate or coating. They are simple to carry out and require to elaborate equipment. Furthermore, they provide a result without any extensive sample preparation. Against this, the outcome is often dependent on the test method used and not too

Table 7.2 Methods for testing adhesion of various metal coatings [13].

Test method	Coating								
	Cr	Ni	Ni+Cr	Ni[1]	Cu	Zn	Ag	Cd	Sn
Bending	●	●	●	●	●				
Deep-drawing	●	●	●	●	●				
Grinding	●	●	●	●					
Filing	●	●	●						
Chiselling	●	●	●	●					
Tearing/cutting	●	●	●	●	●	●	●		
Peening	●	●	●	●	●	●	●	●	●
Thermal shock	●	●	●	●	●	●			
Electrolytic	●	●	●						
Tensile	●	●	●	●	●	●			

[1]Electroless nickel.

reproducible and usually best considered as a pass/fail result. These qualitative methods can simulate compression or tensile conditions, shear force or thermal cycling. Choice of the right method thus depends on the in-service conditions to be expected. Table 7.2 lists a selection of qualitative methods for testing of coating adhesion.

7.4.1.1 Bend test

In this test, a coated metal strip is bent through 180°, then inspected to see whether the coating has lifted from the substrate or not [14]. If the test piece is bent to and fro through an angle of ±90°, the resulting tension/compression action, the coating is also subjected to a severe test, and the coating will usually lift after a few such cycles. It is recommended that the conditions of the test be first devised, in terms of the acuteness of the bending radius and the number of cycles used. In a variant of the method, using thicker gauge metal strips, the testpiece is held in a vice and bent to and fro, either by hand or using a hammer. The bending radius depends on the manner of fixing in the vice. The test is satisfied if the coating remains adherent to the substrate after a specified number of to-and-fro movements.

7.4.1.2 Mandrel bend test

In this test, the sample, usually a plated metal strip, is bent around a mandrel, normally a cylindrical section bar of 4 mm radius, through 90° and then bent back to its original state. The test exposes the sample to shear forces in the plane of the surface, which can result in a lifting of the coating, once the adhesion value is exceeded. After three cycles, the sample is inspected for signs of lifting and a 'pass' is achieved when no cracks or lifting is found. This test is, by its nature, well suited for testing coatings on thin-gauge metal. The outcome is largely a function of the plasticity of the deposit metal, this feature of the coating metal being mainly subjected in the test. To ensure meaningful comparisons, the bending radius and rate of bending should be kept the same in a series of tests.

7.4.1.3 Cross-hatch test

In this test, a hardened steel tip is used to scribe a mesh pattern of 1–3 mm length, over an area of at least 5 cm^2, at three separate locations on the sample surface. The scratches must penetrate down to the substrate. The result is a setting up of lateral forces on the coating. For coatings with good adhesion, the small squares of coating enclosed within the lines of the mesh, will not left. For less well adherent coatings, more than one such square will lift.

In one version of this test, an adhesive tape is carefully applied to the mesh-cut surface, making sure that no air pockets form between tape and coating surface. After 10 s, the tape is lifted up, normal to the surface. The number of small squares detached in this way is noted. Using a special multi-tip scriber and cross-hatching, the test can be made more demanding and is usually thus conducted.

7.4.1.4 Polishing test

The adhesion of metal-on-metal coatings can be assessed by polishing the surface. Using an agate knife, an area of 6.54 cm^2 is scribed out on the surface and then polished with some force for 15 s using a normal polishing wheel. The frictional heat thus generated, causes thermal expansion, and if substrate and coating have different thermal coefficients of expansion, the resulting lateral force will cause a lifting at areas of poor adhesion. For good adhesion, no lifting will be observed. As will be obvious, polishing wheel speed and downward force applied, are critical parameters affecting test outcome, whereas the geometric shape of the test piece is less important. However, the maximum temperature reached during the test – and this is the basis of the method – will also depend on the thermal mass of the testpiece and its ability to conduct heat efficiently from the point where it is generated.

7.4.1.5 File test

To carry out this test, the sample is held in a vice and, as shown in Fig. 7.12, a file is applied to one edge at an angle of 45° [15]. The aim is to so stress the sample that the coating is lifted from the substrate.

Files with various abrasion surface can be used. After filing, the sample is inspected to determine whether the coating has lifted, or simply been abraded together with the substrate. The latter outcome indicates good adhesion. The test can be made more severe by altering the angle of attack of the file, to favour parting of coating from substrate. Test results are strongly dependant on the operator and even then, should not be seen as being reproducible.

Figure 7.12 Qualitative and destructive adhesion testing using a file test.

7.4.1.6 Hammer-blow test

If a coated sample is struck with a hammer, the surface undergoes a plastic deformation, resulting in a decrease in coating thickness and at the same time, an increase in surface area. The shear forces involved, can lead to a detachment of the coating from the substrate. The method has proved especially useful for thicker coatings, and is commended by the ease and speed with which it can be carried out. In practice, an electromagnetically powered hammer is often used, with a diameter of 1.59 mm and a strike rate of 1500–6000 vertical impacts per minute. The momentum thus delivered is typically 0.68 kg s. Poorly adhering coatings show the first signs of blistering or lifting after some 10 s. If no such signs are observed, the coating adhesion can be described as 'sufficient' or 'good'.

7.4.1.7 Cupping test

The Erichsen cupping test can be used to gauge adhesion of a coating on a metal, provided the substrate is no more than 1–2 mm thick. The basis of the method is that, using a press, a cup-shaped indentation is formed in the test piece, and the time required for the coating to lift, is noted. In practice, as shown in Fig. 7.13, a square sample of determined dimensions is clamped between the holder and the anvil or Erichsen platform, with the coating side facing downwards.

The ball-shaped indenter is then pressed down onto the test piece at a constant rate of advance. Depending on the thickness and plastic deformability of the test piece, the coating will peel from the substrate at a given point. The force required for this to occur can be used (other conditions being equal) as a measure of the adhesion. The point at which cracking begins, this immediately preceding coating lift-off, can be more precisely determined as follows. The test sample is immersed in electrolyte before being clamped into the test equipment. If, during the subsequent test, the coating cracks or lifts, the electrolyte permeates through to the substrate and

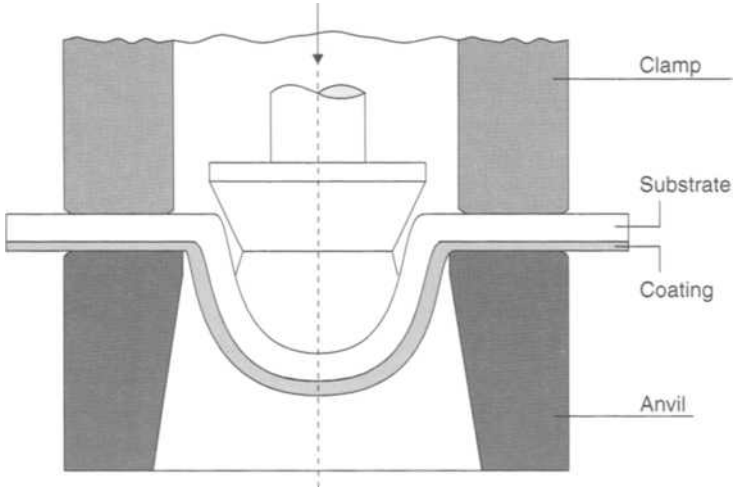

Figure 7.13 Erichsen cupping test for testing coating adhesion [16].

reacts with it. The color formed by this reaction can serve to indicate the onset of cracking etc.

7.4.1.8 Electrolytic test

This electrolytic test can only be used with certain coating metals, namely copper, nickel and chromium. The substrate acts as a cathode, and is immersed in an electrolyte of 5% NaOH or KOH or 5% sulfuric acid. The resulting electrochemical reaction acts to charge the substrate with atomic hydrogen. A steel sheet serves as an anode. The basis of the method rests on the permeability of the coating metal to hydrogen. Results are strongly dependant on the surface pretreatment, but a proper cleaning is essential. The test sample is suspended in the electrolyte with 5 l of solution for 1 m^2 of sample surface. The electrolysis time can range from a few minutes to a few hours, and at temperatures from ambient to 60°C. The cell voltage would be around 10 V. Atomic hydrogen formed at the sample surface diffuses through the coating, and builds up in defect locations at the coating–substrate interface, where it is converted to molecular, gaseous hydrogen. This creates a pressure build-up at the coating-substrate interface which, in many cases, is sufficient to cause lifting of the coating, as a blister. Usually, the sample is removed from the electrolysis cell after 3 min, washed with water and inspected with the naked eye. If no blisters are seen, it is subjected to a further 12 min electrolysis and again inspected. The edges and periphery of the sample should be specially scrutinized. Sample coatings which survive 15 min of this without formation of blisters can be said to be well-adherent.

7.4.1.9 Torsion test

This test requires the sample to be a relatively thin strip of metal, onto which the coating is deposited. The strip is clamped at either end, then slowly twisted until the opposite long edges contact one another. The angle of twist at which the coating begins to lift is a measure of the adhesion. If no lifting takes place, the adhesion can be said to be satisfactory, in that the torsional force proved inferior to the metal-to-metal bonding force. This test can also be modified to test coated wires, in that one records the number of turns on a length of clamped wire required to cause coating lifting.

7.4.1.10 Wrapping test

This test is used for coated wires. It employs a conical, stepped mandrel with 12 steps, each 40 mm wide and of diameter from 2 to 32 mm. The wire sample is wrapped for 10 turns at a constant rate around each step on the mandrel [14]. In order to avoid any increase in the temperature of the mandrel, the rate of winding-on should not be too great. The different diameters of the stepped mandrel correspond to the wire diameter or its 10–20-fold value. The step which results in loss of adhesion of the coating is noted as a guide of adhesion. In the case of zinc-coated copper wire, for example, no loss of adhesion should occur at steps larger than 10 times the wire diameter. As one moves to ever smaller diameters, the maximum strain on the coating occurs when the mandrel diameter is equal to that of the wire. The wrapping test can also be carried out using a smooth barrel-shaped or cylindrical mandrel. In both cases, the wire should be wrapped with each turn immediately adjacent to the

previous one. The mandrel diameter causing the coating to lift is an index of the adhesion. However, the stepped mandrel is the preferred method.

7.4.2 Quantitative Adhesion Tests

In the same way as with qualitative tests, most quantitative tests are based on a measurement of the force required to lift the coating. However, they are more time-consuming to carry out, and require special apparatus. It should also be noted that sample preparation is far more time-consuming than is the case for the previously described qualitative methods. Finally, test methods for relatively thick deposits on some shapes of substrate are very limited in number.

For all these reasons, use of quantitative adhesion testing in working plating shops is but rarely encountered. While numerous methods exist for quantitative adhesion testing for specific coating-substrate combinations, all suffer from possible interfering effects, so they cannot usually be used directly on a component. They do, however, provide absolute values for adhesion, which can be unequivocally cited in standards or in the literature. Adhesion values are quoted in terms of force per unit area. Even here, however, values obtained are very much a function of the method used. With all these methods, there is the common problem of how best to apply the parting force to the sample, since (as seen below) this requires some form of attachment.

7.4.2.1 Peel test

The peel test is widely used, but nowhere more so than in testing the adhesion of copper films laminated with epoxy-resin onto plastic for the printed circuit board industry. A sample of 10–25 mm width is used, and at one end, the copper coating is lifted and then fastened in the direction of the pull-force, to the tester. This then applies a constant pull-off force at an angle of 90° to the plane of the substrate. During the process, the substrate is retained in position by two rollers (Fig. 7.14a) which allow the substrate to move slowly but smoothly in a horizontal plane. Since the tensile strength of the copper film is greater than the adhesive force, it is not torn during this operation (though clearly this would not be true for a very thin film). The adhesion value derived, in this case for copper to epoxy resin, is expressed in newtons per 25 mm [N/25 mm].

The stress–strain diagram affords an insight into the change of pull-off force as a function of path-length. As shown in Fig. 7.14(b), the pull-force rises sharply at the beginning of the test, after which it is broadly constant, with minor variations. The test is carried out over some 75% of the sample length, to give a mean value and at the end of the test, when the copper has been completely detached from the substrate, the pull-force decreases to zero.

Depending on the pull-off angle used, the test data is denoted as 90 or 180° or indeed any other angle. The first two of these, designated as L90° or L180° or T90° are schematically shown in Fig. 7.14(c).

Whatever the sample sizes and test geometries used, it must be noted that test conditions such as pull-rate, test temperature and plastic deformability of the coating layer will all affect the result, and as such, these should not be neglected. It is therefore recommended that these parameters be defined at the outset.

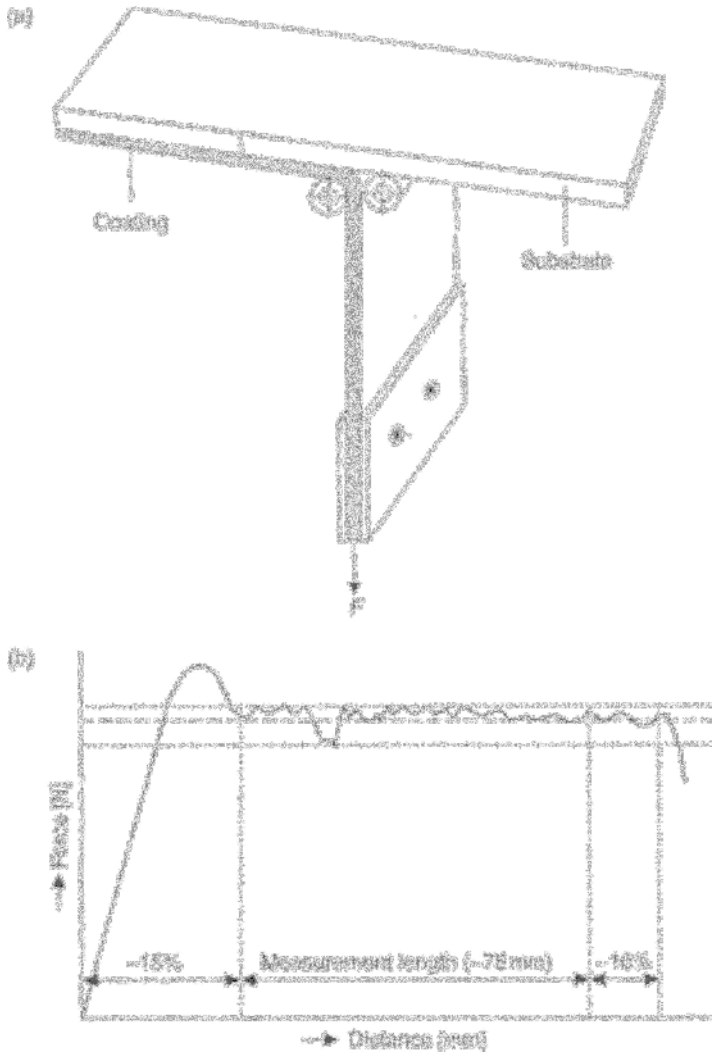

Figure 7.14 (a) Peel test to determine adhesion of copper deposits on plastic substrates [13]. (b) Stress–strain diagram for a peel test for quantitative measurement of copper foil adhesion to a plastic surface. (c) Schematic representation of peel tests using various geometries [6].

7.4.2.2 Cobalt barrel test

In this test, a mushroom-shaped structure made of cobalt is attached to the surface of the coating to be tested, by electrodepositing (or electroforming) it from an appropriate solution. Typically, this would be 2–2.5 mm thick. Deposition of this may take from two to three days. The test sample can then be mounted in a tensile tester, whose jaws grip the cobalt barrel. The force at which detachment of coating from substrate occurs, is noted. Figure 7.15 shows: (a) poor adhesion; (b) high adhesion; and (c) adequate adhesion [13, 16]. In case (a), the coating is readily detached from

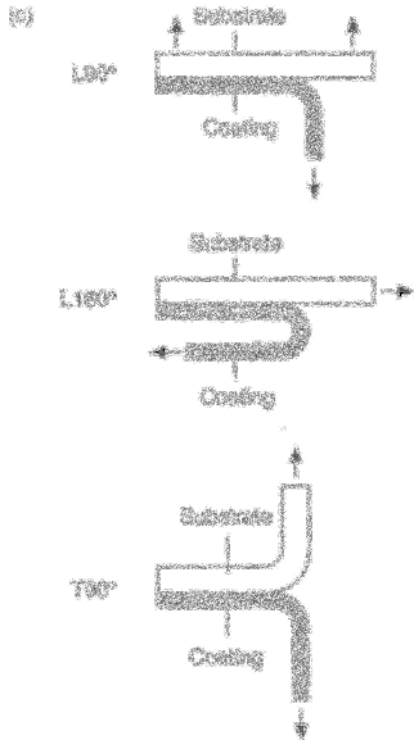

Figure 7.14 (Continued).

the substrate. Where the bonding forces between atoms of the coating (B) and the substrate (A) are greater than those between like atoms, that is $A \leftrightarrow B > A \leftrightarrow A > B \leftrightarrow B$, this indicates a very high adhesion, indeed is greater than the fracture strength of the substrate itself. In this case, the test procedure will lift the coating but with sections of substrate still adhering to it. If the bonding forces between the atoms of the coating material are weaker than those between substrate atoms ($B \leftrightarrow B < A \leftrightarrow A$), then the adhesion test will cause a fracture within the coating itself.

In practice, because it is so time-consuming, this test is rarely used except in respect of nickel coated steel, In many other cases, it is not applicable because of insufficient adhesion between the cobalt barrel and the surface of the metal coating.

7.4.2.3 Ollard test

This test was originally devised for testing nickel plate adhesion to steel, and has since been used for other substrate–coating systems, especially chromium plating, with some success [13–15]. In practice, the end face of a rod-shaped section is plated with the coating to be tested. The rod is typically 3–4 cm long and 2–3 cm in diameter. The deposit thickness is typically 2.5 mm. The rod is then reduced in diameter by turning in a lathe, but leaving the coating protruding, to form a flange as seen in

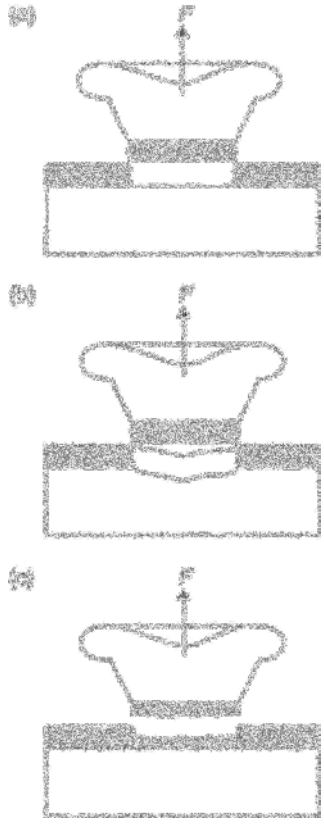

Figure 7.15 Quantitative adhesion testing by means of the cobalt barrel test [13, 16]: (a) poor; (b) high; (c) sufficient.

Fig. 7.16. This bolt-shaped test piece is inserted into a circular steel holder which allows free motion of the sample. This assembly is inserted into a tensile tester and the 'bolt' pulled from below, until the coating (the 'bolt head') is detached from the circular substrate. The resulting adhesion is expressed as N/mm^2. The Ollard test is not suitable for use with brittle deposits, but there are modified versions of the method which can be used in special circumstances.

7.4.2.4 Tensile test

As Fig. 7.17 indicates, the Tensile test is another means of quantitatively determining coating-to-substrate adhesion, based on measurement of the force at which the two separate, or a fracture occurs within either coating or substrate. The method is ideal for use with metallic coatings of gold, copper, nickel, silver, zinc, tin and tin–nickel alloys on metallic substrates. In implementing this test, which is enshrined in DIN Standard DIN EN 13144, it should be appreciated that the results are also affected by sample surface pretreatment. Further details are as follows: a disc-shaped sample coated on one or both sides, and of 30 mm diameter (or a square of 30 mm side) is used. The test-piece should not have been subjected to cold-working.

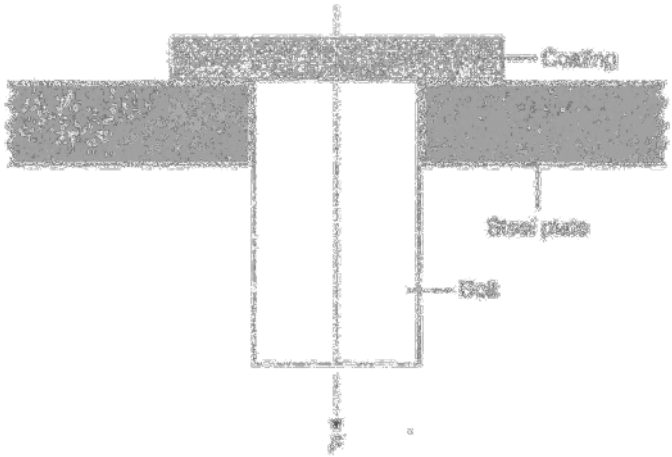

Figure 7.16 Offord adhesion test [13, 16].

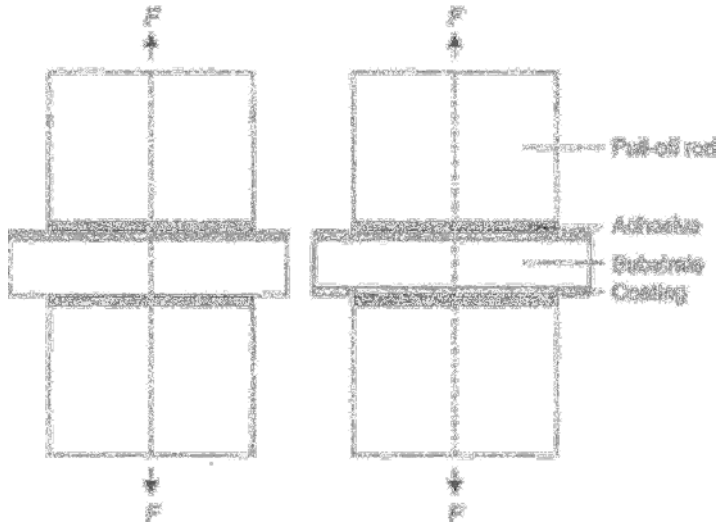

Figure 7.17 Sample arrangement for quantitative adhesion testing using the tensile method. Left: single-sided coating. Right: double-sided coating.

The cylindrical pull-off rods are made of steel, typically of diameter 20 mm. The length of these must not be less than half their diameter and the rods must be such that they undergo no deformation during the test. The end-faces of the pull-off are meticulously cleaned, then coated with special adhesive. This must be prepared and used strictly according to the manufacturer's instructions. The test piece is then inserted between the pull-off rods, coated with adhesive, which are pressed together under constant known pressure. The coating outside the circumference of the pull-off rods is then separated, for example, by selectively removing an annular section, as shown in Fig. 7.17. If required, bonding of the adhesive to the outer coating surface

can be improved by lightly roughening the surface with emery paper before application of the adhesive. The pull-off rods are now subjected to a tensile force, pulling them apart. The tensile force must be applied normally to the plane of the sample, and no bending or any other deformation should take place. The tensile force should be such that fracture takes place within 2 min of initial application of the force. Testing should be carried out at 23±2°C and relative humidity of 50±5%. Adhesion is expressed as σ, given by the expression:

$$\sigma = F/S \ [\mathrm{N/mm^2}] \tag{7.8}$$

where F is the force applied at fracture and S the surface area of the pull-off rods. A detailed subsequent examination of the fracture surfaces and nature of the fracture, form an esential part of the entire procedure.

7.4.3 Non-Destructive Test Methods

Virtually all the foregoing techniques for adhesion measurement, are destructive in nature. For continuous monitoring of production, and especially where testing must not impair the further use of the sample, non-destructive methods are called for. For very high adhesion values, that is, when the adhesion between substrate and coating is greater than the tensile strength of the substrate itself, adhesion testing may result in damage to the substrate (see Fig. 7.15b). At present, there are few non-destructive adhesion test methods, and these are more for laboratory than shop-floor use. Their application in an industrial setting is virtually unknown. The methods are based on various physical effects, which form a basis for adhesion testing.

7.4.3.1 Thermal shock test

This method is based on the fact that if substrate and coating have different thermal expansion coefficients and are subjected to a rapid rise in temperature, there may be loss of contact between the two, especially if adhesion was poor in the first place. Table 7.3 lists the linear coefficients of expansion of some metals and alloys.

Table 7.3 Linear coefficients of thermal expansion of various metals and alloys [17].

Metal	$\alpha\ [\times 10^{-6}]\ [\mathrm{grd^{-1}}]$
Cast iron, grey	7.4
Chromium	8.1
Steel	12.0
Nickel	13.0
Copper	17.0
Bronze	18.8
Silver	19.0
Brass	17.4–19.2
Aluminium	25.7
Zinc die casting	27.7
Lead	28.0
Cadmium	30.0
Indium	56.0

In this method, the sample is rapidly heated to a predetermined temperature, and then rapidly cooled. In practical terms, the sample is held in an oven for around 30 min at 200–350°C, then quenched in water at room temperature. The temperature range chosen, depends on the substrate. In the case of zinc (diecastings), it might be 150±5°C, for copper alloys, 250±5°C. For steels, higher values are necessary, 350±5°C. Silver coatings on electrical contacts are tested by heating for 20 min at around 400°C. This last example reminds us that the time of heating, as well as the temperature selected, must be altered to suit the system being tested. Heating can be carried out using an oil bath, rather than an oven, if desired, and where oxygen uptake, or oxidation is a problem, heating in inert or reducing atmosphere may be necessary. In carrying out this testing, it should be appreciated that heating for extended periods can lead to grain growth in the substrate and so alter its properties, including also adhesion. Heating will also facilitate solid-state interdiffusion between coating and substrate. If this leads to alloying at the interface, adhesion will be substantially increased. However, if an intermetallic compound forms, the reverse may be true.

After quenching, the sample is inspected for local lifting or blistering of the coating. It might be noted that, when gases are trapped or dissolved in the substrate, heating will tend to force these out, again creating a pressure which can cause coatings to lift. This includes hydrogen which is dissolved in the substrate metal. Including this particular test in the 'non-destructive' category, might be questioned by some, since even if the thermal excursion does not cause the coating to lift, it may well affect both properties and appearance of the coated component. The ASTM standards of commonly used temperatures for thermal shock testing are given in Table 7.4.

7.4.3.2 Ultrasound test

The relatively high innate energy of ultrasonic irradiation can be employed to test coating adhesion. The basis of the method rests on the different sound resistance values of coating and substrate (density × sound velocity in that medium) and this causes a sonic effect at the interface, where sound waves can be either reflected back or transmitted. The extent to which either effect occurs is a function of the adhesion, and this in turn depends on surface roughness and other conditions at the interface. The energy of ultrasonic waves reflected from the substrate back to the interface, exerts a force which is directed against the bonding energy of coating to surface, depending on the amplitude and frequency. The effect of ultrasonic energy, in terms of its frequency, can thus be characterised as follows: higher frequencies act at defect

Table 7.4 Commonly used temperatures (±10°C) per thermal shock testing of some substrate–coating combinations (after ASTM).

Substrate	Coating						
	Cr, Ni, NiCr, Cu	Sn	Pb, SnPb	Zn	Au, Ag	Pd	Rh
Steel	250°C	150°C	150°C	150°C	250°C	350°C	185°C
Zinc alloys	150°C	150°C	150°C	150°C	150°C	150°C	150°C
Copper/Copper alloys	250°C	150°C	150°C	150°C	250°C	350°C	185°C
Aluminium/Al alloys	220°C	150°C	150°C	150°C	220°C	220°C	185°C

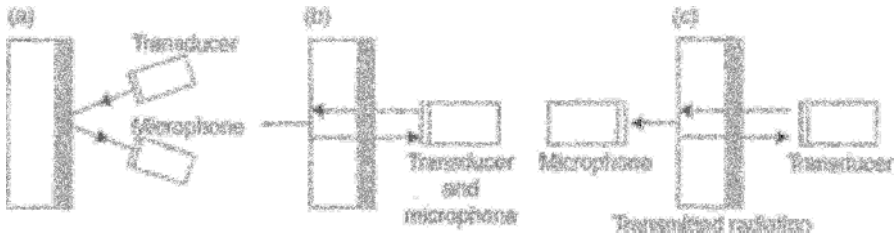

Figure 7.18 Non-destructive adhesion testing by ultrasonics: (a) reflection from the coating–substrate interface; (b) reflection from the rear-side; (c) transmitted radiation [13].

sites at the coating-substrate interface; lower frequencies create stress at the interface which can cause adhesion failure. From use of high and low frequencies, an overall assessment of adhesion can be made.

Thus, this one technique allows adhesion to be assessed at two different levels, localised and over an area as a whole. These approaches are known as reflection and transmission [13]. In the first case, the arrays shown in Fig. 7.18(a) or (b) are used, with the ultrasonic radiation being applied through the coating or from the rear, respectively. In the transmission mode (Fig. 7.18c), transducer and microphone are on opposite sides of the coated sample.

In the case of poorly adherent coatings, higher intensity signals are obtained, whereas for good adhesion, the sample behaves more as a single entity, most of the ultrasonic radiation being then absorbed in the substrate, with only a small percentage being reflected back. The same is true for radiation applied from the rear-side. In the case of poor or largely non-existent adhesion, measurements based on reflected signals are not possible, since these are too weak to reach the receiver. Use of the transmission method is significantly more difficult to carry out, since transmitted radiation intensity measurements are harder to measure, and the method is thus less sensitive than the reflected radiation approach.

7.4.3.3 Acoustic emission (AE) test

A characteristic of all previously described adhesion test methods is that they determine the extent to which adhesion does or does not exist, that is they report on the outcome of the coating process. The acoustic emission (AE), goes further, in that it sheds light on the processes involved in the actual detachment of coating from substrate. The basis of the method is that, as the coating separates from the substrate, energy is released in the form of acoustic waves, at ultrasonic frequencies. By analysing these emissions [18–20] the actual detachment process can be understood. A characteristic of such acoustic emissions is their very small amplitude, the wide range of frequencies over which they form, and the frequency band which they occupy.

AE is the term used to describe, pulsed, elastic pressure waves formed within a material when it is subjected to mechanical or thermal loading. The origin of these lies in stress relaxation processes which occur spontaneously when the material is subjected to loading. They can also be set up by displacements, twinning formation, cracking or delamination processes. The best-known example is the so-called

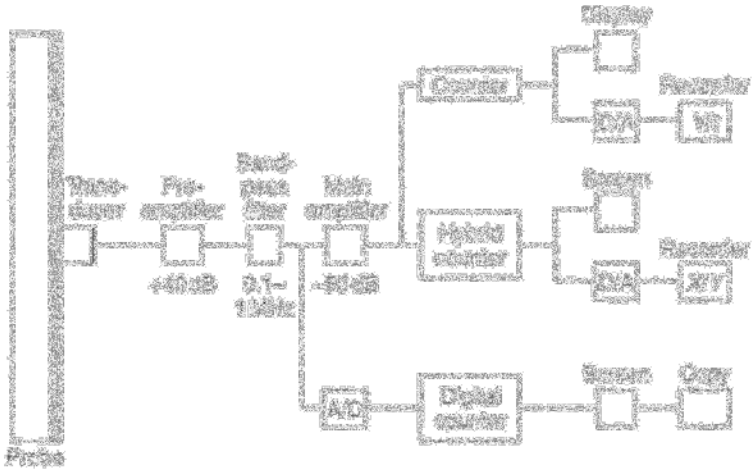

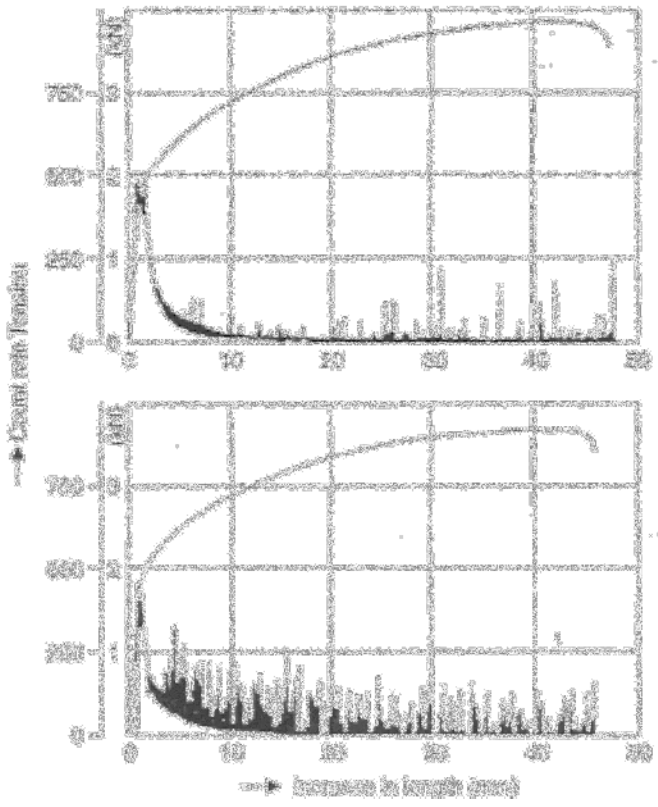

Figure 7.20 Stress–strain plot and acoustic emission recording of copper-plated samples using two different brighteners [20].

'tin-screech' which can be heard when a sample of pure tin is mechanically deformed, and is due to inter-crystalline effects.

Acoustic emission analysis is used to determine adhesion of metallic or non-metallic coatings to metallic substrates. Figure 7.19 shows a block diagram of the apparatus used.

The metal test sample is held in tension, and a stress–strain plot is recorded. At the same time, acoustic emissions are recorded using a piezo-electric microphone. The analog output of this is then subjected to signal processing, allowing the signal output to be characterised in terms of its frequency and amplitude.

The plot shown in Fig. 7.20 offers a comparison between two samples of copper plated onto a copper substrate, both from an acid electrolyte at 6 A/dm^2 but using different brighteners. The results show how use of different brighteners gives rise to different deposit structures, and these provide different values of adhesion and give rise to different acoustic emission 'signatures'.

References

[1] Hornbogen, E., *Werkstoffe*, Springer-Verlag, Berlin, 1973.

[2] Krajewski, W., Legierungsherstellung durch Diffusion in galvanisch abgeschiedenen Schichten, *Metalloberfläche* 37 (1983) 6, 251–255.

[3] Heymann, K., Riedel, W. and Wodt, G., Zur Theorie der Haftfestigkeit galvanischer Schichten auf ABS-Propfpolymerisaten in: *Metallische Überzüge auf Kunststoffen*, Carl Hanser Verlag, München: (1966), pp. 48–63.

[4] Sasse, H.P., Galvanisieren von Kunststoffen, in: *Praktische Galvanotechnik*, Eugen G. Leuze Verlag, Saulgau/Württ., 1984.

[5] Andreas, B., Galvanisieren von Kunststoffen, in: *Technologie der Galvanotechnik*, Eugen G. Leuze, Verlag Saulgau/Württ., 1996.

[6] Bischof, C. and Possart, W., *Adhäsion – Theoretische und experimentelle Grundlagen*, Akademie-Verlag, Berlin, 1983.

[7] Zabach, U., Kunststoffgalvanisierung zwischen Alchemie und Wissenschaft, in: *Fortschritte bei der Galvanisierung problematischer Grundstoffe*, 7. Ulmer Gespräch, Eugen G. Leuze Verlag, Saulgau/Württ., 1984.

[8] Springer, J. and Förster, F., Theorien zur Haftung stromlos abgeschiedener Metallschichten auf Polymeren, Teil I, *Metalloberfläche* 38 (1984) 11, 482–486.

[9] Schammler, G. and Springer, J., Chemische, physikalische und mechanische Bindungscharakteristiken bei stromlos beschichteten Substanzen, *Galvanotechnik* 80 (1989) 5, 1549–1554.

[10] Förster, F. and Springer, J., Theorien zur Haftung stromlos abgeschiedener Metallschichten auf Polymeren, Teil II, *Metalloberfläche* 40 (1986) 10, 417–421.

[11] Schammler, G. and Springer, J., Zur Haftung von Metall auf Nichtleitern, in: *Jahrbuch Oberflächentechnik*, Band 45, Metall-Verlag, Berlin, 1989.

[12] Kanani, N., Schichtprüfungen, in: *Technologie der Galvanotechnik*, herausgegeben von B. Gaida and K. Aßmann, Eugen G. Leuze Verlag, Saulgau/Württ., 1996.

[13] Simon, H. and Thoma, M., *Angewandte Oberflächentechnik für metal-lische Werkstoffe*, Carl Hanser Verlag, München, 1985.
[14] Nitsche, K., *Schichtmeßtechnik*, VEB Deutscher Verlag für Grundstoffindustrie, Leipzig, 1974.
[15] Biestek, T. and Sekowski, S., *Methoden zur Prüfung metallischer Überzüge*, Eugen G. Leuze Verlag, Saulgau/Württ., 1973.
[16] Dettner, H.W. and Elze, E. (Editors): *Handbuch der Galvanotechnik*, Band III, Carl Hanser Verlag, München, 1969.
[17] Kutzelnigg, A., *Die Prüfung metallischer Überzüge*, 2. Auflage, Eugen G. Leuze Verlag, Saulgau/Württ., 1965.
[18] Moslé, H.G. and Wellenkötter, B., Untersuchung des Schädigungsverhaltens beschichteter Bleche mit Hilfe der Schallemission, Teil 1, *Metalloberfläche* 33 (1979) 11, 513–516.
[19] Moslé, H.G. and Wellenkötter, B., Untersuchung des Schädigungsverhaltens beschichteter Bleche mit Hilfe der Schallemission, Teil 2, *Metalloberfläche* 34 (1980) 10, 425–429.
[20] Moslé, H.G., Schichtdicken- und Haftungsmessungen an beschichteten Werkstoffen, *Metalloberfläche* 35 (1981) 12, 473–478.

This Page Intentionally Left Blank

CHAPTER 8

Coating Thickness and its Measurement

8.1 Introduction

A measurement of the thickness of a deposited coating is possibly the most important single test to be carried out after the deposition. Sometimes, if the resulting thickness value is out of specification, further tests will become necessary. It is fair to state that if only a single test is carried out, then this would be a thickness determination.

Of thickness testing it can be said that sometimes, it is a mean value that is required. In other cases, however, it is the value at a particular location that becomes important. Such spot tests yield discrete values, not necessarily typical of the coating as a whole. However if a large enough number of such discrete local values are recorded, it becomes meaningful to use them to derive a mean thickness value. It is thus good practice, whatever the measurement method used, to make as many measurements as possible, not only over the surface of the component, but also more than once at each location. In many cases, there will be locations more prone to wear, and at these, above all, an adequate coating thickness is essential. Though the number of measurements recommended cannot in every case be prescribed, five measurements across the surface of the work, with five values at each location, is sometimes suggested as a guideline.

Because this parameter is so critical, an array of measurement methods has evolved over time, and only the most important are described here [1, 2]. Most such methods can be classified as destructive or non-destructive. In the former case, a distinction can be made between methods where only the coating is destroyed and those where the entire component is sacrificed. Figure 8.1 sets out the various methods.

Both destructive and non-destructive methods can be classified in terms of their underlying physical or chemical principles [2], as shown in Fig. 8.2, which makes no claim to completeness.

8.2 Destructive Processes

These methods have the advantage that on the whole, they can be carried out with relatively simple equipment. Against this, they can, by definition, only be used for random sampling. In spite of the large number of tests shown in Fig. 8.2, only some are described below.

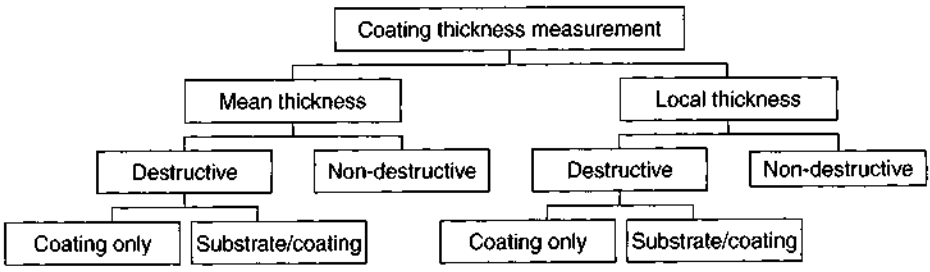

Figure 8.1 Techniques for thickness measurement of metallic coatings.

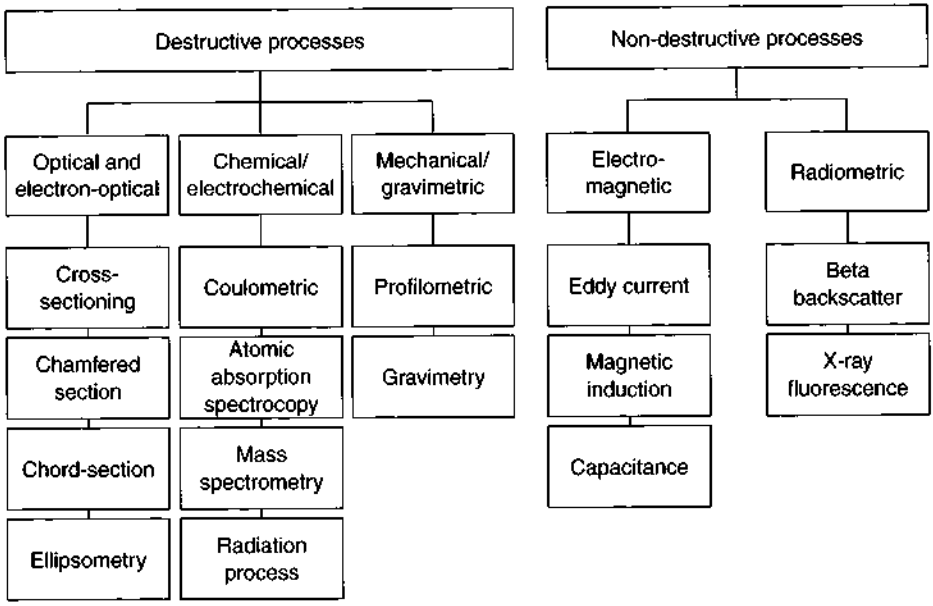

Figure 8.2 Destructive and non-destructive coating thickness measurement techniques and their underlying physical and chemical bases.

8.2.1 Microscopic Methods

Methods based on optical microscopy are not really suitable for coating less than 2 μm thick, owing to the limited resolution of the visible light microscope. By the term 'resolution' is meant the ability of the instrument to distinguish two points or narrow lines, close to and parallel to one another. A formula expressing resolution in terms of the wavelength of radiation used is as follows:

$$d = \frac{\lambda_L}{A} = \frac{\lambda_L}{n_B \sin \omega} \tag{8.1}$$

where d is the spacing between the two points or lines to be distinguished, n_B is the optical refractive index of the medium between the objective and the object viewed (normally this would be air) and ω is half the aperture angle of the objective, that is, the angle subtended by the two light rays emanating from a point object. For instrumental reasons, ω cannot exceed 72°. The expression $A = n_B \sin \omega$ denotes the numerical value of the aperture. For objectives used in air, it is 1.0, while for oil-immersion lenses, it can be up to 1.66. From Eq. (8.1), not only the optical resolution but also the image illumination can be determined. The highest resolutions are those obtained using the shortest wavelength, that is, λ_L is blue light with a wavelength of around 400 nm, while also maximising the refractive index n_B. From this, it follows that the highest possible resolution is found where $d = \lambda_L/A = 240$ nm, corresponding to a magnification of 1500×. Using white light (λ_L = approximately 500 nm), coating thicknesses of down to 0.5 μm can be resolved. However, thanks

to rounded edge effects, actual measurements are not feasible. Increasing the magnification reveals no additional details, since resolution is limited by the objective lens. Thus it is that even with the highest quality objective lens, a magnification of more than 500× to 1000× is pointless, and serves only to increase the image size of details previously visible, while not revealing greater detail. Thus it is that use of optical microscopy is of little use for films ≤2 μm, and at this level, an accuracy of some 10% might be expected.

For coating films ≤2 μm, electron-optical techniques are called for, such as the scanning electron microscope (SEM) (Fig. 8.3). In this instrument, electrons are used as the 'light source', these being emitted from a hot filament in a vacuum chamber. This so-called primary electron source is accelerated by application of a potential gradient, and then focused on the surface of the specimen. The so-called 4QBS electron detector captures the resulting image and enhances contrast. The electron velocity, after acceleration is given by the expression

$$v_E = \sqrt{\frac{2 \cdot e \cdot U}{m_E}} \tag{8.2a}$$

where $e = 1.602 \times 10^{-19}$ (A s) is the charge on the electron and the effective electron mass, m_E is given by:

$$\tag{8.2b}$$

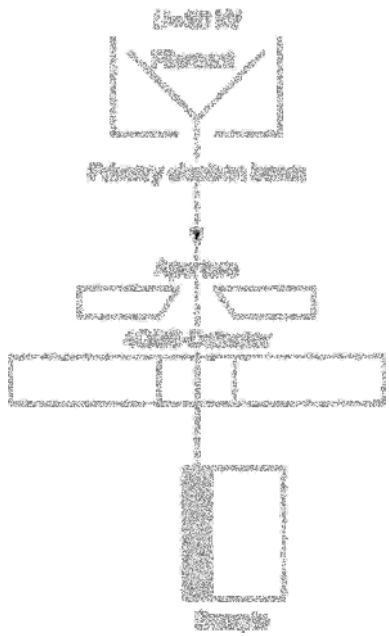

Figure 8.3 Electron-optical configuration of the scanning electron microscope for measurement on thin films.

where $m_o = 9.035 \times 10^{-28}$ (g) is the rest-mass of the electron, and c = velocity of light. According to De Broglie, a wavelength λ_E can then be assigned to an electron, and using Planck's constant, $h = 6.623 \times 10^{-34}$ (J s), the effective mass of the electron and its velocity can be linked by the equation:

$$\lambda_E = \frac{m}{m_E \cdot v_E} \tag{8.2c}$$

The relationship of electron wavelength and accelerating voltage U (V) is:

$$\lambda_E = \frac{1.225}{\sqrt{U}}[\text{nm}] \tag{8.2d}$$

This relationship is shown graphically in Fig. 8.4. From this, it can be seen that for an electron being accelerated through 100 kV, a wavelength value λ_E, of around 0.04 nm or around 0.4×10^{-4} μm can be assigned. This is some four orders of magnitude smaller than the wavelength of white light. Even using an accelerating voltage of 30 kV, as is the case in many instruments, provides an electron wavelength of $\lambda_E = 0.07$ nm. Using this approach drastically increases the useful magnification and resolution and is sufficient for accurate measurement of thin films. An example is shown in Fig. 8.5.

The sample shown is a brass substrate which was first copper plated, then plated with thin films of palladium–nickel and finally silver. In order to avoid distortion during metallographic sample preparation, a final, protective thick deposit of copper was electroplated. Examining the cross-section viewed under optical microscopy, it is

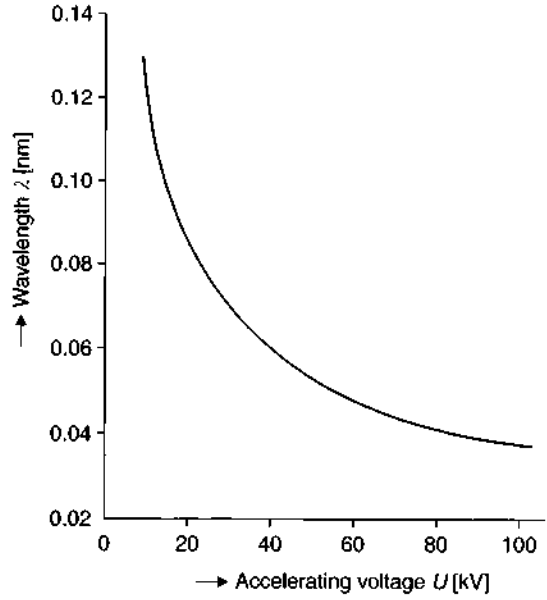

Figure 8.4 Dependence of wavelength of an electron on the accelerating voltage.

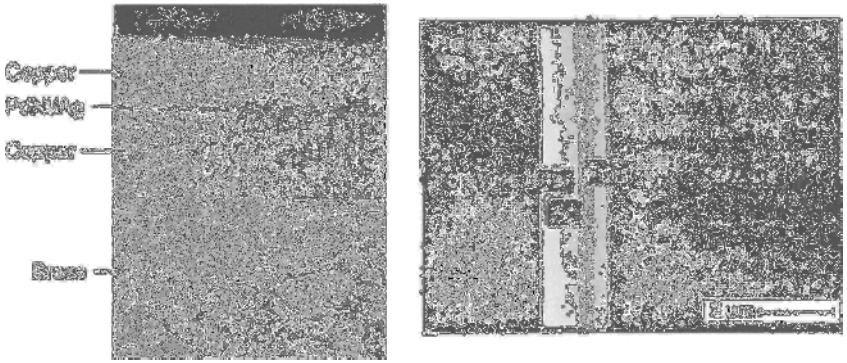

Figure 8.5 Determination of the thickness of thin films. Left: optical microscope cross-section. Right SEM image (d_{Ag} = 0.9 µm, d_{NiPd} = 0.8 µm).

seen that the two thin layers of Pd–Ni and Ag cannot, because of their extreme thinness, be distinguished. The image shows only a single narrow stripe. Use of higher magnifications brings no benefits. Only using an SEM with a voltage of at least 20 kV can the two layers be resolved and quantified. In this case, the respective thicknesses of PdNi and Ag were 0.9 and 0.8 µm.

8.2.1.1 Sample preparation

Microscopic methods for thickness estimation are extremely valuable, especially when the coating is applied over a smooth surface. The approach not only allows thickness to be gauged at a specific location, but gives a (localised) overview of the coating in general, and the extent of its uniformity. The drawback is that sample preparation is somewhat tedious, involving the following steps [3–7]

- taking a sample from a representative location on the work;
- embedding the sample in a suitable potting resin;
- grinding, then polishing (mechanically or electrolytically) the mounted specimen;
- cleaning and etching (chemically or physically) the face of the specimen, and enhancing the contrast for optimum viewing under the microscope.

Figure 8.6 shows these various steps and (insert) a cross-section of a printed circuit board.

Selecting the area from which the sample is taken is critical. Users should bear in mind that if the sample is taken from an unrepresentative area, many misconceptions will follow, not only as to the thickness but perhaps also structure and defects such as cracks.

In order to prevent mechanical damage to the mounted sample during grinding and polishing (when, for example, plastic flow of metal or brittle fracture of a coating could arise) and to retain sharp edges and interfaces, it is common practice to electroplate or electrolessly plate a metal over the top of the sample, to a depth of not

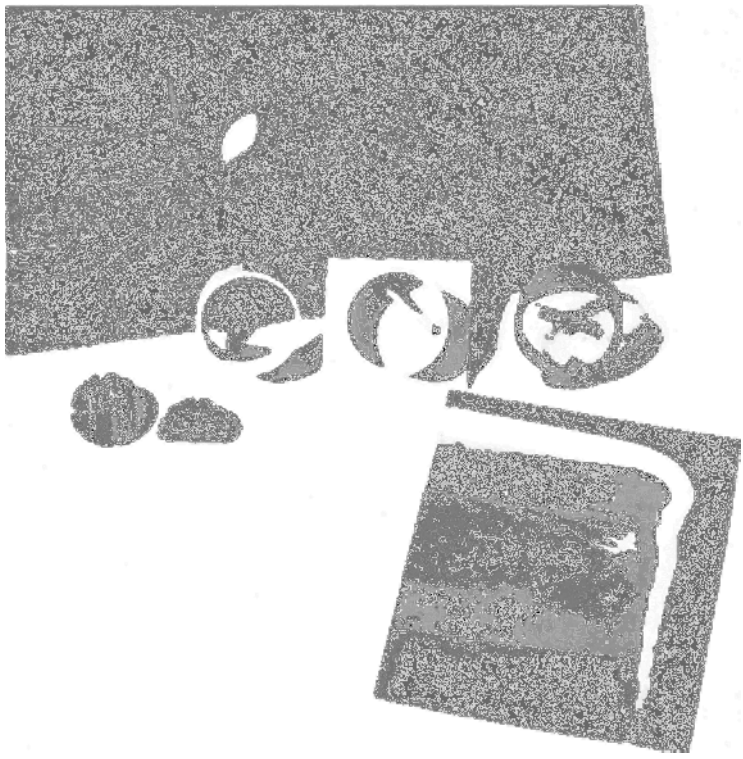

Figure 8.6 Taking of a sample, mounting and embedding in resin and preparation of mounted sample, from a printed circuit board.

less than 5–10 μm. For examination of coatings of tin, silver or zinc, a copper over-plate is ideal. For copper films, a nickel over-plate is recommended.

It should be noted at this point, in respect of the above and what follows, that the methodology described is known as 'metallography' and as such is a long-established procedure, widely used in every laboratory where metals and materials are studied. Specialist companies exist who provide the equipment and materials used, and numerous books are available, exclusively devoted to this technique.

The mounting or 'potting' resin should possess various attributes, such as being room temperature curable and doing so without excessive dimensional changes. Some resins are coloured, others are transparent. The latter offer the advantage that the sample can be viewed from the rear. The subsequent mechanical grinding and polishing are likewise established techniques, widely used by metallurgists and materials scientists. Rotating wheel machines are widely used, and abrasive papers of progressively finer grade are attached in turn to these wheels. The abrasive papers may be based on corundum, silicon carbide or emery (alumina with 15–30% ferric oxide). The process is often carried out under water-wetted conditions. The sample can be hand-held or machine-mounted, and in either case, is subjected to systematic rotation. The surfaces are scratched, with scratches of the size of the abrasive grains

on the paper. The point is then reached where no further polishing takes place, and a finer grade of abrasive is then used.

After working through ever-finer grades of abrasive, the sample is further polished on a wheel covered with felt, baize or chamois leather. These surfaces are lubricated with polishing medium which is an aqueous suspension of a very finely divided and mild abrasive, such as alumina, magnesia, jeweller's rouge or diamond dust, the latter usually as a paste, with particle size $\leq 0.2\ \mu m$. The final stage is copious rinsing with distilled water and drying in air. Rinsing is also crucial between each of the many stages noted above, since if coarser abrasive is carried over to the next stage, the object of moving to finer grade will be defeated. Use of a soft brush or cotton wool tipped stem may be advisable. Use of an ultrasonic cleaning tank is strongly recommended as the final stages are reached. This is an effective means of removing trapped abrasive particles from cracks or micro-pores in the sample as also the interface between sample and mounting resin. In the case of the softest metals, there is a possibility that abrasive particles become embedded in the metal itself. Ultrasonic action, which should be used for 10–30 s, will often remove such embedded particles also.

A further effect which must be borne in mind, is that work-hardening will take place at the outer side of the specimen. This consists of two layers. The outermost is the so-called Beilby layer, which is very thin and often amorphous. Beneath this is a strongly cold-worked crystalline layer which separates the Beilby layer from the unmodified bulk of the substrate (or applied coating). A schematic representation is shown in Fig. 8.7.

A characteristic of the cold-worked zone, which obscures the actual coating structure, is that it often exhibits quite different properties, on account of its strongly

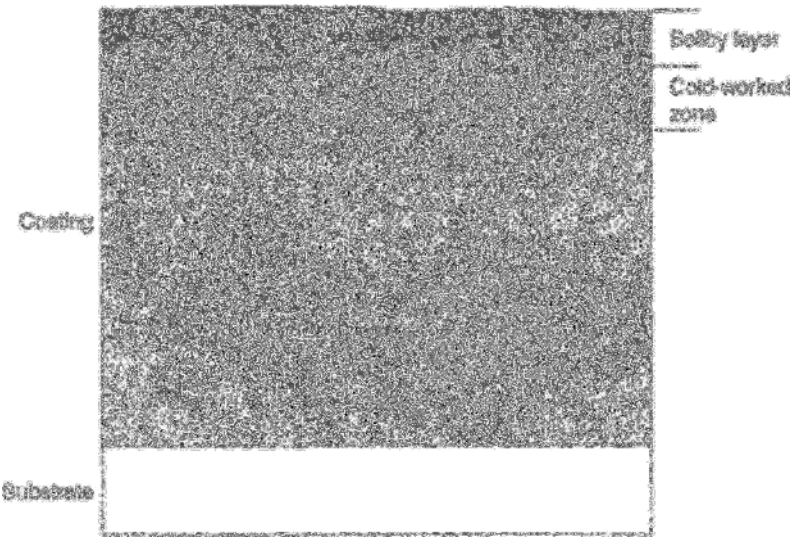

Figure 8.7 Formation of surface layers during grinding and polishing of the surface (Beilby layer and cold-worked zone).

distorted structure with high dislocation density and internal stress, as well as including impurities from the grinding and polishing process which, by their presence, can modify the properties of the coating. Successive etching and polishing will remove much of such cold-working zones, but some may well remain.

In order to obtain a truly unblemished and defect-free surface, electropolishing is normally used. Since this involves no mechanical action, effects due to plastic deformation are avoided. In addition, and in contrast to mechanical processes, no significant temperature increase of the sample takes place. Electropolishing, using equipment sketched in Fig. 8.8 requires little time and gives good reproducibility.

The electropolishing electrolyte is held in a glass vessel with water-cooling jacket. A thermometer and stirrer are shown. The test sample is made anodic, the cathode is a suitably corrosion-resistant material such as stainless steel or a noble metal. Current is controlled with a variable resistor. A levelling action takes place in which peaks and other protrusions are removed in preference to metal along the baseline. The process can be understood in terms of the idealised current–voltage plot shown in Fig. 8.9.

As the voltage is increased, so does the current along the section AB and this reflects an anodic dissolution (or etching) at the sample surface. At point B, a passive film begins to form at the surface, causing the current to drop, along BC. In spite of increasing the voltage between C and D, there is no increase in current, thanks to the barrier effect of the passive layer. It is in this region that the electropolishing effect

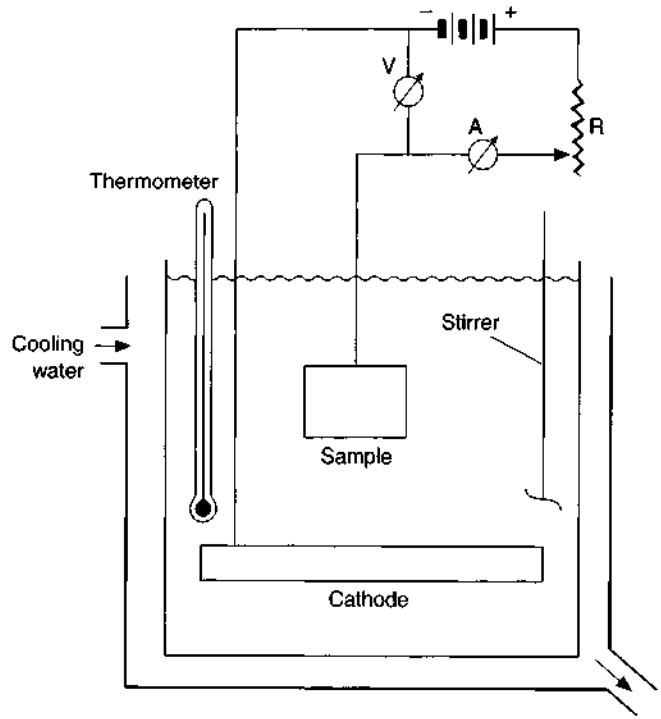

Figure 8.8 Experimental apparatus for electropolishing of metallic surfaces [3].

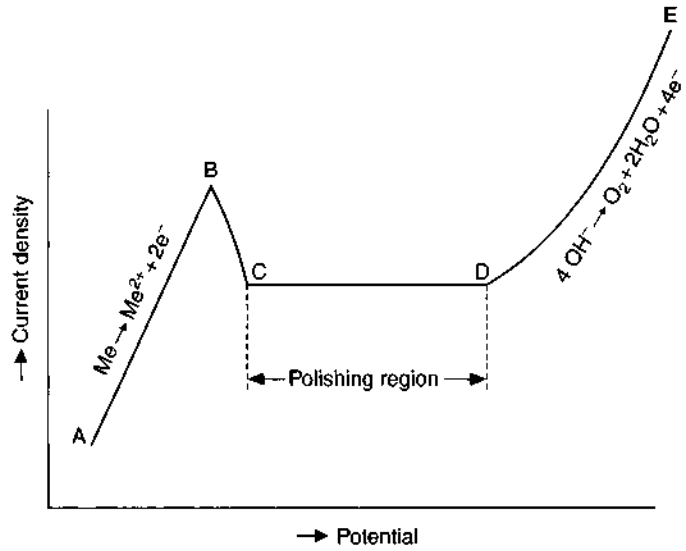

Figure 8.9 Idealised current–voltage plot in electropolishing [3].

takes place. As the voltage is further increased from D onwards, one enters the so-called transpassive region and the current again increases, in part at least due to oxygen evolution, which interferes with the levelling mechanism. The rate of the polishing action is primarily determined by the ratio of anode:cathode areas and the separation of these two electrodes.

The key to successful electropolishing is:

- use of the correct electrolyte,
- setting the correct temperature,
- setting the correct cell voltage.

Bearing in mind the wide range of material to be electropolished and the electrochemical behaviour of substrate and coating, determining the optimum electrolyte is not always straightforward. Likewise, the cell voltage determines not only the current but also the nature of the anodic dissolution process and thus the surface topography.

One drawback of electropolishing is that, in some cases, preferential attack can take place at the edges of the sample, and this makes more difficult, an accurate thickness measurement. Moreover, it has to be noted that the process is not ideal for use with coarse-grained metals. Finally, one should mention problems in dealing with alloys having strongly-defined heterogeneity, that is, multi-phase. Here, as one might expect, preferential dissolution can arise – one, perhaps less noble, phase being selectively dissolved in preference to others. In this case, a form of tampon electropolishing has proved useful, in which electrolytic and mechanical actions are combined [3, 4].

Polishing alone, whether mechanical or electrolytic, will usually result in a very smooth, highly reflective surface, from which little useful information can be gleaned. It is thus customary to follow this with an etching operation. This is known as 'metallographic etching' and is a laboratory process, not to be confused with industrial-scale etching. While the latter is intended for selective metal removal, the laboratory process acts to reveal the structure and different phases of a metal sample with or without coating(s). Metallographic etching methods include purely chemical and also electro-etch processes.

The mechanisms need not concern us here, but there are numerous compilations listing the etching solution composition and conditions of use, for most metals and alloys. Suffice to say that local galvanic couples can form at a sample surface, while structural features such as dislocations and grain boundaries can also result in differential dissolution rates and so reveal themselves. The etching action is often characterised as grain-etching or grain boundary etching.

Grain boundary etching rests on the fact that the crystalline structure is strongly distorted at these locations, in addition to which metallic and non-metallic impurities tend to segregate there. As a result, grain boundaries are usually more strongly attacked than the grains themselves. As a result, the grain boundaries become trenched. Viewed under an optical microscope, normally incident light is diffusely reflected from these trenches, which thus appear darker than the surrounding grain areas.

Etching of the grain surface usually involves a simple anodic dissolution process which takes place at different rates at the various types of grain surface. Depending on the nature and extent of this dissolution, the different grains will have a different appearance under the microscope, thereby appearing as lighter or darker areas.

Etchants can be acidic, basic or neutral solutions. The composition of a few of the most useful for metallographic etching of cross-sections, is shown in Table 8.1, but in fact there are hundreds of suggested formulations. The etch time can vary from a

Table 8.1 Chemical composition of some metallographic etching solutions used at room temperature.

Coating	Substrate	Composition
Cr (hart)	Steel	10 g NaOH[1] + 9.0 ml H_2O 20 s
Cu	Steel, epoxy	10 ml H_2O + 10 ml conc. NH_4OH + 1 ml H_2O_2 5–10 s wipe-etch
Cu	Steel, epoxy	100 g/l Cr(VI)-acid + 100 g/l conc. H_2SO_4 1–3 s wipe-etch
Ni	Copper and alloys	50 ml nitric acid + 50 ml glacial acetic acid 5–6 s
NiP	Steel	17 ml H_2O + 65 ml nitric acid + 18 ml glacial acetic acid 5–6 s
Sn	Steel, Copper and alloys	1 g crystalline ammonium persulfate $(NH_4)_2S_2O_2$ + 1000 ml dist. H_2O
Zn	Steel	200 g chromic acid anhydrous CrO_3 + 1000 ml H_2O
Zn/Zn–Fe	Steel	10 ml H_2O + 10 ml conc. NH_4OH + 1 ml H_2O_2 1–3 s wipe-etch

[1]Electrolytic polishing (high-grade steel as cathode).

few seconds upwards, and is terminated by rinsing with distilled water, then alcohol after which the sample is carefully dried.

Some etch processes which have proved themselves extremely useful, use a physical process to enhance the surface contrast. One such is the use of cathodic sputtering, in which an extremely thin film is deposited on the surface, so causing interference effects. The equipment for this is sketched in Fig. 8.10. As shown, the metallographically prepared sample is locked into the sputter chamber, electrically connected as an anode. Facing it, is the cathode, typically iron. A voltage of some 2 kV is applied, and oxygen introduced into the chamber. After a very short time, a very thin interference film of iron oxide forms, of thickness ≈50 nm, at the sample surface.

The process can be monitored, to ensure the desired contrast, by using the microscope shown in Fig. 8.10, and by systematic variation of the key parameters (voltage, duration, oxygen, type of cathode used), a range of interference colours can be formed, which make readily visible under a microscope, the metallographic features. The basis of this approach is that light incident at the interface between sample and evaporated layer undergoes multiple reflections, which work to increase the contrast. A special advantage of the method is that it is immune to problems which are found in aqueous etching, where the different electrochemical potentials of adjacent phases or features result in undesired etch effects. In addition, the process is inherently a clean one, and the samples so coated are ready for use without further treatment. The cross-sections shown in Fig. 8.11 show the strengths of this method. They show a glass-fibre reinforced epoxy-resin, which has been copper plated. At places, contact between copper and substrate is defective and only after coating with the interference film does this become clearly visible.

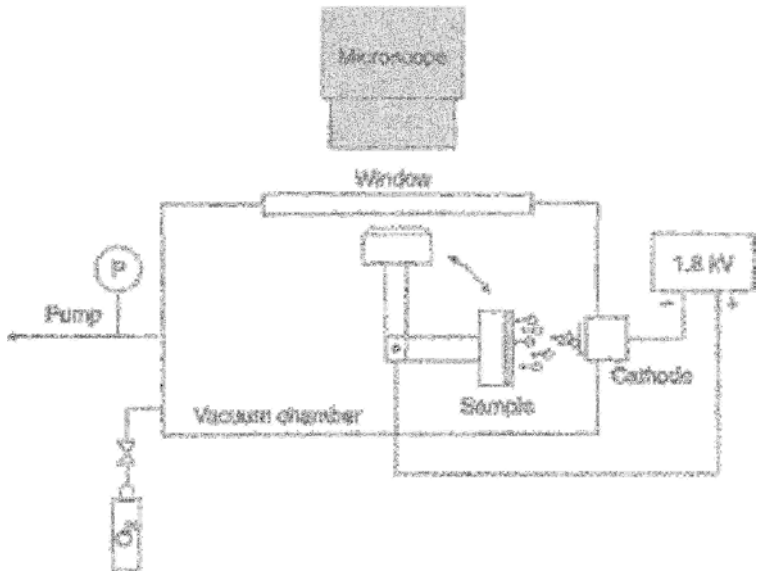

Figure 8.10 Schematic of an evaporation unit for forming interference films on the surface of a metallographic section.

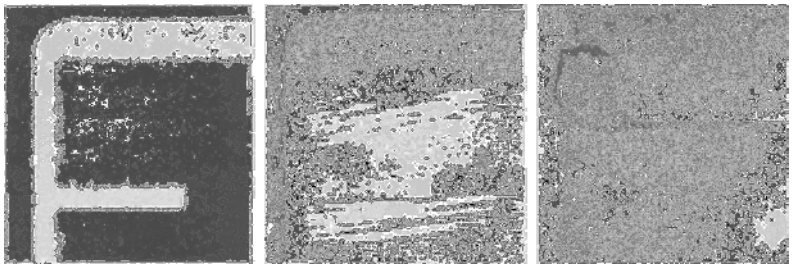

Figure 8.11 Optical microscope images of a multilayer printed circuit board in cross-section with (left) and without (centre) an evaporated interference coating. Defective contacting, right.

8.2.1.2 Types of metallographic section

In preparation of samples for viewing under the optical microscope, three types of section are usually considered. These are the direct cross-section, the oblique section and the chordal section. The first of these is the immediately obvious one, a simple 'slicing' and will not be further discussed. The last two, which will be considered in detail, are a means of 'magnifying' the thickness of a coating, thereby increasing the scope of the optical microscope method.

8.2.1.2.1 Oblique sectioning method

Where the primary purpose is to measure coating thickness, oblique sectioning can give more accurate results, especially for films at the lower limit of useability of the optical microscope. The method is also useful for study of multilayers and alloy deposits. Rather than 'slicing' the sample at right angles to the plane of the coating ($\alpha = 90°$), the sample is 'sliced' at an angle, which can be quite small ($\alpha = 2°$). Figure 8.12 shows such a sample at this very small angle. As will be appreciated, by doing this, the dimension of the thickness becomes the greater, the more oblique the section angle. From simple trigonometry, this is expressed as:

$$d = d' \sin \alpha \tag{8.3}$$

where d is true film thickness and d' the apparent thickness. Table 8.2 lists some values for this equation illustrating the benefits ('magnification' = $d':d$)) of the method at various values of α.

The sectioning procedure is shown in Fig. 8.13. The sample, a coated substrate, is propped-up at a predetermined angle, embedding in mounting resin and then ground and polished along the line AB. Care must be taken that the support which props-up the sample, remains firmly in place. Table 8.2 shows the benefits of this technique. Thus, at an angle $\alpha = 2°17'$, an apparent 25 times magnification (= d') is found. It has been found that in practice, an angle of around this value yields the best results.

The accuracy of this method depends on the precision with which α can be measured. An error $\Delta\alpha \pm 0.5'$ will result in a 1% error in measured thickness [6], and from this, an idea as to the necessary precision of the sectioning can be gathered.

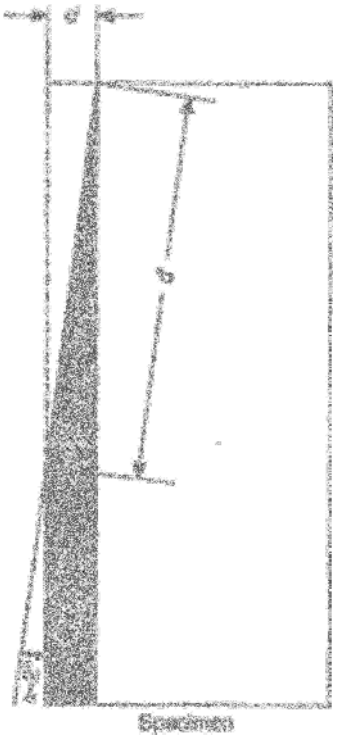

Figure 8.12 Oblique section; d = true thickness; d′ = apparent thickness.

Table 8.2 Apparent increase in coating thickness as a function of the angle of section.

Sectioning angle α	sin α	Advantage d′:d
30° 00′	0.50	2:1
11° 32′	0.20	5:1
5° 44′	0.10	10:1
3° 50′	0.07	15:1
2° 52′	0.05	20:1
2° 17′	0.04	25:1

There are two methods for setting and determining the sectioning angle α. The first, involves carefully selecting the height of the prop used in mounting and embedding the sample (Fig. 8.13), which then (if the mounted specimen is presented at right-angles to the grinding surface) determines the section angle. The second approach is to measure the length of the oblique section after polishing [8]. For this, the mounting resin must be transparent and of known refractive index, n_B. The sample is then viewed under the microscope, as shown in Fig. 8.14, initially at right

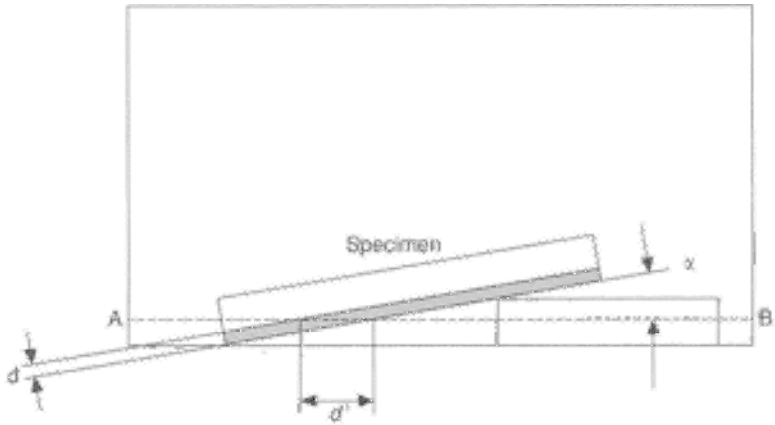

Figure 8.13 Preparation of an obliquely-sectioned specimen for mechanical grinding and polishing along the line AB. α = angle of section.

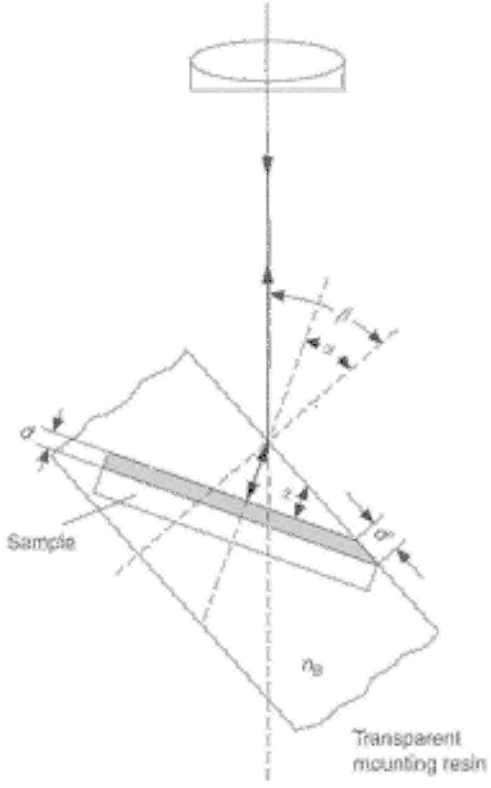

Figure 8.14 Optical microscope used to determine the angle of oblique sectioning, using a transparent mounting resin of known refractive index n_B [8].

angles to the optical axis, and then at a tilted angle such that, viewed through the mounting resin, the sample surface shows maximum brightness. The true film thickness d, and the apparent thickness, d' and the angle of tilt, β, are then related as:

$$d = d' \sin \alpha = d' \sin \beta / n_B \tag{8.4}$$

The error of measurement of angle in this procedure is around $\pm 0.5°$.

In spite of these two methods, it has to be recognised that the accurate determination of α remains a problem and constitutes a drawback of the oblique sectioning method. In addition, the method only a limited microscope magnification to be used, thereby further restricting the resolution achievable. The precision of the oblique sectioning method is thus limited not only by the state of the surface, but also the accuracy of the microscope.

8.2.1.2.2 Chordal sectioning method

This method of sectioning is best understood in visual terms, as shown in Fig. 8.15. Using a grinding disc or grinding burr, a radial or chordal section is cut through the coating and down to the substrate until at least a portion of the latter is visible. The grinding wheel should be mounted on precision bearings, and by 200 mm diameter, 12 mm wide, and of the finest available grade of abrasive.

The grinding disc is applied to the sample with constant downward pressure, the sample being firmly held in position. Since it is difficult to judge precisely the point at which one has ground down to the substrate surface (Fig. 8.15, left), it is usual to end up with the situation shown in Fig. 8.15 (right). Coating thickness is then calculated using the geometry of Fig. 8.16.

This uses a microscope to measure the length of the chord S_2 cut into the coating surface, and S_1 as length of the chord for the substrate; R is the radius of the grinding disk; The following expression is then obtained:

$$d = d_2 - d_1 = \sqrt{R^2 - \left(\frac{S_2}{2}\right)^2} - \sqrt{R^2 - \left(\frac{S_1}{2}\right)^2} \tag{8.5}$$

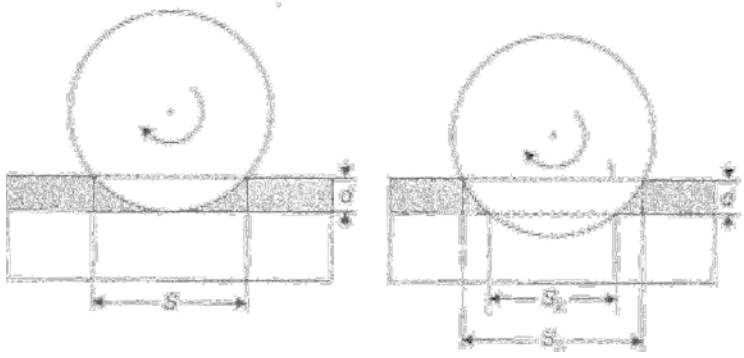

Figure 8.15 Preparation of a chordal section using a rotary grinding disk; left, cut through to substrate surface. Right: cut into the substrate itself.

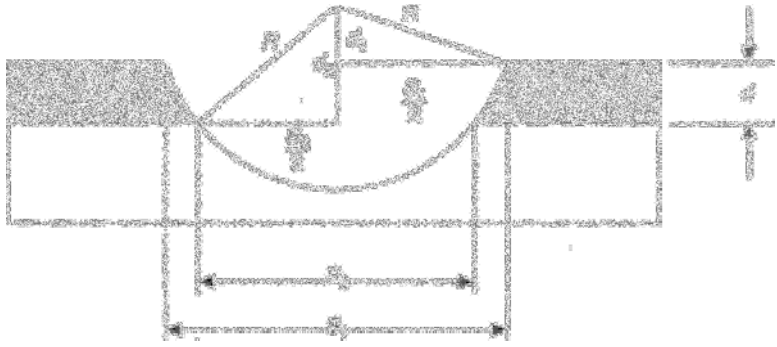

Figure 8.16 Calculation of true coating thickness d, derived from the geometry of the chords formed by grinding.

The accuracy of this method depends mainly on the precision with which the two chord lengths are measured. A drawback of the method, however, lies in the fact that one cannot, as with the preceding methods, improve the sample quality by subsequent polishing. However, a physical or chemical etch treatment can be used to enhance the visual contrast between substrate and coating metals.

The use of this method is recommended where multi-layer coatings are being studied, and where the built-up and thickness of several layers is called for.

A more accurate thickness measurement which is also less time-consuming can be undertaken using a radial section [10] obtained with a grinding ball. A steel ball, typically 6–10 mm in diameter is rotated at 100–1500 rps, a continuous, stepless pressure being applied. Abrasive is simultaneously applied, such as alumina or diamond paste, with grain size 0.25–7 μm. This is distributed over the polishing ball, usually as a slurry with suitable diluent. The foregoing and other parameters are modified as required, bearing in mind the mechanical properties of the coating metal. Finally, with the geometry of the cup-shaped recess in mind, as shown in Fig. 8.17, of diameter D_K, and the apparent coating thickness, d', measurements are made using an optical microscope, the results being interpreted from the equation:

$$d = \frac{(D_K - d')d'}{2R} \tag{8.6}$$

giving the coating thickness d [10].

Given that the angle subtended by the ground section lies in the range 1–2°, magnification factors of 20–60 can be obtained, implying that the method can be used, in the most favourable case, to measure coatings as thin as 0.05 μm. However in this method, as in the preceding case, it is not possible to enhance the section by subsequent polishing.

Figure 8.18 is a graphic representation of measurement errors expected from oblique and radial sectioning methods. Data for rectangular sliced sectioning is also shown.

The graph is based on an assumed optical resolution of 0.5 μm and also assumed is the fact that in practice, such measurements are rarely better than ±3%.

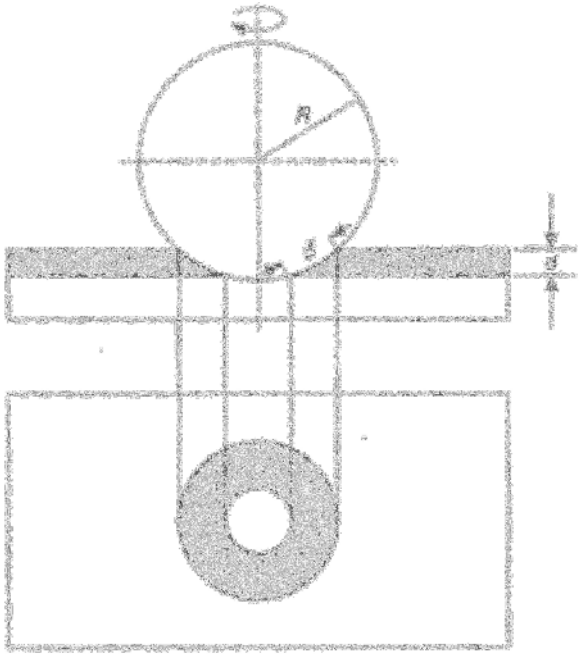

Figure 8.17 Preparation of a radial section using a rotating grinding ball

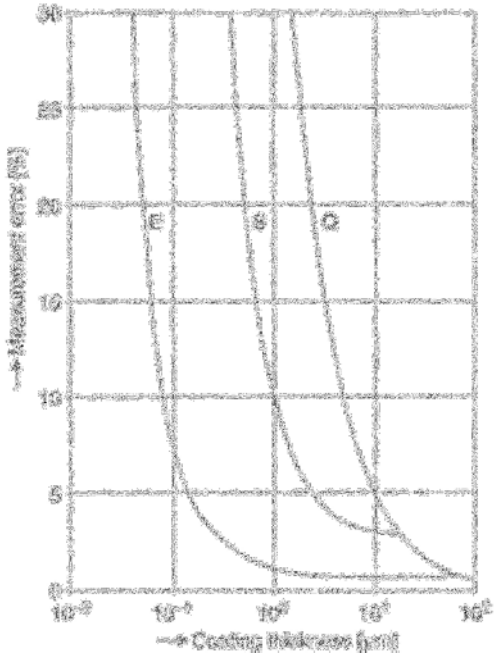

Figure 8.18 Measurement errors as function of coating thickness for different sectioning techniques. Q: simple section; S: oblique section (5× advantage); E: radial sectioning (ball grinding) [8].

The sketch indicates that for coatings >15 μm thick, a normal sectioning (Q) is sufficiently accurate. For thicker films, this method is in fact more accurate than oblique sectioning (S) in which errors due to the need to measure the angle are inherent. Finally, the figure indicates that the radial sectioning method (E), incorporates the fewest errors. Bearing in mind the limit of optical microscope accuracies, in the case of the cup-shaped depression, errors of ≈1% should be assumed. If measurement deviations of ±25% are seen as the highest acceptable limit, the following minimum measurable film thicknesses are found for the three techniques.

- 2 μm for normal sectioning,
- 0.5 μm for oblique sectioning with five-fold advantage,
- 0.05 μm for radial sectioning with 20–60-fold advantage.

8.2.2 Coulometric Methods

This method of coating thickness measurement is based on the reverse of electrodeposition, namely anodic dissolution. Thus the electrical charge required to remove the coating is measured, and using Faraday's Law, the charge is translated into the mass of metal removed [11–13]. On a historical note, it might be mentioned that the method has its roots in an older, superficially similar method. In the BNF jet test, a corroding solution was applied, drop-by-drop, to the coated surface, and the time taken, or the number of drops required, to dissolve away the coating and reveal the substrate, indicated the thickness. However, not only was ambient temperature an important, but uncontrolled parameter in affecting the dissolution rate, but the endpoint detection was also imprecise. The jet test is never used today, but is worth noting as the precursor of the coulometric method. Second, it is worth noting that the coulometric method, though not an electroanalytical technique, shares a key feature, which is that currents, including very small currents, and elapsed times, can both be extremely accurately measured. This is the reason why electroanalytical techniques are capable of very high sensitivities, and the coulometric thickness method shares this advantage.

The equipment is shown in Fig. 8.19. A cylindrical reservoir, usually open-topped, is applied to the surface to be tested. A rubber O-ring makes a liquid-tight seal to the surface. The metal test sample is made anodic, and a cathode is mounted inside the cylindrical reservoir. In most cases, this is made of plastic. In some models, it is made of metal and at the same time is itself the cathode. Provision is also made for agitation of the electrolyte in the reservoir either by mechanical agitation or by using oscillating liquid flow. This ensures that there is no local depletion of electrolyte at the sample surface. The sample surface should be cleaned and degreased, and any passive oxide layer removed, before a measurement, and more than one measurement may be made to provide mean thickness values. After the test, a small circular patch remains where the coating has been dissolved away. Whether this means that the sample is then unusable, or needs re-plating, has to be decided. Once the current has been applied, using a constant current supply, a voltage versus time trace such as that shown in Fig. 8.19(b) is obtained. The sharp elbow on the right of the diagram denotes where the coating metal has completely dissolved away, and the potential is

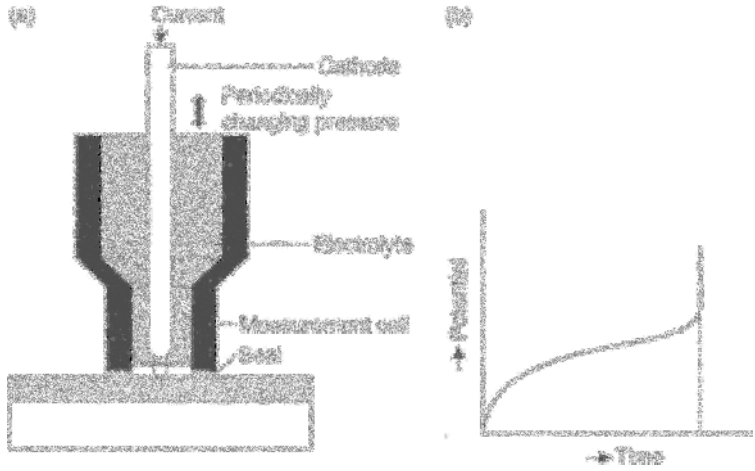

Figure 8.19 Coating thickness measurement by the coulometric technique [11]: (a) sketch of apparatus for anodic coating dissolution; (b) potential–time plot reflecting the anodic dissolution process.

now determined by the newly exposed substrate. In some cases, this will result in a lower potential (if a less noble metal is exposed) but in almost all cases, a sharp change in potential is observed.

The composition of electrolyte used is critical, and usually specific to the coating-substrate combination. It should be so chosen that no dissolution occurs at open circuit, before the current is applied. The accuracy of the result depends on the precision with which the area of the test procedure is known. Typically, this is 1.5–3.2 mm in diameter. Application of excess pressure to the test cell may distort the O-ring and so modify the test area. While any of the coating material remains, it will tend to dictate the potential which will approximate to a plateau, as seen in Fig. 8.19(b), and breathrough to the substrate is marked by a potential jump. In all but the simplest instruments, this potential jump triggers the timer circuit which records total elapsed time, and switches off the current. The instrument then displays elapsed time, or total charge, and in modern instruments, afford a direct reading of thickness, once the information as to the coating metal has been entered. The electrochemical cell, which constitutes the apparatus, may be a two-electrode cell, where the counter-electrode has a large surface area, such as platinised platinum. In this case, the polarisation will be negligible, and change in polarisation during the experiment, even less so. In some instruments, the so-called three-electrode system is used, where there is a reference electrode which is not polarised, and where the potential is recorded with a high impedance circuit.

The coating thickness d (μm) is then given from the dissolution current I (A), duration t (h) using the following equation:

$$d = 10^4 \cdot \frac{A \cdot I \cdot t \cdot \eta}{\rho \cdot F} \tag{8.7}$$

where A is the electrochemical equivalent (atomic weight × valency/26.8) (g/Ah); η the efficiency, that is, actual amount of metal dissolved/theoretical; ρ the density of the coating material and F the test area.

Ensuring a truly constant current, though this is critical, is not usually a problem, while an anodic dissolution efficiency <100% can be troublesome, though efficiencies close to 100% are achieved in most cases, if solution and current density are correctly chosen. The density factor, ρ, raises an interesting point. Many electrodeposited metals have a density significantly less than the accepted value for their massive metal analogues. There are only two solutions to this. Either one measures or at least estimates the density (the literature has numerous values for most electrodeposited metals) or one ignores the issue, and expresses the outcome of the measurement as mass/unit area rather than linear thickness. Apart from distortion of the sealing O-ring and lack of precise definition of the test area, the presence or formation of gas bubbles at the test surface is the most common source of measurement error, and can be avoided by electrolyte agitation or oscillatory movement.

The coulometric thickness method can, in many cases, be used to measure the individual thicknesses of more than one layer, as well as alloys or intermetallic formed at the interface between substrate and a coating. In these cases, a series of plateaus at successively higher overpotentials will be observed, since each layer has its own characteristic potential. Examples of multilayer systems amenable to this approach include duplex nickel (semi-bright and bright), or Cu/Ni–Cr over steel. The method can be used to examine small components which might not lend themselves to other techniques, and can be used to determine thickness values in the range 0.5–50 μm. For coatings ≥50 μm, the accuracy falls off and may be unacceptable. While the accuracy of the method under laboratory conditions is around ±2–3%, a figure of ±4–8% is more realistic for shop-floor use [12]. Instrument manufacturers have developed a range of cells which allow measurements even on curved surfaces. It might also be noted that while many commercial instruments incorporate one or more voltage triggers, for study of multilayer or otherwise more complex systems, an oscilloscope read-out can provide insights which might otherwise be lost.

Films of contaminating species or corrosion layers which restrict access of electrolyte can interfere with measurements, while excessively rough surfaces will also cause problems. It is suggested that mean substrate roughness values (Ra) be ≤0.5 [12].

Conceptually simple though it is, the coulometric method can be time consuming, and for thicker coatings, requires fresh solution to be used. Table 8.3 sets out some widely encountered substrate–coating combinations which lend themselves to use of the method. For the composition of test solutions laid down in the ISO specification, see Table 8.4.

Finally, it might be noted that the coulometric thickness measurement technique has two 'cousins'. Both use the same coulometric and potentiometric principles, and both are known by acronyms. The STEP (simultaneous thickness and electrode potential) makes use of the fact (referred to above) that in multilayer systems, each layer has its own characteristic potential, and is specially used to determine the thickness of duplex nickel coatings. The more recently developed SERA (sequential electrochemical reduction analysis) technique (though the concept is some 70 years

Table 8.3 Substrate–coating combinations for which the coulometric thickness method can be used (EN ISO 2177).

Coating	Substrate							
	Aluminium	Copper and alloys	Nickel	Nickel–Cobalt–Iron	Silver	Steel	Zinc	Non-metallic
Lead	●	●	●	●	●	●		●
Cadmium	●	●	●			●		●
Chromium	●	●	●			●		●
Copper	●	(1)	●			●	●	●
Nickel	●	●		●		●		●
Nickel[2]	●	●	●	●		●		●
Silver	●	●	●			●		●
Zinc	●	●	●			●		●
Tin	●	●	●			●		●
Tin–Lead	●	●	●	●		●		●

[1]Only on copper substrates.
[2]Electroless Ni–P layers, where P concentration is within permitted limits.

Table 8.4 ISO test solutions for coulometric thickness testing [1].

Coating	Substrate				
	Iron	Copper/copper alloys	Nickel	Aluminium	Zinc
Cadmium	A1, B1	A1, B1	A1	A1	
Chromium	A2, B2	A3, B3	A2, B4	A2, B4	
Copper	A4, B5		A4, B6	A4	B7
Lead	B8	B8	B8		
Nickel	A5, B9	A5, B10		A5, B9	
Silver	A6	A7, B11	A6		
Tin	A3, B12	A3, B12	A3	A2, B13	
Zinc	A8, B14	A8, B14	A8	A8	

A1	100 g/l KJ + 0.1 g J_2	
A2	100 g/l Na_2SO_4	
A3	150 g/l NaOH	
A4	80 g $NaK_4H_4O_6$ + 100 g NH_4NO_3/l	
A5	30 g NH_4NO_3 + 30 g NaCNS/l	
A6	100 g $NaNO_3$ + 5 g HNO_3/l	
A7	180 g/l KCNS	
A8	100 g/l NaCl	
B1	30 g KCl + 30 g NH_4Cl/l	
B2	186 g H_3PO_4 + 10 g CrO_3/l	
B3	100 g/l Na_2CO_3	
B4	98 g/l H_3PO_4	
B5	800 g NH_4NO_3 + 10 ml NH_4OH/l	
B6	100 g K_2SO_4 + 20 ml H_3PO_4/l	
B7	30% H_2SiF_6	
B8	200 g CH_3COONa + 200 g CH_3COONH_4/l	
B9	800 g NH_4NO_3 + 3.8 g $(NH_2)_2CS$/l	
B10	42 g/l NCl	
B11	100 g/l KF	
B12	100 g H_2SO_4 + 5 g KF/l	
B13	100 g/l KCl	
B14	100 g/l NaCl	

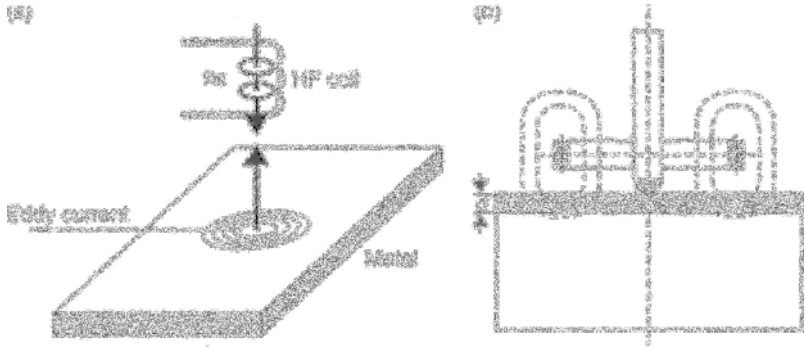

Figure 8.20 Coating thickness measurement using the eddy current method [13, 14]: (a) formation of induced eddy currents in the metallic sample; (b) thickness measurement using a probe.

old) can be used to determine the quantity of oxide layer present on a surface. Both techniques use circuitry and a cell similar to that described above.

8.3 Non-Destructive Methods

Perhaps the main advantage of non-destructive test methods is that, because they do not damage the sample being tested, not only is the cost of making good such damage avoided, but one is able to test much larger numbers, so bringing greater confidence to the results obtained. It also makes possible quality control in real time, for example, when large numbers of small parts are being coated. These methods are all based on physical properties of the materials involved, whether it be atomic number, electrical conductivity or magnetic permeability. In the case of methods based on magnetic properties, it is of course important to know whether substrate and/or coating are ferromagnetic or non-magnetic, or whether electrically conducting or non-conducting species are involved.

As might be guessed, the greater the differences in physical property of coating and substrate, the easier it is to carry out thickness measurements and vice versa. There are too many different methods in use to permit a comprehensive survey, and those that are described below are the most widely used.

8.3.1 Eddy Current Method

The eddy current method is one of the most versatile of the non-destructive techniques, being based on the following physical principle [13–16]. If a small coil is brought close to an electrically conducting surface, while a high frequency current is passed through it (Fig. 8.20a), a circular closed-loop eddy current is induced in the sample, which gives rise to a reverse-coupling in the HF coil. The induced eddy currents are oriented in such a way that they cause the electromagnetic field from the HF coil to weaken. This alters the inductance and effective resistance of the HF coil.

The extent of the weakening depends on the distance between the high-frequency (HF) coil and the substrate. Where this is coated, bringing the coil closer to the surface results in a feedback effect on the primary current in the HF coil, which is a function of the coating thickness [14]. The magnitude of the induced eddy current is, for a given frequency, also a function of the coating thickness and by this means, can be used to measure its thickness. Thus, an electrical signal is created when the electrical conductivities of coating and substrate are different, which is proportional to coating thickness. The coating thickness d can be derived from the following expression:

$$d = \frac{500}{\sqrt{k \cdot f \cdot \sigma \cdot \mu}} \text{ [mm]} \tag{8.8}$$

where k is a constant specific to a given coating metal, f is the frequency (Hz), σ the electrical conductivity (mS/m) and μ is the relative magnetic permeability of the coating metal. Using the appropriate circuitry, the instrument will give a direct read-out of thickness. Figure 8.20(b) is a schematic representation of the instrument.

In making actual measurements, the following points should be borne in mind. Prior to use, the instrument should be calibrated using standards as close as possible to the substrate–coating combination to be measured. Second, measurements should not be made too close to the edge of either plated surface or the sample itself, since eddy current patterns may be distorted here. Most probes today have a diameter of some 2 mm and the electrical measurement field extends to perhaps 3 mm around the centre of the probe. The induced eddy currents, while they form primarily in the near-surface region (so-called skin effect), must not be shielded from the substrate, if a valid measurement is to be made, and factors such as these determine where the probe may or may not be positioned for a valid reading. It follows that in addition to requiring that the sample is electrically conductive, there is also a minimum substrate thickness requirement. In line with this, the method cannot be used to measure the thickness of a metal coating over a thin metal sheet substrate. This restriction can, however, be circumvented by placing the metal sheet over a thicker piece of the same metal, which hopefully simulates thick substrate requirement noted above.

The eddy-current method can also be used to measure thickness of electrically non-conducting or non-ferromagnetic samples on non-ferromagnetic substrates. Likewise, it can be used for measurement of non-ferromagnetic coatings over electrically non-conducting or ferromagnetic substrates. The conditions for satisfactory use of the eddy-current technique are set out in Table 8.5. Here μ_r is the permeability value and σ denotes electrical conductivity. The index 1 denotes the coating material, index 2 the substrate.

The table indicates that optionally, the permeability value of both materials should be 1. The implication is that the eddy current method is specially suited to non-magnetic materials. Good results will be found where the electrical conductivity of the coating material is 0, while the substrate has good electrical conductivity. The method can also be used for metal coatings over metal substrates, providing the two have significantly different electrical conductivity values. This condition can be expressed as $\sigma_1 : \sigma_2 \leq 1:3$ or $\sigma_1 : \sigma_2 \geq 3:1$. The method cannot be used when electrical conductivities of substrate and coating are almost identical [16].

Table 8.5 Conditions for use of the eddy current technique [16].

Optimum conditions	$\mu_{r1} = 1, \sigma_1 = 0$ $\mu_{r2} = 1, \sigma_2 \gg 0$
Can be satisfactorily used	$\mu_{r1} = 1, \sigma_1 < \sigma_2$
Use is permitted	$\mu_{r2} = 1, \sigma_2 < \sigma_1$ $\sigma_1{:}\sigma_2 \leq 1{:}3; \sigma_1{:}\sigma_2 \geq 3$
Cannot be used	$\sigma_1 \approx \sigma_2$
μ_r: permeability value σ: electrical conductivity	Index 1: coating Index 2: substrate

Table 8.6 Effect of various factors on thickness values obtained from eddy current measurements [16].

Parameter	Effect
Distance from edge	Operates up to ca. 3 mm
Substrate thickness	$d_{min} = f(f, \sigma)$ where f = probe supply frequency σ = electrical conductivity
Surface curvature	No effect at large radius. Small radii require calibration on Similarly curved surface. Procedure then as on flat surface
Surface roughness	Rough substrate, levelling deposit. A simulated coating of approx. same thickness can be used with calibration or calculation to give correct readings
Angle of probe	Calibration based on 90° positioned probe. Up to 20° deviation from this is acceptable. Above this, erroneously large thickness values obtained
Interlayers	Electrically conductive interlayers ($\mu_r = 1$) are treated as new substrate. After recalibration, no problems
Coating conductivity	Can affect results; where film conductivity is due to loading with conductive particles or where coating conductivity changes, recalibration required
Extraneous magnetic or electric fields	No effect since instrument uses tuned amplifier

Other parameters which can affect the measurement are noted in Table 8.6. From this, it is seen that by means of appropriate calibration methods, many potentially adverse factors can be taken into account. Use of comparison samples of similar materials and geometry, forms a part of this strategy, especially when the calibrations are based on such reference samples [16].

The eddy current method is an ideal technique when several hundred individual measurements are to be made across the surface of a single sample, in order to provide the most complete picture possible as to coating thickness uniformity. An example of this might be the testing of copper-clad laminated epoxy resin boards, as used in printed circuit manufacture. Bearing in mind the requirements of such boards, the technique is ideal to highlight any variations in electrical conductivity, whatever these may be due to. In addition, the method can be used to monitor the thickness of subsequently electrodeposited copper. In practice, use of manually obtained measurements would be quite impractical and the eddy current method lends itself well

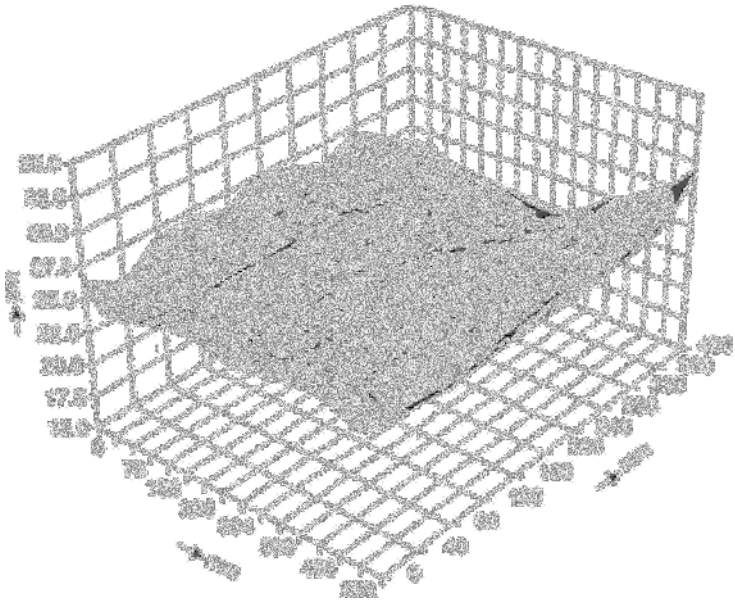

Figure 8.21 Thickness measurements of electroplated copper over an epoxy resin substrate, as measured with an automated scanning eddy current probe.

to various forms of automated operation under computer control. Thus, a routine can be set up in which thickness measurements are reported as an array across the length and breadth of a board, and large numbers of such measurements can be made within a few minutes. The data can then be stored for presentation in two- or three-dimensional format, where any values outside pre-set limits are highlighted in colour on-screen. Figure 8.21 shows an example of such a thickness distribution, based on 150 individual measurements over the surface of a 540×400 mm^2 board. The dark area denotes values outside permitted limits.

The sensitivity of the method can be indicated by the following observation. When measuring the thickness of a copper deposit, a different reading is obtained depending on whether the measurement is made immediately after deposition, or at some later time or after heat-treatment, with a thickness increase being determined in the latter cases. The histograms in Fig. 8.22 show this. In order to bring out this more clearly, the measured thicknesses have been normalised to a value of 25 μm, obtained from micro-sectioning methods.

As the figure shows, the thickness values, as measured by the eddy current method, increases with time in storage. Heat-treatment for 2 h at 140°C has the same effect. The cause of this, on the face of it somewhat surprising, effect, can be explained in terms of changes in the deposit structure, as described in earlier chapters. In the as-deposited state, the copper deposit includes numerous lattice defects, such as vacancies, interstitial atoms and dislocations, all of which adversely affect the electrical conductivity as compare with a relatively defect-free copper sample. Any process which reduces the number of defects will thus improve the conductivity.

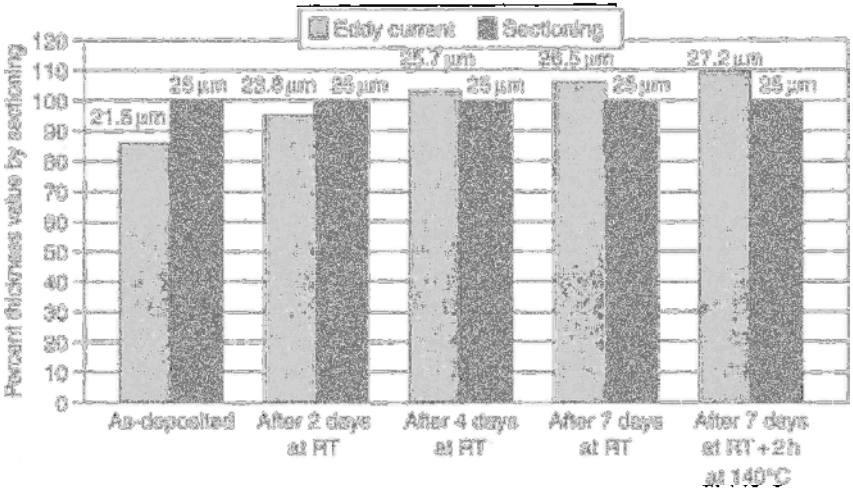

Figure 8.22 Thickness measurements on electrodeposited copper layer as function of storage time or heat-treatment, using the eddy current method.

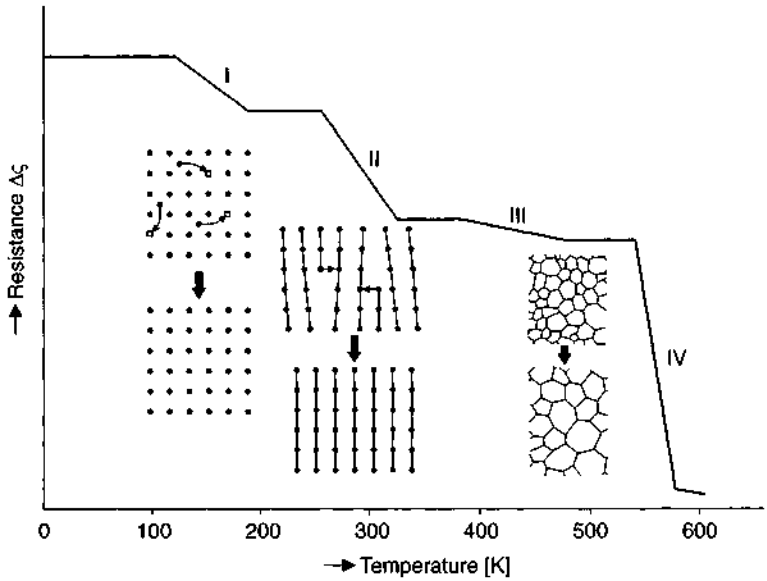

Figure 8.23 Step-wise decrease in electrical resistivity of copper as a function of temperature with associated changes in crystal lattice and structure which contribute to this.

All defects such as those listed above, do have a tendency to heal, at a rate which increases with temperature above absolute zero and up to the melting point, at which point structure disappears. Figure 8.23 depicts in idealised form, the decrease in resistivity with temperature.

Commenting on this graph, the first relatively steep decrease in resistance found at low temperatures (Step 1), is attributed to recombination of so-called Frenkel

pairs. In this, diffusion of twinning atoms into vacant sites results in a healing process and elimination of point defects. Migration and healing of double-vacancies and aggregations of vacancies may also be involved. Step II involves the interaction of dislocations with edges, etc., and gives rise to a further decrease in resistance. This results in a decrease in the number of step-dislocations within an individual copper crystallite. The causes underlying Step III are not clear. However the final steep decline shown in Step IV is attributed to primary recrystallisation, resulting in a significant decrease in dislocation density. This is accompanied by an increase in the mean size of the copper crystallites and ordering in terms of orientation. The result is a reduced number of grain boundaries.

Of interest, in terms of the above description of changes taking place in electrodeposited copper, is the phenomenon known as 'age-softening'. If the hardness of electrodeposited copper is measured, the value for a given sample will progressively decrease over a period of a week or so, after deposition, and this is well-recorded in the literature, though in the past, it has confused those making such measurements.

Further studies confirm the effects of room-temperature storage or brief heating at elevated temperature, and also indicate that heating results in the expulsion of hydrogen, present in the metal as a result of its co-deposition, and this leads to further reduction of resistance. In that thickness values reported using the eddy current method depend on electrical conductivity of substrate and coating, effects such as those described above should be borne in mind when using this otherwise excellent and reliable method.

8.3.2 X-ray Fluorescence Techniques

Fluorescence is, in general, the term used to describe emission of light (or sometimes other wavelengths) when a material is irradiated with electromagnetic radiation. Atoms in the material are promoted to an excited state, which gives rise to such radiation, which is quantized and usually at a somewhat longer wavelength (lower energy) than the exciting radiation. In this particular case, the exciting radiation is in the X-ray band, where energies are some 5000 times greater than those found in the visible region, and of wavelengths 10^{-6}–10^{-10} cm. If an X-ray photon strikes an electron in the atomic nucleus of the material being studied, energy is transferred to that electron, allowing it to escape from the nucleus. The resulting vacancy is spontaneously occupied by another, more energetic electron, which hops into the vacancy from a higher electron shell. Such electronic interactions are shown in Fig. 8.24(a).

The energy differences between the individual electron shells are specific to each type of atom. The energy released by the process described above, manifests itself as X-ray emissions and has a characteristic wavelength for a given atom. It is usual to refer to K_α- or K_β-radiation when the electrons are expelled from the K-shell, and replaced with electrons from the L- or M-shells. In the same way, a distinction is made between L_α- or L_β-radiation when an electron is expelled from the L-shell of the nucleus, with the resulting vacancy being filled with electrons from the M- or N-shells.

In the case of coated substrates, characteristic emissions are produced both from substrate and coating. These can be captured using an energy-dispersive detector,

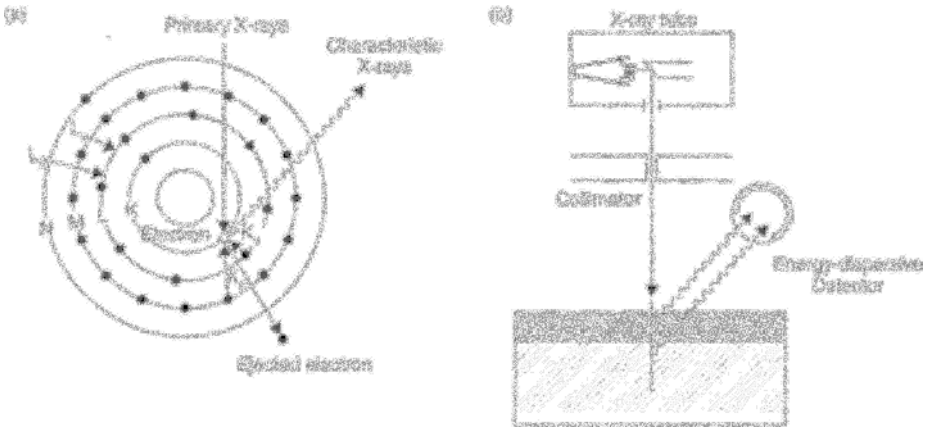

Figure 8.24 Coating thickness measurement by X-ray fluorescence (XRF): (a) interactions between primary X-ray radiation and electrons; (b) apparatus used (schematic).

which records them separately. Provided the exciting radiation is of constant intensity, the emitted radiation is proportional to coating thickness. The technique thus operates as follows: the radiation intensity from a coating of known thickness is measured and compared with the sample being tested [17–20]. In principle, there are two main approaches, the emission and the transmission modes.

In the emission mode, the radiation emerging is taken as a measure of coating thickness. In the transmission method, the emission from the substrate is used. The former method is more widely used, and this is schematically shown in Fig. 8.24(b). The sample is irradiated with collimated X-rays, which is focussed on a given spot. This causes ionisation of the material, that is, radiation of characteristic wavelength is emitted from both substrate and coating and this is received by the energy-dispersive detector. Using appropriate electronic circuitry, the emissions from the coating can be selectively recorded. The size of the detection area is of order 0.2 mm, so that thickness values can be obtained on even the very smallest of samples.

Here, the following points should be noted.

The energy of emitted radiation is a characteristic of the atomic number of the element being irradiated, the higher this is, the greater the energy of such emissions. In line with this rule, emissions from atoms of atomic number <20 are so weak that they are largely absorbed within the sample itself. The signal strength picked up by the detector is little greater than the background noise level. Emissions from elements of atomic number >50, by contrast, are so energetic that they tend to pass right through the detector without eliciting a response. For elements of atomic number <50 and >20, the emitted signals can be processed with no problems. It might be noted that in the characteristic K-radiation, 80% lies in the K_α-region, 20% in the K_β-region. In the case of the L-band radiation, the respective proportions of L_α- and L_β- are 50–50%. Thus, if one wishes to determine thickness of a silver (at. no. = 47) coating over nickel (at. no. = 28), AgK radiation is used for silver thickness measurement. For elements with atomic numbers between 70 and 90, their

characteristic L-radiations are used. So, for measuring gold (at. no. = 79) film thickness on a nickel substrate, AuL radiation is used.

For elements adjacent to one another in the Periodic Table, for example, nickel and copper, the energy difference of their respective emitted radiations is minimal. The discrimination of the energy-dispersive detector is then barely adequate to allow these two elements to be distinguished from one another, and in measurement of the emissions from nickel-coated copper, using the emission method, radiation from both elements is captured and recorded, thereby degrading the measurement accuracy. If the substrate is a copper alloy, such as brass, rather than pure copper, the emissions from the copper atoms are weaker than for pure Cu, on account of interaction between the Cu and Zn atoms, and a different value will be obtained for a nickel coating of unchanged thickness. This illustrates how substrate effects can influence coating thickness measurements. Use of suitable band-pass filters can assist in overcoming this problem.

Thickness values obtained by XRF are largely independent of the physical and structural state of the coating, but far more affected by its chemical composition, and this fact is vital when dealing with alloy coatings. The classic example here is the measurement of tin–lead (solder) coatings of different compositions. This behaviour will be discussed in terms of Fig. 8.25.

Over a copper substrate, an initial layer of nickel, 3 μm thick, is deposited, over which is formed an 8 μm lead–tin coating (Fig. 8.25a). Irradiation with X-rays results in emissions which, as a result of interactions by this composite system, are as shown by the arrows. The processes taking place during such irradiation can be summarized as follows:

In the measurement area, the characteristic K-radiation of tin (at. no. 50) and L-radiation of lead (at. no. 82) are generated. The characteristic nickel signal from the substrate, also produced, is partly absorbed by the tin–lead. The remainder is captured by the detector and can be resolved there. The large energy difference between the radiations from tin and lead allow (as the figure shows), complete discrimination from one another and so permit a determination of each species.

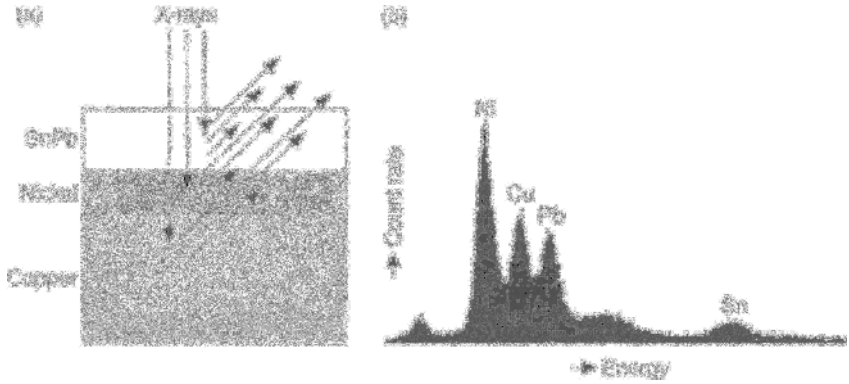

Figure 8.25 XRF thickness and composition determinations of a lead–tin coating: (a) interactions between the primary radiation and the individual layers; (b) energy spectrum.

However depending as to whether the Pb- or Sn-radiation is used as a measure of deposit thickness, different values will be obtained. The reason for this is that the radiation emission intensity from one element is affected by the presence of the other. The characteristic emissions from, for example, the tin atoms, can lead to additional ionisation from the lead atoms. The consequence is that, given the actual composition of the deposit, the tin emissions are lower, and those from lead higher, than one might otherwise expect. In this case, the characteristic radiation from the tin was used to determine thickness and alloy composition. Results from three measurement points gave a thickness value of 7.89 ± 0.33 μm. The tin concentration was found to be $71.3 \pm 0.75\%$. The energy spectrum for this is shown in Fig. 8.25(b) where the various elemental peaks can be seen.

The extent to which mutual interaction of the component elements occurs, depends on the ratio of their concentrations and for this reason, in working with alloy coatings, the two issues of thickness and composition are usually taken together. Typically, accuracies of 0.5–1 wt% are acceptable and for binary alloys this is achievable without undue difficulty, provided the characteristic radiations emitted from the two species can be resolved from one another.

In cases where there is an interlayer between the substrate and the outer coating, for example to improve adhesion or to act as a solid-state diffusion barrier, the thickness of this too, can be determined by XRF, on the basis that the characteristic radiations from the three materials, substrate, coating and interlayer can, in most cases, be resolved by the detector.

A further example is shown in Fig. 8.26, which relates to an examination of a cellphone casing made of ABS, over which a triple-layer copper/nickel/chromium coating has been applied. The function of the copper layer (≈5 μm) is to provide a high level of EMI/RFI screening (shielding) for the device. The nickel layer (≈0.5 μm) serves to protect the softer underlying copper layer. The outer chromium layer (≈0.25 μm) is purely decorative. Because this is so very thin, it presents quite a challenge to the measurement technique.

In cases such as these, the following calibration requirements are called for: coating of the same material of known thickness over an interlayer of sufficient thickness, as well as a sample of interlayer coated substrate, where interlayer thickness is

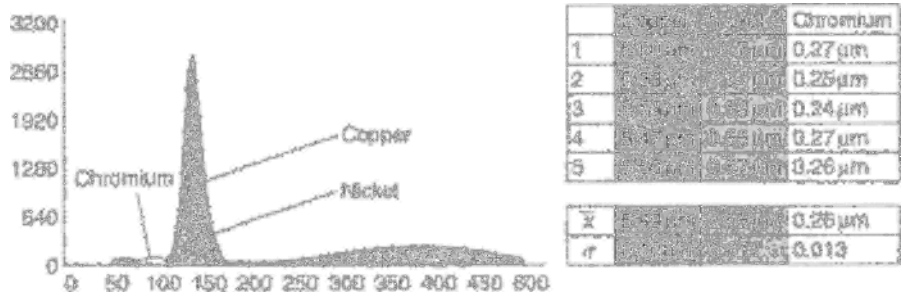

Figure 8.26 Results of a thickness determination of a triple-layer metallised copper/nickel/chromium coating over ABS plastic: (a) spectrum; (b) thickness measurement (courtesy Messrs Roentgen Analytik Messtechnik GmbH).

Table 8.7 XRF thickness measurements for single and multilayer coatings over a range of substrates (courtesy Helmut Fischer GmbH + Co).

Substrate	Coating															
	Ag	Al	Au	Cd	Cr	Cu	Ni	NiZn	Pb	Pd	PdNi	Rh	Sn	SnPb	TiN	Zn
Bronze	●	●	●		●	●	●		●	●	●	●	●	●	●	●
Iron	●	●	●	●	●	●	●	●	●	●			●			●
Epoxy	●					●	●			●						●
Kovar	●	●	●		●	●	●		●	●	●		●	●		●
Copper	●	●	●		●		●		●	●	●	●	●	●		●
Brass	●	●	●		●	●	●		●	●	●	●	●	●		●
Nickel	●	●	●		●	●			●	●	●	●	●	●		
Ceramic oxide	●		●			●	●			●						
Palladium/nickel			●													
Silver		●	●		●	●	●			●		●	●	●		
Tungsten carbide															●	

known and substrate thickness is adequate. Calibration in this case would be based on the pure metals copper, nickel and chromium and the substrate ABS.

The spectra obtained for the individual elements, Cu, Ni, Cr are shown in Fig. 8.26(a) and are used to derive the thickness values of the individual layers. Because copper and nickel possess almost identical energy spectra, the direct analytical discrimination of these two elements is not really possible, although this can be achieved using a special mathematical procedure. The results are listed in tabular form (Fig. 8.26b).

Table 8.7 illustrates how XRF can be used not only with single coatings but also multilayer types, over a range of substrates.

8.3.2.1 Continuous coating thickness measurement

XRF technique is a powerful tool for contactless, non-destructive thickness measurement, affording excellent accuracy and flexibility, and able to handle a wide range of substrate/coating combinations. A further strength of the method is that it can be used for real-time measurements on continuous plating lines, that is, not with test pieces but on the actual strip, etc., being plated [21, 22]. In this type of plant, noble metals or alloys are continuously plated over massive substrates, along the line of their travel through the tanks. Continuous thickness measurements of gold, palladium, silver, nickel, tin and tin–lead coatings on strip or wire is increasingly important. Such coated strip or wire is, for example, widely used in electronics and electrical equipment. Figure 8.27 shows a simplified sketch of such an operation.

In this sketch, it is seen that the measurement head for the thickness determination is positioned directly in the finishing line. The primary X-ray radiation is focused on the work surface, while a detector captures the emitted secondary radiation. A programmable adjustment of the head in the Z-axis is included so that the primary X-rays can be focused at will on the gold or tin–lead layers. In the latter case, both thickness and alloy composition can be determined.

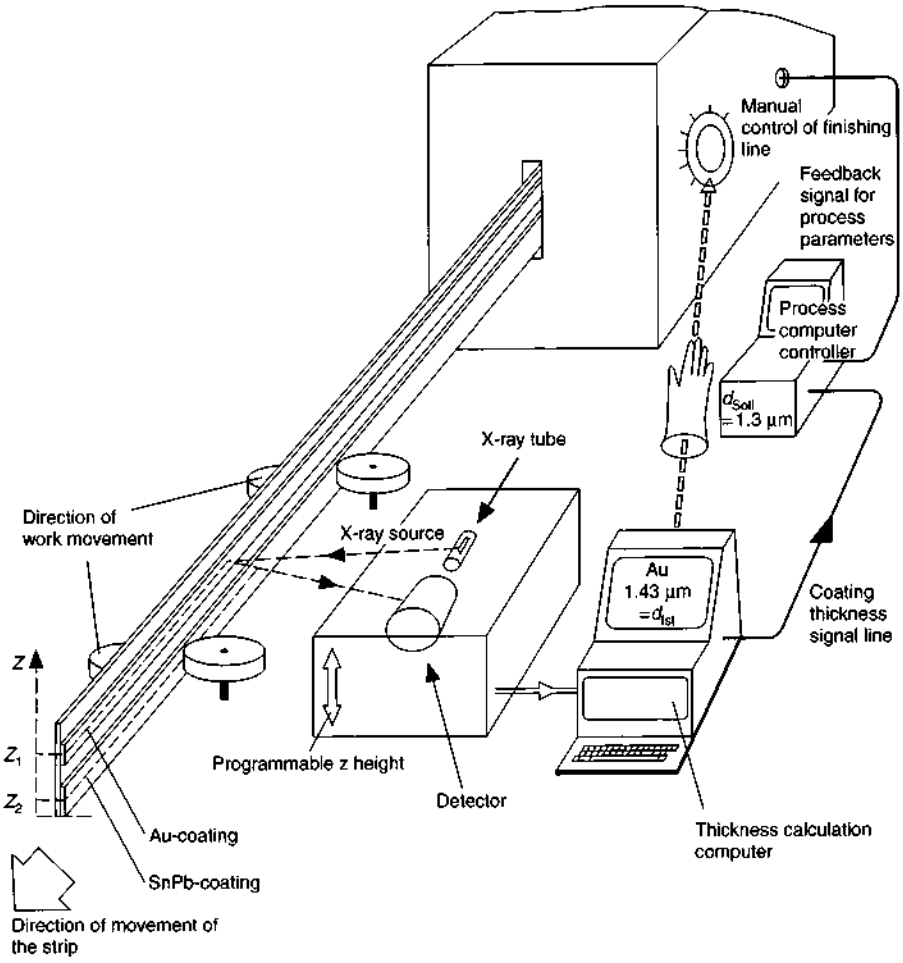

Figure 8.27 Continuous thickness measurement of selectively coated noble metal and alloy deposits on the production line using XRF [21].

Examples of the use of XRF methods for continuous thickness measurements on duplex or alloy coatings are shown in Table 8.8.

8.3.2.2 Standards-free coating thickness measurement

As further demands are made on the performance of electroplated coatings, more complex multilayer systems are devised and introduced in practice. An example is the coating of brass sanitaryware taps. Over the brass, is deposited a pure nickel coating, then palladium–nickel, followed by a top coating of ruthenium. To maintain consistent product quality, accurate thickness control of these layers is essential.

When investigating the properties of newly developed multilayer systems, not least their thickness, reliable standards are essential for calibrating the instrument used. What is understood by this term is a reference sample, in respect of which all

Table 8.8 Examples of the use of XRF for continuous on-line thickness measurements on multilayer or alloy coatings [21].

Coating sequence/substrate	Measurement range
Ag/Ni/Cu	0–3 μm Ag
	0–20 μm Ni
Au/Ni/Cu	0–1.6 μm Au
	0–20 μm Ni
Au/Ni/NiFe	0–1.6 μm Au
	0–20 μm Ni
Au/Ag/Ni	0–3 μm Au
	0–40 μm Ag
Au/Pd/Ni	0–5 μm Au
	0–40 μm Pd
Pd/Ni/Cu	0–3 μm Pd
	0–20 μm Ni
Rh/Au/Ni	0–4 μm Rh
	0–8 μm Au
Sn/Ni/Cu	0–4 μm Sn
	0–20 μm Ni
SnPb/Cu	0–30 μm
SnPb/Ni	0–30 μm

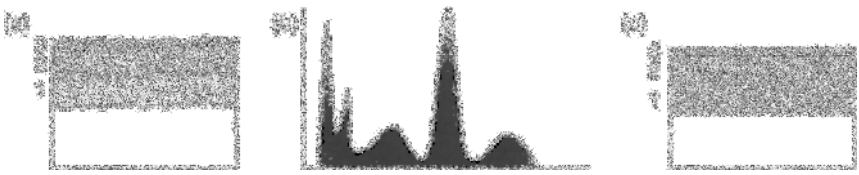

Figure 8.28 Schematic diagram showing principle of standard-free XRF coating thickness measurement

the parameters being measured, are known, including the accuracy of cited values. Preferably some form of certification is provided with such reference standards. Such standards are not usually available off the shelf, and their preparation can be extremely time-consuming. In practice, use is made of so-called comparison standards, until such time as actual standards are available.

It follows that the ability to measure coating thickness and composition reliably but without recourse to standards is a much-desired goal which would bring many benefits. To an extent, achieving this goal has for sometime been possible [23–25]. A much simplified description is shown in Fig. 8.28.

The starting point is a cross-section of a sample consisting of substrate and a three-layer coating (layers 1, 2 and 3) as shown in Fig. 8.28(a). A measurement based on the standard-free approach encompasses this structure and yields a fluorescence spectrum (Fig. 8.28b) which is processed by a special program. This employs information as to the X-ray tube (high voltage and anode current), properties of the instrument itself (angle of incidence of primary radiation, exit angle of

excited emission to the detector) and spectral density data from the primary X-ray source (intensity and energy distribution. Given this information, and using a physical model of the interaction between primary radiation and the sample, the unknown quantities can be determined, in this case, the thickness of the three layers (Fig. 8.28c).

8.4 *In situ* Measurement Methods

According to whether the thickness measurement is made during the actual deposition or thereafter, it is known as *in situ* or *ex situ*. The main drawback of the latter methods is that, in the event they reveal too great or too small a thickness, it is largely too late to correct matters. *In situ* measurements, by contrast, can follow the growth of a coating as it is deposited, in real time, as a function of elapsed time, thereby allowing remedial action or corrective procedures to be applied. The reduction in the amount of defective coatings thereby avoidable needs no elaboration. For this reason, there have been numerous attempts to develop such methods, though time after time, such efforts have been defeated by practical problems.

8.4.1 Island Method

One approach which appears to have been used with remarkable success for thickness measurements in the printed circuit board industry is the so-called island method [26]. The principle of this is shown in Fig. 8.29.

On the surface of a copper-clad epoxy-resin laminate, which is the starting material for most printed circuit boards, circular measurement points, known as islands,

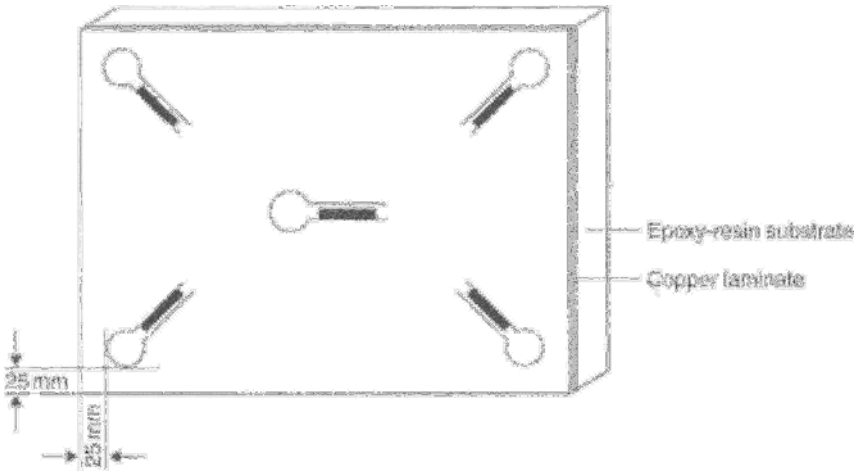

Figure 8.29 Peninsula-shaped measurement areas etched into copper-clad laminate for in situ thickness measurement of the electroplated copper layer.

and of radius r_i, are etched. These are conductively linked, via a small path, to the surrounding copper laminate. The path is partially insulated, using a resist layer (Fig. 8.29). Each island serves, during copper electrodeposition, as a measurement point where local cathodic current densities can be measured. For various technical reasons, the dimensions of these islands must be tightly controlled. The number of these islands and their distribution depends on the size of the board used. In practice, though, five points, configured as shown in Fig. 8.29 has been found satisfactory. This pattern has been shown to be a useful representation of local variations in thickness.

Since electric current can reach the islands only via the narrow path, the dimensions of the path must be so chosen that no excessive ohmic heating occurs, such as changes arising from 'burning' of the deposit. The length l_s and width b_s of such a path can be determined using the criteria noted above. The thickness (height) is determined by the thickness of the copper laminate.

In the case of copper, although a maximum current density of 1000 A/cm^2 is theoretically possible, a value of 600 A/cm^2 should not be exceeded in practice, mainly to avoid burnt deposits. Taking a path b_s of breadth 0.15 cm, and thickness d_s = 17.5 μm, one obtains a current density in the path ($I_s = I/b \times d$) of 610 A/cm^2, still an acceptable value, if the current applied is 160 mA. Given that the current flowing along the path to the island is 160 mA, then the local current density, I_s within the island can be calculated, where F is the surface area, from the formula ($I_i = I/F = I/\pi r^2 = 3$ A/dm^2). If higher current densities are called for, the width of the path must be increased.

The electric current, flowing down the path to the island, gives rise to a voltage drop U_s, the magnitude of which is given by:

$$U_s = I \cdot R = I \cdot \rho_{Cu} \cdot \frac{l_s}{b_s \cdot d_s} \tag{8.9}$$

where ρ_{Cu} is the density of the copper.

Taking typical values for the parameters in the above equation, a voltage drop of around 3.4 mV is obtained, and using a potentiometer of sufficient sensitivity, such small voltages can be accurately measured, thereby obtaining local current densities. One practical approach, shown in Fig. 8.30, is to solder thin wires onto a number of paths, and then measure potentials using a multiplexer, amplifier and ADC, hooked into a computer.

In order to calibrate such measurements, a constant current of 160 mA is allowed to flow from the island (+) to the cathode (−). The potential drop between the two soldered wires in the path is measured and recorded, using this information as a correction factor for each data pair. This can be done using a precision resistor with accuracy of 21 mΩ. This provides the accuracy demanded by the instrumentation being used.

Figure 8.31 shows how the island method is carried out in practice, though for the sake of clarity, the electrical wiring is omitted.

The method provides, within a few minutes, large amounts of data relating not just to deposit thickness distribution but also the rate of deposition in real time.

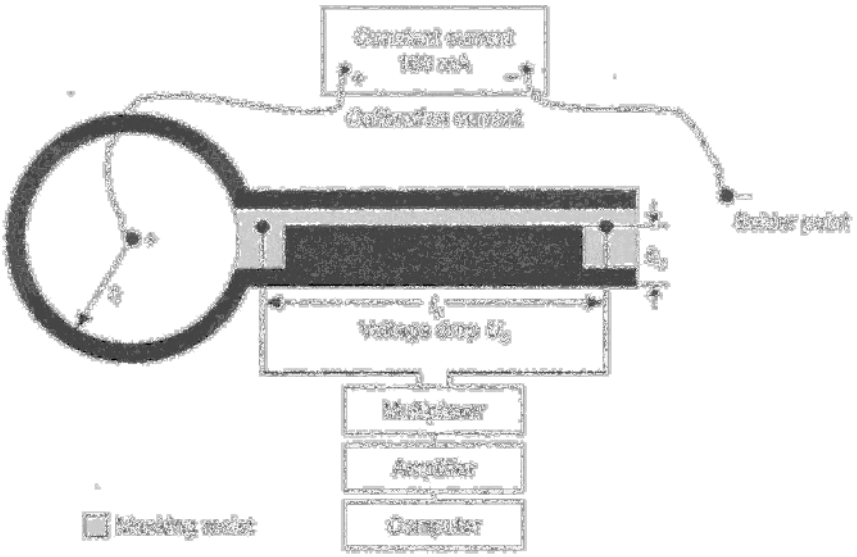

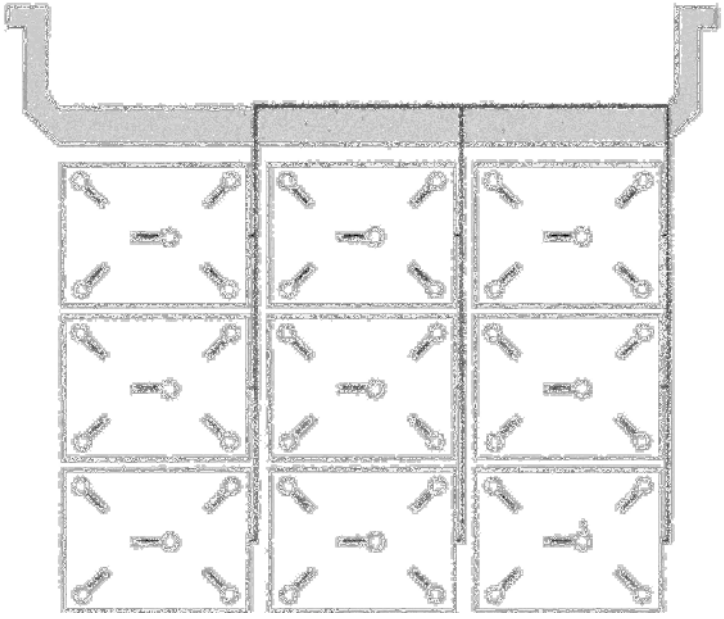

Figure 8.31 Printed circuit board with an array of 'islands', suspended from a rack for in situ monitoring of copper electrodeposition.

If this data is processed to show deviation from target thickness values, the deposition process can be regulated to bring the deposit back into conformity. The following list indicates methods by which such process variations can be effected:

- Separation of anode and cathode
- Varying the number, size, type and positioning of anodes
- Changing the process operating window
- Electrolyte agitation
- Geometry and positioning of shields
- Electrical conductivity of racks used.

*8.4.2 Optipulse Method**

The continued miniaturization of printed circuit boards is also expressed as an ever-increasing aspect ratio. This term describes the ratio of hole depth to diameter, in the printed circuit board. The greater the value of this parameter, the more difficult it is to 'throw' the electrodepositing copper into the full depth of the hole, to create what is known as the 'barrel' (the shape of the deposited copper, as it would appear without the surrounding pcb substrate. Using DC electrodeposition, it then becomes increasingly difficult to deposit, down the entire depth of the hole, as well as on the surface, a 25 μm thick copper deposit. Here, the micro-throwing power of some copper deposition electrolytes (see Chapter 3) comes into its own, but even then calls for special additives to optimise its performance.

The advantages offered by so-called pulse plating (see Chapter 4) have been known for some time, and such processes are now widely used for forming copper tracks and for through-hole plating of printed circuit boards. As Chapter 4 explains, in these processes the cathodic copper deposition is alternated with rest periods or polarity reversals, in the latter case, a small amount of anodic copper dissolution then occurs. The frequency and amplitude of such pulses (usually square wave) is widely variable as Fig. 8.32 shows.

In the case shown, two different cathodic pulses are used I_k^1 and I_k^2 in order to achieve the most uniform possible copper thickness distribution. The short anodic pulse, I_a, serves to dissolve and so remove roughness peaks on the surface. In pulse plating, no less than with DC plating, micro-throwing power in copper deposition is of key importance, and additives must be used to optimise performance. Monitoring the deposition process and thickness distribution can be carried out for pulse plating, as for DC deposition, using the island process (see above), though in the former case, as noted below, some modifications are called for.

The key variables, in the case of pulse plating, are not so much air sparging or work movement, as is the case with DC plating, but rather the pulse program, including a brief anodic pulse. The recording of process data thus calls for a somewhat different approach from that used by the island method as described above. In order to

*Note: Optipulse is a development of the island method, for coating thickness measurement and process optimisation during copper deposition by pulse plating, devised by D. Nitsche (Atotech Deutschland GmbH, Berlin, Materials Science Department).

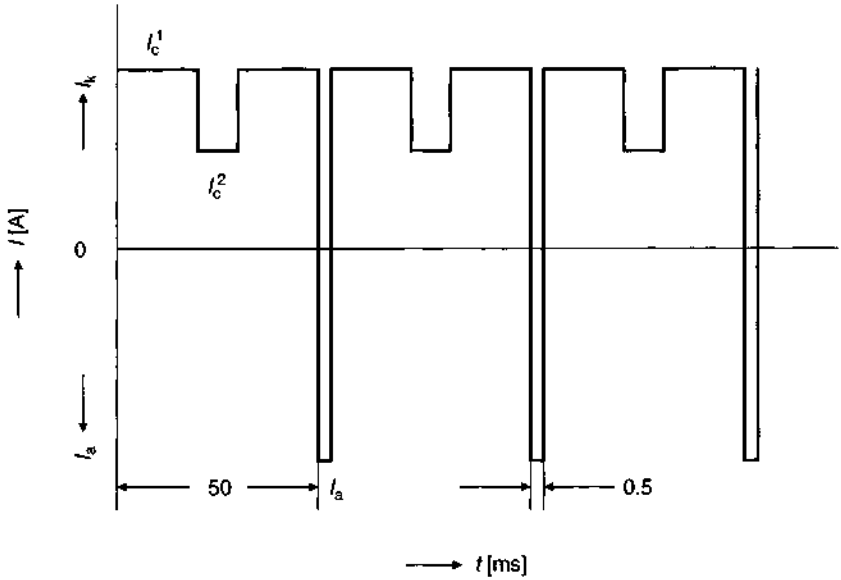

Figure 8.32 Train of cathodic and anodic current pulses for pulse-plating of copper (current–time sequence).

record the short anodic pulse with sufficient accuracy, at least 10 measurements are necessary, that is to say, a measurement is required every 50 μs. Assuming that a typical copper deposition process requires some 30 mins, this requires 36,000,000 measurements for each location be recorded and processed, that is, 20,000 measurements per second per location. Assuming 8 bytes storage capacity per measurement, this calls for a storage capacity for 36,000,000 data values, that is 288 Mb per channel. Two channels are required for handling data from front and rear-sides of the printed circuit board, bringing the required storage capacity to 576 Mb. In order to optimize a typical horizontal printed circuit board plating machine using pulsed currents, some 10 test runs are required.

8.4.2.1 Optimisation procedures

The quality of a pulse-plated copper deposit is determined by the pulse train used and the additives in the electrolyte, and it is with these two elements that optimisation is mainly concerned.

8.4.2.1.1 Effective pulse trains

The current–time charts shown in Fig. 8.33 serve to demonstrate that the parameters set up in defining a pulse-plating programme, are by no means those actually prevailing at the cathode (in this case, a printed circuit board). Examining these *I–t* traces, obtained under real conditions, one can see some typically encountered problems. Thus (Fig. 8.33a) we see a current oscillation following an anodic pule, before the current stabilizes to a defined value. Figure 8.33(b) shows a cathodic current overshoot, indicative of too high a cathodic current density. In the last case (Fig. 8.33c), neither of the foregoing phenomena are seen, but the very short anodic

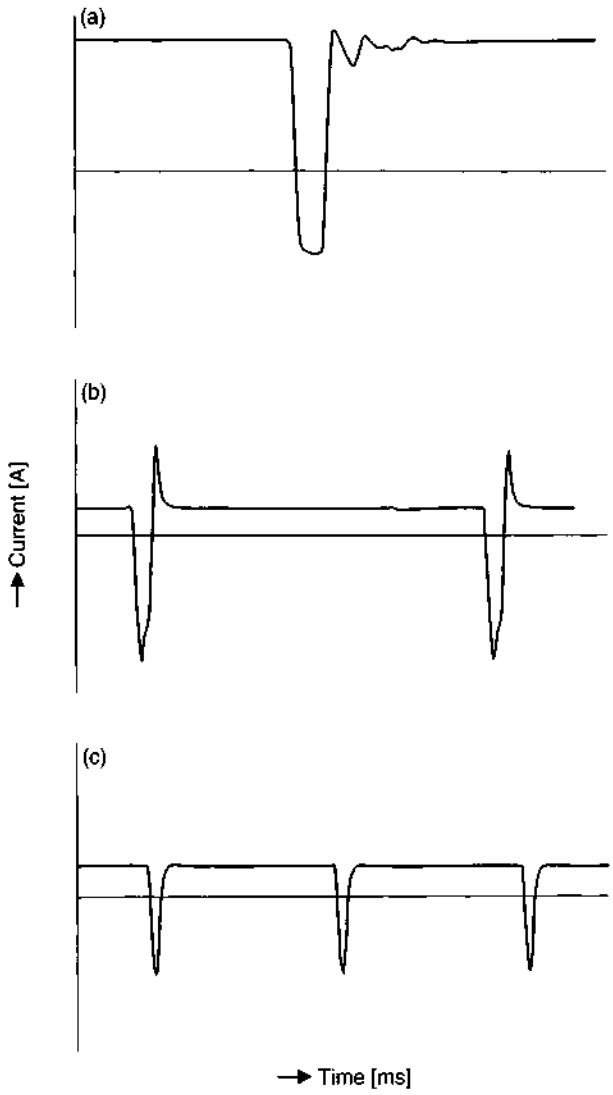

Figure 8.33 Course of a pulse sequence used for copper-plating a printed circuit board. (a) prolonged oscillation/ settling after an anodic current pulse. (b) Pronounced overshoot in the cathodic region. (c) Anodic pulse duration too short.

pulse suggests that the intended anodic copper dissolution process, may not be complete.

Such deviations from the intended pulse program, which would normally be a series of square-waves as shown in Fig. 8.32. have several causes. The main one, is that the electrode-electrolyte system constitute an electrolytic capacitor of extremely high value and, as the current polarity is changed or current value altered, this 'capacitor' has to be charged or discharged. Figure 4.34 (Chapter 4) illustrates admirably how a potential sequence can be distorted by the capacitative

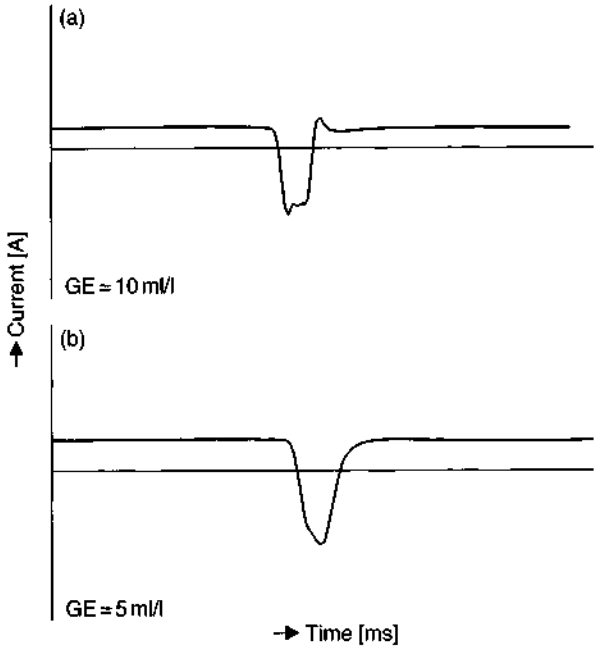

Figure 8.34 Effect of primary levelling agent concentration in a copper plating electrolyte on the shape of a given pulse program.

behaviour of an electrode–electrolyte system. Other factors which can distort a pulse program are inappropriately positioned shields or other components in the plating tank.

The pulse shape is, it must be emphasised, a dominant factor in determining micro-throwing power in a copper electrolyte and the deposit microstructure. The deposition process should be monitored and optimised along the entire length of the plating machine. The Optipulse method allows each current pulse to be recorded and precisely analyzed and to be associated with the position of the pcb in the plating machine.

8.4.2.1.2 Additive dosing

After countless laboratory experiments, it is now well established as to what additive concentrations are necessary to exert a beneficial effect on micro-throwing power. It is now known that their effect can be compared to that of an inhibitor. A result of this is that, for a given pulse program, their effect is different for the anodic and cathodic pulses used, or that the copper deposition potential is shifted to higher values.

This can lead, as seen in Fig. 8.34, to a change in the pulse regime actually reaching the pcb being plated. The Figure shows, for unchanged electrolyte composition and pulse program, but with changes in primary levelling agent (GE) concentration, how sensitive is the Optipulse method to changes in additive concentration of the copper plating electrolyte. These results also show how micro-throwing power can be improved by use of the optimum additive concentration.

8.4.2.1.3 Effect on copper deposit quality

Various methods are available to assess the quality of pulse-plated electrodeposited copper. Ductility measurement is among the most widely used of these, but the method cannot be realistically applied to the copper deposited within a printed circuit board through-hole. Possibly more useful, as a predictive test, is the widely used solder bath thermal shock test, in which plated samples are immersed in molten solder, typically at 260°C for 10 s. The test-piece is suspended in the solder bath (or floated), and a series of three such tests is used. The drawback of the method is that the type and quality of the printed circuit board substrate material used, can influence the test result. A more sophisticated version of this test is the thermal cycling method, which typically involves 1000 or more cycles, between −55 and +125°C, with dwell times of around 15 min. This test, however, suffers the drawback that it takes up to 4 weeks to complete. Relatively recently, a modified and much more rapid such test has been developed. This is the so-called interconnect stress test (IST), which uses test coupons in which the through-holes are electrically connected in a meander manner. The coupons are electrically heated to 150°C within 3 min, and then cooled to room temperature. The IST method can be used to carry out 250 cycles per day. During the heating/cooling sequence, the electrical resistance of the copper plating in the through-holes is continuously recorded. If the measured resistance value exceeds the specified figure by more than 10%, this indicates quality problems with the copper deposit. The method can be complemented by use of electron microscopy to view the test samples. Thus, Fig. 8.35 shows TEM micrographs of copper deposits in a pcb through-hole after thermal loading.

From the left-hand image of Fig. 8.35, it can be seen that at the beginning of electrodeposition, very fine copper crystallites form at the hole wall (dark areas), which continue to grow. The more or less regular structure of the relatively large crystallites can be assumed to indicate good thermal loading behavior. The right-hand image likewise shows growth of copper crystallites at the hole walls (dark areas) taking place. However, in this case, it can be seen that an inhomogeneous and irregular copper microstructure exists, with numerous twinnings present (see Chapter 2). This type of structure is indicative of poor thermal-loading behaviour.

The microstructure of the deposited copper depends mainly on the pulse program applied, and the additives in solution. High ductility, partnered with high

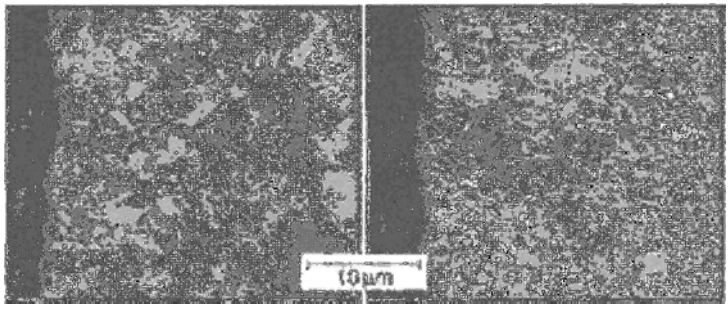

Figure 8.35 TEM images of good and bad pulse-plated copper microstructures. (Left) Good behaviour under thermal loading. (Right) Poor behaviour.

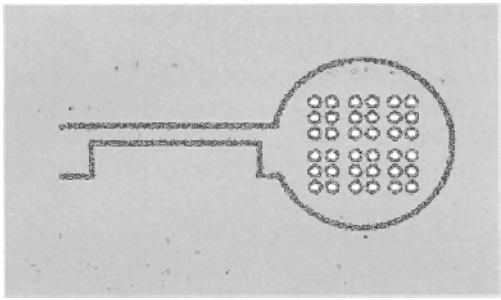

Figure 8.36 Test island etched from copper-clad laminate, with through-holes, for optimising quality of copper deposited in the holes.

tear-strength gives a high toughness deposit, and these are properties which indicate good performance in thermal cycling tests. If, as seen in Fig. 8.36, holes are drilled in an island area etched from a copper-clad laminate, the possibility is then open to modify the microstructure of the copper deposited within the holes, using an appropriate pulse sequence. To do this, the mean values of the successful pulse programs must be determined. The current pulses at the front- and back-side of the printed circuit board are often subject to phase-shift, and by applying a mean value from the two current pulses, it is possible to deposit copper with adequate toughness and ductility within the holes.

8.4.2.2 Determination of deposit thickness

In order to determine the thickness of the copper electrodeposit by means of the Optipulse method, the path leading to the test island must be calibrated, as described in Section 8.3.1. For each measurement point, a characteristic correction factor is found. Based on Eq. (8.9), a voltage drop of 3.4 mV is found for a current density of 3 A/dm^2. Then, if a deposition time of 1 min is used, and the correction factor applied to each measurement in the test island, and a mean value derived from these, then the thickness d can be calculated from the following equation:

$$d = \frac{M_{Cu} \cdot Q \cdot \eta}{z \cdot F \cdot \rho_{Cu} \cdot A} \text{ [cm]} \tag{8.10}$$

where M_{Cu} (g/mol) is the atomic weight of copper, Q (C) is charge passed, η (%) is cathodic current efficiency and A (cm^2) is the area of the test island.

References

[1] Biestek, T. and Sekowski, S., Methoden zur Prüfung metallischer Überzüge, Eugen G. Leuze Verlag, Saulgau/Württ., 1973.

[2] Kanani, N., Schichtprüfungen, in: *Technologie der Galvanotechnik*, herausgegeben von B. Gaida and K. Aßmann, Eugen G. Leuze Verlag, Saulgau/Württ., 1996.

[3] Petzow, G., Metallographisches Ätzen, 5. Auflage, Gebrüder Borntraeger, Berlin, 1976.
[4] Petzow, G. and Exner, E., Die Herstellung von Metallschliffen für lichtmikroskopische Untersuchungen in: *Handbuch der Mikroskopie in der Technik*, Band III, Teil 1, Umschau Verlag, Frankfurt, 1968.
[5] Schumann, H., Metallographie, VEB Deutscher Verlag für Grundstoffindustrie, Leipzig, 1967.
[6] Nitsche, K., Schichtmeßtechnik, VEB Deutscher Verlag für Grundstoffindustrie, Leipzig, 1974.
[7] Vander Voort, G.F., *Metallography – Principle and Practice*, McGraw-Hill Book Company, New York, 1984.
[8] Herff, K. and Roeder, E., Untersuchung und Messung dünner Schichten, *Prakt. Metallogr.* 2 (1972) 11, 615–623.
[9] Whitelam F.E. Jr., Using radial sectioning to measure thin layers, Reprinted from the March 1985 issue of *Metall Progress Magazine*.
[10] Herff, K. and Roeder, E., Vorrichtung zur Messung geringer Schichtdicken, *Prakt. Metallogr.* 5 (1968) 10, 557–566.
[11] Gühring, W.H., Praxisnahe Verfahren, Geräte und Anlagen zur Schichtdickenmessung, *Sonderdruck aus Metalloberfläche* (1976), Heft 3, 4 und 5.
[12] Jojko, Z. and Prušek, J., Schichtdickenmessung – Das coulometrische Verfahren in der Praxis, *Galvanotechnik* 69 (1978) 8 700–703.
[13] Plog, H., *Schichtdicken-Messung, Verfahren und Geräte*, Eugen G. Leuze Verlag, Saulgau/Württ., 1968.
[14] Ott, A., Schichtdickenmessung im Anschluß an die galvanische und stromlose Metallabscheidung, *Galvanotechnik* 1 (1976) 27–36.
[15] Gühring, W.H., Übersicht über die wichtigsten Verfahren und Geräte zur Messung galvanisch oder chemisch abgeschiedener Metallschichten, *Messen + Prüfen* 11 (1977) 731–742.
[16] Schubert, Ch., Schichtdickenmessung mit magnetischen und Wirbelstromverfahren, *Werkstatt und Betrieb* 2 (1979) 123–127.
[17] Latter, T.D.T., X-ray fluorescence for coating thickness measurement, *Circuit World* 10 (1983) 120–25.
[18] Behncke, H.H., Coating thickness measurement by the X-ray fluorescence method, *Metal Finish.* 5 (1984) 33–39.
[19] Lehmann, W., Exakte Schichtdicken-Messung mittels Röntgenfluoreszenz, *Metalloberfläche* 39 (1985) 3 85–88.
[20] Seitz, F. and Käs, H., Schichtdickenmessung an Leiterplatten mit dem Röntgenfluoreszenz-Verfahren, *Materialprüfung* 33 (1991) 1–2, 14–16.
[21] Staib, W., Kontinuierliche Schichtdickenmessung in Durchlauf-Galvanisieranlagen, *Metalloberfläche* 41 (1987) 5 213–219.
[22] Behncke, H., X-ray thickness testing for continuous plating, *Plating Surf. Finish.* 5 (1987) 112–115.
[23] Rößiger, V., Schichtdicke: Messen ohne Standards?, *Metalloberfläche* 47, (1993) 8 400–403.
[24] Rößiger, V., Schichtdicke: Komplexe Schichten sicher messen, *Metalloberfläche* 47 (1993) 9 469–473.

[25] Rößiger, V. and Kaiser, K.-H., Win(dows) FTM: eine neue Software für die Schichtdickenmessung nach dem Röntgenfluoreszenz-Verfahren, in *Jahrbuch Oberflächentechnik* 313–318, Metall-Verlag GmbH, Heidelberg, 1998.

[26] Ehrich, H.-J., Kanani, N., and Nitsche, D., Ein Optimierungsverfahren zur Schichtdickenverteilung beim Leiterbahnaufbau gedruckter Schaltungen in *Jahrbuch Oberflächentechnik* Band 47 175–191, Metall-Verlag GmbH, Berlin/Heidelberg, 1991.

This Page Intentionally Left Blank

CHAPTER 9

Analytical Study of Metallic Layers

9.1 Introduction

By forming a metallic layer on the surface of a component, one seeks to bring about special surface properties, without which the component in question might not be able to function as required. However, such a coating might be applied, and irrespective of whether it is a metal, an alloy or a multi-layer system, the composition of such a coating will determine the chemical, physical, mechanical and technological behaviour of the coating/substrate combination. Under the last of these headings, are included their tribological behaviour, corrosion resistance, electrical contact resistance, solderability and weldability, to name but a few. Then too, it should be borne in mind that on almost all metals, and air-formed oxide layer develops. This, in turn, will have adsorbed on it, water molecules or other contaminant layers derived from air-borne species. In the latter case, these are often organic species, such as hydrocarbons of general formula $C_n H_m$. Figure 9.1 illustrates this. Note that use of a logarithmic scale on the vertical axis, skews the actual film thickness values.

It follows from the above that there is an on-going interest in characterising, as accurately as possible, the chemical properties of such surface coatings using the

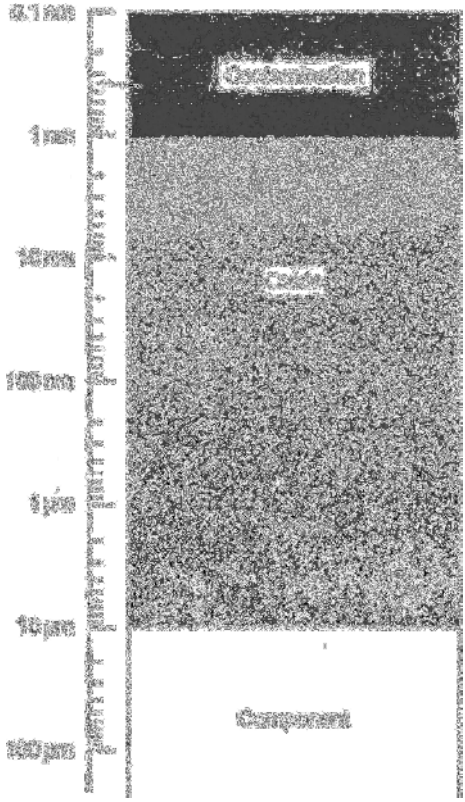

Figure 9.1 Formation of oxide and/or contaminant films over a deposited metal (log scale).

appropriate instrumental techniques. The requirements of this can be classified as follows:

- Analyses of surface composition at various depths, as purpose requires, from a few monolayers to a few micrometres;
- High absolute detection levels;
- High resolution in terms of location, mass, energy;
- Qualitative and quantitative information on the widest range of elements;
- Information on bonding states and chemical compounds;
- Obtaining depth profile analyses;
- Information as to isotopic species.

In recent years, there has been a prodigious development of new analytical techniques with which such requirements can be met [1–46]. Table 9.1 is a listing of most of these [8, 29]. Most of these methods are based on interactions between exciting species, such as ions, electrons or photons, beams of which are focused on the surface to be studied (substrate/coating). This causes various species or forms of energy to be emitted, and these carry the information from which analytical information can be derived. Figure 9.2 shows schematically a few of the most important techniques.

Some of the main options for exciting the surface material and processing the resulting signals are collated in Fig. 9.2 as a matrix. The extent of the excitation and resulting emission is mainly governed by parameters related to the incoming species, such as charge, intensity, energy and mass, as well as angle of incidence onto the sample. These are schematically represented in Fig. 9.3.

Of the long list of methods in Table 9.1, only those most used in the study of electrodeposited films will be considered [1]. These include first and foremost, mass spectrometric methods such as ion-scattering spectrometry (ISS), secondary ion mass spectrometry (SIMS) and secondary neutral particle mass spectrometry (SNMS), together with electron-spectroscopic methods such as auger electron spectroscopy (AES) and electron spectroscopy for chemical analysis (ESCA). The sketches in Fig. 9.4 illustrate the underlying principles of these.

To enable a better appreciation of the similarities and differences of the methods chosen for discussion, some of the most important concepts such as resolution, sampling depth, detection limit and sensitivity will now be discussed and defined.

Resolving power. In the case of optical microscopy, this term is understood to define the closest distance between two points which can be discriminated. Building on this definition, the lateral resolution (local resolution) of an analytical technique can be characterised as follows: two chemically identical adjacent point species, can be distinguished from one another when the intensity minimum between them does not exceed 75% of the peak maximum (Fig. 9.5a). In contrast to this 'qualitative' lateral resolution, the definition of quantitative lateral resolution requires that a given proportion of the measured signal arises from within the layer being analysed, as opposed to the substrate (Fig. 9.5b).

Lateral resolution is governed by the primary radiation, the geometric shape and the extent of interaction volume in the layer being analysed.

Table 9.1 Instrumental methods for surface film analysis.

AEMA	Auger electron microanalysis
AES	Auger electron spectroscopy
ARXPS	Angle-resolved X-ray photoelectron spectroscopy
ASLEEP	Automated scanning low energy electron probe
DIMA	Direct imaging mass analysis
DSIMS	Dynamic secondary ion mass spectroscopy
EDX	Energy dispersive X-ray analysis
EDXRF	Energy dispersive X-ray fluorescence
EELS	Electron energy loss spectroscopy
EID	Electron-induced desorption
EIS	Electron impact spectroscopy
EMPA	Electron microprobe analysis
ESCA	Electron spectroscopy for chemical analysis
ESDN	Electron-stimulated ion desorption
FDMS	Field desorption mass spectroscopy
FEES	Field electron energy spectroscopy
FIMS	Field ion mass spectroscopy
GDMS	Glow-discharge mass spectroscopy
IEX	Ion-excited X-rays
IIXS	Ion-induced X-ray spectroscopy
ILS	Ion loss spectroscopy
IMMA	Ion microprobe mass analysis
NMS	Ionised neutral mass spectroscopy
INS	Ion neutralisation spectroscopy
ISS	Ion scattering spectroscopy
LMMA	Laser microprobe mass analysis
LDMS	Laser desorption mass analysis
LEEIXS	Low energy electron-induced X-ray spectroscopy
LEELS	Low energy electron loss spectroscopy
LEMBS	Low energy molecular beam scattering
LMP	Laser microprobe
LOES	Laser optical emission spectroscopy
MBSS	Molecular beam surface scattering
NIRMS	Noble gas ion reflection mass spectroscopy
NIRS	Neutral impact radiation spectroscopy
PDMS	Plasma desorption mass spectroscopy
QMS	Quadropole mass spectroscopy
RIBS	Rutherford ion backscattering
SAES	Scanning Auger electron spectroscopy
SAM	Scanning Auger microprobe
SDLTS	Scanning deep level transient spectroscopy
SIIMS	Secondary ion-imaging mass spectroscopy
SIMA	Secondary ion microanalysis
SIMS	Secondary ion mass spectroscopy
SIPS	Sputter-induced photoelectron spectroscopy
SNMS	Secondary neutral mass spectroscopy
SPIXE	Scanning photon-induced X-ray emission
SSIMS	Static secondary ion mass spectroscopy
TELESCA	Transmission electron loss spectroscopy for chemical analysis
UMPA	Universal microprobe mass analyser
UPS	Ultra photoelectron spectroscopy
WDX	Wavelength dispersive X-ray analysis
XAES	X-ray-induced Auger electron spectroscopy
XPS	X-ray photoelectron spectroscopy
XRF	X-ray fluorescence
XUPS	Extremely ultraviolet photoelectron spectroscopy

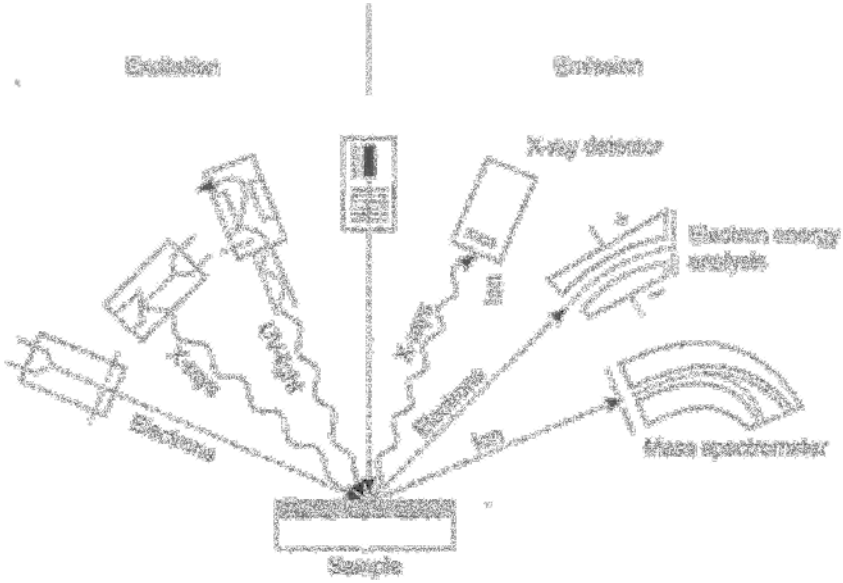

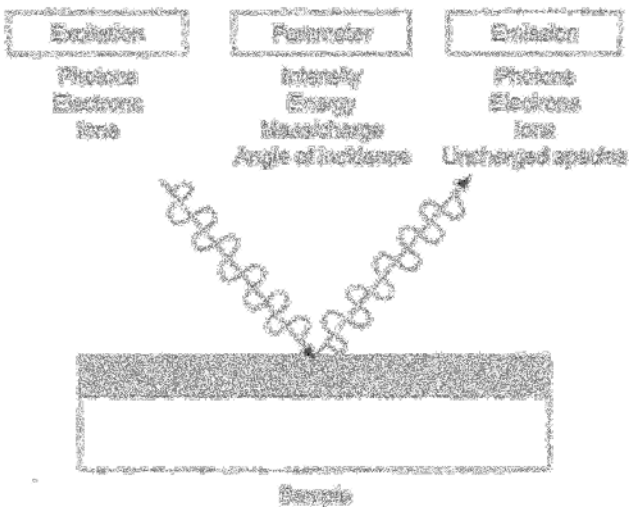

Figure 9.3 Varying intensity, energy, charge and incidence angle of the exciting bam determines the emissions from the surface.

Table 9.2 Overview of the most important analytical methods.

Excitation by/emissions of	Photons	Electrons	Ions
Photons	XRF		IEX
Electrons	ESCA (XPS. UPS)	AES	INS
Ions			ISS/SIMS/GDMS
Uncharged particles			SNMS

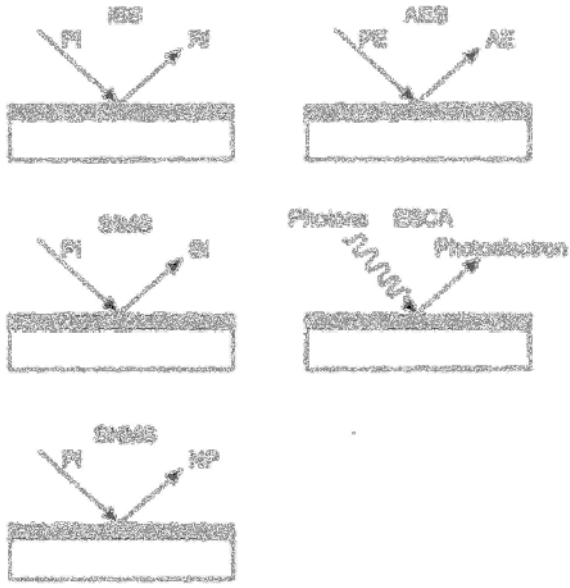

Figure 9.4 Mass spectrometry (left) and electron spectroscopy (right) analytical methods: PI = primary ions; BI = back scattered primary ions; SI = secondary ions; NP = neutral particles; PE = primary electrons; AE = Auger electrons.

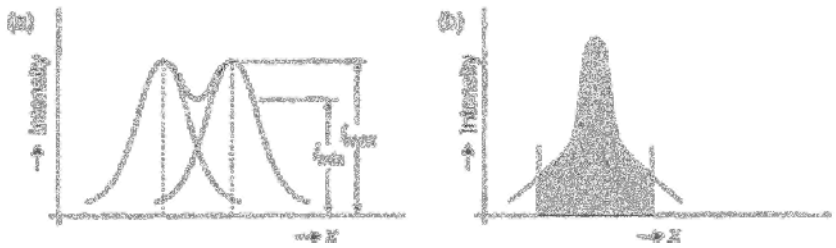

Figure 9.5 Definitions of 'resolving power': (a) qualitative lateral resolution; (b) quantitative lateral resolution [30].

Sampling depth. This is perhaps the most important single parameter for a given analytical method, and designates at what depth below the surface, the method provides information (Fig. 9.6). In simplistic terms, this depth is a function of the extent to which the primary (exciting) radiation penetrates below the surface, and the extent to which the resulting signal can escape from the sample for capture by the detector. Figure 9.7 illustrates some examples of this. On the left, the layer is chemically pure and homogeneous, though covered with a thin film of foreign species. Use of energy dispersive X-ray (EDX) would barely reveal the presence of such a surface film, since the highly energetic primary electrons pass right through the outermost layer and into the coating itself where they cause emissions of secondary electrons (SE) and X-rays.

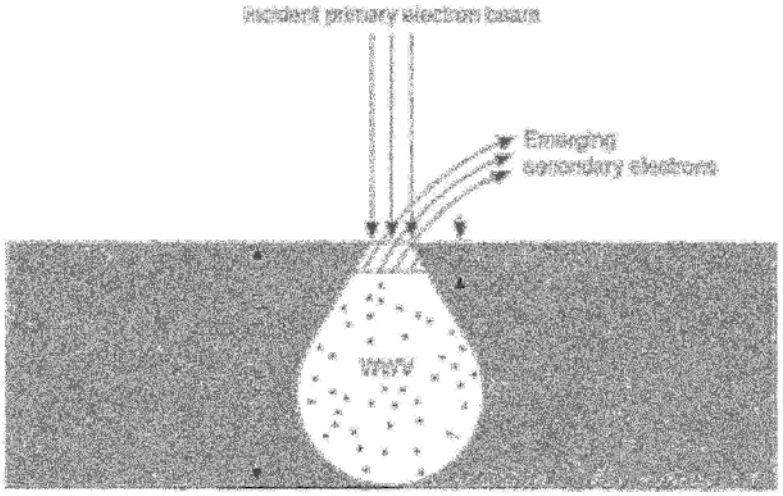

Figure 9.6 Definition of the sampling depth of an instrumental analytical technique, exemplified by primary and secondary electrons (V'eff = sampling volume).

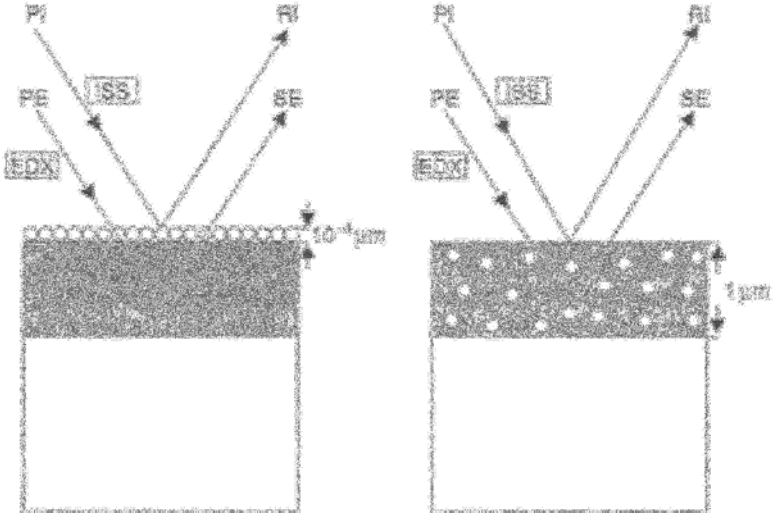

Figure 9.7 Significance of sampling depth of an analytical process in determining the chemical composition of a coating layer.

Were one to use the emitted X-rays for the chemical analysis of the coating, it would appear to be totally pure and homogeneous. If, however, one employed ion-scattering spectrometry (ISS), then the low-energy primary ions (PI) would interact only with the foreign species above the coating and the resulting signal would reflect this, giving analytical information only as to the foreign species on the outer surface. The right-hand side of the figure shows the exact opposite. The coating layer is not chemically pure, but includes atoms of some other species, randomly distributed. EDX, in this

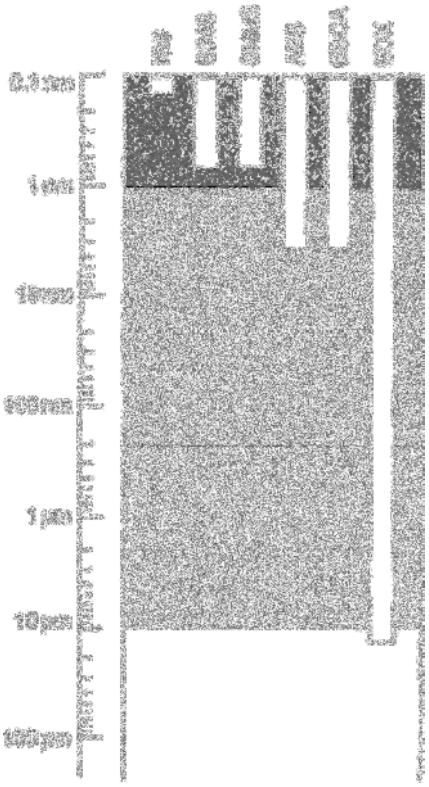

Figure 9.8 Sampling depths of the most important instrumental analysis techniques.

case, yields an overall analysis of the coating and thus will include information as to the presence of the second species with some accuracy. ISS, by contrast, would indicate (falsely) that a chemically pure homogeneous layer was present, since the primary ions would not penetrate deeply enough to detect atoms of the second species.

These two examples indicate clearly, how important it is to choose the appropriate method. Figure 9.8 is another way of distinguishing the scope of some of the various techniques. As this figure makes clear, the sampling depths of ISS, SIMS, SNMS, AES and ESCA (0.1–3 nm) are far more shallow than that of EDX (1–10 μm).

In this sense, SIMS and SNMS, but most of all ISS should be seen as the techniques most sensitive to species actually at the surface and only by using these methods, can information be obtained as to species at the very surface.

Detection limit. For any analytical method, a value can be established denoting the lowest concentration of species detectable by that method, and in this case, for the instrumental methods described, that applies equally, in this case to an element of atomic number Z. The concept applies equally to qualitative analysis (present/not detected) and quantitative analysis (lowest measurable concentration).

The concept can be quantified as the number of atoms of the element in question per unit volume (N/cm^3) in the layer, or as ppma (parts per million atomic). The latter,

often abbreviated to ppm, that is 1 ppm = 1 foreign atom per million. Thus, an analytical method with absolute detection level of 1 ppm can detect, in 1 cm^3 which would typically contain 10^{23} atoms, the presence of 10^{17} foreign atoms, that is, those of some other element. The expression ppmm (parts per million mass) is also used, and 1 ppmm corresponds to 1 μ g/gm. These concepts are very similar to those used in chemistry or metallurgy where compositions are specified either as at. wt% or as wt%.

Sensitivity. In order to determine the concentration c_A of an element A, in the signal of intensity I_A, an additional factor ρ must be taken into account – the sensitivity. This is a function of the element being estimated, the equipment being used and of the layer being examined. It is evaluated by using known standards to calibrate the above factors.

9.2 Mass Spectrometric Methods

If a sample being analysed is bombarded with ions of a few hundred to several thousand electron volts, the returning signal includes not only some of these being back-reflected, but other ions, positively or negatively charged, and neutral species (atoms or molecules) ejected from the surface of the sample. These processes, reflection and emission, are schematically shown in Fig. 9.9.

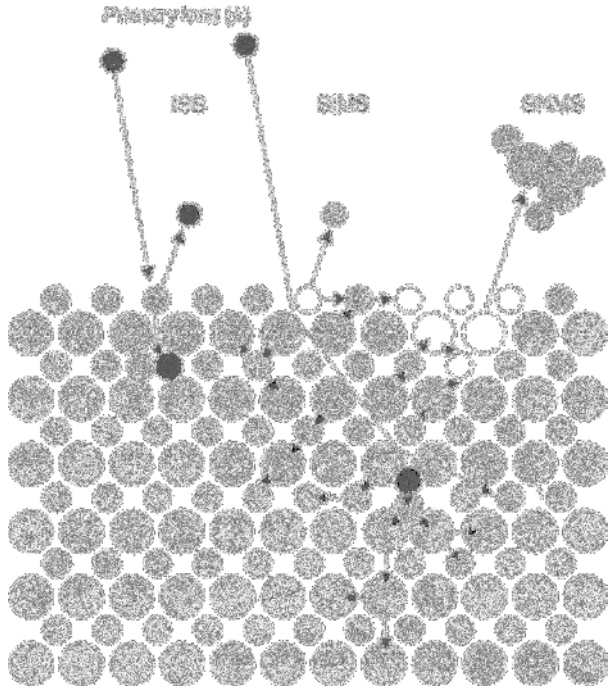

Figure 9.9 Interaction (reflection, emission) between primary ions with various charge values and energies and atoms present in the surface layer [12].

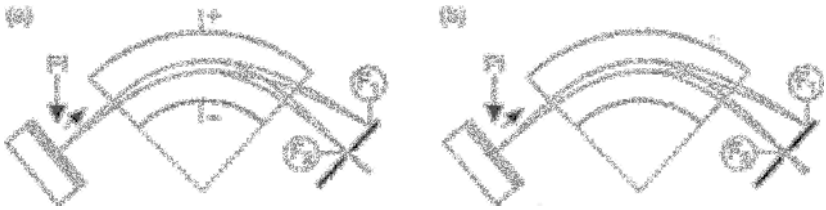

Figure 9.10 (a) Ion beam with two ions of identical mass but differing energies, in an electric field. (b) Ion beam of two ions with the same energies but of different mass, in a magnetic field. F_1 and F_2 are focusing points [46].

The reflected primary ions as well as the emitted secondary ions and uncharged species, which allow a chemical analysis of the sample, can be analysed using a mass spectrometer. Mass spectrometry can be defined as a technique whereby ions are accelerated and then, using electrical and magnetic fields, sorted according to their mass:charge ratio (m/e). This allows singly charged ions of intermediate mass to reach velocities of 10^4–10^5 m/s using an accelerating voltage of 2 kV.

After sorting, the ions are then registered as an ionic current, from which a 'spectrum' is produced. The sorting process is shown in Fig. 9.10.

This figure shows how electric or magnetic fields can be used to separate ions of identical mass or energy, respectively. Ions with larger energy are deflected less than those of smaller energy. In both cases, a directional focusing takes place, which directs the more strongly decelerated ions to the positive condenser plate, these being more strongly deviated (F_2) whereas other ions are accelerated and suffer less deviation, and are directed to the negative condenser plate (F_1). Figure 9.10(b) shows the behaviour of an ion beam with two ions of the same energy but different masses under the influence of a magnetic field. Both suffer deviation, but to differing extents. They are focused such that, behind the magnetic field, they are united as a single 'bundle' of ions of identical mass (F_1 and F_2).

9.2.1 Ion Scattering Spectrometry (ISS)

If the coating layer is bombarded with ions of relatively low kinetic energy, these do not penetrate the surface, but are scattered back from the surface, and their interaction with the solid is limited to the outermost atoms. This is especially the case for LEIS (low energy ion scattering) [9, 10]. Figure 9.11 shows a solid surface being bombarded with a succession of mono-energetic noble gas ions, of mass m and energy E_0.

Following their impact on the surface atoms, the primary ions are back-scattered in a binary elastic collision mode, in which part of their energy is lost. Their kinetic energy after impact is E. The chemical analysis of the surface is then based on an energy analysis by the detector, of the returning primary ions. Figure 9.12 shows in schematic form, an ISS instrument.

The choice of primary ions used depends on the mass of the surface layer atoms. Frequently, H^+, Ne^+ or Ar^+ are chosen, these having energies between 0.5 and 3 keV.

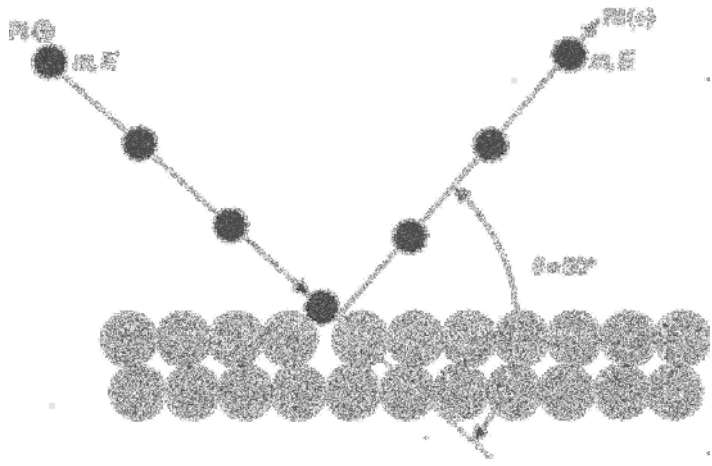

Figure 9.11 Coating layer bombardment by a coherent ion beam (PI) of low kinetic energy and the resulting back-scatter (RI), with back-scatter angle θ.

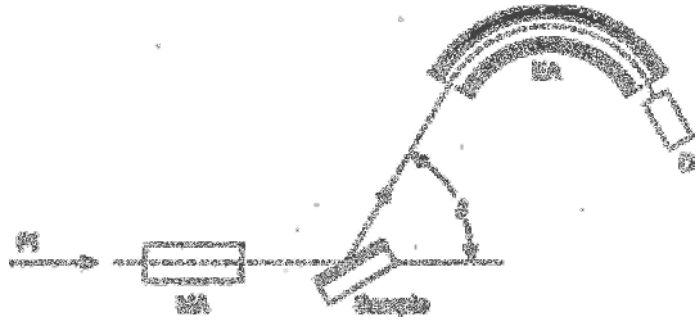

Figure 9.12 Schematic showing ISS technique. PI = primary ion beam, MA = mass analyser, P = sample (substrate + coating), EA = energy analyser, D = detector.

The interaction between incident primary ions and the atoms at the surface depends not only on the atomic mass but also the angle of incidence ψ of the primary ions, that is, once the angle of incidence has been decided, then the energy loss of the primary ions depends solely on the atomic mass of the surface species. Thus, by measuring the energy of he back-scattered primary ions, the atomic composition of the surface can be determined. The equation representing this is [29]

$$\frac{E}{E_0} = \frac{m^2}{(m + M)^2}\left\{\left[\frac{M^2}{m^2} - \sin^2\theta\right]^{1/2} + \cos^2\theta\right\} \tag{9.1}$$

Here, E_0 and E signify the energies of incident and reflected primary ions of mass m respectively; M is the mass of the surface atoms and θ the back-scatter angle. After determining the energy E, one can obtain the mass M. By selecting the experimental condition $\theta = 90°$, the mathematical solution of Eq. (9.1) is greatly simplified.

The analytical scope and accuracy of ion-scattering spectrometry can be gauged from the spectra shown in Fig. 9.13, which shows the intensity, that is, the number of reflected ions per second, in the energy range zero to that of the primary ions themselves.

A homogeneous CuNi layer of composition Cu:Ni = 1:1, and whose ISS spectrum is shown in Fig. 9.13, was subjected to a heat-treatment at 730°C. As might be expected, this thermal treatment resulted in a non-uniform distribution of the two species in the layer and using ISS, the extent of this phenomenon could be recorded. Thus, for the as-deposited specimen, one sees two discrete peaks of similar intensity, indicating a uniform distribution of the two species. The spectrum of he heat-treated sample shows two peaks of very different intensity, indicating a very significant degree of surface-enrichment in copper.

ISS also allows one to study the surface topography of a coating. This is the result of the so-called 'shadowing effect' [2]. If an atom i is adsorbed on the surface, it will then, as Fig. 9.14 shows, it will overshadow a variable number of surface atoms (k_1, k_2, ...) depending on the angle of incidence (ψ_1, ψ_2, ...). By varying this angle, the intensity ratio I_i/I_k also varies. However where the atom I is incorporated into the surface, then its response is virtually independent of the angle of incidence.

Equally, it is possible to study the disposition of chemisorbed molecules on a coating surface to determine, for example, which atom of a molecule is attached to the surface.

The main strengths of the ISS technique can be summarised as follows:

- extremely high sensitivity for surface species,
- non-destructive surface analysis,
- all elements detectable except hydrogen,
- simple and rapid spectrum capture,
- option to obtain depth profiles.

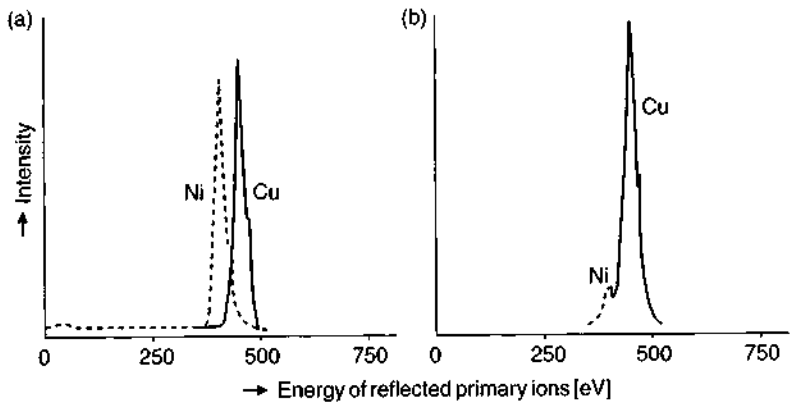

Figure 9.13 ISS spectrum of a copper–nickel alloy: (a) as-deposited; (b) after heat-treatment at 730°C. Bombarded with Ne^+ ions (E_0 = 1.5 keV), angle of incidence ψ = 142°.

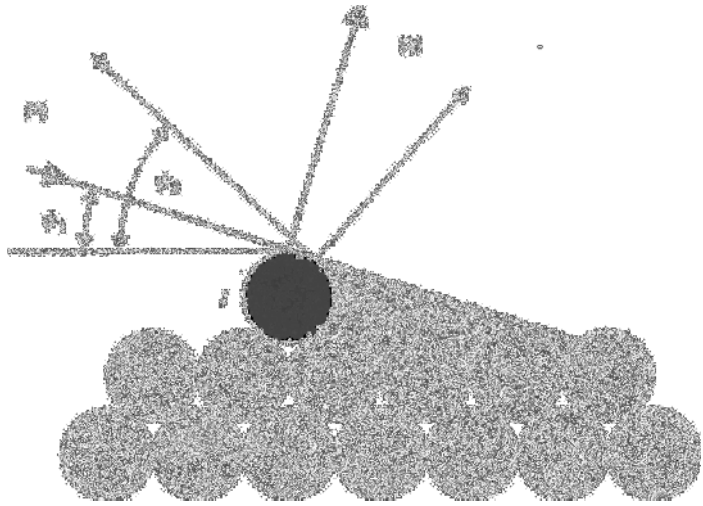

Figure 9.14 Surface topology study of a surface layer with ISS, using the shadowing effect [2].

Minor drawbacks are:

- determination of isotopes and chemical compounds is not possible,
- relatively low lateral resolution.

9.2.2 Secondary Ion Mass Spectrometry (SIMS)

By bombarding a surface with positive or negative primary ions of sufficient energy, a secondary ion emission can be provoked and these too can be of either charge polarity, while yielding information as to the surface composition. This process is schematically shown in Fig. 9.15.

Various models have been proposed to explain this phenomenon. One model that seems most satisfying is based on impulse transfer in the outer layer by cascaded collisions [13]. According to this model, the primary ions will penetrate into the surface layer to a depth determined by their energy, surrendering their kinetic energy as they move downwards, by successive collisions with atoms in the lattice. The result is a sequence of collisions, some of which can emit energetic ions back to the surface. Because the energy of the primary ions is dissipated among so many atoms in the lattice by this sequence of collisions, only a relatively modest energy remains to excite atoms at the surface. However, if that energy is greater than the bond energy of the atoms in the outer layer lattice, it becomes possible for those atoms to be ejected from the surface.

In the course of this emission process, there is a certain probability that, as a result of electron exchange in the conduction band of the surface layer, the atoms ejected from the surface will be ionised. These can be positively or negatively charged. As a rule of thumb, electropositive elements, for example, metals, form positively charged ions. Since secondary ions are formed from virtually all species at the surface, and

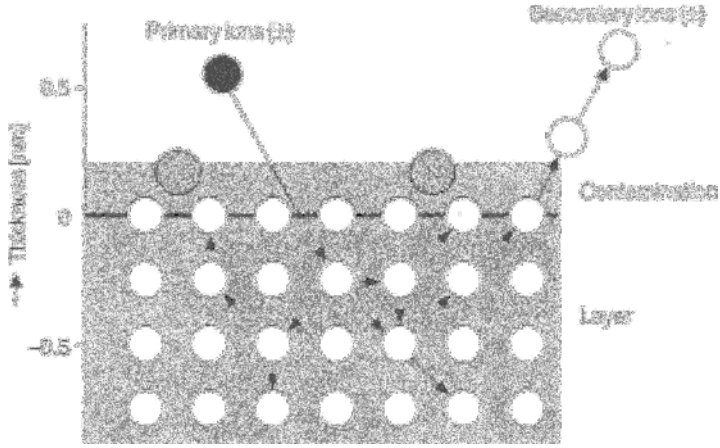

Figure 9.15 Energy transfer and emission of secondary ions resulting from primary ion bombardment with energies of a few kilo electron volts [13].

they are emitted predominantly from the outermost layer, this can yield valuable information as to the outer layer composition. The secondary ion (SI) yield, $S^{\pm}$ is an important concept here, given by the expression:

$$S^{\pm} = \frac{N_{SI}^{\pm}}{N_{PI}} \tag{9.2}$$

where $N_{SI}^{\pm}$ signifies the number of secondary ions (of either charge sign), and N_{PI} is the number of incident primary ions. The SI yield depends not only on the element involved (up to a factor 3×), but also depends strongly of the matrix of the coating layer and the state of the surface. These effects can, in some circumstances, complicate an analytical study. It should further be appreciated that the proportion of secondary ions from the bombarding ions, is very small. Thus, suppose a volume of $100 \times 100 \times 10\,\text{nm}^3$ is sputtered off, this implies that some 10^6 atoms are formed, of which only 10^5 to 10^1 will be ionised. Of these, perhaps only 10% will be detected as ions [19]. In order to increase the SI yield, it is necessary to ionise the excess neutral particles emitted by additional electron bombardment. To bring about this, the use of Cs^+ or O_2^+ ions has proved a useful procedure. In many cases, a mixture of Ar^+ and O_2^+ ions are used to increase the SI yield.

The basic features of a SIMS instrument are shown schematically in Fig. 9.16.

Primary ions are formed either from gas ion sources, in which gaseous atoms or molecules are ionised by electron radiation, or using liquid metal ion sources, where ions are formed from the molten metal by field extraction. Primary ions typically used are O^{2-}, O^-, Ar^+, Ga^+ or Cs^+ with energies of a few hundred electron volts up to 20 keV. After emerging from the ionisation chamber, the primary ions pass through a magnetic field which removes some of the impurities present, and the beam is then aimed at the sample (substrate/coating). The diameter of the ion beam will vary, depending on requirements, from several hundred micrometres down to

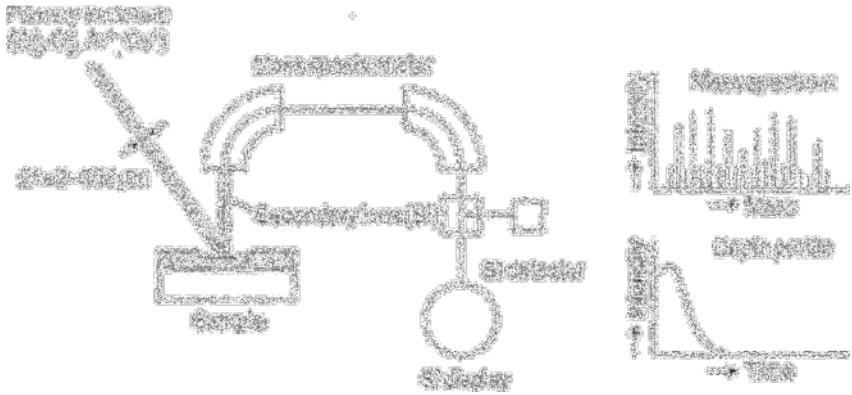

Figure 9.16 Schematic representation of a SIMS instrument for acquisition of mass spectra and depth profiles [16].

100 nm. Using liquid metal ion sources, ion beams of 100 nm (Cs^+) down to 20 nm (Ga^+) can be formed [19]. Sample sizes used depend on the instrument, but are typically <15 mm, and <10 mm thick.

Secondary ions emerge from the surface with moderate velocity and pass through a specially designed ion-optical system which both sorts and collects the ions according to their mass. They are then captured by a highly sensitive SI detector. This registers the incoming ions as cps (counts per second), at rates up to 10^7. A high mass resolution results when the mass difference between primary and secondary ions is large ($m_{PI}/m_{SI} > 10{,}000$). The positive or negative SI current of an element A, incorporated in the coating layer, can be determined as [3]:

$$I_A^{\pm} = k \cdot I_p \cdot S_A^{\pm} \cdot p_A^{\pm} \cdot a_A \int_0^{\infty} c_A(Y)\mathrm{d}Y \tag{9.3}$$

Here, $I_A^{\pm}$ is the measured SI current flux from element A (number of secondary ions/second), k is a constant for the instrument used, I_P is the PI intensity (number of PI/second), $S_A^{\pm}$ is the SI yield (mean number of secondary ions per primary ion), $P_A^{\pm}$ is the ionization probability (proportion of positive or negative secondary ions in the total number of emitted particles), a_A is the isotopic occurrence frequency and c_A the atomic concentration of A as a function of depth Y.

It should also be noted that secondary ions only form at extremely clean surfaces and under ultra-high vacuum (UHV) conditions ($\sim 10^{-8}$ Pa) as a result of so-called kinetic emission. In the case of a contaminated surface (Fig. 9.15), the proportion of secondary ions due to 'chemical emission' is appreciably higher. This can be seen from Table 9.3 which compares measured SI yields for both clean and oxygen-contaminated surfaces of a range of metals.

As the primary ion beam is x–y rastered across the sample surface, so the SI distribution pattern of a given element can be reconstructed (Fig. 9.16). This also allows the detection of certain impurities on the coating surface.

Table 9.3 SI yields S^+ from Ar^+ ion bombardment (2.5 keV) of clean and oxygen-contaminated metal surfaces [12].

Metal	Clean surface	Oxide-coated surface
Mg	0.01	0.9
Al	0.007	0.7
Ti	0.0013	0.4
V	0.001	0.3
Cr	0.0012	1.2
Mn	0.0006	0.3
Fe	0.0015	0.35
Ni	0.0006	0.045
Cu	0.0003	0.007
Sr	0.0002	0.16
Nb	0.0006	0.05
Mo	0.00065	0.4
Ba	0.0002	0.03
Ta	0.00007	0.02
W	0.00009	0.035
Si	0.0084	0.58
Ge	0.0044	0.02

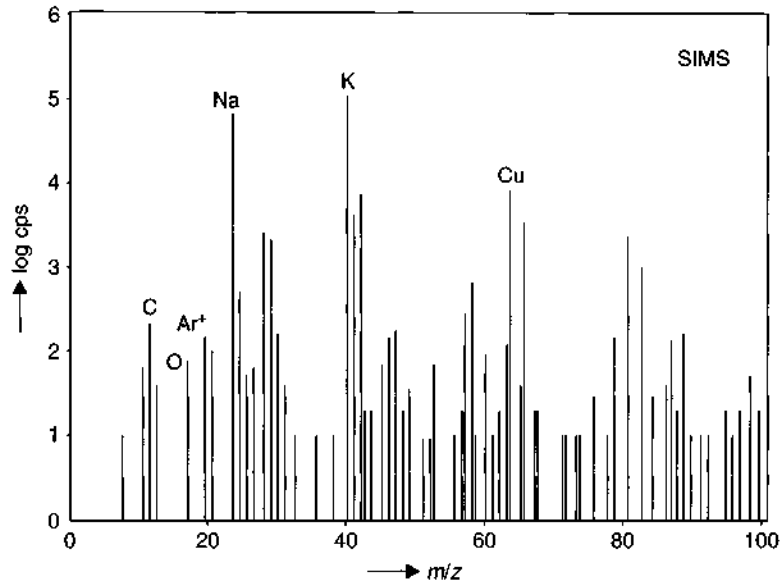

Figure 9.17 SIM spectrum of an electrodeposited copper layer obtained using Ar^+ primary ion bombardment (cps: counts per second).

Depending on the flux density of primary ions, a distinction is made between steady-state and dynamic SIMS [3, 13, 16–19].

In the case of steady-state SIMS (SSIMS), the technique is operated under UHV conditions and with very low current densities (10^{-9} A/cm^2, 0.5–2 keV) with a relatively large target area (0.1 cm^2). The advantage of this is that very little of the

sample surface is sputtered away, usually no more than the outermost monolayer. The process can thus be considered to be non-destructive. Each primary ion impact is separated from the next, not only in time but also spatially [19]. The sensitivity of the method depends on the element(s) to be determined but is of order 1 ppm per monolayer. The technique can also be used to follow oxidation or adsorption processes taking place at the surface, and is well-suited to a study of the outermost layers of organic species. The duration of a measurement might last from 10 s to 1 h.

In the case of dynamic SIMS (DSIMS), a higher primary ion current density is used (10^{-4} A/cm^2, 2–20 keV and this, in contrast to SSIMS, brings about a rapid removal of surface material (up to ca. 1 μm/h). The method allows quantitative depth profiling to be carried out. As successive layers, each one deeper than the preceding one, are bombarded away, the analysis of each allows the depth profile to be constructed. An example of such a depth profile is shown in Fig. 9.16.

Depth profiles in the micrometre range take about an hour to complete, and additional time is required for data-processing. The surface topography also enters into the experiment, since a rough surface may lead to non-uniform material removal and so influence the results of the emerging SI flux and thus the analytical results.

Figure 9.17 shows a SIMS spectrum of an electrodeposited copper layer.

In this case, the spectrum yields useful information as to the purity of the copper deposit. The spectrum shows that, apart from copper, sodium and potassium are the dominant peaks. The latter are probably due to very low concentrations of impurity on the metal surface. Weaker signals for oxygen and carbon are also seen and these are probably from a contaminated layer on the substrate surface prior to copper deposition. The Ar^+ peak arises from the bombardment of the sample with this species. Numerous lesser peaks of varying height would need much additional study to characterise, and are usually not pursued. However, no information as to the presence of hydrogen is available. Other SIMS studies indicate that the level of impurities are of order 1 ppm.

Figure 9.18 shows a surface analysis and depth profile for a pulse-plated copper sample. The copper coating was bombarded with O_2^+ ions and material was sputtered off at a rate of around 90 nm/min. A change of composition with depth can be seen. CuN is seen to be present, though this may result from interaction with nitrogen in the deposit, and does not necessarily imply that CuN as such as present in the sample.

The main strengths of SIMS are:

- provides information at monolayer depths
- offers lateral resolution on the atomic scale
- detection level is at ppm or ppb level (10^{-9}–10^{-12} g)
- all elements including hydrogen can be determined
- chemical compounds (as opposed to elements) can also be determined
- isotopes can be determined
- minimal surface damage (SSIMS)
- quantitative analysis is possible
- depth profiles can be obtained.

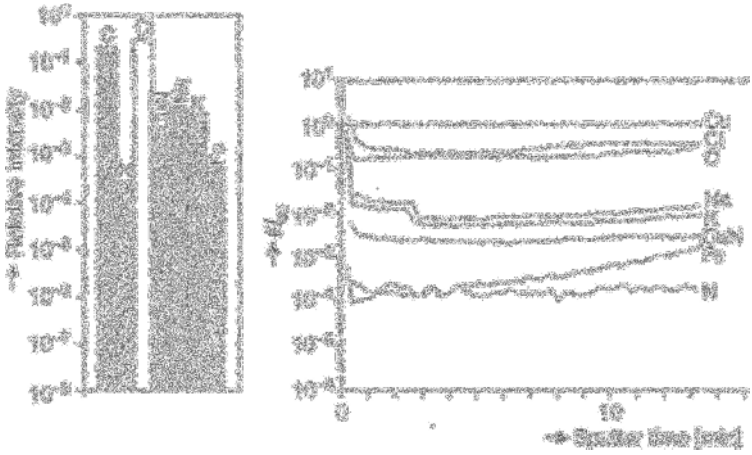

Figure 9.18 Surface analysis (SIMS) and depth profile for a pulse-plate copper sample. (a) Concentration of same elements; (b) depth profile.

Against these advantages, certain drawbacks should be noted:

- sensitivity may vary as function of surface structure
- ion-induced surface reactions can take place
- some destruction of the surface layers may occur (DSIMS)
- quantitative analysis is complicated by pronounced matrix effects.

9.2.3 Secondary Neutral Particle Mass Spectrometry (SNMS)

In recent times, SNMS, as well as SIMS, has assumed in increasing importance in the study of surfaces and surface layers [6, 20, 21]. This technique differs from SIMS in that a flux of neutral atoms or molecules are analysed, after their ejection from the surface due to primary ion bombardment (Fig. 9.9). As a result, SNMS signals are unaffected by an electrical charging of the sample. Whereas secondary ions can be directly recorded by the mass spectrometer, neutral particles must first be ionised before they are determined. This is achieved either using the electronic component of a special HF low-pressure plasma, or using an electron beam. The technique is thus sometimes described as electron-gas SNMS or electron beam SNMS. The more efficient the post-ionisation of the neutral species, the higher is the sensitivity of the method.

By decoupling of the two processes (neutral particle emission and post-ionisation), the quantitative interpretation of SNMS peaks is much simpler than is the case for SIMS peaks. This rests on a knowledge of the element-specific post-ionisation probability and an instrumental constant. It is this greater ease of quantitative analysis that is the strength of SNMS. Depending on the mode of surface bombardment by primary ions, three different variants of the method are used, known respectively as the direct, separate and external modes. Figure 9.19 depicts these.

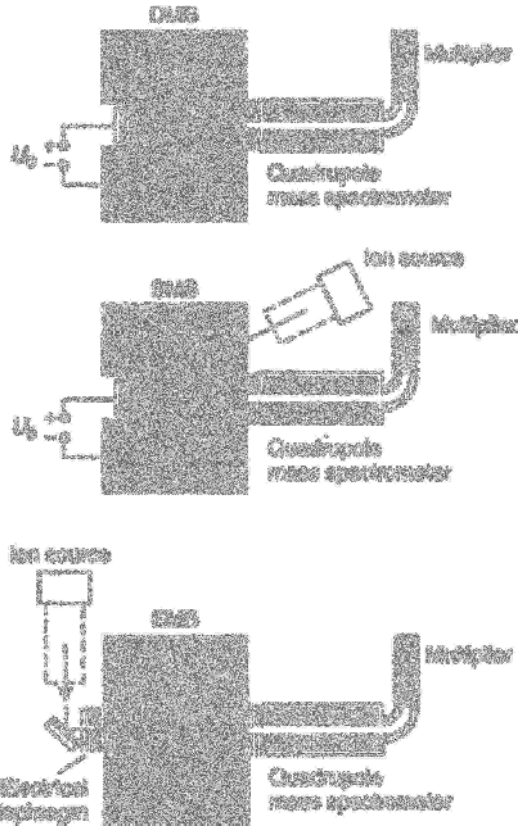

Figure 9.19 Experimental configuration of three variants of SNMS. Top to bottom: direct mode (DMB), separate mode (SMB), and external bombardment (EMB) of the surface with primary ions [21].

The intensity I of a neutral particle X, departing the surface, is given by the following expression [20]:

$$I_X = I_P \cdot S_X \cdot \alpha_X \cdot \eta_{SNMS} \cdot (1 - p_X^+ - p_X^-) \tag{9.4}$$

where I_P is the primary ion current, S_X the partial sputtering yield for particle species X, α_X is the post-ionisation coefficient and η_{SNMS} is a factor involving the geometry, transmission and amplification factors of the particular SNMS instrument. p_X^+ and p_X^- are the ionization probabilities for emission of particles of species X.

Since the sputtering and ionization processes in SNMS are not directly coupled, a sensitivity factor $D_X = \alpha_x \eta_{SNMS}$ is introduced, and this is basically an instrumental constant for species X and is the same order of magnitude for all elements.

It is worth noting that because of the low bombardment energies used in SNMS, there is scarcely any preferential evaporation of elemental species. Although both electron bean SNMS and electron gas SNMS offer good quantitative scope, the latter is the more sensitive, with a detection limit of ≤ 1 ppm for all elements. For electron

Table 9.4 Comparison of analysis data obtained using SNMS and wet chemical methods for an iron alloy (Leybold Heraeus).

Element	Concentration [Atom %]	
	SNMS	Wet chemical
Fe	70.200	70.150
Cr	19.500	19.260
Ni	7.890	8.000
Si	1.360	1.310
Mn	1.030	1.060
P	0.043	0.046

beam SNMS using a fine-focus ion source, lateral resolutions of the order of μm can be obtained. Table 9.4 gives an idea of the confidence with which SNMS can be used for quantitative analysis.

Figure 9.20 shows an SNMS spectrum of electrodeposited copper, using the direct bombardment method

It can be seen in addition to showing copper peaks, the SNMS also shows Ar peaks, this being the bombarding species as well as other species. While all peaks shown can be attributed, not all the data is used in the analysis process. The peak heights can be used to determine the relative concentrations of species present, since SNMS in contrast to SIMS, is virtually matrix-effect free. More detailed analysis reveals that nickel and iron are present as impurities at around the 1 ppm level. Examination of this mass spectrum gives a good idea of the large dynamic range of the technique and in this case, apart from the matrix elements, trace concentrations of other species can be determined in the micrometre per gram range.

As previously noted, SNMS allows one to obtain depth profiles with a high degree of depth resolution and such depth profiles contain all the information one would normally require. Using the electron gas SNMS method in the DBM mode, quantitative depth profile analyses can be obtained with a depth resolution of 1 nm, an example of this being shown in Fig. 9.21.

This spectrum shows that with increasing depth of material removed from the surface, the intensity of the zinc signal decreases, whereas that of iron increases, as one might expect.

The presence of a Cr signal and its intensity decrease, indicates the presence of a chromium layer over the zinc, and the value of this type of data needs no emphasising.

The main advantages of SNMS are:

- all elements can be determined
- highly accurate depth resolution (0.5–1 nm) thanks to use of low energy primary ion bombardment
- direct correlation of SNMS signal intensities and chemical composition of sample
- quantitative depth profile analysis with dynamic range of more than three orders of magnitude
- no problems in analysis of non-conducting materials.

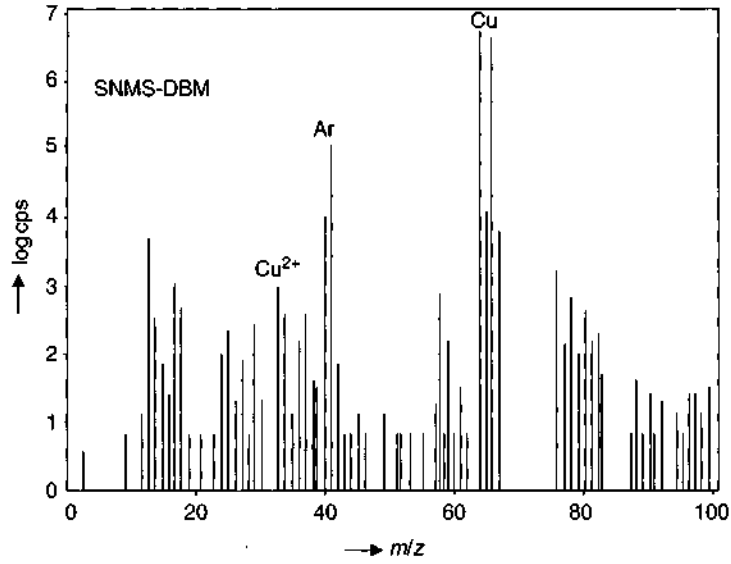

Figure 9.20 SNMS spectrum of electrodeposited copper using the direct bombardment method.

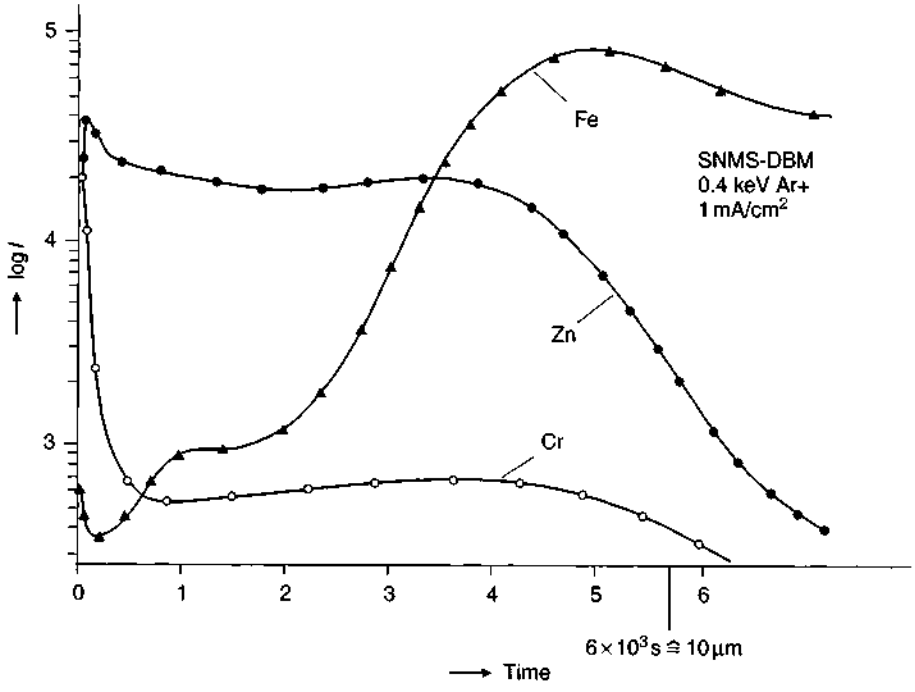

Figure 9.21 SNMS depth profile of a zinc-coated steel sheet (Leybold Heraeus).

Two drawbacks might be noted:

- relatively modest lateral resolution
- damage to sample surface occurs.

9.3 Electron Spectroscopic Methods

Alongside the mass spectrometric methods described above, are a family of techniques based on the use of electrons or photons as the primary or exciting radiation. When a beam of these strikes a substrate, it is partly reflected and partly excites a secondary emission from the surface layers. These processes as well as the energy distribution $N(E)$ of the reflected and emitted species are schematically shown in Fig. 9.22. The term N is plotted as number of electrons versus their energy.

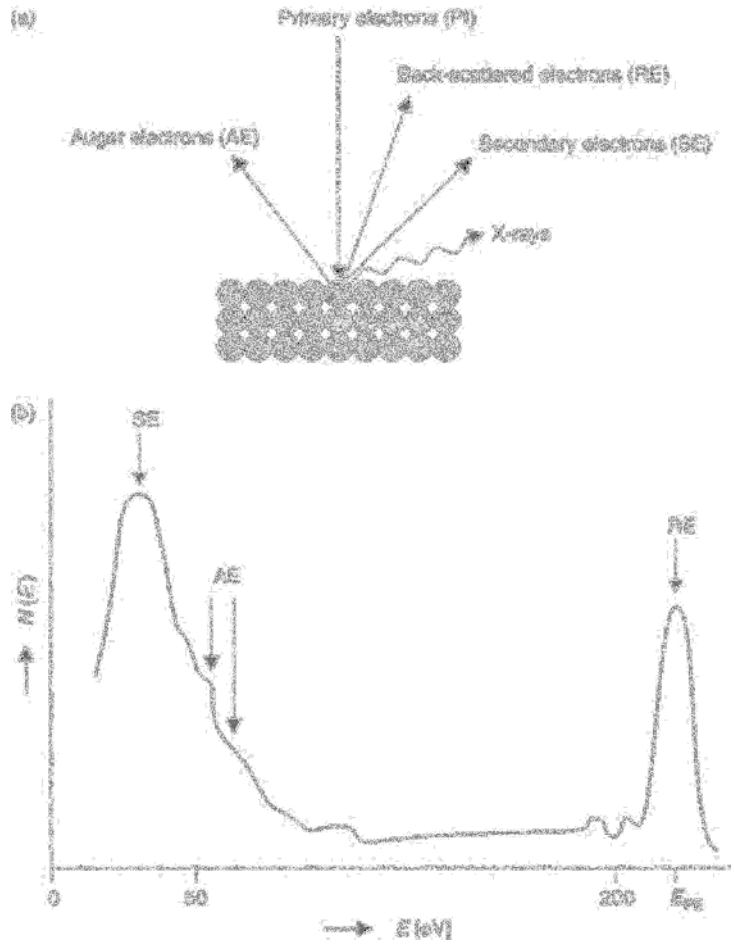

Figure 9.22 (a) Irradiation of surface layer with primary electron beam. (b) Energy distribution plot of the reflected and emitted electrons.

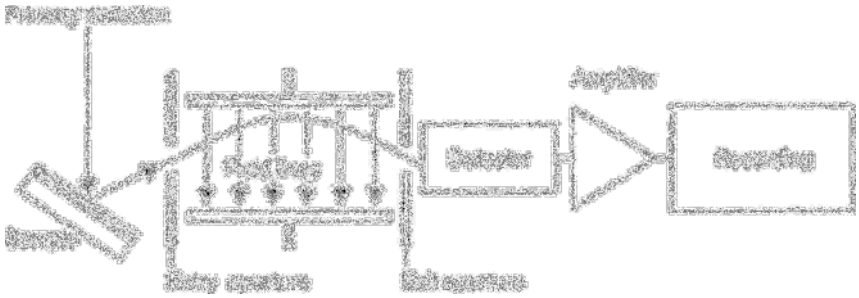

Figure 9.23 Construction of an electron spectrometer for determining the energy and intensity of emitted electrons [30].

The energy distribution plot $N(E) = f(E)$ exhibits three regions, which relate to three different interaction processes. The right-hand peak, RE is due to those electrons, which, after colliding with the surface, are elastically reflected, that is, with no loss of energy. They constitute some 1% of all primary electrons.

A much larger portion of the primary electrons undergoes inelastic scattering, in other words they lose most of their energy following numerous collisions with lattice atoms. The residual energy is then distributed over an extended low-level plateau and this corresponds to the middle part of the energy distribution curve.

The left-hand peak (SE) is due to secondary electrons which are released from the atomic nucleus after collision of primary electrons. These include a group of low-energy electrons, known as Auger electrons, designated AE on the curve.

Figure 9.23 shows the main features of an electron spectrometer, as used to determine electron energy distribution.

By modifying the electric or magnetic fields, electrons emanating from the sample are focused in such a way that they are detected according to their kinetic energies. The energy distribution curve is then obtained by plotting recorded intensities versus applied field strength.

The main variants of this technique include Auger electron spectroscopy (AES) [22–33] and electron spectroscopy for chemical analysis (ESCA) [34–43].

9.3.1 Auger Electron Spectroscopy (AES)

The use of Auger spectroscopy as a non-destructive analytical tool for chemical analysis of surface layers is increasingly employed. Figure 9.24 shows the three-stage re-organisation process which takes place within the electron shells of the excited atom [24, 25, 31]. This embraces excitation, breakdown and relation processes.

If a primary electron with sufficient energy encounters an atom at the sample surface, it is then possible for an electron from the K-shell, that is, the innermost electron shell of the atom, to be ejected, thereby leaving behind it a vacancy (excitation step, Fig. 9.24a). This rapidly gives rise to a re-organisation of the electronic configuration, whereby a more energetic electron from another shell, for example,

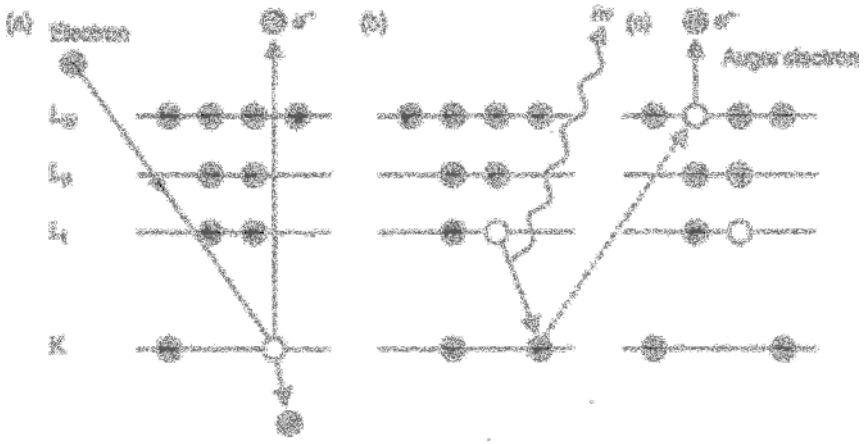

Figure 9.24 Formation of Auger electrons by collision of primary electrons with atoms at the surface. (a) excitation; (b) breakdown; (c) radiationless relaxation.

the L_I-shell hops into the vacant site which is then filled. The energy released by this process is given by the difference

$$\Delta E = E_{L_I} - E_K \tag{9.5}$$

and is usually in the form of an X-ray quantum of frequency $\nu_{LI,K}$ (breakdown process, Fig. 9.24b). It can, however, also result in the ejection of a further electron, for example from the L_{III} shell (radiationless relaxation process, Fig. 9.24c). The kinetic energy of this electron, known as an Auger electron, is then given by the difference between two energy terms:

$$E_{AE} = (E_{L_{III}} - E_{L_I} - E_K) - \Phi_A \tag{9.6}$$

where Φ_A is the work required to expel the electron from the atomic nucleus of the surface material.

Because the Auger electrons possess a characteristic kinetic energy, unequivocal conclusions can be drawn as to the composition of the surface being studied, and these electrons appear as peaks in the energy distribution curve (e.g. Fig. 9.22). Differentiation of this plot renders such peaks more distinct, as seen in Fig. 9.25. By comparing these peaks with data available in tables, elements present can be readily identified while from peak heights (peak-to-trough), the concentrations of these species can be estimated.

Because of the nature of the relaxation process described above, the method is limited to elements of atomic number $Z > 3$. On the other hand, however, the method has the great advantage that the lighter elements, such as boron, carbon, nitrogen, oxygen yield especially high electron efficiencies (Fig. 9.26) and are thus very readily detected in surface layers.

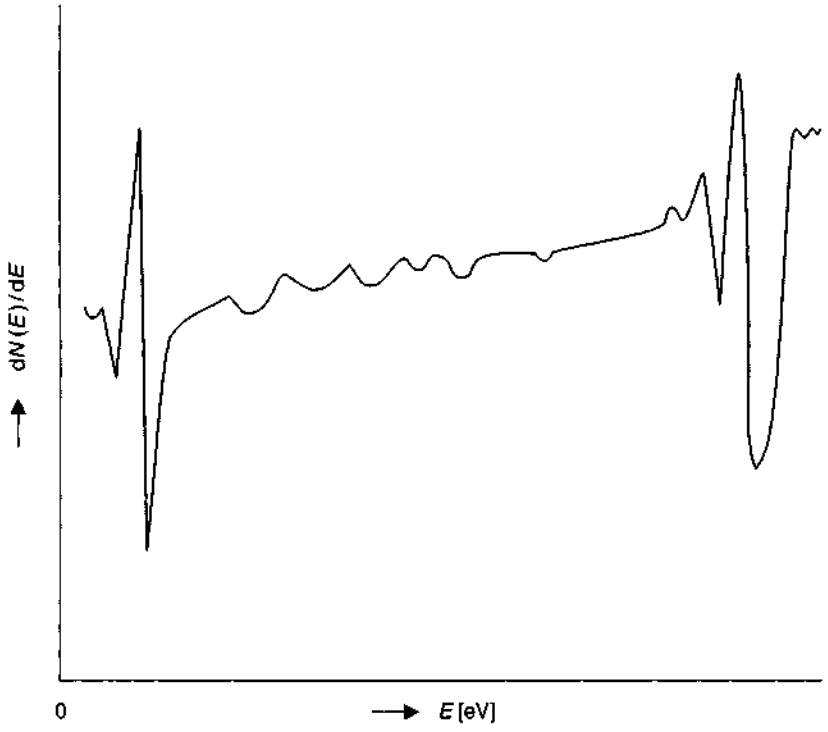

Figure 9.25 Electronically generated first differential, dN(E)/dE of an Auger electron energy distribution curve.

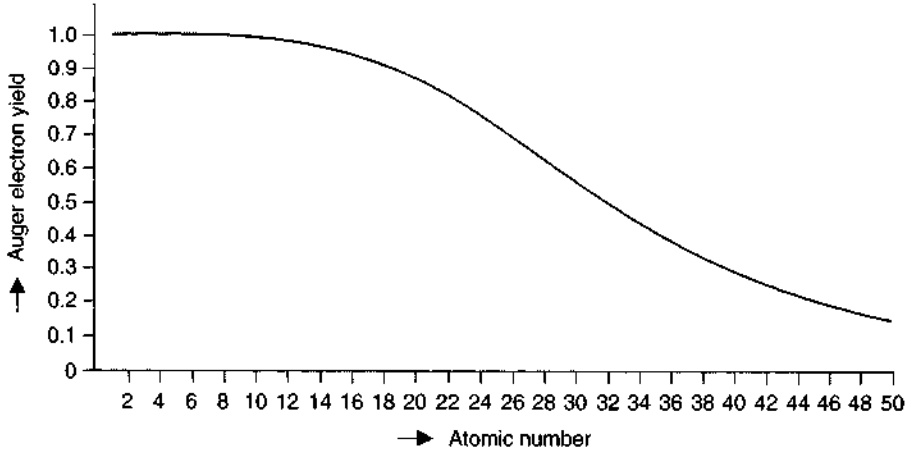

Figure 9.26 Auger electron yield as a function of the atomic number of the element [24].

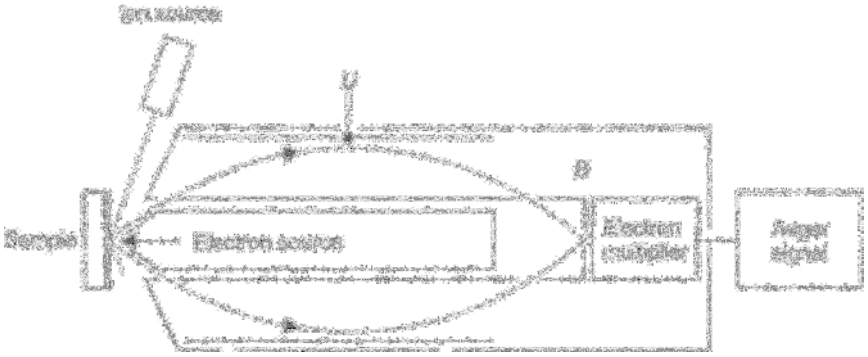

Figure 9.27 Main features of an Auger electron spectrometer with cylinder mirror analyser; B = exit aperture.

Auger instruments often use a special design known as the cylinder mirror analyser, (CMA), the main features of this are seen in Fig. 9.27 [28, 30].

In operation, the sample is normally bombarded with low-energy primary electrons (beam diameter ~3–1 μm, E_{kin} ≈10–1000 eV). These electrons interact with surface atoms and, following loss of kinetic energy, are inelastically scattered. The path length between two consecutive inelastic collisions, known as the mean free path, is a function of the surface composition and the kinetic energy of the primary electrons, and typically will lie between 0.3 and 5 nm. In the case of metals, the values are usually 0.5–1 nm. The useful probing depth of Auger spectroscopy can be taken as three times the mean free path length, and is thus in the range 1–15 nm. The intensity, I_A of a line due to element A present in the surface layers is given by the expression [31]:

$$I_A = I_P \cdot \sigma_A(1 + r_M) \cdot T \cdot D \int_0^\infty c_A \exp\left(\frac{-Y \cdot \cos\theta}{\lambda_M}\right) \cdot dY \qquad (9.7)$$

where I_P is the primary electron current, σ_A is the effective cross-section for emission of Auger lines, λ_M the primary electron back-scatter factor, T is the transmission efficiency of the instrument, D the detector efficiency, θ the electron exit angle (referenced to the normal of the sample plane) and c_A is the concentration of element A as a function of depth Y.

The kinetic energy of the Auger electrons depends slightly on the energy level differences of the electron shells involved in the Auger process and is normally in the range 20–2000 eV. Such low values explain why electrons emerging from the surface originate only from the outermost layers, typically ≈2 nm in depth.

The AES spectrum shown in Fig. 9.28 provides useful data on an electroless copper deposit.

The spectrum provides information on the condition of the surface of the deposit after deposition, indicating the presence of a contamination film containing chlorine, carbon and oxygen atoms which has formed above the copper. Whereas the last of these two elements presumably originated in the instrument, the source of the chlorine is not clear.

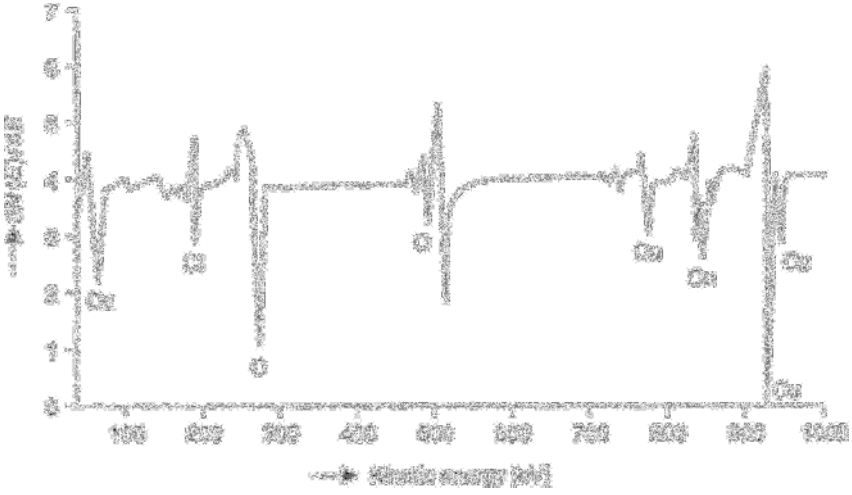

Figure 9.28 Auger full-range spectrum of an electroless copper deposit.

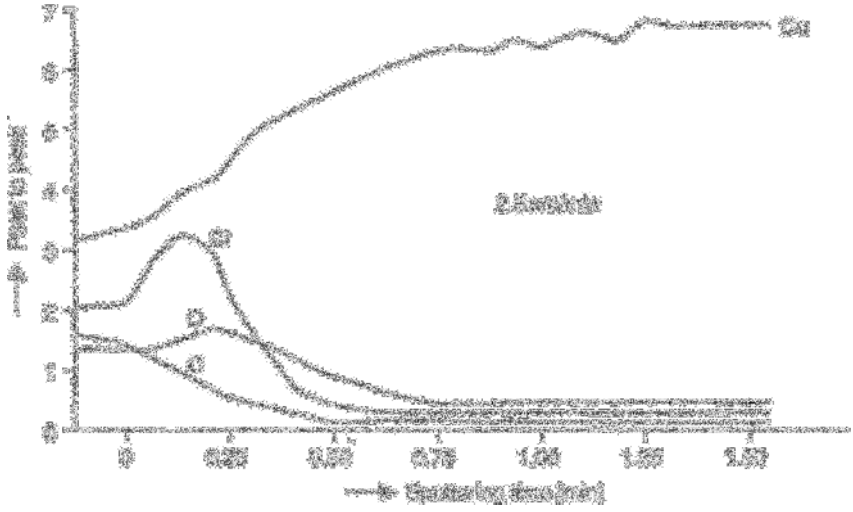

Figure 9.29 Depth profile analysis for the elements C, Cl, O_2 and Cu in an electroless copper deposit.

Apart from these elements, no others can be detected, indicating that the copper deposit itself is of a high purity. In another approach, the ion source of the Auger instrument (Fig. 9.27) can be used either continuously or intermittently to progressively sputter away the surface layers, and by so doing, a depth profile analysis can be produced. This can be done using Ar^+ or Kr^+ ions. Typical material removal rates are 1–100 nm/min and in this way, depths up to 10 μm below the surface can be examined. Figure 9.29 shows how use of a continuous sputtering mode at a rate of 2.5 nm/min can be used to create a depth profile analysis.

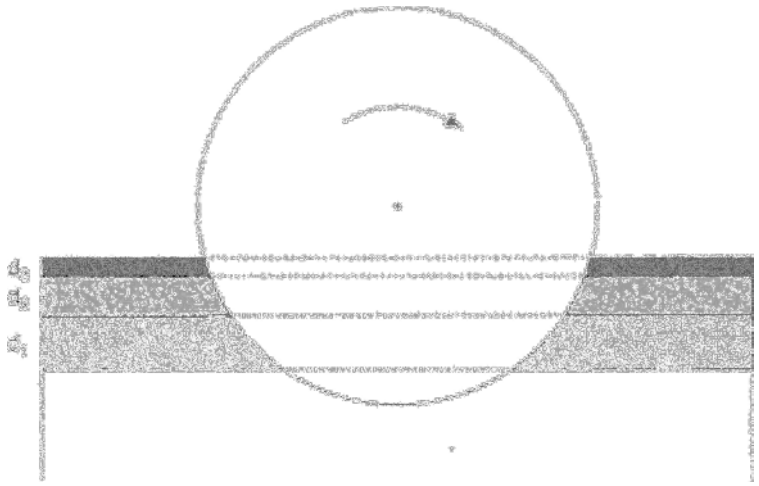

Figure 9.30 Radial sectioning method used to render visible various layers (d_1, d_2, d_3).

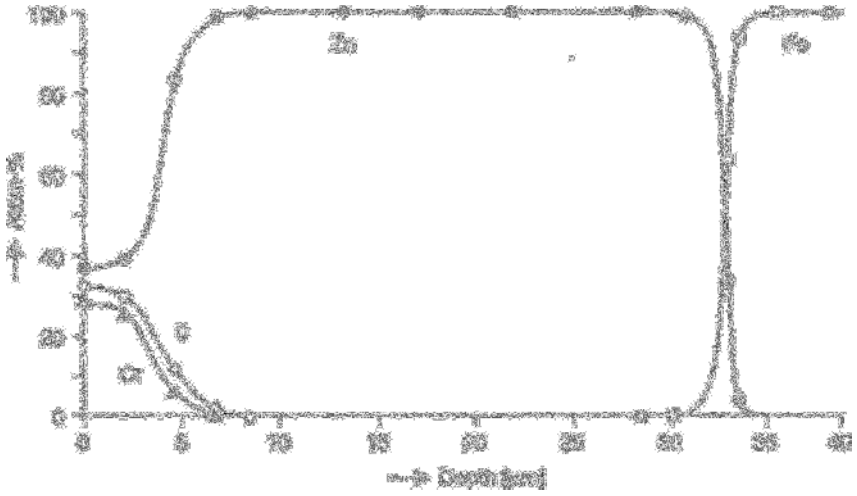

Figure 9.31 Depth profile measurement on a galvanised steel sheet, using radial sectioning to create the cross-section [32].

The results indicate that elements other than copper are present only at the outer surface of the deposit and at depths >1 nm, virtually only copper is present. The so-called radial sectioning method (Chapter 8) widely used for thickness measurement in multilayer systems can also be used for Auger studies to obtain concentration depth profiles in the depth range 1–100 μm (Fig. 9.30) [15, 32]. An example of this is seen in Fig. 9.31, which shows zinc galavnised steel sheet which has then been chromated to improve paint adhesion. The results indicate a zinc thickness of 30–35 μm. It can also be seen that chromium ions have penetrated to a depth of some 5 μm into the zinc layer.

A further development of AES is SAM — scanning Auger microanalysis. Here, the beam can be rastered over the sample surface, thereby allowing a 'map' of elemental distributions to be produced. The primary electron beam is 1 μm down to 25 nm and surface areas of 0.5 cm^2 down to a spot of 1 μm can be thus examined. Using accelerating voltages of up to 35 kV, lateral resolutions of less than 0.1 μm can be obtained (9.20). It should be noted that with such high energies, local surface heating of the sample may occur and other types of damage can be caused by the electron beam, not least in semiconducting materials, as well as electron-induced desorption processes. In conclusion, the main strengths of Auger electron spectroscopy can be listed as:

- sampling depths of 0.5–10 nm
- detection limits typically of order 10^{-2}–10^{-3} of a monolayer
- lateral resolution of ca. 0.2 μm
- all elements detectable except hydrogen and helium
- option of point and line analysis for elements from Li to U
- option of depth profiling used in combination with sputter-etching
- production of 'maps' showing elemental distribution.

Drawbacks include:

- elements of atomic number <3 not detectable
- low sensitivity in the range 0.1–1 at%
- electrostatic charging problems with non-conducting samples
- data interpretation problems with overlapping peaks
- information as to chemical compounds only in restricted cases.

9.3.2 Electron Spectroscopy for Chemical Analysis (ESCA)

ESCA is now widely used as an analytical tool. It is based on photo-effects taking place in the inner atomic orbitals. The surface is bombarded with monochromatic photons (excitation) and the emitted electrons (photo-electrons) are analysed in terms of their energies. The method leaves a surface virtually unaffected, and the principle is shown in Fig. 9.32.

The kinetic energy of the emitted photoelectrons is given by the conservation of energy equation:

$$E_{kin} = h\nu - E_B - \Phi_A \tag{9.8}$$

where $h\nu$ is the energy of the exciting photon and Φ_A is the electronic work function. Since Φ_A is in general <1 eV, this term can usually be neglected. E_B is the electron binding energy and thus specific to the particular atom being studied, provided that the photoelectron does not undergo an inelastic collision in the surface layers.

Because only relatively low kinetic energies are involved in respect of the emitted photoelectrons, the penetration depth of the ESCA technique is little more than 2 nm beneath the surface. This makes it ideal for analyses of species on a surface. In addition, the technique yields information as to the binding states of atoms at the surface being studied. Either UV or X-rays can be used as the excitation source, and

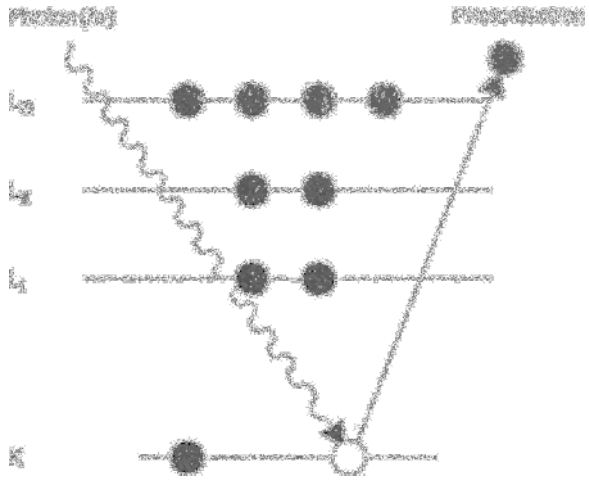

Figure 9.32 Excitation of an atom by bombardedment with photons and emission of photoelectrons.

the technique is then referred to as UPS (ultraviolet photoelectron spectroscopy) or XPS (X-ray PS).

In the former case, monochromatic UV radiation is used, with a low-pressure helium lamp as source. The wavelength $\lambda = 58$ nm, and energy $E = 21.21$ eV. By lowering the pressure still further, He(II) radiation can be obtained ($\lambda = 30.4$ nm, $E = 40.8$ eV). This exciting radiation is introduced into the sample chamber through a capillary, being directed at the sample surface. The energy resolution of the method is so good, thanks to the very narrow line-widths of the He(I) and He(II) radiation (He(I) = 0.003 eV, He(II) = 0.017 eV) that even molecular vibration spectra can be obtained. The UPS variant is then preferable when studies of valence states and conduction band structures are undertaken [3].

In practice, the XPS variant is more widely found. Here, AlK_α radiation ($E = 1.486$ eV, linewidth = 0.83 eV) or MgK_α ($E = 1.253$ eV, linewidth = 0.68 eV) are used. The main features of an XPS instrument are shown in Fig. 9.33.

Emitted electrons are analysed in terms of their kinetic energies, and intensities stored as a function of their kinetic energy. The intensity I_A of a photoelectron from element A is given by the expression [3]:

$$I_A = g \cdot J_P \cdot \sigma_P \int_0^\infty c_A \cdot \exp\left(-\frac{Y}{\lambda_{eff}}\right) \cdot dY \tag{9.9}$$

where g is a constant for the instrument, J_P is the photon flux, σ_P is the photon-efficiency cross-section, c_A is the atomic concentration of element A as a function of depth Y and λ_{eff} is the effective exit depth.

In the same way as for AES, the electrons emitted are counted (cps) and recorded as a function of their energy. Using tabulated data available in the literature, atoms and molecules, as well as the binding states of the latter, can be assigned according

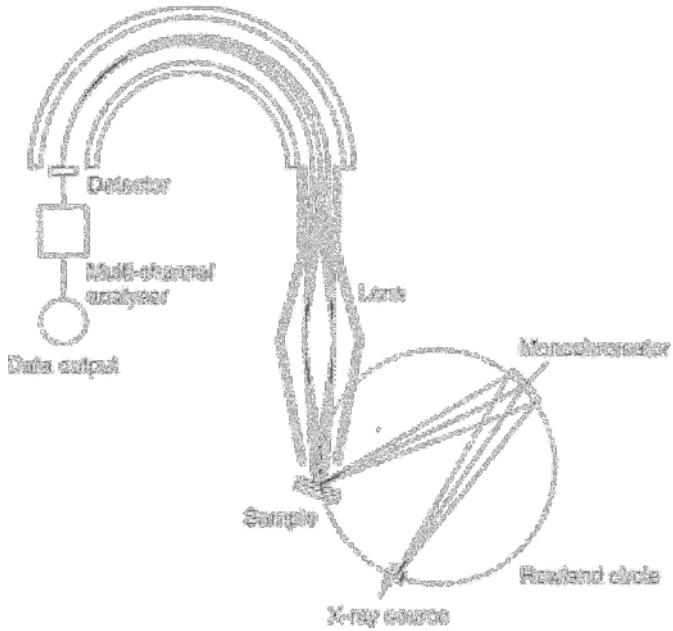

Figure 9.33 Main features of an X-ray photoelectron spectrometer [40].

to their energies. In contrast to AES, where the energy of the Auger electrons emitted depends only on the type of atom being excited, here, the energy of the emitted photoelectrons depends also on the wavelength of the exciting X-rays.

The sampling depth ranges from 0.5 to 10 nm, while the detection limit, on account of the variable photo-efficiency cross-section, ranges from 0.1 to 1.0 at%. In terms of its resolution, the following should be noted. Since X-rays are relatively hard to focus accurately, the irradiated area of the sample will be quite large, perhaps $1 \times 1\ cm^2$. However, in the most modern instruments, a sampling area of diameter as little as 150 μm can be achieved. These instruments are known as 'small spot XPS' (SSXPS) [5]. The price to be paid for this, is a diminution in the signal energy.

Figure 9.34 shows a wide-range XPS spectrum of an electroless copper deposit immediately after its formation.

The individual peaks in this spectrum are due to the different electron relaxation processes which give rise to both photoelectrons and Auger electrons, which explains why both types of peak are seen in the spectrum. The spectrum reveals the presence of a contamination layer above the copper, with oxygen and carbon peaks in evidence (O_{1s} and C_{1s}).

Using the ion source which forms part of this equipment, it is possible to sputter-etch away the sample surface, layer-by-layer, thereby removing surface contamination. This increases the sensitivity of the method to metallic impurities within the copper deposit. The XPS spectrum after removal of the surface impurity layer is shown in Fig. 9.35.

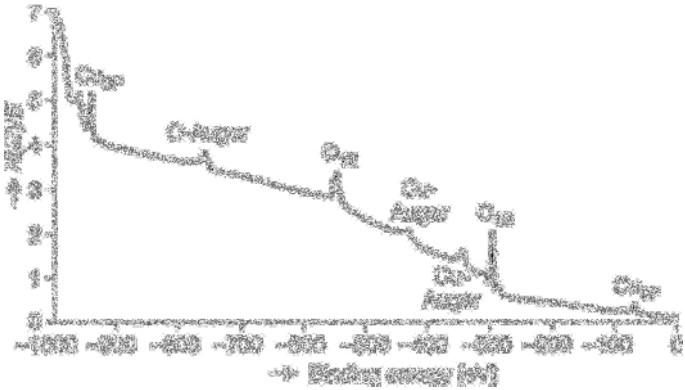

Figure 9.34 XPS wide-range spectrum of electroless copper deposit immediately after its formation.

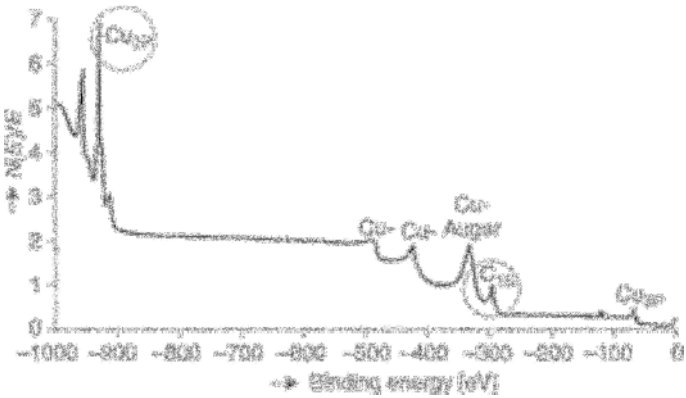

Figure 9.35 XPS wide-range spectrum of electroless copper (as Fig. 9.34) but after removal of outermost contaminated layer by sputter-etching

One special strength of the ESCA technique is that it not only analyses for specific elements, but also provides information on their binding state. This is due to the fact that the binding energy of electrons in the nucleus is affected by their neighbouring atoms. Thus, a different signal will be emitted from atom A, depending on whether it adjoins another atom of the same element, or some other element. This is illustrated in Fig. 9.36 which shows the oxidation of beryllium.

Since oxidation involves loss of electrons, those that remain, become more tightly bound to the atomic nucleus and thus, a higher ionisation energy is required to strip them from the nucleus. This gives rise to the so-called chemical shift observed in the XPS spectrum, which distinguishes a species in its elemental state from the same element as a constituent of a compound. Since sputtering off the contamination film from a copper surface causes changes in binding energies, this too will give rise to peak shifts in the XPS spectrum. Such a shift of the Cu_{2p}- and Cu_{1s} peaks can be

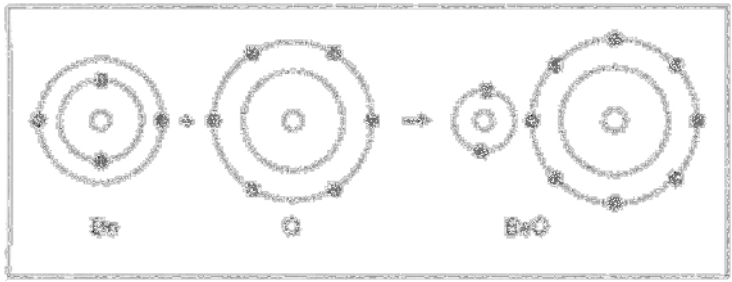

Figure 9.36 Increase in electron binding energy, as shown by a pure metal (beryllium) forming its oxide.

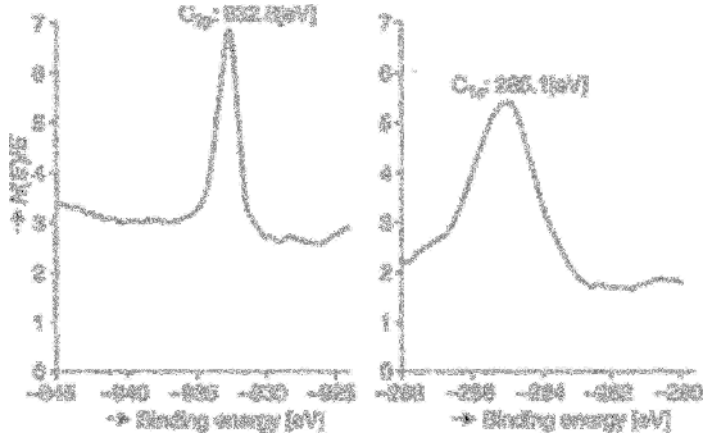

Figure 9.37 Chemical shift of the C_{2p} and C_{1s} peaks after sputter-etching away the outer contamination layer of a copper deposit.

clearly seen in the sectional spectra of Fig. 9.37. From this, it is clear that the Cu_{2p} peak, originally at -934.0 eV has been shifted to -932.8 eV. The corresponding figures for the Cu_{1s} peak are -286.0 and -285.1 eV

With a suitably sensitive instrument, peak shifts of <1 eV can be detected.

In summary, the main advantages of ESCA are:

- sampling depth range ca. 0.5–10 nm
- sensitivity of 10^{-1}–10^{-2} particles per monolayer
- elements from Li to U detectable
- unequivocal assignment of elements
- detailed spectra show binding energies of elements
- oxidation state can be determined using peak shift
- concentrations can be estimated from peak heights or relative heights.

Drawbacks of the method are:

- poor lateral resolution (5–100 μm)
- poor depth resolution
- radiation-induced side-effects impair absolute determinations.

Table 9.5 Methods for study of surfaces and surface coatings and their main features.

Characteristic	Analytical technique				
	ISS	SIMS	SNMS	AES	ESCA
Excitation by	Ions	Ions	Ions	Electrons	Photons
Beam diameter (μm)	100	100	100	0.2–3	~1000
Emission of:	Ions	Ions	Neutral-particles	Electrons	Electrons
Sampling depth (monolayers)	1	1	1	1–10	10
Elements detectable	$Z > 1$	All	All	$Z > 2$	$Z > 1$
Isotope detection	No	Yes	Yes	No	No
Detection of compounds	No	Yes	Yes	Possible	Yes
Detection limit (ppm)	1000	1	1	100	1000
Sampling area (mm^2)	0.5–5	0.1–10	0.1–10	10^{-10}–10^{-2}	2–100
Lateral resolution (μm)	100	0.1–1	100	0.1–3	150–1000
Variation of atomic sensitivity	×50	$\times 10^4$	$\times 10^4$	×10	×10
Quantitative analysis	Possible	Possible	Possible	Yes	Possible
Depth profile analysis	Possible	Yes	Yes	Yes	Possible
Damage to sample surface	No	Yes	Yes	Minimal	Minimal
Analysis of non-conductors	Yes	Yes	Yes	No	Yes

Table 9.5 collates the main features of the analytical techniques described in preceding sections, with a view to allowing selection of the most suitable method for a particular task.

9.4 Microanalysis

The techniques described above can more or less be described as *surface analysis methods* describing the condition and composition of what is on or very near the surface. In order to determine the composition of a coating, other techniques, capable of probing more deeply below the surface, must be used. Foremost among these are methods employing X-rays, whose high energy allows them to penetrate more deeply into solids.

Depending on the magnitude of the accelerating voltage, U and the material of the solid coating, the primary electrons (PE) will penetrate more or less deeply beneath the surface. Within the so-called excitation volume (electron diffusion zone), the electrons are retarded by the atoms in the solid, and deviated or scattered or involved in other interactions. In the case of the lighter elements, the excitation volume is pear-shaped while for heavier elements, it is more spherical in shape [47, 49]. Its precise geometry is influenced by the acceleration voltage and the extent of radial electron scattering in the solid layer (Fig. 9.38).

The effective range or penetration depth R (μm) of the primary electrons into the solid is not only a function of acceleration voltage U (kV) and the atomic number, but also the mean relative atomic weight A, the density ρ (g/cm^3) of the coating layer

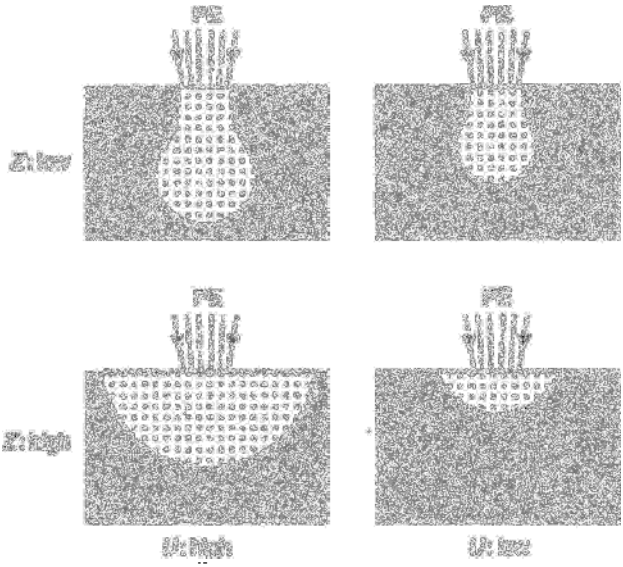

Figure 9.38 Effect of atomic number and acceleration voltage U on the shape and size of the excitation volume.

and also the critical excitation voltage U_c (kV). Below this value, no excitation occurs. Castaing [1] derived the following expression:

$$R = 0.0033 \cdot (U^{1.7} - U_c^{1.7}) \cdot \frac{A}{\rho \cdot Z} \tag{9.10}$$

For an acceleration voltage 30 kV, often used in practice, the penetration depth of primary electrons into aluminum is ~5 μm, into copper ~2 μm and for lead, 1 μm. At 10 kV, the corresponding values for aluminium and lead are ~1 and 0.2 μm, respectively.

The primary electrons trigger a range of processes below the surface of the solid giving rise to the emission of numerous signals, including secondary electrons (SE), back-scattered electrons (RE), bremsstrahlung** and characteristic X-rays (γ). These can be distinguished from one another in terms of the various size of diffusion zone within the solid, from which they can be emitted. The loci where these are generated are shown schematically in Fig. 9.39.

Secondary electrons: These are formed within a thin zone of the surface layer, up to a depth determined by the penetration of the primary electrons. They are used in scanning electron microscopy, since they provide a high degree of lateral resolution of order 10 nm and allow surface images with a high depth of focus.

Back-scattered electrons: Back-scattered electrons offer a poorer lateral resolution than their secondary analogs, since they derive from a larger and deeper-lying

** Bremsstrahlung – a German term with apparently no English equivalent, and the German expression is used as such in English language publications. Heterochromatic or continuous ('white') X-ray radiation.

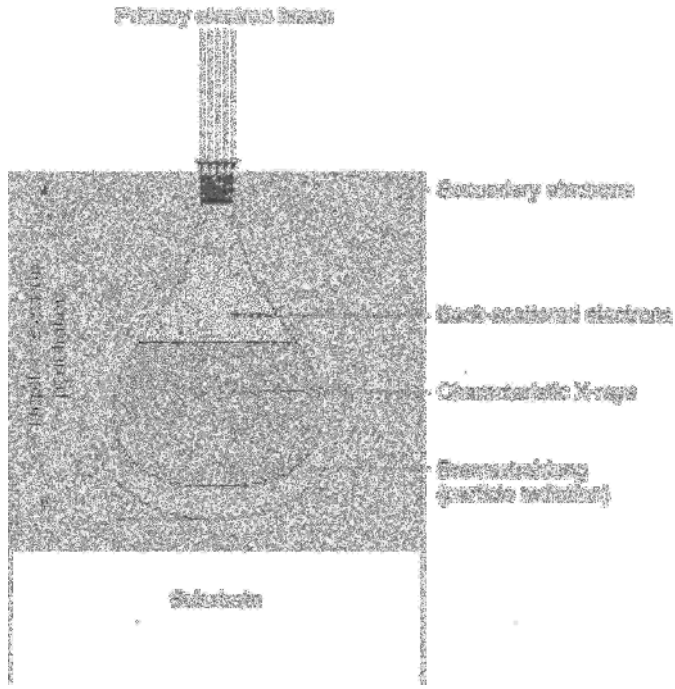

Figure 9.39 Formation of secondary and back-scattered electrons as well as characteristic X-ray emissions and bremsstrahlung from within the excitation volume.

volume beneath the surface. Images based on these electrons cannot thus be usefully be magnified beyond about 2000×. However, they allow surface contours to be shown with remarkably plastic form. This is due to the direct line of travel of back-scattered electrons to the detector, thereby creating shadow effects on features at the far side of the detector. In addition, the back-scatter coefficient, that is the number of back-scattered electrons as function of the number of primary electrons, depends on the mean atomic number. The resulting high-contrast image from back-scattered electrons can thus be invaluable in some types of structure investigation.

The curves in Fig. 9.40 show the resolving power of secondary and backscattered electrons as a function of the diameter of the primary electron beam.

This shows how the achievable resolution compares with that using X-rays. It is seen that in the latter case, a resolution of only a few micrometres can be hoped for, provided the diameter of the primary electron beam is <1 μm. The three plots should not be considered as more than an idealized notion of the resolving power of which the three methods are capable.

X-rays: X-ray emissions from a solid are due to two processes. When primary electrons, encountering atoms beneath the solid surface are scattered, they lose kinetic energy which is then emitted as so-called bremsstrahlung (Fig. 9.41a). This consists of a continuous X-ray spectrum (Fig. 9.41b), which, though it includes the full range of energies, contains no information that might allow chemical analysis of

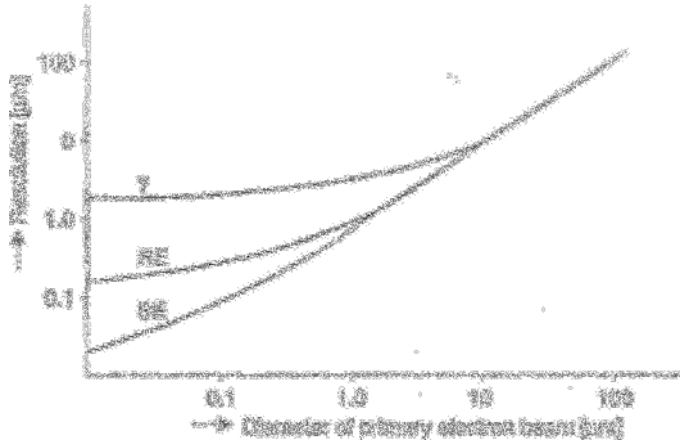

Figure 9.40 Resolving power of secondary and backscattered electrons and X-ray emissions as a function of the diameter of the primary electron beam [57].

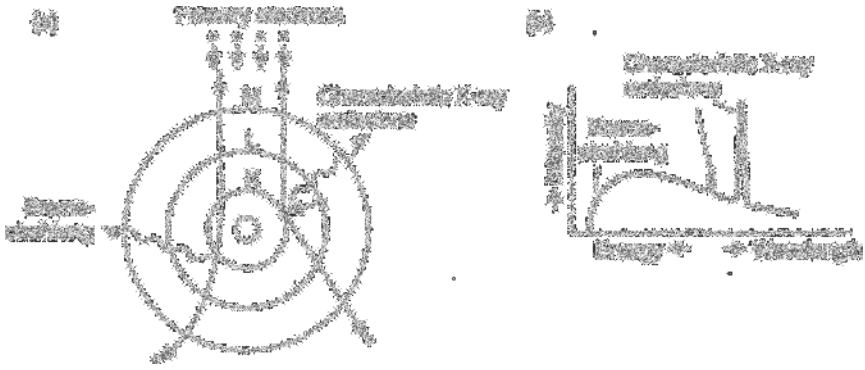

Figure 9.41 Formation of continuous bremsstrahlung and characteristic X-rays: (a) interaction between incident primary electrons and atoms; (b) X-ray spectrum.

the solid from which it is emitted. Instead, it forms a background noise level which degrades the actual signals with informational content, and which must be filtered out as far as possible.

If, by contrast, the primary electrons impact electrons in the atomic orbitals of the sample, thereby ejecting these from their shell, the resulting vacancies are then filled within less than 10^{-15} s, by electrons from other shells (Fig. 9.41a). This energy difference is then released in the form of characteristic X-rays (Fig. 9.41b). Depending on the shell from which this emanates, one refers to K-, L- or M-radiation.

A characteristic X-ray spectrum, in contrast to bremsstrahlung, exhibits a number of lines or peaks, each of which can be unequivocally assigned to a particular element, in terms of its location. These X-ray signals can be characterised in terms of their wavelength and energy. Where peak height (intensity) is displayed as a function of energy ($I = f(E)$), the technique is known as energy-dispersive X-ray analysis

[47–55]. If, instead, peak height is displayed as function of wavelength, $I = f(\lambda)$, the method is known as wavelength dispersive X-ray analysis [56–60]. The physical basis is the general relationship between energy and wavelength, given by the expression:

$$E = \frac{h \cdot c}{\lambda} \tag{9.11}$$

Here, h and c are Planck's constant and the velocity of light, respectively. The intensity I_o of the X-rays, that is, their peak height, can be derived from the equation:

$$I_o = k \cdot (U - U_c)^{5/3} \tag{9.12}$$

where k is a constant.

9.4.1 Energy-Dispersive X-Ray Analysis (EDX)

The equipment used for this technique employs a semiconductor X-ray detector, a multichannel analyser and data display instrumentation. The basics of such an instrument are seen in Fig. 9.42 [47, 52]. To protect the detector from contamination, etc., a 7.5 μm X-ray transparent beryllium window is provided.

For chemical analysis of a sample, the detector is brought up close to the surface so that the emitted X-rays subtend the greatest possible solid angle. The widely used 45° inclination of the detector (Fig. 9.43) maximises secondary electron capture and also ensures a favourable exit angle, θ for the characteristic X-ray emissions. Under most conditions, (plane-polished sample surface and unchanged position of the X-ray detector), θ is then a constant for the experimental set-up. Inclination

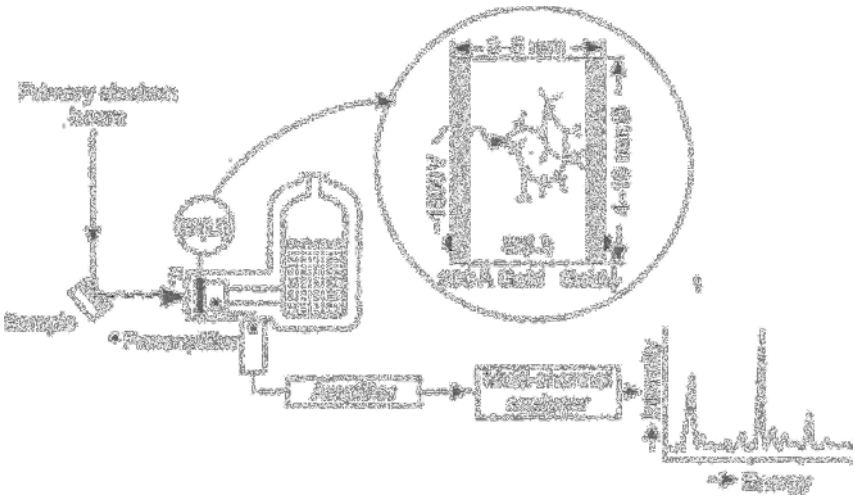

Figure 9.42 Main features of an EDX spectrometer (F = beryllium window).

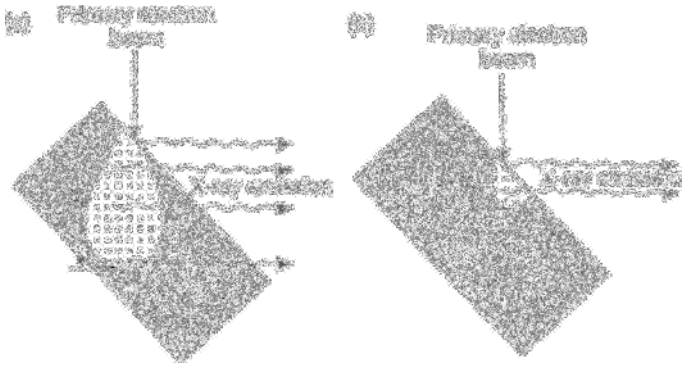

Figure 9.43 The 45° sample inclination for increased SE yield and increased excitation (sampling) volume: (a) light element; (b) heavier element.

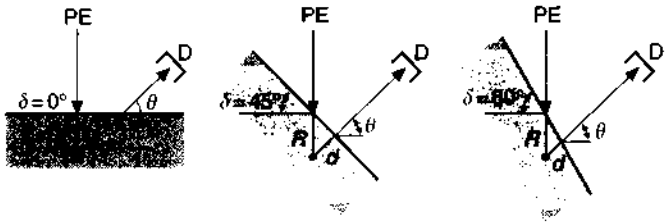

Figure 9.44 Decrease in path-length d with increasing angle of tilt δ (PE = primary electron beam, θ = exit angle, D = X-ray detector [49].

of the sample also brings about an increase in the area exposed to the X-rays, so making the resulting output signal more representative.

The characteristic X-rays are partly absorbed, in their transit through the surface coating. The extent of this is a function of path length and the specific absorption of the material in question, μ. From Fig. 9.44 it is seen that the path-length d becomes smaller as the angle of tilt of the sample increases. The path length d, for an untilted sample ($\delta = 0$) is:

$$d = R \cdot \frac{1}{\sin \theta} \tag{9.13a}$$

While for a tilted sample, it is smaller as:

$$d = R \cdot \frac{\cos \delta}{\sin(\theta + \delta)} \tag{9.13b}$$

Decreasing the absorption path-length as the angle of tilt increases, leads to an increase in the intensity of the emitted X-rays. If this intensity is designated as I_0 for

$\delta = 0$, then for the case $\delta \neq 0$:

$$I = I_0 \cdot e^{-\mu \cdot d} = e^{-\mu \cdot R \cdot (\cos\delta / \sin(\theta + \delta))} \tag{9.14}$$

The characteristic X-rays emitted from the surface layer, of intensity I are captured by the semiconductor detector, absorbed in the p–n transition zone where they initiate an ionization (Fig. 9.42). Charge carriers formed by ionization, the number of which is proportional to the energy of the X-ray quanta, migrate under the potential field towards the gold electrode (Fig. 9.42). Given that for every ionization taking place in the Si(Li), that is, for formation of an electron – hole pair, according to the equation:

$$n \cdot Si + \gamma \rightarrow n \cdot Si^+ + n \cdot e^- \tag{9.15}$$

an energy of 3.8 eV is required [52], the value n, for the maximum possible number of ionisations is readily calculated. Conversely, if the number of ionisations is known, the energy of an X-ray quantum can be derived. Using the preamplifier shown in Fig. 9.42, a voltage pulse can be recorded, whose height is proportional to the electron flux and thus the energy of the X-ray quanta. After further amplification, the voltage signal is fed into a multichannel analyser and sorted according to energy. Having selected the desired range of energies, the output can then be displayed on screen.

9.4.1.1 Qualitative EDX analysis

In a qualitative EDX analysis of an electroplated or electroless layer, the issue is simply one of which elements are present. Subjected to this technique, an EDX spectrum is obtained. This consists of a slightly bent baseline, which is the manifestation of bremsstrahlung, together with discrete lines corresponding to elements present in the sample. The height of these peaks allows the relative concentrations of elements to be estimated. Figure 9.45 shows such a spectrum for a 10 μm thick electrodeposit of lead–tin over a copper substrate.

The Cu peaks derive from the substrate. EDX will detect elements from $Z \geq 11$ (sodium), since the characteristic X-rays from elements $Z < 11$ is largely absorbed by the beryllium window of the X-ray detector. Thus, for example, 40% of Na-Kα radiation and 98% of oxygen-Kα radiation fail to penetrate the beryllium window.

An element can be detected with confidence when its peak is at least three standard deviations above the background level, in other words the relevant peak must be clearly visible above the background due to bremsstrahlung. The energy-resolution of the X-ray detector, which determines its ability to separate adjoining peaks is specified for an energy value of 5.894 keV (manganese Kα-line). For the Si(Li) detector, this has a theoretical value of 79 eV, though in practice, a value of 150 eV is more realistic. For this reason, the technique cannot be used to detect elements below carbon in the Periodic Table.

The detection limits for EDX are at or less than 0.1 wt% for count rates of 100–500s. Increasing the accelerating voltage allows the detection limit to be improved. Qualitative EDX can be used to study a sample in several modes, namely point and line analyses as well as creating elemental distribution maps.

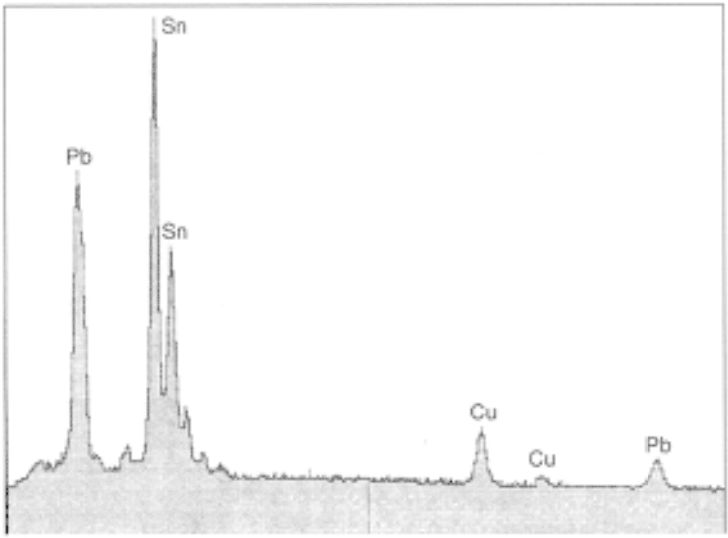

Figure 9.45 EDX spectrum of a 10 μm thick PbSn eutectic deposit over a copper substrate (U = 20 kV).

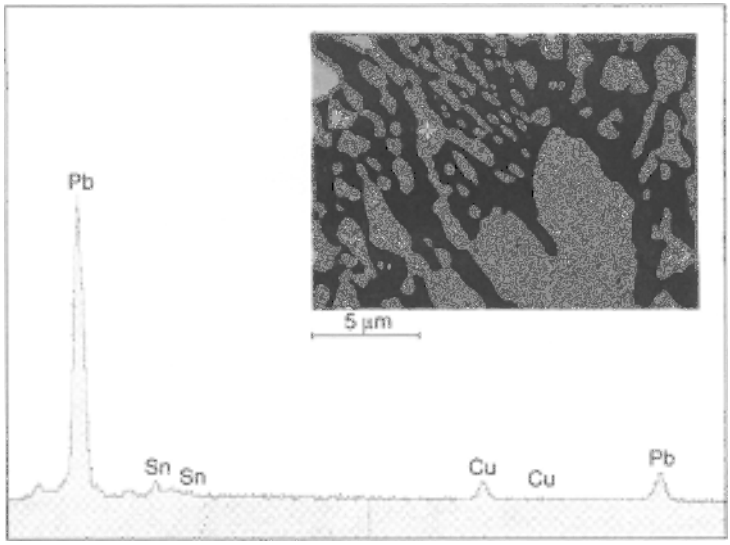

Figure 9.46 Back-scattered electron image and spot analysis (+) from a 10 μm thick tin–lead deposit (U = 20 kV).

Point analysis: The aim here is to provide analytical data for specific locations at a surface. The primary electron beam is thus steered, using the image formed on-screen by secondary or back-scattered electrons, to the location required, after which the analysis is carried out. Figure 9.46 shows a back-scattered electron image and a point analysis for a tin–lead deposit. That part of the structure on the image

marked with a (+) can be seen to consist mainly of lead with only modest amounts of tin. The copper peaks are due to the underlying copper substrate.

Line analysis: Should it be that several point analyses give rather different values for a given element, it is good practice and often insightful to conduct a line analysis where the concentration of an element is tracked along an arbitrarily chosen line. The detector is set that only a narrow sector of the total energy spectrum is registered and then slowly tracked along the prescribed line. In this way, the incoming X-ray pulses are collected at constant time intervals in the appropriate channels of the multichannel analyser. Figure 9.47 shows a back-scattered electron image and the corresponding line concentration profile analysis for a tin–lead deposit. The light areas of the structure are found, on the basis of the analysis, to be predominantly lead, embedded in a tin-rich matrix.

Elemental distribution visualisation: EDX, as with certain other techniques noted in this chapter, can be used to 'map' the distribution of a given element over a two-dimensional surface. Using the same X-ray conditions as for point analysis, the beam is rastered over an area demarcated by the user. Although the sensitivity of the resulting map is less than would be obtained from a point analysis, this means of presenting data is extremely valuable. To create such an image, some 50,000–100,000 pulses are required. The example of a tin–lead coating shown in Fig. 9.48

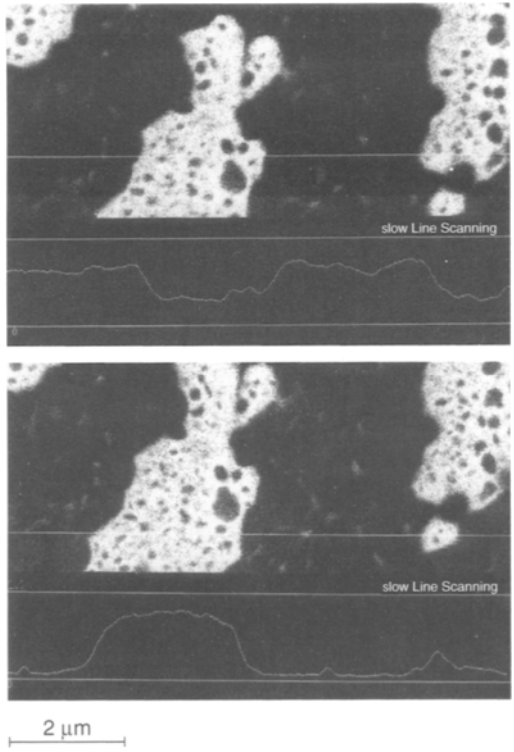

Figure 9.47 Back-scattered electron image and concentration profile (line analysis) for tin (top) and lead (below) in a 10 µm thick tin–lead deposit (U = 20 kV).

confirms that the areas appearing light in the back-scattered electron image of the structure are mainly lead.

9.4.1.2 Quantitative EDX analysis

The purpose of this technique is to carry out a complete and accurate analysis of all species present in a surface layer. This calls for a high-quality plane-polished sample surface, if reliable and reproducible results are called for. Without such sample preparation, spurious results may be found. The schematic in Fig. 9.49 illustrates how surface topography can adversely affect an EDX analysis [48, 55].

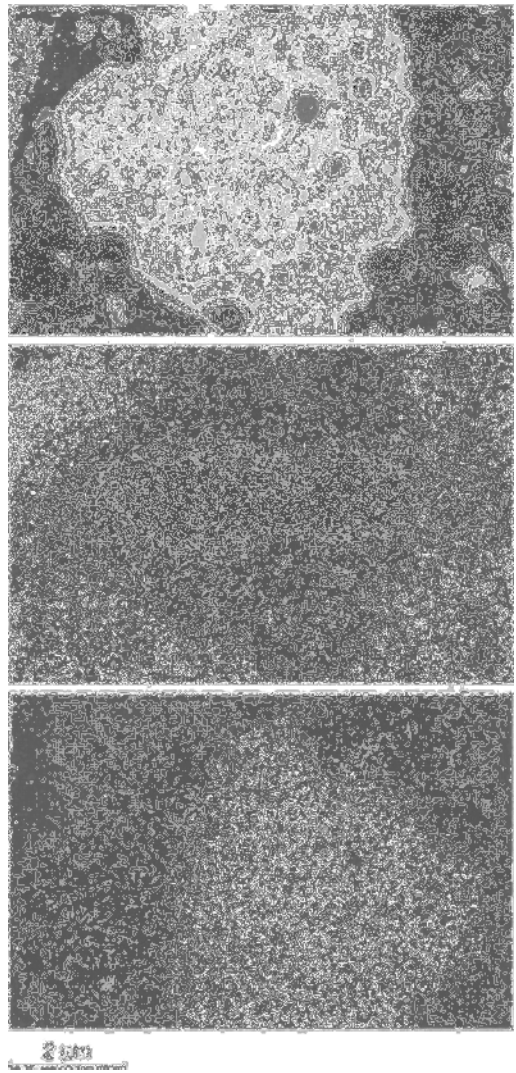

Figure 9.48 Back-scattered electron image and elemental distribution images of tin and lead from a 10 µm thick tin–lead coating (U = 20 kV).

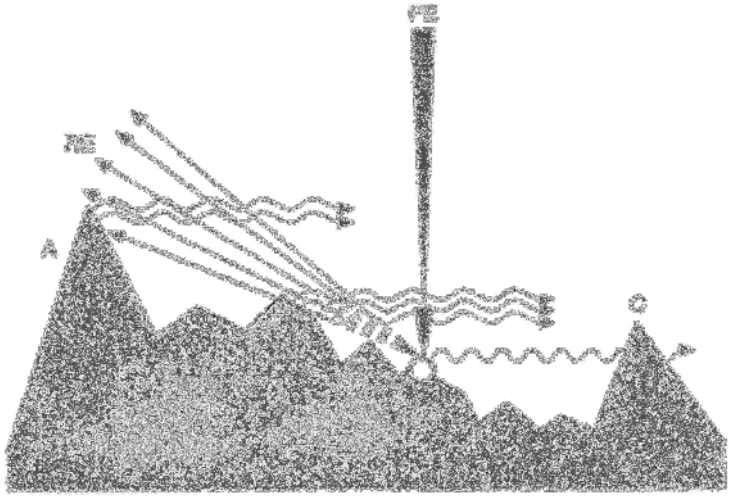

Figure 9.49 Effect of surface roughness on results from an X-ray point analysis.

The back-scattered electrons emerging from the particles to be analysed, P, cause characteristic X-rays to be formed from the protruding edges A and B. At the same time, similar X-rays emitted from the particles are largely absorbed before reaching the detector, by roughness peaks C. In consequence, little data are gathered as to the composition of particles P. Instead, signals relate to the composition of edges A and B.

The implication is that, when examining rough surfaces, neither the angle of tilt of the sample, nor angle of the X-ray detector to the plane of the sample surface are in any sense defined.

Surface topography apart, certain other factors need to be taken into account in that they can affect results of X-ray analysis [50, 52] and these are summarised below.

If, in determining the concentration c_x of an element x in a coating, one assumes a linear relationship between c_x and peak height, I_x, one can proceed as follows. The X-ray intensity of x in the layer is measured (I_x^{layer}). Then, under otherwise unchanged experimental conditions, a similar determination is carried out using a calibrated standard (I_x^{standard}). The value of c_x is then given by

$$c_x = \frac{I_x^{\text{Layer}}}{I_x^{\text{Standard}}} \tag{9.16}$$

However, the assumption of a linear relationship, noted above, may not hold. The cause lies in the so-called matrix effect, which can strongly affect an EDX result. Certain correction factors are then required to obtain valid results, and the most important of these are F_z–, F_A- and F_F– correction factors, briefly described below.

Atomic number correction factor F_Z: This relates to the number of X-ray quanta generated in the sample. It corrects for the fact that electrons undergoing back-scattering deeper down in the sample do not contribute to formation of X-ray quanta. It also takes into account the extent to which fast electrons are slowed by passage through

the material of the sample. These may not generate X-ray quanta in that much of their energy is lost as they transit the solid of the sample.

Absorption correction factor F_A: As X-ray quanta are formed at varying depths within the sample, more or less of their number will be lost as a result of being absorbed, and their having different path lengths through the solid, before reaching the detector. The extent of such losses are a function of the sample composition.

Fluorescence correction factor F_F: This factor notes that as X-rays are formed, on their way through and out of the sample, can generate further X-rays from other elements lower down in the atomic number series. The extent of such secondary X-ray formation depends on the energies of the primary X-ray emissions, but such secondary X-rays are formed within a larger sampling volume than those initially generated.

Taking these factors into account, for a quantitative determination of element X, c_x, we have:

$$c_x = (F_Z)_x \cdot (F_A)_x \cdot (F_F)_x \cdot \frac{I_x^{\text{layer}}}{I_x^{\text{Standard}}} \tag{9.17}$$

The so-called ZAF correction software, which incorporates the above corrections, allows good quantitative analysis data to be obtained.

The advantages of EDX analysis can be summarised as:

- simple and rapid analyses in point, line or areal form, for flat or curved surfaces, both smooth or rough
- simultaneous determination of all elements from sodium to uranium
- option of quantitative analyses on smooth and plane-polished surfaces
- detection limit at or below 0.1 wt%
- delicate samples not damaged thanks to low irradiation fluxes of order 0.5 nA.

As drawbacks, the following should be noted:

- analysis of lighter elements, notably carbon and oxygen, is not possible
- resolution of adjacent elements using low acceleration voltages can be difficult
- determining low concentrations of adjacent elements is difficult
- analysis of thin films complicated by excessive penetration of primary electrons
- analysis of very small inclusions, of approximately the size of the sampling volume (~1 μm) not always possible
- analysis may be complicated by appearance of extraneous peaks in the EDX spectrum, resulting from quantum loss in the detector (escape lines) or overlapping pulses (pile-up effect).

9.4.2 Wavelength Dispersive X-Ray Analysis (WDX)

WDX rests on a spectroscopic resolution of the characteristic X-rays emitted from the sample in terms of their wavelength and as such, resembles infrared or UV–visible spectroscopy. It uses a so-called analyser crystal, at the planes of which the X-rays are resolved according to their wavelength and then reflected

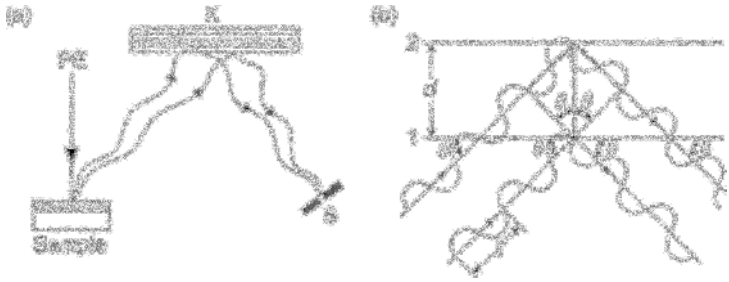

Figure 9.50 Wavelength-dispersive X-ray analysis: (a) schematic showing principle; (b) derivation of the Bragg equation (K is analyser crystal, S is detector slit).

(Fig. 9.50a). Using a detector, amplifier and on-line computer, qualitative or quantitative analyses are then possible.

The resulting coherent scattering of X-rays gives rise to interference bands, determined by the separation of the crystal planes in the analyser. This behaviour, which is expressed by Bragg's reflection equation, rests on the following assumption.

If two X-ray waves, of wavelength λ and exit angle θ, also known as the angle of reflection, fall onto the analyser crystal, whose planes are spaced distance d apart, they will then be reflected at the crystal plane at the same angle. However, the beam reflected from crystal plane 2 (Fig. 9.50b) has a longer path to travel than the beam reflected from plane 1. The difference in distance of travel (drawn as heavy line in Fig. 9.50b) equals $2d \sin\theta$. Only where this distance is equal to wavelength λ or exact multiples thereof, are the reflected beans amplified. This is mathematically expressed in the Bragg reflection equation:

$$n \cdot \lambda = 2 \cdot d \cdot \sin\theta \tag{9.18a}$$

where n can be 1, 2, 3 ... the first, second, third reflections, etc., that is the number of crystal planes at which the X-ray beams are reflected.

A drawback of this technique is the profusion of peaks or lines which are observed, and this arises from the fact that each reflected beam can be duplicated or triplicated, etc., according to the order of reflections involved (though their intensity diminishes at each further order). Equation (9.18a) formalises this.

A key criterion in choosing the analyzer crystal is its resolving power, defined mathematically as $d\theta/d\lambda$. Differentiating the Bragg equation, one obtains:

$$\frac{d\theta}{d\lambda} = \frac{n}{2 \cdot d} \cdot \frac{1}{\cos\theta} \tag{9.18b}$$

From which it is seen that the smaller the separation of the crystal planes in the analyzer, the greater its resolving power. Increasing the angle of reflection θ has the same effect. One therefore uses different analyser crystals with variously separated planes in order to be able to determine as many elements as possible. Table 9.6 presents a small selection of the many different analyser crystals available [56, 60].

Table 9.6 Selection of some of the most widely used X-ray analyser crystals.

Crystal	Lattice plane spacing (Å)	Wavelength range (Å)
LiF (lithium fluoride)	2.01	0.7–3.5
Quartz	4.23	1.5–7.0
EDDT (ethylenediamine-D-tartrate)	4.35	1.5–7.0
PET (pentaerythritol)	4.39	1.5–7.0
ADP (ammonium dihydrogen-phosphate)	5.30	2.0–9.0
KAP (Calcium-Phthalate)	13.30	5.0–25.0
Lead stearate	49.00	15.0–100.0

LiF is the most widely used crystal (reflection plane = (200)). In addition to its good reflectivity, it offers relatively good resolving power and is largely unaffected by temperature changes and irradiation. It can be used for detection of all elements from calcium to uranium. For analysis of the lighter elements (from Al to Cl), EDDT is used (Table 9.6) with reflection plane 020, or PET (reflection plane 002). Compared with EDDT, PET offers similar resolution but superior reflection, but is susceptible to temperature and radiation effects [60]. Salts of phthalic acid, especially calcium (KAP) are notable for their larger plane spacing and good reflectivity and are used in analysis of magnesium, sodium and fluorine.

To cover all elements from Z = 4 to Z = 92, the wavelength range 0.5–100 Å must be covered and this requires use of at least three different crystal analyzers, having different plane spacings. WDX instruments are thus equipped with turret-mounted analyzers, within an evacuable, thermostatted chamber, to avoid temperature-induced changes in plane spacing.

The longest wavelength capable of being reflected by the analyzer is theoretically $\lambda = 2d$, when $\theta = 90°$. In practice, however, instrumental limitations restrict this to $\lambda = 1.6d$. From the Bragg equation, however, it follows that, by rotating the analyzer crystal, resolution of an incident X-ray beam can be accomplished within the wavelength range $\lambda = 2d$. For instruments with flat and smooth analyzers, only a small portion of the reflected X-rays can be captured by the detector (Fig. 9.51a). To optimise focusing, completely or semi-automatic focusing is used, in which non-linear analyser crystals can be used. Thus, as shown in Fig. 9.51(b), a greater solid angle can be obtained [56–59].

In the optimum instrumental configuration, with automatic focusing and maximum reflectivity, the main components, namely sample, point X-ray source, non-linear analyzer and detector slit, all lie around the circumference of a circle, the so-called Rowland circle, of radius R (Fig. 9.51b). The radius of curvature of the analyser is $2R$ and in order to conform snugly to the Rowland circle, the crystal is ground to a concave form.

To record a WDX spectrum, the angle of reflection θ is continuously varied using a servo-motor, thus covering the desired wavelength range. Peak height is then recorded as a function of λ. While θ is varied, the other components remain in their constant positions on the Rowland circle. This ensure that the relationship between

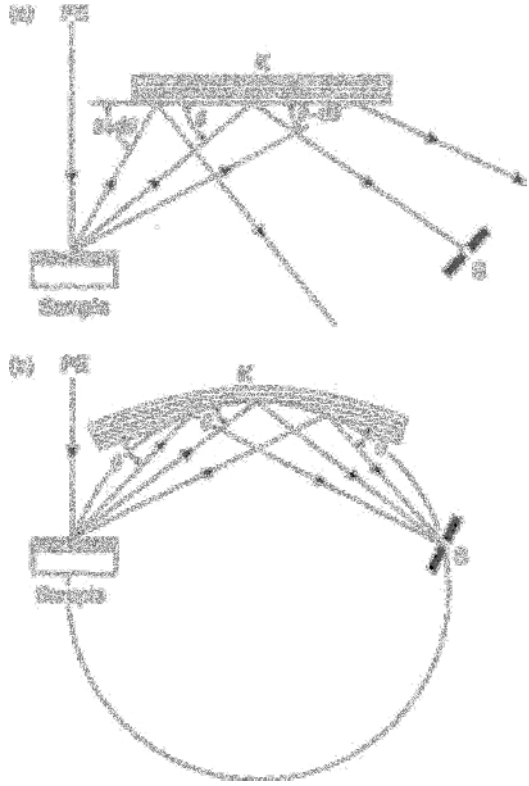

Figure 9.51 Wavelength dispersive X-ray spectrometer; (a) plane, smooth analyser crystal; (b) curved and concave-ground analyser crystal.

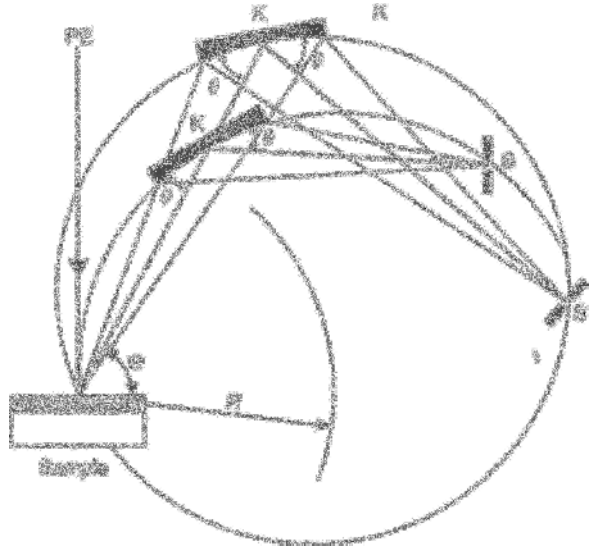

Figure 9.52 Linear WDX spectrometer with curved and concave-ground crystal analyser crystal and variable-radius Rowland circle [59].

Table 9.7 Quantitative determination of chemical composition of a Ni–P alloy deposit, obtained using WDX spectroscopy.

Ni	P	Cl	Si	S
87.6482	12.0858	0.0155	0.0170	0.0425
87.7610	12.0240	0.0052	0.0158	0.0025
87.7333	12.2272	0.0181	0.0063	0.0151
87.3573	12.4953	0.0181	0.0088	0.0176
87.3127	12.6112	0.0285	0.0284	0.0176
87.5564	12.3897	0.0000	0.0101	0.0250
87.5434	12.3885	0.0361	0.0094	0.0225
87.4427	12.5296	0.0129	0.0148	0.0000
87.5675	12.3906	0.0155	0.0114	0.0151
87.4243	12.4054	0.0000	0.0217	0.0151

Table 9.8 Comparison of EDX and WDX X-ray analysis techniques.

Comment	EDX	WDX
Spectral resolution	Low	High
Signal/noise ratio	Low	High
Count rate	High	Low
Sample exposure	Low	High
Sample surface	Can be rough	Plane-polished
Degree of freedom		
Spectrum recording	Simultaneous	Sequential
Analysis time	Short	Long
Data output	On-screen, x–y recorder	x–t recorder
Range of elements	$_9$F–$_{92}$–	$_4$Be–$_{92}$U
Solid angle of capture	Large	Small
Exit angle	Variable	Fixed
Quantitative analysis	In some cases	Yes

the detector slit and the analyser are unchanged as does that of the sample to the analyser.

The so-called linear spectrometer (Fig. 9.52), widely used, is based on a further development of the fully focusing spectrometer and allows the incidence angle θ to be held constant. This is achieved by altering the radius R of the Rowland circle, for each value of θ and thus λ.

WDX spectrometers are specially suitable for routine qualitative analysis of the chemical composition of coatings, though they are also used in R&D. They can be used equally well for reliable quantitative analysis, as shown in Table 9.7. This illustrates an analysis of a 30 μm thick nickel–phosphorus alloy deposit where P ~ 12%.

The comparisons set out in Table 9.8 offer an objective comparison of the strengths and weaknesses or energy-dispersive and wavelength-dispersive X-ray analysis techniques [52].

References

[1] Benninghoven, A., Neue Methoden zur Untersuchung von Festkörperoberflächen, *Phys. Blätter* 32 (1976) 298–308.

[2] Frommeyer, G. and Sölter, H.-J., Anwendung spektroskopischer Analysemethoden für Oberflächen- und Grenzschichtuntersuchungen. Teil 1 and 2, *Metalloberfläche* 33, 12 (1979) 546–550 and 34, 1 (1980) 19–23.

[3] Mathieu, H.J., Moderne Oberflächen-Analysenmethoden. Teil 1 and 2, *Oberfläche-Surface* 24, 2 (1983) 40–44 and 24, 3 (1983) 78–83.

[4] Hantsche, H., Grundlagen der Oberflächenanalysenverfahren AES/SAM, ESCA (XPS), SIMS und ISS im Vergleich zur Röntgenmikroanalyse und deren Anwendung in der Materialprüfung, *Microscopica Acta* 87, 2 (1983) 97–128.

[5] Bilger, G., Meßverfahren für die Oberflächenanalytik, *Oberfläche + JOT*, 8 (1989) 32–37.

[6] Braun, W. und Bradshaw, A.M., Methoden der Oberflächenanalytik, *Vakuum in der Praxis* 4 (1989) 291–300.

[7] Kanani, N., Oberflächenanalyse: technische Möglichkeiten, praktische Anwendungen im Berichtsband Vorbehandlung – Grundlage erfolgreicher Oberflächentechnik der DGO-Bezirksgruppe Berlin, Eugen G. Leuze Verlag, Saulgau/Württ., 1993.

[8] Hantsche, H., Abreviation for microscopical and analytical methods, *Microscopica Acta* 87 (1983) 3, 217–276.

[9] Smith, D., Analysis of surface composition with low-energy back-scattered ions, in: *Modern Methods of Surface Analysis*, P. Mark and J.D. Levine (Editors), North-Holland Publishing Company, Amsterdam, 1971.

[10] Armour, D.G., Ion scattering spectroscopy, in: *Methods of Surface Analysis – Techniques and Application*, J.M. Walls (Editor), Cambridge University Press, Cambridge, 1992.

[11] Buhl, R., Huber, W.K., und Löbach, E., Messung von Konzentrationsprofilen dünner Schichten mit der Sekundärionenmassenspektrometrie (SIMS), *Vakuum-Technik* 24 (1975) 7, 189–193.

[12] Benninghoven, A., Development in secondary ion mass spectroscopy and application to surface studies, *Surf. Sci.* 53 (1975) 596–625.

[13] Düsterhöft, H., Sekundärionen-Massenspektroskopie, in: *Handbuch Festkörperanalyse*, VEB Verlag, Berlin, 1979.

[14] Richter, C.-E., Sekundärionen-Massenspektrometrie und Ionenstrahl-Mikroanalyse, in: Ausgewählte Untersuchungsverfahren in der Metallkunde, VEB Verlag, Leipzig, 1982.

[15] Wall, J.M., Surface analytical techniques: their developing role in the characterisation of surfaces, thin films and surface coatings, *Trans. Inst. Metal Finish.* 62 (1985) 2, 163–168.

[16] Grasserbauer, M., Sekundär-Ionen-Massenspektrometrie (SIMS), in: *Angewandte Oberflächenanalyse*, Springer-Verlag, Berlin, 1986.

[17] Vickermann, J.C., Static secondary ion mass spectroscopy, in: *Methods of Surface Analysis – Techniques and Application*, J.M. Walls (Editor), Cambridge University Press, Cambridge, 1989.

[18] Sykes, D.E., Dynamic secondary ion mass spectroscopy, in: *Methods of Surface Analysis – Techniques and Application*, J.M. Walls (Editor), Cambridge University Press, Cambridge, 1989.

[19] Grasserbauer, M., Sekundärionen-Massenspektrometrie, *Chemie in unserer Zeit*, 28 (1994) 5, 222–232.

[20] Müller, K.-H., Oberflächenanalytische Verfahren zur Charakterisierung von Festkörperoberflächen und dünnen Schichten, *Nachr. Chem. Tech. Lab.* 37 (1989) 11, 3–11.

[21] Oechsner, H., Surface and depth profile analysis of insulator materials, in: *Oberflächentechnik SURTEC '89*, Hanser Verlag, München, 1989.

[22] Chang, C.C., Auger Electron Spectroscopy, *Surf. Sci.* 25 (1971) 53–79.

[23] Dini, J.W. and Musket, R.G., Application of Auger electron spectroscopy in electroplating, *Plating* 8 (1973) 811–814.

[24] Stupian, G., Auger electron spectrometry, in: *Systematic Materials Analysis*, Vol. I, J.H. Richardson and R.V. Peterson (Editors), Academic Press, New York, 1974.

[25] Rivière, C.J., Auger spectroscopy, in: *Modern Physical Techniques in Materials Technology*, T. Mulvey and R.K. Webster (Editors), Oxford University Press, Oxford, 1994.

[26] Hofmann, S., Oberflächen- und Tiefenanalyse mit der Auger-Elektronen-Spektroskopie (AES), *Mikrochim. Acta*, Suppl. 7 (1977) 109–128.

[27] Klau, M. and Oertel, G., Auger-Elektronenspektroskopie in: *Handbuch Festkörperanalyse*, VEB Verlag, Berlin, 1979.

[28] Klöber, J., Auger-Elektronenspektroskopie, in: *Ausgewählte Untersuchungsverfahren in der Metallkunde*, VEB Verlag, Leipzig, 1982.

[29] Seah, M.P., Auger electron spectroscopy, in: *Microscopic Methods in Metals* U. Gonser (Editor), Springer-Verlag, Berlin, 1986.

[30] Dudek, J., Auger Elektronen-Mikroanalyse, Grundlagen und Anwendungen, in: *Angewandte Oberflächenanalyse*, herausgegeben von M. Grasserbauer, H.J. Dudek und M.F. Ebel, Springer-Verlag, Berlin, 1985.

[31] Jitschin, W., Augerelektronen-Spektroskopie (AES), *Physik in unserer* Zeit, 20 (1989) 35–39.

[32] Bishop, H.E., Auger electron spectroscopy, in: *Methods of Surface Analysis – Techniques and Application*, J.M. Walls (Editor), Cambridge University Press, Cambridge, 1992.

[33] Shew, B.-Y. and Huang, J.-L., Quantitative AES investigation of magnetron sputtered Ti–Al–N film, *Surf. Coat. Technol.* 73 (1995) 66–72.

[34] Trautwein, A. and Keune, W., Photoelektronenspektroskopie: Prinzip und Anwendung in der Metallphysik, *Metall* 26 (1972) 5, 435–442.

[35] Holm, R., ESCA – eine neue Methode zur Bestimmung von Elementen und ihren Bindungszuständen in der Oberfläche von Festkörpern Teil 1 und 2, *G-I-T Fachzeitschrift* 16 (1972) 1, 12–19 und 112–116.

[36] Holm, R., Photo- und Augerelektronenspektroskopie (ESCA) und Sekundärionenmassenspektroskopie (SIMS), *Metalloberfläche* 27 (1973) 6, 199–207.

[37] Hagström, S., Photoelectron spectroscopy of surfaces, *Vakuum-Technik* 23 (1974) 2, 46–53.
[38] Proctor, W.G., X-ray photoelectron spectrometry (ESCA), in: *Systematic Materials Analysis*, Vol. II, J.H. Richardson and R.V. Peterson (Editors), Academic Press, New York, 1974.
[39] Berg, U., Photoelektronenspektroskopie, in: *Handbuch Festkörperanalyse*, VEB Verlag, Berlin, 1979.
[40] Werfel, F., Photoelektronen-Spektroskopie, in: *Ausgewählte Untersuchungsverfahren in der Metallkunde*, VEB Verlag, Leipzig, 1983.
[41] Ebel, M.F., Röntgen-Photoelektronen-Spektrometrie, in: *Angewandte Oberflächenanalyse*, herausgegeben von M. Grasserbauer, H.J. Dudek und M.F. Ebel, Springer-Verlag, Berlin, 1985.
[42] Wertheim, G.K., X-ray photoelectron spectroscopy, in: *Microscopic Methods in Metals*, U. Gonser (Editor), Springer-Verlag, Berlin, 1986.
[43] Christie, A.B., X-ray photoelectron spectroscopy, in: *Methods of Surface Analysis – Techniques and Application*, J.M. Walls (Editor), Cambridge University Press, Cambridge, 1992.
[44] Critchlow, G.W., Instrumental techniques for the surface analysis of materials, *Trans. IMF*, 74(3) (1997) 108–114.
[45] Madelung, O.W., *Oberflächenanalyse, Verfahren, Anwendung, Anbieteradressen*, VDI-Verlag GmbH, Düsseldorf, 1989.
[46] Bock, R., *Methoden zur Analytischen Chemie*, Bd. 1, Verlag Chemie GmbH, Weinheim, 1974.
[47] Engel–Klingele, Rasterelektronenmikroskopische Untersuchungen von Metallschäden, Gerling Institut für Schadenforschung und Schadenverhütung GmbH, Köln, 1974.
[48] Hantsche, H., Zur quantitativen Röntgenmikroanalyse: Die Ermittlung notwendiger geometrischer Daten für energiedispersive Systeme mit verschiebbarem Detektor, *Beitr. elektronenmikrokop. Direktabb. Oberfläche* 7 (1974) 531–625.
[49] Hantsche, H., Messung zur Abhängigkeit des Röntgensignals vom Kippwinkel der Probenoberfläche, *Beitr. elektronenmikrokop. Direktabb. Oberfläche* 10 (1977) 615–626.
[50] Schlüter, P., Mikroanalyse am Rasterelektronenmikroskop, *Sonderdruck aus LaborPraxis*, Heft 6 (1979).
[51] Hillmer, T., Praktische Erfahrungen bei der Werkstoffmikroanalyse mit dem Raster-Elektronenmikroskop, Teil 1 und 2, *Prak. Metallogr.* 16 (1979) 465–479 und 521–536.
[52] Hantsche, H., Energiedispersive Röntgenmikroanalyse – Anwendungsgebiete, Grenzen und Fehlermöglichkeiten, *GIT Fachzeitschrift für das Laboratorium* 25 (1981) 682–689.
[53] Statham, P.J., Prospects for improvement in EDX microanalysis, *J. Microanal.* 130, Pt 2 (1983) 165–176.
[54] Lewis, D.B., Scanning electron microscopy and X-ray microanalysis, *Inst. Metal Finish.* 70(40) (1992) 198–202.

[55] Bomback, J.L., Practical limitations of X-ray analysis in the scanning electron microscope, *73rd Annual Meeting ASTM*, Toronto/Canada, June 1970.

[56] Brown, L.C. and Thresh, H., Electron-probe microanalysis, in: *Tools and Techniques in Physical Metallurgy*, Vol. 2, F. Weinberg (Editor), Marcel Dekker, Inc., New York, 1970.

[57] Gullasch, J., Elektronenstrahlmikroanalyse, Physikalisch Grundlagen und Grenzen dieser Analysenmethode, *GIT Fachzeitschrift für das Laboratorium*, Heft 12 (1970) 1397–1403.

[58] Beier, W., Röder, A. and Brümmer, O., Elektronenstrahl-Mikroanalyse, in: *Handbuch Festkörperanalyse mit Elektronenstrahl, Ionen und Röntgenstrahlen*, Autorenkollektiv, VEB Deutscher Verlag für Grundstoffindustrie, Berlin, 1979.

[59] Hunger, H.-J., Elektronenstrahl-Mikroanalyse und Rasterelektronen-Mikroskopie, in: *Ausgewählte Untersuchungsverfahren in der Metallkunde*, Autorenkollektiv, VEB Deutscher Verlag für Grundstoffindustrie, Leipzig, 1983.

[60] Ritschel, B., Die wellenlängendispersive Röntgenfluoreszenzanalyse, *CLB Chemie für Labor und Betrieb*, Heft 1 und 2 (1985) 14–17 und 73–74.

This Page Intentionally Left Blank

Index

This Page Intentionally Left Blank